Jianqi Wu

Advanced Metric Wave Radar

國防工業出版社
National Defense Industry Press
Springer

Advanced Metric Wave Radar

Jianqi Wu

Advanced Metric Wave Radar

國防工業出版社
National Defense Industry Press

Springer

Jianqi Wu
China Electronics Technology Group
Corporation
Hefei, China

ISBN 978-981-10-7646-6 ISBN 978-981-10-7647-3 (eBook)
https://doi.org/10.1007/978-981-10-7647-3

Jointly published with National Defense Industry Press, Beijing
The print edition is not for sale in China Mainland. Customers from China Mainland please order the print book from: National Defense Industry Press.

Translation from the Chinese language edition: *Xian Jin Mi Bo Lei Da* by Jianqi Wu, © National Defense Industry Press 2015. All Rights Reserved.
© National Defense Industry Press, Beijing and Springer Nature Singapore Pte Ltd. 2020
This work is subject to copyright. All rights are reserved by the Publishers, whether the whole or part of the material is concerned, specifically the rights of translation, reprinting, reuse of illustrations, recitation, broadcasting, reproduction on microfilms or in any other physical way, and transmission or information storage and retrieval, electronic adaptation, computer software, or by similar or dissimilar methodology now known or hereafter developed.
The use of general descriptive names, registered names, trademarks, service marks, etc. in this publication does not imply, even in the absence of a specific statement, that such names are exempt from the relevant protective laws and regulations and therefore free for general use.
The publishers, the authors, and the editors are safe to assume that the advice and information in this book are believed to be true and accurate at the date of publication. Neither the publishers nor the authors or the editors give a warranty, express or implied, with respect to the material contained herein or for any errors or omissions that may have been made. The publishers remain neutral with regard to jurisdictional claims in published maps and institutional affiliations.

This Springer imprint is published by the registered company Springer Nature Singapore Pte Ltd.
The registered company address is: 152 Beach Road, #21-01/04 Gateway East, Singapore 189721, Singapore

Preface

It was metric wave radar that became my research topic when I started my work more than 20 years ago. The idea to write this book relates to the International Radar Conferences that I attended. The International Conferences on Radar were held in China, America, Britain, France, and Australia in turn. The 2013 International Conference on Radar was held in Adelaide, Australia. About 300 radar experts and scholars from more than 20 countries and regions attended this conference. In the a.m. of the opening ceremony day, I and Professor Griffiths, a famous British radar expert, were arranged to give plenary meeting reports. The title of my report was "Some Issues in the Development of Metric Surveillance Radar". In the report, I introduced my technological research efforts and some experimental results achieved in advanced metric wave radar. And, the communions were also conducted with the conference representatives. The report aroused strong responses. Australian Defense Magazine (ADM) issued a special report titled as "Radar smarts on show in Adelaide", with emphasis on what I reported. The 2014 International Conference on Radar was held in France, and the theme of conference was "Catch invisible". On invitation of the honorary president of this International Conference on Radar, Francois Le Chevalier, I gave a plenary report titled as "Research on Improvements of VHF-band Radar Performance". The report described metric wave radar how to overcome multipath effects and improve height finding performance in complex environment, as well as the novel methods to make metric wave radar have a certain target recognition capability under narrowband condition. My report also aroused great responses. During the conference, some famous radar experts, including the honorary president, Francois Le Chevalier, made deep discussions with me on some relevant problems about metric wave radar. They all showed great interests.

Attended the International Conference on Radar two times, I realized that the international radar community is interested in anti-stealth technologies, and the development and advancement of advanced metric wave radar. In future, this field will become one of the research hotspots of the international radar community. By looking up the sci-tech books at home and abroad, no book concerning this aspect

has been found. Therefore, an idea burgeoned in my mind to write a book about advanced metric wave radar for readers.

"Advanced metric wave radar", different from traditional metric wave radar, is a new type of metric wave radar, where the major problems of traditional metric wave radar have been solved by using the novel theory, idea of system design and by combining the applications of new methods, such as modern array signal processing, etc. In the past, metric wave radar was considered to be simple and backward because it not only failed to measure height owing to its poor measurement accuracy but also had large low-elevation blind zone and discontinuous coverage resulting from its beam cocking-up and beam splitting due to ground reflection. At one time, the radar experts widely considered that high frequency band radar would be the direction of radar development. Even more, the Western countries have gotten rid of the development of metric wave radar on one occasion. The need to counter stealth aircraft brings a new chance of developing metric wave radar. Metric wave radar has advantages in both countering stealth in frequency band and large power-aperture product at relatively low cost. With the superposition effect of the two factors, metric wave radar can achieve a gain of 40dB above in detecting stealth aircraft under the condition of equivalent cost in comparison with microwave frequency band radars, for example, S-band radar. If the main problems of metric wave radar mentioned above are overcome, metric wave radar can become the backbone anti-stealth equipment. That is to say, an economic and effective anti-stealth technological path can be found.

However, the problems of traditional metric wave radar lasted over a long period of time and the relative recognitions were also deepseated. Taking the height finding of metric wave radar as an example, the previous viewpoints of many experts were that metric wave radar could not realize accurate height finding due to its severe beam deformation resulting from ground reflections. And, the super-resolution techniques are not used successfully in radar for a long term because the radar community generally considers that the super-resolution algorithms require such a high signal-to-noise ratio that radar cannot meet the requirement. Also, the traditional thinking believes that metric wave radar certainly has poor low-elevation performance due to its beam cocking-up, so that it can be used only as middle and high-altitude detection radar. To solve the problems of metric wave radar, first, we should dare to break the bondage of traditional thinking and seek breakthrough by innovation. I started to bend myself to the research on metric wave radar anti-stealth technologies at the beginning of 1990s. On the basis of my investigations and experimental results, I have concluded that the most root cause resulting in the above problems of traditional metric wave radar is that the serious ground or water multipath interference existing in metric wave band cannot be well solved. During the research of more than 20 years, I and my team have gradually explored and formed our theory and method. I call them "Multiple phase centers" theory and "Multi-freedom terrain matching" theory. The former means that multiple sufficiently separated independent phase centers are used to complement and smooth multipath interference fringes, which supports and produces a multi-phase-center radar system. It is a new system, and I call it "Synthetic impulse

and aperture radar". For details, please read the monograph *Synthetic Impulse and Aperture Radar (SIAR)–A Novel Multi-Frequency MIMO Radar*, which has been written cooperatively by me and Professor Chen Baixiao. The latter means that the flexibility brought by multiple independent transmit/receive channels of array antenna, namely multi-freedom, is utilized to realize good terrain matching, which can improve the multipath interference fringes. Along this direction, we have explored the partitioned reshaping beam design methods to solve the problems about low-elevation blind zone and airspace coverage discontinuity. By keeping experiments and modifications, these methods can adapt well to various terrain environments so as to make metric wave radar glow with new vigorous vital force. The book summarizes our scientific research practices and gives emphasis to the novel methods and designs aiming at increasing the height finding accuracy and improving the coverage performance of metric wave radar. The experiment results are given.

To break the limit set by the narrow absolute bandwidth of metric wave radar and further bring the potential of metric wave radar into play, the book arranges a chapter to devote the narrowband target recognition methods suitable for metric wave radar, along with relevant experiment results. Aiming at the particular interference environment faced by metric wave radar, a special topic is established in this book to study the anti-interference methods for metric wave radar. The book gives a special discussion on the cooperative detection of metric wave radar network. Furthermore, the book also gives detailed descriptions of antenna mechanical structure design, antenna techniques, and transmit/receive techniques of metric wave radar. The theories, methods, and technologies introduced in this book are also applicable to UHF radar.

The author thanks Professor Chen Baixiao, Researcher Hu Kunjiao, Doctor Yang Xueya, Doctor Zhu Wei, Doctor Tian Xilan, Researcher Hu Yuankui, Researcher Sun Shaoguo, Researcher Wang Bing, Senior Engineer Wang Mei, Researcher Zhu Qingming, and Doctor Liu Guanghong for their help in writing this book. The author would also like to thank Academicians Wang Xiaomo and Lu Jun for their comments on the manuscript.

Hefei, China Jianqi Wu

A Brief Introduction to This Book

The advanced metric wave radar presented in this book is a novel metric wave radar, which is different from traditional metric wave radar. The advanced metric wave radar is based on active electronic scanning array (AESA) or digital array (DA) radar technology. With new theory, method, and system design idea, as well as modern array signal processing technique, the advanced metric wave radar can solve the major problems of traditional radar and achieve a leap in the performance of metric wave radar.

In this book, the author gives a systemic description of the advanced metric radar in combination with engineering practical application. A comprehensive introduction to the advanced metric wave radar techniques is also given from the theory and method to solve the major problems of metric wave radar to system design, antenna/feed, transmitting/receiving subsystem, and mechanical structure design. As the emphasis, the methods to solve large blind zone and discontinuity in detection coverage and the height finding method of metric wave radar are studied. Moreover, this book gives detailed accounts of how to use the super-resolution technique for solving the low-angle height finding problem in metric wave radar. In addition, as for the unique jamming environment faced by metric wave radar, the anti-jamming method is introduced. In order to cope with the limitation of narrow absolute bandwidth in metric wave radar and further exploit the potential of metric wave radar, a special introduction to narrowband target recognition method is given. About the metric wave radar netting, the cooperative detection is covered in this book. Finally, the main experimental results are shown. The theories, methods, and technologies researched in this book are also applicable to UHF radar.

This book is intended for the professional engineers as well as the graduate students who engage in radar system engineering, electronic engineering, and signal processing.

Contents

1 Introduction 1
1.1 Anti-stealth and Metric Wave Radar 1
1.2 The Major Problems in Metric Wave Radar 3
1.3 The Development of Metric Wave Radar in China 4
1.4 Development of Direction of Metric Wave Radar and Theory and Method of Advanced Metric Wave Radar 7
Bibliography 9

2 Target Characteristics in Metric Wave Band 11
2.1 Overview of Stealth Technologies 11
2.2 Counter-Stealth Mechanism at Metric Wave Band 14
2.3 Electromagnetic Computation and Analysis of Stealth Aircraft RCS 16
2.3.1 Electromagnetic Computation Methods 16
2.3.2 Electromagnetic Computation Results 19
Bibliography 24

3 System Design of Advanced Metric Wave Radar 27
3.1 Technology Scheme of Advanced Metric Wave Radar 27
3.1.1 Multipath Effect in Metric Wave Band 27
3.1.2 General Consideration for Radar Technology Scheme 29
3.1.3 Principle of Metric Wave Digital Array Radar 30
3.1.4 Features of Metric Wave Digital Array Radar System 30
3.2 Polarization Selection 32
3.2.1 Impacts of Different Polarizations on Metric Wave Radar Performance 32
3.2.2 Principles of Metric Wave Radar Polarizations Selection 34

3.3 Frequency Selection . . . 35
3.3.1 Frequency Regulations of Radio Committee . . . 35
3.3.2 Avoiding Television, FM Broadcasting and Radio Paging Frequencies . . . 35
3.3.3 Comprehensive Discussion on Radar Performance . . . 39
3.4 Technical Approaches Analysis of Metric Wave Radar Height Finding . . . 40
3.4.1 Common Height Finding Methods . . . 40
3.4.2 Superresolution Angle Measurement Methods . . . 42
3.5 Optimal Design of Airspace Coverage . . . 44
3.5.1 Design of Independent Beam . . . 44
3.5.2 Design of Improved Volume Coverage Diversity . . . 47
3.5.3 Optimal Design of Pulse Energy . . . 47
3.6 Design of Work Modes . . . 48
3.6.1 Design of Common Work Mode . . . 48
3.6.2 Design of Special Work Mode . . . 50
Bibliography . . . 51

4 Height Finding Technique of Metric Wave Radar . . . 53
4.1 Introduction . . . 53
4.2 Height Finding Model of Metric Wave Radar . . . 54
4.2.1 Typical Multipath Signal Model . . . 55
4.2.2 Multipath Signal Model Taking into Account Earth Curvature . . . 57
4.2.3 Reflection Coefficients . . . 60
4.2.4 Effective Reflection Area . . . 61
4.3 Lobe Split Method . . . 66
4.4 Array Super-Resolution Algorithms . . . 70
4.4.1 Spatial Smoothing MUSIC . . . 71
4.4.2 Maximum Likelihood Algorithm . . . 75
4.4.3 RELAX Algorithm . . . 81
4.4.4 Sparse Solution Method . . . 83
4.5 Terrain Matching MUSIC/ML Algorithm . . . 86
4.6 Multipath Distributed Source Model Height-Finding Method . . . 89
4.6.1 Distributed Source Model . . . 89
4.6.2 Multi-dimensional Alternate Projection ML . . . 92
4.7 Height-Finding Based on Self-Adaptive Beam Forming . . . 93
4.8 Conclusion . . . 95
Bibliography . . . 96

5 Metricwave Radar Anti-jamming Technology . . . 101
5.1 Particularity of Metricwave Radar Anti-jamming . . . 101
5.1.1 Electromagnetic Environment of Metricwave Band . . . 101

5.2 Advanced Metricwave Radar Anti-jamming Technology 104
5.2.1 Airspace Domain Anti-jamming Technology 104
5.2.2 Waveform Domain (Time, Frequency and Intra-pulse) Anti-jamming Technology 112
5.2.3 Anti-jamming Technology in Energy Field 115
5.2.4 Anti-jamming Technology in Processing Domain 117
Bibliography 128

6 Metric Wave Antenna Techniques 131
6.1 Antenna Scheme 131
6.2 Main Parameters of the Antenna 132
6.2.1 Beamwidth 132
6.2.2 Sidelobe Level 133
6.2.3 Gain 133
6.2.4 Others 135
6.3 Array Analysis and Design 136
6.3.1 Array Arrangement Mode 136
6.3.2 Grid Form and Array Element Spacing 142
6.3.3 Common Aperture Distribution 147
6.3.4 Intelligent Algorithms for Pattern Synthesis 152
6.3.5 Mutual Coupling 155
6.4 Antenna Array Element 157
6.4.1 Symmetrical Dipole 158
6.4.2 Folded Dipole 161
6.4.3 Directional Antenna 163
6.4.4 Log Periodic Antenna 168
6.4.5 Tapered Slot Antenna 170
6.4.6 Lon Slot Array Antenna 175
6.5 Antenna Tolerance 176
6.6 Impact of Metric Wave Multipath Effect 179
6.7 Antenna Monitoring and Calibration Techniques 185
Bibliography 189

7 Metric Wave Transmit and Receive Techniques 191
7.1 Overview 191
7.2 Composition and Realization of Transmit/Receive System 192
7.2.1 Composition of Transmit/Receive System 192
7.2.2 Realization of Transmit/Receive System 195
7.3 RF Digitalized Transmitter Technique 196
7.3.1 Requirements of Digital Array Radar on Transmitter 196
7.3.2 Realization of RF Digitalized Transmitter 199

7.4 RF Digitalized Receive Technique . . . 209
7.4.1 Features and Composition of Advanced Metric Wave Radar Receiver . . . 209
7.4.2 Receiver Noise . . . 213
7.4.3 Dynamic Range of Receiver . . . 222
7.4.4 Realization of Multi-Channel RF Digitalized Receiver . . . 225
7.4.5 Optical Transmission and Synchronization of Data . . . 230
7.5 Electromagnetic Compatibility Design . . . 238
7.6 Super-Low Phase Noise Frequency Source Technique . . . 248
7.6.1 Analysis on the Effect of Frequency Source Phase Noise on Radar System . . . 248
7.6.2 Realization of Frequency Source . . . 250
7.6.3 Techniques for Distributed Frequency Sources . . . 252
Bibliography . . . 252

8 Target Classification and Identification Techniques for Advanced Metric Wave Radar . . . 255
8.1 Overview . . . 255
8.1.1 Status of Radar Target Classification and Identification . . . 255
8.1.2 Target Classification and Identification Process in Metric Wave Radar . . . 258
8.2 Feature Extractions . . . 259
8.2.1 Basic Motion Features . . . 259
8.2.2 Resonant Frequency Features . . . 261
8.2.3 Micro-Doppler Modulation Feature . . . 264
8.2.4 Polarization Features . . . 271
8.3 Target Classification and Identification . . . 274
8.3.1 Decision Synthesis . . . 275
8.3.2 Data Analysis . . . 277
8.4 Classification and Identification Database . . . 288
8.4.1 Construction Approach . . . 288
8.4.2 Content and Storage Rule . . . 290
8.4.3 Realization Measures . . . 291
Bibliography . . . 293

9 Cooperative Detection Metric Wave Radar Techniques . . . 295
9.1 Overview . . . 295
9.2 Development Trend of Cooperative Detection Technique . . . 297
9.2.1 CEC System Technique . . . 297
9.2.2 MIMO Radar Techniques . . . 298
9.2.3 Distributed Array Coherent-Synthesis Radar Technique . . . 300

9.3 Typical Operation Modes . . . 301
9.3.1 Self-transmitting/Self-receiving Mode . . . 302
9.3.2 MIMO Mode . . . 305
9.3.3 Transmitting/Receiving Full-Coherence Mode . . . 306
Bibliography . . . 309

10 Structural Design of Large Metric Wave Radar . . . 311
10.1 Introduction . . . 311
10.2 Overall Design of Metric Wave Radar . . . 312
10.2.1 Outline of Overall Design . . . 312
10.2.2 Overall Layout Design . . . 313
10.2.3 Radar Erection and Assembly . . . 314
10.2.4 Transportation and Packing Design . . . 315
10.3 Key Technologies in Structural Design of Metric Wave Radar . . . 316
10.3.1 Antenna Framework Configuration Design Technologies . . . 316
10.3.2 Wind-Resistant Safety Design Technology . . . 331
10.3.3 Automatic Erection Design Technology for Metric Wave Radar . . . 340
10.3.4 Cooling Design Technology . . . 352
Bibliography . . . 357

11 System Tests and Demonstrations . . . 361
11.1 Introduction . . . 361
11.2 Test and Demonstration of Transmitting/Receiving Calibration . . . 361
11.2.1 Interior Field Calibration of the Transmitting Channel . . . 361
11.2.2 Interior Field Calibration of the Receiving Channel . . . 362
11.3 Antenna Test and Demonstration . . . 362
11.3.1 Antenna Outfield Calibration Test and Demonstration . . . 362
11.3.2 Low Sidelobe Antenna Outfield Test . . . 364
11.3.3 Test of the Sidelobe Cancellation Performance . . . 369
11.4 Test and Demonstration of Metric Wave Radar Airspace Coverage . . . 371
11.4.1 Test Method . . . 371
11.4.2 Performance Evaluation Based on Tested Data . . . 373
11.4.3 An Example of Performance Evaluation . . . 375
11.5 Height-Finding Tests and Demonstrations in Different Terrain Environments . . . 376
11.5.1 Test Method . . . 376
11.5.2 Performance Evaluation Based on Test Data . . . 377
Bibliography . . . 384

Chapter 1
Introduction



1.1 Anti-stealth and Metric Wave Radar

The first radar system was born in World War II, which was invented and used by the British. The radar system changed British-German air warfare situation and had a major influence on the outcome of the warfare between England and Germany. From then the development of radar has progressed from lower frequency range to higher frequency range because the higher the radar frequency is, the easier the measurement precision of radar can be achieved. In the past, it was widely believed that the high frequency radar is an inevitable trend of radar development. For a long time, the metric wave radar has been even abandoned by the western radar community.

The stealth targets put forward a severe challenge to the development of radar technology. On December 19, 1989, the F-117A Stealth Fighter was first used in combat during operation JUST CAUSE in Panama. F-117A was again called into action during Operation DESERT SHIELD STORM in 1990–91. The combination of stealth aircraft with precision attack set the tone for the modern air force. Since the fifth-generation fighters such as F22, F35 entered service in batches as well as the rise of stealth bombers and stealth unmanned aerial vehicle (UAV), the capability of traditional radar network was near to be reset. Compared with the fourth-generation fighter, the Radar Cross Section (RCS) of the fifth-generation fighter has decreased about by 2–3 orders of magnitude in microwave band. According to the radar equation:

$$R_{max}^4 = P_{av} A_e \sigma E_i(n) F^4 t_s / (4\pi k T_0 F_n (S/N)_1 L_s \Omega) \tag{1.1}$$

where σ is the Radar Cross Secton (RCS), when σ has decreased by 2–3 orders of magnitude, the power-aperture product of radar P should increase correspondingly by 2–3 orders of magnitude for the same distance if the operating frequency and other conditions remain unchanged. How much will the cost of the radar increase accordingly? For convenience and intuition, we assume that the radar antenna is a planar array with the rectangular aperture, and the receiving array shares the same aperture

© National Defense Industry Press, Beijing and Springer Nature Singapore Pte Ltd. 2020

J. Wu, *Advanced Metric Wave Radar*, https://doi.org/10.1007/978-981-10-7647-3_1

and the same element number with the transmitting array. In order to increase the power-aperture product 200 times, the element number of the radar must be increased 14 times. Considering the proportion between the element number and the whole system cost, it can be concluded that the whole system cost of radar will increase about one order of magnitude. In the operation cost, only the power consumption will also increase one order of magnitude. If the anti-stealth performance is achieved completely by increasing the power-aperture product, it's a huge financial burden for updating and operating the whole radar network.

It's the most direct and efficient measure to detect the stealth aircraft by low-frequency radars with their metric and even longer wavelengths because the Rayleigh scattering or the resonance scattering of electromagnetic waves are not sensitive to the aircraft configuration, and the absorbing properties of the radar absorbing coating are limited by the relationship between thickness and wavelength. After a lot of calculation, simulation and test analysis, it's generally acknowledged that the radar cross section (RCS) of a stealth aircraft on metric wave frequency bands is about 2–3 orders of magnitude greater than on microwave frequency bands. It's called the anti-stealth frequency advantage of metric wave radar. In addition, compared to the microwave radar, the metric wave radar also has a most significant advantage in the power-aperture product. To illustrate this point, let's make a comparison. By assuming their costs are equal, we can compare a metric wave radar at 300 MHz with a S-band microwave radar at 3000 MHz so as to see how different their power-aperture product is? For simplicity, we assume that they are the active phased array radars with the planar rectangular aperture antenna, where the number of radar elements (channels) determines the complexity of radar and also the cost of radar. For larger phased array radar, the cost of the active array and the processing equipments such as the A/D converter, data transmission and data processing equipments contribute to more than 80% of the total cost of the radar. Calculated by 80%, we can draw a conclusion that the antenna area of the metric wave radar is 80 times the size of the microwave radar antenna at the same cost. The next thing to consider is the effective radiated power. Statistically, the cost of unit radiant power for the final stage power transistor at metric wave band is about a quarter compared to S-band power transistor, and the cost of unit radiant power for whole transmit channels is no more than one-third compared to S-band power transistor. This means that the power-aperture of metric wave radar is 240 times larger than the S-band microwave radar at the same cost, up to 2 orders of magnitude. For the stealth aircraft, the overall advantages of the frequency and the power-aperture product together can be achieved above 4 orders of magnitude. The metric wave radar can counteract the effects of the reduced warming time caused by the supersonic cruise stealth aircraft since it can not only counteract the effects of the reduced RCS of stealth aircraft but also double nearly the radar detection range.

Besides, the metric wave radar may also offer many advantages, such as no clutter interference from cloud and rain, weaker clutter interference from ground and sea relative to the microwave radar, lower Doppler ambiguity and effective anti-ARM ability.

1.2 The Major Problems in Metric Wave Radar

Then, can we solve the anti-stealth problem by just using metric wave radar to replace microwave radar? This is not so simple. The traditional metric wave radar has the serious problems such as inaccurate height finding, discontinuous coverage, large low-angle blind zone, and poor site adaptability. This is why the West has abandoned the development of metric wave radar for a long time. If these problems cannot be solved, the metric wave radar acts as only a complementary instrument rather than backbone equipment. Conversely, all of these problems can be solved so as to achieve high measurement accuracy, good terrain environment adaptability, nice low-altitude coverage performance, and etc., then the metric wave radar can be used as the backbone radar in air defense network and take on the anti-stealth responsibility.

What is the ultimate cause of these problems that make metric wave radar different from microwave radar? At microwave frequency band, the roughness of the earth surface causes strong diffuse reflection and the surface vegetation has high absorptivity, so that the reflection coefficient is small. Additionally, the microwave antenna has narrow beam, which makes it possible to use the direction selectivity of the antenna for further suppressing multipath signal, thus the multipath effect is not very severe in many conditions. However, at metric wave frequency band, there is a very great earth surface reflection coefficient, which even approaches to 1. The multipath component and the direct arrival component are comparable. The metric wave antenna has wide beam at elevation, which makes it impossible to use the direction selectivity of the antenna for rejecting multipath signal. Therefore, the multipath effect is very serious in various terrain conditions. There exists strong coherence between multipath signal and direct arrival signal, and the coherently-superposed interferences at some angles may enlarge the detection range significantly. At the same time, the destructive interferences at other angles may greatly shorten the detection range, resulting in discontinuous airspace coverage. Moreover, the destructive interference makes the low-elevation coverage performance more worse. Multipath interference destructs the lobe configuration of antenna, which makes the conventional amplitude-comparison/phase-comparison methods inoperative, so it is unable to do the measurement of target height.

Furthermore, numerous civil and commercial services have crowded in metric wave frequency band and its neighboring frequency bands, such as television, FM broadcasting, and etc. The external noise level entering into radar via its antenna is higher than that in microwave frequency band. The frequency spectrum width of radar is narrow in general, its target discrimination and recognition capabilities are poor. Also, wide antenna beamwidth brings difficulty in realizing low sidelobe and results in weak anti-interference capability.

1.3 The Development of Metric Wave Radar in China

Since 1930s, the development of metric wave radar has experienced a palingenesis, from naissance to early flourishing, gradual decline, and then growing up once again. As described above, metric wave radar has a number of unique merits. In history, metric wave radar was attached importance and found wide applications like microwave radar. However, because of its so many demerits, it was thought as a type of radar with poor performance, namely, it was used only for surveillance rather than guidance, which has limited the development of metric wave radar. For many years, the United States as well as many NATO countries have already eliminated metric wave radar, except that Russia and some of the former Warsaw Pact countries still use many metric wave radars in their early warning systems.

From 1950s to 1960s, the former Soviet Union developed and deployed a great number of metric wave radars. But in 1970s and 1980s, most of these radars were replaced by S-band radars with higher accuracy and performance. Many old metric wave radars were sold or presented to the countries of the Third World. At the end of 20th century, Kosovo War broke out. F-117A stealth aircraft was shooted down by SAM missile. It was believed that P18 metric wave radar (Fig. 1.1) played a key role in finding and tracking target. After this, the business that solid-state technology and digital processing technique were used to modify metric wave radar proliferated in Russia. In recent years, metric wave radar was focused and developed again, which is considered as an important technical reversion.

In the family of metric wave radars, the most of them are two-dimensional radars and mechanical scanning radars. No report is seen so far about the Western countries developing and deploying metric wave three-dimensional radar. The most famous



Fig. 1.1 P18 metric wave radar

metric wave radar in Russia is "Nebo" UE (Fig. 1.2). It includes a horizontal antenna and a height finding antenna. The horizontal antenna is responsible for searching and finding target as well as measuring the azimuth and range of target, whereas the height finding antenna is used to measure the height. The radar uses two fan beams rather than pencil beam to realize three dimensional measurements, so that, in strict meaning, it is not a real modern three-dimensional (3D) radar. The radar still has the defects of traditional metric wave radar.

The follow-up metric wave 3D radars of "Nebo" family mainly include "Nebo" SVU, "Nebo" M RLM-ME, and "Nebo" UME. All of these radars adopt active phased arrays. According to the report by Russian media in October, 2013, Nizhniy Novgorod Research Institute of Radio Engineering (NNIIRT) has developed a new dual-band 3D early warning radar, named as "Nebo" UME (Fig. 1.3). It uses metric wave band to measure range and L-band to measure height. Thus, it can be inferred that, in Russia, although the new metric wave 3D radar adopts active phased array, the issues in metric wave band are not well solved, still needing other assistant height finding measures.

Influenced by the former Soviet Union, a number of metric wave radars have been held for a long time in China, including shipboard and ground-based radars.

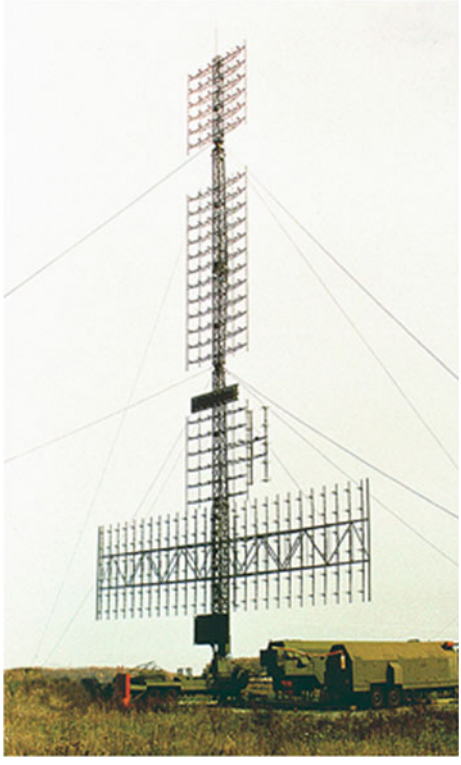


Fig. 1.2 "Nebo" UE



Fig. 1.3 "Nebo" UME

After 1990s, some backbone ones among these radars have been updated by use of full solid-state, digital signal processing, and computer techniques. But there are all two-dimensional (2D) radars, as shown in Fig. 1.4. Entering into the 21st century, China has set up projects to develop modern metric wave 3D radars. These radars were deployed from 2010. At the same time, JY-27A metric wave 3D radar for export was developed and produced, as shown in Fig. 1.5.



Fig. 1.4 Chinese 107D metric wave radar



Fig. 1.5 Chinese JY-27A metric wave 3D radar for export

1.4 Development of Direction of Metric Wave Radar and Theory and Method of Advanced Metric Wave Radar

Metric wave possesses a unique advantage in countering stealth but the traditional metric wave radar also has obvious disadvantages. Can we find out effective technical approaches that not only bring into play the advantages of metric wave radar but also solve the major problems of the traditional radar so as to make metric wave radar glow with vital force and play the main role in modern air defense and surveillance system again? If we can, metric wave radar will have not only excellent performance but also low purchase cost and operational cost, which will realize an economic and effective anti-stealth approach. This is a huge attraction, drawing the development of metric wave radar.

Nevertheless, the problems of traditional metric wave radar lasted over a long time, and the relative recognitions were also deepseated. For example, the previous viewpoints of many experts for the height finding of metric wave radar, were that metric wave radar could not realize accurate height finding due to its severe beam deformation resulting from ground reflections. And, the super resolution technique has not been used successfully in radar for a long term, because the radar community generally considered that the super resolution algorithms require such a high signal-to-noise-ratio that radar cannot meet the requirement. Also, the traditional thinking believed that metric wave radar certainly has poor low-elevation performance due to its lobe cocking-up, so that it can be used only as middle and high-altitude detection radar. To solve the problems of metric wave radar, firstly we should dare to break the bondage of traditional thinking, and seek breakthrough by innovation. The theory and method of advanced metric wave radar emerge as the times require.

Now that the ultimate cause resulting in the problems of metric wave radar is multipath interference, then the direction of solving the problems is how to eliminate the

influences due to multipath interference. Being a single-phase center system, the old metric wave radar had fixed and baneful multipath interference fringe. If metric wave radar can operate in multiple phase centers and has an enough separation between the phase centers, multiple sets of different interference fringes can be formed. They are complementary and produce smoothing effect. If the number of phase centers is sufficient, there is a trend to free-space detection coverage performance. We call it "multiple phase centers" theory and method. The metric wave radar, developed according to this theory and method, is suitable for stationary rather than mobile operation because of its many large and independent antennas.

To solve the mobile operation problem, being established in single phase center, the utilization of the flexibility brought from multiple independent transmit/receive channels of array antenna (called freedom in array signal theory) makes antenna performance match with efficiently practical terrain so as to change the baneful multipath interference fringes. In this book, it is known as "multiple-freedom terrain matching" theory. Based on this theory, we have explored "partitioning beam shape keeping" and "terrain matching super resolution height finding" methods for solving the three problems of metric wave radar: large low-elevation blind zone, discontinuous detection coverage, and poor height finding accuracy.

Other than the above problems, the anti-interference of metric wave radar is also an important issue. The anti-interference of metric wave radar itself has particularities: congested frequency band, severe electromagnetic environment interference and strong sky noise interference at low frequency band. In receive chain, the hybrid design of multiple measures, such as preselection filtering, anti-aliasing narrowband filter bank, and high-performance digital filtering, can effectively suppress the electromagnetic environment interference. When the operating frequency is below 100 MHz, there is a great influence of sky noise, mainly composed of galaxy noise and sun noise, which has obvious directivity and can be rejected by use of spatial filtering method. As far as countering enemy jamming is concerned, the comprehensive countermeasures involving low intercept probability, spatial filtering, and jamming elimination can be taken. Low sidelobe beam agile scanning, protecting pulse, low pulse power waveform, and etc., are the efficient means to counter intercept. Large dynamic range and multi-freedom adaptive sidelobe cancellation can be counter strong noise jamming. Pulse jamming can be suppressed by sidelobe blanking, jamming recognition and elimination. For further removal of jamming, the methods, such as multi-frame data correlation, multi-parameter (velocity, position, and etc.) correlation filtering, can also be used.

There is another important issue, that is target recognition. In metric wave band, absolute majority of wideband recognition methods cannot be used due to narrow absolute bandwidth, so that metric wave radar mainly adopts narrow band recognition methods. Making use of target motion characteristics and such characteristic quantities as waveform modulation, resonance, polarization, and so on, there are many methods suitable for target classification and recognition. The experiments show that very high recognition probability can be achieved.

The advanced metric wave radar introduced in this book is based on active electronic scanning array (AESA) or digital array (DA) radar technology. Using novel

theory and system design idea, and combining with modern array signal processing technique, the main problems of traditional metric wave radar can be overcome, resulting in new efficient metric wave radar.

Bibliography

1. Randy L. Haupt, Yahya Rahmat-Samii. Antenna array Developments: A Perspective on the Past, Present and Future[J]. IEEE Antennas and Propagation Magazine, 2015, 57(1):86–96.
2. Carlo Kopp. Russian VHF Counter Stealth Radars Proliferate[J]. Defense Today, 2008:32–36.
3. Balajti I, Kende Gy, Sinner Ed. Increased Importance of VHF Radars in Ground-Based Air Defense[J]. IEEE Aerospace and Electronic Systems Magazine, 2012, 27(1):4–18.
4. Cherneyak V S, Immoreev I Ya, Vovshin B M. Radar in the Soviet Union and Russia: A Brief Historical Outline[J]. IEEE Aerospace and Electronic Systems Magazine, 2003, 18(12):8–12.
5. Barton David K. Recent developments in Russian Radar Systems[C]// Proceedings of the 1995 IEEE International Radar Conference, 1995:340–346.
6. Zachepitsky A. VHF (Metric Band) Radars from Nizhny Novgorod Research Radiotechnical Institute[J]. IEEE Aerospace and Electronic Systems Magazine, 2000, 15(6):9–14.
7. Carlo Kopp. Advances in Russian and Chinese Active Electronically Steered Arrays (AESAs)[C]// IEEE 2013 International Symposium on Phased Array systems & Technology, 2013:29–42.
8. Skolnik M. Radar Handbook[M]. Third Edition, 2008.
9. Skolnik M. Introduction to Radar Systems[M]. Third Edition, 2001.
10. Chen Baixiao, Wu Jianqi. Synthetic Impulse and Aperture Radar (SIAR): A Novel Multi-Frequency MIMO Radar[M]. Singapore: John Wiley & Sons Singapore Pte Ltd, 2014.
11. Wu Jianqi, Xu Jin. Some Issues in the Development of Metric Surveillance Radar[C]// 2013 International Conference on Radar, Adelaide, SA: IEEE, 2013:6–10.
12. Wu Jianqi. Anti-Stealth and Development of Advanced Metric-Wave Radar[J]. Radar Science and Technology, 2015, 13(1):1–4.
13. Wu Jianqi, Yang Xueya. Novel Height Finding Technique Based on Spatial Filtering in Meter-wave Radar[J]. Modern Radar, 2015, 37(3):1–4.

Chapter 2
Target Characteristics in Metric Wave Band



2.1 Overview of Stealth Technologies

Since engaging in its first actual battle, the stealth aircraft has appeared for 25 years. During this period, the U.S. armed force put its stealth aircraft into the several local wars launched by America and excellent operational efficiency was achieved. The most famous stealth fighters are F-117A, F-22, and F-35. Among them, the F-22 and F-35 have not only stealth performance, but also supersonic cruise, super-maneuver, and beyond-light-of-sight (BLOS) attack capabilities. In addition, the U.S. also possesses B2 stealth strategic bomber and many types of stealth UAV. Russia, China, and India develop their stealth aircraft one after the other. And many countries have developed and equipped various stealth UAVs. The age of stealth aircraft is coming.

The essential idea of stealth is to reduce the detectable signal features of air flight objects so as to shorten the detection range of the enemy sensor. The signal features of the most significance are radar cross section (RCS), RF radiation signal feature, and infrared signal feature. Radar and passive radiation location system can penetrate cloud and rain, but the infrared signal disables. So that these signal features are commonly considered to be more important than thermal feature.

In order to achieve full "stealth" effect, combined technologies should be adopted. Low interception probability technology can be used to decrease the active radiation from airborne radar and data link. By using of very wideband frequency hopping, noise-like modulation, and time or pattern pseudo-random sweeping, the low interception probability technology makes the detection of its radar and data link/network radiations become very difficult. Modern AESA (active electronically scanned array) radars have the capability of hopping over kMHz or greater bandwidth and use spread spectrum modulated pulse train. They are almost invisible for the radar warning system that uses crystal video frequency receiving technique.

As for stealth technology, how to decrease the radar signal features of aircraft and missile is a greater challenge. The most outstanding is that the enemy radar can operate across multiple frequency bands, wavelength going from about ten meters till to one centimeter or less. This becomes a very great difficulty for the two main

© National Defense Industry Press, Beijing and Springer Nature Singapore Pte Ltd. 2020

J. Wu, *Advanced Metric Wave Radar*, https://doi.org/10.1007/978-981-10-7647-3_2

technologies to produce stealth capability, that is, the shape design technology and the wave absorbing material technology.

(1) Shape stealth

Under the condition of satisfying the aerodynamic requirement of aircraft, the shape stealth means that the energy reflected from target to radar is minimized by designing or selecting target's surface shape, profile, and edge. The main forms of radar stealth shape design used currently are:

(1) Airframe-wing, airframe-cockpit fusion and integration.
(2) Skin edges and blocks are required to be parallel in space so as to make the energy reflected from aircraft be centralized at only several directions and very weak at other directions, resulting in very narrow three-lobe reflection pattern or four-lobe reflection pattern.
(3) Wing and airframe are fully fused into an integrated flying wing.
(4) Angular cone-shaped aircraft nose, polyhedron airflame, and low winglet only produce weak radar echoes with instantaneous flicker.
(5) Canted twin-vertical tail, V-shape tail or no tail.
(6) Stealth antenna radome, planar phased array antenna.
(7) Flush-mounted conformal phased array antenna.
(8) Retractable radio communication and navigation antennas.
(9) Removing all external stores and their pylons, for example, external weapons, pods, and auxiliary fuel tanks.
(10) Engines are mounted in semi-buried or full in-airframe and in-wing mounting modes.
(11) Adopt conformal inlet, sawtooth lip, adding inlet screen grid or metal net mash.
(12) Adopt S-shaped inlet and shelter inlet and exhaust nozzle by use of airframe or empennage.

Shape stealth is the major measures for reducing RCS. However, it will sacrifice the weapon loading capability and even decrease the aircraft maneuverability and agility.

It can be seen through the electromagnetic simulation and time-frequency characteristic analysis of RCS of F-22 aircraft at different frequency bands and angles that large RCS values present in the relatively fixed angle ranges near 40°, 90°, 140°, and 160°. Combined with the shape structure feature of F-22 aircraft, the analysis shows that local strong scattering centers appear at the edge of inlet, edge of wing, edge of vertical tail, edge of horizontal tail, exhaust nozzle, and the joint between airframe and wing.

(2) Stealth material

For some positions of aircraft, such as inlet, ideal stealth effect cannot be achieved only by shape stealth design. The radar absorbing material should be used at these positions to decrease RCS. The radar absorbing material is such a kind of material that can absorb and attenuate the incoming electromagnetic waves and transfer the

electromagnetic energy into heat energy to dissipate out, or disperse the electromagnetic energy to other directions. Using radar absorbing material, the aircraft can make use of its special electromagnetic characteristics to significantly reduce its RCS. The demands on the radar absorbing material are: under the precondition of satisfying electromagnetic wave absorbing attenuation rate (commonly going beyond −10 dB), the frequency range should be as wide as possible; light weight, thin thickness, and corresponding bearing capacity; weakening infrared radiation as small as possible. The radar absorbing material can be divided into coating type and structure type according to its function. The coating-type radar absorbing material is characterized by convenient construction and low cost, suitable for complex shape; the structure-type radar absorbing material is a structural composite material formed by dispersing the absorbent into the special fiber (for example, glass fibre and quartz fiber) enhanced structural material. Its typical characteristics are that it can not only bear but also reduce target's RCS. Currently, the main radar absorbing materials are nano material, metamaterial, intelligent material, conductive polymer wave absorbing material, and so on.

Some researchers in western countries stated that the aircraft could disappear from the opponent's display by using this kind of mysterious coating material. The actual situation is that the coating and material are generally only effective in very narrow frequency band and has a certain depth or thickness so as to obtain good effect, which will have an influence on the weight and volume of the aircraft. The major difficulty of the radar absorbing material and dissipative material is "skin effect", that is, the RF current induced by incident electromagnetic wave trends towards centralizing at the target surface. If the conductive material is adopted, such as aluminium skin, it will become an excellent reflector due to its very thin coating thickness. However, the conductivity of the wave absorbing or dissipating coating must be low enough to make is effective, which leads to thicker skin. As a result, with the skin thickness becoming several millimeters or centimeters, the thin coating that can effectively counter the radar operating at 10 GHz may be disable to counter the radar operating at 10 MHz or 100 MHz.

The most common method to solve this problem is to use radar absorbing structure. For instance, the front edge of the wing of B-2A bomber, its thickness can accommodate the wave absorbing structure, so that it is very effective in very wide bandwidth. But this is impossible for fighter because of volume and weight limits.

In the realization of aircraft stealth, the airframe shape design achieves the greatest gain. Actually, the initial 100 times of radar signal reduction is brought by ingenious airframe shape design, only a small part of reflection is absorbed by wave absorbing material. For example, in centimeter wave band, the RCS of traditional fighter is 1 m^2, but the same design using proper stealth shape design may make its RCS to be 0.01 m^2 only. Further application of wave absorbing material to right position may decrease its RCS to 0.001–0.0001 m^2.

Like the coating material, the efficiency of airframe shape design is also correlative closely to radar wavelength. At the places much greater than the radar wavelength in size, such as plane, small plane, or front edge of wing, the rules of geometric optics are applicable, thus the reflected waves can depart from the threat radar very

accurately. For F-117A, B-2A, and F-22A, their adjusted front edges of wings, platforms, and small planes or planes are very effective for the wavelength down to several centimeters, and, for B-2A, even down to metric wave. As far as frequency is concerned, fighter is easy to realize stealth at X band and S band, and B-2A can realize stealth at a certain degree even at metric wave band.

2.2 Counter-Stealth Mechanism at Metric Wave Band

Both stealth and counter-stealth follow the basic electromagnetic scattering theory. For a simple object, such as a sphere, the RCS is normalized to optical area, and the relationship of the RCS and the target relative to the size of wavelength (ratio of perimeter to wavelength) is shown in Fig. 2.1. The diagram is divided into three regions: Rayleigh region, resonant region, and optical region. $2\pi r/\lambda < 1$ is Rayleigh region, in which the RCS increases with the fourth power of sphere radius. This is the general characteristic of electrically small structure. $2\pi r/\lambda > 10$ is optical region, where the RCS approaches to the optical area of the sphere. Located between the Rayleigh region and the optical region is resonant region, where the fluctuation of the RCS is caused by the interaction between the specular reflection and the creeping wave rounded the shadow region.

For typical aircraft target, because of the reflection, diffraction, and travelling wave, there are seven echo sources: groove structure, mirror scatter, travelling wave echo, top/edge and corner diffractions, surface discontinuity, creeping wave, and

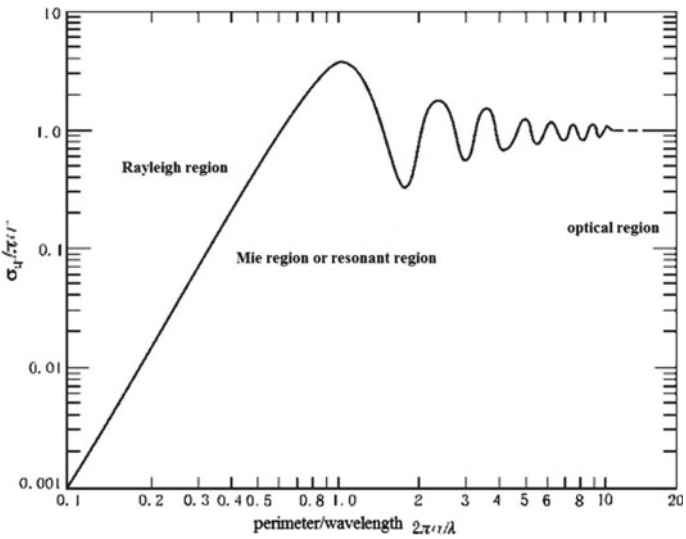


Fig. 2.1 Normalized RCS of an ideal conductive sphere

interaction. The echoes observed by radar are commonly the signals superposing the full or partial energies of these seven echo sources. The electromagnetic computation and the scaled model test of typical aircraft target show that the RCS and size of aircraft target and wavelength also have the similar basic relations of the above Rayleigh region, resonant region, and optical region.

When the effective size of target is equivalent to the radar wavelength, that is, locating in the resonant region, the RCS of target generates resonance, resulting in a big difficulty to control reflection direction and distribution. The region with the greatest resonance amplitude is called as "main resonant region". When the size of target falls into the main resonant region, the RCS of target will increase significantly. With the wavelength increasing further, enter into Rayleigh region. At this time, the RCS is dependent on the effective physical size of the reflection part and has no close relation to the aircraft shape, that is to say, the shape stealth almost fails to function.

The targets nowadays used for actual battle have the effective sizes equivalent to the wavelength of metric wave radar, For example, the effective sizes of various aircraft fall into the range of about 0.5–5 m and the effective sizes of various missiles are about 0.1–2 m, while the wavelength range of metric wave radar is 1–10 m. Therefore, as long as the operating frequency of radar is selected to be in metric wave band, the scattered waves of the most targets are in Rayleigh region and resonant region. The shape stealth design will not act as the function of reducing RCS. In some countries, large amount of test accumulations about the RCS frequency characteristics of the targets of interest show that the resonant region almost locates at metric wave band. For example, The RCS of American stealth fighter F-117 is only 0.01 m^2 about in microwave band, but 10–20 m^2 in the main resonant region, increasing 1000–2000 times. Different aircraft have different resonant frequency points. Making use of this characteristic can distinguish the types of stealth aircraft.

The basic characteristic of radar absorbing material is that the dielectric constant or magnetic permeability is a complex. When electromagnetic waves are illuminated on the target coated with wave absorbing material, some electromagnetic waves are absorbed by the wave absorbing material, realizing the stealth purpose. The wave absorbing performance of the wave absorbing material is relevant to its electromagnetic parameters (ε, μ) and thickness relative to wavelength. In general, the lower the operating frequency is, the greater the required thickness of wave absorbing coating is. Because of the limits imposed by weight and mechanical strength, the thickness of the wave absorbing coating on aircraft surface is usually smaller than 2 mm. This may have good wave absorbing effect at higher frequency band. For the technology of coating wave absorbing material on target surface to realize stealth, in order to effectively absorb the radar incident wave, the coating thickness must be greater than 1/10 of the wavelength of incident wave. As for the metric wave radar operating at VHF band, the coating thickness at least reaches to the magnitude of 0.1–1 m. Actually, it is impossible to coat the wave absorbing material of such thickness on the moving targets of high speed and high sensitivity, for example, aircraft or missile. So the material stealth method is also ineffective to metric wave radar.

Currently, the stealth frequency range of all kinds of stealth aircraft is limited to 1–20 GHz due to the limits of aerodynamics and the frequency response of wave

absorbing material. If the operating frequency range of radar oversteps this range, the stealth effect of aircraft will be rebated greatly, so that the counter-stealth purpose can be realized. Modern metric wave radar operates at VHF band of 30–300 MHz and thus has prominent frequency-band counter-stealth advantage.

2.3 Electromagnetic Computation and Analysis of Stealth Aircraft RCS

In designing counter-stealth advanced metric wave radar, the first problem should be concerned is what the RCS of each type of stealth target is under heaven. This problem is very important but not simple. A large number of factors can make influences on target RCS: the relation to target's azimuth and elevation, the relation to frequency, the relation to polarization, and etc. It is impossible that some one wants to obtain enough data through practical target detection. The electromagnetic scattering characteristic of target can be researched via experiments, but the acquisition of target RCS using measurement method is limited by many factors, such as target size, dielectric attribute, test field, environmental condition, time, weather, and so on. Additionally, there is an expensive test cost, so that it is not an effective method. It is obvious that the theoretical estimation and accurate computational solution of target RCS become an essential and important measure.

2.3.1 Electromagnetic Computation Methods

The methods to solve target's electromagnetic scattering characteristics mainly include analytical method, high-frequency method, and numerical method.

The numerical method, also called as full-wave numerical method, is a class of electromagnetic simulation algorithms to solve differential forms of Maxwell's equations or equivalent integral equations by using of numerical computation method, mainly including the method of moment (MoM), the finite difference time domain (FDTD) method, and the finite element method (FEM). The numerical method has found wide applications due to its ability to compute the complex target with arbitrary shape, high computation precision, and flexibility. The multilevel fast multipole algorithm (MLFMA) using multilevel cluster technique can further decrease the storage and computational amount to the magnitude of $O(N\lg N)$, which significantly enhances simulation capability and enlarges the electric size scale of solving scattering problem. The primary simulation softwares based on MLFMA are FISC and FEKO.

The ANSYS is used to set up the geometric modeling of the stealth aircraft target to be computed and complete the geometrical partition of target surface. On this basis, the strict MLFMA is used to realize the electromagnetic scattering computation of

target at given frequency points. The impedance boundary condition—multilevel fast multipole algorithm (IBC-MLFMA) is used to realize the electromagnetic scattering computation of the target coated with thin stealth material.

Large amount of tests and engineering applications show that, in order to accomplish the accurate computation of the RCS of a complex target in practical engineering application, it is required to have a deep understanding of electromagnetic scattering theory and correctly set the various operational parameters according to different target shape characteristics. The key techniques to enable correct operation of algorithm include geometric modeling, electromagnetic modeling and electromagnetic computation, and verification of solution accuracy.

(1) Geometric modeling

Geometric modeling is the foundation for solving the numerical value of electromagnetic scattering of target. Geometric modeling is to make curve fitting and element partition of target. As for computer numerical program, its solving object is the "target" in mathematics of a real target fitted by curve after discretization. Thus the accuracy of this "target" approaching to the original physical target determines the credibility of the computed RCS curve. In addition, the curve-partitioned element is the definition domain of basis functioning in MLFMA program, reflecting directly the change rule of induced current density of target surface, so that the geometric modeling is also affected by electromagnetic scattering mechanism. If the "target" formed by geometric modeling of a target is completely in accordance with the original target but the element density cannot reflect the actual surface current distribution, a large computation error of the target RCS still presents.

In computing actual engineering problem, the geometric modeling and target surface partitioning have very important significance. The geometric model of stealth aircraft obtained through modeling by the CAD software ANSYS is shown in Fig. 2.2. Making discrete partition of target shape can obtain geometric information about target for electromagnetic modeling and electromagnetic computation.

(2) Electromagnetic modeling and electromagnetic computation

The CRWG basis function based on curved-surface triangle partition is used to solve the electromagnetic scattering problem of stealth aircraft on the basis of

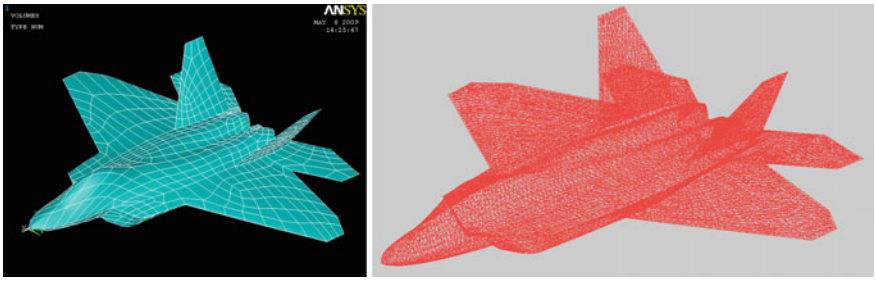


Fig. 2.2 Schematic diagram of CAD model of F-22 stealth aircraft and its partitioning

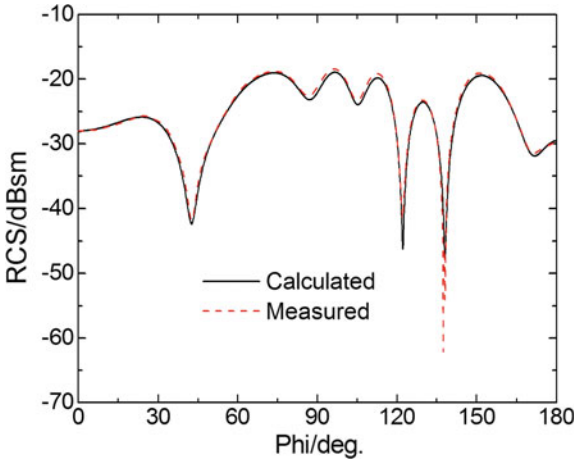


Fig. 2.3 Backscatter RCS of NASA almond: horizontal polarization

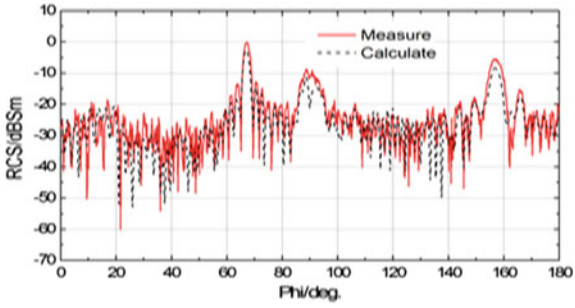


Fig. 2.4 Backscatter RCS of diamond with coating

MLFMA, and a series of improved and accelerating computation methods are used for improving computation efficiency; the IBC-MLFMA is applied to the analysis of the target coated with thin stealth material; in order to solve the electromagnetic scattering problem of electrically large-size target at microwave band, the MPI and OPENMP parallel computation techniques based on 64-bit platform are adopted. The applications of the above methods and measures can greatly increase the computing speed and computing capability of the electromagnetic analysis of complex target.

(3) Verification of computation accuracy

First, the monostatic RCS of Benchmark target—NASA almond under horizontal polarization was investigated. The comparison between the computed RCS curve and the tested resulted is shown in Fig. 2.3, the root mean square error is 0.8889 dB.

Then, the model to be computed was chosen as a diamond model coated partially with metal. The parameters of the coating material are: $\varepsilon_r = 1.1634 + i4.0755$, $\mu_r = 4.0755 + i1.9731$, and the incident wave frequency is 3 GHz. The comparison between the computed backscatter RCS curve and the tested resulted is shown in Fig. 2.4, indicating a good agreement the computed curve and the tested curve.

2.3.2 *Electromagnetic Computation Results*

Taking the two typical stealth aircraft, F-35 and F-22, into consideration, their RCS results of electromagnetic computations under different attitude angles, different polarizations, and different frequencies are given below respectively.

(1) F-35 aircraft

(1) RCS results under different attitude angles

Under the condition of 100 MHz and horizontal polarization, the RCS results of F-35 are about 3.2 m^2 at nose direction, near 31.6 m^2 at tail direction, and almost 100 m^2 in maximum at lateral direction respectively, as shown in Fig. 2.5.

(2) RCS results under different polarizations

For F-35 stealth aircraft, its RCS results at nose direction, tail direction, and the most of azimuth angles under horizontal polarization excel those under vertical polarization, but at the part of angles of lateral direction, the RCS results under vertical polarization excel those under horizontal polarization, as shown in Fig. 2.6.

(3) Variation of RCS with frequency

The maximum RCS of F-35 stealth aircraft under horizontal polarization presents at 20 MHz, and the maximum RCS under vertical polarization presents at 30 MHz, as shown in Fig. 2.7.

Figure 2.8 gives a RCS comparison of F-35 in a larger frequency range. Generally, the RCS results at VHF band (30–300 MHz) near the nose direction and the tail direction are above 0 dBsm (i.e., 1 m^2), but obviously decrease at UHF band.

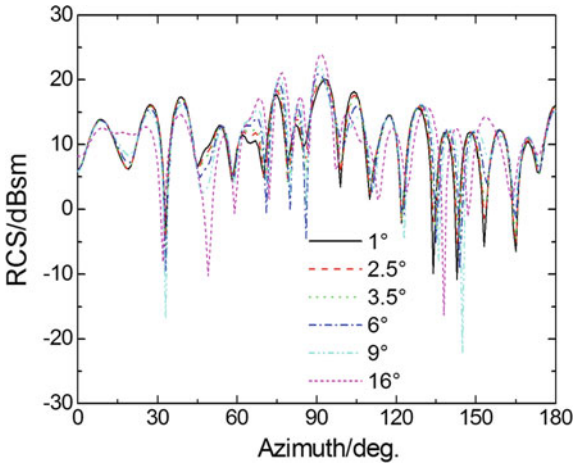


Fig. 2.5 Variation of backward RCS of F-35 with azimuth angle under horizontal polarization and 100 MHz

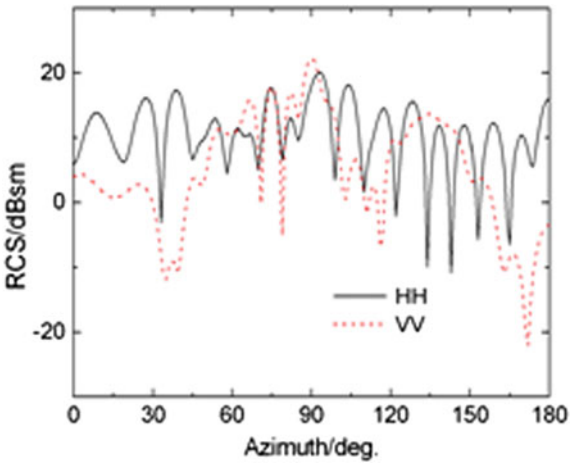


Fig. 2.6 Variation of backward RCS of F35 with azimuth angle under HH and VV polarizations and 1° of elevation

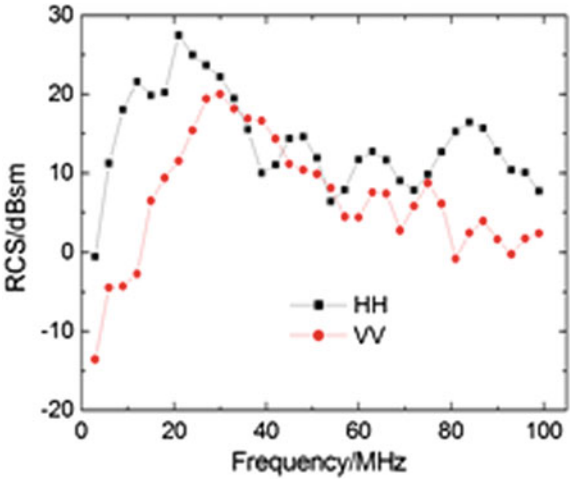


Fig. 2.7 RCS variation of stealth aircraft F-35 with frequency

(4) Computed bistatic radar RCS result

Figure 2.9 gives the computed RCS results of F-35 aircraft at different bistatic angles. With the bistatic angle increasing, RCS becomes large, reaching up to above 30 and 20 dBsm respectively under horizontal polarization and vertical polarization.

(2) F-22 aircraft

(1) RCS results at different attitude angles

Under the condition of 100 MHz and horizontal polarization, the RCS results of F-22 are about 1.8 m^2 at nose direction, near 10 m^2 at tail direction, and almost 100 m^2 in maximum at lateral direction respectively, as shown in Fig. 2.10.

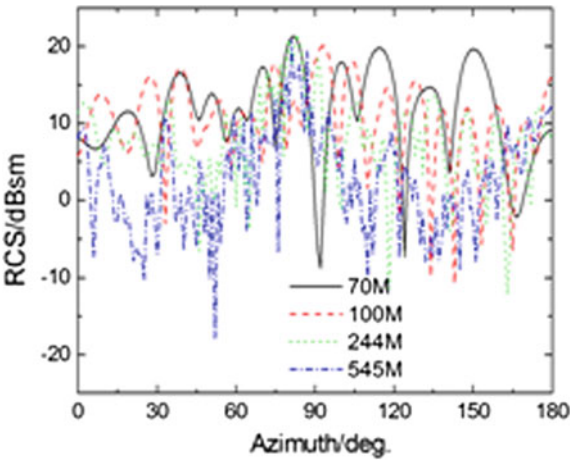


Fig. 2.8 RCS comparison of stealth aircraft F-35 at typical frequencies

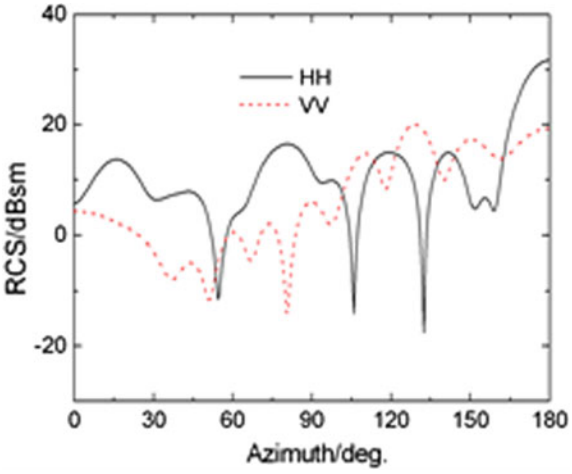


Fig. 2.9 Bistatic RCS of F-35 stealth aircraft at 100 MHz

(2) RCS results under different polarizations

For F-22 stealth aircraft, its RCS results at nose direction and tail direction under vertical polarization excel those under horizontal polarization, but at the most of azimuth angles, the RCS results under horizontal polarization excel those under vertical polarization, as shown in Fig. 2.11.

(3) Variation of RCS with frequency

The maximum RCS of F-22 stealth aircraft under horizontal polarization appears at 18 MHz and the miximum RCS under vertical polarization appears at 25 MHz, as shown in Fig. 2.12.

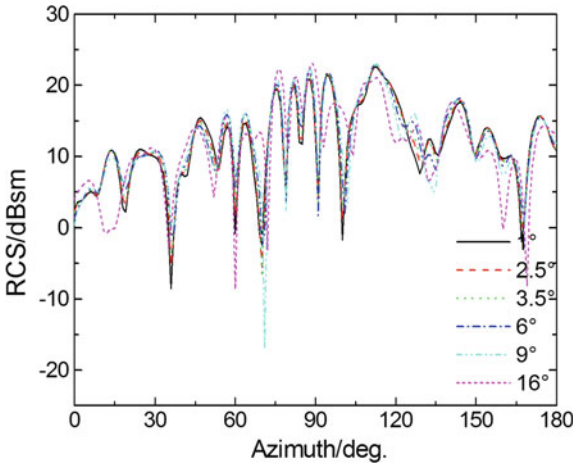


Fig. 2.10 Variation of backward RCS of F-22 with azimuth angle under horizontal polarization and 100 MHz

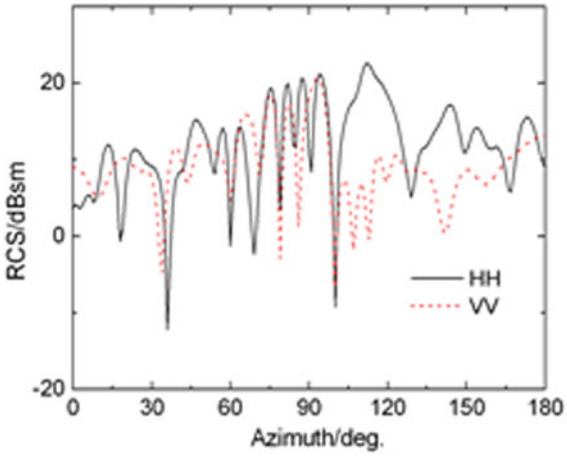


Fig. 2.11 Variation of backward RCS of F-22 with azimuth angle under HH and VV polarizations and 1° of elevation

Although RCS is relatively large at some frequency points blow 100 MHz, this phenomenon cannot simply be used as the basis for selecting the operating frequency to counter stealth target. This is because the antenna noise temperature will sharply rises with frequency dropping blow 100 MHz. Thus comprehensive considerations are needed.

A RCS comparison of F-22 in a larger frequency range is shown in Fig. 2.13. Generally, the RCS results at VHF band (30–300 MHz) near the nose direction and the tail direction are above 0 dBsm (i.e., 1 m^2), but obviously decrease at UHF band.

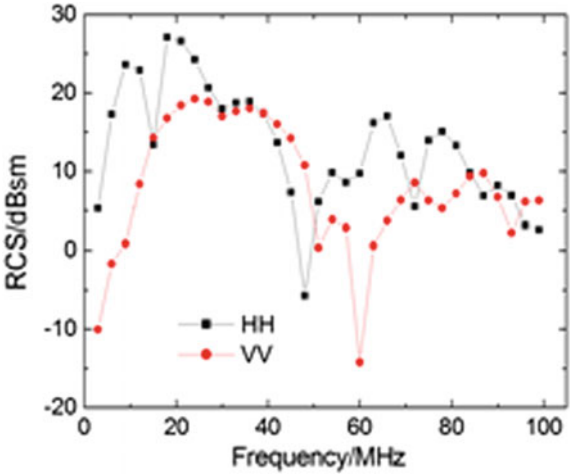


Fig. 2.12 RCS variation of F-22 stealth aircraft with frequency

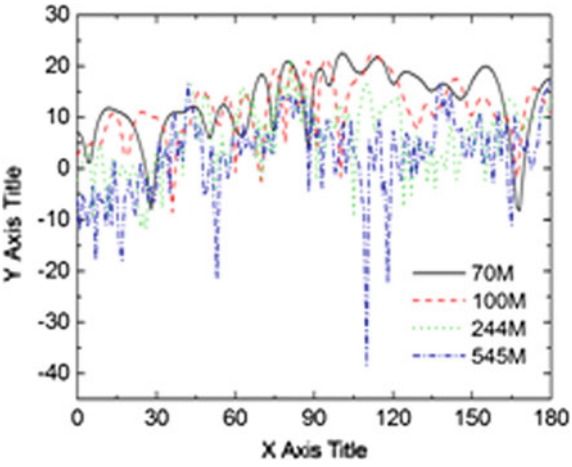


Fig. 2.13 RCS comparison of F-22 stealth aircraft at typical frequencies

(4) Computed bistatic radar RCS result

Figure 2.14 gives the computed RCS results of F-22 aircraft at different bistatic angles. With the bistatic angle increasing, RCS becomes large, reaching up to above 30 and 20 dBsm respectively under horizontal polarization and vertical polarization.

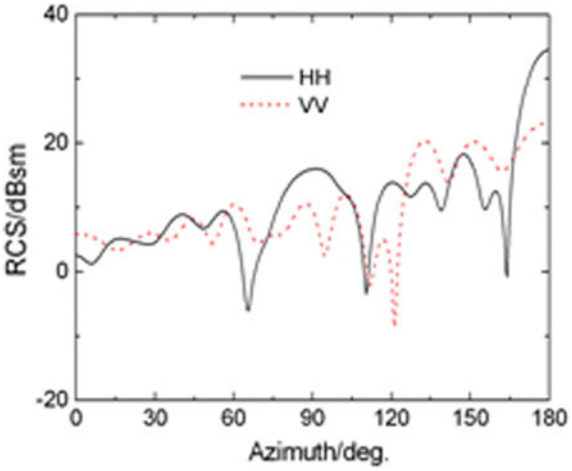


Fig. 2.14 Bistatic RCS of F-22 stealth aircraft at 100 MHz

Bibliography

1. Wolfgang Holpp. The Century of Radar[EB/OL]. http://100-jahre-radar.fraunhofer.de/Vortraege/Holpp-The_Century_of_Radar.pdf.
2. Carlo Kopp. Russian VHF Counter Stealth Radars Proliferate[J]. Defense Today, 2008(4):32–36.
3. Liu Falai. Radar Stealth and Counter-Stealth[J]. Avionics Technology, 1995(4):27–34.
4. Ruan Yingzheng. Radar Cross-Section and Stealth Techniques[M]. Beijing: National Industry Press, 1998.
5. Ling Xiaoshu. Stealth and Anti-Stealth Techniques of Radar[J]. Shipboard Electronic Countermeasure, 2007(3):40–42.
6. Chen Changxing, Gong Linyu, Ban Fei, et al. Research into Anti-Stealth Technology of Meter-Wave Resonance Radar[J]. Shipboard Electronic Countermeasure, 2009(4):34–37.
7. Li Jinliang, Li Yongzhen, Wang Xuesong. Study on Anti-Stealth with Meter-Band Polarimetric Radar[J]. Radar Science and Technology, 2005(6):321–327.
8. Nie Zaiping, Que Xiaofeng, Fu Jun. Numerical Computation Techniques of Target RCS[R]. RCS Computation and Analysis Report, 2009.
9. Kuschel H. VHF/UHF Radar, Part 1: Characteristics[J]. Electron. Commun. Eng. Journal, 2002, 14(2):61–72.
10. Kuschel H. VHF/UHF Radar, Part 2: Operational Aspects and Applications[J]. Electron. Commun. Eng. Journal, 2002, 14(3):101–111.
11. Huang Peiking, Yin Hongcheng, Xu Xiaojian. Radar Target Characteristics[M]. Beijing: Publishing House of Electronic Industry, 2005.
12. He Guoyu, Lu Caicheng, Hong Jiacai. Computation and Measurement of Electromagnetic Scattering[M]. Beijing: Beihang University Press, 2006.
13. Nie Zaiping. Target and Environment Electromagnetic Scattering characteristics Modeling-Theory, Method, and Realization[M]. Beijing: National Industry Press, 2009.
14. Skolnik M I. Radar Handbook[M]. 3rd ed. McGraw-Hill, 2008.
15. Zhuang Zhaowen, Yuan Naichange, Mo Jinjun. RCS Estimation and Measurement of Military Target[M]. Beijing: Science Press, 2007.
16. Chen Baixiao. RCS Measurement of Scaled Model of Stealth Target Under Low Frequency Band and Different Polarizations[C]// Eleventh Chinese Radar Conference, Changsha, China, 2010.

17. Zhang Xinglong. Study on Full-Polarization Radar and Polarization Information Processing[D]. Xian: Xidian University, 2010.
18. Chen Baixiao, Hu Tiejun, Zhu Wei, et al. RCS Measurement for Scale Model of Stealth Targets in VHF Band[J]. Chinese Journal of Radio Science, 2011(3):480–485.
19. Zhang Linxi, Li Nanjing, Hu Chufeng. Test and Image Diagnosis of Radar Target Scattering Characteristics[M]. Beijing: China Astronautic Publishing House, 2009.
20. Hu Mingchun. Simulation and Measurement of Radar Target Electromagnetic Scattering[J]. Modern Radar, 2012(10): 1–5.
21. Tan Huaiying, Guo Jianming. VHF/UHF Radar Characteristics and Applications[C]// China Radar Technology Forum, Nanjing, 2006:83–87.
22. Zhou Wei. Study on Low Elevation Heigh-Finding Methods for Metric Wave Digital Array Radar[D]. Xian: Xidian University, 2013.
23. Ding Guosheng. Study on Analysis of Electromagnetic Radiation Field Strength from Ship-Borne High Power Radar and Improvement Technology[D]. Nanjing: Nanjing University of Science and Technology, 2012.
24. Yang Xueya. Research on Super resolution and Height-Finding Methods for Metric Wave Radar Array[D]. Xian: Xidian University, 2011.

Chapter 3
System Design of Advanced Metric Wave Radar



3.1 Technology Scheme of Advanced Metric Wave Radar

3.1.1 Multipath Effect in Metric Wave Band

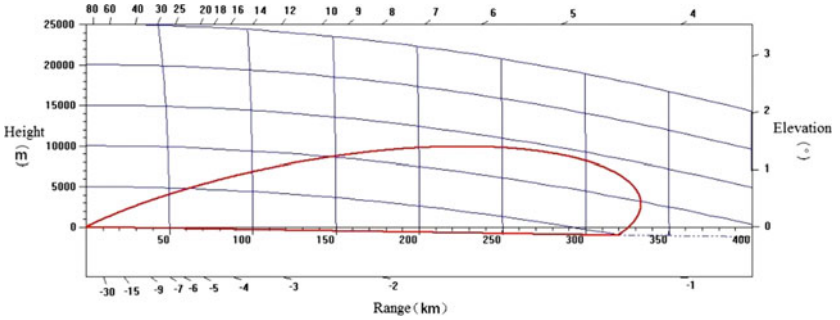
The multipath effect in metric wave band is stronger in comparison with microwave radar. In metric wave band, there are long wavelength, large earth surface reflection coefficient (near 1 in low elevation area especially), and comparative amplitudes and strong correlation between direct-wave and multipath reflection signal. Also, for the radar operating in metric wave band, it has broad beams, and the included angle between the direct-wave incident angle and the multipath reflection wave incident angle is very small and they are usually within one beam width, which results in the difficulty to differentiate them generally by the directional selectivity of antenna. Due to the limited operational bandwidth in metric wave band, it is also difficult to differentiate the direct-wave and the multipath echo signal by means of high range resolution. Multipath effect mainly impacts the airspace coverage performance and height finding performance of radar.

(1) Impact of multipath effect on the airspace coverage of metric wave radar

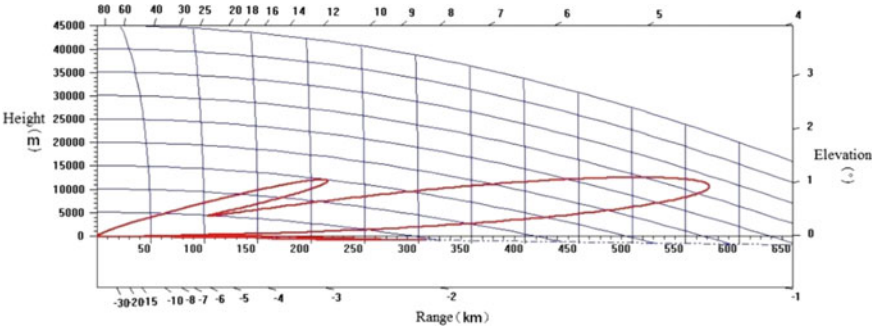
Figure 3.1 illustrates the schematic diagram of airspace coverage of typical single-beam metric wave radar. Fig. 3.1a and b are respectively the airspace coverage diagram in free space and the airspace coverage diagram in ground reflection condition. It can be seen that the impact of multipath effect on the airspace coverage of metric wave radar. The benefit is that the maximum detection range of radar is significantly enlarged in a certain elevation range. The disbenefits are: (1) the low-elevation blind zone resulted from beam tilting has influence on the low altitude detection performance; (2) the notch resulted from beam splitting has influence on the continuity of radar airspace coverage, resulting in severe problems such as discontinuous track and lost track. Traditional metric wave radar, usually adopting single beam and uniform time and energy distribution, is unable to realize the optimization in spatial domain and temporal domain. Therefore, it cannot overcome the problems of poor

© National Defense Industry Press, Beijing and Springer Nature Singapore Pte Ltd. 2020

J. Wu, *Advanced Metric Wave Radar*, https://doi.org/10.1007/978-981-10-7647-3_3



(a) Free space



(b) Ground reflection

Fig. 3.1 Schematic diagram of single-beam metric wave radar airspace coverage

low-elevation detection performance and poor high-altitude airspace coverage continuity.

(2) Impact of multipath effect on metric wave radar height-finding accuracy

Modern air surveillance radars are imposed the operational tasks on interruption and guidance and thus usually are required to have three-dimensional measurement capability. How to achieve good height-finding performance for metric wave radar is always a difficult problem. In low elevation area, especially, direct-wave and multipath reflection signal have comparative amplitudes and strong correlation; the included angle between the target direct-wave incident angle and the multipath reflection wave incident angle is very small and they are often within one beam width; beam tilting or splitting can make the level of received signal decrease and flicker, as a result, the signal-to-noise ratio (SNR) is low and the fluctuation is large. The height-finding problem of metric wave radar can be viewed as an problem of target DOA (direction of arrival) estimation under a low SNR, strongly correlated source. The phase information about target elevation carried by the received echo is damaged by multipath echo, so the conventional amplitude-comparison and

phase-comparison techniques will bring significant height-finding error, unable to meet the measurement requirement.

3.1.2 General Consideration for Radar Technology Scheme

Radar technology scheme is a common technical term in radar community. It generally means the set of the most notable one or more technical features, which may be the technical features at system level or the important technical features of major subsystems that dominate the radar performance and complexity. For example, the full-coherent system, continuous-wave system, and active phased array system are well known. Advanced metric wave radar need to overcome major shortages of traditional metric wave radar. This cannot be achieved by such technology scheme as traditional mechanical scan, single-beam or fixed beam design, and amplitude comparison/phase comparison angle measurement. Novel technology scheme must be established.

Firstly, consider the beam scanning technology scheme. If a single broad fixed-beam is used at elevation to realize airspace coverage, it is difficult to focus on both low-elevation detection performance and high-altitude continuous coverage performance. The independent beam and subarea reshaping design should be adopted and the matching optimization should be made according to the terrains in different azimuth sections. Thus, both transmit beam and receive beam are required to perform subarea scanning at elevation, and their directions and shapes to vary agilely with different azimuths. In the optimized design of elevation coverage, to achieve a good effect, the optimization of energy and dwell time distributions should be done except for the optimization of beam direction and shape. That is, the transmitting and receiving need to have flexible beam agility and waveform agility, which means electric scanning system.

Second, consider height-finding technology scheme. Under the precondition that the subarea independent beam design flexibility is available, the elevation coverage area can be divided into high elevation area and low elevation area. In engineering, the beam width can be used as the boundary to separate high elevation area form low elevation area. Through antenna sidelobe or "nulling" design, the multipath signal in high elevation area can be reduced so small as to be ignored. Then, the height-finding in high elevation area can be made by means of conventional monopulse angle measurement and multi-beam amplitude comparison/phase comparison angle measurement. In low elevation area, the multipath signal and the direct signal are comparable, and their coherent effects cause the beam shape to deform. The conventional angle measurement methods are no longer applicable, so that superresolution methods or diverse height-finding systems must be adopted, of which a dedicated description will be given in Sect. 3.3.

Thirdly, determine radar's technology system according to its operating mission. Advanced metric wave radar is supposed to be a new generation of mainstay radar. Its principal mission is to detect and track stealth aircrafts. Besides strong anti-stealth

capability, it is required to have good tracking performance for super-maneuver aircrafts, namely, capability of tracking with high data rate. Paying attention to search performance and tracking performance, TAS (tracking and search) operation mode is needed. To realize this operation mode, the antenna should be equipped with two-dimensional electric scanning ability; usually a two-dimensional phased array antenna is chosen. Additionally, the modern new radar must have good anti-jamming performance in order to adapt to the electronic countermeasures environment in modern war. The strong airspace filtering performance is the most important anti-jamming capability. The advanced metric wave radar, therefore, should have multi-freedom jamming cancellation or nulling capability. The digital beamforming (DBF) and the adaptive signal processing techniques are the optimal choice to realize this capability.

Summarized the above considerations, the technology system of advanced metric wave radar is determined to be digital array radar and superresolution height-finding system. Digital array radar is the latest development of active phased array radar. Different from the analog beam forming of traditional phased array radar, it's transmit and receive both adopt digital beam forming technique.

3.1.3 Principle of Metric Wave Digital Array Radar

The basic operational principle of metric wave digital array radar is given as follows. In transmit mode, digital beamformer generates the amplitude and phase control words required for transmit beam and sends to digital transmit/receive (DTR) module. The DTR module produces the RF signal of a certain frequency, phase, and amplitude. Up converted and amplified, the RF signal is radiated out and power combined in space. In receive mode, the T/R module receives the microwave signal from antenna element. Down converted, the signal is transformed into IF signal. After IF A/D conversion and digital orthogonal sampling, I/Q echo signals are output and sent to digital beamformer, signal processor, and data processor for software-based processing. The basic architecture of digital array radar is shown in Fig. 3.2.

3.1.4 Features of Metric Wave Digital Array Radar System

In metric wave digital array radar, there are several main modes as follows:

(1) Single-beam mode with transmit DBF and receive DBF (single transmit and single receive mode)

In analog beamforming radar, the beamforming is executed before receiver, thus the receiver is needed to provide very high dynamic range level for countering the strong jamming source in the main lobe of receive beam. To resolve this problem, digital array radar (DAR) digitalize the receive aperture. Then the jamming gain entering

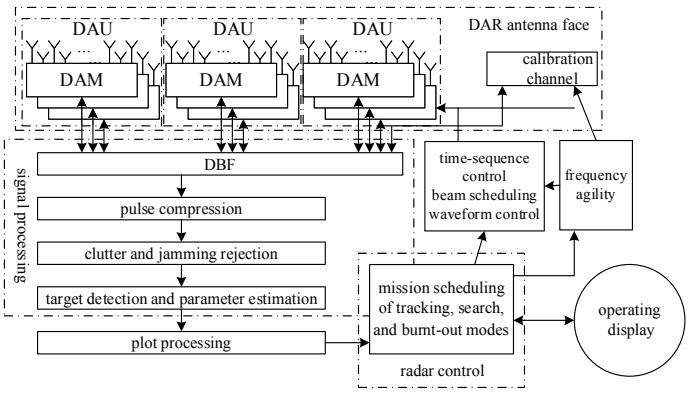


Fig. 3.2 Basic architecture of digital array radar

into each receiver can be decreased thus the requirement on the dynamic range of receiver is mitigated. The outputs from different receivers are synthesized by DBF.

(2) Broad transmit beam and DBF receive multi-beam mode (single transmit and multiple receive mode)

To shorten the time for searching an airspace, DAR can broaden its transmit beam. The transmit beam illuminates an angular section, and multiple beams are simultaneously used to receive in the coverage range of the whole broad transmit beam, which is equivalent to beam scanning continuously. Because of low transmit antenna gain, long transmit and integration time is needed. In addition, the Doppler resolution can be improved.

(3) DBF transmit and receive beam mode in MIMO operation (multiple transmit and multiple receive mode)

The optimal mode for omnidirectional radar is to operate in multiple input multiple output (MIMO) mode. At the transmit end, DAR aperture is divided into M low gain array elements, each element radiating a single orthogonal coded waveform. At the receive end, there are N receive channels. A received signal passes through M matching filters and is matched with a transmit waveform, so that MN matching filter outputs are obtained. These MN signals can form one or more pointing beams.

In comparison with traditional metric wave radar system, the metric wave digital array radar has the following advantages:

(1) Large dynamic range. It preserves small target information without loss under strong clutter background, and facilitate improving small target detection capability.
(2) Flexible multiple beams. The width of transmit beam can be adjusted arbitrarily, realizing either high-gain narrow beam in any direction or board beam for full airspace coverage. Multiple receive beams can be formed without SNR loss.

(3) Ultralow sidelobe. DDS is used to produce the exciting signal for every antenna element with flexible phase control and high accuracy, which can realize active ultralow sidelobes. The ultralow sidelobe antenna is propitious for improving radar ECCM capability and reducing the influence of sidelobe clutter on target detection.
(4) Short production period and low cost. Without RF beamforming network and feedline network, DAR adopts modular design and can be produced by DAM assembling, which shortens development and production period and reduces cost.
(5) Easy software implementation. The main radar functions are implemented by programming, thus allows to change radar function or improve radar performance through software upgrade instead of replacing hardware platform.

3.2 Polarization Selection

3.2.1 Impacts of Different Polarizations on Metric Wave Radar Performance

(1) Impacts of different polarizations on radar coverage

With the multipath effect, radar echo is supperposition of direct wave and ground reflected wave. If the direct wave and the reflected wave were equal in amplitude and phase, the total received voltage will be 4 times of that in free space. That means the signal power is increased by 16 times, so the target detection range is twice of the free space detection range. Sea surface fluctuation, earth surface curve, and atmosphere loss usually degrade this range.

Compared with free space, therefore, multipath effect may change radar detection range significantly. Depending on horizontal polarization or vertical polarization, the influence of multipath effect on radar coverage may be different somewhat. Figure 3.3 gives the simulation results.

Figure 3.3 shows that the reflected energy under horizontal polarization is greater than that under vertical polarization. The energy gains are different for these reflection surfaces, in which the maximum gains occurring in the cases of salty water surface and fresh water surface, are about 4–6 dB, but the energy gains for other reflection surfaces are only 0.5–1.7 dB.

(2) Influences of different polarizations on height-finding accuracy

The echo of metric wave radar is the vector synthesis of direct wave and ground reflected wave. When a target locates at low elevation, the reflected wave energy is strong and the phase information about target elevation carried by echo is damaged. In this case, conventional amplitude comparison height-finding method certainly brings error and the angle measurement errors under different polarizations are also

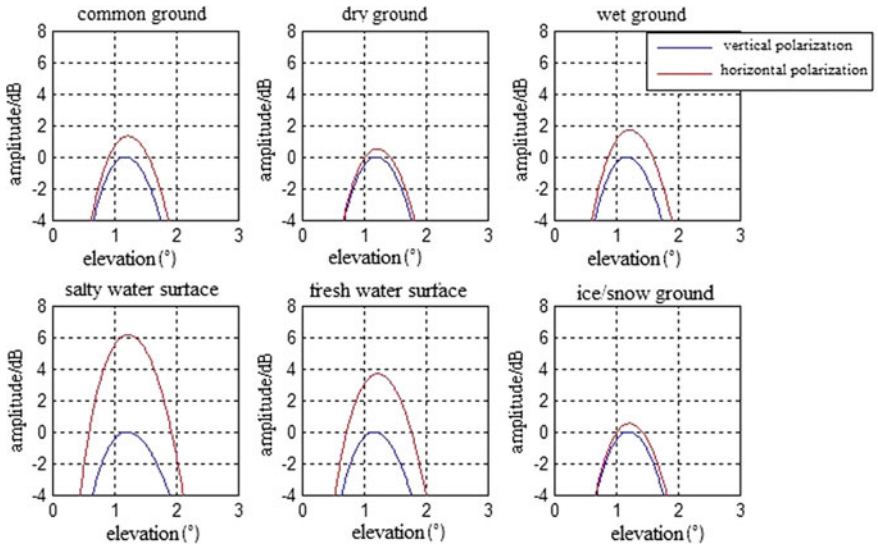


Fig. 3.3 Comparison of radar low-elevation energies under horizontal/vertical polarization

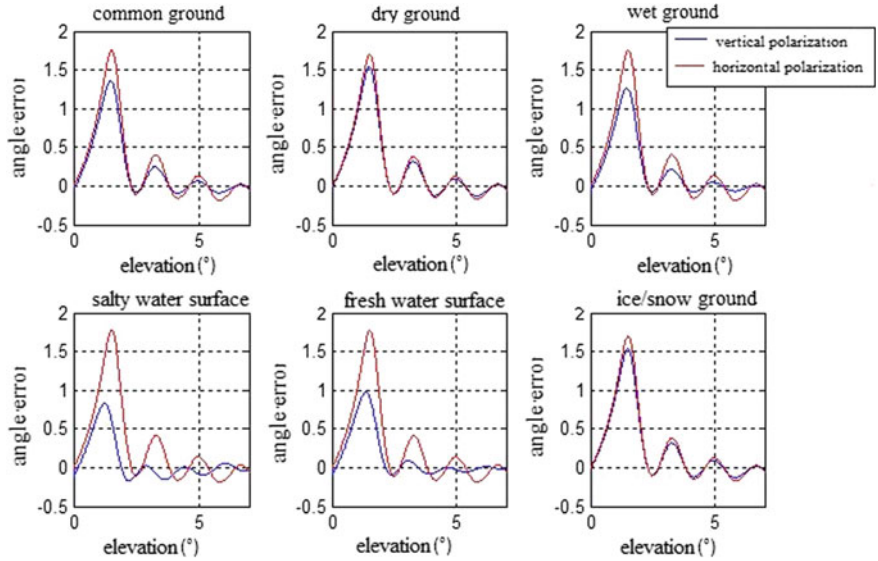


Fig. 3.4 Angle measurement errors resulted from multipath effect under horizontal/vertical polarization

different. Figure 3.4 gives the simulation results of angle measurement errors resulted from multipath effect under vertical polarization and horizontal polarization.

It can be seen from the simulation results that, for different reflection surfaces, the angle measurement errors under vertical polarization are smaller than those under horizontal polarization.

3.2.2 Principles of Metric Wave Radar Polarizations Selection

Consider the radar coverage. The reflected energy gain obtained under horizontal polarization is greater than that under vertical polarization and the energy gains for different reflection surfaces are not equal. In view of the gain of radar coverage, metric wave radar should use horizontal polarization.

Consider the height-finding accuracy. For different reflection surfaces, the multipath effect under vertical polarization is smaller than that under horizontal polarization, and the corresponding angle measurement errors are also smaller than that under horizontal polarization. To reduce the influence of multipath effect on elevation angle measurement accuracy, the metric wave radar should use vertical polarization.

Consider the target detection stability. Illuminated by electromagnetic waves in different polarizations, a flying target has somewhat different RCS characteristics. The polarization mode, single polarization or dual polarizations, is chosen according to the target RCS characteristic. Compared with the target RCS flicker loss due to single polarization, dual polarizations, the detection and tracking of stealth aircraft are made more stable through independently receiving and processing horizontal/vertical polarization component of target echo.

Consider the polarization matching of target echo. When passing through the ionosphere, the polarization of electromagnetic wave will be rotated (Faraday rotation effect), thus the polarization mode of target echo is difficult to predict. Transmitting and receiving in single polarization may result in polarization mismatch. However, dual-polarization receiving can reduce the polarization mismatch loss brought by Faraday rotation effect as much as possible. The detection of near space target will become more stable.

Consider the ECCM capability. Polarization agility may be used to adjust the polarization state of radar system according to the polarization state of foe jamming source to make them orthogonal. In addition, by independently receiving and processing the horizontal and vertical polarization components of target echo, the electromagnetic wave of any polarization state can be synthesized, which allows both the mainlobe and sidelobe interference of the antenna to be suppressed as much as possible.

Consider the target recognition. Target polarization characteristic is another feature of radar echo signal except for amplitude, phase, and Doppler shift. Polarization information in radar echo is an important resource to enhance radar detection capability. The electromagnetic scattering theory shows that the polarization scattering characteristic of target is closely related to its physical characteristic, which provides a promising way to enhance target classification and recognition for radar system.

The polarization mode selection of metric wave radar is a comprehensive consideration course. There are many factors to be considered. Detailed demonstration should be made according to practical requirements.

3.3 Frequency Selection

Metric wave frequency band is a crowded frequency band, occupied by various electronic applications for communications, navigation, satellites, weather, television, and so on. Thus careful consideration should be given to the frequency selection of metric wave radar so as to minimize the interferences.

The following factors should be considered during the selection of operating frequency of metric wave radar: according with the frequency usage regulations of radio committee; avoiding the frequency bands for television, FM broadcasting, and radio paging; bringing radar performance into play.

3.3.1 Frequency Regulations of Radio Committee

In "People's Republic of China Regulations of the Radio Frequency Allocation", the allocation of radio frequency in metric wave band (30–300 MHz) in the mainland of PRC is listed in Table 3.1.

To select the operating frequency of metric wave radar, large operating frequency band should be retained, and, in this frequency range, there are wide frequencies used for radiolocation as the primary service, so as to avoid the interferences with other services and increase the validity of radar operation.

3.3.2 Avoiding Television, FM Broadcasting and Radio Paging Frequencies

In PRC, television channels 1–12 fall into the operating frequency range of metric wave radar. Their frequency distribution is given in Table 3.2.

In general, the bandwidth of television image is 5 MHz above, but the bandwidth of sound is narrow, only several kHz. The frequency of metric wave radar should be selected far from the image and sound carrier frequencies. If the operating frequency of metric wave radar covers television frequency, it is necessary to make careful selection of radar frequency points and fine design of frequency spectrum control so as to minimize the impacts on television.

The frequency range occupied by FM broadcasting is 88–108 MHz, with frequency interval of 100 kHz and offset frequency of 75 kHz. From four-level hybrid

Table 3.1 Allocation of radio frequency in metric wave band in the mainland of PRC

Serial no.	Frequency band (MHz)	Service name
1	30.005–30.01	Space operation (satellite identification) Fixed, mobile, space research
2	30.01–37.5	Fixed, mobile
3	37.5–38.25	Fixed, mobile, [radioastronomy] [1]
4	38.25–39.986	Fixed, mobile
5	39.986–40.02	Fixed, mobile,[space research]
6	40.02–40.98	Fixed, mobile
7	40.98–41.015	Fixed, mobile [space research]
8	41.015–44	Fixed, mobile
9	44–48.5	Fixed, mobile
10	48.5–50	Fixed, mobile, broadcasting
11	50–54	Amateur, broadcasting, fixed, mobile
12	54–64.5	Fixed, mobile, broadcasting
13	64.5–72.5	Fixed, mobile, broadcasting, radiolocation
14	72.5–74.6	Fixed, mobile, radiolocation
15	74.6–75.4	Aeronautical radionavigation
16	75.4–76	Fixed, mobile, radiolocation
17	76–84	Broadcasting, fixed, mobile, radiolocation
18	84–87	Fixed, mobile, radiolocation
19	87–108	Broadcasting, [radiolocation]
20	108–117.975	Aeronautical radionavigation
21	117.975–137	Aeronautical mobile
22	137–137.025	Space operation (space to ground), satellite meteorological (space to ground) Satellite mobile (space to ground), space research (space to ground) Fixed, mobile, (except for aeronautical mobile(R))
23	137.025–137.175	Space operation (space to ground), satellite meteorological (space to ground) Space operation (space to ground), fixed Mobile (except for aeronautical mobile(R)) [Satellite mobile (space to ground)]
24	137.175–137.825	Space operation (space to ground), satellite meteorological (space to ground) Satellite mobile (space to ground), space research (space to ground) Fixed, mobile, (except for aeronautical mobile(R))

(continued)

Table 3.1 (continued)

Serial no.	Frequency band (MHz)	Service name
25	137.825–138	Space operation (space to ground), satellite meteorological (space to ground) Space research (space to ground), fixed, mobile, (except for aeronautical mobile(R)) [Satellite mobile (space to ground)]
26	138–143.6	Fixed, mobile, radiolocation [Space research (space to ground)]
27	143.6–143.65	Fixed, mobile, space research (space to ground) (space to ground) Radiolocation
28	143.65–144	Fixed, mobile, radiolocation [Space research (space to ground)]
29	144–146	Amateur, amateur-satellite [Radiolocation], [aeronautical mobile(OR)]
30	146–148	Amateur, fixed, mobile, [radiolocation]
31	148–149.9	Fixed, mobile, satellite mobile (space to ground)
32	149.9–150.05	Satellite mobile (space to ground), satellite radionavigation
33	150.05–156.4875	Fixed, mobile, radiolocation
34	156.4875–156.5625	Maritime mobile (distress and safety calling using DSC)
35	156.5625–156.7625	Fixed, mobile
36	156.7625–156.8375	Maritime mobile (distress and calling)
37	156.8375–157.45	Maritime mobile
38	157.45–160.6	Maritime mobile, land mobile
39	160.6–160.975	Maritime mobile,[land mobile]
40	160.975–161.475	Fixed, mobile
41	161.475–162.05	Maritime mobile,[land mobile]
42	162.05–167	Fixed, mobile Space operation (space to ground), radiolocation
43	167–174	Broadcasting, [fixed], [mobile], [radiolocation]
44	174–184	Broadcasting Space operation (space to ground), space research (space to ground) [Fixed], [mobile], [radiolocation]
45	184–216	Broadcasting, [fixed], [mobile], [radiolocation]
46	216–223	Broadcasting, [fixed], [mobile]
47	223–225	Fixed, mobile, aeronautical radionavigation, radiolocation
48	225–230	Fixed, mobile, aeronautical radionavigation, radiolocation
49	230–235	Fixed, mobile, aeronautical radionavigation, radiolocation
50	235–267	Aeronautical mobile, [radiolocation]
51	267–272	Aeronautical mobile, [space operation (space to ground)] [radiolocation]

(continued)

Table 3.1 (continued)

Serial no.	Frequency band (MHz)	Service name
52	272–273	Space operation (space to ground) Aeronautical mobile, [radiolocation]
53	273–279	Aeronautical mobile, [radiolocation]
54	279–281	Fixed, aeronautical mobile, [radiolocation]
55	281–312	Aeronautical mobile, [radiolocation]

Table 3.2 Frequency distribution of television channels 1–12 in PRC

Channel	Frequency range (MHz)	Center frequency (MHz)	Image/sound carrier frequencies (MHz)
1	48.5–56.5	52.5	49.75/56.25
2	56.5–64.5	60.5	57.75/60.25
3	64.5–72.5	68.5	65.75/68.25
4	76–84	80	77.25/83.75
5	84–92	88	85.25/91.75
6	167–175	171	168.25/174.75
7	175–183	179	176.25/182.75
8	183–191	187	184.25/190.75
9	191–199	195	192.25/198.75
10	199–207	203	200.25/206.75
11	207–215	211	208.25/214.75
12	215–223	219	216.25/222.75

coverage networks planning, it is known that the receiving field strengths in urban area and rural area in China are respectively 60 dBμV/m and 46 dBμV/m and there are 4–5 channels for choice. In the environment of such dense broadcasting channels, the metric wave radar in the frequency band cannot operate.

The frequency regulation of radio paging system issued by the China National Radio Committee is given in Table 3.3. The frequencies already put into operation are 150.725, 151.305, 152.650 MHz (for local network and national network), and 156.725 MHz (for local network). The frequencies that can be requested are Group D28, D29, and D30.

To avoid the cross interferences, the frequency of metric wave radar should be chosen away from the operating frequencies of television, FM broadcasting, and radio paging.

Table 3.3 Frequencies for radio paging system

Group no.	Frequency band (MHz)	Number of frequencies
D06	43.675–43.775	5
D28	152.500–152.700	9
D29	156.050–156.300	11
D30	156.500–156.700	9
D50	410.600–410.900	13
D51	419.300–419.600	13

3.3.3 Comprehensive Discussion on Radar Performance

(1) Anti-stealth performance: as described in Chap. 2, metric wave radar has inherent anti-stealth advantage. Metric wave radar should operate near the possible harmonic frequency of target. For example, the RCS of F-117A stealth aircraft will increase significantly when the radar operating frequency is lower than 200 MHz. If the major operational target is known, the operating frequency favorable for detecting this type of aircraft may be chosen.
(2) Anti-jamming performance: local warfare in modern high-tech conditions requires radar to have good anti-jamming performance. Frequency agility is one of the important technologies to enhance radar anti-jamming performance. From this point of view, the bandwidth of frequency hopping is required to be as wide as possible. When It happened that the radar frequency conflicts with the frequencies used for distress calling, communications concerning foreign affairs, and international lifesaving, the radar needs to take measures to resolve them, such as frequency range limiting and automatic/manual hoping.
(3) Mobility: Considering the radar mobility requirement, the operating frequency of radar should be selected to be in the higher frequency range of metric wave band so as to decrease the antenna mobility design difficulty brought by large antenna aperture.
(4) Detection performance: Influenced by ground reflection, metric wave radar suffers from beam splitting due to antenna driving up. If frequency diversity is used to overcome multipath effect, sufficient operating bandwidth should be taken to compensate for the detection blind zone resulted from beam splitting.

In a word, for the frequency selection of metric radar, it is needed to consider various factors and make tradeoffs among radar performance, electromagnetic compatibility, and beam splitting. The relevant technical solutions and frequency limiting should be used to minimize the cross interferences between radar and other electronic equipments.

3.4 Technical Approaches Analysis of Metric Wave Radar Height Finding

3.4.1 Common Height Finding Methods

In metric wave radar, both high-elevation height finding and azimuth angle measurement can be done by amplitude comparison and target height is calculated from the amplitudes of echo signals received at different elevations (beams). Thus the consistency of amplitude signals of various beams is critical. Only the comparability of amplitude signals of various beams is ensured, the height finding accuracy can be guaranteed. For ensuring the comparability, the amplitude signals entering into the signal processor should be consistent, and it is required that the amplitude signals output from the signal processor are comparable. As far as MTD system is concerned, if the data after peak selection are taken to conduct amplitude-comparison height finding, the gains of various channels are required to consistent. If each channel outputs signal respectively, the gains of NCFAR channel, KALMUS channel, and CFAR channel should be consistent basically. At the same azimuth and the same range, according to the beam number at which the signal of the maximum amplitude locates, the signals of the right beams and left beams that have the same parameter components as the amplitude signal of the center beam are taken to make amplitude-comparison height finding. For MTI system, the amplitude signals of NCFAR channel and zero-velocity channel are the raw signals, the gain of MTI output signal is normalized to the normal channel. The over-threshold signals of normal channel and MTI channel should be output in pairing with their amplitude signals each. In the same way, when performing height finding computation, three-dimensional plot clotting is done firstly, and then, the signal feature of the center beam is made as the reference and the signals with the same feature of the adjacent channels are used for amplitude-comparison to ensure the height-finding accuracy.

Monopulse eccentric angle measurement is a mature technique. It usually uses a special type of antenna feeding so that only one pulse is needed to generate four beams. Through antenna or the mixer of RF front-end, the “sum beam”, “azimuth difference beam”, and “elevation difference beam” can be formed. As for two-dimensional (2D) digital array radar, there are hundreds of antenna elements and the antenna aperture is large. Microwave network cannot be used to form the sum and difference beams for monopulse tracking. Only by signal processing can sum and difference beams be formed, which is called as digital monopulse measurement. Traditional monopulse measurement is realized through lookup of the error curve table. In 2D digital array radar, there are many beams at azimuth and elevation and many operating frequency points, and the differences in the equivalent antenna apertures of beams can bring angle measurement errors. If monopulse measurement is conducted in traditional monopulse angel measurement mode, it is necessary to set up a monopulse angle measurement error curve table for each frequency point and beam, which will produce large loads on radar data processing. For example, the APG-77 multifunction phased array radar onboard American F-22 aircraft and the

Russian Don-2 phased array radar adopt frequency grouping, scan angel partitioning plus modification to make tradeoffs, but high angle measurement accuracy cannot be achieved.

For the low-elevation height-finding in metric wave radar, the methods studied early are multi-frequency smoothing, spatial-domain filtering, complex indicated angel technique, correlation height method, and range high-resolution height finding.

The multi-frequency smoothing method adopts frequency diversity technique. The angle measurement error depends on the operating frequency of radar and is decreased by averaging many times. But its angle measurement accuracy is still low. When target range is short, the required frequency hopping bandwidth is small, however, for the target at long range, the frequency hopping bandwidth is required to be greater than 50%, which is difficult to accommodate.

The basic idea of spatial filtering method is that, the weighting of antenna array element signal is used to make the gain of antenna receive pattern at negative elevation direction decrease significantly and then reduce multipath effect. However, this method requires antenna array to have large vertical electrical length, which is difficult for metric wave radar.

The principle of complex indicated angle technique is that an orthogonal channel signal is added when monopulse radar phase detection is performed and the actual elevation value is obtained by use of the relationship between in-phase error signal and quadrature error signal. Elevation ambiguity is the shortage of this technique. In application, it is needed to calibrate the relationship curve of in-phase error signal and quadrature error signal in advance.

In correlation height method, the data should be received by radar are simulated at all possible target heights according to target height characteristics and multipath reflection model, the correlation function of target measurement height and estimation height is set up, and then the precise height-finding and tacking are realized through the correlation function. Nevertheless, the height-finding ambiguity often appears and the correlation function reaches its maximal values possibly at multiple heights.

The height finding method based on range high-resolution uses radar wideband signal to generate range high-resolution signal and then discriminates the target echo from the ground/sea reflected echo to achieve the precise height of target. In metric wave radar, unfortunately, the range resolution usually is low and the travel route difference between the direct wave and the reflected echo is much smaller than range resolution. Thus, it is difficult to discriminate direct wave from multipath signal.

In metric wave radar, beam splitting is caused by ground reflection because of its wide beam. The beam splitting method realizes low-elevation height finding of metric wave radar through phase comparison and amplitude comparison. This method uses the array elements at different heights. There is a phase relationship between the split beams at different heights. The elevation region at which the target locates can be determined by the phase relationship. The amplitudes of the signals received by antenna are used to perform amplitude comparison to extract the normalized error signal and the target height is obtained by looking up table. The influence of ground fluctuation on height finding performance is analyzed and the formula

for computing error curves in different sites is deduced. In this method, when the mean square deviation of ground fluctuation is not beyond 1 m and the SNR reaches 16 dB, the height-finding precision can reach up to 1% of the range. If the method is used, it is not needed to enlarge the elevation aperture of antenna and perform the array superresolution processing. And the radar is not required to set up in a very high site. On the other hand, the method needs small computational load and is easy to implement. The DBF technique and the beam splitting method are combined to enlarge the height-finding range. The DBF technique can be used to combine the multiple-channel signals received by antenna in a weighted manner. Combining the DBF technique with the beam splitting method can realize the height-finding in a large range of elevation. Impacted by the change and fluctuation of multipath reflection surface, the height-finding method based on beam splitting is not very stable in performance and has no very high accuracy.

3.4.2 Superresolution Angle Measurement Methods

The major methods for superresolution height-finding are:

(1) Eigen-subspace algorithms. The category of algorithms includes multiple signal classification (MUSIC) algorithm, estimation of signal parameters via rotational invariance technique (ESPRIT), and etc. When these algorithms are used for low elevation height-finding, the coherence problem of direct wave and multipath signal will be faced. When signal sources are fully coherent, the order of covariance matrix of the data received by array reduces to 1, which may cause the dimension of signal subspace smaller than the number of signal sources. That is, the presence of coherent sources makes signal subspace and noise subspace permeate each other. Then the steering vectors of some coherent sources are not orthogonal fully to the noise subspace, resulting in performance degrade or malfunction of many eigen-subspace algorithms. In the case of coherent sources, the core of correctly estimating signal direction is to recover effectively the order of covariance matrix of signal, i.e., decoherence or decorrelation. There are two categories of methods for the estimation of DOA (direction of arrival) of coherent source: reduced dimension processing and non-reduced dimension processing. Among the reduced-dimension processing algorithms, the typical ones are spatial smoothing algorithms and matrix reconfiguration algorithms. The decoherence performance of this kind of algorithms is achieved at the cost of reduced freedom. The basic idea of spatial smoothing is that the equidistant uniform linear array is divided into some subarrays overlapping each other, the coherence is realized by averaging the covariance matrixes of subarrays, and finally DOA estimation is done in combination with eigen-subspace algorithms. The algorithms based on matrix reconfigurations mainly include matrix decomposition algorithm and vector singular value algorithm. The non-reduced dimension processing algorithms include the Toeplitz algorithm, the virtual

array transformation algorithm, and so on. The major advantage is no loss in array aperture. In the Toeplitz algorithm, the covariance matrix of the received data is made to approach to the covariance matrix of the real data. But the estimation derivation of Toeplitz method is large. The virtual array transformation algorithm is mainly used for non-equidistant array.

(2) Maximum likelihood (ML) and subspace fitting algorithm. The maximum likelihood method is a special case of Bayesian estimation method and is the optimal estimation under white noise. In the maximum likelihood algorithm, the likelihood function of the observed signal is defined as the conditional probability density function including unknown parameters. The purpose is that the unknown parameters can be selected so as to make the likelihood function as great as possible. The idea of the subspace fitting algorithm is that there is a fitting relation between the array manifold matrix and the subspace of the data received by array. This fitting relation is a problem of optimize maximum likelihood function. Currently, this kind of algorithms mainly include maximum likelihood algorithm, multidimensional MUSIC algorithm, weighted subspace fitting algorithm, and weighted noise subspace fitting algorithm. The performance of this kind of algorithms approaches to the Cramer-Rao lower bound under high SNR. And they can work well even under low SNR. However, the likelihood function maximization problem to be solved is a nonlinear multidimensional optimizing problem, which needs multidimensional search. As a result, the computational amount increases exponentially as the number of targets rises and the realization process is complex. The effective multidimensional fast search algorithms includes the alternating projection method, iterative quadratic ML, MODE algorithm, and genetic algorithm.

On the basis of the relevant height finding methods and the prior information such as antenna height, distance between target and radar, earth curvature, and atmosphere refraction, the precise multipath reflected signal model should be set up by taking such factors as the polarization information of incident signal, the mirror reflection, the scattering, diffuse reflection, sea state, and the grazing angle into consideration. The ML algorithm based on precise multipath reflected signal model is used and the all unknown parameters (except for target angle) are expressed to be the functions of target angle, which can reduce the number of the parameters to be estimated and improve the estimation precision of low-elevation DOA.

Through modification of the precise multipath reflected signal model, we have developed a ML height finding algorithm based on terrain parameter matching. Making use of the terrain information of reflection site, the fluctuation information of the reflecting points to which each elevation angle corresponds can be obtained by means of measurement. The information is used to calculate path difference and multipath factor precisely during height-finding processing, so the matching with the actual echo signal model can be achieved. Compared with conventional array superresolution algorithms, this algorithm improves significantly the height-finding accuracy of metric wave radar, especially in low-elevation area, which makes metric wave radar have a breakthrough in height-finding technique. The height finding problem

of metric wave radar in the case of a relatively flat reflection site is solved effectively. Nevertheless, if a reflection site with big fluctuation is faced, the terrain fluctuation at low elevation has a great influence on the measurement result. In particular, the rugged ground surfaces, buildings, and mountains cause the multipath signal have irregular reflections, for example, diffuse reflection and scattering. These uneven and irregular reflection surfaces have a great impact on height finding. The reflection site with big fluctuation makes terrain parameters very difficult to obtain. At this time, the ML height-finding algorithm based on terrain matching is no longer applicable. Aimed at the height-finding problem in the case of a site with fluctuation, we have developed a height-finding algorithm based on adaptive DBF. It is applicable for both complex site and flat site.

At present, the research on the low-elevation estimation technique of metric wave radar has achieved breakthroughs. Significant results have been acquired and successful applications are found. These will be described in detail in Chap. 4.

3.5 Optimal Design of Airspace Coverage

3.5.1 Design of Independent Beam

Metric wave radar operates in low frequency band and wide beam, easy to suffer from ground (water) surface reflections. The vertical plane beam of antenna will change due to the influences of ground (water) surface multipath signals. Assume that the vertical plane amplitude beam function of antenna in free space is $f_0(\theta, \theta_0)$. The variables of the formulas in this section is defined as follows: θ_0 is the pointing of the maximum value of beam, δ is wave path difference between direct wave and reflected wave at target, S_d is the electric field intensity of direct wave at target, S_r is the electric field intensity of reflected wave at target, φ_d is the phase of antenna beam at elevation angel θ_d of direct wave in free space, φ_r is he phase of antenna beam at elevation angel θ_r of direct wave in free space, $f_0(\theta_d, \theta)$ is the amplitude value of antenna beam at elevation angel θ_d of direct wave in free space, $f_0(\theta_r, \theta)$ is he amplitude value of antenna beam at elevation angel θ_r of direct wave in free space, ρ is the amplitude value of ground reflection coefficient, and ϕ_g is the phase of ground reflection coefficient.

In our discussion, only the influences of electric property and roughness of ground surface are taken into consideration, rather than the influence of earth curvature. From superposition principle, the electric field intensity at target is the vector addition of the direct wave electric field intensity and the reflected wave electric intensity and is expressed as:

$$S_t = S_d + S_r \tag{3.1}$$

It can be known from electromagnetic field theory:

$$S_d = Af_0(\theta_d, \theta_0)e^{j\phi_d} \tag{3.2}$$

$$S_r = A\rho f_0(\theta_r, \theta_0)e^{j(\phi_g+\varphi_r-2\pi\delta/\lambda)} \tag{3.3}$$

Substituting (3.2) and (3.3) into (3.1) results in the antenna beam considered multipath effect

$$f(\theta, \theta_0) = \sqrt{f_0^2(\theta_d, \theta_0) + \rho^2 f_0^2(\theta_r, \theta_0) + 2\rho f_0(\theta_d, \theta_0) f_0(\theta_r, \theta_0) \times \cos(\varphi_d - \varphi_r - \varphi_g + 2\pi\delta/\lambda)} \tag{3.4}$$

Let $\Delta\varphi = \varphi_d - \varphi_r - \varphi_g + 2\pi\delta/\lambda$

(1) When $\Delta\varphi = (2n+1)\pi, n = 0, 1, \ldots, f_{\min}(\theta, \theta_0) = f_0(\theta_d, \theta_0) - \rho f_0(\theta_r, \theta_0)$ is the minimal value of the antenna beam reflected by ground surface. When $\rho = 1, f_0(\theta_d, \theta_0) = f_0(\theta_r, \theta_0), f(\theta, \theta_0) = 0$ indicates that the antenna beam shows zero-point (blind point). This is the worst case.

(2) When $\Delta\varphi = 2n\pi, n = 0, 1, 2, \ldots, f_{\max}(\theta, \theta_0) = f_0(\theta_d, \theta_0) + \rho f_0(\theta_r, \theta_0)$ is the maximal value of the antenna beam reflected by ground surface.

From the analysis above we can see that, different from microwave radar, conventional metric wave radar has wider vertical beam and its main beam touches the ground, so the influence of ground reflection is greater and multipath effect is more significant; if the vertical beam tilts up, there is larger low-altitude blind area (Fig. 3.5). A method for reducing low-altitude area is to drive up the antenna for lowering its beam down. But this will result in beam splitting, which causes notches appear in the observation airspace and detection discontinuous (Fig. 3.6).

Good result can be achieved through optimization of the elevation beam distribution and design of radar working mode. It is required to design low elevation beam and medium/high elevation beam respectively and independently. In designing medium/high elevation beam, the control of ground-touching level is very important. For both transmit beam and receive beam, the nulls or very low sidelobe levels should be directed towards the high reflecting region. In designing low-elevation beam, the beam width should be as narrow as possible to achieve good low-elevation coverage and measurement performance, which is beneficial for both elevation and azimuth estimation. Also, it is necessary for the lower edge of elevation beam to have steep drop characteristic. These designs are all based on the foundation that the radar antenna should possess flexible 2D beam shape agility, which calls for 2D transmit and receive full DBF antenna.

Figure 3.7 shows the coverage diagram of a metric wave radar after optimal design (the thin line). The center height of the radar antenna is 15 m. The thick line is the elevation airspace coverage diagram realized by a single wide beam. Making a comparison, we can see that the effect is obvious.

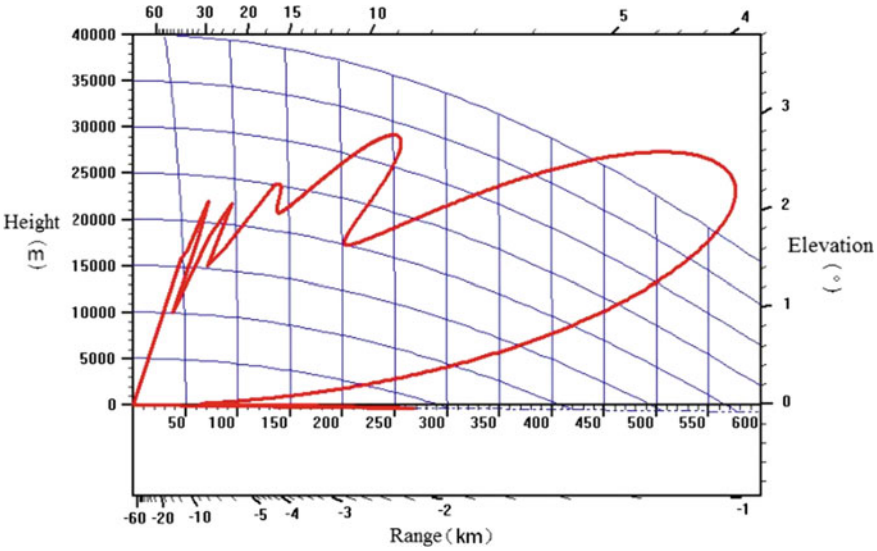


Fig. 3.5 Large low-altitude blind area of conventional metric wave radar

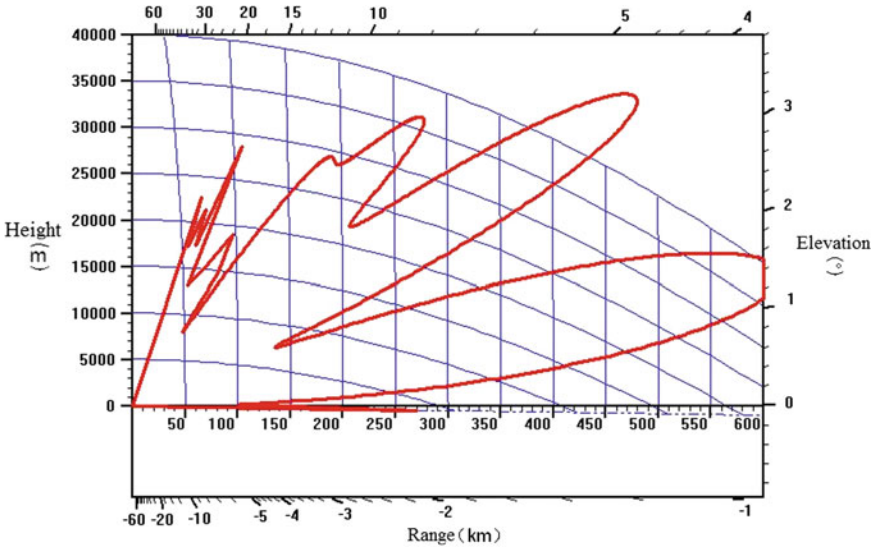


Fig. 3.6 Beam splitting of conventional metric wave radar after antenna driving up

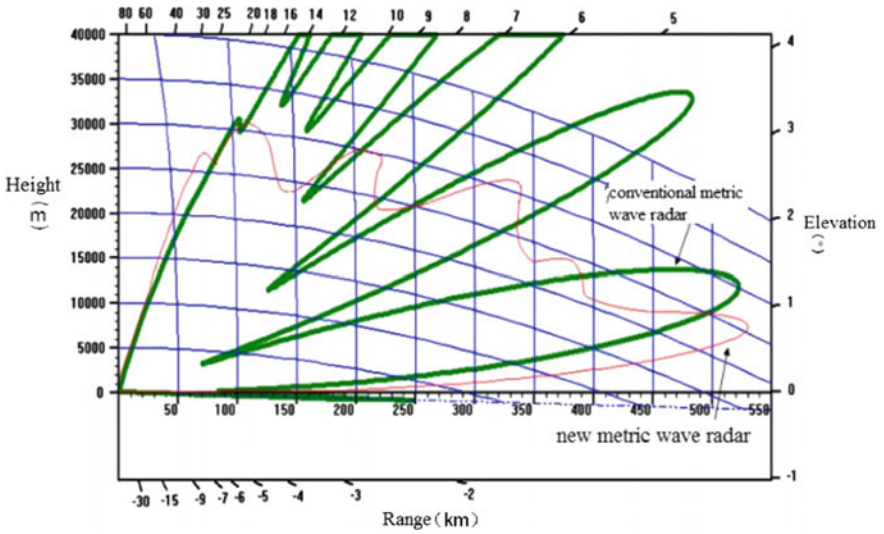


Fig. 3.7 Airspace coverage of a metric wave radar

3.5.2 Design of Improved Volume Coverage Diversity

For metric wave radar, the elevation beam splitting appears under the influence of ground (sea) surface multipath signal, that is, the peak value appears at the elevation angle $\theta_n = n\lambda/2h$, $(n = 1, 2, \ldots)$ (λ is wavelength, h is center height of antenna) and the valley value appears at the elevation angle $\theta_n = \left(n + \frac{1}{2}\right)\lambda/2h$, $(n = 1, 2, \ldots)$. The airspace coverage of metric wave radar can be improved by frequency diversity (changing wavelength λ) or antenna height diversity (changing center height of antenna). In frequency diversity, the radar operates at the waveforms of different operating frequencies simultaneously or alternatively to achieve the complement peak value and valley value of the split beams. In theory, the full peak value complement can be achieved only when the wavelength strides over the octave. In antenna height diversity, the different phase center heights of antenna elements are used to realize the complement peak value and valley value of the spatial beams. The precondition is that the transmitted signals of individual antenna elements are orthogonal and do not overlap coherently in space. The metric wave synthetic impulse and aperture radar, for example, is a typical multi-frequency MIMO radar.

3.5.3 Optimal Design of Pulse Energy

The detection range equation is

$$R_{\max} = 239.4\left[\frac{P_t \times \tau \times G_t \times G_r \times \sigma \times F_t^2(\theta) \times F_r^2(\theta)}{f^2 \times T_s \times D_0 \times C_B \times L_{\sum}}\right]^{1/4} \tag{3.5}$$

where τ is the transmitting pulse width, D0 is the detectability factor. The detectability factor depends on the number of beam position dwell pulses. The larger the number is, the smaller the detectability factor is. Actually, the two parameters represent the pulse energy distribution and have direct impacts on radar detection range. Thus, the radar airspace coverage can be optimized by adjusting pulse energy.

It can be seen from the radar equation that the pulse width is proportional to the radar detection range. The greater the pulse width is, the longer the detection range is. The design of pulse width is limited mainly by two factors. The first is the maximal duty ratio of transmitter. It lies on the transmitter operation mechanism, system power dissipation, heat resistance of power device, cooling system performance, and so on, which needs comprehensive considerations. The second is the minimal pulse width. It lies on the minimal detection of radar system. Generally, the maximal range blind-zone cannot be greater than the minimal detection range.

The number of pulses is proportional to the radar detection range. The larger the number of dwell pulses, the longer the detection range is. The design of pulse number is limited mainly by two factors. One is the beam position dwell time and the pulse repetition period. The beam position dwell time lies on the search data rate and beam width of radar system. The pulse repetition period lies on the maximal unambiguous range. In general, for long range surveillance radar, it is unambiguous in range and its maximal unambiguous range is greater than its maximal detection range. The other is the clutter rejection requirement. To satisfy the improvement factor requirement for rejecting ground clutter and moving clutter, enough number of pulses must be needed.

3.6 Design of Work Modes

The advanced metric wave radar that adopts digital array technique has not only strong spatial-domain filtering capability, but also high flexibility in time and energy distributions. Multiple operating modes can be designed according to mission requirement. Also, the combined applications of various operating modes can be supported to meet various application requirements of user to the maximum.

3.6.1 Design of Common Work Mode

Advanced metric wave radar takes stealth aircraft detection as its main task. Its common work mode is air surveillance mode. A basic design idea and the typical work follow are given hereafter. The antenna adopts full-array transmitting and receiving.

On transmitting, the low-elevation pencil beam and the high-elevation low-sidelobe wide beam scan mode are used to mitigate the impact of multipath effect on low-altitude blind zone and height finding error. On receiving, the DBF technique is used to form multiple receive beams that perform scan synchronous with transmit beam to cover the designated airspace. Mechanical scan and electric scan are used to realize azimuth coverage.

For the airspace coverage notch problem in metric wave radar, except for the optimal design of space beams, the optimal distribution of space energy can be made to further weaken the notches resulted from multipath effect and achieve continuous coverage of the whole airspace.

The typical radar work follow is given as follows.

(1) Site selection and optimization evaluation

Based on its location, the radar firstly exploits the geological information database to acquire the information about the terrain and physiognomy around the site in the range of 450 km, providing the geological information for site selection and beam scheduling and supporting radar airspace coverage evaluation.

(2) Environment sensing supports the radar to intelligently choose the optimal processing mode

Once powered on, the radar chooses the operating frequency suffered the least interference under the support of the reconnaissance receiving subsystem. The system enters the standard search processing mode (the default processing mode). At the same time, the radar signal processing subsystem analyzes the ground clutter, meteorological clutter, and sea clutter around the site. The results are sent to the intelligence analysis unit for environment analysis so as to support the radar choosing intelligently the optimal processing mode and realizing the environment matching detection.

(3) Target tracking

The TWS (track-while-scan) mode is used to track the common target. The track initiation may be either the multi-frame initiation or the single-frame initiation realized in electronic scanning confirmation mode during a mechanical scanning period. The electronic scanning flyback mode is used to track the important target and the high-speed and high-maneuvering target. This mode can increase the sweeping times and the dwell time, which is beneficial to the improvement of detection ability and tracking performance and the realization of target classification and identification. For the target according with TBM (tactical ballistic missile) motion feature, the radar enters the TBM tracking mode.

(4) Target attribute analysis

Detected target, the system makes comparative analysis on the newly received target and the target information saved in target database and received from other intelligence sources (exterior intelligence, IFF/secondary radar), and then updates the information about attribute, type, and amount of target. The result of target attribute

analysis gives a warning. For the target whose attribute cannot be determined, a suggestion is given on the basis of the air situation treating rule so as to make further check and treatment.

(5) Target classification and identification

For the tracked target to which attention should be paid, the classification and identification mode is used to acquire the information about target, sortie, classification and identification result. Metric wave radar can use narrow processing mode to complete the classification and identification of aircraft target. In narrow processing mode, the classification and identification of aircraft target are realized based on the combination of motion feature and modulation feature of target.

(6) Analysis of air attack grade and threat grade

After judgment on target attribute, classification and identification result, and aircraft fleet sortie, it is needed to make an analysis on the missions to be executed by the target. For the cooperative airplane target, the correlation to the information about its flight No. is conducted directly. For friendly military airplane, the correlation to the flight plan, prediction, flight report, activity airspace, and activity rule is made and then the target's task is determined. For the noncooperative aerodynamic target, the analysis and verification is done to determine the target's task in combination with exterior multiple-source intelligence, such as technical reconnaissance, superior aviso, intelligence from friendly neighbor, and activity rule of foe airplane. For the target that has foe attribute shows threat intent, it is necessary to build the knowledge base of target air attack grade and threat grade judgment rules. Based on the knowledge base, a combined judgment on target model, sortie, flight track, and tactical attempt can be made to give a threat grade. The computations about collision avoidance, off-course judgment, responsibility zone entry/exit, air defense identification zone, and forbidden zone are performed so as to send out relevant warning and cuing information in time.

3.6.2 Design of Special Work Mode

To make metric wave radar work well on high-mountain sites, a high-mountain work mode should be designed. At low beam position, multiple frequency points are utilized, and the complementation of the notches at different frequency points is conducted to enhance the low-altitude coverage continuity. In addition, the height finding results are weighted according to the SNRs of target echoes at various frequency points and then averaged for high height finding accuracy.

The TBM detection mode is designed to detect and track TBM target. The radar operates in 2D electronic scan mode. Search screen is set at a certain elevation direction. The range extending effect of ground reflection should be used for the setting of search screen. The screen traversing time is determined according to TBM firing range. The sweeping times for a single screen-traversing are determined by the

requirement of intercept probability. In turn, the frame period of search screen can be determined. Once confirmed, the target to be intercepted is switched to tracking. The TAS mode is used to arrange the search and tracking beam positions. The time and energy for tracking lies on the data rate for tracking target and the largest number of targets to be tracked.

Several anti-jamming modes may be designed to achieve good anti-jamming performance, such as frequency agility, waveform, random scan, and etc. Sidelobe cancellation and sidelobe blanking can be added to the normal work mode. In addition, the protecting pulse can also be inserted into the normal work time sequence.

The work modes mentioned above can be applied in a combined manner. For example, the air surveillance mode and the TBM mode can be combined to form an air and missile defense mode to accommodate the requirement of air and missile defense integrated operation mission.

Bibliography

1. Chen Baixiao, Wu Jianqi. Synthetic Impulse and Aperture Radar (SIAR): A Novel Multi-Frequency MIMO Radar[M]. Singapore: John Wiley & Sons Singapore Pte Ltd, 2014.
2. Heiner Kuschel. VHF/UHF Radar Part 1: Characteristics[J]. Electronics & Communication Engineering Journal, 2002:61–72.
3. Heiner Kuschel. VHF/UHF Radar Part 2: Operational Aspects and Applications[J]. Electronics & Communication Engineering Journal, 2002:101–111.
4. Li Jinliang, Li Yongzhen, Wang Xiesong. Study on Anti-Stealth with Meter-Band Polarimetric Radar[J]. Radar Science and Technology, 2005, 3(6):321–326.
5. Tan Huaiying, Guo Jianming. VHF/UHF Radar Characteristics and Applications[C]// Forum of China Radar Technologies, Nanjing, 2006:83–87.
6. Gu Ao. Development Status of Metric Wave 3D Radar[J]. Modern Weaponry, 2009(4):50–51.
7. Li Te. Development Situation of Three-Dimensional Radar at Home and Abroad[J]. 2006, 29(1):23–26.
8. Yang Xueya. Study on Array Super-Resolution and Altitude Measurement in VHF Radar[D]. Xi'an: Xidian University, 2011.
9. Zhu Wei. Study on Low-Angle Altitude Measurement in VHF Radar[D]. Xi'an: Xidian University, 2013.
10. Hu Xiaoqin, Chen Jianwen, WANG Yongliang. Research on Meter-Wave Radar Height-Finding Multipath Model[J]. Chinese Journal of Radio Science, 2008, 23(4):651–657.
11. Wu Manqing. The Development of Digital Array Radar[J]. Journal of China Academy of Electronics and Information Technology, 2006, 1(1):11–16.
12. Tang Xiaowei, Tang Jun, Peng Yingning. Parallel Algorithm for Digital Array Radar and its Implementation[J]. Information and Electronic Engineering 2009, 7(4):294–299.
13. Ding Lufei, Geng Fulu. Radar Principle[M]. Xi'an: Xidian University Press, 2003.
14. Skolnik M I. Radar Handbook[M]. McGraw-Hill, 1990.
15. Zhu Qingming. An Overview of Digital Array Radar Development[J]. 2004, 2(3):136–141.
16. Kahrilas P J, Miller T W, Lazzara S P. Digital Beamforming for Multiple Independent Transmit Beams: U.S. Patent 4,965,602[P]. 1990-10-23.
17. Xu Guangzheng, Ji Bao. Beam Control of Future Phased Antenna[C]// Tenth Annual Conference of Radar Specialty Information, 1993:238–243.
18. Garrod A. Digital Modules for Phased Array Radar[C]// 1996 IEEE International Symposium on Phased Array Systems and Technology, 1996:81–86.

19. Wu Manqing. DDS Technique and Its Application in Transmit DBF[J]. Modern Electronics, 1996(2):9–13.
20. Wu Manqing, Wang Yan. T/R DBF Phased Array Technology Based on DDS[J]. High Technology Letters, 2000, 10(8):42–44.
21. Edward M. Digital Beamforming Phased Array Transmit Antenna[C]// AP2000 Millennium Conf. on Antennas & Propagation, 2000:426–429.
22. Rudish R M, Magill E G. Direct Digital Synthesizer Driven Phased Array Antenna: U.S. Patent 5,764,187[P]. 1998-6-9.
23. Yu Hongbiao. The Study of DBF Transmitting Technology on Digital T/R Modules[J]. Modern Radar, 2001, 23(1):77–80.
24. Wu Manqing, Wang Yan, Jin Xueming. Research on Key Technology of DBF Phased Array Radar[J]. Systems Engineering and Electronics, 200l, 23(4):45–47.
25. Wu Manqing. Development and Future Design of Digital Array Radar[J]. Radar Science and Technology, 2009, 6(6):401–405.
26. Xu Haizhou, Wu Manqing. Study of the Digital Array Radar System[J]. Journal of Hefei University of Technology(Natural Science), 2008, 31(5):718–720.
27. Zhang Mingyou. Digital Array Radar and Software Defined Radar[M]. Beijing: Publishing House of Electronics Industry, 2008.
28. HU Kunjiao. Design of Digital Array Radar in Meter-Wave Band[J]. Radar Science and Technology, 2009, 6(6):422–425.
29. Chen Zengping, Zhang Yue, Bao Qinglong. Advance in Digital Array Radar and Its Key Technologies[J]. Journal of National University of Defense Technology, 2011(6):1–7.
30. Long M W. Radar Scattering Characteristics of Ground and Sea Surfaces[M]. Beijing: Science Press, 1981.
31. Blake L V. Radar Range-Performance Analysis[M]. Artech House, Inc., 1986.
32. Zhu Wei, CHEN Baixiao, Zhou Qi. Angle Measurement Method with Digital Monopulse for 2-Dimensional Digital Array Radar[J]. Systems Engineering and Electronics, 2011, 33(7):1503–1509.

Chapter 4
Height Finding Technique of Metric Wave Radar



4.1 Introduction

The main difficulties in low-elevation height finding of VHF radar are as follows:

(1) VHF radar is characterized by long wavelength, wide beam, low angle resolution and high accuracy of measurement.
(2) Pitch beam is easy to illuminate the ground, so the received beams include not only the direct wave signals reflected from the targets, but multipath signals reflected from the ground (the sea surface) because it tracks targets in low elevation, which results in lobe splitting. It causes the detection and measurement errors increase.
(3) When detecting low elevation targets, multipath reflections and strongly correlated direct waves enter the receiving beam mainlobe simultaneously.
(4) The included angle between the direct wave and multipath echoes is very small and is usually within one beamwidth, so the conventional angle measurement method by amplitude comparison becomes invalid.
(5) Reflections of undulating surfaces and irregular reflectors (such as vegetation and buildings) will result in complicated multipath reflections, such as diffuse reflections and scattering, which are difficult to model and will have a strong impact on the height-finding performance of metric wave radar.
(6) Height-finding technique of metric wave radar is not only suitable for complanate site, but also for a variety of other environments, such as rough terrain, mountain environment and some complex sites.

To avoid the impact of multipath effects on height-finding, some of the main technical approaches are given as follows:

(1) To increase the antenna size, especially the aperture in altitude, which can reduce the beamwidth of the antenna in perpendicularity, and thereby increasing the angular resolution, and allow the mainlobe "no-grounding" and reduce the sidelobe "grounding" level for higher elevation.

© National Defense Industry Press, Beijing and Springer Nature Singapore Pte Ltd. 2020

J. Wu, *Advanced Metric Wave Radar*, https://doi.org/10.1007/978-981-10-7647-3_4

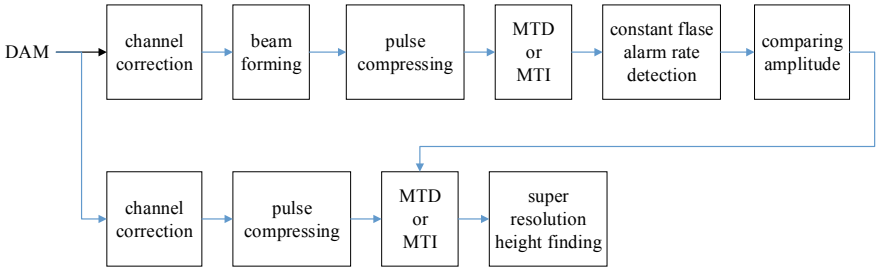


Fig. 4.1 Flow diagram of signal processing system

(2) To increase the antenna set-up height, optimize the energy distribution in airspace, reduce beam raising upwarping, enhance the target's signal-to-noise ratio in low elevation area, and adopt lobe splitting and array super-resolution technologies, to resolve the height-finding problem.

4.2 Height Finding Model of Metric Wave Radar

In respects of the height-finding of VHF radar, the whole elevation coverage can be divided into high elevation and low elevation areas. By means of controlling the "grounding" energy, the range where multipath effects can be ignored is the high elevation one, whereas is the low elevation one. In high elevation coverage, the height finding can be completed by applying conventional angular measurement methods, such as monopulse angular measurement. In low elevation coverage, some new methods must be applied to resolve the problem related with height finding due to the beam distortion generated by severe multipath effects. The implementation of the height finding in low elevation coverage is given as follows.

The signal processing of the advanced VHF radar is mainly composed of two branches, the conventional processing branch and height finding processing branch, as shown in Fig. 4.1. After channel correction, beam forming, pulse compression, filtering and conventional processing checks, the data received by Digital Array Module (DAM) will be used to transmit the plots information into the height finding branch, and then the height finding branch will transmit the data corresponding to current plots by channel correcting, pulse compressing and filtering into the height finding module.

The row antenna beam forming is executed on the echo signal received from N_y antenna elements in every row in the height finding branch, the resulting signals in N_z channels are sent to a general signal processing board to implement pulse compression and filtering. According to the detection results in the conventional branch, the multi-pulse data in the corresponding row synthetic beam are chosen, and then the multi-pulse data processed in N_z row antennas is transmitted into the

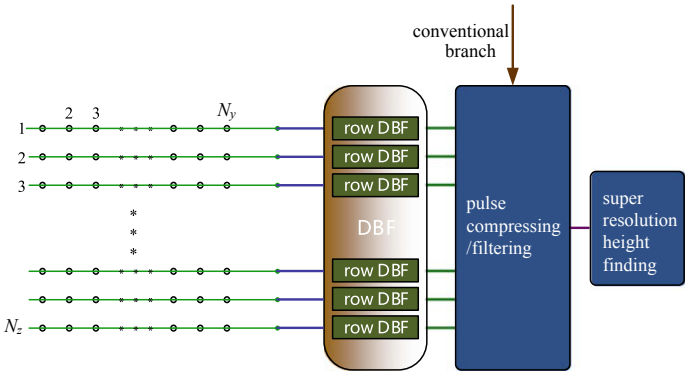


Fig. 4.2 Processing flow diagram in height-finding branch

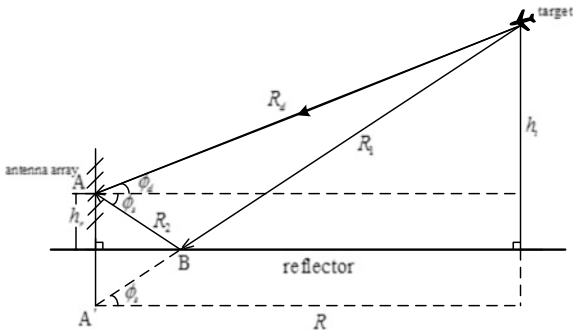


Fig. 4.3 Wave propagation schematic diagram for received signal from the array antenna

super-resolution height-finding module to complete the elevation super-resolution and height finding. The whole data flow is shown in Fig. 4.2.

4.2.1 Typical Multipath Signal Model

For Uniform Line Array (ULA) with space separation of d, which is composed of N arrays placed perpendicularly, supposing that the target echoes are incident upon ULA via direct path R_d and surface path $R_s(= R_1 + R_2)$ in consideration of smooth reflection ground, the incidence pitch angles are ϕ_d and ϕ_s respectively, as shown in Fig. 4.3. When sampling No. l, the data vector received from the array is,

$$\boldsymbol{x}_l = \boldsymbol{A}\boldsymbol{s} + \boldsymbol{n}_l = [\boldsymbol{a}(\phi_d)\boldsymbol{a}(\phi_s)] \cdot [s_d(t_l)\rho s_s(t_l)]^{\mathrm{T}} + \boldsymbol{n}_l \tag{4.1}$$

where, $\boldsymbol{A} = [\boldsymbol{a}(\phi_d)\boldsymbol{a}(\phi_s)]$ is array flow pattern, $\boldsymbol{s} = [s_d(t_l)\rho s_s(t_l)]^{\mathrm{T}}$ is the complex envelope vector of the signal. $\boldsymbol{a}(\phi_d) = \left[1, \exp(\mathrm{j}2\pi(d/\lambda)\sin(\phi_d)), \ldots, \exp(\mathrm{j}2\pi((N-1)d/\lambda)\sin(\phi_d))\right]^{\mathrm{T}}$

is steering vector of the direct wave. $\boldsymbol{a}(\phi_s) = \left[1, \exp(\mathrm{j}2\pi(d/\lambda)\sin(\phi_s)), \ldots, \exp(\mathrm{j}2\pi((N-1)d/\lambda)\sin(\phi_s))\right]^{\mathrm{T}}$ is steering vector of the corresponding specular reflection wave, ρ is corresponding reflected coefficient in reflected area, and $\boldsymbol{n}_l$ is complex gauss white noise vector disrelated with the signal.

As for the reference sub-array of array centre, the difference in distance between reflected wave and direct wave is $\Delta R = R_s - R_d$, taking notice of $s_s(t_l) = \rho\exp(-j2\pi\Delta R/\lambda)s_d(t_l)$, therefore,

$$\boldsymbol{x}(t_l) = \left[\boldsymbol{a}(\phi_d) + \rho\exp(-\mathrm{j}2\pi\Delta R/\lambda)\boldsymbol{a}(\phi_s)\right]\cdot s_d(t_l) + \boldsymbol{n}(t_l), \quad l = 1, \ldots, L \tag{4.2}$$

The receiving data for L snapshots can be indicated as,

$$\boldsymbol{X} = \boldsymbol{A}\boldsymbol{S} + \boldsymbol{N} = [\boldsymbol{a}(\phi_d)\boldsymbol{a}(\phi_s)]\cdot\begin{bmatrix} s_d(t_1) & s_d(t_2) & \cdots & s_d(t_L) \\ \rho s_s(t_1) & \rho s_s(t_1) & \cdots & \rho s_s(t_L) \end{bmatrix} + \boldsymbol{N} \tag{4.3}$$

The covariance matrix of array signal can be estimated as,

$$\hat{\boldsymbol{R}} = \mathrm{E}\left[\boldsymbol{X}\boldsymbol{X}^{\mathrm{H}}\right] = \frac{1}{L}\sum_{l=1}^{L}\boldsymbol{x}_l\boldsymbol{x}_l^{\mathrm{H}} \tag{4.4}$$

As for the schematic diagram of wave propagation in Fig. 4.3, if not specifically described, the assumptions mentioned in the full text of the multipath reflected signal are as follows,

(1) The ground reflection point of return waves received from all antenna arrays is on the same horizontal plane.
(2) The Fresnel reflection plane is an ideal flat position, which satisfies the specular reflection condition, and also the ground reflection coefficient is same (ground reflection coefficient $\rho \approx -1$ with respect to horizontal polarization wave).
(3) Object height $h_t \ll R_d$, both direct wave and reflected wave are plane wave, incident angle (ϕ_d, ϕ_s) of the echo signals received from each array element is same, and the difference in distance between the direct wave and the reflected wave received from adjacent two array element are $d\sin(\phi_d)$ and $d\sin(\phi_s)$ respectively.
(4) The antenna center height h_r and object height h_t take the altitude of ground reflected point B as reference point.

Regardless of earth curvature, the direct path R_d and reflected path R_s can be respectively indicated as,

$$R_d = \left[R^2 + (h_t - h_r)^2\right]^{1/2} \tag{4.5}$$

$$R_s = \left[R^2 + (h_t + h_r)^2\right]^{1/2} \tag{4.6}$$

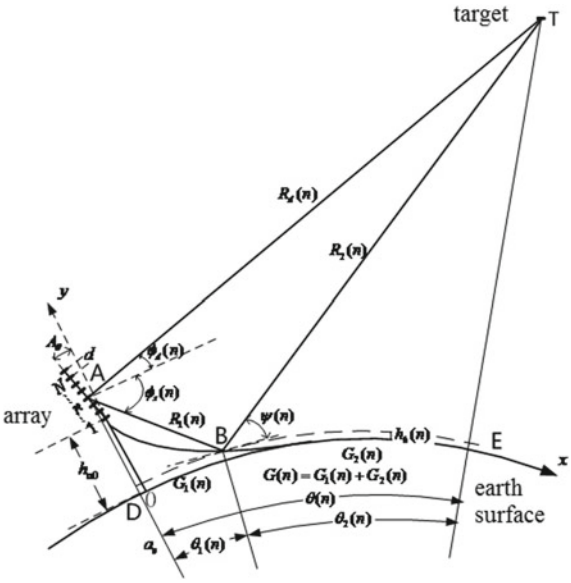


Fig. 4.4 Multipath geometry of spherical surface mode

Equations (4.5) and (4.6) can be expanded according to the binomial theorem, thanks to R $\gg h_t$ and R $\gg h_r$ typically, therefore the first two item of the extended equation can just be retained, but the high-order terms can be omitted, where,

$$\Delta R \approx R + \frac{(h_t + h_r)^2}{2R} - \left(R + \frac{(h_t - h_r)^2}{2R} \right) \approx \frac{2h_t h_r}{R} \tag{4.7}$$

The object reflection angle ϕ_s can be calculated by Eq. (4.8),

$$\phi_s = -\arctan(\tan(\phi_d) + 2h_r/R) \tag{4.8}$$

4.2.2 Multipath Signal Model Taking into Account Earth Curvature

Earth plane model can't be merely taken into account simply due to larger impact of the earth curvature on object height finding at long distance. In order to obtain a more accurate signal model, apart from the signal path bending caused by tropospheric refraction and earth curvature itself, terrain parameter etc. in reflection area must also be taken into account, as shown the spherical-surface mode in Fig. 4.4.

Considering one uniform linear array composed of isotropy obliquely placed array elements, the incidence signal is a narrowband spherical-surface wave. A curve coordinate is built based on the first antenna, where the projection of the reference

antenna at sea level is the origin of coordinate, along earth surface is axis X, and perpendicular to earth surface is axis Y. The tilt of the array face is A_θ, namely the height above sea level of the first antenna is h_{a0}, array element space is d, A is the nth array element, whose horizontal coordinate and vertical coordinate are $h_{ax}(n)$ and $h_{ay}(n)$ respectively:

$$h_{ax}(n) = -d(n-1)\sin A_\theta, \quad n = 1, 2 \ldots, N \tag{4.9}$$

$$h_{ay}(n) = h_{a0} + d(n-1)\cos A_\theta, \quad n = 1, 2 \ldots, N \tag{4.10}$$

where, point D is the projection of the nth array element on the ground; point T is the target, whose horizontal coordinate and vertical coordinate are h_{tx} and h_{ty} respectively; point E is the projection of the target on the ground/sea level; a_e is the equivalent earth radius; point B is the ground reflection center corresponding to the nth array element, and the height above sea level of the reflection point is $h_b(n)$; arc length $G(n)$ and $G_1(n)$ denote the curve length between ground projection of the nth array element and ground/sea level projection of the target, and the curve length between ground projection of the nth array element and the reflection point respectively. $\theta(n)$ and $\theta_1(n)$ denote corresponding geocentric angle respectively. Target's direct-arrival wave path of the nth array element and wave path of the ground reflecting is $R_d(n)$ and $R_s(n)$, and $R_s(n) = R_1(n) + R_2(n)$, where $R_1(n)$ and $R_2(n)$ represent the distance between point B and A, point B and T respectively. $\phi_d(n)$, $\phi_s(n)$ and $\psi(n)$ denote the incidence direct-arrival angle, reflecting incidence angle and grazing angle, corresponding to the nth array element repectively.

Base on the geometric relation in Fig. 4.4, the vertical coordinate and horizontal coordinate of the target can be figured out using direct-arrival angle ϕ,

$$h_{ty}(\phi) = \sqrt{(h_{a0} + a_e)^2 + R_d^2(1) - 2(h_{a0} + a_e)R_d(1)\cos(\pi/2 + \phi)} - a_e \tag{4.11}$$

$$h_{tx}(\phi) = G(1) = a_e\theta(1) = a_e \cos^{-1}\left[\frac{(h_{ty}(\phi) + a_e)^2 + (h_{ay}(1) + a_e)^2 - R_d^2(1)}{2(h_{ty}(\phi) + a_e)(h_{ay}(1) + a_e)}\right] \tag{4.12}$$

Therefore, the distance $G(n)$ and geocentric angle $\theta(n)$ from ground projection points of each array element to target ground projection point respectively are,

$$G(n) = h_{tx}(\phi) - h_{ax}(n), \quad n = 1, 2 \ldots, N \tag{4.13}$$

$$\theta(n) = G(n)/a_e, \quad n = 1, 2 \ldots, N \tag{4.14}$$

According to $\theta(n)$, the direct-arrival distance and direct-arrival angle between the target and each array element can be obtained:

$$R_{\mathrm{d}}(n)=\sqrt{(h_{\mathrm{ay}}(n)+a_{\mathrm{e}})^2+(h_{\mathrm{ty}}(\theta)+a_{\mathrm{e}})^2-2(h_{\mathrm{ay}}(n)+a_{\mathrm{e}})(h_{\mathrm{ty}}(\phi)+a_{\mathrm{e}})\cos\theta(n)} \tag{4.15}$$

$$\phi_{\mathrm{d}}(n)=\cos^{-1}\left[\frac{(h_{\mathrm{ay}}(n)+a_{\mathrm{e}})^2+R_{\mathrm{d}}^2(n)-(h_{\mathrm{ty}}(\phi)+a_{\mathrm{e}})^2}{2(h_{\mathrm{ay}}(n)+a_{\mathrm{e}})R_{\mathrm{d}}(n)}\right]-\frac{\pi}{2} \tag{4.16}$$

The height of reflection point is $h_{\mathrm{b}}(n)$, so the earth radius, array element height and the target height can be considered to be equivalent to,

$$\overline{a}_{\mathrm{e}}=a_{\mathrm{e}}+h_{\mathrm{b}}(n)\cong a_{\mathrm{e}} \tag{4.17}$$

$$\overline{h}_{\mathrm{ay}}(n)=h_{\mathrm{ay}}(n)-h_{\mathrm{b}}(n) \tag{4.18}$$

$$\overline{h}_{\mathrm{ty}}(\phi)=h_{\mathrm{ty}}(\phi)-h_{\mathrm{b}}(n) \tag{4.19}$$

Therefore, the curve distance from ground projection points of each array element to target ground projection point is,

$$G(n)=\overline{a}_{\mathrm{e}}\theta(n) \tag{4.20}$$

The other parameters can be resolved based on Fishback cubic equation:

$$\begin{aligned}&2G_1^3(n)-3G(n)G_1^2(n)+[G^2(n)-2\bar{a}_{\mathrm{e}}(\bar{h}_{\mathrm{ay}}(n)+\bar{h}_{\mathrm{ty}}(\phi))]G_1(n)\\&\quad+2\bar{a}_{\mathrm{e}}\bar{h}_{\mathrm{ay}}(n)G(n)=0\end{aligned} \tag{4.21}$$

The solution of the equation is,

$$G_1(n)=\frac{G(n)}{2}-p\sin\frac{\xi}{3} \tag{4.22}$$

There into,

$$p=\frac{2}{\sqrt{3}}\sqrt{\overline{a}_{\mathrm{e}}(\overline{h}_{\mathrm{ay}}(n)+\overline{h}_{\mathrm{ty}}(\phi))+(G(n)/2)^2} \tag{4.23}$$

$$\xi=\sin^{-1}\frac{2\overline{a}_{\mathrm{e}}G(n)\left(\overline{h}_{\mathrm{ty}}(\phi)-\overline{h}_{\mathrm{ay}}(n)\right)}{p^3} \tag{4.24}$$

Other parameters can be obtained by geometric relations:

$$\theta_1(n)=G_1(n)\big/\overline{a}_{\mathrm{e}} \tag{4.25}$$

$$\phi_2(n)=(G(n)-G_1(n))/\overline{a}_{\mathrm{e}}=G_2(n)/\overline{a}_{\mathrm{e}} \tag{4.26}$$

$$R_1(n) = \sqrt{\overline{a}_e^2 + (\overline{a}_e + \overline{h}_{ay}(n))^2 - 2\overline{a}_e(\overline{a}_e + \overline{h}_{ay}(n))\cos\theta_1(n)} \tag{4.27}$$

$$R_2(n) = \sqrt{\overline{a}_e^2 + (\overline{a}_e + \overline{h}_{ty}(n))^2 - 2\overline{a}_e(\overline{a}_e + \overline{h}_{ty}(n))\cos\theta_2(n)} \tag{4.28}$$

$$R_s(n) = R_1(n) + R_2(n) \tag{4.29}$$

$$\phi_s(n) = -\left(\cos^{-1}\frac{R_1^2(n) + R_d^2(n) - R_2^2(n)}{2R_1(n)R_d(n)} - \phi_d(n)\right) \tag{4.30}$$

$$\psi(n) = \left(\pi - \cos^{-1}\frac{R_1^2(n) + R_2^2(n) - R_d^2(n)}{2R_1(n)R_2(n)}\right)/2 \tag{4.31}$$

The distance difference ΔR will be easily obtained:

$$\Delta R(n) = R_1(n) + R_2(n) - R_d(n) \tag{4.32}$$

4.2.3 Reflection Coefficients

In light of the direct-arrival signals and the reflection signals within the echoes received from radar antenna, the product factors which are used to describe the differences between the two signals, contain phase difference caused by the path difference and specular reflection coefficient ρ.

For rather smooth reflection surface ($\sigma_h < \lambda/(16\sin(\psi))$), the calculation expressions for vertical polarization and horizontal polarization respectively are,

$$\rho_v = \frac{\varepsilon\sin(\phi_s) - \sqrt{\varepsilon - (\cos(\phi_s))^2}}{\varepsilon\sin(\phi_s) + \sqrt{\varepsilon - (\cos(\phi_s))^2}} \tag{4.33}$$

$$\rho_h = \frac{\sin(\phi_s) - \sqrt{\varepsilon - (\cos(\phi_s))^2}}{\sin(\phi_s) + \sqrt{\varepsilon - (\cos(\phi_s))^2}} \tag{4.34}$$

Complex permittivity ε usually can be denoted by relative permittivity ε_r and surface substance conductivity σ_e,

$$\varepsilon = \varepsilon_r - \mathrm{j}60\lambda\sigma_e \tag{4.35}$$

Electrical characteristics of some typical surface are shown in Table 4.1.

For coarse reflector $\sigma_h \geq \lambda/(16\sin(\psi))$, reflection coefficient is the product of three factors: reflection coefficient of ideal flat reflector ρ_v or ρ_h, dispersion factor D and reflection attenuation factor caused by surface coarseness γ, the relation can be expressed by,

Table 4.1 Electrical characteristics of some typical surface

Serial number	Medium	ε_r	σ_e
1	Favorable soil (wet soil)	25	0.02
2	Ordinary soil	15	0.005
3	Barren soil (dry soil)	3	0.001
4	Snow, ice	3	0.001
5	Fresh water	81	0.7
6	Brine	75	5

$$\rho = \rho_{(y,h)} D_\gamma \tag{4.36}$$

where D is defined as,

$$D \approx \frac{1}{\sqrt{1 + \frac{2r_1 r_2}{r_e r \sin(\phi_s)}}} \tag{4.37}$$

Here, $r_1 = |\mathrm{OB}|$, $r_2 = |\mathrm{BC}|$, $r = |\mathrm{OC}|$, $r_e = \frac{4}{3} \times 6370\,\mathrm{km}$ is the effective radius of the earth. The expression of γ is,

$$\gamma = \exp\left[-2\left(\frac{2\pi}{\lambda}\Delta h \sin(\phi_s)\right)^2\right] \cdot I_0\left(\left(\frac{2\pi}{\lambda}\Delta h \sin(\phi_s)\right)^2\right) \tag{4.38}$$

where $I_0(\cdot)$ is the modified Zeroth-Order Bessel Function.

Figure 4.5 gives the flat position level and reflection coefficient of the vertical polarization under various reflecting surfaces. For horizontal polarization, the reflection coefficient amplitude of low-elevation for common reflection position is above 0.9, and that phase is around 180°. Different from the slowly change for horizontal polarization, the reflection coefficient of the vertical polarization attenuates quickly as with the grazing angle.

4.2.4 Effective Reflection Area

As the electromagnetic waves radiated by the antenna project on the ground, each ground point will excite electric current, and reradiate into the space. Therefore, the ground reflected signals are actually composed of the reflected signals of ground points. However, the functions of each ground point on generating reflected signal are different, and the area made up of mostly function point is called effective reflecting surface of radar position. It is significantly important to know the location and size

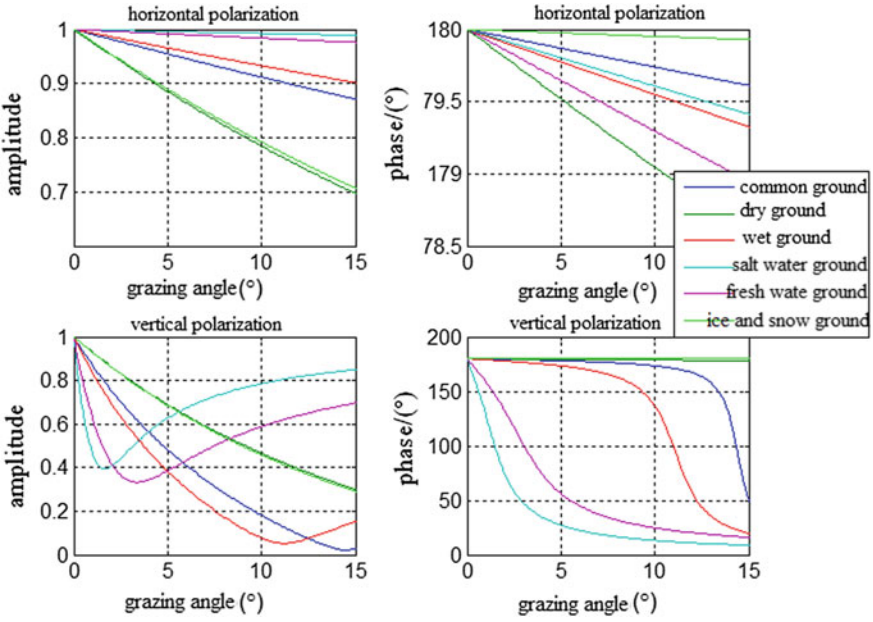


Fig. 4.5 Reflection coefficient under various positions

of effective reflecting surface for effectively and accurately measuring the radar position.

Figure 4.6 gives the effective reflection area, point B is the center of ground reflection, and we suppose the phase difference led by the wave path difference of reflected signals between other ground reflected points and point B is $\Delta\varphi$. According to the value range of $\Delta\varphi$, the resulting effective reflection areas are different, and the precondition for the effective reflection area generated in the classical first Fresnel range is $|\Delta\varphi| < \pi$. Vector diagram which analyzes the optimal value range of $\Delta\varphi$ is given as follows. As shown in Fig. 4.7, u_1 is reference vector (superposition with axis y), the included angle between vector u_2 and vector u_1 is $\Delta\varphi$. As shown in Fig. 4.7, when u_2 is in the first and second quadrant, namely $|\Delta\varphi| < 2k\pi + \pi/2$, $(k = 0, \pm 1, \ldots)$, the projection of u_2 on u_1 will be strengthened; while u_2 is in the third and fourth quadrant, namely $2k\pi + \pi/2 < |\Delta\varphi| < 2k\pi + \pi$, $(k = 0, \pm 1, \ldots)$, the projection of u_2 on u_1 is reduced. Therefore, in order to ensure that the filed strength of each reflection point is always strengthened, the value range of $\Delta\varphi$ is preferably in the first and second quadrant. Point B is corresponds to the geometric optics reflection of Point T, i.e. the filed strength of Target T is mainly determined by the ground reflection signal together with the direct signal near Point B. Therefore, the area one ($|\Delta\varphi| < \pi/2$) determined by Point B is the effective reflection area of radar position for Target T, and the phase difference will be divided into one reflection area every other $\pi/2$, thereby obtaining the area two and three shown as

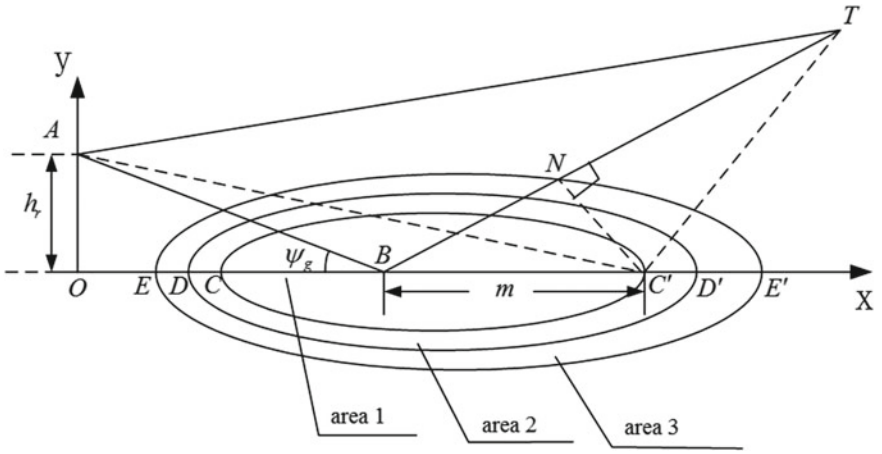


Fig. 4.6 Effective reflection area

Fig. 4.7 Vector analyzing diagram

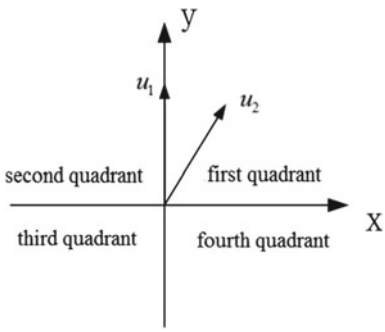


Fig. 4.6. How to obtain the location and size of the effective reflection surface will be discussed in detail as following.

As $|\Delta\varphi| < \pi/2$, wave path difference is within 1/4 wavelength, so the relations for calculating critical value,

$$\overline{AB} + \overline{BT} + \lambda/4 = \overline{AC'} + \overline{C'T} \tag{4.39}$$

Here, horizon line denotes the distance between the two points.

Make the vertical line of $\overline{BT}$ from point C' $\overline{NC'}$, and under the circumstance of height finding for metric wave radar $\overline{NT} \approx \overline{C'T}$. Suppose the distance between point C' and point B at the edge of effective reflection surface is m, and within the right-angled triangle $BC'N$, $\overline{BN} = m\cos\psi_g$, so,

$$\overline{BT} = \overline{BN} + \overline{C'T} = m\cos\psi_g + \overline{C'T} \tag{4.40}$$

Substitute Formula (4.40) into (4.39), and eliminate $\overline{C'T}$, hence

$$\overline{AB} + m\cos\psi_g + \lambda/4 = \overline{AC'} \tag{4.41}$$

Within the right-angled triangles AOC' and AOB, the results are obtained respectively,

$$\overline{AC'} = \sqrt{h_r^2 + \left(h_r \mathrm{ctg}\,\psi_g + m\right)^2} \tag{4.42}$$

$$\overline{AB} = h_r / \sin\psi_g \tag{4.43}$$

So (4.41) can be expressed as,

$$h_r / \sin\psi_g + m\cos\psi_g + \lambda/4 = \sqrt{h_r^2 + \left(h_r \mathrm{ctg}\,\psi_g + m\right)^2} \tag{4.44}$$

Square the both side of the above expression and simplify,

$$m^2 - m\frac{\lambda\cos\psi_g}{2\sin^2\psi_g} - \frac{1}{\sin^2\psi_g}\left(\frac{h_r\lambda}{2\sin\psi_g} + \frac{\lambda^2}{16}\right) = 0 \tag{4.45}$$

Two solutions m_1, m_2 can be obtained based on the formula of finding roots, that is,

$$m_{1,2} = \frac{\lambda\cos\psi_g \pm \sqrt{\lambda^2 + 8h_r\lambda\sin\psi_g}}{4\sin^2\psi_g} \tag{4.46}$$

There into,

$$m_1 = \frac{\lambda\cos\psi_g + \sqrt{\lambda^2 + 8h_r\lambda\sin\psi_g}}{4\sin^2\psi_g} > 0 \tag{4.47}$$

It indicates that point C' is farther than point B.

$$m_2 = \frac{\lambda\cos\psi_g - \sqrt{\lambda^2 + 8h_r\lambda\sin\psi_g}}{4\sin^2\psi_g} < 0 \tag{4.48}$$

It indicates that point C is closer than point B.

Get the farthest reflection region boundary $\overline{OC'}$, the nearest reflection region boundary $\overline{OC}$ of region one respectively is,

$$\overline{OC'} = \overline{OB} + m_1 = h_r \mathrm{ctg}\,\psi_g + \frac{\lambda\cos\psi_g + \sqrt{\lambda^2 + 8h_r\lambda\sin\psi_g}}{4\sin^2\psi_g} \tag{4.49}$$

$$\overline{OC} = \overline{OB} + m_2 = h_r \text{ctg}\,\psi_g + \frac{\lambda\cos\psi_g - \sqrt{\lambda^2 + 8h_r\lambda\sin\psi_g}}{4\sin^2\psi_g} \tag{4.50}$$

Usually, the size of effective reflection surface can be estimated by estimating the maximum value of first lobe pattern, thus,

$$\sin\psi_g = \lambda/(4h_r) \tag{4.51}$$

$$\cos\psi_g = \sqrt{1-\sin^2\psi_g} = \sqrt{16h_r^2 - \lambda^2}/(4h_r) \tag{4.52}$$

$$\text{ctg}\,\psi_g = \cos\psi_g/\sin\psi_g = \sqrt{16h_r^2 - \lambda^2}/\lambda \tag{4.53}$$

Substitute Formulae (4.49)–(4.51) into expression of (4.47) and (4.48), and the resulted farthest reflection region boundary and nearest reflection region boundary are shown as follows respectively,

$$\overline{OC'} = \overline{OB} + m_1 = \frac{4h_r^2}{\lambda}\left(2\sqrt{1-\left(\frac{\lambda}{4h_r}\right)^2} + \sqrt{3}\right) \tag{4.54}$$

$$\overline{OC} = \overline{OB} + m_2 = \frac{4h_r^2}{\lambda}\left(2\sqrt{1-\left(\frac{\lambda}{4h_r}\right)^2} - \sqrt{3}\right) \tag{4.55}$$

Usually, $\left(\frac{\lambda}{4h_r}\right)^2 \ll 1$ can be omitted, that is $\left(\frac{\lambda}{4h_r}\right)^2 \approx 0$, thus the farthest reflection region boundary and nearest reflection region boundary can be further simplified as,

$$\overline{OC'} \approx 14.9\frac{h_r^2}{\lambda} \tag{4.56}$$

$$\overline{OC} \approx 1.1\frac{h_r^2}{\lambda} \tag{4.57}$$

So the effective reflection region of the ground region one is,

$$\overline{OC}\sim\overline{OC'} = (1.1\sim14.9)\frac{h_r^2}{\lambda} \tag{4.58}$$

Suppose the antenna height is 8 m, and the wavelength of the metric wave radar is 2 m (namely frequency is 150 MHz), so some important parameters and the corresponding grazing angle and Rayleigh undulated height are shown in Table 4.2.

For flat radar position (less than 1 m), the sensitivity of electromagnetic wave on ground undulation is not high in metric wave band and can meet Rayleigh criterion (shown in Table 4.2). Therefore, only specular reflection should be taken into account, and the effect of diffuse reflection can be omitted.

Table 4.2 some important parameters in region one

Parameter	Range (m)	Grazing Angle (rad)	Rayleigh Undulated Height (m)
$\overline{OC}$	35.2	0.2235	1.1279
$\overline{OB}$	127.8	0.0625	4.0026
$\overline{OC'}$	476.8	0.0168	14.8817

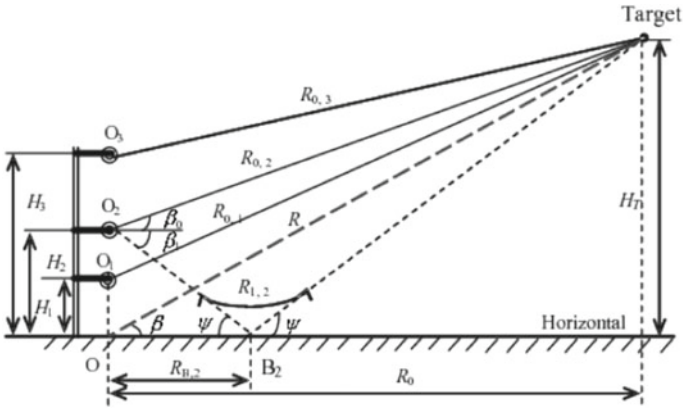


Fig. 4.8 Multipath geometrized structure diagram of plane low-altitude target

4.3 Lobe Split Method

Conventional radar should usually avoid multipath effect generated by ground reflection. There is lobe split led in metric-wave band radar due to ground reflection by width beam, which is unavoidable. The split lobe for various altitude antennas are different and keep certain phase relationship, so the low-elevation height finding method for metric-wave band radar by lobe split method is designated phase-amplitude-comparison method.

Beam sensitivity at pitch is required to be high in height finding. The beam split makes it narrow, which makes height finding for metric-wave radar possible. Single receiving antenna cannot confirm which beam the target is in, thereby several receiving antennas must be adopted. Supposing three receiving antennas at high, middle and low positions for measuring height, and the heights are H_1, H_2 and H_3 respectively, as shown in Fig. 4.8. The target's height is H_T, elevation is β, and the cross range between target and antenna is R_0, so resulted $H_T = R_0 \tan\beta \geq H_i$, $R^2 = R_0^2 + H_T^2$, the following expression can be obtained by the geometric relations,

$$R_{0,i} = \sqrt{R_0^2 + (H_T - H_i)^2} = \sqrt{R_0^2 + H_T^2 + H_i^2 - 2H_T H_i}$$

$$= \mathrm{R}\sqrt{1+\frac{H_i^2-2H_TH_i}{R^2}} \approx \mathrm{R}\left(1+\frac{H_i^2-2H_TH_i}{2R^2}\right)$$
$$\approx \mathrm{R}\left(1-\frac{H_TH_i}{R^2}\right) \approx \mathrm{R}-H_i\sin\beta, \quad i=1-3 \tag{4.59}$$

$$R_{1,i} = \sqrt{R_0^2+(H_T+H_i)^2} = \sqrt{R_0^2+H_T^2+H_i^2+2H_TH_i}$$
$$= \mathrm{R}\sqrt{1+\frac{H_i^2+2H_TH_i}{R^2}} \approx \mathrm{R}\left(1+\frac{H_i^2+2H_TH_i}{2R^2}\right)$$
$$\approx \mathrm{R}\left(1+\frac{H_TH_i}{R^2}\right) \approx \mathrm{R}+H_i\sin\beta, \quad i=1-3 \tag{4.60}$$

where, $R_{0,i}$ and $R_{1,i}$ denote direct irradiation distance and multi-path distance respectively, and the range difference is,

$$d_{R,i} = \mathrm{R_{1,i}} - \mathrm{R_{0,i}} \approx 2H_i\sin\beta \tag{4.61}$$

Considering the multipath effect, the radiation intensity at the direction of β is,

$$F_i(\beta) = F(\beta_0) + \Gamma F(\beta_\mathrm{i})\exp\left(-\mathrm{j}\frac{4\pi}{\lambda}H_i\sin\beta\right) \tag{4.62}$$

where, λ is wavelength, and $\Gamma = \rho_r\exp(j\varphi_r)$ is the reflection coefficient of the earth surface.

When incident electromagnetic wave is horizontal polarized at ground plane, $\Gamma = -1$, $\rho_r = 1, \varphi_r = \pi$. $F(\beta)$ is the pitching pattern of antenna without considering the ground reflection. For wide beam, the gain can be approximated as a constant, for example, $F(\beta_0) \approx F(\beta_1)$ near Zero-degree. If antenna altitude is far lower than target one at the far field, and $\beta_0 \approx \beta$, the expression (4.62) can be written as,

$$F_i(\beta) = F(\beta)\left[1-\exp\left(-\mathrm{j}\frac{4\pi}{\lambda}H_i\sin\beta\right)\right]$$
$$= F(\beta)2\sin\left(\frac{2\pi}{\lambda}H_i\sin\beta\right)\mathrm{e}^{j\varphi_i} \tag{4.63}$$

$$|F_i(\beta)| = F(\beta)2\left|\sin\left(\frac{2\pi}{\lambda}H_i\sin\beta\right)\right| \tag{4.64}$$

where, $\varphi_i = \frac{\pi}{2} - \frac{2\pi}{\lambda}H_i\sin\beta$. The conclusion can be easily gained according to the Formulae (4.63) and (4.64):

(1) When $\frac{2\pi}{\lambda}H_i\sin\beta = n\pi$, $|F_i(\beta)| = 0$, and beam split. When $\frac{2\pi}{\lambda}H_i\sin\beta = \frac{2n+1}{2}\pi$, $F_i(\beta)$ reaches the maximum value, so $F_i(\beta)$ is obviously related with antenna altitude and wavelength.

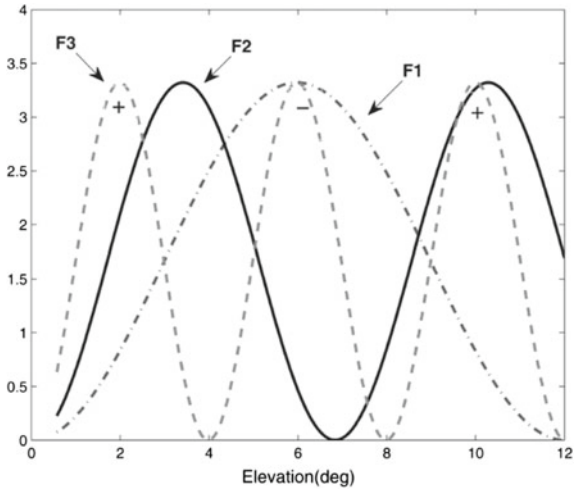


Fig. 4.9 Antenna beam pattern

(2) When the value of $\frac{2\pi}{\lambda}H_i \sin\beta$ is within section $[2n\pi, (2n+1)\pi]$ or $[(2n+1)\pi, (2n+2)\pi]$, this means $\sin\beta$ is within section $\left[\frac{n\lambda}{H_i}, \frac{(2n+1)\lambda}{2H_i}\right]$, or $\left[\frac{(2n+1)\lambda}{2H_i}, \frac{(n+1)\lambda}{H_i}\right]$, and phase $F_i(\beta)$ is equal to φ_i or $\pi+\varphi_i$. As shown in Fig. 4.9, there is 180° phase difference among split beams. In Fig. 4.9, the altitudes of antennas are 4, 7 and 12 m respectively. Positive and negative signs are used to denote reversed phase relationship among phases. As can be seen from the figure, the peaks and troughs for every beam present the trend of interleaving arrange.

Suppose the height difference among antennas is far smaller than the radar range resolution, including far field direct wave, and the baseband signal model for reflecting wave signal is

$$\begin{aligned} U_i(\beta) &= \left[\exp\left(-\mathrm{j}kR_{0,i}\right) + \Gamma\exp\left(-\mathrm{j}kR_{1,i}\right)\right]F(\beta) \\ &\approx \exp(-\mathrm{j}kR)F(\beta)\left[1-\exp(-\mathrm{j}2kH_i\sin\beta)\right] \\ &= F(\beta)2\sin(kH_i\sin\beta)\exp(-\mathrm{j}\varphi_i) \end{aligned} \tag{4.65}$$

where, wave number $k = \frac{2\pi}{\lambda}$, $\varphi_i = \frac{\pi}{2} - kH_i\sin\beta - kR$.

If $0 < kH_i\sin\beta < \pi$, for example, if $0 < \sin\beta < \frac{\lambda}{2H_i}$, and the phase difference between the two receiving antennas is

$$\varphi_{1,2} = \Phi[U_1(\beta)] - \Phi[U_2(\beta)] \approx k(H_2 - H_1)\sin\beta \tag{4.66}$$

where, $\Phi[x]$ denotes the phase of x. Seen from expression (4.66), phase difference can be used to define the information of elevation angle β. However, when

Table 4.3 Pitching code information

$C_{1,2}$	$C_{1,3}$	$C_{2,3}$	Elevation angle (°)
1	1	1	0.5–4.0
1	0	0	4.0–6.6
0	0	1	6.6–8.0
0	1	0	8.0–11.5

$\lambda = 1.7\,\text{m}$, $H_i = 12\,\text{m}$, $\beta < 4°$, it is difficult to measure angle directly due to the restriction of elevation.

For measuring target altitude effectively, firstly we should know which area the target is within the split beam or altitude range. As can be seen from expression of (4.65), the phase of receiving antenna is φ_i or $\varphi_i + \pi$, so the phase difference $\phi'_{1,2}$ between the two antennas is $\varphi_{1,2}$ or $\pm\pi + \varphi_{1,2}$. $\varphi'_{1,2}$ is a multivalue variable quantity, which can not be used to measure target elevation angle directly. However, we can confirm the approximate range of $\varphi'_{1,2}$, so

$$C_{1,2} = \text{sign}[\cos\varphi'_{1,2}] = \begin{cases} 1, & \cos(\varphi'_{1,2}) \geq 0 \\ 0, & \cos(\varphi'_{1,2}) < 0 \end{cases} \tag{4.67}$$

The phase denotation between antennas (1, 3) and (2, 3) can be obtained by the same way, which can be written as $C_{1,3}$ and $C_{2,3}$ respectively. The combination of $C_{1,2}$, $C_{2,3}$ and $C_{1,3}$ is nominated as pitching code, which can be denoted as $C_{1,2}C_{2,3}C_{3,1}$. As antenna altitudes are 4, 7 and 12 m respectively, and carrier frequency is 180 MHz, we can calculate the pitching code information by expressions (4.63) and (4.67), and the results are shown in Table 4.3. When angle $\beta > 11.5°$, pitching code is multivalue variable quantity, and we denominated the instance as "subdomain ambiguity". Here we discuss mainly the measurement methods of low-altitude target.

After determining the pitching code, the error signal can be calculated by expression (4.68) while comparing the receiving signal amplitudes from different antennas:

$$E_{12}(\beta) = \frac{|U_1(\beta)|^2 - |U_2(\beta)|^2}{|U_1(\beta)|^2 + |U_2(\beta)|^2} \tag{4.68}$$

Similarly, error signal $E_{13}(\beta)$ and $E_{23}(\beta)$ can be generated. The amplitudes of each pair of antennas can be calculated from the error curve obtained by the carrier wave, antenna altitude and pitching angle range ($0.5° < \beta < 11.5°$) before estimating the target altitude. On account of the single value of error signal within each pitching interval, it is necessary to determine which error curve it corresponds to and also which portion it corresponds to according to the pitching coding information. For example, if $\beta < 4°$, the errors signal of $E_{13}(\beta)$ can be applied. However, when β is around 4°, error signal of $E_{12}(\beta)$ is prior comparing with $E_{13}(\beta)$. The peak value of $E_{13}(\beta)$ is around 4.3°, so its sensitivity is very low. It is necessary to choose

the error curve with large slope within different pitching interval. Sometimes, height finding can be improved by combining two or three curve values.

The above height finding method is feasible under the following conditions:

(1) Same radiation pattern $\Gamma(\beta)$ for all antennas;
(2) All receiving channels are same;
(3) Set-up and tear-down ground is flat, and the reflection point and radar are at the same plane.

As mentioned above, the detail signal processing for height finding is shown as follows:

(1) The error curve is generated by simulation according to the radar frequency, antenna altitude and terrain condition;
(2) Transmit test signals to each receiving channel, and balance the impact of inconsistency in receiving channels;
(3) Calculate the pitching coding information $C_{1,2}$, $C_{2,3}$ and $C_{1,3}$ by expression (4.67), and then evaluate which pitching spacing the target is in;
(4) Compare the amplitudes of the pair receiving channels, and obtain the error signals by expression (4.68);
(5) Look up the error curve, and obtain the pitching information;
(6) Considering that the earth is a spherical surface, so the target height can be modified as,

$$H \approx R_0 \sin\beta + H_a + \frac{R_0^2}{2R_e} \tag{4.69}$$

where, R_e is the earth radius, H_a is antenna height, and R_0 the horizontal distance of the target to the antenna.

4.4 Array Super-Resolution Algorithms

An early method of evaluating the arrival angle of the space signal is the mechanical beam scanning, which is a simple air-domain expand for traditional time-domain Fourier spectral estimation. Same as Fourier restriction, the angle resolution is restricted by array physical aperture. And that is Rayleigh limit, which is impartible in one beam width. In order to break through the restriction of Rayleigh limit and improve the angle measurement accuracy, a number of research has been done on space spectral estimation since the 1970s. Among them, Multiple Signal Classification (MUSIC) algorithm proposed by Schmidt is the most outstanding, which divided the receiving data into two mutually orthogonal subspaces by mathematics decomposing on the array receiving data which are signal subspace and noise subspace. The space spectral was built by adopting the orthogonality of signal subspace and noise subspace. Since the 1980s, another space fitting algorithm emerged, and

the maximum likelihood (ML) algorithm is the most representative one, which is a typical and useful estimation in parameter estimation theory. In 1988, Ziskind applied maximum likelihood parameter estimation to direction-of-arrival estimation. Multi-dimension space-spectral searching and huge computation are required during the solving process due to the direction estimation likelihood function is nonlinear. Wax proposed an alternating projection (AP) algorithm for a seeking optimal solution of likelihood function that can reduce the computation effectively.

Array super-resolution technology deals with the airspace sampling snapshots obtained from different space locations by super-resolution algorithm, with higher angle resolution and measurement accuracy, which can break through the Rayleigh limit of array angle resolution. The technology has been applied in the direction-of-arrival estimation extensively and has expansive potential applications in height-finding of metric wave radar.

4.4.1 Spatial Smoothing MUSIC

Multiple Signal Classification (MUSIC) algorithm was proposed by Dr. R. O. Schmidt in 1979, which opened up a new era of space spectral estimation, and promoted the emergence and development of characteristic structure algorithms, becoming a symbolic algorithm for space spectral estimation. The before space spectral estimation algorithms, such as MVM, MEM, Lp and CBF, directly address covariance matrix of array receiving data. The essential idea of MUSIC is to execute eigen-decompose of covariance matrix of the output data from arbitrary arrays, and thereby to obtain the signal subspace corresponding to signal components and the noise subspace orthogonalize with signal components, and then to estimate the signal parameters, such as incidence, polarization and signal intensity, by the orthogonality of the two subspaces. It is the high resolution, estimation accuracy and stability of MUSIC algorithms in given condition that attracted many researchers to conduct in-depth research and analysis.

To execute eigenvalue decompose on covariance matrix $\hat{\boldsymbol{R}}$ of array receiving signal in expression (4.4),

$$\hat{\boldsymbol{R}} = \hat{\boldsymbol{U}}_{\mathrm{S}} \hat{\boldsymbol{\Sigma}}_{\mathrm{S}} \hat{\boldsymbol{U}}_{\mathrm{S}}^{\mathrm{H}} + \hat{\boldsymbol{U}}_{\mathrm{N}} \hat{\boldsymbol{\Sigma}}_{\mathrm{N}} \hat{\boldsymbol{U}}_{\mathrm{N}}^{\mathrm{H}} \tag{4.70}$$

In light of the property, signal subspace and noise subspace in data space are orthogonal to each other under ideal conditions, namely steering vector in the signal subspace is orthogonal to the noise subspace,

$$\boldsymbol{a}^{\mathrm{H}}(\phi) \boldsymbol{U}_{\mathrm{N}} = 0 \tag{4.71}$$

$\boldsymbol{a}(\phi)$ and $\hat{\boldsymbol{U}}_{\mathrm{N}}$ can not be orthogonalized entirely due to the presence of noise, so DOA calculation is implemented in reality by optimize searching, so

$$\phi_{MUSIC} = \arg\min_{\phi} \boldsymbol{a}^{\mathrm{H}}(\phi)\hat{\boldsymbol{U}}_{\mathrm{N}}\hat{\boldsymbol{U}}_{\mathrm{N}}^{\mathrm{H}}\boldsymbol{a}(\phi) \tag{4.72}$$

Therefore, the spectral estimation expression for MUSIC algorithm is,

$$P_{MUSIC} = \frac{1}{\boldsymbol{a}^{\mathrm{H}}(\phi)\hat{\boldsymbol{U}}_{\mathrm{N}}\hat{\boldsymbol{U}}_{\mathrm{N}}^{\mathrm{H}}\boldsymbol{a}(\phi)} \tag{4.73}$$

The MUSIC algorithm is given as following steps,

(1) To obtain data covariance matrix $\hat{\boldsymbol{R}}$ by the array receiving data, namely expression (4.70)
(2) To execute eigen-decompose on $\hat{\boldsymbol{R}}$
(3) To judge the amount of the signal source by eigenvalue of $\hat{\boldsymbol{R}}$
(4) To confirm the signal subspace $\hat{\boldsymbol{U}}_{\mathrm{S}}$ and noise subspace $\hat{\boldsymbol{U}}_{\mathrm{N}}$
(5) To search in light of signal parameter range
(6) To find the angle corresponding to the maximum value, which is the signal incidence direction

Several aspects on the above MUSIC algorithm should be given as follows,

(1) The eigenvalue of covariance matrix are obtained under non-ideal circumstance.

$$\lambda_1 > \lambda_2 > \cdots > \lambda_K > \lambda_{K+1} > \cdots > \lambda_N \tag{4.74}$$

So the methods related to signal number estimation are required for determining the signal number, such as AIC rule, MDL rule and CCT.

(2) In light of $\boldsymbol{U}_{\mathrm{S}}\boldsymbol{U}_{\mathrm{S}}^{\mathrm{H}} + \boldsymbol{U}_{\mathrm{N}}\boldsymbol{U}_{\mathrm{N}}^{\mathrm{H}} = \boldsymbol{I}$, the MUSIC algorithm shown in expression (4.73) can be simplified as follows,

$$P_{MUSIC} = \frac{1}{\boldsymbol{a}^{\mathrm{H}}(\phi)(\boldsymbol{I} - \hat{\boldsymbol{U}}_{\mathrm{S}}\hat{\boldsymbol{U}}_{\mathrm{S}}^{\mathrm{H}})\boldsymbol{a}(\phi)} \tag{4.75}$$

According to the above expression, signal parameter estimation by noise subspace is consistent with the one by signal subspace, but the two methods are different from estimation capability in practice, especially in the case where the number of signals or the estimation error is unknown.

(3) Search range for signal parameter of linear array is at $[-90°, 90°]$, while the one for planar array is at $[-180°, 180°]$. In addition, steering vector for an assured array is confirmed uniquely by array element position.
(4) When steering vector belongs to the signal subspace, $\boldsymbol{a}^{\mathrm{H}}(\phi)\hat{\boldsymbol{U}}_{\mathrm{N}}$ is a value that is approximately zero, however when it does not belong to signal subspace, $\boldsymbol{a}^{\mathrm{H}}(\phi)\hat{\boldsymbol{U}}_{\mathrm{N}}$ is a non-zero value, so a very peaky spectrum peak will be produced by the space spectrum from expression (4.73) at the direction of signal source, while it is smooth relatively at other direction.

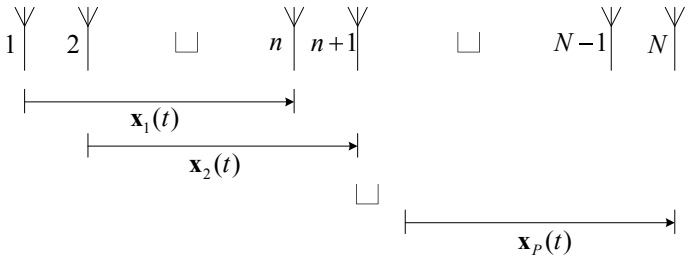


Fig. 4.10 Diagram of ULA spatial smoothing

There is another normalized form for MUSIC algorithm in expression (4.73),

$$P_{MUSIC} = \frac{\boldsymbol{a}^{\mathrm{H}}(\phi)\boldsymbol{a}(\phi)}{\boldsymbol{a}^{\mathrm{H}}(\phi)\hat{\boldsymbol{U}}_{\mathrm{N}}\hat{\boldsymbol{U}}_{\mathrm{N}}^{\mathrm{H}}\boldsymbol{a}(\phi)} \tag{4.76}$$

The expression for one-dimension steering vector in practice is given as follows,

$$\boldsymbol{a}^{\mathrm{H}}(\phi)\boldsymbol{a}(\phi) = N \tag{4.77}$$

Namely, minimum optimized search is changed as,

$$\hat{\phi}_d = \arg\min_{\phi} \frac{\boldsymbol{a}^{\mathrm{H}}(\phi)\hat{\boldsymbol{U}}_{\mathrm{N}}\hat{\boldsymbol{U}}_{\mathrm{N}}^{\mathrm{H}}\boldsymbol{a}(\phi)}{\boldsymbol{a}^{\mathrm{H}}(\phi)\boldsymbol{a}(\phi)} = \arg\min_{\phi} \mathrm{tr}\left\{\boldsymbol{P}_{\boldsymbol{a}}\hat{\boldsymbol{U}}_{\mathrm{N}}\hat{\boldsymbol{U}}_{\mathrm{N}}^{\mathrm{H}}\right\} \tag{4.78}$$

Here, $\boldsymbol{P}_{\boldsymbol{a}} = \boldsymbol{a}(\theta)\left(\boldsymbol{a}^{\mathrm{H}}(\theta)\boldsymbol{a}(\theta)\right)^{-1}\boldsymbol{a}^{\mathrm{H}}(\theta)$ is the projection matrix of $\boldsymbol{a}(\theta)$, which shows the above MUSIC algorithm is essentially the noise subspace algorithm based on one dimension search.

The above MUSIC algorithm which is based on the eigen-subspace estimation has not made decorrelation processing. Provided that the echo signal contains correlated sources, the signal subspace will diffuse into noise subspace, and the obtained orthonormality for signal subspace and noise subspace will be destroyed, which will result in a miss alarm for correlated signals, and the peak value in spatial spectrum will depart from the target's true direction, thus resulting in no exact angle estimation. Therefore, if there are correlated echo signals, super-resolution algorithms such as subspace are employed, decorrelation processing is required.

The most common decorrelation processing is spatial smoothing. The principle of forward spatial smoothing is shown in Fig. 4.10, where ULA is divided into P subarrays interleaved one another, and the number of array element for each subarray $n = N - P + 1$. The data vector for Pth subarray is,

$$\boldsymbol{x}_p(t) = [\,x_p\ x_{p+1}\ \cdots\ x_{p+n-1}\,]^{\mathrm{T}} = \boldsymbol{A}\boldsymbol{D}^{(p-1)}\boldsymbol{s}(t) + \boldsymbol{n}_p(t) \tag{4.79}$$

where, $\boldsymbol{D}$ is the diagonal rotation matrix, and it is defined as,

$$\boldsymbol{D} = \begin{bmatrix} \mathrm{e}^{\mathrm{j}\beta_1} & 0 & \cdots & 0 \\ 0 & \mathrm{e}^{\mathrm{j}\beta_2} & \cdots & 0 \\ \vdots & \vdots & \ddots & \vdots \\ 0 & 0 & \cdots & \mathrm{e}^{\mathrm{j}\beta_K} \end{bmatrix} \tag{4.80}$$

where, $\beta_k = (2\pi/\lambda)d\sin(\theta_k)$. The data covariance matrix of the subarray is,

$$\boldsymbol{R}_p = \boldsymbol{A}\boldsymbol{D}^{(p-1)}\boldsymbol{R}_s(\boldsymbol{D}^{(p-1)})^{\mathrm{H}}\boldsymbol{A}^{\mathrm{H}} + \sigma_0\boldsymbol{I} \tag{4.81}$$

where, $\boldsymbol{R}_s = \mathrm{E}[\boldsymbol{s}\boldsymbol{s}^{\mathrm{H}}]$ is the covariance matrix of signal vector $\mathbf{s}(t)$,

$$\boldsymbol{R}_s = \begin{bmatrix} \sigma_1 & \rho_{12}\sqrt{\sigma_1\sigma_2} & \cdots & \rho_{1K}\sqrt{\sigma_1\sigma_K} \\ \rho_{12}^*\sqrt{\sigma_1\sigma_2} & \sigma_2 & \cdots & \rho_{2K}\sqrt{\sigma_2\sigma_K} \\ \vdots & \vdots & \cdots & \vdots \\ \rho_{1K}^*\sqrt{\sigma_1\sigma_K} & \cdots & \cdots & \sigma_K \end{bmatrix} \tag{4.82}$$

The covariance matrix after forward spatial smoothing is,

$$\boldsymbol{R}^f = \frac{1}{P}\sum_{p=1}^{P}\boldsymbol{R}_p = \boldsymbol{A}\left(\frac{1}{P}\sum_{p=1}^{P}\boldsymbol{D}^{(p-1)}\boldsymbol{R}_s(\boldsymbol{D}^{(p-1)})^{\mathrm{H}}\right)\boldsymbol{A}^{\mathrm{H}} + \sigma_0\boldsymbol{I} \tag{4.83}$$

Suppose $\boldsymbol{Q} = \frac{1}{P}\sum_{p=1}^{P}\boldsymbol{D}^{(p-1)}\boldsymbol{R}_s(\boldsymbol{D}^{(p-1)})^{\mathrm{H}}$, for any $l, k \in [1, K]$, obviously when $l = k$, $q_{lk} = \sigma_l$; when $l \neq k$, let $\alpha = l\sin(\theta_l) - k\sin(\theta_k)$, that

$$\begin{aligned} q_{lk} &= \frac{1}{P}\sum_{p=1}^{k}\rho_{lk}\sqrt{\sigma_l\sigma_k}\mathrm{e}^{j(2\pi/\lambda)ld\sin(\theta_l)}\mathrm{e}^{-j(2\pi/\lambda)kd\sin(\theta_k)} \\ &= \frac{1}{P}\rho_{lk}\sqrt{\sigma_l\sigma_k}\sum_{p=1}^{P}\mathrm{e}^{j(2\pi/\lambda)d(p-1)\alpha} \\ &= \rho_{lk}\sqrt{\sigma_l\sigma_k}\mathrm{e}^{j(\pi/\lambda)d(P-1)d\alpha}\left(\frac{\sin(\pi/\lambda)Pd\alpha}{P\cdot\sin(\pi/\lambda)d\alpha}\right) \end{aligned} \tag{4.84}$$

Thus, the related coefficient,

$$\gamma_{lk} = \frac{q_{lk}}{\sqrt{\sigma_l\sigma_k}} = \rho_{lk}\mathrm{e}^{j(\pi/\lambda)(P-1)d\alpha}\left(\frac{\sin((\pi/\lambda)Pd\alpha)}{P\cdot\sin((\pi/\lambda)d\alpha)}\right) \tag{4.85}$$

Obviously,

$$|\gamma_{lk}| = |\rho_{lk}| \cdot \left| \left(\frac{\sin((\pi/\lambda) P d\alpha)}{P \cdot \sin((\pi/\lambda) d\alpha)} \right) \right| \leq |\rho_k| \tag{4.86}$$

Therefore, spatial smoothing technology is capable of reducing relativitity. It has been proved that if array element number of subarray $n \geq K$, and when $P \geq K$, the special smoothing technology can renew $\boldsymbol{R}^f$ to full rank.

The data vector for the pth subarray of the backward special smoothing can be defined as,

$$\boldsymbol{x}_p^b(t) = \left[x_{N-p+1} \; x_{N-p} \; \ldots \; x_{N-p-n+2} \right]^* \tag{4.87}$$

The relationship between covariance matrix $\boldsymbol{R}_p^b$ for the Pth subarray data of the backward spatial smoothing and $\boldsymbol{R}_p$ is,

$$\boldsymbol{R}_p^b = \boldsymbol{J}_n \boldsymbol{R}_p^* \boldsymbol{J}_n \tag{4.88}$$

where, $\mathbf{J}_n$ is the permutation matrix of $n \times n$, and its all anti-subdiagonal element is 1, and others are 0. Forward-and-Backward spatial smoothing is averaged by forward spatial smoothing and backward spatial smoothing.

$$\boldsymbol{R}^{fb} = \frac{1}{2P} \sum_{p=1}^{P} \left(\boldsymbol{R}_p + \boldsymbol{R}_p^b \right) \tag{4.89}$$

Compared with forward (backward) spatial smoothing, the array aperture loss of the bidirectional one is smaller. At the same time, unidirectional spatial smoothing can distinguish $\lfloor N/2 \rfloor$ coherent sources at most, while unidirectional spatial smoothing can distinguish $\lfloor 2N/3 \rfloor$ coherent sources, which can boost up the overloading capability.

4.4.2 Maximum Likelihood Algorithm

It is well-known that Bayesian methods based on statistical theory is a classical method, which is suitable for related parameter estimation problem. The Maximum Likelihood (ML) estimation is a special case of the Bayesian methods, which is the optimal Bayesian estimation under the known white noise environment. Although the parameter space requires high-dimensional nonlinear search for azimuth estimation, its estimation performance under the condition of finite snapshots and low signal-to-noise ratio shall be better than subspace algorithm (such as MUSIC and MNM) based on one-dimensional parameter search, and its application has no restriction on array geometric structure. It is more important that it can carry out azimuth estimation on space coherent source. ML is one gradual unbiased estimation that can reach the boundary of Cramer-Rao, which is characteristic with low signal-to-noise ratio

threshold and less required snapshots, and so it can obtain better results in the angle estimation of related signals.

According to the array receiving data in expression of (4.1), the unite probability density function for sample data is given as follows,

$$f(\boldsymbol{X}) = \prod_{l=1}^{L} \frac{1}{\pi \det[\sigma^2 \boldsymbol{I}]} \cdot \exp\left(-\frac{1}{\sigma^2} |\boldsymbol{x}(t_l) - \boldsymbol{A}(\boldsymbol{\theta})\boldsymbol{s}(t_l)|^2 \right) \tag{4.90}$$

The logarithm likelihood function that neglects the constants is given as an expression of (4.80),

$$L_f = -LN \log \sigma^2 - \frac{1}{\sigma^2} \sum_{l=1}^{L} |\boldsymbol{x}(t_l) - \boldsymbol{A}(\boldsymbol{\theta})\boldsymbol{s}(t_l)|^2 \tag{4.91}$$

For calculating the maximum likelihood function, it is necessary to fix $\boldsymbol{\theta}$ and $\boldsymbol{s}$ firstly. L_f will be maximized by the estimated σ^2, which can obtained from the following expression,

$$\hat{\sigma}^2 = \frac{1}{LN} \sum_{l=1}^{L} |\boldsymbol{x}(t_l) - \boldsymbol{A}(\boldsymbol{\theta})\boldsymbol{s}(t_l)|^2 \tag{4.92}$$

Substituting the above expression into the logarithm likelihood function and neglecting the constants, thus the maximum likelihood estimation can be addressed by solving the following maximum problem.

$$\max_{\boldsymbol{\theta},\boldsymbol{s}} \left\{ -LN \log \left(\frac{1}{LN} \sum_{l=1}^{L} |\boldsymbol{x}(t_l) - \boldsymbol{A}(\boldsymbol{\theta})\boldsymbol{s}(t_l)|^2 \right) \right\} \tag{4.93}$$

Although logarithmic function is monotone function, the above maximum issue is the minimum issue in expression (4.83).

$$\min_{\boldsymbol{\theta},\boldsymbol{s}} \sum_{l=1}^{L} |\boldsymbol{x}(t_l) - \boldsymbol{A}(\boldsymbol{\theta})\boldsymbol{s}(t_l)|^2 \tag{4.94}$$

The above expression is minimized by estimation of $\boldsymbol{s}$ with fixing $\boldsymbol{\theta}$, so,

$$\hat{\boldsymbol{s}}(t_l) = \left(\boldsymbol{A}^{\mathrm{H}}(\boldsymbol{\theta})\boldsymbol{A}(\boldsymbol{\theta}) \right)^{-1} \boldsymbol{A}^{\mathrm{H}}(\boldsymbol{\theta})\boldsymbol{x}(t_l) \tag{4.95}$$

where, $(\cdot)^{\mathrm{H}}$ denotes Hermite conjugate transpose. Substituting the above expression, the minimum issue given in expression (4.96) can be obtained.

$$\min_{\boldsymbol{\theta}} \sum_{l=1}^{L} \left| \boldsymbol{x}(t_l) - \boldsymbol{A}(\boldsymbol{\theta}) \left(\boldsymbol{A}^{\mathrm{H}}(\boldsymbol{\theta}) \boldsymbol{A}(\boldsymbol{\theta}) \right)^{-1} \boldsymbol{A}^{\mathrm{H}}(\boldsymbol{\theta}) \boldsymbol{x}(t_l) \right| \tag{4.96}$$

The above expression can be rewrited as,

$$\min_{\boldsymbol{\theta}} \sum_{l=1}^{L} \left| \boldsymbol{x}(t_l) - \boldsymbol{P}_{\boldsymbol{A}(\boldsymbol{\theta})} \boldsymbol{x}(t_l) \right|^2 \tag{4.97}$$

$\boldsymbol{P}_{\boldsymbol{A}(\boldsymbol{\theta})}$ is the space projection spanned by column vector of matrix $\boldsymbol{A}(\boldsymbol{\theta})$, and the expression is given as follows,

$$\boldsymbol{P}_{\boldsymbol{A}(\boldsymbol{\theta})} = \boldsymbol{A}(\boldsymbol{\theta}) \left(\boldsymbol{A}^{\mathrm{H}}(\boldsymbol{\theta}) \boldsymbol{A}(\boldsymbol{\theta}) \right)^{-1} \boldsymbol{A}^{\mathrm{H}}(\boldsymbol{\theta}) \tag{4.98}$$

So the maximum likelihood estimation of parameter $\boldsymbol{\theta}$ can be obtained by maximizing the logarithm likelihood function in expression (4.99).

$$L_f(\boldsymbol{\theta}) = \sum_{l=1}^{L} \left| \boldsymbol{P}_{\boldsymbol{A}(\boldsymbol{\theta})} \boldsymbol{x}(t_l) \right|^2 \tag{4.99}$$

Simplified by:

$$\begin{aligned} L_f(\boldsymbol{\theta}) &= \sum_{l=1}^{L} \left| \boldsymbol{P}_{\boldsymbol{A}(\boldsymbol{\theta})} \boldsymbol{x}(t_l) \right|^2 = \sum_{l=1}^{L} \boldsymbol{P}_{\boldsymbol{A}(\boldsymbol{\theta})} \boldsymbol{x}(t_l) \boldsymbol{x}^{\mathrm{H}}(t_l) \boldsymbol{P}_{\boldsymbol{A}(\boldsymbol{\theta})}^{\mathrm{H}} \\ &= \boldsymbol{P}_{\boldsymbol{A}(\boldsymbol{\theta})} \sum_{l=1}^{L} \boldsymbol{x}(t_l) \boldsymbol{x}^{\mathrm{H}}(t_l) \boldsymbol{P}_{\boldsymbol{A}(\boldsymbol{\theta})}^{\mathrm{H}} = \mathrm{tr} \left(\boldsymbol{P}_{\boldsymbol{A}(\boldsymbol{\theta})}^2 \sum_{l=1}^{L} \boldsymbol{x}(t_l) \boldsymbol{x}^{\mathrm{H}}(t_l) \right) \end{aligned} \tag{4.100}$$

Due to projection matrix $\boldsymbol{P}_{\boldsymbol{A}(\boldsymbol{\theta})} = \boldsymbol{P}_{\boldsymbol{A}(\boldsymbol{\theta})}^2$ with $\hat{\boldsymbol{R}} = \frac{1}{L} \sum_{l=1}^{L} \boldsymbol{x}(t_l) \boldsymbol{x}^{\mathrm{H}}(t_l)$, so the maximum likelihood solution of $\boldsymbol{\theta}$ is shown as expression (4.101).

$$\boldsymbol{\theta} = \arg\max \left(\mathrm{tr}(\boldsymbol{P}_{\boldsymbol{A}(\boldsymbol{\theta})} \hat{\boldsymbol{R}}) \right) \tag{4.101}$$

ML height-finding needs multi-dimensional space spectrum search, namely the two-dimensional space spectrum of direct angle and reflection angle search for their corresponding maximum in expression (4.101). Based on the geometry relationship shown in Fig. 4.4, the corresponding reflection angle can be calculated by searching direct angle, and the two-dimensional angle search can be simplified as one-dimensional angle search, which reduces the computational complexity significantly.

The flow of maximum likelihood algorithm in height-finding of metric wave radar is shown in Fig. 4.11.

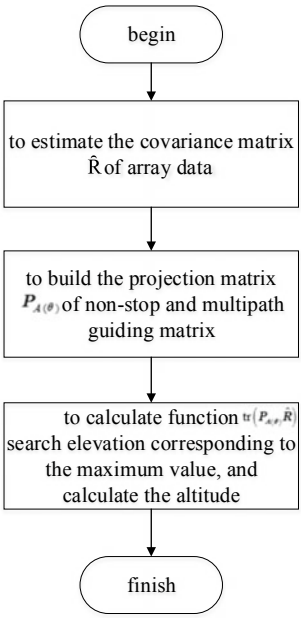

begin
to estimate the covariance matrix $\hat{R}$ of array data
to build the projection matrix $P_{A(\theta)}$ of non-stop and multipath guiding matrix
to calculate function $\mathrm{tr}(P_{A,\theta}\hat{R})$ search elevation corresponding to the maximum value, and calculate the altitude
finish

Fig. 4.11 ML algorithm height-finding flow

The maximum likelihood algorithm is a non-linear multi-dimension optimization problem, which needs multi-dimensional search for global extremum and huge computation. The two-dimensional downward one-dimensional search method based on geometry relationship reduces the computational complexity significantly, but the precondition of the simplification is that ground reflection can be considered as specular reflection. Otherwise, it will seriously affect the performance of dimension-reduction ML algorithm. Afterward, some ML simplification algorithms are given, such as genetic algorithm (GA), iteration quadratic-form maximum likelihood (IQML), bearing estimation method (MODE) and alternate projection (AP). Let's introduce the AP algorithm in the following paragraphs.

Alternate projection (AP) algorithm is a method of alternate optimization and projection matrix factorization. Alternate optimization is a simple solution method related with multi-dimensional optimization which is implemented by iterating. Every step of the iteration optimizes one parameter, while the other parameters remain the same, so the $i+1$th iteration for $\hat{\theta}_k^{(i+1)}$ can be obtained by the following one-dimensional optimization.

$$\widehat{\theta}_k^{(i+1)} = \max_{\theta_k} tr\left(\boldsymbol{P}_{[A(\widehat{\Theta}_{(k)}^{(i)}),a(\widehat{\theta}_k)]} \hat{\boldsymbol{R}} \right) \tag{4.102}$$

In the expression, $\boldsymbol{P}$ is alternate projection matrix, $\hat{\boldsymbol{R}}$ is the covariance matrix of the echo signal, and $\Theta_k^{(i+1)}$ denotes the calculated parameter vector for dimension of $\mathrm{N}-1$, so $\Theta_{(k)}^{(i)} = \left[\widehat{\theta}_1^{(i)}, \ldots, \widehat{\theta}_{k-1}^{(i)}, \widehat{\theta}_{k+1}^{(i)}, \ldots, \widehat{\theta}_K^{(i)}\right]$.

For each parameter optimization, the algorithm can find an extreme point of its likelihood function along the parameter's axis direction, while the search speed lies on the speciality in close proximity to the peak of likelihood function. The following is a brief introduction to an effective initialization.

Firstly, the DOA estimation of the first signal is given as follows,

$$\widehat{\theta}_1^{(0)} = \max_{\theta_1} tr\left(\boldsymbol{P}_{\boldsymbol{a}(\widehat{\theta}_1)}\hat{\boldsymbol{R}}\right) \tag{4.103}$$

Then, suppose the first signal source lie in $\widehat{\theta}_1^{(0)}$, the DOA estimation of the second signal is solved,

$$\widehat{\theta}_2^{(0)} = \max_{\theta_2} tr\left(\boldsymbol{P}_{[\boldsymbol{a}(\widehat{\theta}_1)^0, \boldsymbol{a}(\widehat{\theta}_2)]}\hat{\boldsymbol{R}}\right) \tag{4.104}$$

According to the above method, namely for the ith iteration while keeping the former $k-1$th calculated value unchanged, $\widehat{\theta}_k^{(0)}$ is given herein until the Kth initialization is solved. The alternate optimization method is to simplify the complicated multi-dimensional search issues into several simple one-dimensional search issues, which can reduce the optimization computation cost significantly. However, the computation cost remains rather huge, because it needs to calculate the projection matrix when solving the issues and it involves matrix inverse and multiplication operations. One upgrade expression for matrix projection will be introduced in the following paragraph as to simplify the operation of each iteratation.

Let $\boldsymbol{B}, \boldsymbol{C}$ as two arbitrary column full rank matrix with same rows, and supposing $\boldsymbol{P}_{[\boldsymbol{B},\boldsymbol{C}]}$ as subspace projection matrix spanned by the column of matrix $[\boldsymbol{B}, \boldsymbol{C}]$, so according to the inversion formula for partitioning Hermite matrix, we can obtain

$$\begin{aligned}\boldsymbol{P}_{[\boldsymbol{B},\boldsymbol{C}]} &= [\boldsymbol{B}, \boldsymbol{C}]\begin{bmatrix}\boldsymbol{B}^{\mathrm{H}}\boldsymbol{B} & \boldsymbol{B}^{\mathrm{H}}\boldsymbol{C} \\ \boldsymbol{C}^{\mathrm{H}}\boldsymbol{B} & \boldsymbol{C}^{\mathrm{H}}\boldsymbol{C}\end{bmatrix}^{-1}\begin{bmatrix}\boldsymbol{B}^{\mathrm{H}} \\ \boldsymbol{C}^{\mathrm{H}}\end{bmatrix} \\ &= \boldsymbol{P}_{\boldsymbol{B}} + (\boldsymbol{I}-\boldsymbol{P}_{\boldsymbol{B}})\boldsymbol{C}\left[\boldsymbol{C}^{\mathrm{H}}(\boldsymbol{I}-\boldsymbol{P}_{\boldsymbol{B}})\boldsymbol{C}\right]^{-1}\boldsymbol{C}^{\mathrm{H}}(\boldsymbol{I}-\boldsymbol{P}_{\boldsymbol{B}})\end{aligned} \tag{4.105}$$

Supposing $\boldsymbol{C}_{\boldsymbol{B}} = (\boldsymbol{I}-\boldsymbol{P}_{\boldsymbol{B}})\boldsymbol{C}$, the upgrade expression of the projection matrix is given by

$$\boldsymbol{P}_{[\boldsymbol{B},\boldsymbol{C}]} = \boldsymbol{P}_{\boldsymbol{B}} + \boldsymbol{P}_{\boldsymbol{C}_{\boldsymbol{B}}} \tag{4.106}$$

Substituting the above expression into (4.94) and optimizing, we can obtain

$$\boldsymbol{P}_{[\boldsymbol{A}(\widehat{\Theta}_{(k)}^{(i)}),\boldsymbol{a}(\widehat{\theta}_k)]} = \boldsymbol{P}_{\boldsymbol{A}(\widehat{\Theta}_{(k)}^{(i)})} + \boldsymbol{P}_{\boldsymbol{a}(\widehat{\theta}_k)_{\boldsymbol{A}(\widehat{\Theta}_{(k)}^{(i)})}} \tag{4.107}$$

Here, $\boldsymbol{a}(\theta_k)_{\boldsymbol{A}(\widehat{\Theta}_{(k)}^{(i)})} = \left(\boldsymbol{I} - \boldsymbol{P}_{\boldsymbol{A}(\widehat{\Theta}_{(k)}^{(i)})}\right)\boldsymbol{a}(\theta_k)$.

$$\boldsymbol{P}_{\boldsymbol{A}(\widehat{\Theta}_{(k)}^{(i)})} = \boldsymbol{A}(\widehat{\Theta}_{(k)}^{(i)})\left(\boldsymbol{A}^{\mathrm{H}}(\widehat{\Theta}_{(k)}^{(i)})\boldsymbol{A}(\widehat{\Theta}_{(k)}^{(i)})\right)^{-1}\boldsymbol{A}^{\mathrm{H}}(\widehat{\Theta}_{(k)}^{(i)}) \tag{4.108}$$

$$\boldsymbol{P}_{\boldsymbol{a}(\widehat{\theta}_i)_{\boldsymbol{A}(\widehat{\Theta}_{(k)}^{(i)})}} = \boldsymbol{a}(\widehat{\theta}_i)_{\boldsymbol{A}(\widehat{\Theta}_{(k)}^{(i)})}\left(\boldsymbol{a}^{\mathrm{H}}(\widehat{\theta}_k)_{\boldsymbol{A}(\widehat{\Theta}_{(k)}^{(i)})}\boldsymbol{a}(\widehat{\theta}_k)_{\boldsymbol{A}(\widehat{\Theta}_{(k)}^{(i)})}\right)^{-1}\boldsymbol{a}^{\boldsymbol{H}}(\widehat{\theta}_k)_{\boldsymbol{A}(\widehat{\Theta}_{(k)}^{(i)})} \tag{4.109}$$

If the constant term independent of θ_k are ignored, we can obtain

$$\widehat{\theta}_k^{(i+1)} = \max_{\theta_k} tr\left(\boldsymbol{P}_{\left[\boldsymbol{A}(\widehat{\Theta}_{(k)}^{(i)}),\boldsymbol{a}(\widehat{\theta}_k)\right]}\widehat{\boldsymbol{R}}\right) \tag{4.110}$$

Or

$$\widehat{\theta}_k^{(i+1)} = \max_{\theta_k}\left(\boldsymbol{X}^{\mathrm{H}}\boldsymbol{P}_{\left[\boldsymbol{A}(\widehat{\Theta}_{(k)}^{(i)}),\boldsymbol{a}(\widehat{\theta}_k)\right]}\boldsymbol{X}\right) \tag{4.111}$$

The AP algorithm introduced above is essentially the method that combines alternate optimization and projection matrix factorization, translating the complicated multi-dimensional search issue into several simple one-dimensional ones, which reduces the computation complexity of ML algorithm signicantly.

If there are only two signal sources, the original value should be solved firstly. Assuming that there is only one signal source θ_1, so the original value $\theta_1^{(0)}$ is

$$\theta_1^{(0)} = \arg\max_{\theta_1} tr\left(\boldsymbol{P}_{[\boldsymbol{a}(\theta_1)]}\widehat{\boldsymbol{R}}\right) \tag{4.112}$$

Then, to iterate the value of the second signal source $\theta_2^{(1)}$, and to suppose the first signal source lie in $\theta_1^{(0)}$, so

$$\theta_2^{(1)} = \arg\max_{\theta_2} tr\left(\boldsymbol{P}_{[\boldsymbol{a}(\theta_1^{(0)}),\boldsymbol{a}(\theta_2)]}\widehat{\boldsymbol{R}}\right) \tag{4.113}$$

Then, $\theta_1^{(2)}, \theta_2^{(3)}, \theta_1^{(4)}, \ldots, \theta_1^{(2p)}, \theta_2^{(2p+1)}, \theta_1^{(2p+2)}, \theta_2^{(2p+3)}$ can be solved by iterating in turn, until $\theta_1^{(2p)} = \theta_1^{(2p+2)}, \theta_2^{(2p+1)} = \theta_2^{(2p+3)}$, and the iteration digraph is given as Fig. 4.12.

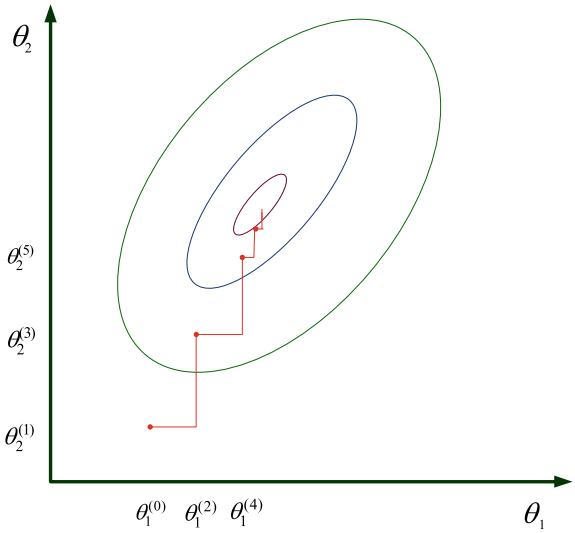


Fig. 4.12 Two-dimensional alternate projection process

4.4.3 RELAX Algorithm

RELAX algorithm proposed by Li Jian and Stoica is a so-called flabby solid algorithm for system error and environment additive noise distribution suppose hypothesis, and is also one mix spectrum used for estimating coloured noise, which only needs simple FFT operation during search.

To construct the cost function related with arrival angle $\boldsymbol{\theta}$ and signal waveform $\boldsymbol{s}(t_l), l = 1, \ldots, L$,

$$F_1(\boldsymbol{\theta}, \boldsymbol{s}(t_1), \boldsymbol{s}(t_2), \ldots, \boldsymbol{s}(t_L)) = \sum_{l=1}^{L} \left\| \boldsymbol{x}(t_l) - \sum_{k=1}^{K} \boldsymbol{a}(\theta) s_k(t_l) \right\|_F^2 \tag{4.114}$$

where, $\|\cdot\|_F$ denotes Frobenius norm.

Supposing there are $\overline{K}(1 \leq \overline{K} \leq K)$ signals, and the signal matrix $\boldsymbol{x}_k(t_l)$ is given as follows:

$$\boldsymbol{x}_k(t_l) = \boldsymbol{x}(t_l) - \sum_{i=1, i\neq k}^{\overline{K}} \boldsymbol{a}(\theta_i)\hat{s}_i(t_l) \tag{4.115}$$

where, $\{\theta_i\}_{i=1,i\neq k}^{\overline{K}}$ is the estimated value.

Therefore, the cost function of the kth signal parameter is given by,

$$F_2(\theta_k, s_k(t_1), s_k(t_2), \ldots, s_k(t_L)) = \sum_{l=1}^{L} \|\boldsymbol{x}_k(t_l) - \boldsymbol{a}(\theta_k) s_k(t_l)\|_F^2 \tag{4.116}$$

Derivation on $s_k(t_1), s_k(t_2), \ldots, s_k(t_L)$ and θ_k by F_2, the parameter estimation of minimum F_2 is given by,

$$\hat{s}_k(t_l) = \left. \frac{\boldsymbol{a}^{\mathrm{H}}(\theta_k)\boldsymbol{x}_k(t_l)}{N} \right|_{\theta_k = \hat{\theta}_k}, \quad l = 1, 2, \ldots, L \tag{4.117}$$

$$\hat{\theta}_k = \arg\max_{\theta_k} \sum_{l=1}^{L} \left| \boldsymbol{a}^{\mathrm{H}}(\theta_k)\boldsymbol{x}_k(t_l) \right|^2 \tag{4.118}$$

The estimation value of $\hat{\theta}_k$ is corresponding to the maximum of $\left|\boldsymbol{a}^{\mathrm{H}}(\theta_k)\boldsymbol{x}_k(t_l)\right|^2/N$, therefore, it can be achieved by Zero-Padding (ZP) FFT on $\boldsymbol{x}_k(t_l)$. The above angle and waveform estimation may be implemented by iteration process, and the steps are given by,

(1) Suppose $\overline{K} = 1$, here $\boldsymbol{x}_1(t_l) = \boldsymbol{x}(t_l)$, the estimation of $\hat{\theta}_1$ and $\hat{s}_1(t_l)$ can be implemented by expressions (4.118) and (4.117).
(2) Suppose $\overline{K} = 2$, substitute $\hat{\theta}_1$ and $\hat{s}_1(t_l)$ obtained by step one into expression (4.115) to calculate $\boldsymbol{x}_2(t_l)$, and similarly for $\hat{\theta}_2$ and $\hat{s}_2(t_l)$. Then, substitute $\hat{\theta}_2$ and $\hat{s}_2(t_l)$ into expression (4.115) to recalculate $\boldsymbol{x}_1(t_l)$, reestimate $\hat{\theta}_1$ and $\hat{s}_1(t_l)$ by expressions (4.118) and (4.117), and iterate repeatedly untill convergence.
(3) Suppose $\overline{K} = 3$, substitute $\hat{\theta}_1$, $\hat{s}_1(t_l)$ and $\hat{\theta}_2$, $\hat{s}_2(t_l)$ obtained by step (2) into expression (4.104) to calculate $\boldsymbol{x}_3(t_l)$, and $\hat{\theta}_3$ and $\hat{s}_3(t_l)$ may be obtained by expressions (4.118) and (4.117). Then, to calculate $\boldsymbol{x}_1(t_l)$ by $\hat{\theta}_2$, $\hat{s}_2(t_l)$ and $\hat{\theta}_3$, $\hat{s}_3(t_l)$, and to reestimate $\hat{\theta}_1$ and $\hat{s}_1(t_l)$. And then recalculate $\boldsymbol{x}_2(t_l)$ by $\hat{\theta}_1$, $\hat{s}_1(t_l)$ and $\hat{\theta}_3$, $\hat{s}_3(t_l)$, to estimate $\hat{\theta}_2$ and $\hat{s}_2(t_l)$, and iterate repeatedly untill convergence.
(4) Let $\overline{K} = 4, 5, \ldots$, untill $\bar{K} = K$; angle and waveform estimation of K incidence signal can be implemented by similar iteration process.

The zero padding FFT does not add any new information, but there will be more points after transforming the frequency domain. Therefore, the calculation amounts of zero padding still remain huge when high angle precision or two-dimensional angle estimation is required. The following interval FFT method can avoid huge calculation complexity.

The FFT for Point N on receiving array data X, direction cosine corresponding on grid is $\Delta\omega = \frac{\lambda}{Nd}$, and obviously it can not satisfy the required accuracy. Suppose that the grid corresponding to the maximum value is $\hat{\omega}$, so the maximum value should appear around $\hat{\omega}$, for about half of grid. We didn't carry on thinning search on $\left[\hat{\omega} - \Delta\omega/2, \hat{\omega} + \Delta\omega/2\right]$, but to choose three points $\left(\hat{\omega} - \Delta\omega/2, \hat{\omega}, \hat{\omega} + \Delta\omega/2\right)$, and compensate on $\boldsymbol{X}$ by phases corresponding to the three points. The direction cosine with biggest amplitude will be chosen, such as $\hat{\omega} - \Delta\omega/2$, and then choose one point each on left and right which is centered on $\hat{\omega} - \Delta\omega/2$, to rebuild three points and search for the biggest one. To choose one point as $\left(\hat{\omega} - \Delta\omega/4, \hat{\omega} + \Delta\omega/4\right)$

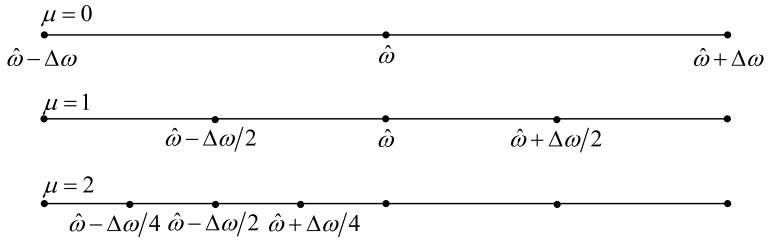


Fig. 4.13 Dichotomy search diagram

from left and right, its direction cosine interval chooses half of the former one. Such process is repeated M times until the interval $\Delta\omega/2^M$ is less than the positive number ε (very small) of the given value, and the gained direction cosine for the maximum of "one from the three" is corresponding to the target angle. The above direction cosine interval selected by per iteration is half of the last time, therefore it is also called dichotomy. The search process is shown in Fig. 4.13, and μ denotes the iteration times.

To choose the sequence length M of zero-padding FFT according to required search accuracy (grid size), and the required frequency precision is λ/Md. FFT needs $M \log_2 M$ times of complex multiplication, while the dichotomy search needs $2\log_2 (M/N) + N \log_2 (N)$ times, and for $N = 22$ and $M = 512$, the computation complexity of dichotomy is about 1/15 of zero-padding FFT search.

4.4.4 Sparse Solution Method

Sparse representation has drawn more and more developer's attention due to its application in various fields, such as blind signal separation, Inverse Synthetic Aperture Radar (ISAR), band-limited function extrapolation and spectral estimation, and also signal reconstruction and classification. It is used to show some signal features by seeking certain transformation relationships in a group of primer vectors which correspond to one sparse vector of the signal, and to carry out virtual extension on length of the original data under restriction condition, which is characterised with higher resolution and lower sidelobe.

$\boldsymbol{Y}$ is the sparse solution of $M \times L$, which is expatiated as minimum vector (element) founded in overcomplete vector (element) set which is used to represent the data matrix $\boldsymbol{X}$ received by the array. It can be expressed as the following solution issue for underdetermined equation:

$$\boldsymbol{FY} + \boldsymbol{V} = \boldsymbol{X} \tag{4.119}$$

where $\boldsymbol{F}$ is one matrix for $N \times M$ ($N \ll M$ is to ensure sparsity), Usually, to suppose $\boldsymbol{F}$ is roll full rank, which can be expressed by DFT coefficient matrix, such as $F[n,m] = (1/M)\mathrm{e}^{j2\pi nm/M}$, and also can be used with beam scanning coefficient $F[n,m] = \exp\left(j\frac{2\pi}{\lambda}(n-1)d\sin(\phi_m)\right)$, where ϕ_m denotes mth angle for the sparse solution within pitch angle. Most elements of the column vector used for sparse solution $\boldsymbol{Y}$ is 0, and $\boldsymbol{V}$ is the additive white Gaussian noise independent of $\boldsymbol{Y}$. That is, data matrix $\boldsymbol{X}$ can be represented by the minority column of $\boldsymbol{F}$. The maximum a posteriori estimation of R_s can be expressed as,

$$\begin{aligned}\boldsymbol{Y}_{MAP} &= \arg\max_{\boldsymbol{Y}} \ln f(\boldsymbol{Y}|\boldsymbol{X}) \\ &= \arg\max_{\boldsymbol{Y}} [\ln f(\boldsymbol{X}|\boldsymbol{Y}) + \ln f(\boldsymbol{Y})] \\ &= \arg\max_{\boldsymbol{Y}} [\ln f_{\boldsymbol{v}}(\boldsymbol{X} - \boldsymbol{F}\boldsymbol{Y}) + \ln f(\boldsymbol{Y})] \end{aligned} \tag{4.120}$$

Suppose element $\boldsymbol{V}$ subject to the Gaussian distribution of the zero mean, and each element is independent and identically distributed, while Probability Density Function (PDF) is $f_{V[n.l]}(u) = \frac{1}{\sqrt{2\pi}\sigma}\exp\left(-u^2/2\sigma^2\right), 1 \le n \le N, 1 \le l \le L$, where σ^2 is noise variance. Similarly, suppose $Y[m,l]$ is independent and identically distributed that satisfies the random variables of generalized Gaussian distribution,

$$f_{Y[m,l]}(u) = \frac{p}{2\sqrt[p]{2}\beta\Gamma\left(\frac{1}{p}\right)}\exp\left(-|u|^p/2\beta^p\right) \tag{4.121}$$

where, $p(\le 1)$ is used to control the form of probability density function, β is the generalized variance, $\Gamma(\cdot)$ denotes the standard Gamma function. Sparse solution can be achieved by choosing $0 < p \le 1$, which is discussed in a great many literatures.

Substituting $f_{V[n.l]}(u)$ and $f_{Y[m,l]}(u)$ obtained from above into the expression (4.120), hence

$$\boldsymbol{Y}_{MAP} = \arg\min_{\boldsymbol{Y}} J(\boldsymbol{Y}) \tag{4.122}$$

where, cost function $J(\boldsymbol{Y})$ can be expressed as,

$$J(\boldsymbol{Y}) = \left[\|\boldsymbol{F}\boldsymbol{Y} - \boldsymbol{X}\|_F^2 + \gamma E^{(p)}(\boldsymbol{Y})\right] \tag{4.123}$$

Here, $\|\cdot\|_F$ denotes F norm, $E^{(p)}(\boldsymbol{Y}) = \sum_{m=1}^{M}\|\boldsymbol{Y}[m]\|_2^p = \sum_{m=1}^{M}\left(\sum_{l=1}^{L}|Y[m,l]|^2\right)^{p/2}$ is sparsity, $\gamma = \frac{\sigma^2}{\beta^p}$ is to trade fitting-quality $\|\boldsymbol{F}\boldsymbol{Y} - \boldsymbol{X}\|_F^2$ and sparsity $E^{(p)}(\boldsymbol{Y})$. The larger γ emphasizes minimized $\Delta R = R_s - R_d$, which will generate many sparse solutions with lower non-zero elements. At the same time, the fitting-error will be increased, and vice versa.

Derivating $J(\boldsymbol{Y})$ on $\boldsymbol{Y}$ and set it to zero, and

$$\boldsymbol{Y} = \boldsymbol{W}\boldsymbol{F}_W^{\mathrm{H}}\left[\boldsymbol{F}_W\boldsymbol{F}_W^{\mathrm{H}}+\kappa\boldsymbol{I}_N\right]^{-1}\boldsymbol{X} \tag{4.124}$$

where, $(\cdot)^{\mathrm{H}}$ denotes conjugate transpose, $\boldsymbol{W} = \mathrm{diag}\left(\|\boldsymbol{Y}[m]\|_2^{1-(p/2)}\right)$, $m = 1,\ldots,M$, $\boldsymbol{F}_W \triangleq \boldsymbol{F}\boldsymbol{W}$, $\boldsymbol{Y}[m]$ denotes the m row of $\boldsymbol{Y}$, $\|\boldsymbol{Y}[m]\|_2 = \left(\sum_{l=1}^{L}|Y[m,l]|^2\right)^{1/2}$, $\kappa = \frac{p}{2}\frac{\sigma^2}{\beta^p}$, $\boldsymbol{I}_N$ is the unit matrix of $N \times N$.

The suffix μ denotes iteration number, and the iteration process for solution sparsity is,

(1) Initialize $\boldsymbol{W}_1 = \boldsymbol{I}_M$, $\boldsymbol{F}_{W_1} = \boldsymbol{F}$, for array data $\boldsymbol{X}$, the initial value $\boldsymbol{Y}_1$ for sparsity solution obtained by expression $\boldsymbol{Y} = \boldsymbol{F}^{\dagger}\boldsymbol{X}$, and calculate $c_1[m], m = 1,2,\ldots,M$ by expression (4.125).

$$c_\mu[m] = \left\|\boldsymbol{Y}_\mu[m]\right\|_2 = \left(\sum_{l=1}^{L}\left|Y_\mu[m,l]\right|^2\right)^{1/2} \tag{4.125}$$

(2) For $\mu \geq 2$, calculate $\boldsymbol{W}_{\mu+1}$ by expression (4.126),

$$\boldsymbol{W}_{\mu+1} = \mathrm{diag}\left(\left[c_\mu[m]\right]^{1-p/2}\right), \quad m = 1,\ldots,M \tag{4.126}$$

(3) Calculate $\boldsymbol{F}_{W_{\mu+1}}$ by expression (4.127),

$$\boldsymbol{F}_{W_{\mu+1}} = \boldsymbol{F}\boldsymbol{W}_{\mu+1} \tag{4.127}$$

(4) Obtain $\boldsymbol{Y}_{\mu+1}$ by expression (4.128), and calculate $c_{\mu+1}[m], m = 1,2,\ldots,M$ by expression (4.125),

$$\boldsymbol{Y}_{\mu+1} = \boldsymbol{W}_{\mu+1}\boldsymbol{F}_{W_{\mu+1}}^{\mathrm{H}}\left[\boldsymbol{F}_{W_{\mu+1}}\boldsymbol{F}_{W_{\mu+1}}^{\mathrm{H}}+\kappa\boldsymbol{I}_N\right]^{-1}\boldsymbol{X} \tag{4.128}$$

When ratio factor $\frac{\|\boldsymbol{Y}_\mu-\boldsymbol{Y}_{\mu-1}\|_F}{\|\boldsymbol{Y}_{\mu-1}\|_F} < \delta$, if it meets convergent condition, the iteration process will end, otherwise $\mu \to \mu+1$, and to repeat the iteration of steps (2)–(4). The selection of parameter p is determined by the convergence speed and sparsity of the sparse solution. It has been proved that a smaller p can make the iterative algorithm converge faster, however, but it also makes it possible for the algorithm to get into a local minimum value.

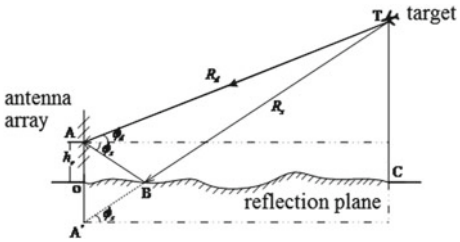


Fig. 4.14 Multipath echo diagram of flat position

4.5 Terrain Matching MUSIC/ML Algorithm

The conventional ML algorithm introduced in Sect. 4.4.2 carry out two-dimensional matching by building guiding matrix for direct wave and reflection wave, which can achieve high efficiency for high-finding in very smooth position environment. However, for certain undulate reflection position, the multipath reflection is no more a strict point-reflection mirror echo signal, so there is a certain mismatch between practical echo signals and theoretical signal model, resulting in poor high-finding performance, where one high-finding algorithm that fit for smoother position ($0 < \sigma_h < \lambda/(16\sin(\psi))$) should be adopted. Considering the reflection coefficient and the phases produced by distance difference for multipath reflection and direct wave, an accurate multipath reflection signal model should be created so as to reduce the parameter numbers to be evaluated, to improve the parameter estimation accuracy, and a maximum likelihood algorithm based on terrain parameter matching is given.

The reflector with certain undulation is given in Fig. 4.14, and the multipath echoes are still stressed on mirror reflection. Similar as expression (4.1), the echo signal $x_n(t)$ received by the nth array element is,

$$\begin{aligned} x_n(t) &= x_{\mathrm{dn}}(t) + x_{\mathrm{sn}}(t) + e(t) \\ &= s_0(t)\mathrm{e}^{-\mathrm{j}\frac{2\pi}{\lambda}R_{\mathrm{d}}(n)} + s_0(t)\rho(n)\mathrm{e}^{-\mathrm{j}\frac{2\pi}{\lambda}(R_1(n)+R_2(n))} + e(t) \end{aligned} \tag{4.129}$$

where, $x_{\mathrm{dn}}(t)$ is direct wave signal, $x_{\mathrm{sn}}(t)$ is multipath signal, $e(t)$ is white Gauss noise with variance of σ^2, output noise for each array element is counted independently, $s_0(t)$ is target's scattering signal, and $\rho(n)$ is reflection coefficient.

Similarly, the receiving model in expression (4.129) can be written in the form of vector,

$$\boldsymbol{X}(t) = (\boldsymbol{a}(\phi_d) + \boldsymbol{\rho} \odot \mathbf{K} \odot \boldsymbol{a}(\phi_s)) \cdot s_0(t) + \boldsymbol{E}(t) \tag{4.130}$$

In the expression: $\boldsymbol{X}(t)$ is the receiving data of each array element, $\boldsymbol{a}(\phi_d)$ and $\boldsymbol{a}(\phi_s)$ is the guiding vector for direct wave and multipath signal respectively, $\boldsymbol{\rho} = [\rho(1), \rho(2), \cdots, \rho(N)]^{\mathrm{T}}$ denotes the reflection coefficient vector, $\boldsymbol{K} = [\kappa_1\ \kappa_2\ \cdots\ \kappa_N]^{\mathrm{T}}$, where $\kappa_n = \exp\left[-\mathrm{j}2\pi(R_1(n) + R_2(n) - R_d(n))/\lambda\right]$ is the

phase difference caused by the multipath distance difference, which is called multipath factor, and $\boldsymbol{E}(t)$ is noise vector.

According to the derivation from Sect. 4.2.2, reflection angle and distance difference can be represented by direct wave ϕ_d and the altitude difference h_r between reflection point and array centre, and guiding vector $\boldsymbol{a}(\phi_s)$ is the function of searching elevation ϕ and terrain parameter h_r. The corresponding target elevation can be obtained by the two-dimensional spectrum searching of ML or MUSIC algorithm in elevation domain and altitude difference h_r.

Firstly, to estimate the covariance matrix $\hat{\boldsymbol{R}}$ of the array with receiving signals by expression (4.4), and gained noise subspace $\hat{\boldsymbol{U}}_{\mathrm{N}}$ with eigenvalue decomposition by expression (4.70).

Then, to construct the compound guiding vector $\boldsymbol{a}_{sum}(\phi, h_r)$

$$\boldsymbol{a}_{sum} = \boldsymbol{a}(\phi_d) + \boldsymbol{\rho} \odot \mathbf{K} \odot \boldsymbol{a}(\phi_s) \tag{4.131}$$

Finally, the estimation value $\hat{\phi}_d$ and $\hat{h}_r$ of target's elevation and reflector gap will be obtained by two-dimensional MUSIC spectrum searching on target's elevation and reflector gap.

$$\left(\hat{h}_r, \hat{\phi}_d\right) = \underset{h_r \in H, \phi \in \Phi}{\arg\max} \left(\frac{1}{\left\| \boldsymbol{a}_{sum}^{\mathrm{H}}(\phi, h_r) \hat{\boldsymbol{U}}_{\mathrm{N}} \right\|_F^2} \right) \tag{4.132}$$

where, Φ is the given elevation searching range, and H is the terrain parameter searching range.

For ML algorithm, the process is similar. Firstly, to construct the project matrix $\boldsymbol{P}_{\boldsymbol{a}_{sum}}$ of the compound guiding vector $\boldsymbol{a}_{sum}(\phi, h_r)$,

$$\boldsymbol{P}_{\boldsymbol{a}_{sum}} = \boldsymbol{a}_{sum}\left(\boldsymbol{a}_{sum}^{\mathrm{H}} \boldsymbol{a}_{sum}\right)^{-1} \boldsymbol{a}_{sum}^{\mathrm{H}} \tag{4.133}$$

Then, $\hat{\phi}_d$ and $\hat{h}_r$ will be obtained by maximizing likelihood function,

$$\left(\hat{h}_r, \hat{\phi}_d\right) = \underset{h_r \in H_r, \phi \in \Phi}{\arg\max} \left(\mathrm{tr}\left(\boldsymbol{P}_{\boldsymbol{a}_{sum}}(\phi, h_r) \hat{\boldsymbol{R}} \right) \right) \tag{4.134}$$

According to the derivation from Sect. 4.2.2, multipath distance difference $R_1(n) + R_2(n) - R_d(n)$ is determined by reflection point height $h_{\mathrm{b}}(n)$, and the horizontal coordinate $h_{\mathrm{b}x}(n)$ and vertical coordinate $h_{\mathrm{b}y}(n)$ for reflection point meet the following relationship, and at the same time, the reflection point is at the terrain curve:

$$\begin{cases} h_{\mathrm{b}x}(n) = G_1(n) + h_{\mathrm{a}x}(n), & n = 1, 2 \ldots, N \\ h_{\mathrm{b}y}(n) = h_{\mathrm{b}}(n), & n = 1, 2 \ldots, N \end{cases} \tag{4.135}$$

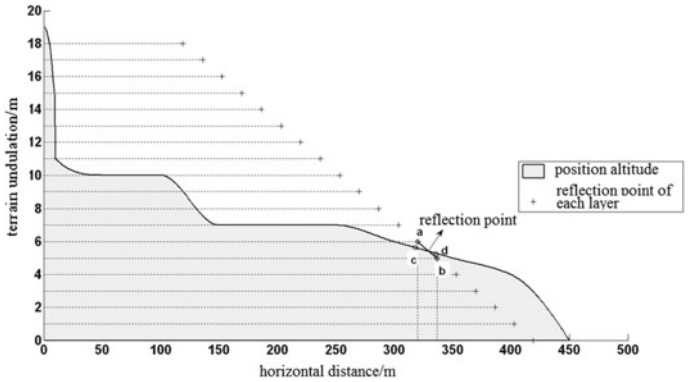


Fig. 4.15 Reflection point calculation sketch map

The terrain curve is difficult to present in math expression due to practical terrain undulation, therefore the expression (4.50) is difficult to solve. It can be solved approximately by terrain stratification and curve fitting according to Fig. 4.15, and the steps are given as followings.

Step 1: Stratify the reflection terrain based on undulations, and then according to searching elevation, account the horizontal coordinate $h_x(n, m)$ and vertical coordinate $h_y(n, m)$ of reflection point for nth array element at the layer of m. In Fig. 4.15, the horizontal axis represents the horizontal distance from the radar position, the vertical axis represents the terrain undulation height, shadow represents the radar position terrain, sidelong broken line indicates terrain stratification, and "+" indicates the reflection point of the array element at each layer.
Step 2: Lookup the nearest reflection points up and down sides in the radar position map, then take record as a and b.
Step 3: Project point "a" and "b" vertically on the map of the radar position, and the projection point "c" and "d" will be obtained. The upright dashed in Fig. 4.15 represents vertical projection. The position altitude between point "c" and "d" will be used to achieve curve fitting, and the curve "cd" will be obtained.
Step 4: The intersection of the line "ab" and the curve "cd" is approximately the reflection point of the array element on the undulation terrain.

It uses the information related with reflection position terrain and a high-accuracy three-dimensional digital elevation map, combined with in situ measurement, to search for the elevation data around the radar position coordinate and also the attributes and height of reflection surface. The undulation information of the reflection point corresponding to each elevation by inversion calculation is obtained, and create the curve for terrain undulation parameter. Through the checking table, you can find the terrain undulation parameters corresponding to each search elevation, and calculate a more accurate distance difference, and create a multipath factor κ_n to

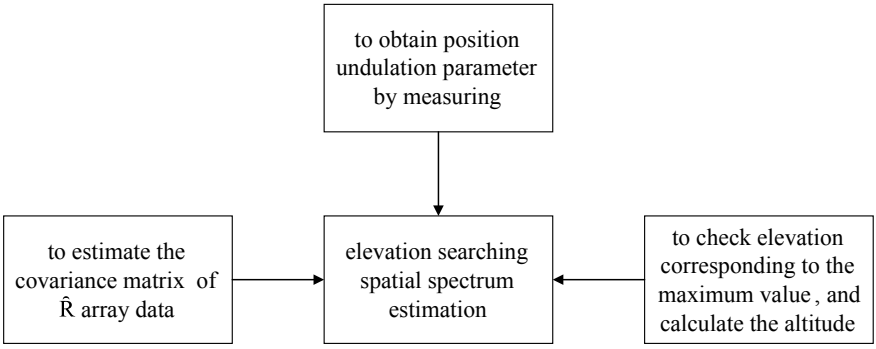

to obtain position undulation parameter by measuring
to estimate the covariance matrix of $\hat{R}$ array data
elevation searching spatial spectrum estimation
to check elevation corresponding to the maximum value , and calculate the altitude

Fig. 4.16 Process flow for terrain matching ML algorithm

achieve the matching with practical echoes signal model. The process flow is given as Fig. 4.16.

4.6 Multipath Distributed Source Model Height-Finding Method

Although multipath is considered to be an approximate analysis method produced by only one point of the terrain geometrical reflection point, it can give some reasonable results. Practically, due to some roughness on the ground, it is obviously unfeasible to present multipath phenomenon through only one image source. The area around the ground geometrical reflection point has a large effect on the signal received by the radar antenna, especially for greater ground roughness. The multipath model created in Sect. 4.2 is inapplicable, so the rough surface diffuse scattering should be built.

4.6.1 Distributed Source Model

When the rough surface of the ground is increased to the Rayleigh criteria, the signal from target to the rough surface is not the entire mirror reflection, but also scattered at other incident angle. The signals received by the radar antenna should be the sum of mirror reflection component and diffuse reflection. On unit area, the diffuse power is much less than the mirror reflection power. It can be considered that the total mirror reflection power is from the point source of target's mirror image, while the total diffuse reflection power includes the whole area between the target and the receiver. The rougher the surface, the lower the height, so diffuse reflection power is at the dominant status.

According to the Rayleigh criteria, the effective ground roughness is direct proportional to $\sigma_h \sin\psi/\lambda$, so the reflection coefficient of rough surface for diffuse reflection should also be a function of surface roughness, grazing angle and incident wavelength. The reflection coefficient of rough surface for diffuse reflection can be represented as,

$$\Gamma_{\mathrm{d}} = \Gamma \Re_{\mathrm{d}} \tag{4.136}$$

where, $\Re_{\mathrm{d}}$ is the correction coefficient of surface rough diffuse reflection that is related with surface roughness $\sigma_h \sin\psi/\lambda$, and $\Re_{\mathrm{d}}$ is the mean value scattering around 0.30–0.35 whose measured value is mostly between 0.2 and 0.4.

Considering the diffuse reflection of surface, the receiving signal corresponding to (4.129) can be represented as,

$$\begin{aligned} x_n(t) &= x_{\mathrm{dn}}(t) + x_{\mathrm{sn}}(t) + n(t) \\ &= s_0(t)\mathrm{e}^{-\mathrm{j}2\pi R_{\mathrm{d}}(n)/\lambda} + \iint\limits_{\Omega} \Gamma_{dk}(n)\mathrm{e}^{-\mathrm{j}2\pi R_{sk}(n)/\lambda} s(k,t) + e(t) \end{aligned} \tag{4.137}$$

where, the second item is the integral of the diffuse reflection within effective surface reflection area Ω, $R_{sk}(n)$ denotes wave-path of kth diffuse reflection signal within reflection area Ω, $\Gamma_{dk}(n)$ is surface reflection coefficient of kth reflection signal, and $s(k,t)$ is kth reflection signal.

For the convenience of analysis, only one-dimensional reflection area is considered, so the multipath distributing source can be represented as,

$$\begin{aligned} x_{sn}(t) &= \int_{R\mathrm{min}^{(n)}}^{R\mathrm{max}^{(n)}} \Gamma_{dk}(n)\mathrm{e}^{-\mathrm{j}2\pi R_{sk}(n)/\lambda} s(k,t)\mathrm{d}R_{sk}(n) \\ &= \Gamma(n)s_0(t) \int_{R\mathrm{min}_{(n)}}^{R\mathrm{max}^{(n)}} \mathrm{e}^{-\mathrm{j}2\pi R_{sk}(n)/\lambda} g(k)\mathrm{d}R_{sk}(n) \end{aligned} \tag{4.138}$$

where, $R_{\mathrm{min}}(n)$ and $R_{\mathrm{max}}(n)$ are the minimum and maximum multipath wave-path within 1st Fresnel zone of the nth array element, $\Gamma_{dk}(n)s(k,t) = \Gamma(n)g(k)s_0(t)$, $g(k)$ is the amplitude of kth reflection signal. When $g(k)$ is a function of δ, the multipath reflected signal is obviously the signal source of the point target.

It is difficult to determine the $R_{\mathrm{min}}(n)$ and $R_{\mathrm{max}}(n)$ in expression (4.138), so substitution is the simple distributed signal source mathematic model, and to converse the integral in expression (4.138):

$$x_{sn}(t) = \Gamma(n)s_0(t)\int_{R\min_{(n)}}^{R\max^{(n)}} \mathrm{e}^{-\mathrm{j}2\pi R_{sk}(n)/\lambda} g(k)\mathrm{d}R_{sk}(n)$$
$$= \Gamma(n)s_0(t)\int_{-\pi}^{\pi} \mathrm{e}^{-\mathrm{j}2\pi d(n-1)\sin\beta/\lambda} g(\beta-\theta_\mathrm{i})\mathrm{d}\beta \tag{4.139}$$

where, θ_i is the direction of arrival of the distributed multipath signal centre, $g(\beta-\theta_\mathrm{i})$ is the angle signal distributing function, and when $g(\beta-\theta_\mathrm{i})$ is the function of $\delta(\beta-\theta_\mathrm{i})$, the multipath reflection signal is the signal source of point target.

Write the receiving signal model in expression (4.137) to vector form:

$$\boldsymbol{X}(t) = (\boldsymbol{A}_\mathrm{d} + \boldsymbol{\Gamma} \odot \boldsymbol{A}_s)s_0(t) + \boldsymbol{E}(t) \tag{4.140}$$

where,

$$\boldsymbol{A}_\mathrm{d} = \left[1, \mathrm{e}^{-\mathrm{j}2\pi d\sin\phi_\mathrm{d}/\lambda}, \ldots, \mathrm{e}^{-\mathrm{j}2\pi d(N-1)\sin\phi_\mathrm{d}/\lambda}\right]^\mathrm{T} \tag{4.141}$$

$$\mathbf{A}_s = \int_{-\pi}^{\pi} \mathbf{a}(\beta)g(\beta-\phi_s)\mathrm{d}\beta \tag{4.142}$$

$$\boldsymbol{a}(\beta) = \left[1, \mathrm{e}^{-\mathrm{j}2\pi d\sin\beta/\lambda}, \ldots, \mathrm{e}^{-\mathrm{j}2\pi d(N-1)\sin\beta/\lambda}\right]^\mathrm{T} \tag{4.143}$$

In fact, the surface multipath signal mode is difficult to determine, so only the mathematical expression for angle signal distributed function subjected to Gaussian distribution is given here. When the angle signal distributing function subjects to Gaussian distribution,

$$g(\beta-\phi_s) = \frac{1}{\sqrt{2\pi\,\Delta^2}}\exp\left(-\frac{(\beta-\phi_s)^2}{2\Delta^2}\right) \tag{4.144}$$

Substitute the above expression into expression (4.143),

$$\boldsymbol{A}_s = \left[1, \mathrm{e}^{-\Delta^2/2}\mathrm{e}^{-\mathrm{j}2\pi d\sin\phi_s/\lambda}, \ldots, \mathrm{e}^{-(N-1)^2\Delta^2/2}\mathrm{e}^{-\mathrm{j}2\pi d(N-1)\sin\phi_s/\lambda}\right]^\mathrm{T} \tag{4.145}$$

When $\Delta = 0$, $\boldsymbol{A}_s = \boldsymbol{a}(\phi_s)$.

Substitute (4.144) into expression (4.142),

$$[\boldsymbol{A}_s]_m = \int_{-\pi/2}^{\pi/2} \exp(\mathrm{j}\kappa dn\sin(\beta))\frac{1}{\sqrt{2\pi}\,\Delta}\exp\left(-\frac{(\beta-\phi_s)^2}{2\Delta^2}\right)\mathrm{d}\beta \tag{4.146}$$

Approximate the expression (4.146),

$$[\boldsymbol{A}_s]_m \approx \exp(\mathrm{j}\kappa dn\sin(\phi_s)) \cdot \int_{-\pi/2}^{\pi/2} \exp\left(\mathrm{j}\kappa dn\tilde{\beta}\cos(\phi_s)\right)\frac{1}{\sqrt{2\pi}\,\Delta}\exp\left(-\frac{\tilde{\beta}^2}{2\Delta^2}\right)\mathrm{d}\tilde{\beta}$$
$$= \exp(\mathrm{j}\kappa dn\sin(\phi_s)) \cdot [\boldsymbol{h}]_n \tag{4.147}$$

where,

$$[\boldsymbol{h}]_n = \int_{-\pi/2}^{\pi/2} \exp\left(\mathrm{j}\kappa dn\tilde{\beta}\cos(\phi_s)\right)\frac{1}{\sqrt{2\pi}\,\Delta}\exp\left(-\frac{\tilde{\beta}^2}{2\Delta^2}\right)\mathrm{d}\tilde{\beta} \tag{4.148}$$

According to integral formula,

$$\int_{-\infty}^{\infty} \exp\left(-f^2x^2\right)\exp(jl(x+v))\mathrm{dx} = \sqrt{\pi}\exp\left(-\frac{l^2}{4f^2}\right)\frac{\exp(jlv)}{f} \tag{4.149}$$

The expression (4.147) can get a closed expression,

$$[\boldsymbol{A}_s]_n \approx \exp(\mathrm{j}\kappa dn\sin(\phi_s))\exp\left(-(\kappa d)^2n^2\cos^2(\phi_s)\Delta^2/2\right) \tag{4.150}$$

Therefore, expression (4.142) can be written as,

$$\boldsymbol{A}_s \approx \boldsymbol{a}(\phi_s) \odot \boldsymbol{h} \tag{4.151}$$

where, $\odot$ denotes Schur-Hadamard product, $[\boldsymbol{h}]_n = \exp\left(-(\kappa d)^2n^2\cos^2(\phi_s)\Delta^2/2\right)$.

4.6.2 Multi-dimensional Alternate Projection ML

Actually, due to complex surface reflections, it is not possible to determine which distribution the multipath signal angle function subject to and what the distribution parameters of angle signals distribution function is. Take Gaussian distribution as example, there are three unknown parameters: ϕ_d, ϕ_s and Δ. If three-dimensional searching is used, the computation is too complex, so a simple multi-dimensional alternate projection algorithm is given here. The algorithm flows are given as follows,

(1) Suppose that multipath signals are point signal sources, $\hat{\phi}_\mathrm{d}$ and $\hat{\phi}_s$ can be calculated using generalized constrained MUSIC algorithm. It will be used as the initial value for subsequent iterations.

(2) Search Δ initial value using compound guiding vector ML algorithm, and fix up $\hat{\phi}_{\mathrm{d}}$ and $\hat{\phi}_s$, then estimate Δ.

$$\hat{\Delta} = \underset{\Delta \in \Delta_{\overline{\text{range}}}}{\arg\max} \left(\mathrm{tr} \left\{ \boldsymbol{A}_{\mathrm{sum}} \left[\boldsymbol{A}_{\mathrm{sum}}^{\mathrm{H}} \boldsymbol{A}_{\mathrm{sum}} \right]^{-1} \boldsymbol{A}_{\mathrm{sum}}^{\mathrm{H}} \boldsymbol{R} \right\} \right) \tag{4.152}$$

where, $\boldsymbol{A}_{\mathrm{sum}} = \boldsymbol{A}_{\mathrm{d}} + \boldsymbol{\Gamma} \odot \boldsymbol{A}_s$ is compound guiding vector, $\boldsymbol{A}_{\mathrm{d}} = \left[1, \mathrm{e}^{-\mathrm{j}2\pi d \sin \hat{\phi}_{\mathrm{d}}/\lambda}, \ldots, \mathrm{e}^{-\mathrm{j}2\pi d(N-1) \sin \hat{\phi}_{\mathrm{d}}/\lambda} \right]^{\mathrm{T}}$ is direct wave guiding vector, $\boldsymbol{A}_s = \left[1, \mathrm{e}^{-\Delta^2/2} \mathrm{e}^{-\mathrm{j}2\pi d \sin \hat{\phi}_s/\lambda}, \ldots, \mathrm{e}^{-(N-1)^2\Delta^2/2} \mathrm{e}^{-\mathrm{j}2\pi d(N-1) \sin \hat{\phi}_s/\lambda} \right]^{\mathrm{T}}$ is multipath guiding vector, Δ_{range} is the searching range of Δ.

(3) Fix $\hat{\phi}_s$ and $\hat{\Delta}$, and estimate the direct wave DOA.

$$\hat{\phi}_{\mathrm{d}} = \underset{\phi_{\mathrm{d}} \in \Phi}{\arg\max} \left(\mathrm{tr} \left\{ \boldsymbol{A}_{\mathrm{sum}} \left[\boldsymbol{A}_{\mathrm{sum}}^{\mathrm{H}} \boldsymbol{A}_{\mathrm{sum}} \right]^{-1} \boldsymbol{A}_{\mathrm{sum}}^{\mathrm{H}} \boldsymbol{R} \right\} \right) \tag{4.153}$$

where, Φ is the searching range of ϕ_{d}.

(4) Repeat step (2), step (3) and step (4) until the $\hat{\phi}_{\mathrm{d}}$ is unchanged.

4.7 Height-Finding Based on Self-Adaptive Beam Forming

For height-finding on rough position, after long-term analysis of the meterwave radar data, a meterwave radar height-finding algorithm based on adaptive beam forming is proposed, which can solve the height-finding problem of the rough position.

Adaptive beamforming is a airspace filtering technology that can restrain space interference and noise, and increase useful signal energy effectively. It has been extensively used. Adaptive beamforming method has been introduced into the meterwave radar height-finding, because radar height-finding branch has passed through traveling wave formation, pulse compression and filter processing, and target's echos are characterized with higher signal noise ratio (SNR). Target direct echo and reflection multipath echo are considered to be sidelobe jamming in two unknown direction, and two nulling generated during the search which correspond to the adaptive beam of current search height and its multipath reflection angel, and also carry out beamforming on the array data. If beam nulling only eliminates the echo, then the energy after beamforming here is minimal, and the angle corresponding to the nulling is the target elevation.

In height-finding module, it is necessary to realize one-dimensional angle searching. Setting current searching elevation as ϕ_i, the reflection angle can be calculated by direct angle with geometrical relationship, as shown in expression (4.30).

Set direct wave as unit signal, and set ϕ_i and ϕ_j as target direct wave angle and reflection wave elevation respectively, and combine the expression (4.140), the covariance matrix of echoes received by the array is given as follows,

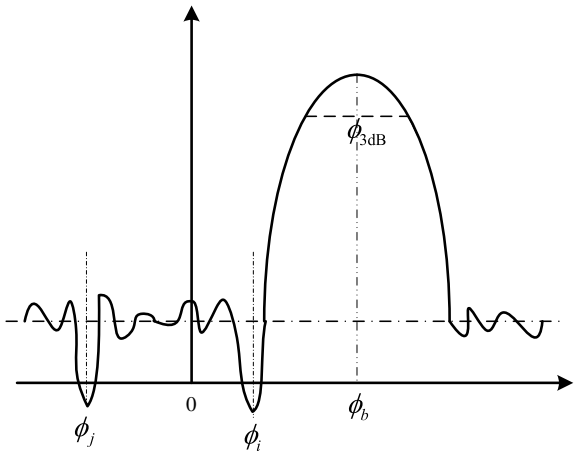


Fig. 4.17 Adaptive beamforming diagram

$$\boldsymbol{R}_i = \left(\boldsymbol{A}_{\mathrm{d}}(\phi_i)\boldsymbol{A}_{\mathrm{d}}^{\mathrm{H}}(\phi_i) + \left(\boldsymbol{\Gamma} \odot \boldsymbol{A}_{\mathrm{s}}(\phi_j)\right)\left(\boldsymbol{\Gamma} \odot \boldsymbol{A}_{\mathrm{s}}(\phi_j)\right)^{\mathrm{H}}\right) \tag{4.154}$$

Calculate the array weight vector $\boldsymbol{W}_i$ and eliminate the jamming of ϕ_i and ϕ_j by the beam whose direction is ϕ_b, that is to calculate the criteria resolution based on the minimum noise difference:

$$\boldsymbol{W}_i = \underset{\boldsymbol{W}^{\mathrm{H}}a(\phi_b)=1}{\arg\min}\left(\frac{1}{2}\boldsymbol{W}^{\mathrm{H}}\boldsymbol{R}_i\boldsymbol{W}\right) \tag{4.155}$$

Here, Lagrange multiplier method is used to obtain,

$$\boldsymbol{W}_i = \mu\boldsymbol{R}_i^{-1}\boldsymbol{a}(\phi_b) \tag{4.156}$$

The adaptive beamforming coefficient $\boldsymbol{W}_i$ obtained in this way will form nulling in place of ϕ_i and ϕ_j, as shown in Fig. 4.17,

In order to overcome beam distortion and sidelobe level increase, covariance matrix will generally be used for diagonal loading technology, namely,

$$\boldsymbol{R}_i = \left(\boldsymbol{A}_{\mathrm{d}}(\phi_i)\boldsymbol{A}_{\mathrm{d}}^{\mathrm{H}}(\phi_i) + \left(\boldsymbol{\Gamma} \odot \boldsymbol{A}_{\mathrm{s}}(\phi_j)\right)\left(\boldsymbol{\Gamma} \odot \boldsymbol{A}_{\mathrm{s}}(\phi_j)\right)^{\mathrm{H}}\right) + \varepsilon \cdot \mathrm{eye}(N) \tag{4.157}$$

where, eye(N) is the unit matrix of $N \times N$, and ε is the smallest positive constant.

Three issues should be settled during the algorithm implementation.

(1) Selection of main beamforming direction

Consider two aspects of the main beamforming selection:

(a) Close the "jamming" angle as much as possible and ensure a larger interference-to-noise ratio for cancelling.

(b) Keep away from the nulling to avoid the problems of waveform direction offset and distortion.

Combine theoretical simulations and measured data, and it is relatively appropriate to choose $\phi_b \in (\phi_i + 1/2 \cdot \phi_{3\text{dB}}, \phi_i + \phi_{3\text{dB}})$, where $\phi_{3\text{dB}}$ is 3 dB beamwidth.

(2) Calculate adaptive beamforming coefficient off-line

During the elevation searching, if it is necessary to calculate the adaptive beamforming coefficient in real time, the coefficient of each searching angle needs to be calculated independently. Due to the complex covariance matrix operation and matrix inversion, the requirements on hardware resource are higher. The adaptive beamforming coefficient is generated off-line, namely to calculate the adaptive beamforming coefficient corresponding to each searching angle beforehand, including amplitude weighted, and then import it into the SDRAM of height-finding hardware processing platform. The relevant coefficient will be folded in for beamforming during angle searching. The relevant coefficient produced in advance for each searching angle by computer within interested elevation range will reduce the amount of computation, reduce resource requirements and save processing time significantly.

(3) Combine with position peculiarity

The height-finding algorithm based on adaptive beamforming is suitable for both flat position and rough position. Therefore, for positions where the tilt position is inclined at a certain angle and the is likely to cause severe diffuse reflection, it can improve the algorithm stability and height-finding accuracy by combining with position peculiarity.

The height-finding processing based on adaptive beamforming is given in Fig. 4.18. All data generated by beam from each row is firstly calculated as the array covariance matrix, then the beamforming coefficient corresponding to searching elevation is read on the SDRAM of signal processing board, and finally the height of the target is calculated according to the searching elevation corresponding to the minimum of beamforming energy.

4.8 Conclusion

Due to advantages in anti-stealth targets and counter anti radiation missile (ARM) of meterwave digital array radar, it plays more and more important roles in modern radar network. However, since it is easier to be affected by surface reflection and leads to wavebeam splitting because of its longer wavelength, width wavebeam, especially when measuring low-angle targets, the waveform irradiates on the ground, intensive surface reflection and serious target's multipath phenomena, meterwave radar have poor height-finding performance and even completely failure. Apart from electric wave refraction effect caused by the inhomogeneity of the low-layer atmosphere, the received signals also include multipath interference effect by the mirror reflection

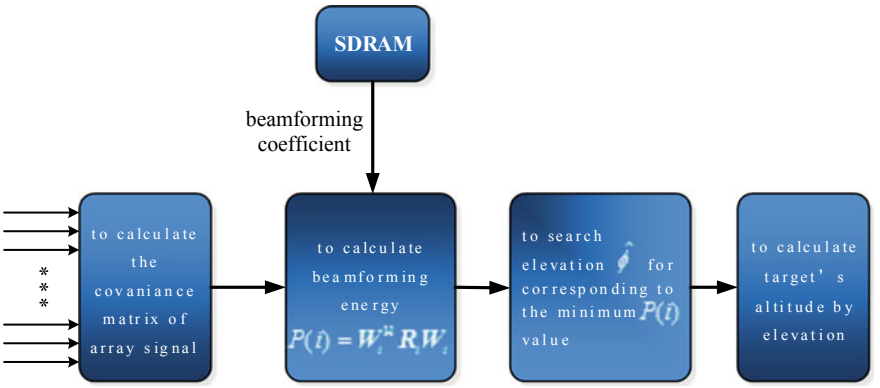

SDRAM
beamforming coefficient
to calculate the covaniance matrix of array signal
to calculate beamforming energy
$P(i) = W_i^H R W_i$
to search elevation $\hat{\phi}$ for corresponding to the minimum $P(i)$ value
to calculate target's altitude by elevation

Fig. 4.18 Height-finding processing based on ADBF

and diffuse scattering of surface. Therefore, it is an urgent and critical key issue to improve the angle-measuring accuracy of meterwave digital array radar.

This chapter carries out angle resolution and height-finding on the low-elevation target direct wave and multipath reflection echoes received by radar by reasonable algorithm design. Firstly, the height-finding principle and signal model of multipath reflection under condition of flat and spherical model are given. Then, some classical height-finding methods of meterwave radar are introduced, including beam splitting height-finding methods and common array super-resolution height-finding algorithm. The multipath echoes signal modeling method is given for actual undulation and complicated reflection position, and super-resolution height-finding method based on terrain matching, multi-dimensional alternate projection ML algorithm and height-finding method based on adaptive beamforming are proposed, which effectively solve the challenges of high resolution, high measurement accuracy and position applicability that meterwave radar faces.

Bibliography

1. Barton D K. Low-Angle Radar Tracking [J]. Proceedings of the IEEE, 1974, 62(6):587–704.
2. White W D. Low-Angle Radar Tracking in the Presence of Multipath [J]. IEEE Trans on Aerospace and Electronic Systems, 1974, 10(6):835–852.
3. Giuli D, Tiberio R. A Modified Monopulse Technique for Radar Tracking with Low-Angle Multipath [J]. IEEE Trans on Aerospace and Electronic Systems, 1975, 11(5):741–748.
4. Mrstik A V, Smith P G. Multipath Limitations on Low-Angle Radar Tracking [J]. IEEE Trans on Aerospace and Electronic Systems, 1978, 14(1):85–102.
5. Reilly J, Litva J, Bauman P. New Angle-of-Arrival Estimator: Comparative Evaluation Applied to the Low-Angle Tracking Problem [J]. IEE Proceedings F, Communications, Radar and Signal Processing, 1988, 135(5):408–420.
6. Sword C K, Simaan M, Kamen E W. Multiple Target Angle Tracking Using Sensor Array Outputs [J]. IEEE Trans on Aerospace and Electronic Systems, 1990, 26(2):367–373.

7. Bruder J A, Saffold J A. Multipath Effects on Low-Angle Tracking at Millimeter-Wave Frequencies [J]. IEEE Proceedings F, 1991, 138(2):172–184.
8. Zoltowski M D, Lee T-S. Maximum Likelihood Based Sensor Array Signal Processing in the Beamspace Domain for Low Angle Radar Tracking [J]. IEEE Trans on Signal Processing, 1991, 39(3):656–671.
9. Rahamim D, Tabrikian J, Shavit R. Source Localization Using Vector Sensor Array in a Multipath Environment [J]. IEEE Trans on Signal Processing, 2004, 52(11):3096–3103.
10. Hurtado M, Nehorai A. Performance Analysis of Passive Low-Grazing-Angle Source Localization in Maritime Environments Using Vector Sensors [J]. IEEE Trans on Aerospace and Electronic Systems, 2007, 43(2):780–789.
11. LI Jinliang, LI Yongzhen, WANG Xuesong. Study on Anti-Stealth with Meter-Band Polarimetric Radar [J]. Radar Science and Technology, 2005, 3(6):321–326.
12. Wan Shanhu, Din Jianjiang. Key Technology for Improving Four Countermeasures of Meter-Wave Radar [J]. China Radar, 1998(2):1–4.
13. Dong Zhiwen, Qu Xiaoguang. Anti-stealth Performance Analysis for Guidance Radar in Air Defense System [C]//Tenth Annual National Radar Conference, 2008:376–379.
14. Tao Fuyu. Introduction of Modern Meter-wave Radar [J]. Ground Air Defense Weapon, 2002(4):34–38.
15. CHEN Changxing, GONG Linyu, BAN Fei. Research into Anti-Stealth Technology of Meter-wave Resonance Radar [J]. Shipboard Electronic Countermeasures, 2009, 32(4):34–37.
16. CHEN Zhiming. Stealth Waveform for Airborn Radar [J]. Modern Radar, 2006, 28(9):24–26.
17. Wang Pai, Xia Mingyao, Zhou Lezhu. Scattering Characteristics Comparison Analysis of Stealth Aircraft with Different Methods [J]. 2004(19):69–72.
18. Shi Xiaoling. Analysis on Target Track of Meter-wave Radar [J]. Modern Electron, 2000, 73(4):8–12.
19. Sheng Jingtai. Multipath Height Finding Method Used in Meter-Wave RADAR [J]. Journal of China Academy of Electronics and Information Technology, 2008, 3(5):510–514.
20. Hu Kunjiao, Wu Jianqi. Low-Elevation Height-Finding Experiment Research for Meter-Wave Radar [C]// Tenth Annual National Radar Conference, 2008:63–66.
21. Hu Xiaoqin, Chen Jianwen, Chen Hu. Artificial Neural Network Diction for Height-Finding of Meter-Wave Radar [J]. Transaction of Air Force Radar Academy, 2004, 18(3):16–19.
22. Dong Mei, Zhang Shouhong, Wu Xiangdong. Range High-Resolution Height-finding Technology[J]. Fire-Control Radar Technology, 2006, 35(1):10–14.
23. Capon J. High-Resolution Frequency-Wavenumber Spectrum Analysis [J]. IEEE Proceedings, 1969, 57(8):1408–1418.
24. Schmidt R O. Multiple Emitter Location and Signal Parameter Estimation [J]. IEEE Trans on Antennas and Propagation, 1986, 34(3):276–280.
25. Pillai S U, Kwon B H. Forward/Backward Spatial Smoothing Techniques for Coherent Signal Identification [J]. IEEE Trans on Acoustic, Speech and Signal Processing, 1989, 37(1):8–15.
26. Rao B D, Hari K V S. Performance Analysis of Root-MUSIC [J]. IEEE Trans on Acoustic, Speech and Signal Processing, 1989, 37(12): 1939–1949.
27. Roy R, Kailath T. ESPRIT-a Subspace Rotation Approach to Estimation of Parameters of Cissoids in Noise [J]. IEEE Trans on Acoustic, Speech and Signal Processing, 1986, 34(10):1340–1342.
28. Haardt M, Nossek J A. Unitary ESPRIT: How to Obtain Increased Estimation Accuracy with a Reduced Computational Burden [J]. IEEE Trans on Signal Processing, 1995, 43(5):1332–1242.
29. Stoica P, Sharman K. C. Maximum Likelihood Methods for Direction-of-Arrival Estimation [J]. IEEE Trans on Acoustic, Speech and Signal Processing, 1990, 38(7):1132–1143.
30. Ziskind I., Wax M. Maximum Likelihood Localization of Multiple Sources by Alternating Projection [J]. IEEE Trans on Acoustic, Speech and Signal Processing, 1988, 36(10):1553–1559.
31. Zhao Yiongbo, Zhang Shouhong. Height-Finding Technology Research on Meter-Wave Radar [D]. Electronics Engineering Institute of Xidian University, 2003.
32. Li Ping, Russian Air defense System Began to Deploy Meter-Wave Anti-Stealth Digital Phased Array Radar. Aerospace Electronic Warfare, 2004(4):42.

33. Bao Zheng Zhang Qingwen. A New Style Metric Wave Radar-Synthetic Impulse and Aperture Radar. Modern Radar, 1995, 17(1):1–13.
34. Zhang Qinwen. System Performance Analysis and Research on Synthetic Impulse and Aperture Radar [D]. Xian: Doctor's Degree Thesis of Xidian University, 1994.
35. Chen Baixiao. SIAR and its Four-Dimensional Tracking Processing Technology Research [D]. Xian: Doctor's Degree Thesis of Xidian University, 1997.
36. Chen Baixiao, Zhang Shouhong, Wu Jianqi, et al. Analysis and Results on Sparse-Array Synthetic Impulse and Aperture Radar [C]//Proc. of 2006 CIE International Conf. on Radar, Beijing: IEEE, 2001:76–80.
37. Wu Jianqi, He Ruilong, Jiang Kai. Research and Experimentation on Sparse-Array Synthetic Impulse and Aperture Radar [J]. Modern Electron, 1998, 64(3):1–5.
38. Yang Kehu, Bao Zheng. Performance Improvements of Multi-Frequency Application on Low-Angle Tracking Direction Estimation [J]. Journal of Xidian University, 1993, 20(4):181–193.
39. Zhang Ping, Zhang Xiaohua. One New Method for Low-Elevation Tracking [J]. Modern Radar, 2001, 12(6):9–12.
40. HE Zishu, LI Min, JING Yulan. Target Multipath DOA Estimation Algorithm Based on Frequency Agility for Phased Array Radar [J]. Systems Engineering and Electronics, 2005, 27(11):1880–1882.
41. Sherman S M. Complex Indicated Angles Applied to Unresolved Radar Targets and Multipath [J]. IEEE Trans on AES, 1971(1):160–170.
42. Peyton P Z, Goldman L. Radar Performance with Multipath Using the Complex Angle [J]. IEEE Trans on AES, 1971, 7(1):171–178.
43. Howard D D, Sherman S M, Campbell J J. Experimental Results of the Complex Indicated Angle Technique for Multipath Correction [J]. IEEE Trans on AES, 1974, 10(6):779–787.
44. Knepp D L. Variance and Bias of Angle Estimation Radars [J]. IEEE Trans on Antennas and Propagation, 1976, 24(4):518–521.
45. Zheng Y B, Tseng S M, Yu K B. Closed-Form Four-Channel Monopulse Two-Target Resolution [J]. IEEE Trans on AES, 2003, 39(3):1083–1089.
46. Nickel U, Fhr F. Overview of Generalized Monopulse Estimation [J]. IEEE A&E Systems Magazine, 2006, 21(6):27–56.
47. FAN Zhijie, SHANG She. A New Method for Low Altitude Target Detection and Tracking [J]. Radar Science and Technology, 2004, 2(3):153–157.
48. Jia Yongkang, Bao Zheng. Maximum Likelihood DOA Estimation by Using Doppler Information [J]. Acta Electronica Sinica, 1997, 25(6):71–76.
49. Jia Yongkang, Bao Zheng. Wave Arrive Direction Estimation Method and Performance Analysis Under the Model of Time-Space Two-Dimensional Signal [J]. Acta Electronica Sinica, 1997, 25(6):69–73.
50. Zhao Guanghui, Chen Baixiao, Dong Mei. A New DOA Estimator Based on Alternating Projection and Its Application in VHF Radar [J]. Journal of Electronics & Information Technology, 2008, 30(1):224–227.
51. Hu Tiejun, Yang Xueya, Chen Baixiao. Application of Beamspace ML Algorithm Based on Array Interpolation in Height Measuring Using VHF Radar [J]. Journal of Electronics & Information Technology, 2009, 24(4):660–666.
52. Wu Xiangdong, Zhang Shouhong, Dong Mei. An Algorithm Based on Linear Preprocessing for Meter-Wave Radars to a Target at Low Altitude [J]. Acta Electronica Sinica, 2006, 34(9):1668–1671.
53. Zhang Wenjun, Zhao Yongbo, Zhang Shouhong. Altitude Measurement of Meter-Wave Radar Using the General MUSIC Algorithm and Its Improvement [J]. Journal of Electronics & Information Technology, 2007, 29(2):387–390.
54. Liu Jun, Liu Zheng, Liu Yunfo. Elevation Angle and Multipath Fading Coefficient Joint Estimation Algorithm in VHF Radar [J]. Journal of Electronics & Information Technology, 2011, 33(1):33–37.
55. Chen Baixiao, Hu Tiejun, Zheng Ziliang. Method of Altitude Measurement Based on Beam Split in VHF Radar and Its Application [J]. Acta Electronica Sinica, 2007, 35(6):1021–1025.

56. Chen Baixiao, Zhao Guanghui, Zhang Shouhong. Altitude Measurement Based on Beam Split and Frequency Diversity in VHF Radar [J]. IEEE Trans on Aerospace and Electronic Systems, 2010, 46(1):3–13.
57. Lo T, Litva J. Low-Angle Tracking Using a Multifrequency Sampled Aperture Radar [J]. IEEE Trans on AES, 1991, 27(5):797–805.
58. Lo T, Litva J. Use of a Highly Deterministic Multipath Signal Model in Low-Angle Tracking [J]. IEE Proceedings-F, 1991, 138(2):163–171.
59. Lo T, Wong T, Litva J. New Technique for Low-Angle Radar Tracking [J]. Electronics Letters, 1991, 27(6):529–531.
60. Zhu Wei. Study on Low-Angle Altitude Measurement in VHF Radar [D]. Xian: Xidian University, 2013.
61. Hu Xiaoqin. Basis Study on the Application of Super-Resolution Spatial Spectrum Estimation Technique [D]. Changsha: National University of Defense Technology, 2009.
62. Xu Liang. The Study of Target Echo Extraction in Active Sonar Signal Processing Based on Blind Source Separation and Array Extension [D]. Harbin: Harbin Engineering University, 2010.
63. Jin Rong. Spatial Spectrum Estimation Calibration Algorithm in Microwave Radiation Receiving System [D]. Wuhan: HuaZhong University of Science and Technology, 2008.
64. Yang Lingling. The Research on the Algorithm for Spatial Spectrum Estimation [D]. Wuhan: HuaZhong University of Science and Technology, 2007.
65. Fu Na. Research on Communication and Direction-finding System of Multi-Beam Modulation Carrying Directional Information [D]. Nanjing: Nanjing University of Aeronautics and Astronautics, 2008.
66. Zhang Yufeng. DOA Algorithms Research [D]. Wuhan: HuaZhong University of Science and Technology, 2008.
67. Lei Yuan. Research of MUSIC Algorithm and Implementation on DSP [D]. Qingdao: Ocean University of China, 2009.
68. Yang Xueya. Study on Array Super-Resolution and Altitude Measurement in VHF Radar [D]. Xian: Xidian University, 2011.
69. Wan Xin. Study on Application of Computational Intelligence Methods to the DOA Estimation [D]. Harbin: Harbin Engineering University, 2008.
70. Chai Xuyang. Method and Implementation of Height-Finding Processing in VHF Radar [D]. Xian: Xidian University, 2011.
71. YANG Xueya, YANG Guangyu. Method of Height Measuring Based on Sparse Solution in Meter-Wave Radar [J]. Radar Science and Technology, 2012, 10(6):629–632, 638.
72. SONG Xiufen, ZHU Wei, XIE Tengfei, et al. Study on Low-Angle Height-Finding Algorithm of VHF Radar in Complex Terrain [J]. Radar Science and Technology, 2014, 12(2):156–160.

Chapter 5
Metricwave Radar Anti-jamming Technology



5.1 Particularity of Metricwave Radar Anti-jamming

Apart from radar signals, there are a great deal of civil television, modulation frequency radio and communication signal in crowded metricwave frequency bands, which are usually adjacent to radar operation frequency, with very high power and incessancy, therefore metricwaver radar should firstly be characteristized with anti-jamming capability in strong civil electromagnetic signals. Mostly, civil jamming signals are continuous or quasi-continuous, and they are very difficult to be suppressed effectively in time domain, so some measures taken in frequency domain and space domain will be more effective. The technical measures taken for space domain filtering mainly include antenna low-sidelobe design and sidelobe cancellation or nulling. The key solution for frequency filtering is the receiving channel design. Moreover, the detail methods will be introduced in Chap. 6.

With aspect of anti-jamming, metricwave radars are usually characteristized with wide antenna lobe, higher sidelobe level, and weak direction selection. Furthermore, the narrower frequency of metricwave radar is easier to be reconnaissance and intercepted; therefore the hostile jamming will be more pertinent, which can adopt jamming measures efficiently, such as spot jamming and deception jamming. So the first issue should be taken into account for metricwave radar anti- jamming is how to reduce interception probability, and the methods for antenna low sidelobe, random access scanning, spectrum spread, frequency agility and variable polarization.

5.1.1 Electromagnetic Environment of Metricwave Band

(1) Civil Radio and TV Jamming

The frequency band of metricwave, civil radio and TV have some overlap section, so there is mutual jamming between radar signals and TV ones. Chinese television

© National Defense Industry Press, Beijing and Springer Nature Singapore Pte Ltd. 2020

J. Wu, *Advanced Metric Wave Radar*, https://doi.org/10.1007/978-981-10-7647-3_5

Table 5.1 Radiovision signal distributing in metricwave band

Channel	Frequency range	Image carrier frequency (MHz)	Sound carrier frequency (MHz)
6	167–175	168.25	174.75
7	175–183	176.25	182.75
8	183–191	184.25	190.75
9	191–199	192.25	198.75
10	199–207	200.25	206.75
11	207–215	208.25	214.75
12	215–223	216.25	222.75

is the version of PAL D/K, and the channel frequency similar to metricwave radar can be divided as Table 5.1.

The main jamming within the working band is TV signal jamming whose interferential value is similar to the central frequencies of TV image and TV sound.

Due to receiving DBF carried out in digital domain, wider single antenna element beam, and less main and sidelobe are achieved. Therefore, whether radar mainlobe aims in the direction of TV tower transmitting antenna, there exists certain jamming. The radar anti-jamming capability can be improved by the inhibitory effect channelized filter and digital filter, which requires better rectangle coefficient in design.

The sidelobe jamming impact of radio and TV frequency on radar mainly embody enabling receiving channel saturation. Under the circumstances of un-saturated channel, sidelobe TV jamming can achieve main and sidelobe rejection ratio and sidelobe cancellation ratio after DBF, which will be reduced about 30 dB, thus to decrease the jamming on radar.

(2) Universe Noise Jamming

In metricwave band, antenna noise is stronger, and the noise in low-end higher than high-end, which mainly caused by the Sun noise and the Milky Way noise, where the two biggest ones are the Milky Way central area and the Sun. The field angle of the Sun corresponding to radar observation point is about 0.53°, and at the low end of metricwave band (<100 MHz), when the Sun is quite the equivalent noise temperature in the angle is about 10^6 K, while it will be about 10^7 K during several hours after Solar burst.

Universe noise distributions are given in Fig. 5.1, in which Milky Way noise is mainly used. The Milky Way central noise is the strongest, and the filed angle of the strongest corresponding to radar observation point is about $3° \times 3°$, while the maximum equivalent noise temperature at the low-end of metricwave band is up to 10^5 K; the weakest noise is at the direction of the Milky Way pole, and the equivalent noise temperature at the low-end of metricwave band is about 3000 K; geometric mean of hemispherical coverage at the low-end of metricwave band is about 15,000 K.

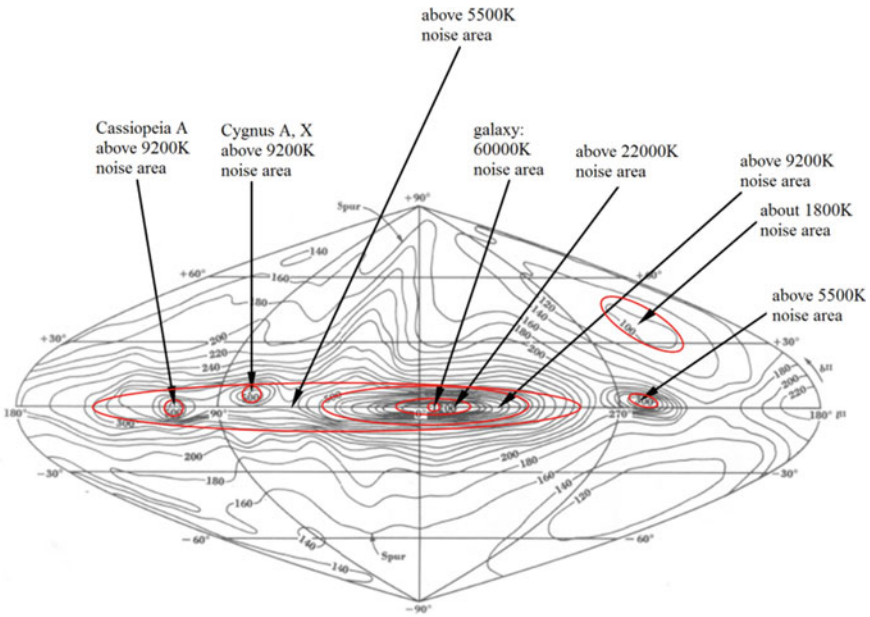


Fig. 5.1 Universe noise distribution

Antenna noise temperature is the space angle weighted average of various noise source temperatures within the receiving antenna lobe. Metricwave radar is used to design one fixed value for antenna noise temperature, which usually derives from geometric mean of hemispherical coverage. It is very irrational for new AESA metricwave radar. For example, when the beam points at the Sun in burst, the radar background noise (hemispherical average noise) at the low-end of metricwave will be 5 dB higher than the designed one; when beam points at the central area of the Milky Way, the radar background noise will be 3 dB higher than the designed one; when the beam points at the direction of the Milky Way pole, the radar background noise will be 6 dB lower than the designed one. If the system design according to average noise ground, then the beam points at the Sun or point through the Milky Way central area within the scope of beam scanning, radar detection performance will obviously decrease. Moreover, if the beam points are at other areas, there will be much design margin. Therefore, by way of obtaining uniformed detection performance, the AESA metricwave radar working on low frequency should adjust the dwell time and pulse width according to the difference of the background noise of each position corresponding to hemispherical average noise.

5.2 Advanced Metricwave Radar Anti-jamming Technology

The main advanced metricwave radar anti-jamming technologies will be introduced in terms of following airspace, waveform domain, energy domain and processing domain.

5.2.1 Airspace Domain Anti-jamming Technology

Airspace domain anti-jamming technology for new system of metricwave radar mainly include jamming orientation and adaptive beam nulling, random access scanning, sidelobe blanking and sector silence.

5.2.1.1 Adaptive Beam Nulling

New metricwave radar adopts adaptive array antenna and digital beam forming technology, which can realize adaptive beam nulling in the direction of jamming source to improve anti-jamming efficiency.

The purpose of adaptive beam nulling is mainly to counter the active jamming from the sidelobe. Firstly, jamming source direction should be measured based on the space spectrum estimation of jamming source signal, and simultaneously to form multi-assistant beams pointing to jamming source, and Fig. 5.2 shows the flow chart.

(1) Jamming Orientation

Jamming orientation technology is mainly to analyse spatial sampling data by signal processing, to form spatial distribution of jamming signal, to estimate jamming azimuth and elevation, and then the accurate jamming angle information is sent to carry out tracking and estimation by data processing.

Jamming source orientation and analysis processing flow chart are given as Fig. 5.3.

Angle measuring accuracy and signal to noise ratio (SNR), antenna beam width is subjected to the following relationships:

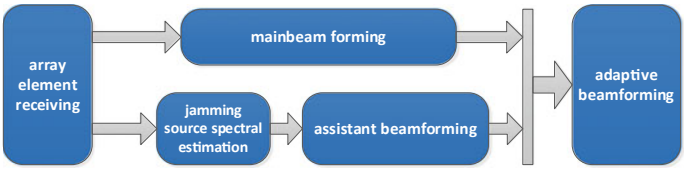


Fig. 5.2 Adaptive beam nulling flow chart

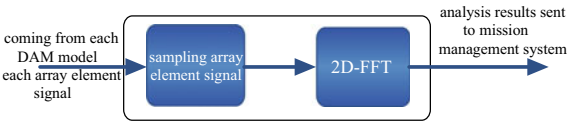

coming from each DAM model each array element signal
sampling array element signal
2D-FFT
analysis results sent to mission management system

Fig. 5.3 Jamming orientation and analysis processing flow

$$\delta_{\Delta\theta n} = \frac{0.51}{\sqrt{J/N}} \Delta\theta_{\frac{1}{2}} \tag{5.1}$$

(2) Adaptive Nulling

Adaptive nulling forming technology mainly adopts AA adaptive processing technology, which ranges part adaptive beam forming method of sub-beam. Firstly, it estimates the active jamming direction by beam scanning, and then to form assistant beam of pointing jamming at the direction of active jamming, thus to reduce the high-dimensional covariance matrix into (J + 1) × (J + 1) covariance matrix, where J is the active jamming number. The cancellation of jamming can be achieved by main beam and assistant beam adaptive processing. Figure 5.4 shows the realization principle of AA algorithm.

Let $y(t)$ as the response of main beam, $x_i(t), i = 0, 1, \cdots, J-1$ is the assistant beam response of J pointing jammings. One covariance matrix for main beam and assistant beam response can be achieved by N snapshots on jamming background in far zone.

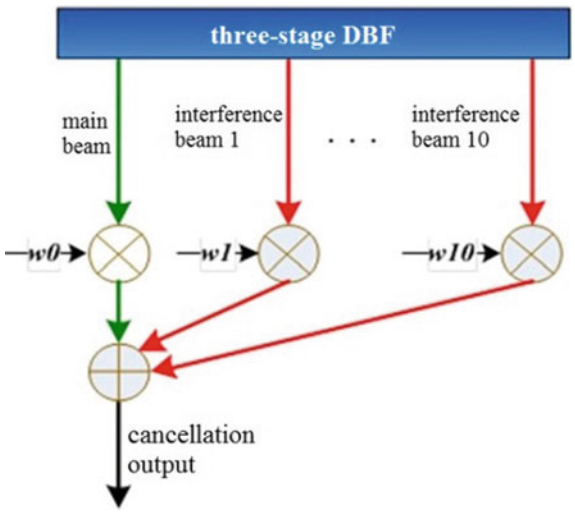


Fig. 5.4 AA algorithm realization principle

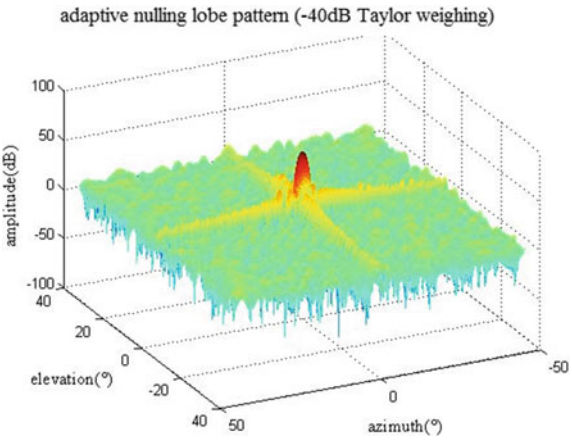


Fig. 5.5 Adaptive nulling lobe pattern

$$R_x = \frac{1}{N}\sum_{n=0}^{N-1}[y(t_n), x_1(t_n), x_2(t_n)\ldots x_{J-1}(t_n)]^H[y(t_n), x_1(t_n), x_2(t_n)\ldots x_{J-1}(t_n)] \tag{5.2}$$

Thus, the optimum weight after dimension reduction is,

$$\mathbf{w}_{opt} = \mu R_x^{-1} T^H \mathbf{a}(\theta_s, \varphi_s) \tag{5.3}$$

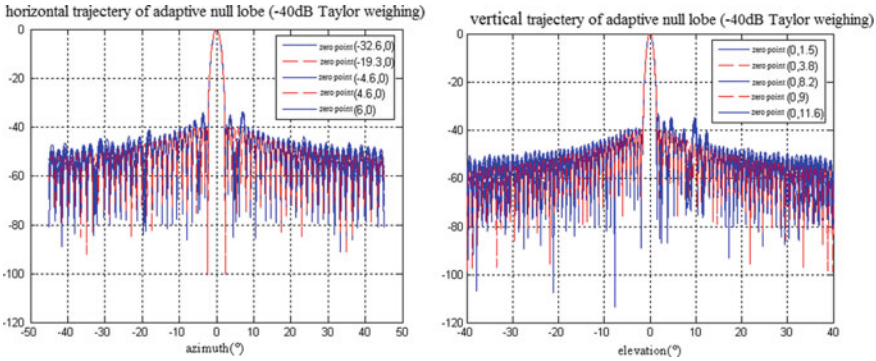
where, $T = [a(\theta_m, \varphi_m), a(\theta_0, \varphi_0), a(\theta_1, \varphi_1), \cdots, a(\theta_{J-1}, \varphi_{J-1})]$ is the transformation matrix after dimension reduction, (θ_s, φ_s) is the target direction, (θ_m, φ_m) is main beam direction, (θ_j, φ_j), $j = 0, 1, \cdots, J-1$ is jamming direction, $y = a^H(\theta_m, \varphi_m)a(\theta_s, \varphi_s)$ is main beam output, and $x_j = a^H(\theta_j, \varphi_j)a(\theta_s, \varphi_s)$, $j = 0, 1, \cdots, J-1$ is the assistant beam output. The array optimum output is,

$$y_{opt}(t) = [y(t)x_1(t)x_2(t)\ldots x_{J-1}(t)]\mathbf{w}_{opt}^* \tag{5.4}$$

(3) Simulation Verification

Suppose there are 10 active jammings, all element's jamming-to-noise ratio is 48 dB, amplitude weighted is −40 dB Taylor weighting, snapshot number is 32, root-mean square error for array receiving channel amplitude is 0.5 dB and phase root-mean square error is 2°. Assistant beam pointings that take jamming pointing as mean value disturb uniformly, assistant beam and jamming direction are shown in Figs. 5.2 and 5.3, and the lobe pattern after cancellation is shown in Figs. 5.5, 5.6 and Tables 5.2, 5.3).

The simulation results show that with higher jamming-to-noise ratio, better cancellation effects are achieved. When the jamming-to-noise ratio is higher than 10 dB, the null depth employing the algorithm in the direction of jamming is better than −55 dB.



(a) Horizontal profile (b) Vertical profile

Fig. 5.6 Lobe pattern after adaptive jamming cancellation

Table 5.2 Beam pointing

Beam pointing	Azimuth (°)	Elevation (°)
Main beam pointing	0	0
Assistant beam pointing jamming 1	−32.2	0.2
Assistant beam pointing jamming 2	−19.3	0.1
Assistant beam pointing jamming 3	−4.6	0.3
Assistant beam pointing jamming 4	4.7	0.2
Assistant beam pointing jamming 5	6.1	0.2
Assistant beam pointing jamming 6	0	1.7
Assistant beam pointing jamming 7	0.3	4.1
Assistant beam pointing jamming 8	0.4	8.2
assistant beam pointing jamming 9	0.2	9.4
Assistant beam pointing jamming 10	0.3	11.9

Table 5.3 Jamming direction

Target Classes	Intensity (dB)	Azimuth (°)	Elevation (°)
Signal	0	0	0
Jamming 1	20	−32.6	0
Jamming 2	20	−19.3	0
Jamming 3	20	−4.6	0
Jamming 4	20	4.6	0
Jamming 5	20	6	0
Jamming 6	20	0	1.5
Jamming 7	20	0	3.8
Jamming 8	20	0	8.2
Jamming 9	20	0	9
Jamming 10	20	0	11.6

5.2.1.2 Random Scanning Technology

New metricwave radar employing random scanning mainly is used for anti-reconnaissance and countering deceptive jamming. The prerequisite condition for deceptive jamming is that denseness false targets distribute comparatively sparse. Under typical working condition, all beam position for the new metricwave radar employ random phase scanning to achieve target searching, to complete airspace coverage within certain period, and at the same time to keep no certain relationship between scanning frames of fixed position in one space, namely radar searching frame period is randomly various, which significantly reduce its reconnaissance probability by electronic device, and at the same time effectively counteract the active deceptive jamming.

Beam position sort for conventional ranking two-dimensional scanning is shown in Fig. 5.7.

The random scanning beam position is shown in Fig. 5.8.

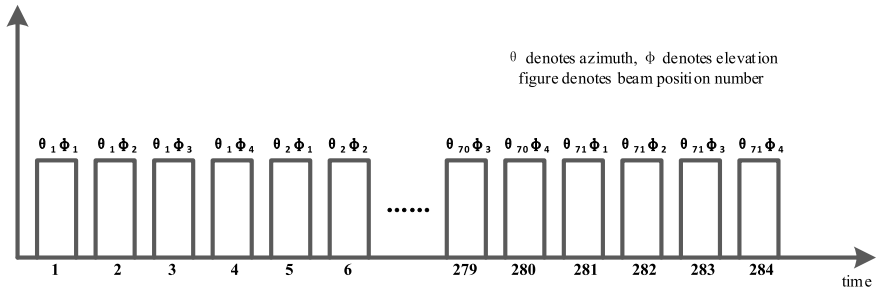

θ denotes azimuth, ϕ denotes elevation
figure denotes beam position number
θ1ϕ1 θ1ϕ2 θ1ϕ3 θ1ϕ4 θ2ϕ1 θ2ϕ2 ..... θ70ϕ3 θ70ϕ4 θ71ϕ1 θ71ϕ2 θ71ϕ3 θ71ϕ4
1 2 3 4 5 6 279 280 281 282 283 284
time

Fig. 5.7 Conventional scanning sequence sketch

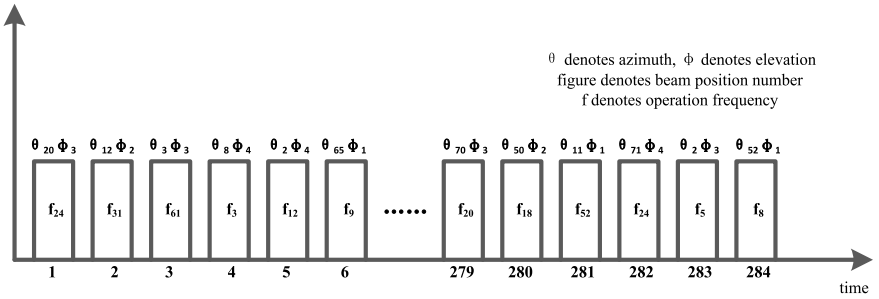


Fig. 5.8 Random scanning sequence sketch

5.2.1.3 Sidelobe Blanking

(1) Principle of Sidelobe Blanking

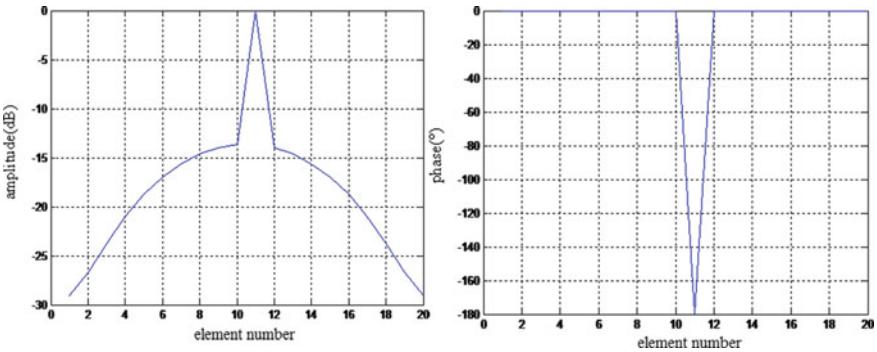
The main function of sidelobe blanking antenna is to provide spatial overlapping level converging all sidelobe of primary radar antenna beam, which employs separated blanking antenna design, namely azimuth coverage by employing horizontal surface omni-directional antenna and enhancing antenna gain in vertical surface array. Conventional blanking antenna is characterised with large size, low gain and small range blanking in vertical surface. Taking account of digital array radar beamforming speciality, choosing some elements from the array, employing element re-using and achieving blanking beam with DBF, the blanking antenna design can be simplified.

Through adjusting weighting coefficients of two-row elements and simulation calculation, it can be seen azimuth surface gain for overlapping level of blanking channel is −28 dB, which can cover −30 dB sidelobe for primary antenna of azimuth surface; the gain overlapping (−20 dB) in pitching surface (main cut) is better than 50°. The aperture distribution of blanking antenna is shown in Fig. 5.9, and the overlapping relationship between the blanking channel and the primary antenna beam coverage is shown in Fig. 5.10. Figure 5.11 shows the simulation three-dimensional lobe pattern of blanking channel.

(2) Engineering Realization of Sidelobe Blanking

Sidelobe blanking processing flow chart is shown in Fig. 5.12. Sidelobe blanking processing is aimed at each beam position, each distance cell and each filter channel, i.e. to add one beam processing channel, the main channel will be closed when both main channel and blanking channel pass the threshold after pulse compression, filtering and threshold detection, and also the amplitude of latter is larger than former one. The detailed processing flow can be given as the following three steps:

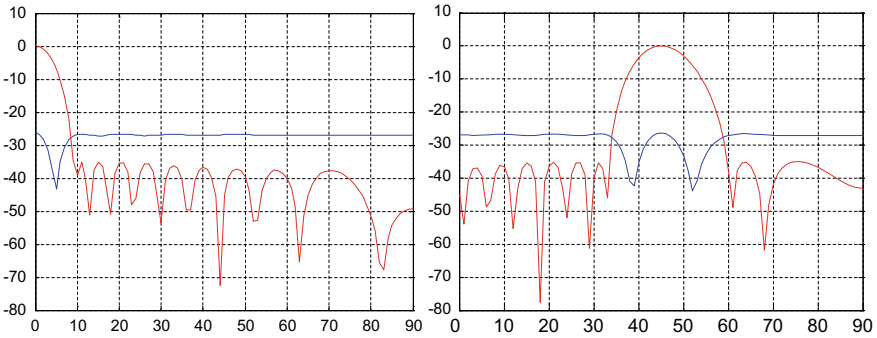
(a) to judge whether the blanking channel is saturated or not, where to saturated is supposed as 1, unsaturated as 0, and the judgment basis is saturation threshold.



(a)Three-dimensional lobe pattern for primary antenna

(b)Blanking antenna aperture distribution

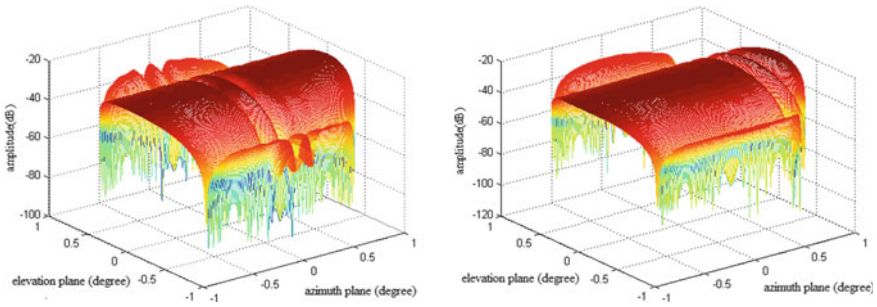
Fig. 5.9 Blanking antenna aperture distribution



(a) lobe overlapping patter for primary cut in azimuth

(b)lobe overlapping patter of primary cut for azimuth scanning

Fig. 5.10 Lobe overlapping comparatione between primary antenna and blanking channel



(a) 0º lobe for azimuth surface scanning

(b) 45º lobe for azimuth surface scanning

Fig. 5.11 Three-dimensional lobe pattern for blanking channel

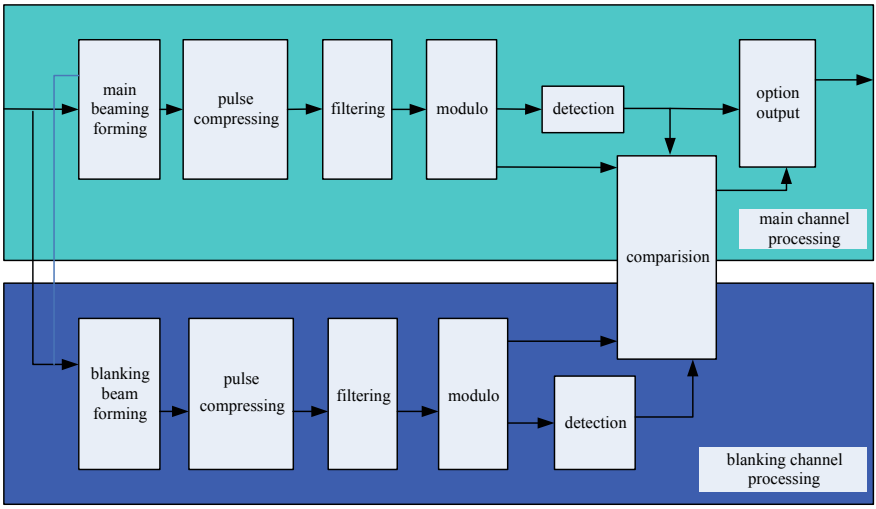


Fig. 5.12 Sidelobe blanking processing flow chart

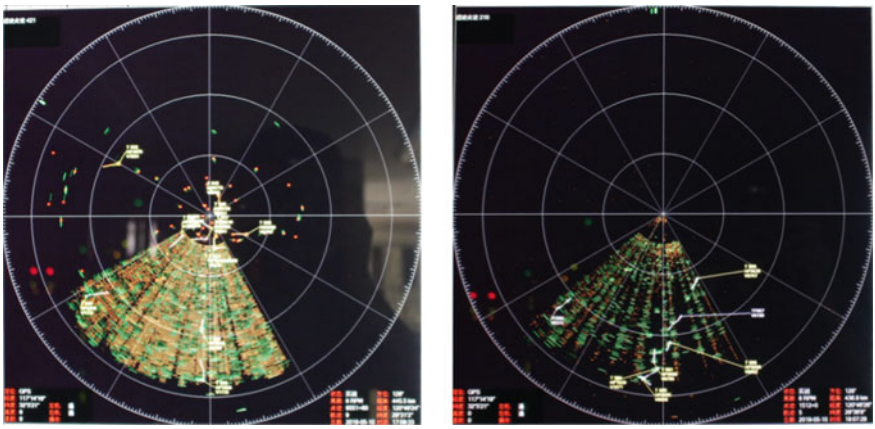
(b) to carry out fast threshold-crossing detection on blanking channel, and to suppose passed as 1, no passed as 0, and the judgement basis is that distance element chooses large threshold and detection threshold.
(c) to compare blanking channel and main channel intensity, and the judgement basis is comparison threshold.

When the above three steps are satisfied, it is to determine whether to blank the distance element and filter output or not, and the detailed judgment criteria are shown in Table 5.4, where "1" denotes closing main channel output, "0" denotes not closing main channel output and "X" denotes the item unimportant.

Actual measurements of counter active jamming during flight test are shown in Fig. 5.13. By actual comparison on measurements picture, apart from parts of falsehood plots in the direction of mainlobe, there are no falsehood targets in the azimuth of sidelobe after the radar system starts up sidelobe blanking anti-jamming, therefore the anti-jamming measurements take effect.

Table 5.4 Blanking processing judgement criteria

Blanking channel saturated	Blanking channel threshold-crossing detection	Blanking channel larger than main channel	Closing main channel output
No	N	X	0
No	X	No	0
No	Yes	Yes	1
Yes	X	X	1



(a) No anti-jamming measures (b) With anti-jamming measurements

Fig. 5.13 Sidelobe blanking test

5.2.2 *Waveform Domain (Time, Frequency and Intra-pulse) Anti-jamming Technology*

5.2.2.1 Complex Waveform

Advanced metricwave radar can offer thousands of waveform combination in light of arbitrary operational parameter collocation, and the detail criterion is given as following.

The operational parameters will be arbitrary combined in light of detection distance in practice. There are supposed K waveforms within each range and the transmitting repetition frequencies corresponding to K waveforms are $(fr_1, fr_2, \cdots, fr_K)$, therefore corresponding duty ratio is $(blind_1, blind_2, \cdots, blind_K)$, corresponding pulse width is $(\tau_1, \tau_2, \cdots, \tau_K)$, corresponding pulse number is $(n_1, n_2, \cdots, n_K)$ and the predictive value for researched target is R. Let $midr_k = \mathrm{mod}(\frac{C}{2fr_k})$, and according to the following expression,

$$\begin{aligned} r_k &= \min(|\ \mathrm{mod}\ (R, midr_k) - midr_k \times blind_k|, |\ \mathrm{mod}\ (R, midr_k) \\ &\quad - (1 - blind_k) \times midr_k|)/midr_k \\ [void, k_0] &= \max(r_1, r_2, \cdots, r_K) \\ R_{\max} &= 239.4\left(\frac{P_t \tau_k n_k G_t G_r \sigma F_t^2 F_r^2}{f^2 F_n T_s D_0 C_B L}\right)^{1/4} \end{aligned} \tag{5.5}$$

The corresponding transmitting repetition frequencies, pulse width and pulse number are given, adding transmitting waveform of related range bin formed by corresponding waveform modulation type. Several signal waveforms arrange as

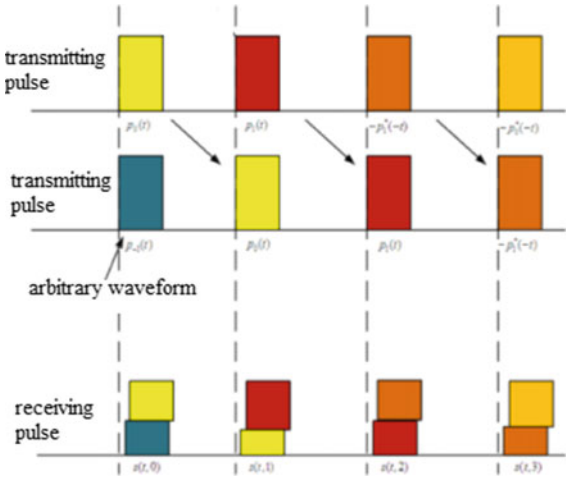


Fig. 5.14 Confrontating deceptive jamming waveform sketch

pseudo-random sequence, to ensure different waveform within each pulse-to-pulse, so as to increase the difficulty of jammer reconnaissance, analysis and sorting association.

5.2.2.2 RF Protecting Signal

RF protecting signal is used to differentiate targets and interferes or eliminate jamming signals by constructing certain transmitting waveform sequence employing signal replications with a jammer. Certain time source will be lossed with the method, and at the same time detection coverage will also be affected.

The advanced metricwave radar employing RF protecting signal is mainly used for electronic anti-reconnaissance and countering mainlobe deceptive jamming.

Usually, jammer can only forward the radar signal intercepted by the former pulse repeat period due to the restriction of processing delay. The jammer can only forward the radar signal intercepted by the former pulse repeat period to protect self object more closed to the radar, even the jammer can receive, replicate and forward current signal within short time, namely the interface signal always lag behind real target echoes.

Therefore, it transmits multi-pulse signals on deceptive jamming. Due to the signal modulation rule within impulse signal of radar itself, which is unknown for jammer, therefore the relativity between jamming signals forwarded by current transmitting signal and jammer replication modulation is reduced. The reference signals that radar pulse compression employs are corresponding to current transmitting pulse, which results jamming signal mismatch thereby to decrease jamming effects, effectively restraining deceptive jamming. The waveform sketch is given in Fig. 5.14.

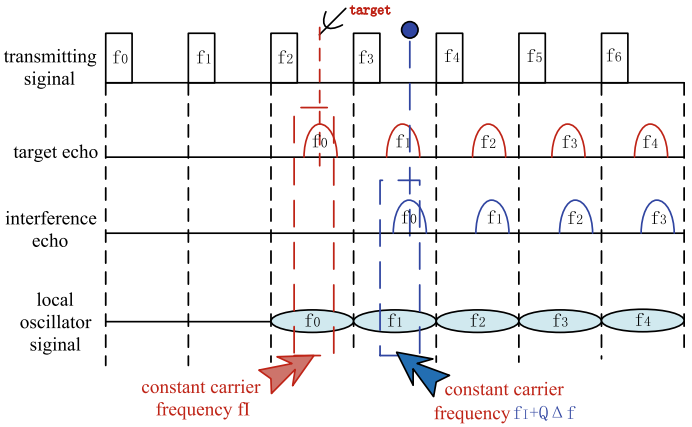


Fig. 5.15 Stepped-frequency radar transmitting pulse and local oscillator signal sequence

5.2.2.3 Pulse Stepped-Frequency

The advanced metricwave radar can employ pulse stepped-frequency to confrontate mainlobe narrowband noise suppression, mainlobe wideband noise suppression and mainlobe deceptive jamming. The prerequisite of employing the method is that radar system has precisely tracked targets.

The stepped-frequency radar can cover with the whole operating range by moving range window. As shown in Fig. 5.15, different range window can set by the start time of stepped-frequency receiver local oscillator.

Frequency difference that is smaller than bandwidth of intermediate frequency receiver can only pass through intermediate frequency receiver. The target range corresponding to range widow can be changed by altering basic frequency pulse position of stepped-frequency within local oscillator signals. The interested target range will be covered by continuously adjusting the basic frequency pulse position and moving range widow. The jamming coming into the receiver can be restrained by confining the receiver bandwidth. The stepped-frequency radar can choose targets to be processed by setting up receiver bandwidth (Fig. 5.16).

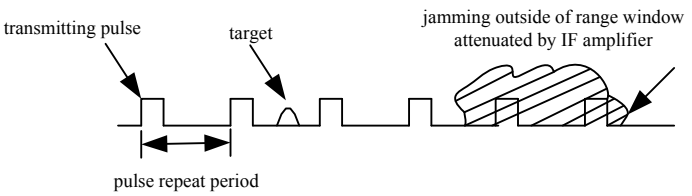


Fig. 5.16 Jamming restraining by intermediate frequency amplifier

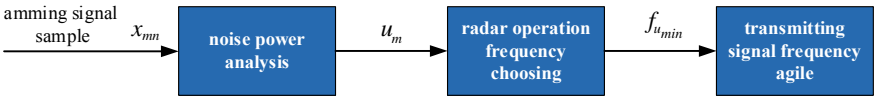


Fig. 5.17 Pulse-to-pulse adaptive agility flow

5.2.2.4 Frequency Agility

Frequency Agility can be divided into pulse-to-pulse random frequency agility, pulse-to-pulse adaptive frequency agility and pulse cluster frequency agility.

Pulse-to-pulse random frequency agility is that radar transmits signals working on the chosen frequency points randomly, which makes frequency measurement system of spot jammer that can not keep up with the variety of radar work frequency.

The purpose of pulse-to-pulse adaptive agility used in advanced metricwave radar is to choose the method for confrontating wideband barrage jamming, as shown in Fig. 5.17.

Jamming signal sample should be chosen from the radar interruption period, so as to avoid the effect of close distance clutter. Then, the interruption period will be divided into some time interval, corresponding to M working frequency points that can be separated into M segments. The radar working on M frequency points by turns receives jamming signals within M time interval, takes samples from all received jamming signals within M time intervals after signal processing, and then to calculate all mean value u_m (being directly proportional to jamming average power) of jamming sampling. Let there N sampling points at each time interval, then,

$$u_m = \frac{1}{N}\sum_{n=0}^{N-1} x_{mn};\ m = 0, 1, \ldots, M-1 \tag{5.6}$$

$$u_{min} = \min[u_m];\ m = 0, 1, \ldots, M-1 \tag{5.7}$$

It is obvious that, u_{min} is the low jamming average power within the M time intervals, therefore the receiver working frequency $f_{u_{min}}$ corresponding to this time interval is the frequency point with weakest jamming power to be find. As a result, the central frequency for next radar transmitting pulse should be shifted agilely into this frequency, so as to reduce the effect of the jamming on radar working. In this way, it achieves pulse-to-pulse adaptive frequency agility.

5.2.3 Anti-jamming Technology in Energy Field

Anti-jamming in energy field is an important measure for confrontating active jamming, namely power countermeasure, especially for confrontating mainlobe compression jamming. The echo signal power can be augmented by increasing

transmitting power, delaying the beam dwell time on target, or increasing the gain, thus to improve receiving signal to jamming ratio, which is beneficial for target detection.

Advanced metricwave radar design is based on high power-aperture product anti-stealth idea, and the power countermeasures include pulse compression technology and long-time pulse integration.

(1) Pulse Compression

Pulse compression is an ordinary but effective measure to counter the power. Radar pulse compression refers to the course that echoes corresponding to wide pulse transmitting signals with TBP above 1 are transformed into narrow pulse after matched filtering. Pulse compression signal is usually linear frequency modulation signal, and its mathematical expression is given as following,

$$s(t) = u(t)e^{j2\pi ft} = A \cdot rect(t/T)e^{j2\pi(f_0 t + 0.5kt^2)} \tag{5.8}$$

Based on matched filtering theory, its frequency characteristic acts as conjugate of input signal spectrum, thus its time domain pulse response is,

$$h(t) = rect(t/T)e^{j\pi kt^2}e^{j2\pi f_0 t} \tag{5.9}$$

After matched filtering processing, the output signal is,

$$s_0(t) = A\sqrt{TB}\frac{\sin[\pi B(t - t_d)]}{\pi B(t - t_d)}e^{j2\pi f_0(t-t_d)} \tag{5.10}$$

It is the signal with fixed carrier frequency as f_0, envelopment is close to sinc function, and TB is compression ratio D. According to expression (5.10), after matched filtering, peak voltage becomes $\sqrt{D}$ times of the former one, and peak power becomes D times of the former one. It can be inferred that when implement noise jamming on radar, the signal to noise ratio output from a filter will increase D times, because radar signal processor match's with signals but mismatches with noise jamming signals. For noise jamming to be effective, the jamming power of jammer at receiver input end must be D times than echo signal power, which is difficult for jammer power level, therefore pulse compression radar is characterised with strong confrontating noise suppression performance. The anti-jamming benefit value of the radar is approximately equal to time width and bandwidth product.

(2) Long-time Pulse Integration

According to radar equation and jamming equation,

$$S = \frac{P_t G_t G_r \lambda^2}{(4\pi)^3 R^4} \tag{5.11}$$

$$J = \frac{P_j G_a G_j \lambda^2}{(4\pi)^2 R_j^2} \tag{5.12}$$

where, P_t is transmitting power, G_t is transmitting gain, G_r is receiving gain, P_j is jammer power, G_a is the gain in the direction of jamming signal, G_j is jammer gain, σ is the target's RCS, and λ is radar operating wavelength.

Under the condition of pressing noise jamming, the phased radar beam aims at the jammer direction for long time, thus signal jamming ratio (SIR) will be increased by N times by pulse accumulation, where N is the integration multiple under conditions of being-jamming and no-jamming. When signal jamming ratio (S/J) reach the target detection threshold, target burned-out detection under condition of jamming can be realized. In practice, the gain from long-time pulse accumulation anti-jamming is also related with accumulation method and target motion character.

5.2.4 Anti-jamming Technology in Processing Domain

5.2.4.1 Jamming Elimination Based on Amplitude Deviation Coefficient

Amplitude deviation coefficient is a physical quantity used to characterize signal stability. The jamming elimination method based on amplitude deviation coefficient can be used to counter mainlobe deception jamming. The jamming using false targets during missile terminal phase penetration is a typical mainlobe jamming, which can be use to differentiate true targets and false targets effectively, and then some integration anti-jamming measures will be taken according to target's speed and distance relativity. The method is an effective and truthful after measured data validation.

(1) Introduction

The stability of echo complex envelope and echo signal is related with jammer structure, flight attitude, radar parameter, radar working state and data length. Signal echo is difficult to cover the modulation period of target's rotating structures due to its short transmitting period <5 ms usually. Modulation period characteristics should be extracted from a set of echoes (azimuth-distance two-dimensional complex envelope) swept targets by radar antenna, namely batch processing on transversal echo. A set of echoes swept targets by air defense radar antenna include stationary and non-stationary components, thus two-dimensional complex envelope processing can be implemented by stationary and non-stationary signal processing approaches. The number of effective echoes in transversal wave filtering of air defense radar is determined by antenna scanning speed and radar repeated period. To ensure signal stationary concurrently, the more effective echoes are more convenient for modulation characteristics extract.

During target's moving going with jammer, one same radial velocity is almost constant in the short time when antenna sweeps targets, while the jammer executes multi-dimensional modulation on targets all the time. The resulted echoes energy does not centralized as target's echoes due to the echoes stability produced by jamming itself, is certainly not higher than the target one. The physical mechanism has

been proven by the data analysis results from the practical exercise of the real shell in observation data.

The mechanism gives us a very good suggestion, namely to estimate amplitude modulation character by the variation of pulse-to-pulse amplitude. The amplitude deviation coefficient g_a can be defined as,

$$g_a = \frac{\sigma_a}{\overline{a}} \tag{5.13}$$

where, amplitude mean value and variance can be denoted as, $\overline{a} = \frac{1}{N_a}\sum_{i=1}^{N_a} a_i$, $\sigma_a^2 = \frac{1}{N_a - 1}(\sum_{i=1}^{N_a} a_i^2 - N_a \overline{a}^2)$.

According to the expression, amplitude deviation coefficient g_a is a relative quantity, and with the more value of g_a, it shows the more amplitude standard deviation, σ_a deviates mean value $\bar{a}$, namely the echoes extent fluctuates significantly. The modulation component of jammer on targets occupies a large portion within the whole echoes, which suggests that the modulation of jammer on target's echoes is significant. Whereas, if the value of g_a smaller, it shows that the stable missile target echoes take priority in the echoes. Therefore, amplitude deviation coefficient reflects the stability of jammer and targets. On the other hand, g_a can remove the influence of missile average components, azimuth and distance factor, which will be more effective than the identification of jammer and target stability by RCS features.

It has preferable invariability to choose amplitude deviation coefficient g_a to denote the amplitude modulation character of echoes, and all reflect the complexity of target and jammer, which can be directly used to classify the targets and jammers. To compare characteristic parameters g_a and $\bar{a}$, it is suboptimal from an theoretical perspective, but according to N_a coherent echoes of targets when air defense radar antenna scans, it can directly estimate the g_a characteristics parameter conveniently in time domain in real time, and it has also no obvious character loss.

(2) Function Validation

To acquire some deceptive jamming test data, there are totally 300 tracking wave positions required calculation according to practical measured data, and the amplitude deviation coefficient comparison analysis between real targets and jamming signals for each wave position are shown in Fig. 5.18.

(a) Identify Flow

Velocity compensation on radar echoes will make the results envelop that implemented pulse compression aligning. The results will be stored, and the targets and jamming in distance element position will be extracted from the detection module after a series of signal processing flows. The pulse compression breadth of N_a coherent echoes where radar antenna scans targets in the distance element from the stored pulse compression results. Then, to estimate g_a characteristic parameter directly in

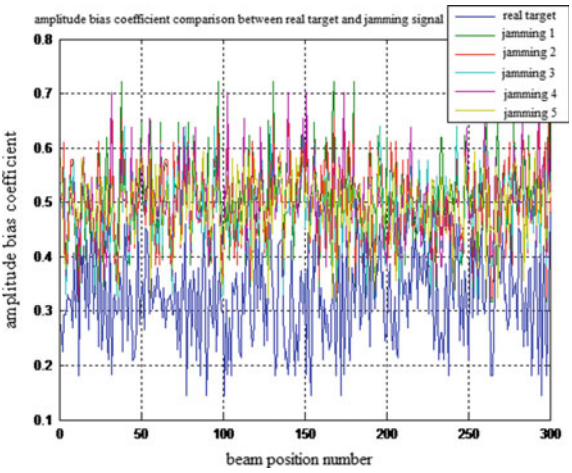


Fig. 5.18 Amplitude deviation coefficient comparison analysis between real targets and jamming signals

time domain, and its real-time characteristic satisfies radar signal processing requirement. Two types of targets will be separated according the above method, and then real targets and jamming will be distinguished based on target velocity and distance relativity. The identify flow will be given as Fig. 5.19.

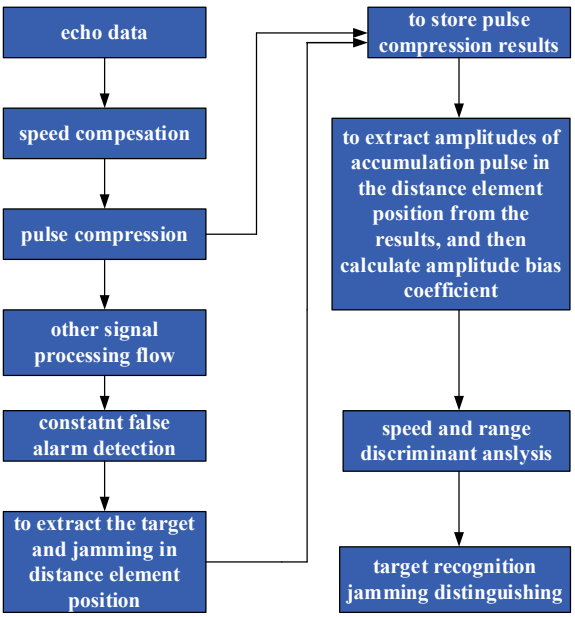

echo data
speed compesation
pulse compression
other signal processing flow
constatnt false alarm detection
to extract the target and jamming in distance element position
to store pulse compression results
to extract amplitudes of accumulation pulse in the distance element position from the results, and then calculate amplitude bias coefficient
speed and range discriminant anslysis
target recognition jamming distinguishing

Fig. 5.19 Identify algorithm flow

Table 5.5 Identify results

	Real targets	Jamming signal	Recognition rate (%)
Real targets	287	13	95.7
Jamming signal	44	1456	97.1

(b) Identify Performance Analysis

By choosing 300 real targets and 1500 jamming signal, the jamming recognition is implemented according to the above algorithm, and the results are shown as Table 5.5.

5.2.4.2 Jamming Recognition Based on Spectrum Feature

Man-made intentional passive jamming mainly refers to chaff jamming, which is relatively an important and mature jamming device in passive electronic countermeasure. Because it has low price, convenient and large area jamming, chaff technology can carry out jamming on multi-radar with different directions, different frequencies, different types and systems, even we do not know about radar parameters. (Confusing sentence please rephrase it) Chaff jamming is an important way of passive jamming, which usually launch a large number of randomly distributed chaff cloud or chaff corridor composed of half-wavelength chaffs, to disturb, puzzle, transfer and draw in missile or other aerospace vehicles. Chaff jamming substantively makes use of reradiated electromagnetic wave produced by induction alternating current in the affection of alternating electromagnetic field according to electromagnetic radiation theory, to passive jamming on radar.

Usually, ground radar employs MTI/MTD technology to restrain chaff jamming, but there is broadening phenomenon of Doppler due to wind and gravitation on chaff jamming, so as to discriminate targets or jamming, one effective way is to increase coherent integration time, and to identify chaff jamming or targets by using the spectrum characteristics of chaff jamming.

(1) Chaff cloud radar echoes model

There are two phases from chaff bomb launch to disperse: diffusion phase and stabilization phase. In diffusion phase, chaff bomb has already blasted, but it didn't diffuse completely, therefore chaff cloud density decreased, backscatter cross section increased, and chaff space distributed unsymmetrically and variationally. In stabilization phase, chaff cloud diffuses completely, its effective radar cross section reaches maximum, when the chaff cloud has ability to defend targets in deed, and it is the most difficult time for identifying chaff cloud. In stabilization, each signal in chaff cloud echo is the vector sum of single chaff echo. So our research on chaff cloud echo signals is based on stabilization phase, and also the prerequisite is targets and staff cloud is within radar beam completely. Expression (5.14) is the chaff cloud.

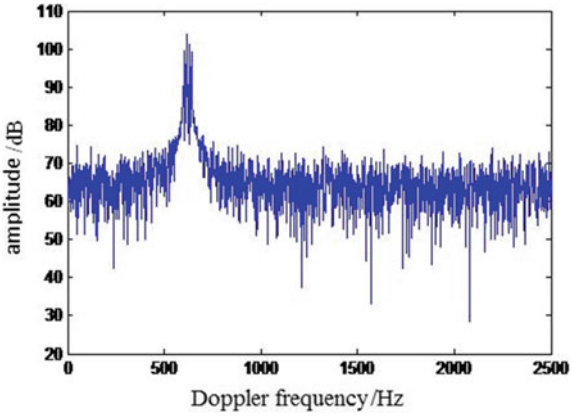


Fig. 5.20 Chaff cloud spectrum diagram for 20 chaffs

$$s(t) = \sum_{i=1}^{N} \gamma_i a^0 \exp(j2\pi(f_0 - f_{Di})(t - \frac{2r_i}{c})) = \sum_{i=1}^{N} \gamma_i a^0 \exp(j2\pi\ f_0 t) \exp(-j2\pi\ f_{Di} t) \exp(-j2\pi\ f_0 \frac{2r_i}{c}) \quad (5.14)$$

where, a^0 is transmitting signal amplitude, f_0 is centre frequency of transmitting signal, γ_I is backscattering coefficient, $i = 1, 2, \ldots, N$, and N is total chaff number. The radial distance for I chaff apart from radar is r_i, and its Doppler shift is f_{Di}.

On the assumption that the staff total number is 20, 50 and 100 respectively, the spectrum characteristics is analyzed as followings, and the spectrum diagrams are shown in Figs. 5.20, 5.21 and 5.22.

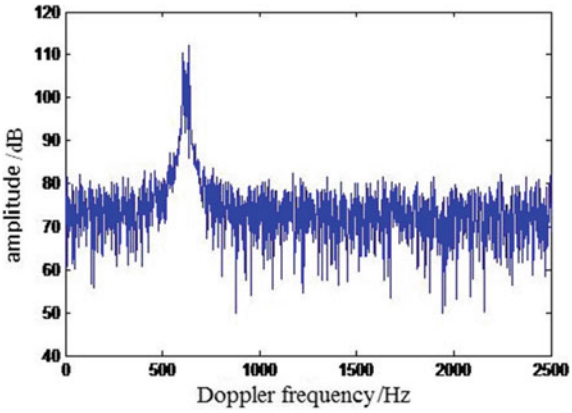


Fig. 5.21 Chaff cloud spectrum diagram for 50 chaffs

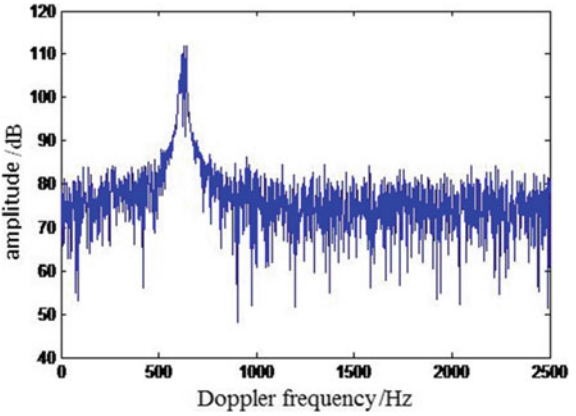


Fig. 5.22 Chaff cloud spectrum diagram for 100 chaffs

(2) Aircraft echo model

For jet, helicopter and prop aerodynamic target, excluding ground clutter and other electronic jamming, the complex envelop obtains from low resolution radar receiver at least include airframe component, rotating structures (JEM component) and noise component, which can be expressed synthetically as,

$$s(t) = a_s(t)\left\lfloor C_f S_f(t) + C_{JEM} S_{JEM}(t) \right\rfloor + C_n w_n(t) \tag{5.15}$$

where, $a_s(t)$ is the overall restriction of radar system on JEM characteristic, including transmitting signal, receiving fashion and antenna fashion effectives. $S_f(t)$, $S_{JEM}(t)$ and $\omega_n(t)$ are airframe component, rotating structure component and noise component. C_f, C_{JEM} and C_n are intensity coefficients for airframe component, rotating structure component and noise component. Suppose there are M ideal rotating parts in radar far-field distance R_0, azimuth angle α and elevation angle β, thus the echo for basic frequency rotating parts is,

$$\begin{aligned} S_{JEM}(t) = \sum_{m=0}^{M-1} \sum_{k=0}^{N_m-1} & G(L_{2m} - L_{1m}) \cos\ \beta' \cos(\theta_{k_m} + \omega_{r_m} t - \alpha) \\ & \cdot \exp\left\{ -j2\pi f_d t - j\frac{4\pi}{\lambda}\left[R_0 + \frac{L_{2m} + L_{1m}}{2} \cos\ \beta' \cos(\theta_{k_m} + \omega_{r_m} t - \alpha) \right] \right\} \end{aligned} \tag{5.16}$$

where, $G = g_{1m} + g_{2m}(\theta_{km} + \omega_{rm} - \alpha)$, the rotate speed for the mth rotating parts is ω_{rm}, the distance from blade root and blade needle to blade centre are L_{1m}, L_{2m}, M is number of rotor, fan or propeller, N_m is the blade number for the mth rotating parts, airframe Doppler $f_d = 2v/\lambda$, v is the projection of airframe velocity on the ranging from radar to target, $\theta_{km} = \theta_0 + 2\pi k/N_m$, $k = 0, 1, \cdots, N_m - 1$, θ_0 is the initial rotation angle of the 0th blade, and θ_m denotes blade angle.

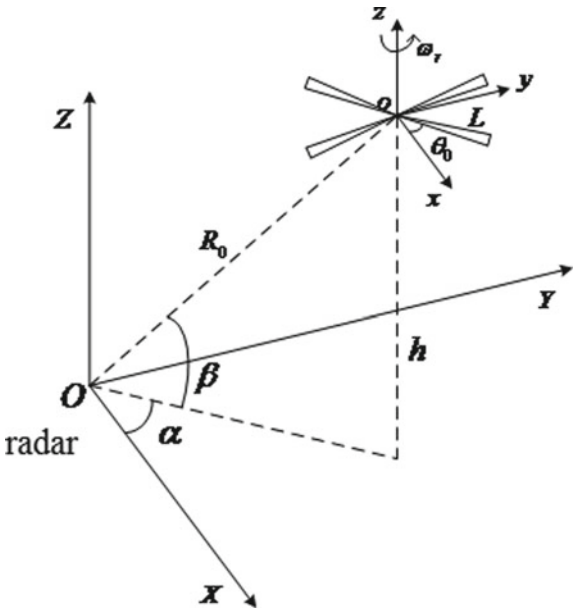


Fig. 5.23 Position sketch for rotor and radar relative position

$$g_{1m} = \sin(|\beta'| + \theta_m) + \sin(|\beta'| - \theta_m),$$
$$g_{2m} = sign(|\beta'|)[\sin(|\beta'| + \theta_m) + \sin(|\beta'| - \theta_m)] \quad (5.17)$$

When rotation surface is parallel to flight direction, $\beta' = \beta'$; and vertical to flying direction, $\beta' = \pi/2 - \beta$. Figure 5.23 shows the geometric relation between radar and rotor taking example by parallel flight direction in rotation plane. Rotation plane vertical to flight direction is similar rotor coming from far off along α direction in azimuth, and the rotor is vertical to radar ranging when it approaches on the radar, therefore the vertical rotor at range R_0, azimuth angle α and elevation angle β are equivalent to horizontal rotor at the range R_0 azimuth α and elevation angle $\pi/2 - \beta$.

The spectrum characteristics of jet, helicopter and rotor aircraft are analyzed respectively by taking measured data as background (Figs. 5.24, 5.25 and 5.26).

(3) Recognition Algorithm Flow

The engineering realization of anti-chaff jamming method by employing spectral broadening of chaff cloud is shown in Fig. 5.27. Signal processor firstly implements echo spectrum analysis and CFAR processing to obtain the echo power spectrum, and then to obtain the echo spectral width according to the spectral line number beyond threshold. The echoes for strongest spectral line present in detection element whose range element and Doppler element are R_n and F_n respectively, and then for echo

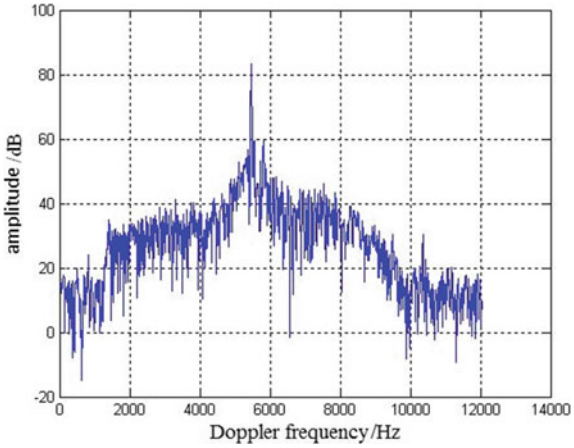
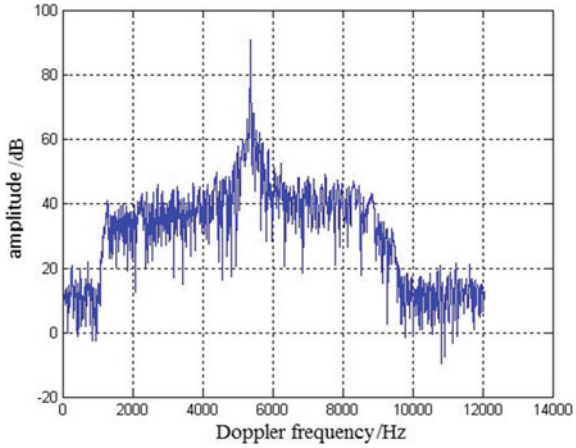


Fig. 5.24 Helicoptor frequency spectrogram

(a) Range 8km, modulation sideband SNR=22.6dB, modulation spectral width 8061Hz



(b)Range 6km, modulation sideband SNR=28.4dB, modulation spectral width 8116Hz

signal whose range element in different repeated period, to counter the spectral line number above false alarm threshold on both side centred in F_n on the dimension of Doppler. The resulted W_n is the spectral width of current detected echo. Once more, to compare adjudge W_n with spectral threshold T_n, and if it exceeds the threshold, it can be determined as chaff cloud, otherwise as aircraft. For spectral threshold T_n, its initial presetting position is T_0. The spectral width determined as chaff cloud is implemented by weighted processing as new threshold during detection, enabling spectral width adaptive regulating ability.

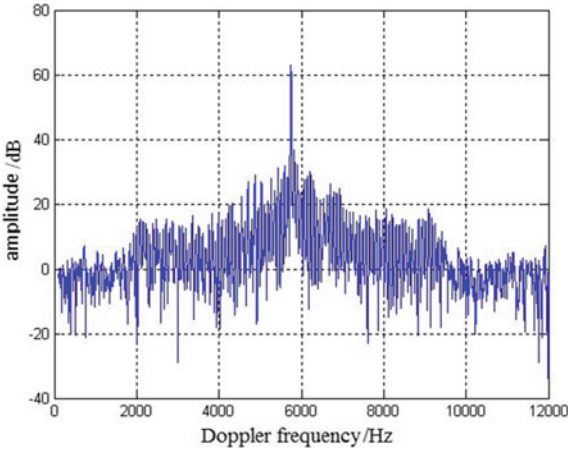
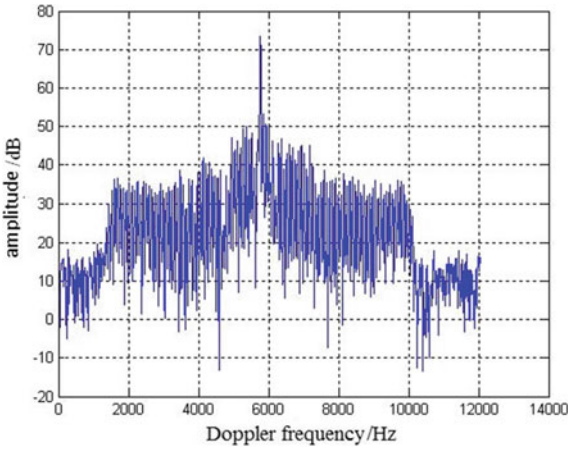


Fig. 5.25 Rotor aircraft frequency spectrogram

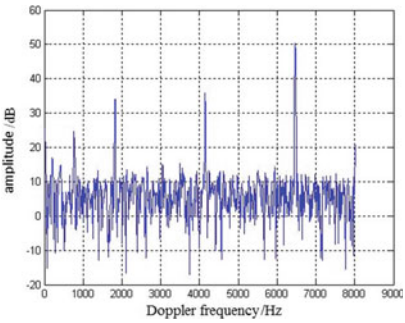
(a) Range 8km, modulation sideband SNR=9.84dB, modulation spectral width7725HZ



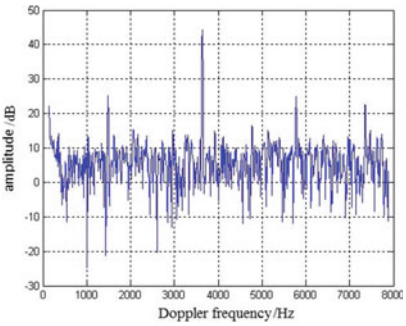
(b) Range 8km, modulation sideband SNR=25.7dB, modulation spectral width 8311Hz

(4) Recognition Performance Analysis

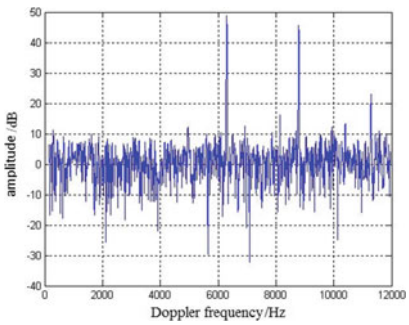
Simulation verification according to chaff cloud and aircraft echo model, and here 300 group simulation data of chaff cloud are chosen. Each 100 group data are chosen for 20, 50 and 100 chaffs, and their velocity change are restricted within 3–5 m/s. 300 groups simulation data are chosen for aircraft, where 100 groups data are chosen for helicopter, rotor aircraft and jet aircraft each. Chaff cloud is implemented jamming recognition according to the algorithm flow in Fig. 5.27, and the results are shown in Table 5.6.



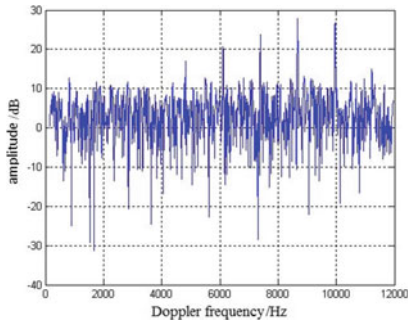
(a) Toward-station target, range 48km, modulation sideband SNR=27.76dB,modulation spectral width 5691Hz



(b) Toward-station targtet,range 76km, modulation sideband SNR=15.91dB, modulation spectral width 5837Hz



(c) Toward-station targtet, range 48km, modulation sideband SNR=29.83dB,modulation spectral width 5241Hz



(d) Toward-station targtet, range 75km, modulation sideband SNR=16.84dB,modulation spectralwidth 5216Hz

Fig. 5.26 Jet aircraft frequency spectrogram

Table 5.6 Recognition results

	Chaff cloud	Aircraft	Recognition rate (%)
Chaff cloud	278	22	92.7
Aircraft	28	272	90.1

(5) Conclusion

According to the above classification recognition results, spectral characteristics can be used effectively by differentiating aircrafts and chaff cloud. Combined with target velocity and range relativity, the method can effectively eliminate chaff jamming. The test results show the method is stable and effective.

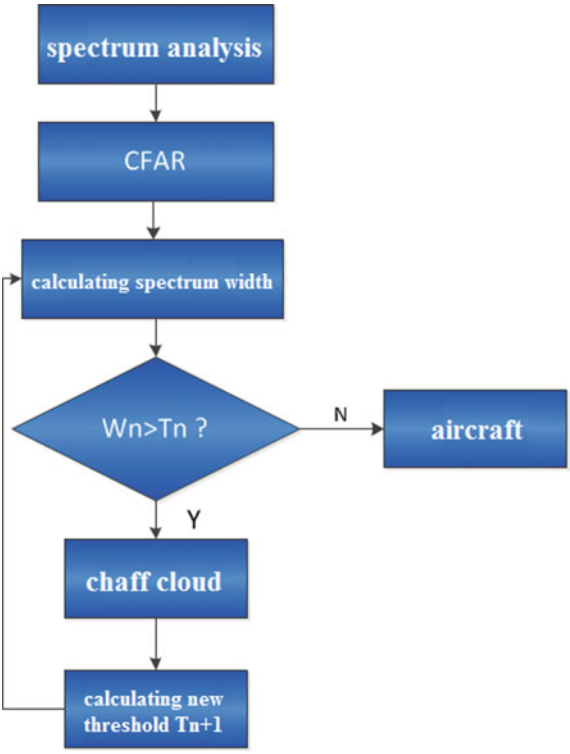


Fig. 5.27 Recognition algorithm flow

5.2.4.3 Counter Asynchronous Pulse Jamming Elimination

Asynchronous pulse jamming is part of regular pulse jamming, whose amplitude, width and repeated period are stable relatively, and they don't have integral multiple relationships with radar pulse repeated period, resulting in target echo presenting come-and-go moving periodically at range.

Advanced metricwave radar will restrain jamming signal (I and Q signal output from receiver) before pulse compression. The concrete method is: firstly, to confirm the jammed element, and then to substitute the jammed element content with sampled signal received from the same cluster of pulses, thus to decrease the jammer affection, especially on pulse compression processing. The method for confirming jammed element is: to compare the amplitudes of sampling signals in adjacent repetition periods, if the amplitude discrepancy is above certain threshold, the strong amplitude signal is regarded as jamming signal, so the element content of strong amplitude signal is substituted with sampling signal with different repeated periods from same pulse group. The reflection signals of real targets will form echoes with near amplitudes at the same range element with multiple repeated periods or multiple pulse group, while jamming signals usually only present echoes at the same range element within single or a few repeated periods.

Table 5.7 Asynchronous jamming distinguishing sheet

	Range element 1	Range element 2	Range element 3	…	Range element n
Fr2-fr1	1	1	0		0
Fr3-fr2	0	1	0		1
Judgement results	1	0	0		0

Clutter area and clean area should be differentiated for restraining asynchronous jamming. Ground clutter and jamming signal are superposed together in clutter area, therefore firstly to eliminate ground reserving jamming by two-pulse cancellation, and to position and eliminate jamming signals. Distinguishing criteria is: if three continuous FR present one jamming at most within the same range element, after the two pulses cancellation, the first row and the second row are elemented exclusive OR, if the exclusive OR is 1, the current row should be reserved (the first row saves corresponding value); if exclusive OR is 0, to execute nulling. The distinguishing method is shown in Table 5.7.

To judge whether there are jamming for the first fr within one range element by distinguishing the sheet value, if the value is 1, then it shows that there are jamming with the range element for the pulse, so to substitute the signal with adjacent fr, thus to eliminate the asynchronous jamming.

This counter asynchronous pulse jamming method has been successful applied in foreign Master-M, Track 2000 radar, and multiple domestic radars.

Bibliography

1. Zhang Yuan, Zhang Linrang, Ma Jianying. Modeling and Simulation for Low Altitude Multi-Path Echo of UWB Radar[J]. Signal Processing, 2005, 21(4A):571–574.
2. ZHOU Zhizeng, LIU Peng, GU Rongjun. Analysis of Radar Detection Under Multi-path Effect[J]. Journal of Terahertz Science and Electronic Information Technology, 2013, 11(5):736–740.
3. WANG Lijun, GUO Jianming, HAO Jing. The Influence of Multi-Path Effect on Low Altitude Cruise Missile Detection in Radar[J]. Radar Science and Technology, 2010, 18(1):7–14.
4. ZHANG Yu, MIAO Huifeng, ZHANG Xi. A Method of Improving Adaptive Nulling Performance at Low Sample Rate[J].Journal of China Academy of Electronics and Information Technology, 2013, 8(4):433–436.
5. Shengxian Sun, Jun Tong, Yaohuan Gong. Recursive Nulling in Adaptive Arrays[J]. Signal Processing, 2001, 20(4):403–405.
6. Chen Zhongxian. Design Principles for Low Probability of Intercept Guide Radar[J]. Systems Engineering and Electronics, 1999, 21(10):35–37.
7. Zhou Chang, Zhu Zhenbo, Tang Ziyue. Study on Operating Mode and Anti-Jamming Performance of Sidelobe Blanking in Pulse-Compression Radar[J]. Aerospace Electronic Warfare, 2014, 30(1):47–51.
8. He Zhen, Zhang lingjun, Liu FuQiang. Radar-Waveform and Anti-Jamming[J]. Aerospace Electronic Warfare, 2011, 27(4):22–24.

9. Wang Xiaonian, Dang Likun, Zhang Jianke. Considerations on Complicated Wave Antijamming of Digital Store Frequency[J]. Modern Defence Technology, 2011, 39(4):100–105.
10. Jin Shanshan, Wang Chunyang, Qiu Cheng. Design of RF Protecting Signal for Transponder Jamming Suppression[J]. Journal of China Academy of Electronics and Information Technology, 2014, 9(4):377–381.
11. Gan Rongbing, Ma Kangwei, Chang Jindan. Anti-Jamming Capability of High Resolution Stepped-Frequency Radar[J]. Electronic Information Warfare Technology, 2011, 26(11):36–40.
12. Huang Hongxu, Xu Hui. Performance Analysis and Estimation Research on Radar Frequency Agility Anti-Jamming[J]. Aerospace Electronic Warfare, 2001(1):21–24.
13. Ren Yi. Design of Self-Adaptive Frequency Agility of Warning Radar and Anti-Jamming Analysis[J]. Shipboard Electronic Countermeasure, 2008, 31(3):21–24.
14. Zhang Juquan, Li Chao. Anti-Jamming Efficiency Estimation Research on Frequency Agility Radar[J]. Aerospace Electronic Warfare, 2003(5):23–26.
15. Chen Yong, Shi Yinshui, Zhu Yan. The Analysis and Simulation of LFM Pulse Compression Radar Antijamming Ability[J]. Modern Defence Technology, 2008, 36(5):146–152.
16. Wu Wei, Wang Guohong, Li Shizhong. Research on Optimum Radar Pulses Accumulation in Emission Time and Energy Constraints[J]. Modern Defence Technology, 2011, 39(4):118–123.
17. Wang Cunwei, Wang Yongliang, LI Rongfeng. An Effective Technique for Smart Jamming Elimination[J]. Journal of Air Force Radar Academy, 2010, 24(4):244–247.
18. Hu Fenggang, Ruan Huailin. Characteristic Analysis of Pulse Doppler Radar and The Study of Jamming Recognition Method[J]. Shipboard Electronic Countermeasure, 2007, 30(3):30–33.
19. Fu Hongwei, Zhang Shanwen, LI Xiaoman. A Recognition Method of Chaff Jamming Based on Gray Principle[J]. Electronics Optics & Control, 2003, 10(3):42–44.
20. Yan Yan, Li Ming, Lu Yunlong. Multi-Feature-Based Identification of Smart Noise Jamming[J]. Radar Science and Technology, 2011, 33(5):39–43.
21. Gu Haiyan, Lu Gang, Tang Bin. A Method of Characteristic Analysis and Identification on Convolution Jamming[J]. Modern Radar, 2011, 33(3):39–43.
22. Li Jianxun, Tang Bin, Lü Qiang. Bispectrum Feature Extraction Used in Deceptive Jamming Modes Recognition[J]. Journal of University of Electronic Science and Technology of China, 2009, 38(3):329–332.
23. Xu Ruijie. Research on Speech Endpoint Detection Technology and DSP Implementation[D]. Beijing: Beijing University of Technology, 2010.
24. Chen Yapei. Research on Methods Against Radar Range Deception Jamming[D]. Xian: Xidian University, 2012.
25. Zhou Hang. Algorithm and Application for Active Jamming Environment Analysis Based on Radar Echo [D]. Xian: Xidian University, 2013.
26. Hu Wunyan. Research on Doppler Effect to Anti-RGPO[D]. Beijing: Beijing University of Technology, 2010.
27. Liu Qiang. Research on Radar Anti-jamming Technology-Research on Chaff Jamming Autosuppressing[D]. Zhenjiang: Jiang Su Technology University, 2007.
28. QU Changwen, LI Yanan. Research on Simulation of Radar Echo from Chaff Cloud[J]. Fire Control & Command Control, 2012, 37(7):47–50.
29. Chen Feng. Radar Target Recognition Based on HRRP and JEM Signal[D]. Xian: Xidian University, 2009.
30. Shang Wei. Theory Research and Design of a Coherence Terminal Guidance Radar Signal Processor[D]. Xian: Xidian University, 2007.

Chapter 6
Metric Wave Antenna Techniques



The antenna is a transducer for transmitting and receiving electromagnetic wave energy. In transmitting, it radiates the electromagnetic wave into the free space. In receiving, it collects the electromagnetic wave from the free space and provides signals for the receiving equipment. The antenna has an excellent directionality and is the most important component necessary for radar system. Compared with microwave band antenna, the antenna design of advanced metric wave radar has its unique particularity. For example, it is required to achieve low sidelobe and large scanning angle with few antenna elements. The calibration of a metric wave antenna is susceptible to environment, and the validation method of antenna design is different, such as antenna test. In addition, the antenna elements are required work under various extreme environments without protection of the antenna radome.

6.1 Antenna Scheme

The choice of the antenna scheme is very crucial, it is closely related to the functions that need to be performed by the radar and usually plays a crucial role. To overcome some inherent drawbacks in the conventional metric wave radar, such as low angular resolution, poor low altitude detection performance, and susceptibility to interferences, the advanced metric wave radar uses a new theory and a new technique (like DBF and super resolution) in signal processing. The digital array design concept that uses digital beamforming technique for transmission and reception is a design innovation for multifunction active phased array; its engineering realization settles a foundation for the development of multifunction phased array radars, suitable for multiple purposes. The system with digital beamforming (DBF) technique has many advantages. It can achieve optimal adaptive pattern in ECM environment. Likewise, while forming instantaneous multiple beams, adaptive nulling of jamming source can be realized and super resolution, super low sidelobe performance can be achieved. The beamforming can be adjusted according to the clutter requirement, which enables flexible and convenient beamforming. The advanced metric wave

© National Defense Industry Press, Beijing and Springer Nature Singapore Pte Ltd. 2020

J. Wu, *Advanced Metric Wave Radar*, https://doi.org/10.1007/978-981-10-7647-3_6

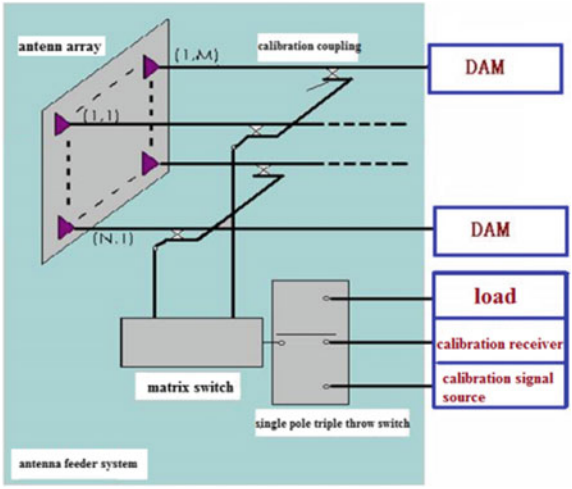


Fig. 6.1 Basic composition of digital array antenna

radar antenna adopts digital array antenna solution, which combines ultra wideband antenna array technique with fully digital array module (DAM) technique. Through the cooperative operations of antenna array, digital transmit/receive channel, calibration system, frequency synthesizing system, and digital beamforming system, the digital synthesis and control of transmit/receive beams and inner calibration of transmit/receive statuses are realized. Figure 6.1 shows the basic composition of a digital array antenna.

6.2 Main Parameters of the Antenna

The main specifications that characterize the antenna are antenna beam width, sidelobe level, and antenna gain.

6.2.1 Beamwidth

Antenna beamwidth means the mainlobe width of the antenna pattern, generally, the corresponding beamwidth at half-power of the antenna patterm. The antenna beamwidth is related to the antenna aperture, the operating frequency, and the amplitude and phase distributions at the antenna element. It determines the angular resolution of the radar and also has an effect on the antenna gain. The narrower the antenna beam, the higher the antenna gain. The antenna beamwidth can be denoted by

$$\Delta\theta_{3dB} = k\frac{\lambda}{D} \tag{6.1}$$

where, k is a constant and related to the weight of the antenna aperture. λ is the operating wavelength in frequency band, D is the aperture size of the antenna array. For phased array antennas, the beamwidth should be modified as follows

$$\Delta\theta_{3dB} = k\frac{\lambda}{D\cos\theta} \tag{6.2}$$

where, θ is the included angle between the antenna beam and the normal direction of the antenna array. When the antenna beam scans, the beamwidth widens. It can be known from the expressions (6.2) that the antenna beamwidth is inversely proportional to the antenna size and directly proportional to the wavelength. The narrow beamwidth means large antenna aperture and short wavelength.

6.2.2 Sidelobe Level

In antenna radiation pattern, there are some small sidelobes around the mainlobe. These sidelobes are called antenna sidelobes. The sidelobe level means the magnitude of the sidelobe with respect to the mainlobe. In radar systems, the antenna sidelobe level affects the radar performance. In transmitting, high sidelobe level implies a waste of the radiation power. In receiving, some unwanted energy, such as jamming and clutter, will get into the receiver through the sidelobes. That's why, for a radar system, the antenna sidelobe level has to be as low as possible.

Decreasing sidelobe levels can be done by weighting the antenna aperture illumination, however, the antenna aperture efficiency will decrease as well, which lowers the antenna gain and broadens the beamwidth. Table 6.1 gives the antenna performance parameters for some common aperture illumination functions.

6.2.3 Gain

Antenna gain represents the degree of the energy (transmitted or received by antenna) centralizing in a specific direction and is a parameter related to the antenna aperture area and aperture utilization efficiency. There are two concepts related to the antenna gain: direction gain and power gain. The direction gain is commonly called as directivity factor and the power gain is the conventional antenna gain. The directivity factor is defined as the ratio of the maximum radiation intensity and the average radiation intensity. As shown in Fig. 6.2, assume that the antenna is located in the plane XOY, $p(\theta, \varphi)$ is the radiation intensity of the antenna.

Then the total radiation intensity of the antenna is

Table 6.1 Antenna parameters for common aperture illumination functions

Aperture shape	Illumination function		Max sidelobe level (dB)	Mainlobe width	Efficiency
Rectangle aperture	Uniform		−13.2	50.8λ/D	1
	Cos		−23	68.2λ/D	0.81
	Cos^2		−32	82.5λ/D	0.67
	10 dB step Cos^2		−26	62λ/D	0.88
	20 dB step Cos^2		−40	73.5λ/D	0.75
	Hamming		−43	74.2λ/D	0.73
	Dolph-Chebyshev		−50	76.2λ/D	0.72
	Taylor	$\bar{n} = 3$	−25	60.1λ/D	0.9
		$\bar{n} = 5$	−35	67.5λ/D	0.8
		$\bar{n} = 8$	−45	74.5λ/D	0.73
Circular aperture	Uniform		−17.6	58.2λ/D	1
	Taylor	$\bar{n} = 3$	−26.2	64.2λ/D	0.91
		$\bar{n} = 5$	−36.6	70.7λ/D	0.77
		$\bar{n} = 8$	−45	76.4λ/D	0.65

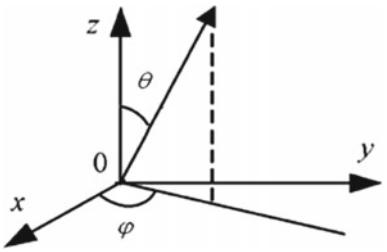


Fig. 6.2 Coordinate system of antenna radiation

$$p = \int_0^{2\pi} \int_0^{\pi} p(\theta, \varphi) d\theta d\varphi \tag{6.3}$$

The average radiation intensity of the antenna is

$$p_{av} = \frac{p}{4\pi} \tag{6.4}$$

The direction gain of the antenna is

$$D = \frac{p(\theta, \varphi)\text{max}}{p_{av}} = \frac{p(\theta, \varphi)\text{max}}{\frac{p}{4\pi}} = \frac{4\pi p(\theta, \varphi)\text{max}}{\iint p(\theta, \varphi) d\theta d\varphi} \tag{6.5}$$

If $\Delta\theta_{3dB}$ and $\Delta\varphi_{3dB}$ represent the antenna beamwidth at elevation and the antenna beamwidth at azimuth respectively, then the direction gain can be written as

$$D = \frac{4\pi p(\theta, \varphi)\max}{\iint p(\theta, \varphi) d\theta d\varphi} \approx \frac{4\pi}{\Delta\theta_{3dB}\Delta\varphi_{3dB}} \tag{6.6}$$

If $\Delta\theta_{3dB}$ and $\Delta\varphi_{3dB}$ are measured in degree, for an aperture weighted antenna array, the direction gain can be approximated as

$$D \approx \frac{27000}{\Delta\theta_{3dB}\Delta\varphi_{3dB}} \tag{6.7}$$

Because the beamwidth in two planes is equal to the ratio of wavelength and antenna aperture, that is,

$$\Delta\theta_{3dB}\Delta\varphi_{3dB} \approx \frac{\lambda}{L_1}\frac{\lambda}{L_2} = \frac{\lambda^2}{A} \tag{6.8}$$

L_1 and L_2 are the sizes of horizontal plane and vertical plane of the antenna respectively; A is the aperture area of the antenna array.

So the direction gain can also be written as

$$D = \frac{4\pi A}{\lambda^2} \tag{6.9}$$

The product of the antenna direction gain and the antenna radiation efficiency is the usual antenna gain.

$$G = D\eta \tag{6.10}$$

where η is the antenna radiation efficiency factor. For uniform illumination aperture, $\eta = 1$; for plane array antenna, taking weight influence and loss into considerations, the value of η is 0.5–0.9.

6.2.4 Others

Except for the most important specifications discussed above (beamwidth, sidelobe level, and antenna gain), there are other technical specifications required for an antenna: operating frequency, bandwidth, polarization, voltage standing wave ratio (VSWR), antenna power capacity, etc.

The operating frequency of an antenna is the operating frequency of the radar system, which is determined according to the comprehensive consideration of the functions to be performed by radar.

The bandwidth means the frequency range in which some electric specifications of the antenna may drop to their allowable values. There are two methods to define the antenna bandwidth. One is the absolute bandwidth, that is, the difference of high-end frequency and low-end frequency. The other one is the relative bandwidth, which is the percentage of absolute bandwidth to the center frequency. There are different bandwidth standards proposed for different systems and different functions, for example, the pattern bandwidth, impedance bandwidth, and gain bandwidth, or the synthetic bandwidth including multiple performance requirements.

The polarization is a parameter for describing the space pointing of the electromagnetic wave field vector radiated by antenna. There is a constant relation between electric field and magnetic field, thus the space pointing of the electric field vector is generally taken as the polarization direction of the antenna, including linear polarization, circular polarization, elliptic polarization, and etc. Both circular polarization and linear polarization are special examples of elliptic polarization. The polarization selection should be set by taking into consideration both target echo intensity and environment echo intensity effects.

VSWR shows if the input impedance and the output impedance of the antenna are in good matching or not. The closer to 1 the antenna VSWR is, the higher the antenna radiation efficiency is. Especially for phased array antennas, due to the effects of mutual coupling between the array elements, there are big changes of VSWR at different antenna scanning angles. When an important change of the antenna VSWR occurs at a specific angle, the antenna reflection is great, and "blind spot" phenomenon will even occur.

The antenna power capacity means that the antenna has no arcing or cannot be damaged when the power feeding the antenna is very high. The antenna power capacity requirement must be proposed.

6.3 Array Analysis and Design

Array antenna is a kind of combined antenna consisted of at least two elements arranged regularly or randomly and drived properly to achieve expected radiation property. By selecting reasonably and optimizing the configuration, arrangement mode, and amplitude and phase excitation, the excellent radiation property that is difficult to be realized for a single antenna can be realized to ensure various functions of radar.

6.3.1 Array Arrangement Mode

The advanced metric wave radar antenna adopts the digital array solution based on active phased array. Planar array and three-dimensional array form the view of different arrangements of array elements. The concept of three-dimensional array

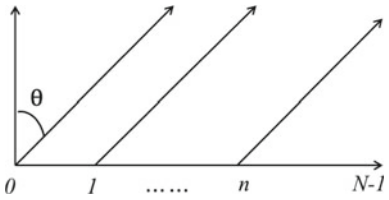


Fig. 6.3 Geometric sketch diagram of linear array

proposed here is mainly relative to planar array. The antenna elements in an array do not completely locate in a plane. The polyhedral array (trihedral array or tetrahedral array) and cylindrical array can be assorted into three-dimensional array.

(1) **Planar array**

Planar array is featured by simple structure and wide applications and is the most common array arrangement mode for phased array antenna. Linear array can be viewed as the simplest planar array. For a linear array of N elements spaced by d, its sketch diagram is shown in Fig. 6.3.

In the analysis of large phased array antenna, antenna array factor is a very important guiding index. The directivity and gain of antenna can be calculated via the antenna array factor. The design optimization of antenna array factor can make antenna achieve specific beam shape.

The array factor of linear array is

$$F(\theta) = \sum_{n=0}^{N-1} I_n \exp[jknd(\sin\theta - \sin\theta_s)] \tag{6.11}$$

where, I_n is the real current distribution of array element, d is the element spacing, k is the wave vector, and θ_s the scanning angle.

In the expression,

$$k = \frac{2\pi}{\lambda} \tag{6.12}$$

Based on actual excitation requirement, I_n can be set pertinently. The Taylor distribution can be used to obtain the required low sidelobe level pattern. In addition, according to the required pattern, the value of I_n can be determined by the shaping design. If uniform excitation mode is used, then $I_n = 1$(n = 0,1, …, N − 1),so Expression (6.11) is simplified to be

$$F(\theta) = \left| \frac{\sin(\frac{N\mu}{2})}{\sin(\frac{\mu}{2})} \right| \tag{6.13}$$

$$\mu = kd(\sin\theta - \sin\theta_s) \tag{6.14}$$

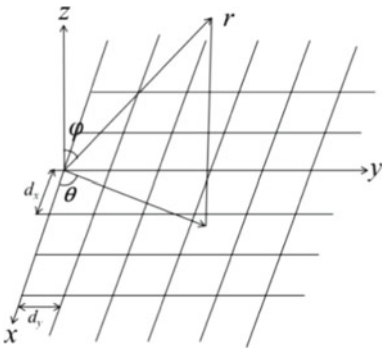


Fig. 6.4 Illustrative diagram of rectangular grid planar array

The phase difference between adjacent elements is $\varphi_s = -kd\sin\theta_s$. Changing the phase difference between elements can realize different beam direction of antenna array. This is the basic principle of phased array antenna scanning.

The planar array can be thought as the combination of multiple linear arrays. Assume an antenna array consisting of M × N similar elements arranged in rectangular grid. Its arrangement is illustrated in Fig. 6.4.

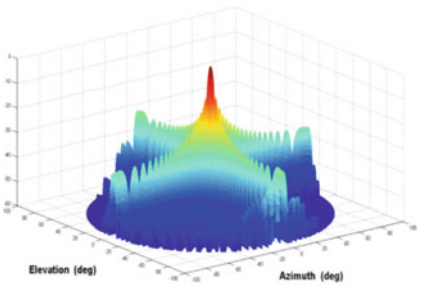
If $r(\theta_s, \varphi_s)$ is the beam pointing angle of antenna array, the array factor of rectangular grid antenna array is expressed as follows:

$$F(\theta_s, \varphi_s) = \sum_{m=0}^{M-1} \sum_{n=0}^{N-1} I_{mn} \exp[jk(md_x U + nd_y V)] \tag{6.15}$$

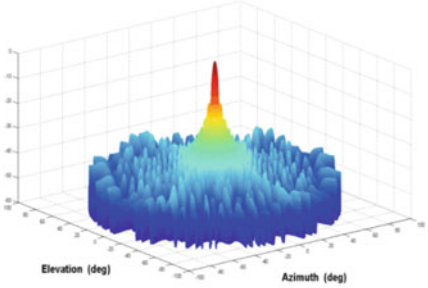
where, $U = \sin\theta\cos\varphi - \sin\theta_s\cos\varphi_s$, $V = \sin\theta\cos\varphi - \sin\theta_s\sin\varphi_s$, $k = \frac{2\pi}{\lambda}$. I_{mn} is the real current distribution of the stimulated array elements, d_x and d_y are the element spacings along the x axis and y axis, and λ is the operating wavelength of antenna.

There are three common planar array aperture shapes: rectangular aperture, circular aperture, and octagonal aperture. The ground-based large phased array radars designed by United States of America usually use circular apertures, while the Russian design uses rectangular apertures. Different antenna aperture shapes have different beam space distributions. Figure 6.5 gives the three-dimensional pattern distributions of different antenna aperture shapes with the same number of elements.

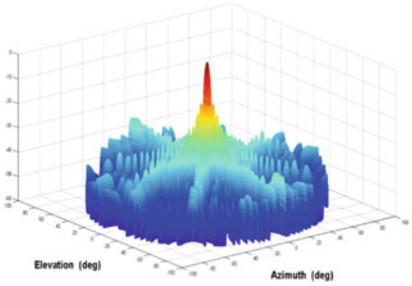
Among the above three aperture shapes, except the circular aperture, the antenna patterns of the rectangular aperture and the equilateral octagonal aperture have principal axis surfaces. From the view of antenna design, the efficiency of circular aperture is higher than rectangular aperture. Under the condition of having the same maximum designed sidelobe, the circular aperture has top aperture efficiency. From another point of view, in the case of having the same aperture weighting efficiency, the circular aperture has the least full-space theoretical maximum sidelobe and the



(a) Rectangular aperture



(b) Circular aperture



(c) Equilateral octagonal aperture

Fig. 6.5 Three-dimensional patterns of three antenna aperture shapes

more uniform full-space sidelobe property. It also has better beam symmetry and sidelobe symmetry and has problem of large main-section sidelobe.

(2) **Three-dimensional array**

For a large metric wave antenna, its array size is generally up to several tens of meters or even one thundered of meters, unabling to rotate. Thus, three-dimensional array arrangement is commonly taken to realize 360° spatial coverage. The common three-dimensional arrays are polyhedral array and cylindrical array.

A polyhedral array combines several planar arrays back to back. Obviously, a polyhedral array should have 3 arrays at least, commonly the trihedral array and tetrahedral array. The more the arrays are, the smaller the required scanning angle is. The decreasing of the maximum scanning angle implies that the gain degradation because of scanning gets small. However, at the same time, the effective area of each array decreases with the number of arrays increasing. For a polyhedral array, the normalized performance-cost ratio index q can be introduced to assess its performance. The index represents the ratio of the effective area of antenna and the number of required antenna elements (cost).

$$q = \frac{(\cos\frac{\pi}{n})^k}{n(1+\sin\frac{\pi}{n})} \tag{6.16}$$

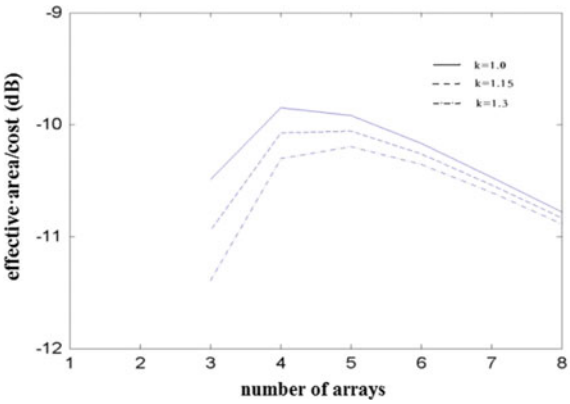


Fig. 6.6 Omnidirectional coverage normalized performance index versus number of arrays

In the formula, n is the array number of a polyhedral array, k is the factor denoting the array scanning mismatch loss, with typical value of 1.0–1.3 representing the ideal match.

Figure 6.6 shows the relation between the omnidirectional coverage normalized performance index and the array number of polyhedral array. It can be seen that the tetrahedral array and the pentahedral array basically have the same performance and the former is almost perfect.

Polyhedral array can also realize hemispheric airspace coverage. Figure 6.7 gives the structure of a trihedral array. The maximum inclination angle should be choosed so that the maximum scanning angles of all arrays is the same and the numerical value is the least. Knittel made analysis of using 3, 4, 5, and 6 arrays respectively to realize the upper half space coverages. In the case of 3 arrays, the included angle between the normal directions of the arrays and the zenith is 63°, and the maximal scanning angel of each array is 63°. For a tetrahedral array, the angle between the normal directions of the arrays and the zenith is 55°, and the maximal scanning angel of each array is 55°. For a pentahedral array, the normal direction of an array points to the zenith, and the angle between the normal directions of other 4 side arrays and the zenith is 72°. The maximal scanning angle of each array is 47°. For a hexahedral array, its arrangement is similar to a pentahedral array, which has one zenith array and five side arrays. The angle between the normal directions of side arrays and the zenith is 69°, and maximal scanning angle of each array is 41°.

Trihedral array and tetrahedral array are common. If the same gain at the minimal scanning angle is required, the needed element number of a trihedral array is 1.22 multiples of a tetrahedral array and the array area is 1.35 multiples of a tetrahedral array. If the same scanning beamwidth is required at the minimal scanning angels, the needed element number of a trihedral array is 1.45 multiples of a tetrahedral array and the array area is 1.59 multiples of a tetrahedral array.

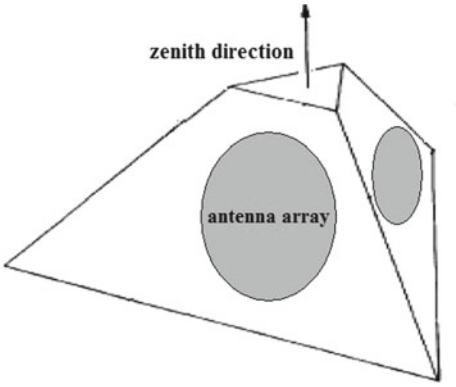


Fig. 6.7 Structural sketch diagram of a trihedral array

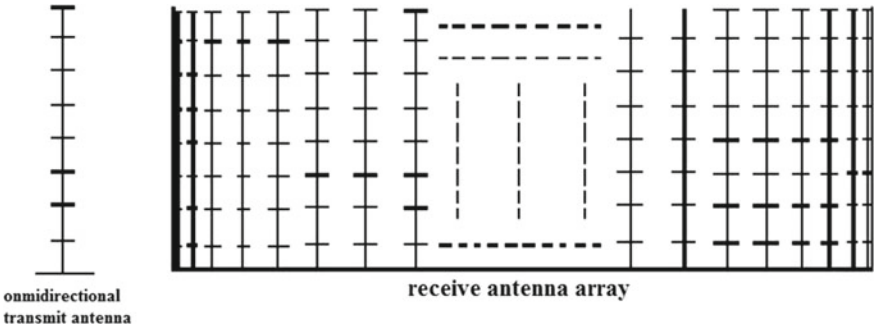


Fig. 6.8 Configuration of metric wave circular cylinder array

The commonest in cylindrical array is the circular cylinder array. Generally, its transmitting antenna array and receiving antenna array are separated. As shown in Fig. 6.8, the transmitting array is an omnidirectional antenna array and the receiving array takes the form of circular cylinder array. The elements are regularly distributed on the circular cylinder, with each antenna element connecting a digital receiver. By DBF beamforming technique, the received signals from various receivers are summed under different weights to form beams of different directions in space, realizing 360° coverage. Without beam scanning, the echo signals from the entire space can be received simultaneously.

The beam coverage of circular cylinder array is realized by selecting the receive channels of the elements in different sectors to form multiple beams simultaneously, without scanning. So that, compared with polyhedral array, the beam gain of circular cylinder array is constant, unchanging with the scanning angles.

For a circular cylinder array, the effective central angle of sector should be as large as possible. Considering the elements at edges has small contribution to coverage,

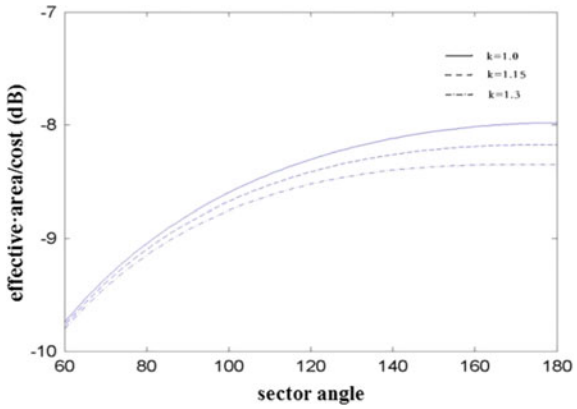


Fig. 6.9 Relationship between the omnidirectional coverage normalized performance index and the sector angle

the effective central angle of sector angle is limited to 120°. The performance-cost index of circular cylinder array, q_c, is expressed as

$$q_c = \frac{\int_0^{\Delta\phi/2} (\cos\theta)^k d\theta}{\pi(1 + \sin\frac{\Delta\phi}{2})} \tag{6.17}$$

In the expression, $\Delta\phi$ is the effective central angle of sector of circular cylinder.

Figure 6.9 gives the relationship between the omnidirectional coverage normalized performance index and the central angle of sector. It can be seen that the circular cylinder array is 1.5 dB better than polyhedral array.

Taking the minimal gain as the selection criterion, the element number of circular cylinder array is much lesser than tetrahedral array. If need low sidelobe, this advantage will weaken. The major reason is that, if excellent sidelobe control is required for a circular cylinder array, its array element spacing must be near $\lambda/2$, otherwise, large grating lobes will appear in some angular regions due to different element beam directions.

6.3.2 Grid Form and Array Element Spacing

Grid form and array element spacing are the basic parameters of phased array antenna. The phased array antenna design includes the reasonable determination of these parameters. Selection of array element spacing should be dependent on grating lobe suppression and wide angle impedance matching. It is related to the performance and manufacturing cost of antenna. For a given aperture size, the larger the array element spacing is, the samller the number of the elements set in the aperture is.

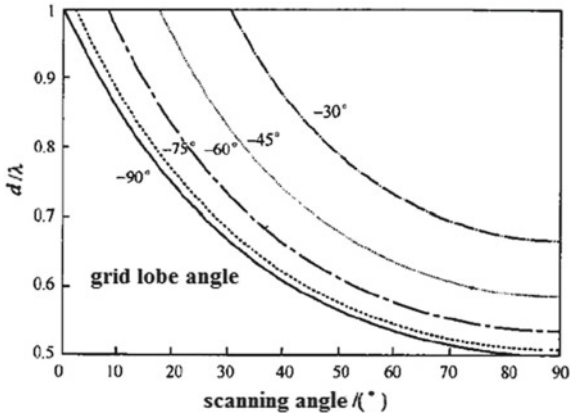


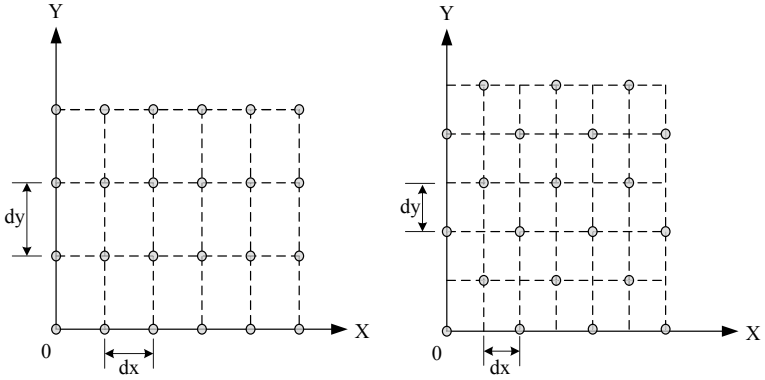
Fig. 6.10 Curve of grid lobe position versus scanning angle and array element spacing

Correspondingly, the scale and complexity of active transmitting/receiving channels can be decreased thus reducing costs. In phased array antenna, however, the array element spacing is limited by the scanning beam quality. Scanning in a preset airspace, only one mainlobe is allowed. Large array element spacing causes grating lobes that decrease the gain and singularity in the active input impedance of array element. The relationship curve of the grating lobe position varying with the scanning angle and the array element spacing is given in Fig. 6.10.

As far as planar phased array antenna is concerned, for engineering design convenience, the arrangement mode of array elements is usually the uniform regular grid. Currently, there are two kinds of familiar element arrangement modes: rectangular grid, shown in Fig. 6.11a, and triangular grid, shown in Fig. 6.11b. The rectangular grid is widely used because of its simple arraying mode, good beam characteristics, and simple feeding. The triangular grid adopts less radiation elements (with respect to the rectangular grid) and corresponding signal channels, which can save the system cost. Thus, it has been found more applications in large active phased array system with two-dimensional large scanning angle. The research for years shows that, for a two-dimensional phased array antenna with conical scanning, when the array is triangular grid, the array elements can be decreased by 13% at most. When the absolute element number is large, the decreasing of radiation elements is favorable for system cost reduction. For a phased array antenna with elevation and azimuth scanning modes, however, the array elements can be decreased only by 4–5%.

As for rectangular grid, to assure the strongest scanning capabilities in azimuth and elevation without grating lobes, the separation distances along azimuth between the radiation elements, dx and dy, need to respectively satisfy that:

$$d_x \leq \frac{\lambda_{\min} \cdot (1 - \Delta_x)}{1 + |\sin \theta_{az} \max|} \tag{6.18}$$



(a) Rectangular grid (b) Triangular grid

Fig. 6.11 Two grid arraying modes of planar array antenna

$$d_y \leq \frac{\lambda_{\min} \cdot (1 - \Delta_y)}{1 + |\sin \theta_{el}\max|} \tag{6.19}$$

where, $\lambda_{\min}$ is the least operating wavelength of antenna.

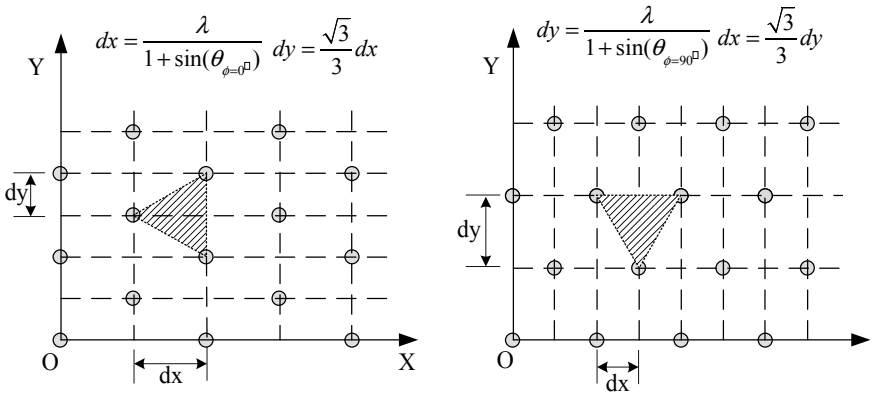
Δ_x and Δ_y are the reciprocals of the numbers of the radiation elements in azimuth and elevation respectively.

$\theta_{az}\max$ and $\theta_{el}\max$ are the maximal scanning angles in azimuth and elevation respectively.

We can see that, for a rectangular grid antenna, the grid height and width of antenna are determined respectively by azimuth scanning angle and elevation scanning angle independently.

For triangular grid, its grid from is determined jointly by two dimensions. According to the grid orientations, the triangular grid can be divided into two forms. One is side triangular grid that its dx is determined by azimuth scanning angle and then its dy is optimized by the whole scanning region. The other is regular triangular grid that its dy is determined by elevation scanning angle and then its dx is optimized by the whole scanning region. For conical scanning, the grid shapes are all the equilateral triangles, as illustrated in Fig. 6.12. The effects for reducing element number are the same; the difference is the orientations of equilateral triangles in array. For non-conical scanning airspace, the two kinds of triangular grids are the same in element number reduction.

Based on the required airspace scanning range, the element numbers of the rectangular grid-arraying mode and the two kinds of triangular grid-arraying modes are different. For the convenience of quantitative comparison, the occurrence of grating lobes in visible region is the condition, and the possible maximum spacing of each kind of grids can be found. Then, the element number of unit area is determined. Assume that an array adopts conical scanning and the scanning angle is 45°, then:



(a) Side triangular grid with its dx determined firstly

(b) Regular triangular grid with its dy determined firstly

Fig. 6.12 Two angular grids in conical scanning solution

(1) For rectangular grid: dx = 0.585 λ, dy = 0.585 λ, the element number of unit area is

$$\sigma_e = \frac{1}{dx \cdot dy} = 2.912\lambda^{-2} \tag{6.20}$$

(2) For the side triangular grid with its dx being determined firstly by azimuth scanning angle: dx = 0.585 λ, dy = 0.337 λ, the element number of unit area is

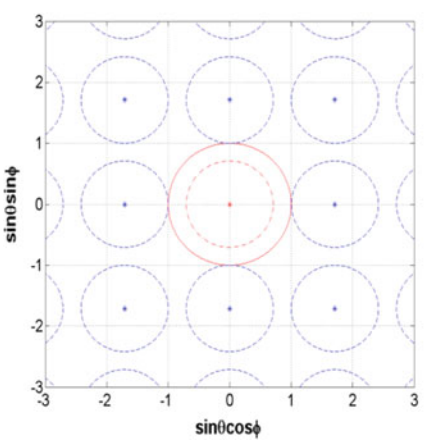
$$\sigma_e = \frac{1}{2dx \cdot dy} = 2.536/\lambda^{-2} \tag{6.21}$$

(3) For the regular triangular grid with its dy being determined firstly by elevation scanning angle: dx = 0.337 λ, dy = 0.585, the element number of unit area is

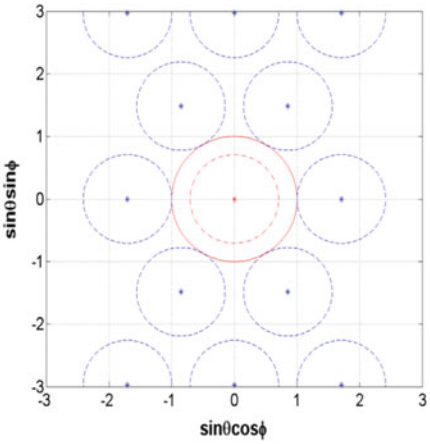
$$\sigma_e = \frac{1}{2dx \cdot dy} = 2.536/\lambda^{-2} \tag{6.22}$$

The analysis results show that, the two kinds of triangular grid structures have the same array elements and the numbers of their reduced elements are equivalent on the whole. Compared with rectangular grid, the elements can be decreased approximatively by $1 - 2.536/2.912 = 13\%$.

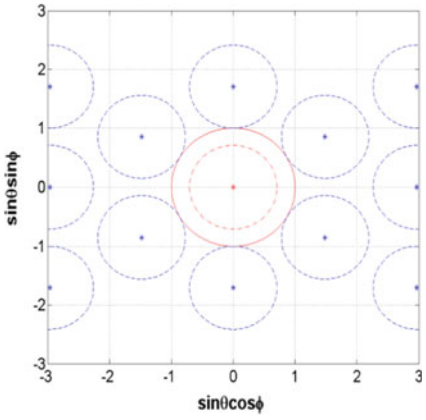
For a two-dimensional conical scanning array, if the spacing is greater than the maximum spacing limitation, there will be grating lobes entering into real space. For a straight view, Fig. 6.13 gives the distributions of the scanning airspaces of these three grid array antennas in real space and virtual space. In the figure, the dashed circles are grating lobe airspaces and the real line circle is real space region. The



(a) Distributions of rectangular grid scanning airpace in real space and virtual space



(b) Distributions of side triangular grid scanning airpace in real space and virtual space



(c) Distributions of regular triangular grid scanning airpace in real space and virtual space

Fig. 6.13 Distributions of the scanning airspaces of three arraying grid antennas in real space and virtual space

dotted line circle in the real space region is the mainlobe airspace when the array scanning 45°. The element spacing choices of the three kinds of grids are idem. It can be known from Fig. 6.13 that, when performing 45° conical scanning, the grating lobes do not enter into real space, so no grating lobes.

Table 6.2 Radiation characteristics of Hamming distribution

Aperture edge level(dB)	−21.94
Half-power beamwidth (degree)	$74.26\ \frac{L}{\lambda}$
Max sidelobe level(dB)	−42.8
Aperture efficiency	0.73

6.3.3 Common Aperture Distribution

The beam direction and beam shape of phased array antenna can be controlled in a flexible mode, which owes to the amplitude and phase distributions of array antenna aperture. The array aperture distribution has a direct effect on the total performance indexes of antenna array (including beam width, sidelobe level, and antenna gain). The following will introduce the common aperture distributions of array antenna; see the references for more distributions. The actual array aperture distribution is the discrete sampling of continuous distribution function. The theory proves that they two are in close agreement when the sampling is in conformity with Nyquist theorem.

6.3.3.1 Separable Distributions

(1) **Hamming distribution**

Hamming distribution is a low sidelobe distribution. If the aperture distribution function *g(x)* is

$$g(x) = 0.54 + 0.46\cos(\frac{2\pi x}{L})(-\frac{L}{2} \le x \le \frac{L}{2}) \tag{6.23}$$

Then the antenna pattern can be expressed as

$$E(u) = \frac{\sin(u)}{u} + 0.426(\frac{\sin(u+\pi)}{u+\pi} + \frac{\sin(u-\pi)}{u-\pi}) \tag{6.24}$$

where, $u = \frac{\pi L}{\lambda}\sin\theta$ is the general angle variable of linear aperture.

Hamming distribution has good radiation characteristics, see Table 6.2.

(2) **Taylor distribution**

Taylor distribution is characterized by high aperture efficiency and easy engineering implementation, so it has found wide applications.

For an antenna aperture with a length of *L*, if it's current distribution function *g(x)* is

$$g(x) = 1 + 2\sum_{m=1}^{N-1} E_m \cos(\frac{2m\pi x}{L})(-\frac{L}{2} \le x \le \frac{L}{2}) \tag{6.25}$$

where, N is the number of equal-level sidelobles.

$$E_m = \frac{[(N-1)!]^2}{(N-1+m)!(N-1-m)!}\prod_{n=1}^{N-1}\left[1-(\frac{m}{Z_n})^2\right]$$

Here, Z_n is

$$Z_n = \begin{cases} \pm\sigma\left[A^2 + (n-\frac{1}{2})^2\right]^{\frac{1}{2}} & (1 \le n < N) \\ \pm n & (N \le n) \end{cases}$$

$$\sigma = \frac{N}{\left[A^2 + (N-\frac{1}{2})^2\right]^{\frac{1}{2}}}$$

$$A = \frac{1}{\pi}\text{ar}\cosh t$$

t is the ratio of mainlobe level to sidelobe level, then the radiation pattern is

$$F(\frac{u}{\pi}) = \frac{\sin(u)}{u}\prod_{n=1}^{N-1}\frac{\left[1-\left(\frac{u}{\pi Z_n}\right)^2\right]}{\left[1-\left(\frac{u}{n\pi}\right)^2\right]} \tag{6.26}$$

The half-power beamwidth of Taylor distribution is

$$BW_{3dB} = \frac{\sigma\lambda}{L}\beta \tag{6.27}$$

In the formula, $\beta = \frac{2}{\pi}\left[(\text{ar}\cosh t)^2 - \left(\text{ar}\cosh\frac{t}{\sqrt{2}}\right)^2\right]^{\frac{1}{2}}$

The aperture efficiency of Taylor distribution, η is

$$\eta = \frac{1}{1 + 2\sum\limits_{n=1}^{N-1}|E_n|^2} \tag{6.28}$$

Choosing over-low sidelobe level, that is, over-large t, will decrease the array aperture efficiency. In general, when t = 20 ~ 30 dB, take N = 4 ~ 6; when t = 30 ~ 40 dB, take N = 7 ~ 11.

Table 6.3 Typical data of Ω_m and A

t(dB)	15	20	25	30	35	40
A	1.0079	1.2247	1.4355	1.6413	1.8431	2.0415
Ω_1	1.5124	1.6962	1.8826	2.0708	2.2602	2.4504
Ω_2	2.2561	2.3698	2.4943	2.6275	2.7675	2.9123
Ω_3	3.1693	3.2473	3.3351	3.4314	3.5352	3.6452
Ω_4	4.1264	4.1854	4.2527	4.3276	4.4093	4.4973

(3) **Bayliss difference distribution**

For an antenna aperture with a length of L, the current distribution function $g(x)$ is

$$g(x) = \sum_{n=0}^{N-1} B_n \sin\left[\left(n + \frac{1}{2}\right)\frac{2\pi x}{L}\right](-\frac{L}{2} \le x \le \frac{L}{2}) \tag{6.29}$$

In the expression, N is the number of equal-level sidelobles.

$$B_m = \begin{cases} (-1)^m (m + \frac{1}{2})^2 \dfrac{\prod_{n=1}^{N-1}\left[1-\left(\frac{m+\frac{1}{2}}{\sigma Z_n}\right)^2\right]}{\prod_{\substack{n=0 \\ n\neq m}}^{N-1}\left[1-\left(\frac{m+\frac{1}{2}}{n+\frac{1}{2}}\right)^2\right]} & n = 0, 1, 2 \ldots (N-1) \\ 0 & n \ge N \end{cases}$$

where, $\sigma = \frac{N+\frac{1}{2}}{(A^2+N^2)^{\frac{1}{2}}}$

$$Z_m = \begin{cases} 0 & m = 0 \\ \pm\Omega_m & m = 1, 2, 3, 4 \\ \pm\sqrt{A^2 + m^2} & m = 5, 6, 7 \cdots (N-1) \end{cases}$$

Then the Bayliss difference pattern function of the array is

$$F(\frac{u}{\pi}) = u\ \cos(u)\frac{\prod_{m=1}^{N-1}\left[1 - \left(\frac{u}{\pi\sigma Z_m}\right)^2\right]}{\prod_{m=0}^{N-1}\left[1 - \left(\frac{u}{(m+\frac{1}{2})\pi}\right)^2\right]} \tag{6.30}$$

Here, Ω_m and A are obtained by approximating the polynomials, and their typical data are given in Table 6.3.

6.3.3.2 Inseparable Distributions

For a two-dimensional array, its aperture distribution function can be divided into the products of two independent one-dimensional linear arrays. The separable distributions discussed in above section can be used; otherwise, the aperture current inseparable distributions should be employed.

(1) **Taylor distribution of circular aperture**

If a circular aperture antenna with a radius of a has current distribution $I(\rho)$, then

$$I(\rho) = \sum_{m=0}^{N-1} \frac{F_m J_0\left(\mu_m \frac{\pi\rho}{a}\right)}{\left[J_0(\mu_m \pi)\right]^2} (0 \le \rho \le a) \tag{6.31}$$

In the expression, N is the number of equal-level sidelobes, $F_0 = 1$.

$$F_m = -J_0(\mu_m \pi) \frac{\prod_{n=1}^{N-1} \left[1 - \left(\frac{\mu_m}{z_n}\right)^2\right]}{\prod_{\substack{n=1 \\ (n \ne m)}}^{N-1} \left[1 - \left(\frac{\mu_m}{\mu_n}\right)^2\right]} (1 \le m \le N-1)$$

μ_m is the mth root of $J_1(\pi x)$.

$$z_n = \pm\sigma \left[A^2 + \left(n - \frac{1}{2}\right)^2\right]^{\frac{1}{2}}$$

$$\sigma = \frac{\mu_N}{\left[A^2 + \left(N - \frac{1}{2}\right)^2\right]^{\frac{1}{2}}}$$

$$A = \frac{1}{\pi} \operatorname{arcosh} t$$

t is the ratio of mainlobe level to sidelobe level, the radiation pattern $F(u)$ is

$$F\left(\frac{u}{\pi}\right) = \frac{2J_1(u)}{u} \prod_{n=1}^{N-1} \frac{\left[1 - \frac{\left(\frac{u}{\pi}\right)^2}{z_n^2}\right]}{\left[1 - \frac{\left(\frac{u}{\pi}\right)^2}{\mu_n^2}\right]} \tag{6.32}$$

Table 6.4 gives the null position μ_m of $J_1(\pi x)$

(2) **Bayliss difference distribution of circular aperture**

If a circular aperture antenna with a radius of a has current distribution $I(\rho, \varphi)$, then

Table 6.4 Null position μ_m of $J_1(\pi x)$

m	μ_m	m	μ_m
1	1.2196699	6	6.2439216
2	2.2331306	7	7.2447598
3	3.2383155	8	8.2453948
4	4.2410629	9	9.2458927
5	5.2427216	10	10.2462933

Table 6.5 Root of first-order Bessel function derivative $\boldsymbol{J_1'(\pi\mu_m)}$

m	μ_m	m	μ_m
0	0.5860670	5	5.7345205
1	1.6970509	6	6.7368281
2	2.7171939	7	7.7385356
3	3.7261370	8	8.7398505
4	4.7312271	9	9.7408945

$$I(\rho,\varphi)=\cos\varphi\sum_{m=0}^{N-1}B_m J_1\left(\frac{u_m\pi\rho}{a}\right)(0\le\rho\le a) \tag{6.33}$$

where, N is the number of equal-level sidelobes.

$$B_m=\frac{\mu_m^2}{J_1(\mu_m\pi)}\frac{\prod_{n=1}^{N-1}\left[1-\left(\frac{\mu_m}{\sigma z_n}\right)^2\right]}{\prod_{\substack{n=1\\(n\neq m)}}^{N-1}\left[1-\left(\frac{\mu_m}{\mu_n}\right)^2\right]}$$

μ_m is the root of first-order Bessel function derivative $J_1'(\pi\mu_m)$, see Table 6.5.
$\sigma=\frac{\mu_N}{(A^2+N^2)^{\frac{1}{2}}}$, $A=\frac{1}{\pi}\text{ar}\cosh t$, t is the ratio of mainlobe level to sidelobe level.

$$Z_m=\begin{cases}0 & m=0\\ \pm\Omega_m & m=1,2,3,4\\ \pm\sqrt{A^2+m^2} & m=5,6,7\cdots(N-1)\end{cases}$$

See Table 6.3 for the data of Ω_m and A.
Thus the radiation pattern $F(u,\varphi)$ is

$$F(u,\varphi)=uJ_1'(u)\cos\varphi\frac{\prod_{n=1}^{N-1}\left[1-\left(\frac{u}{\pi\sigma z_n}\right)^2\right]}{\prod_{n=0}^{N-1}\left[1-\left(\frac{u}{\pi\mu_n}\right)^2\right]} \tag{6.34}$$

6.3.4 Intelligent Algorithms for Pattern Synthesis

The pattern shape obtained from the aperture distribution discussed in the above section is pencil sum beam or difference beam. By parameter setting, the mainlobe level, sidelobe level, and aperture effectiveness of the pattern can be synthesized. For the pattern of specially-required shape, however, it is synthesized usually by means of function approximation. Among the common synthesizing method, the Fourier synthesizing method is often used for the synthesis of the shaped beam with wide beamwidth and the Woodward synthesizing method is used to control pattern shape and sidelobe null. These methods apply constraints to both amplitude and phase of array aperture, which limits their applications. For the required pattern shapes (e.g., shaped beam, beam broadening, and sidelobe nulling), it is usually required to make synthesis of amplitude or phase of the exciting current only in practical engineering applications. The transmit shaped beams in fully digital phased array, for example, because of their transmitting power are equal, only phase synthesis is made to realize the required beam shapes. In addition, some array antennas achieve the required beam shapes through adjustment of the positions of their array elements (sparse array). The syntheses in these special cases are usually realized by use of intelligent algorithms. Currently, the effective and practical intelligent algorithms used for array antenna pattern synthesis are mainly the genetic algorithms and the particle swarm optimization algorithm.

(1) Genetic algorithm (GA)

Genetic algorithm has unique superiority in solving complex problem, such as large space, nonlinear, and global optimization, and has found wide applications in many fields. In recent years, generic algorithm has been used in electromagnetic field and antenna design, realizing parameter synthesis of array pattern successfully.

With its investigation starting from the 1960s, genetic algorithm is an adaptive search process based on genetics and natural choice. As an effective means to solve complex problem, genetic algorithm becomes the hotspot in artificial intelligence and system optimization fields currently. Starting from an initial population, genetic algorithm selects the individuals with excellent performance. Biology-like breeding is gone among these excellent individuals. Moreover, they evolve generation after generation into the zone in which the solution space becomes better and better. As long as search time is long enough and the optimal solution of each generation is held, global optimal solution can be achieved finally. In comparison with other optimization algorithms, genetic algorithm describes all of the optimization problems in the form of a single string and performs optimization computation only by use of fitness function values without other assistant information. The main characteristics of genetic algorithm are:

a. Genetic algorithm uses the code form of parameters of the problem to be solved, rather than the parameters themselves, and the operation is carried out on the given stirng.

b. Genetic algorithm needs only a fitness function, that is, the optimization object, not requiring the continuity of objective function.
c. Genetic algorithm uses probabilistic rule rather than certain rule to guide search and is able to search discrete and noisy multi-peak complex space.
d. Genetic algorithm starts to search the solution from multiple points in the solution space of problem rather than a point, thus fast global convergence can be achieved.

The basic procedures of genetic algorithm are:

(1) Generate an initial population randomly, the number of individuals is definite and each individual shows the gene code of chromosome.
(2) Compute the fitness of individuals and judge whether the optimization criteria is accorded with or not. If accordant, output the optimal individual and the optimal solution it represents and end the computation. Otherwise, go to step (3).
(3) Choose renewable individuals according to fitness. The individuals with high fitness have high probability to be chosen and those with low fitness may be eliminated.
(4) Generate new individuals according to a certain crossover probability and crossover method.
(5) Generate new individuals according to a certain mutation probability and mutation method.
(6) Generate a new generation of population and return back to step (2).

For basic principle and detailed description of genetic algorithm, please see relative literatures.

For example, consider an array aperture L. It is a linear array of N array elements. Grating lobe suppression and sidelobe level reduction are reached by optimizing the positions of array elements

The far radiation field of the linear array is

$$F(\theta) = \sum_{n=1}^{N} A(n) e^{-jkd_n \sin(\theta)} \tag{6.35}$$

where, dn represents the position of nth element, $A(n)$ is the excitation coefficient of element (also can be viewed as a optimization variable, here, $A(n) = 1$), wave number $k = 2\pi/\lambda$, λ is wavelength; θ is elevation angle, and $-\pi/2 \leq \theta \leq \pi/2$. To hold the array aperture to be L, let $d_1 = 0$, $d_N = L$, the positions of other array elements $d_2, \ldots\ldots, d_{N-1}$, meet $\min\{di - dj\} \geq C$, here C is the given minimal element distance constraint value, $1 \leq j < i \leq N$. On the basis of array constraint condition and taking the array element position as the optimization parameter, the fitness function is defined as $ffit(d_1, d_2, \ldots\ldots, d_N) = \min(F(\theta)/F_{max})$, here, F_{max} is the peak value of mainlobe, the value range of θ should exclude the mainlobe region.

Consider a linear array of 33 elements. Its aperture length is 20.48 λ and element distance constraint is $C \geq 0.5\lambda$. For equal-amplitude and in-phase excitation, when array elements are distributed and arranged uniformly, the array element distance is 0.64λ and the maximal sidelobe level is -13.2 dB. By optimizing

the array element positions, the maximal sidelobe level decreases to −22.6 dB, and the optimal array element position after optimization are: 0, 0.81, 2.04,2.65, 3.52, 4.29, 4.83, 5.41, 5.99, 6.55, 7.08, 7.61, 8.13, 8.64, 9.14, 9.64, 10.14, 10.64, 11.14, 11.64, 12.14, 12.64, 13.14, 13.64, 14.16, 14.7, 15.3, 15.97, 16.68, 17.33, 18.9, 19.67, 20.48 (unit: λ).

(2) **Particle swarm optimization (OPS) algorithm**

OPS algorithm is an evolutionary computation technique, proposed by Eberhart and Kennedy in 1995 and rooted from the research on bird flock preying behavior. Similar to genetic algorithm, it is an optimization algorithm based on iteration. The algorithm takes a set of random numbers as its initial value and searches the optimal solution via iteration. Without crossover and variation in genetic algorithm, OPS algorithm carries out the search through following the optimal particle in solution space. In comparison with genetic algorithm, OPS algorithm is characterized by few adjustable parameters, simpleness, fast convergence, and easy realization. In recent years, OPS algorithm has been widely used to solve the optimization problem of antenna array.

OPS algorithm initializes a group of random particles, and then finds out the optimal solution through iteration. In each iteration, the particles update themselves by following two extremums. One is the optimal solution found by a particle itself, that is, individual extremum, the other is the optimal solution found by the whole population, called as global extremum. Found the two extremums, the particle update their velocities and positions over again. The new velocity and position are given by

$$v_i = \omega \cdot v_i + c1 \cdot rand1() \cdot (p\_best - x_i) + c2 \cdot rand2() \cdot (g\_best - x_i) \quad (6.36)$$

$$x_i = x_i + v_i \quad (6.37)$$

where, ω is inertia weight, generally taking 0.9–0.4. c1 and c2 are acceleration constants, selected to be 2 generally. rand1() and rand2() are the random functions varying in the range of [0,1], p_best is the optimal solution of individual particle and g_best is the global optimal solution of all particles. By learning and updating continuously, the position of the optimal solution is obtained and the search process is ended.

It can be seen that OPS algorithm and genetic algorithm have some common points, such as initializing population randomly, evaluating system by use of fitness value, and conducting random search with fitness value. But OPS algorithm has no crossover and variation. It performs search at its own speed. The two algorithms are different in information sharing mechanism. In genetic algorithm, the chromosomes share information each other and the whole population moves somewhat uniformly toward the optimal region. In OPS algorithm, however, only *g_best* transfers information to other particles. This is a single-way information flow and the whole search process is a process to follow the current optimal solution. Compared with genetic algorithm, it can converge faster at the optimal solution. In genetic algorithm, many parameters are needed to adjust, such as selection probability, crossover probability,

variation probability, and so on, which lies on the experience in a great degree. As a contrast, OPS algorithm is simple in its usage and easy to master and use, without intervening parameters manually.

The basic procedures of OPS algorithm are:

(1) Initialize a group of particles in the interval to be solved, including the initializing position and speed of particle.
(2) Calculate the fitness value of each particle.
(3) For each particle, make a comparison between its fitness value and its best position experienced, p_best. If better than the later, substitute the current fitness value for the original postion.
(4) For each particle, make a comparison between its fitness value and its best position experienced globally, g_best. If better than the later, substitute over again.
(5) Update the speed and position of particle according to the formulas (6.36) and (6.37).
(6) If the finish condition has been met (generating good enough fitness value or achieving the preset largest algebra), end the computation. Otherwise, jump to step (2).

In realizing the algorithm, the particle out-of-bound problem should be taken into consideration. That is, the particle is out of bound in a dimension in the solution space according to the computation by iteration speed computing formula. Three methods can be used to solve this problem. The first is the absorbing bound. The particle takes bound value at this dimension. The second is the reflective bound. The particle holds its velocity invariable in magnitude but inverse in direction at this dimension. The third is the invisible bound. If a particle is out of bound, then its fitness value will not be estimated and it will not participate in the optimal individual competition next turn.

6.3.5 Mutual Coupling

In phased array antenna, mutual coupling exists objectively between antenna elements. Especially in the case of wideband large scan angle, the mutual coupling has severe influences, mainly exhibiting in the following aspects:

a. The element input impedance changes acutely with scan angle and operating frequency, which causes element impedance mismatch and blind point at some scan angles. This will has significant impact on system detection capability.
b. Make element beam change. In finite array, the mutual coupling environments the elements face are different, so the changes are different. Especially for the elements at the array edges, their beam shapes have great changes.
c. Change the exciting coefficient of array aperture and make the actual aperture distribution deviate from the design value, which will affect the realization of low sidelobe level and then depress the radar ECCM capability.

d. Generate parasitic radiation on the accessorial structures of antenna elements, affecting the sidelobe level and scan capability of the antenna.

Once antenna element form and element grating lobe has been determined, it is necessary to analyze and compensate for the influences resulted from mutual coupling. In particular, the active impedances of array elements should be matched well to make them have wide angle and wide band abilities.

At present, there are three main methods for achieving the active impedances of array elements:

(1) Finite small array method (experiment and simulation);
(2) Infinite array waveguide simulator method (experiment and simulation);
(3) HFSS LBC method—joint boundary conditions method.

The experiment method is a commonly used test method. In this type of experiment, the reflection coefficient of an element is measured directly via a standing wave bridge or indirectly via testing mutual coupling coefficient matrix under the environment of whole array exciting (according to the required scan angle). This experiment method is able to measure the direct relation between scan angle and element mismatch. At the same time, the measurement of the passive beam of array element can reveal preliminarily some severe "beam missing" or resonant effect, and then the possible blind point effect can be judged. This method needs to have the feeding network with beam control ability. As for the metric wave antenna operating at lower frequency, a small array often has an aperture of more than ten meters, which makes test difficult. On the other hand, the external interferences affect the test accuracy. Theoretically, commercial high-frequency structure simulation softwares can simulate and compute directly the S parameter of the experimental small array and the beams of array elements. With the increment of computer capacity and data processing capability, the computation scale and precision of antenna array can meet the engineering design requirement.

Assume that the exciting signal voltages of N array elements are V_1, V_2, … V_N, and the reflected signal voltages are e_1, $e_{2,}$… e_N. Taking the influences of mutual coupling among array elements into consideration, we can obtain:

$$[e] = [S][V] \tag{6.38}$$

That is,

$$\begin{bmatrix} e_1 \\ e_2 \\ \dots \\ e_N \end{bmatrix} = \begin{bmatrix} S_{11} & S_{12} & \dots & S_{1N} \\ S_{21} & S_{22} & \dots & S_{2N} \\ \dots & \dots & \dots & \dots \\ S_{N1} & S_{N2} & \dots & S_{NN} \end{bmatrix} \cdot \begin{bmatrix} V_1 \\ V_2 \\ \dots \\ V_N \end{bmatrix}$$

where, [S] is the mutual coefficient matrix, S_{ii} is the reflection coefficient of ith element, and S_{ij} is the coupling coefficient from jth element to ith element.

Then, the active reflection coefficient of kth antenna element is

$$r_k = e_k / v_k \tag{6.39}$$

The mutual coupling coefficient matrix of the small array, [S], can be obtained through simulation and computation by use of high-frequency simulation software. According to the known exciting voltage matrix, [V], the active reflection coefficients of array elements can be calculated by expressions (6.38) and (6.39). Consequently, the change of active impedance can be seen. Through modification and adjustment, the ideal matching can be reached.

Making use of two basic theorems, that is, the guided mode in rectangular waveguide being the overlapping of four decomposed plane waves at specific incident angles and the mirror image principle of electromagnetic field, and placing few antenna elements into rectangular waveguide, the waveguide simulator method can simulate the active impedance of antenna element in infinite array under specific scan angle. The benefits of the experimental simulation method are lower cost than the small array method and strong ability to reflect the characteristics of large-scale antenna array. But it has the drawbacks as follows. First, a kind of metal waveguide simulator can simulate a kind of scan angle under a specific frequency and the simulated scan angle varies with the change of frequency. Second, it cannot simulate side-fire beam state. Third, some scanning states cannot be simulated because of the discreteness of waveguide mode and the certainty of grid shape. Fourth, the simulation of some scanning states requires the waveguide simulator to work in higher mode, which results in difficult to design mode exciter. The greatest advantage of the waveguide simulator method is its fast simulation speed with high precision. In addition, the ideal magnetic wall can be set and the mode separation can be done in simulation, so that the second and fourth drawbacks may be overcome.

HFSS LBC method is a simulation and analysis method for infinite array by use of the periodical structure of array antenna. Its advantage is that the active impedance characteristics of the elements in infinite antenna array under various scanning angles can be obtained by simulating only one antenna element. In this way, not only the frequency characteristic of active impedance under specific scanning angle can be obtained conveniently, but also the beam scanning characteristic of active impedance at specific frequency point. It is an effective method with common use for large periodical structure array.

The uses of the above methods in combination with the traditional mutual coupling analysis theory can realize the compensation and matching of array elements and meet the engineering design requirements.

6.4 Antenna Array Element

Antenna radiation element is an important factor for array antenna composition. Its performance has a direct influence on the performance of the whole antenna. Especially for phased array antenna, the comprehensive performance of array element will widely impact the antenna array in its bean scanning performance, gain,

structural design complexity, mobility, and etc. In this section, the designs and usages of some wideband array elements with a certain scanning ability will be discussed as viewed from metric wave radar antenna. The principles will be described briefly with emphasis on engineering applications.

Metric wave antenna operates at VHF band, with wavelength from 1–10 m. The selection of array element is limited by the large sizes of antenna array and array element. Except for electric performance, the structural size, weight, assembly and setup, feeding protection complexity, and cost should be taken into consideration. The array element suitable for metric wave antenna mainly takes the structural form of rod or frame.

6.4.1 Symmetrical Dipole

Symmetric dipole antenna is a common element form in metric wave radar antenna. It takes metal rod as its radiation body and is characterized by simple structure, small longitudinal size, high intensity, wide frequency band, and easy wide angle scanning impedance matching. Figure 6.14 gives a simple model of symmetric dipole with length of $2l$ and radius of 2a.

Its field strength pattern function is

$$F(\theta, \varphi) = \frac{\cos(kl\ \cos\theta) - \cos(kl)}{\sin\theta} \tag{6.40}$$

It is obvious that the pattern is constant and independent of φ in the plane vertical to the dipole. Whatever value l/λ takes, at $\theta = 0°$ direction, the radiation field always is zero, no radiation at axial direction. When $l/\lambda < 0.7$, the maximal radiation direction is $\theta = 90°$. For common half wave dipole, $2l = 0.5\lambda$, its field strength pattern function is $F(\theta) = \frac{\cos(\frac{\pi}{2}\cos\theta)}{\sin\theta}$, the corresponding beamwidth is $\theta_{3dB} \approx 78°$.

Symmetric dipole usually operates during $0 < l/\lambda \leq 0.35$ and $0.65 < l/\lambda \leq 0.85$, its input impedance can be approximated as

$$Z_{inA} = \frac{R_m}{\sin^2(\alpha l)} - jZ_{0av}ctg(\alpha l) \tag{6.41}$$

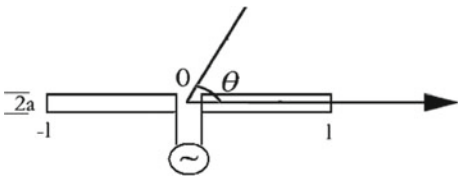


Fig. 6.14 Coodinate relation of symmetric dipole model

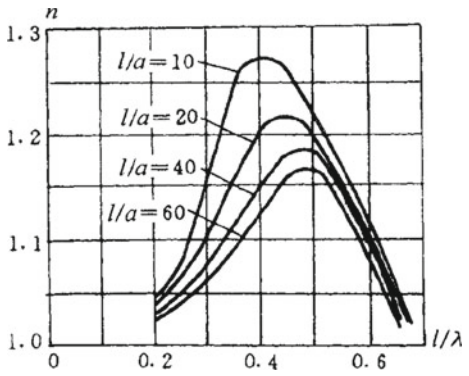


Fig. 6.15 Relation curves of wavelength shortening factor of symmetric dipole

where, l is the increased length of dipole due to ignoring end effect. Z_{0av} is the average characteristic impedance of symmetrical dipole. The characteristic impedances are different for the different positions of symmetric dipole center. The characteristic impedance of symmetric dipole is described by use of average characteristic impedance as $Z_{0av} = 120(\ln \frac{2l}{a} - 1)$. Here, $\alpha = nk$, n is the wavelength shortening factor, the relationship of n between l/λ and l/a is shown in Fig. 6.15. R_m is the radiation resistance of symmetric dipole. For a half-wave dipole, $R_m = 73.1\ \Omega$.

The average characteristic impedance becomes lower with the arm of symmetric dipole getting bigger. The flatter the input impedance varies with frequency, the easier the matching is realized in wide frequency band. In view of the size and weight of metric wave antenna, the dipole arms are often arranged to be a circle by use of multiple cables, forming a cage antenna. Also, the dipole arm can be made in the form of planar plate. For the symmetric dipole with noncircular cross section, its characteristics can be viewed to be same as the cylindrical dipole with equivalent radius.

The equivalent radius of elliptical cross section can be found by

$$a_e = (p + q)/2 \tag{6.42}$$

where, p and q are the long axis and short axis of ellipse respectively.

The equivalent radius of rectangular cross section can be obtained by searching the cure shown in Fig. 6.16.

In engineering, for the convenience of matching, the symmetrical dipole is expected to work at the state that its input impedance is the pure resistance, that is, the imaginary part is zero. Its input impedance can be approximated as

$$R_{in} = \begin{cases} 20(kl)^2 & 0 < l/\lambda \le 0.125 \\ 24.7(kl)^{2.4} & 0.125 < l/\lambda \le 0.25 \\ 11.14(kl)^{4.17} & 0.25 < l/\lambda \le 0.3185 \end{cases}$$

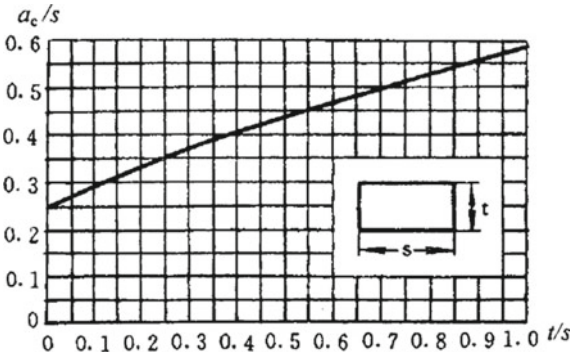
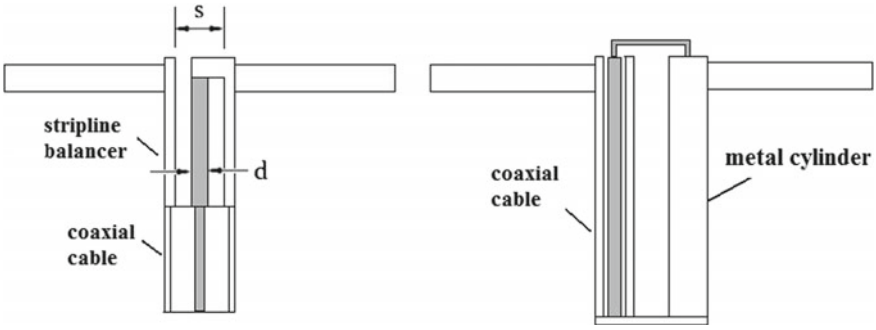


Fig. 6.16 Equivelant radius of rectangular cross section



(a) Feeding via stripline balance converter

(b) Feeding via balance converter with additional balance segment

Fig. 6.17 Feeding symmetric dipole via two balance converters

The current symmetry of two arms of symmetric dipole ensures its good electric performance. When the symmetric dipole at metric wave band is fed via double cables, the currents of its two arms can be thought to be symmetric. When feeding via coaxial cables, balance conversion is needed to ensure the current balance of two arms. Nowadays, the wideband balancers in common use are the stripline balance converter and the balance converter with additional balance segment, as illustrated in Fig. 6.17.

The stripline balance converter is a modificated design based on the traditional coaxial slotted balance converter. The two external conductors of the slotted coaxial cable are changed into two parallel plates, similar to stripline structure. This structure has larger power capacity and wider wideband characteristics. Its characteristic impedance is

$$Z_{01} = 15 + 60 \ln \frac{s}{d} (\mathrm{s/d} > 1.5) \tag{6.43}$$

$$Z_{02} = 173[\cos(90^\circ \frac{d}{s})]^{0.5} (\mathrm{d/s} < 0.6) \tag{6.44}$$

where, d is the diameter of the inner conductor between plates, s is the plate spacing. The input impedance of the stripline balance converter should be equal to the characteristic impedance of the feeding coaxial cable so as to realize good matching within wide frequency band.

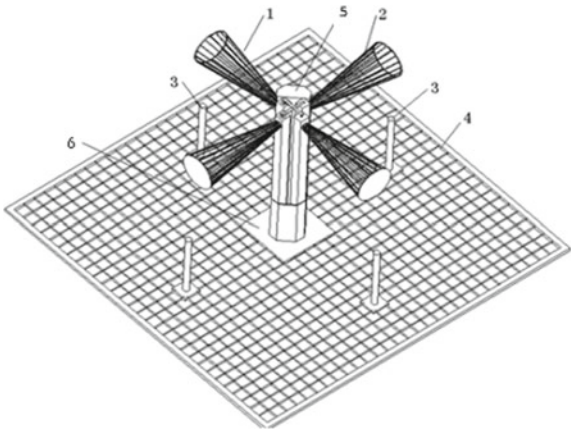
The connection form of the balance converter with additional balance segment is: the external conductor of coaxial cable is connected to an arm of dipole, the internal conductor of coaxial cable is connected to a segment of metal cylinder (0.25λ in length, the balance converter with additional segment) and then to the other arm through the metal cylinder. The structural size of the metal cylinder is equal to the structural size of the external conductor of the coaxial cable. They both are fixed on a metal base and form the 0.25λ short circuit line for terminal short circuit. As far as the above mentioned symmetric dipole antenna is concerned, because of structural symmetry, the input impedance of the short circuit line acts as a compensation for the resistance of dipole, expanding the operational bandwidth. At the same time, the shunt current on the outer wall of the external conductor of coaxial cable is equal to the current on the metal cylinder, ensuring the symmetric distribution of the currents on the two arms of dipole.

It can be seen that the symmetric dipole antenna fed using the balance converter with additional balance segment is easy to form a dual-polarization antenna element. Dual polarizations can be realized by placing two symmetric dipoles vertically and crosswise. Changing the feeding phases of the two dipoles can also form left-handed (right-handed) circular polarization operating state. What shown in Fig. 6.18 is a dual-polarization element fed using the above-mentioned feeding structure. The dipole arm is a cone cage structure with its diameter getting greater gradually along axis. The combination of metal material and feeding balancer enlarges the operating bandwidth. On the other hand, it is featured by light weight, high intensity, and low wind resistance. The parasitic posts take a metal cylinder structure and locate at two sides of symmetric dipole antenna. Choosing adequate spacing and height widens the E-plane lobe of the dipole antenna and realizes good lobe equalizing. The reflection grid increases the forward radiation efficiency of the antenna element and decreases the back lobes of the antenna significantly. Also, it is featured by light weight and low wind resistance. The relative bandwidth at an antenna standing wave ratio smaller than 2 is greater than 50% and the element isolation is greater than 30 dB.

6.4.2 Folded Dipole

The folded dipole antenna can be viewed as two half wave dipoles spacing very closely ($d \ll \lambda$), as shown in Fig. 6.19. The two top ends are the current wave nodes and the middle is the current wave antinode.

The input impedance of folded dipole is



(1, 2 —cone cage dipole arm, 3— parasitic post,
4—reflection grid, 5—antenna radome, 6—metal base)

Fig. 6.18 Wideband dual-polarization cone cage antenna

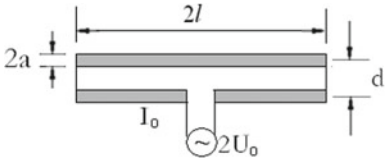


Fig. 6.19 Schematic diagram of folded dipole antenna

$$Z_{in} = \frac{2U_0}{I_0} = \frac{4Z_{inA}Z_b}{2Z_{inA} + Z_b} \tag{6.45}$$

Here, Z_{inA} is the input impedance of symmetric dipole, Z_b is the input impedance of short circuit line of l in length, $Z_b = jZ_{0b}tg(kl)$, $Z_{0b} = 120\ln(d/a)$. When $2l = \frac{\lambda}{2}$, $Z_{in} = 4Z_{inA} \approx 300\,\Omega$.

The folded dipole is equivalent to the symmetric dipole enlarged in diameter. Its equivalent radius is

$$a_e = \sqrt{ad} \tag{6.46}$$

where, a is the radius of cylinder conduct wire of folded dipole. If the radius of the two conduct wires of folded dipole are different, a_1 and a_2 respectively, then the equivalent radius is $\ln a_e = (a_1^2 \ln a_1 + a_2^2 \ln a_2 + 2a_1a_2 \ln d)/(a_1 + a_2)^2$.

The folded dipole is a kind of wide frequency band antenna element with simple structure and light weight, widely used in metric wave band. The structural model of folded dipole is illustrated in Fig. 6.20.

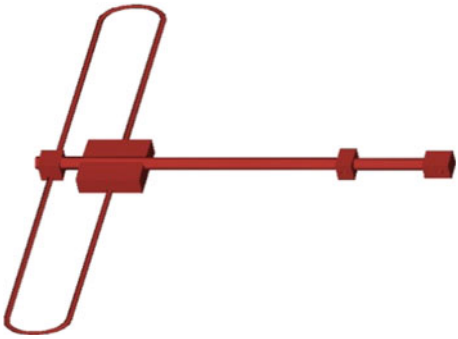


Fig. 6.20 Structural model of folded dipole

6.4.3 Directional Antenna

Directional antenna is also called as Yagi antenna. It is simple both in structure and feeding. It has found wide applications in radio equipments operating at metric wave band, such as communication, radar, television, and so on. Its structure is shown in Fig. 6.21, consisting of an active dipole, a reflector, and multiple directional passive dipoles. The active dipole may be the half wave dipole or folded dipole introduced previously. In general, the folded dipole is selected due to its higher input impedance and convenience of matching with feed line. The reflector and passive dipoles are all the isolated metal poles, disconnected to the active dipole. All dipoles are arranged in a plane, centered along a straight line and parallel each other. In operation, the active dipole radiates electromagnetic waves, which will produce induced current on the passive dipoles. By adjusting the lengths of reflector and passive dipoles and the spacings of adjacent dipoles to make the phases of induced currents on the isolated dipoles lag in turn from the reflector to the final passive dipole, the antenna radiating maximal energy toward the passive dipoles can be realized. These passive dipoles are called as director.

Directional antenna has excellent directivity. Actually, the radiation from passive dipole to reflector is very weak, so only a reflector is usually used. Adding more directional dipoles in front of the active dipole can improve the antenna gain significantly, but the number should not be over 10. Because the induced current on the directional dipole far from the active dipole away is very weak, it acts less for enhancing antenna directivity. In order to reduce the sidelobes of directional antenna and increase the forward gain, the reflector is often fabricated as a rectangular grid structure, with its grid strips being parallel to dipole.

Directional antenna is a travelling-wave antenna with slow wave structure. Its gain is approximated as

$$G \approx 10\frac{L}{\lambda} \tag{6.47}$$

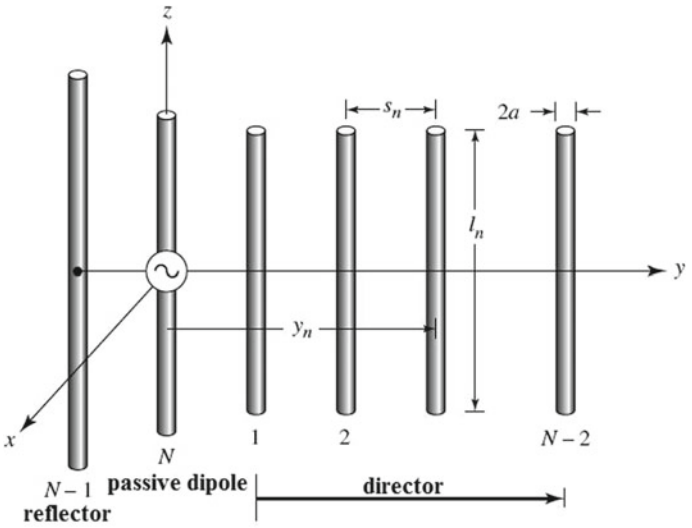


Fig. 6.21 Structrual diagram of directional antenna

Here, L is the total length. The beamwidth is approximated as

$$\theta_{3dB} \approx 55\sqrt{\frac{L}{\lambda}} \tag{6.48}$$

In designing, the structural parameters of directional antenna are determined according to the gain and beamwidth requirements. Because the parameters are restricted each other, computer aided optimization design is used in general. It is shown in practice that the parameters should be selected usually in a certain range.

The spacing between the directors of directional antenna is chosen usually in the range of (0.15–0.4) λ. When a large value is chosen, the beamwidth is narrow. There is flat frequency response characteristic of impedance, but the sidelobes are great. When a small value is chosen, the sidelobes are low, but the gain is small.

The spacing between reflector dipole and active dipole often takes (0.15–0.23) λ. It has an influence on the ratio of forward field intensity and backward field intensity and the input impedance of directional antenna. When the spacing is (0.15–0.17) λ, the ratio of forward field intensity and backward field intensity is great, the input impedance of antenna is small (15–20Ω). When the spacing is (0.2–0.23) λ, the ratio of forward field intensity and backward field intensity is small, the input impedance of antenna is great (50Ω–60Ω).

Table 6.6 gives some reference data for the selection of spacings.

As for the selection of dipole length, the reflector dipole is often within (0.5–0.55) λ. The reflector length should not be less than 1/2 of the shortest operating wavelength. The directional dipole is within (0.4–0.44) λ. The lengths of all dipoles may

Table 6.6 Optimal equal-spacing data of directional antenna

Number of dipoles N	d_r/λ	d_{01}/λ	d_{12}/λ	d_{23}/λ	d_{34}/λ	d_{45}/λ	d_{56}/λ
2	0.15–0.2						
2		0.07–0.11					
3	0.16–0.23	0.16–0.19					
4	0.18–0.22	0.13–0.17	0.14–0.18				
5	0.18–0.22	0.14–0.17	0.15–0.2	0.17–0.23			
6	0.16–0.2	0.14–0.17	0.16–0.25	0.22–0.3	0.25–0.32		
8	0.16–0.2	0.14–0.16	0.18–0.25	0.25–0.35	0.27–0.32	0.27–0.33	0.3–0.4

(d_r is the spacing between reflector and active dipole, $d_{n(n+1)}$ is the spacing of adjacent dipoles)

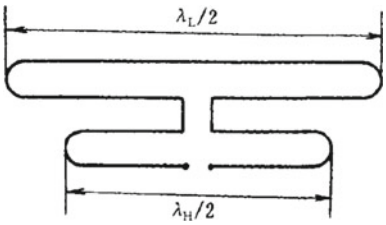


Fig. 6.22 Type H hybrid folded dipole

be equal and can be decreased gradually with the spacing increasing. The length of active dipole is about 0.475λ. The length should be short with dipole getting bigger.

The radius of passive dipole can be determined according to the antenna frequency band requirement. The bigger the dipole is, the lower the characteristic impedance is and the wider the antenna frequency band is. According to the bandwidth △f, the characteristic impedance of dipole is

$$Z_0 = (9.6 \sim 12.8) f_0/\Delta f \tag{6.49}$$

In the formula, f_0 is the center frequency. From the characteristic impedance of dipole, we can find the radius of dipole, generally being (1/500–1/80)λ_0. Table 6.7 lists the typical characteristics of several spacing-equal directional antennas for reference in design (in the table, the radius of conduction line is 0.0025λ).

The directional antenna has narrow frequency band, especially, the higher the gain is, the narrower the bandwidth is. To expand the bandwidth, the hybrid folded dipole is used as active dipole in general. Shown in Fig. 6.22 is a kind of hybrid folded dipole.

In Fig. 6.22, λ_L is the low-frequency wavelength, λ_H is the high-frequency wavelength. In this case, the input impedance of the hybrid folded dipole is about 300 Ω.

Table 6.7 Characteristics of some spacing-equal directional antennas

Element number	Spacing (wavelength number)	Element length (wavelength number)			Gain (dB)	F/B ratio (dB)	Input impedance (Ω)	H plane		E plane	
		Reflector	Exciter	Director				θ_{3dB} (°)	Sidelobe(dB)	θ_{3dB} (°)	Sidelobe (dB)
3	0.25	0.479	0.453	0.451	9.4	5.6	22.3 + j15.0	84	−11	66	−34.5
4	0.15	0.486	0.459	0.453	9.7	8.2	36.7 + j9.6	84	−11.6	66	−22.8
4	0.20	0.503	0.474	0.463	9.3	7.5	5.6 + j20.7	64	−5.2	54	−25.4
4	0.25	0.486	0.463	0.456	10.4	6.0	10.3 + j23.5	60	−5.8	52	−15.8
4	0.30	0.475	0.453	0.446	10.7	5.2	25.8 + j23.2	64	−7.3	56	−18.5
5	0.15	0.505	0.476	0.456	10.0	13.1	9.6 + j13.0	76	−8.9	62	−23.2
5	0.20	0.486	0.462	0.449	11.0	9.4	18.4 + j17.6	68	−8.4	58	−18.7
5	0.25	0.477	0.451	0.442	11.0	7.4	53.3 + j6.2	66	−8.1	58	−19.1
5	0.30	0.482	0.459	0.451	9.3	2.9	19.3 + j39.4	42	−3.3	40	−9.5
6	0.20	0.482	0.456	0.437	11.2	9.2	51.3 − j1.9	68	−9.0	58	−20
6	0.25	0.484	0.459	0.446	11.9	9.4	23.2 + j21.0	56	−7.1	50	−13.8

(continued)

Table 6.7 (continued)

Element number	Spacing (wavelength number)	Element length (wavelength number)			Gain (dB)	F/B ratio (dB)	Input impedance (Ω)	H plane		E plane	
		Reflector	Exciter	Director				θ_{3dB} (°)	Sidelobe(dB)	θ_{3dB} (°)	Sidelobe (dB)
6	0.30	0.472	0.449	0.437	11.6	6.7	61.2 + j7.7	56	−7.4	52	−14.8
7	0.20	0.489	0.463	0.444	11.8	12.6	20.6 + j16.8	58	−7.4	52	−14.1
7	0.25	0.477	0.454	0.434	12.0	8.7	57.2 + j1.9	58	−8.1	52	−15.4
7	0.30	0.475	0.455	0.439	12.7	8.7	35.9 + j21.7	50	−7.3	46	−12.6

F/B ratio = ratio of forward field intensity and backward field intensity

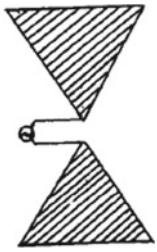
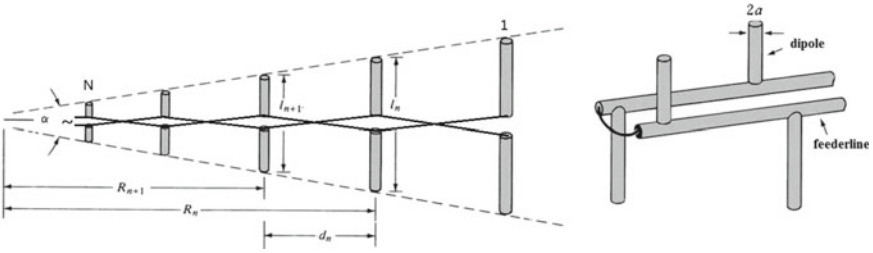


Fig. 6.23 Bow-tie antenna



(a) Geometric structure (b) Schematic diagram of feeding

Fig. 6.24 Log periodic dipole antenna

6.4.4 Log Periodic Antenna

Log periodic antenna (LPD) is a frequency-independent antenna, initially proposed by Isbell and Duhamel and modified by Isbell. After that, Carrel made detailed theoretical and experimental researches on it and proposed concrete design procedures. Log periodic antenna is a discrete self-similar structure, meeting self-similar structure at some frequency points. That is, when an antenna has been transformed at a scale factor, τ, it still holds its original structure. Thus, the characteristic of the antenna varies periodically with the logarithm of frequency.

Log periodic antenna evolved from bow-tie antenna (also called as double-fin antenna) at the very beginning. As shown in Fig. 6.23, the antenna radiates linearly polarized waves bidirectionally in the direction vertical to the antenna plane. However, it only has limited bandwidth because radial current suddenly cuts off at the end of antenna.

At the beginning of 1960s, further advance was achieved in log periodic antenna. The log periodic dipole antenna (LPDA) was developed, as illustrated in Fig. 6.24. It has found wide applications in communications, broadcasting, and television at HF, VHF, and UHF frequency bands.

The log periodic dipole antenna is composed of N symmetric dipoles in parallel arrangement. Its structural characteristics are that the sizes and positions of individual dipoles are determined according to a scale factor, τ, that is,

$$\tau = \frac{d_{n+1}}{d_n} = \frac{l_{n+1}}{l_n} = \frac{R_{n+1}}{R_n} = \frac{a_{n+1}}{a_n} \tag{6.50}$$

In the expression, τ is called as period rate, the footnote, n, indicates the serial number of dipole, $n = 1, 2, 3 \ldots N$, the small serial number means large size, d represents the spacing between dipoles, l is the full length of dipole, R is the vertical distance from the antenna geometric top, O, to dipole, a is the radius of dipole.

The whole structure of antenna relies on period rate τ, structure angel α, and spacing factor σ. α is the included angle of all dipole final-end connection lines. σ is equal to the ratio of the spacing between two adjacent dipoles and the double length of the longer dipole, that is

$$\sigma = \frac{d_n}{2l_n} \tag{6.51}$$

We can obtain

$$\alpha = 2tg^{-1}\left(\frac{1-\tau}{4\sigma}\right) \tag{6.52}$$

Therefore, among three structure parameters τ, α, and σ, only two may be selected independently. In general, all dipoles are fed via a pair of dual-wire transmission lines. The signal source is connected to the end of the short dipole. The adjacent two pairs of dipoles are cross fed, as shown in Fig. 6.24b.

The operating bandwidth of LPDA is mainly limited by geometric sizes, that is, the length of the longest dipole and the length of the shortest dipole. Nowadays, the frequency range above 10:1 has been realized.

The lengths of the longest dipole and the shortest dipole of log periodic antenna are respectively the half wavelengths of the lowest frequency and the highest frequency of the operating bandwidth, which will result in a large size metric wave antenna and inconvenience in use. On the other hand, the operating frequency band of antenna often is the bandwidth of octave. When arranging array, element spacing is determined according to the wavelength of high frequency, but the longest dipole is designed according to the wavelength of low frequency, so that the antenna will not be arranged due to the limited spacing. Thus, log periodic dipole antenna has many variations occupying reduced space in order to meet the requirements of low frequency operation and array arrangement.

Figure 6.25 shows a tree-like fractal log periodic dipole antenna. Through first-order or second-order tree-like fractal of the dipole of conventional log periodic antenna, the dipole arm length can be decreased. In this way, the horizontal size of antenna element can be decreased to be the half of conventional log periodic antenna. The combination of the dipole arm length decreasing and the loading part introducing makes the parasitic impedance decrease. In corresponding, the length of the feeding parallel dual-line can be reduced to 53% of conventional periodic antenna. Therefore,

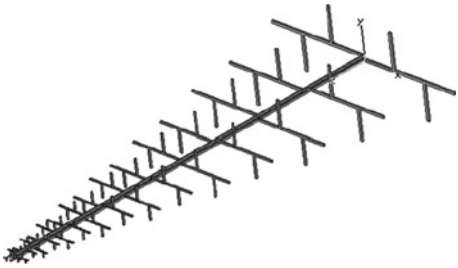


Fig. 6.25 Tree-like fractal structure

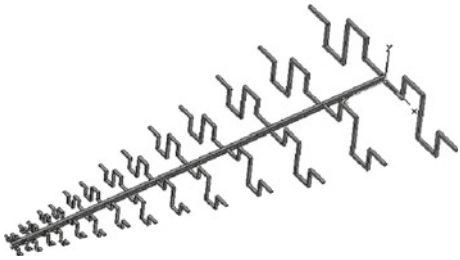


Fig. 6.26 3/2 Curve fractal structure

the antenna area is reduced to 30% of conventional periodic antenna, reducing the antenna area greatly. The array arrangement can be realized at metric wave band.

Except for tree-like fractal, Koch fractal or 3/2 Curve fractal can be applied to the dipoles of conventional log periodic dipole antenna. Figure 6.26 gives a 3/2 Curve fractal log periodic dipole antenna. The size and area of the antenna can also be reduced.

In another variation of log periodic dipole antenna, the dipoles of conventional log periodic antenna take the shape of plane rather than line. In this way, a plate dipole log periodic antenna is formed. Its horizontal size and height can be reduced to 80% of conventional log periodic dipole antenna.

6.4.5 Tapered Slot Antenna

In 1974, Lewis put forward a kind of microstrip line feed waveguide slot antenna. This antenna structure with end-firing toward open direction is thought as the origin of slot antenna. The antenna structure proposed by Lewis is illustrated in Fig. 6.27. In the slot antenna, two slots with two curved edges are opened on two layers of external conductor and the open-circuit orthogonal conductor is used for excitation.

The radiation mechanism of this antenna can be described as follows: TEM electromagnetic wave is fed from stripline transfers to slot position then excites induced

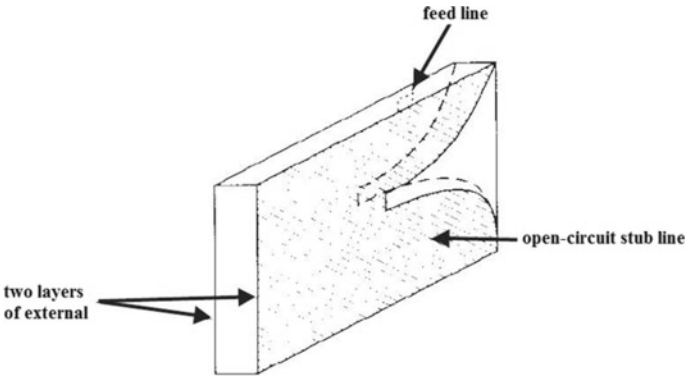


Fig. 6.27 Slot antenna structure proposed by Lewis

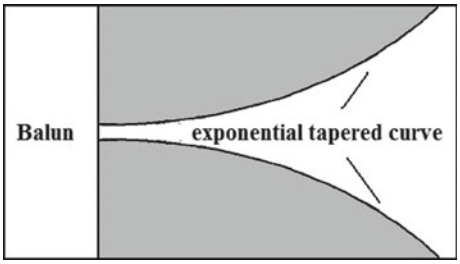


Fig. 6.28 Basic structure of Vivaldi antenna

voltage at two sides of the slot and correspondingly generates induced electromagnetic wave. The induced electromagnetic wave radiates out along the direction vertical to slot width. The electromagnetic wave radiated by the antenna is the polarizated wave, belonging to travelling wave radiation.

In 1979, a kind of exponential tapered slot antenna was proposed by Gibson and named as Vivaldi that is the name of a violinist. The structure of Vivaldi antenna is shown in Fig. 6.28. The exponential tapered metal layer is printed on the dielectric substrate. The other side of the substrate has no metal layer. The curves including in the antenna are the blocklines of exponential curve. Exponential function is defined as $y = \pm ce^{Rx}$, here y is the half of slot width, x is the length of slot, R is the tapered curvature of exponential curve. The radiation process of Vivaldi antenna is: the guided travelling wave is fed into the slot via Balun; the electromagnetic wave is tied in the slot and then propagates toward the opening direction of the slot; when the electromagnetic energy arrives at the largest opening place, the antenna starts to radiate electromagnetic wave along the direction vertical to the slot opening.

The most important structure feature of tapered slot antenna is the tapered slot. This tapered slot is the radiating region of tapered slot antenna. Generally, the portion for feeding energy in is the narrow slot portion with equal width, but this is not necessary. Electromagnetic energy can be directly fed to the tapered slot portion. In tapered

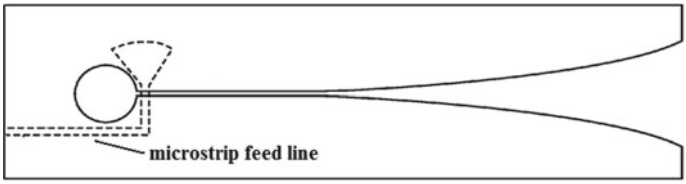


Fig. 6.29 Schematic diagram of classical tapered slot antenna structure

region, the electromagnetic energy is radiated toward the opening direction into free space via the tied electromagnetic wave. With the distance between the metalized curves becoming bigger, the tying on the electromagnetic wave becomes smaller. When the tying weakens to a certain degree, the electromagnetic wave starts to radiate. The electromagnetic signals of different frequencies are radiated via different portions of the slot. The narrow opening end radiates higher frequency electromagnetic wave and the wide opening end radiates lower frequency electromagnetic wave, showing the feature of the travelling wave antenna.

Tapered slot antenna has very wide impedance bandwidth, in general, the bandwidth at standing wave ratio smaller than 2 can reach up to 5 octaves. Its bandwidth is impacted by slot width, exponential curve form, and feeding mode. Firstly, as for slot width, narrow width corresponds to the upper limit of operating frequency and the largest opening corresponds to the lower limit of antenna operating frequency. Secondly, the curvature of exponential curve has influence on impendence bandwidth. The tapered curves in linear tapered form or other forms have different influences on impedance bandwidth. Finally, once antenna slotting structure has been fixed, the feeding mode adopted by antenna also has influence on impedance bandwidth, mainly including energy conversions at two places, one is feeding energy from feed structure to narrow slot, and the other is the electromagnetic energy tied in radiation region being converted into free space. Especially, the wideband characteristic of initial feeding is a difficult point of this antenna. Figure 6.29 gives the structural schematic diagram of classical tapered slot antenna. It adopts mcirostrip—slot coupling feeding mode.

As far as metric wave antenna is concerned, due to large antenna size, the metal portion of the above-mentioned tapered slot antenna often adopts metal plate, and, on the other hand, the feeding portion is deformed, using coaxial cable feeding structure. For further decreasing weight and wind resistance, the metal portion of tapered slot antenna usually is fabricated in frame structure, see Fig. 6.30.

Advanced metric wave radar antenna is expected to have perfect characteristic in both wide frequency band and wide scanning range. In antenna array, to avoid grid lobes when beam making wide angle scanning, the arrangement spacing should be determined according to the wavelength of higher frequency. Therefore, the element spacing is required to be very small. Under this condition, widening the array bandwidth can be realized by two methods. One is that the antenna element composing the array is a miniaturized ultra wideband antenna. The antenna size is much smaller

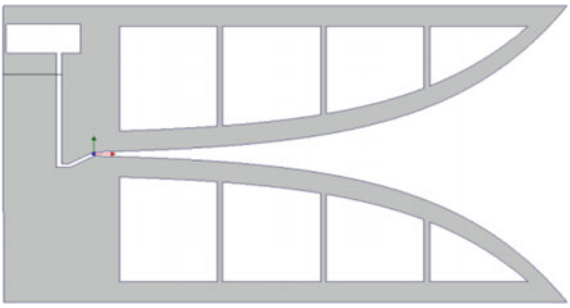


Fig. 6.30 Schematic diagram of coaxial cable feeding tapered slot antenna structure

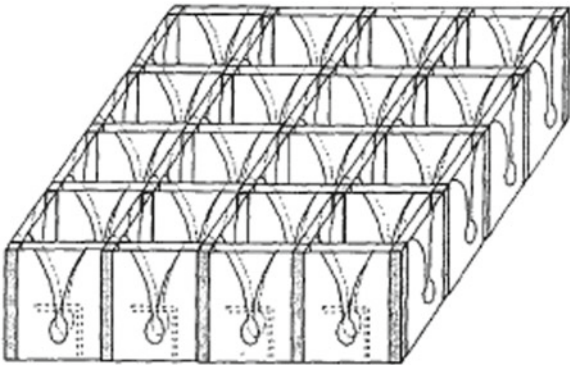


Fig. 6.31 Closely arranged array of wideband and wide angle dual-polarization tapered slot antenna

than the wavelength of lower frequency in operating bandwidth. There is excellent wideband performance within the limited element spacing. However, according to the antenna radiation principle, its physical size has a limit, which results in difficulty in realization. Another method for widening array bandwidth is to consider how antenna elements can operate in the array at the lower frequency than the frequency at which individual elements operate, that is, the mutual coupling between elements is used to make small-sized elements have larger bandwidth so as to widen the bandwidth of the whole array. For tapered slot antenna, in the case of horizontal size being limited by element spacing, through close arrangement, the bandwidth at lower frequency can be effectively widened by making use of the mutual coupling between array elements. Thus, good wide-angle scanning performance can be achieved within wide frequency band. Shown in Fig. 6.31 is a wideband and wide angle dual-polarization antenna array consisting of the tapered slot antennas in close arrangement. Scanning 45° within 4:1 bandwidth, the standing wave ratio is smaller than 2.

The basic principle of widening bandwidth by means of close arrangement is described as: in the array, because the size of tapered slot antenna is very small

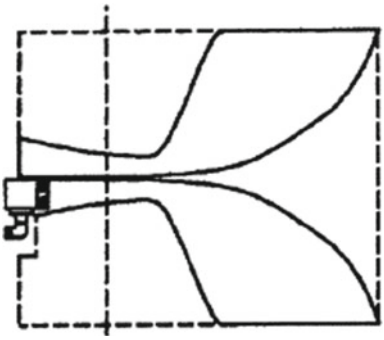


Fig. 6.32 "Bunny Ear" antenna structure

compared with the corresponding lower frequency wavelength, we can view it as short dipole with uniform current. The short dipole has very low radiation effectiveness due to its very small radiation resistance. The radiation resistance r is

$$r = 20\pi^2(l/\lambda)^2 \tag{6.53}$$

In the expression, l is the length of dipole, λ is the operating wavelength. For short dipole, $l \ll \lambda$, the radiation resistance is only several ohms. After an array has been formed, the current is nearly uniform, which means the length increasing equivalently. This makes radiation resistance increase effectively and then the radiation capability is carried to a new and higher level. Its operating bandwidth can be expanded effectively toward lower frequency. For instance, when $l = \lambda/2, r \approx 49\,\Omega$. If reaching up to the 73 ohms radiation impedance of half wave dipole, the length should be slightly larger than a half of wavelength. Taking boundary truncation effect into consideration, only the length reaches up to a wavelength of lower frequency, the ideal matching requirement can be met.

On the basis of tapered slot antenna structure, Lee and some other scholars brought forward a double exponential tapered antenna, called as "Bunny Ear" antenna. The antenna has excellent performance on 5:1 bandwidth. It is much shorter than tapered slot antenna and thus has much smaller horizontal current. Additionally, the antenna exhibits lower cross polarization performance and has simple feed line, so that it is more suitable for meeting the setup of metric wave antenna. As shown in Fig. 6.32, one of its important features is that the isolated element is not placed in the continuous metal structure.

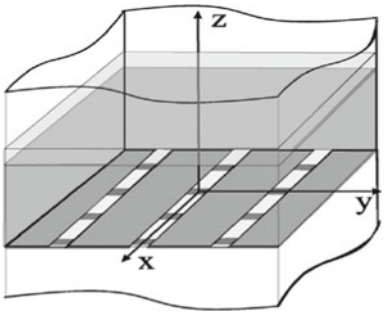


Fig. 6.33 Schematic diagram of infinite bandwidth long slot array antenna structure

6.4.6 Lon Slot Array Antenna

Long slot array is a type of ultra wideband antenna. Its basic principle is on the basis that a finite number of slots of infinite length spacing by half wavelength λ/2 of higher frequency, excited in λ/2 equal spacing along slot direction, radiate plane waves toward two sides without grid lobes. According to the dispersionless characteristic of plane wave, the array has no cut-off frequency at lower frequency band. In theory, it has infinite bandwidth. Placing metal back-cavity at one side of long slot array can realize unidirectional radiation, but the bandwidth infinity is broken. At present, it is reported in literatures that the demonstrated operational bandwidth in experiment (experimental small array) is about 4:1. The principle of long slot array antenna is given in Fig. 6.33.

In general, long slot antenna is suitable for various working environments. The use of metric wave large array antenna is mainly limited by the wind resistance and mobility of antenna structure (structure blocking design, mobile transportation structure design).

The array elements of long slot array are connected each other rather than discrete. There is strong mutual coupling between array elements. Its wideband characteristic profits just from the utilization of the mutual coupling between array elements. Shown in Fig. 6.34 is a long slot antenna structure. The long slot array antenna is across-slot excited through the interconnected dipoles located between the slot surface and the back-cavity. Array element spacing is often determined by the minimal wavelength in the operating frequency band. The selection of the feeding modes is critical, including the selection of wideband impedance conversion, balance to imbalance conversion, and feeding transmission line. Nowadays, parallel dual transmission lines are used for feeding the dipoles. The parallel dual transmission lines pass through the back cavity and connect to the transformer Balun. Such structure imposes a strict requirement on the size of antenna back-cavity structure. Meanwhile, the transformer Balun shows greater loss at higher frequency end.

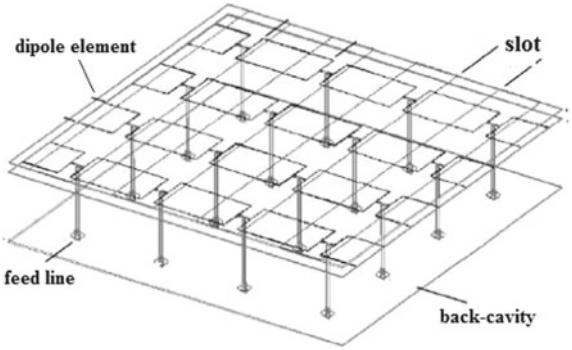


Fig. 6.34 Long slot antenna structure excited by dipole

6.5 Antenna Tolerance

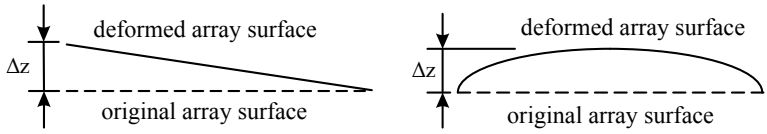
As for active phased array antenna system, the presence of various errors leads to the aperture distribution of phased array antenna deviating from the theoretical design value inevitably, which will make the antenna performance degrade, for example, sidelobe rising up, beam direction deviating, and gain dropping. There are many types of errors affecting antenna aperture distribution, usually dividing into three classes: slowly-changed error, systematic error, and random error.

In general, the slowly-changed errors result from array surface roughness, gravity deformation, and wind force deformation. The influences of this class of errors appear near the mainlobe.

The systematic errors include the inconsistent frequency characteristics among circuit components, imperfect design, structural asymmetry, and so on, usually presenting periodicity. The features of the above two classes of errors are that their influences on antenna performance can be strictly computed and controlled in advance.

The random errors involve element active channel error, manufacture tolerance, mount tolerance, element malfunction, and etc. This class of errors is random and thus difficult to strictly analyze and compute in advance. They are finally equivalent to the random changes of amplitude and phase distributions of array antenna aperture current and should be analyzed by use of statistical theory. The mount tolerance means the mount position error of array element. It introduces the phase error of element. If the position deviations of antenna element on x, y, z three axial lines are Δx, Δy, Δz respectively, then their variances are $\sigma_{\Delta x}^2, \sigma_{\Delta y}^2, \sigma_{\Delta z}^2$. If the mount tolerances of antenna element on three axial lines are identical, that is, $\sigma_{\Delta x}^2 = \sigma_{\Delta y}^2 = \sigma_{\Delta z}^2$, it can be shown that the root-mean-square of the total phase error resulted from element mount tolerance $\sigma_{\Delta\varphi}$ is

$$\sigma_{\Delta\varphi} = \frac{2\pi}{\lambda}.\sigma_{\Delta x} \tag{6.54}$$



(a) Linear deformation model (b) Secondary deformation model

Fig. 6.35 Deformation models of antenna array surface

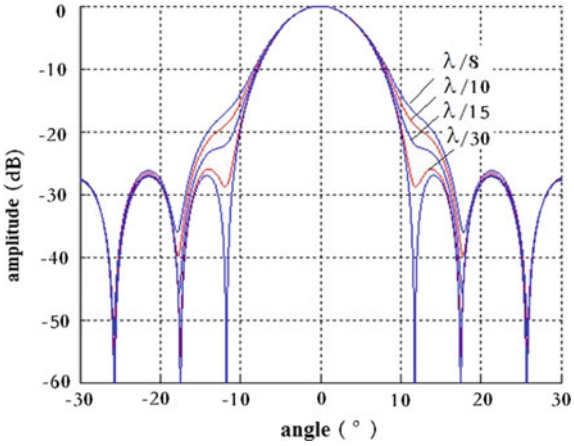


Fig. 6.36 Impact of secondary deformation of antenna structure on antenna pattern (The greatest deformation amounts are λ/8, λ/10, λ/15, and λ/30 respectively)

On the basis of structural mechanics analysis of large metric wave antenna array surface, the forced deformation of antenna can be divided into linear deformation and secondary deformation. Figure 6.35 give the linear deformation model and the secondary deformation model of antenna array surface.

It is easy to understand that the linear deformation mainly has effects on the pointing accuracy of antenna. For instance, considering a metric wave antenna with aperture being 10λ, when the greatest deformation amount of linear deformation is λ/15, the beam pointing deviation is 0.38°. The secondary deformation of array surface will add a secondary phase error to the antenna aperture, leading to antenna beam root segment widening and gain dropping. Figure 6.36 illustrates the change of antenna pattern under secondary deformation of antenna structure relative to non-deformation.

For a large array antenna, it is required to make analysis on its aperture amplitude and phase errors using statistical theory. The sidelobes having errors obey Rice distribution in probability. Therefore, when antenna beam pointing direction is (θ, φ), the mainlobe-to-sidelobe ratio of antenna R is not beyond the probability p distribution of the required value R_T, expressing by

$$p[R(\theta,\varphi) < R_T] = \int_0^{R_T} \frac{R}{\sigma_R^2} e^{-\frac{R^2+\overline{R}^2}{2\sigma_R^2}} \cdot I_0\left(\frac{R\overline{R}}{\sigma_R^2}\right) dR \tag{6.55}$$

From the expression, we can obtain the relation curve between the probability that antenna can reach a certain sidelobe level (R_{T}) and the mean square sidelobe level (σ_{R}) under the given theoretical design sidelobe level $\overline{R}$. In the expression, the mean square sidelobe level of antenna σ_R^2 is expressed by

$$\sigma_R^2 \approx \frac{1}{2}\left[\frac{f(\theta,\varphi)}{f(\theta_0,\varphi_0)}\right]^2 \cdot \frac{\varepsilon^2(\theta,\varphi)}{\eta p N} \tag{6.56}$$

Here,

$$\varepsilon^2(\theta,\varphi) = (1-p) + \sigma_A^2(\theta,\varphi) + p \cdot \sigma_{\Delta\varphi_i}^2(\theta,\varphi)$$

$\sigma_A^2(\theta,\varphi)$	amplitude variance of element
σ_R^2	variance of sidelobe-mainlobe ratio
$\sigma_{\Delta_{\varphi i}}^2(\theta,\varphi)$	phase variance
η	Antenna effectiveness
pN	Effective element number
p	Effectiveness

Assume that antenna element has no directivity, that is, $\frac{f(\theta,\varphi)}{f(\theta_0,\varphi_0)} = 1$, and the variances of amplitude and phase errors are independent of the beam scanning angle, then we have

$$(1-p) + \sigma_A^2 + p\sigma_{\Delta\varphi_i}^2 = 2 \cdot \eta p N \sigma_R^2 \tag{6.57}$$

Figure 6.37 gives the relation curves between the probabilities that the antenna reaches −25 dB and −30 dB sidelobe levels (R_{T}) respectively and the mean square sidelobe level σ_R under the aperture distribution is designed according to -35 dB Taylor distribution.

It is obvious that lower sidelobe requires smaller mean square sidelobe level σ_R under the same probability. Given the probability that the required sidelobe can be reached, the mean square sidelobe level σ_R can be calculated. Making use of the above relationship expression, the aperture amplitude and phase errors can be distributed and constrained.

In the case of having or no amplitude and phase errors, the influence of phased array antenna element on antenna gain relies on element amplitude and phase errors and effective element number of array. The correlation can be expressed as

$$\Delta G = 10 \cdot \lg\left(\frac{D(\theta_0,\varphi_0)}{D_0(\theta_0,\varphi_0)}\right) = 10 \cdot \lg\left(\frac{1}{1+\frac{\varepsilon^2}{p}}\right) \tag{6.58}$$

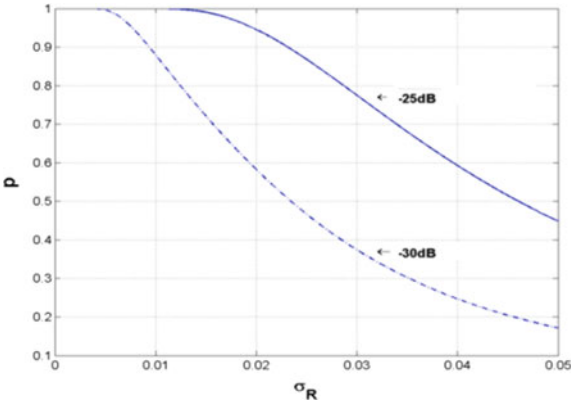


Fig. 6.37 Relation curves between the probabilities that the antenna reaches sidelobe levels and the mean square sidelobe level

Here, $D(\theta_0, \varphi_0)$ is the directivity coefficient in the case of having random amplitude and phase errors of element, $D_0(\theta_0, \varphi_0)$ is the directivity coefficient in the case of no random amplitude and phase errors of element, ΔG is the relative variation of gain. For a large phased array antenna, the random amplitude and phase errors of element channel have greater impacts on the antenna gain. In considering error distribution, special attention should be paid to antenna gain dropping.

In designing phased array radar system, the formula of beam pointing direction error is

$$\begin{aligned}\sigma_{\Delta\theta} &= \frac{\sqrt{12}}{\left(\frac{2\pi}{\lambda}d\right)N}\sigma_c \\ \sigma_c^2 &= \left[1+\sigma_A^2\right]\sigma_{\Delta\varphi}^2 \\ \sigma_{\Delta\varphi}^2 &= \sigma_{\delta i}^2 + \sigma_{\phi i}^2\end{aligned} \tag{6.59}$$

where,

σ_A^2 amplitude variance of element;
$\sigma_{\delta i}^2$ phase variance introduced by element position accuracy;
$\sigma_{\phi i}^2$ phase variance introduced by the exciting current of element channel;
N Number of elements.

6.6 Impact of Metric Wave Multipath Effect

When radar beam illuminates target, except for the echoes directly scattered back from target, there are also target echoes indirectly scattered from ground surface (sea surface) and barriers. All of these echoes arrive at radar receiver at the same time. They

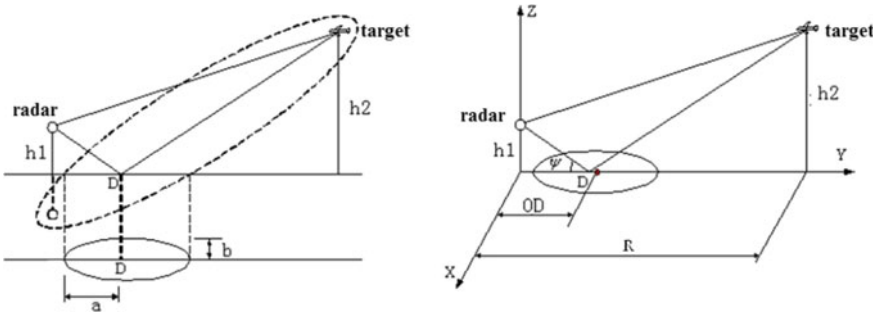


Fig. 6.38 Schematic diagram of effective reflecting zone

overlap each other and generate interference effect, usually called as multipath effect. As far as metric wave radar is concerned, ground surface and sea surface reflections are the main reasons to cause multipath effect. Multipath effect has a severe impact on antenna patter shape and makes the beam split, thus has a significant impact on radar detection performance, especially the low-altitude detection performance.

The reflection intensity is related to the roughness of ground surface (sea surface). When the mean square deviation of asperity height Δh meets $\Delta h \sin\psi \leq \lambda/8$, rough surface can be viewed as flat surface. When the grazing angle is very small and the wavelength is big, it is easy to generate multipath interference effect. The amplitude of diffuse reflection caused by the rougher surface is very small compared with the direct wave. It only causes small ripples in the direct wave, thus can be ignored.

When considering the impacts of reflection, the effective reflecting zone should be determined firstly, generally called as the first Fresnel elliptical zone in engineering. As shown in Fig. 6.38, it is an elliptical zone in which the ellipsoid making radar image and target as its two focal points intersects the ground surface. The reflection and scatter in this zone have big influences on antenna pattern. Their positions and covering ranges can be defined by the center, semi-major axis, and semi-minor axis of ellipse. Section 4.2.4 introduces the simplified method for defining effective reflecting zone from the view of site measurement required for terrain correction algorithm. In this section, the effective zone will be analyzed more fully and deeply from the view of impact on antenna performance.

When the antenna height h_1, target height h_2, and target range R are all far greater than the operating wavelength, the parameters of Fresnel elliptical zone can be computed by the following formulas respectively:

Elliptical center:

$$OD = R(1 - F_2)/2 \tag{6.60}$$

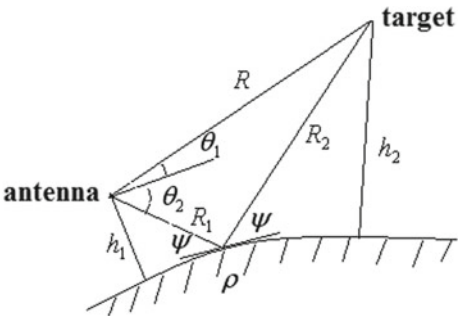


Fig. 6.39 Multipath effect model of electromagnetic wave propagation

Semi-major axis:

$$a = RF_1\sqrt{(1 + F_2^2 - 2F_3)} \tag{6.61}$$

Semi-minor axis:

$$b = R\sqrt{(F_1^2 - 1)(1 + F_2^2 - 2F_3)} \tag{6.62}$$

Here,

$$F_1 = \frac{N\lambda}{2R} + \sec(\psi)$$
$$F_2 = \frac{h_2^2 - h_1^2}{(F_1^2 - 1)R^2}$$
$$F_3 = \frac{h_2^2 + h_1^2}{(F_1^2 - 1)R^2}$$
$$\psi = arctg(\frac{h_1 + h_2}{R})$$

Considering the influence of earth curvature, the radio wave propagation can be divided into three zones: interference zone, middle zone, and diffraction zone. Multipath effect mainly appears in interference zone. The multipath effect model of electromagnetic wave propagation transmitted by the antenna set up on the ground surface is shown in Fig. 6.39.

In the multipath effect model shown in Fig. 6.39, the antenna height is h_1, the target height is h_2, the direct route of electromagnetic wave transmitted by antenna to the target is R, the reflection route of electromagnetic wave from the target is $R_1 + R_2$. According to the propagation path of electromagnetic wave, the total propagation factor to the target, F, is

$$F = f(\theta_1) \cdot \sqrt{1 + X^2 + 2X\ \cos(\alpha)} \tag{6.63}$$

where, the parameters in (6.63) are defined and described as:

$$X = \frac{\rho f(\theta_2)}{f(\theta_1)} = \frac{r D \rho_0 f(\theta_2)}{f(\theta_1)} \tag{6.64}$$

Here, ρ_0 is the amplitude value of ground surface or sea surface reflection coefficient; r is the roughness coefficient of surface; D is the diffusion factor; $f(\theta_1)$ is the antenna pattern factor of direct wave; $f(\theta_2)$ is the antenna pattern factor of reflected wave.

Phase difference:

$$\alpha = \frac{2\pi\delta}{\lambda} + \varphi + \beta_1 - \beta_2 \tag{6.65}$$

In the expression, φ is the phase loss resulted from surface reflection; β_1, β_2 are the initial phases of the antenna direct wave and the reflected wave respectively.

While the path difference:

$$\delta = R_1 + R_2 - R = \frac{2h_1h_2}{d} J(S, T) \tag{6.66}$$

In the formula, d is the horizontal distance from antenna to target, J(S,T) is the path difference correction factor considering the earth curvature and can be solved by the following formulas. For the convenience of computation, two intermediate variables S_1 and S_2 are introduced.

$$S = \frac{d}{\sqrt{2a_e}(\sqrt{h_1} + \sqrt{h_2})} = \frac{(S_1 + S_2 T)}{1 + T} \tag{6.67}$$

$$T = \sqrt{\frac{h_1}{h_2}} \tag{6.68}$$

$$S_2 = \frac{\sqrt{(1 - S_1^2)^2 + 4S_1^2T^2} + S_1^2 - 1}{2S_1T} \tag{6.69}$$

where a_e is the equivalent radius of the earth which is about 8500 km. From formulas (6.67), (6.68), and (6.69), we can find out parameters S, T, S_1, and S_2.

Then,

$$J(S, T) = (1 - S_1^2)(1 - S_2^2) \tag{6.70}$$

Diffusion factor:

Table 6.8 Relative dielectric constants and conductivities of common earth materials

Material	Relative dielectric constant ε_1	Conductivity σ (S/m)
Low-salt sea water	80	1
Mean-salt sea water	70	5
Fresh water	80	0.003
Wet soil	30	0.01
Medium-dry ground	15	0.001
Dry ground	7	0.0003

$$D = (1 + \frac{4S_1^2 S_2 T}{S(1 - S_1^2)(1 + T)})^{(-0.5)} \tag{6.71}$$

As for the roughness coefficient r, if the height distribution of rough surface obeys Gaussian distribution, then the roughness coefficient is

$$r = \exp(-2(\frac{2\pi H \sin(\psi)}{\lambda})^2) I_0(2(\frac{2\pi H \sin(\psi)}{\lambda})^2) \tag{6.72}$$

where, H is the standard deviation of Gaussian height distribution; I_0 is the zeroth-order modified Bessel function; ψ is the grazing angle and can be found by the following formula after correction taking the earth curvature into consideration:

$$\tan(\psi) = (\frac{h_1 + h_2}{d}) * (\frac{(1 - S_1^2) + T^2(1 - S_2^2)}{1 + T^2}) \tag{6.73}$$

For vertical polarization antenna, the ground surface reflection coefficient is:

$$\rho_v = \rho_{0v} e^{-j\varphi_v} = \frac{\varepsilon_c \sin(\psi) - \sqrt{\varepsilon_c - \cos^2(\psi)}}{\varepsilon_c \sin(\psi) + \sqrt{\varepsilon_c - \cos^2(\psi)}} \tag{6.74}$$

For horizontal polarization antenna, it becomes:

$$\rho_h = \rho_{0h} e^{-j\varphi_h} = \frac{\sin(\psi) - \sqrt{\varepsilon_c - \cos^2(\psi)}}{\sin(\psi) + \sqrt{\varepsilon_c - \cos^2(\psi)}} \tag{6.75}$$

where, $\varepsilon_c = \varepsilon_1 - j60\lambda\sigma$ is the complex dielectric constant of surface material; ε_1 is the relative dielectric constant; σ is its conductivity whose unit is S/m. λ is the wavelength whose unit is m. Table 6.8 gives characteristic parameters of some common earth materials.

The above two formulas show that the surface reflection coefficient of horizontal polarization radio wave becomes large, the amplitude value approaches to 1 and is not sensitive to the change of frequency. Compared with horizontal polarization, the surface reflection coefficient of vertical polarization radio wave is small and has an

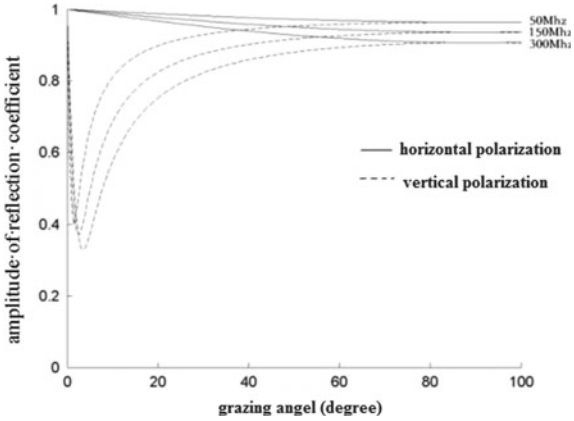


Fig. 6.40 Amplitude change curve of reflection coefficient

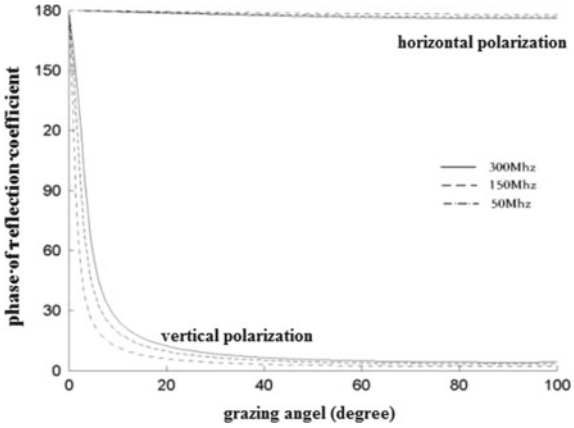


Fig. 6.41 Phase change curve of reflection coefficient

obvious change with frequency. Figs. 6.40 and 6.41 respectively show the curves of amplitude and phase of sea surface reflection coefficient changing with incident angle at different frequencies.

Figure 6.42 shows the lobe changes of the antenna set up 20 m impacted by dry ground and sea surface multipath effects.

It can be understood from the above analysis that multipath effect leads to antenna beam splitting and significantly tilting up, which has a great influence on the radar low-altitude detection performance. In the same state, sea surface multipath reflection contributes an influence on antenna lobe greater than dry ground. Under the same reflection surface, the higher the antenna is set up, the larger the influence of multipath effect is, leading to the antenna pattern splitting to generate more and denser lobes. Under the same antenna height, in comparison with the wavelength, the smoother

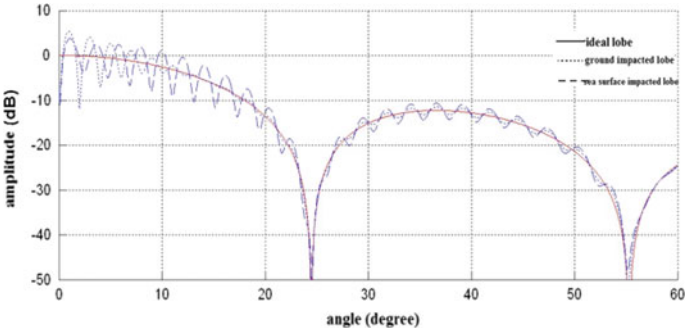


Fig. 6.42 Lobe changes of the antenna set up 20 m impacted by dry ground and sea surface multipath effects

the reflection surface is, the severer the influence of multipath effect is. This further shows that the multipath reflection has a greater impact on metric wave antenna beam compared with other microwave antennas.

6.7 Antenna Monitoring and Calibration Techniques

In active phased array antenna, because of various factors such as inconsistency of components, manufacturing tolerance, assembling error, replacement of component, mutual influence between elements, environment temperature, certainly, there are initial amplitude and phase errors existing in the channels of phased array antenna. These errors will severely damage the antenna pattern characteristics, resulting in antenna gain dropping, sidelobe level rising, and beam pointing accuracy decreasing. Therefore, for ensuring phased array antenna in normal operation, the system must have flexible, reliable, accurate amplitude and phase online monitoring and correction abilities. Through accurate measurement, calibration, and compensation of the amplitude and phase characteristics of each channel, the antenna reaches the required technical specifications.

To realize the antenna calibration, the first is able to make accurate measurements of the amplitude and phase differences between the element channels of antenna array. For this, it is necessary to add monitoring equipment into antenna array, mainly including the exciting signal source, calibration coupling path, amplitude and phase receiver, and channel control device. Based on the different positions of calibration coupling path at which signals are extracted, the calibration methods can divided into the external calibration method and the internal calibration method.

(1) **External calibration method**

The so called external calibration method means that the coupling path for extracting signal is placed outside the antenna array, able to be in either far field or near

field; the external correction is accomplished by respectively detecting and compensating the transmit/receive channels of individual elements. This method can detect the amplitude and phase errors resulted from the mount tolerance of antenna element and the pattern difference due to the mutual impacting between elements. Its advantages are reflected by no complex coupling calibration network, simple calibration system, and the ability to conduct calibration and fault monitoring of the whole transmit/receive channel. However, its calibration accuracy is sensitive to the environment, which imposes special requirement on the site, especially in the metric wave band of lower frequency.

Based on the difference in correction principles, the external calibration has the direct method, matrix inversion method, FFT method, middle field calibration method, and etc. The direct method is a near field measurement method. Making use of near field sweeping system, the test antenna is placed in the reactance region closely near radiation elements and moved along the element grid positions one by one. In this way, the amplitude and phase distributions of individual element channels in antenna array can be measured directly. The merit of this method is simple and direct. Nevertheless, it needs a long period for a large phased array antenna. In addition, it is difficult to measure directly a large phased array antenna in a microwave anechoic chamber. Particularly, the direct method has a great limitation for large metric wave antenna array.

The matrix inversion method, proposed by Davis, is a far field calibration method. All the technical measures for accurately achieving the far-field amplitude and phase lobes of antenna array can be used in this calibration method. In this method, a far distance test field is needed. The phased array antenna to be measured is mounted on a rotation pedestal and receives a far-field radiation signal. The amplitude and phase of the total port of antenna are measured at the preset angular position. Through matrix inversion, the amplitude and phase values of antenna element channels can be obtained. The merit of this method is the inclusion of the influences of mutual coupling between elements, mounting tolerance of array elements, and element inconsistency. In theory, the matrix inversion method is an accurate calibration method.

The FFT method is basically consistent with the matrix inversion method in algorithm principle. It is also a far-field calibration method without rotation positioning and assistant far-field radiation signal. In addition, it adopts faster FFT algorithm rather than matrix inversion.

In the middle field calibration method, the antenna array is measured by placing the assistant reference antenna at the several specific positions away from the front of antenna array to be measured. The position means radiation near field for the whole array but far field for the elements in array. Corresponding to 1D scanning and 2D scanning phased array antennas, the middle field calibration technique can be divided into middle field two-point method and middle field three-point method. The position of the assistant reference antenna is identical to the grid spacing of array and the calibration wires are parallel to antenna array.

The advantages of middle field calibration method are simple, low construction cost, not high requirement on test site, and able to test the transmit/receive performance of antenna. Thus, the method is particularly suitable for the outfield

calibration of large phased array antenna. But its disadvantages are: (1) good consistence is required between element patterns, if necessary, modification should be made; (2) test results are easy to suffer the influences of environmental reflection and interference, for this, measurements at multiple times and multiple points should be made to further increase test data and improve test precision.

In addition, some elements in the antenna array can also be used as an assistant antenna and the mutual coupling between elements is used to complete the amplitude and phase measurements of each element channel. This is called as mutual coupling calibration method. In the method, additional assistant coupling channel is not required, but the coupling coefficients of antenna elements of the same position relationship are required to be identical. Through the coupling coefficient transfer, the relative transmission coefficient is obtained, with which, however, error accumulation accompanies.

Several external calibration methods commonly used for phased array antenna have been described briefly above. The reader who is interesting can refer to the relative literatures in which the more detailed descriptions about their theoretical algorithms and realization processes have been given.

(2) **Internal calibration method**

When internal calibration method is adopted, the coupling path is placed into the feed channel of antenna array, the extraction of calibration signal is realized via coupler or switch plus calibration network, and the calibration signal is transferred in a closed structure. The benefits are small impact of exterior environment, fixed state, and high calibration precision. But the shortpoints are complex calibration feed network and unable to make test and modification on antenna elements.

It can be seen from the above analysis that the major similarities of external calibration and internal calibration are that their calibration principles and test processes are basically identical. Both of them acquire initial amplitude and phase data of the transmit/receive channels in antenna array via coupling path and can accomplish modification and compensation in a fast and automatic manner. Their differences are represented by the following aspects. First, the amount of test equipments is different. For internal calibration, the amplitude and phase data are obtained by directly coupling from the transmit/receive channel in antenna array. There are couplers or switches between transmit/receive channel and array element. At the same time, complex calibration network and large amount of cables are required. For external calibration, only assistant antenna is needed to place outside the antenna array. Due to simple structure, external calibration exceeds internal calibration in maintainability and reliability. Second, for internal calibration, the calibration signal is coupled directly in the channel and is transferred internally, thus, there is a small fluctuation in the amplitude of each element and no strict requirement on the dynamic range of calibration receive channel. Nevertheless, in external calibration, the calibration signal is transferred via space to the assistant antenna. Because there are different angles and distances relative to different positions of individual elements, the calibration signal level of each channel presents a large fluctuation. Considering exterior multi-reflection interference, the calibration receive channel is required to have a wide

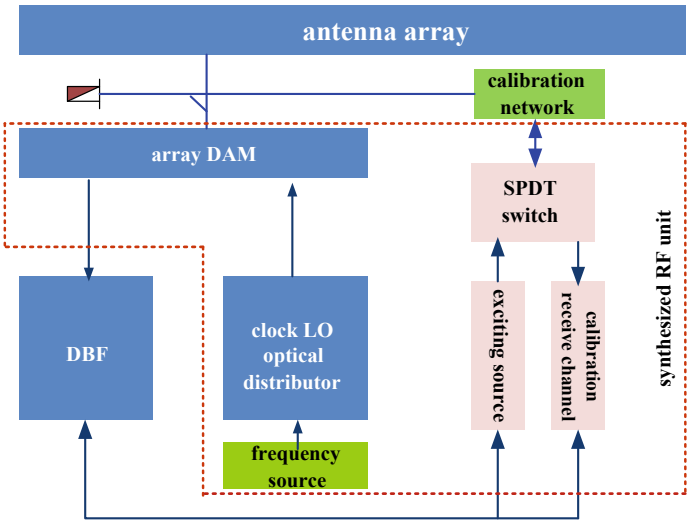


Fig. 6.43 Composition block diagram of internal calibration system for digital array

dynamic range in external calibration, generally greater than 45 dB. Finally, because calibration signal transmission environments are different, internal calibration has small inter-channel effect and is almost not impacted by environment. Compared with external calibration, internal calibration has smaller errors and higher stability, but it does not include antenna element errors.

Both internal calibration and external calibration have their own shortages and excellences. The selection of calibration methods should be dependent on different antenna arrays and requirements. For metric wave phased array antenna, external calibration method should not be used due to its large array size and the interferences resulted from celestial body radiations, communication signals, broadcasting and television signals, and etc. To ensure the test and calibration precision, internal calibration method is commonly selected. Especially for the metric wave antenna that communication signals, broadcasting and television signals are included in its frequency band, it is required to adopt the switch matrix system composed of high-isolation switches and feed network to isolate the exterior interference signals received by antenna elements. The accurate calibration of the whole array is realized through self-check one by one.

Figure 6.43 gives a basic composition block diagram of the internal calibration system for typical metric wave full-digital antenna array, mainly including coupler or switch, calibration network, single pole double throw (SPDT) switch, exciting source, calibration receive channel, and etc.

For receive calibration, the exciting source outputs RF signal which is sent to each directional coupler via SPDT switch and calibration network and is injected into the receive channel of array DAM through the coupler. The element channels can receive the signal independently at the same time. Due to high insolation, the

relative amplitude and phase data of each receive channel can be obtained. The comparison between the data and the receive reference calibration data is made in the DBF computer to obtain the amplitude and phase calibration codes under receive state. In operation, the DBF system will use the data to make amplitude and phase corrections of the receive DBF.

For transmit calibration, each transmit channel can be turned on or off independently and the one-by-one self-check calibration mode is adopted. Under the control of initial phase-shift code, the transmit channels transmit signals one by one. The coupled signals pass through the calibration network and the SPDT switch and enter into the calibration receive channels. Then the relative phase data of each channel can be extracted. Through comparison with the transmit reference calibration data, the phase calibration code under transmit state can be obtained. In operation, the DBF computer will send the calibration data to the digitalized active channel to realize the corrections of the transmit beams.

Bibliography

1. Zhang Guangyi. Phased Array Radar System[M]. Beijing: National Defense Industry Press, 1994.
2. Wang Puzhong, Shi Changsheng. Antenna Principles[M]. Beijing: Tsinghua University Press, 1993.
3. Wang Yuankun, Li Yuquan. Wide Frequency Band Techniques of Linear Antenna[M]. Xi'an: Xidian University Press, 1995.
4. Shu Xianrong, He Bingfa, Gao Tie. Phased Array Radar Antennas[M]. Beijing: National Defense Industry Press, 2007.
5. Zhang Zuji, Jin Lin, Shu Xianrong. Radar Antenna Techniques[M]. Beijing: Publishing House of Electronics Industry, 2005.
6. Yao Yuan. Wideband Antenna and Antenna Array[M]. Beijing: Beijing University of Posts and Telecommunications Press, 2012.
7. Robert J M. Phased Array Antenna Handbook[M]. 2rd ed, 2005.
8. Yang Shenyuan, Ma Huizhu, Zhang Chaozhu. Modern Antenna Techniques[M]. Beijing: Beijing Institute of Technology Press, 2009.
9. Ben De, Wei Chuanan, LinYouquan. Airborne Radar Techniques[M]. Beijing: Publishing House of Electronics Industry, 2004.
10. Jiao Peinan, Zhang Zhongzhi. Radar Environment and Wave Propagation Characteristics[M]. Beijing: Publishing House of Electronics Industry, 2004.
11. Lamont V B. Machine Plotting of Radio/Radar Vertical-Plane Coverage[R]. Naval Research Laboratory, Washington, D.C. 1970:3–5.
12. Mao Naihong, Ju Xinde. Antenna Measurement Handbook[M]. Beijing: National Defense Industry Press, 1987:12.
13. Lee J J, Livingston S, Koenig R. A Low-Profile Wide Band (5:1) Dual Polarized Array[J]. IEEE Antennas and Wireless Propagation Letters, 2003(2):46–49.
14. Lee J J. Compact Light Weight UHF Arrays Using Long Slot Apertures[J]. IEEE Trans on Antennas and Propagation, 2006, 54(7):2009–2015.
15. Hansen R C. Phased Array Antennas[M]. New York: John Wileys &Sons Inc, 1998.
16. Hansen R C, et al. Microwave Scanning Antennas[M]. New York: Academic Press, 1966.
17. Rudge, A W, et al. The Handbook of Antenna Design[M]. Peter Peregrinus Ltd, 1982.
18. Mailloux R J. Phased Array Antenna Handbook[M]. London: Artech House, 1994.

19. Lu Shanwei. Antenna Array Synthesis[M]. Beijing: Beihang University Press, 1988.
20. Lin Changlu, Chenhai, Wu Weigong. Modern Antenna Design[M]. Beijing: Posts and Telecom Press, 1990.
21. Hansen R C. Current Induced on a Wire: Implications for Connected Arrays[J]. IEEE Antennas and Wireless Propagation Letter, 2003, 2(1):288–289.
22. Hood A Z, Karacolak T, Topsakal E. A Small Antipodal Vivaldi Antenna for Ultrawide-Band Applications[J]. IEEE Antennas and Wireless Propagation Letter, 2008(7):656–660.
23. Niu Baojun. Outer Surveillance System for Large Phased Array[J]. Modern Radar, 1999, 26(1):53–57.
24. Lin Changlu. Antenna Measurement Techniques[M]. Chengdou: The University of Electronic Science and Technology Press, 1987.
25. Shu Xianrong. The Analysis of Electromagnetic Relationship on External Monitor System of Phased Array and Its Optimal Design[J]. Journal of Microwaves, 2002, 18(2):45–48.
26. Zheng Xuefei, Gao Tie. Study on Mid-field Calibration Technique of Phased Array Antenna[J]. Journal of Microwaves, 2005, 21(5):22–25.
27. Zhang Zijing, Zhao Yongbo. The Genetic Algorithms for Array Antennas[J]. Journal of Electronics (China), 2000, 22(1).
28. Shu Xianrong, Li Jianxin. Analyses on Utmost Scan Coverage of Planar Phased Array Antenna[J]. Modern Radar, 2005, 27(7):51–53.
29. Yang Enyao, Du Jiacong. Antenna[M]. Beijing: Publishing House of Electronics Industry, 1984.
30. Li Jinhua. Study on Adaptive Pattern Synthesis Algorithms of Array Antenna[D]. Shanghai: Shanghai Jiao Tong University, 2003.
31. Sun Shaoguo. Unequally Spaced Sparse Array Synthesis Based on Particle Swarm Optimization[J]. Fire Control Radar Technology, 2014, 43(1):14–17, 50.
32. Fan Yu. Evolutionary Computation and Its Application in Array Antenna Pattern Synthesis[D]. Shanghai: Shanghai Jiao Tong University, 2005.
33. Zhang Feng. Development and Realization of Passive Radar Antenna System[D]. Zhengzhou: Information Engineering University, 2006.
34. Mo Jiaqing. Applications of Bluetooth Underlying Protocol in RF Engineering[D]. Beijing: Beijing University of Technology, 2004.
35. Sheng Haiqiang. On the Multi-Band Base-Station Antenna Elements[D]. Xi'an: Xidian University, 2005.
36. You Qidi. Application Research of Several Fractal Technologies on Antenna[D]. Harbin: Harbin Institute of Technology, 2006.
37. Sun Shaoguo. Analysis of the Influence of Multipath Effect on Meter-Wave Antenna Pattern[J]. Telecommunication Engineering, 2008, 48(2):52–56.

Chapter 7
Metric Wave Transmit and Receive Techniques



7.1 Overview

The rapid development of semiconductor industry brings along the revolution of information technology. The digitalization is becoming a trend of information technology. In the radio technology areas of communication, radar, electronic warfare, and etc., the software radio model proposed by J. Mitola is the target promoted by digitalization technique. In the software radio system, A/D and D/A are required to approach to antenna as close as possible and the software is used to realize various functions on a general platform, emphasizing the programmability and the software redefinability. On this basis, the America initiated the SPEAKEASY plan, which realized the multimode and multiband speaking among its armed forces. And, the joint tactical radio system (JTRS) had been realized in 2010. In the nineties of the 20th century, Japan and some developed countries in Europe started the research and development of the software radio system. In China, software radio system was also placed in the "863" high-tech development plan. Accommodating to the development of software radio, the radar community presented such concepts as "digital radar" and "software radar". The wide applications of digital technique in radar will be a trend. To bring "digital radar" into realization, the longitudinal topological structures of receive and transmit channels in radar should be simplified. The radio frequency digitalized transmit/receive technique is an ideal technical means of this simplification.

In new radar system, the transmit and the receive systems should be integrated in the design of T/R module form. Further, the integrated design of multiple channel digital T/R modules can produce a novel comprehensive radar front-end functional module; we call it "digital array module". The integrated design of digital T/R module changes people's knowledge about the phased array radar that lasting for a long time. The digital array module design technique based on optical fiber signal transmission can configure large and complex phased array radar in "building block" fashion and is characterized by modularization, scalability, easy reconfiguration, and high reliability, which greatly improves the agility of radar system.

© National Defense Industry Press, Beijing and Springer Nature Singapore Pte Ltd. 2020

J. Wu, *Advanced Metric Wave Radar*, https://doi.org/10.1007/978-981-10-7647-3_7

With the developments of high-speed A/D and D/A converter techniques and high-speed digital signal processing techniques, the high resolution RF digitalization technique has been realized firstly at metric wave band. It is the radar system that approaches to the ideal software RF model under the present technical condition. RF digitalization is the technical foundation for realizing fully digitalized array radar and also an important emerging radar technology.

Optoelectronics technique has been widely applied for civil communications. Optical fiber data transmission technique is getting mature and is used in multi-channel, large capacity, and high-speed radar baseband data transmission system. At present, the optical fiber transmission technique of above 10 Gbps each channel has been used widely. More than ten channels can be integrated into an area of several square centimeters, completely meeting the requirements of radar, communication, and electronic countermeasure at the present stage. Optical fiber data transmission is featured as strong anti-interference capability, long transmission distance, and stable data transmission. The applications of optoelectronics technique in radar and so on are not only limited in high-speed data transmission, but also the transmission of microwave signal, clock signal, and synchronizing signal. The mature applications of optoelectronics technique significantly reduce the complexity of large radar system and make the interconnections more simple and reliable. Nowadays, the microwave and optical signals, which have different physical characteristics, have been fused by the advanced radar systems.

The application of metric wave radar has a long history. The radars in British "Home Chain" in WWII, the large metric wave phased array radars in ballistic missile early warning system of the former Soviet Union, and the metric wave multi-static phased array in the American naval space surveillance system (NAVSPASUR) show that this type of radar has unique feature. For the observation of stealth target, the metric wave phased array radar is paid more attention. Starting from improving detection range or resolution and angle measurement accuracy, it is necessary to enlarge antenna aperture or use multiple disperse metric wave radars to construct large radar detection systems. It is required to increase significantly the channel number of the transmit/receive system. And the realization of its critical specifications also decides the tactical performance of the radar system. In this chapter, the transmit/receive system of new metric wave radar will be discussed on the basis of RF digitalized transmit/receive technique.

7.2 Composition and Realization of Transmit/Receive System

7.2.1 Composition of Transmit/Receive System

In this book, a new type of active phased array radar is introduced, called as "digital array radar". The digital array radar is a fully digitalized array scan radar in which both

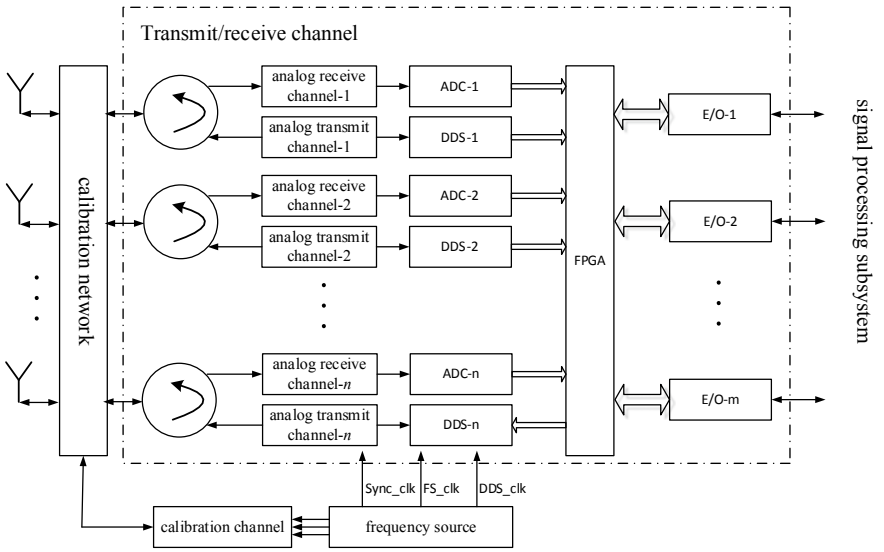


Fig. 7.1 Transmit/receive system composition of metric wave digital array radar

transmit DBF and receive DBF techniques are used. The amplitude-phase weighting is implemented in digital domain. In general, its transmit/receive system comprises RF digital receiver (including A/D conversion), RF digitalized transmitter (including waveform generation), frequency source, and calibration channel, as shown in Fig. 7.1. It can be seen that this novel metric wave digital array radar is different from the traditional active phased array radar. To what its antenna element corresponds is not only an active T/R module, but also a digital T/R module. That is, a T/R channel is composed of two parts: analog transmit/receive channel and digital transmit/receive channel (including ADC and DDS). And, optical fiber is used as data transmission medium. It fuses several types of signals, such as strong microwave signal, weak microwave signal, digital signal, and optical signal, representing a new concept for the design of radar transmit/receive system.

The receive channel receives echo signal from active antenna array. In analog receive channel, the echo signal is processed by a series of components and devices, including the limiter used for protecting the receiver from burn-out or saturation, low noise amplifier (LNA), directional coupler and compensation amplifier set for built-in-test (BIT), and matched or quasi-matched filter. Under existing technical conditions, metric wave radar doesn't need mixing. The RF signal can be digitalized directly. The echo processed by an analog receive channel is sent directly into a digital receiver. The analog echo signal is sampled and quantized by high-speed A/D converter into the digital signal of specific word length and specific data rate. The digital signal after sampling completes RF digital demodulation in special-purpose digital down-conversion (DDC) chip or by use of numerical control oscillator (NCO) in FPGA to output digital baseband signal. At the same time, for matching with the

data rate of the following signal processor, it is often required to extract high-rate digital signal and then make digital matched filtering. In general, in order to meet system dynamic range, the resolution of an ADC in radar system should be the all-important factor to be considered in device selection. Meanwhile, the specifications such as the RF bandwidth and the sampling rate should be taken into account as well.

In metric wave digital array radar, the RF digitalized transmitter is mainly divided into four parts: exciting signal generator, matched filter, power amplification chain, and circulator (or isolator). The exciting signal generator produces the signal of the waveform required for radar by DDS chip. The signal characters, i.e., frequency, bandwidth, modulation mode, pulse duration, and etc., can be all controlled by external parameters. The waveform signal from DDS is firstly filtered to complete the purification of the transmitting signal and remove those frequency spectrum components that are not needed by the system. The power amplification chain, commonly divided into front-stage amplification and final-stage amplification, is the core of transmit channel. The development of solid-state transmitter started from the end of 1960s. Till now, the solid-state transmitter has been used in almost all phased array radars and has become one of the mainstream design techniques of modern radar systems. The other important part in the transmit channel is circulator, or isolator. Its function is to achieve the isolation of transmit channel between receive channel and the isolation of the transmit signal between the reflected signal at the port. In a phased array radar, the scan of the transmit beam can cause a change of the active standing wave of antenna, to which should be paid attention when designing the transmit channel.

The calibration channel is the auxiliary function channel to implement the internal and external calibrations in phased array radar. For transmit calibration, it performs the function of extracting amplitude and phase information of calibration signal. For receive calibration, it generates calibration signal. And the calibration channel can also generate the analog target signal and BIT signal used for radar system test. It is convenient for test and repair.

The other important component in transmit/receive system is frequency source, sometimes called as frequency synthesizer. Making a high-quality oscillator as frequency reference, it synthesizes and forms various clock frequencies required for radar system through different methods Frequency source is mainly divided into three types: direct analog frequency source, phase-locked frequency source, and direct digital frequency source. Also, the above three realization methods can be used comprehensively to produce all frequency clock signals used in radar system. In RF digitalized transmit/receive system, the frequency source is mainly used to produce the sampling clock signal, the waveform generation clock signal, and the reference clock signal used by radar timer, but the LO signal in heterodyne system, which simplifies the design of the frequency source.

7.2.2 *Realization of Transmit/Receive System*

As mentioned in Sect. 7.1, in the advanced digital array radar, the transmit/receive system is no longer an independent system or equipment, but an integrated product designed with high integration degree. We call it digital array module (DAM). Its typical features are: the transmit channel and receive channel adopt integrated design in a certain scale; each transmit channel has independent direct digital frequency synthesis (DDS) or digital-analog conversion (DAC) chip and each receive channel has independent analog-digital conversion (ADC) chip; all transmit/receive channels of this module share a control and data transmission interface, usually a high-speed optical fiber module; all transmit/receive channels share unitive clock, LO (without LO signal but direct digitalization at metric wave band) and power supply system. The benefits of this design are to greatly simplify the external interface of the module and make the digital array module more suitable for constructing large phased array radar with compact system and strong ECCM capability. Figure 7.2 illustrates its operation principle block diagram.

Based on the above technical features of digital array module, we can propose a novel integrated design architecture of transmit/receive system. That is to take the form of frequency source + clock distribution net + digital array module to realize the integrated design of transmit/receive system as shown in Fig. 7.3.

In metric wave digital array radar, the transmit/receive system adopting this design architecture can lead to the following benefits:

First, by having the integrated digital array module, the radar can have a simple active antenna array, flexible function realization, and strong reconfigurability and scalability.

Second, in metric wave band, the traditional multi-core data transmission line is liable to interference due to complex electromagnetic environment and long

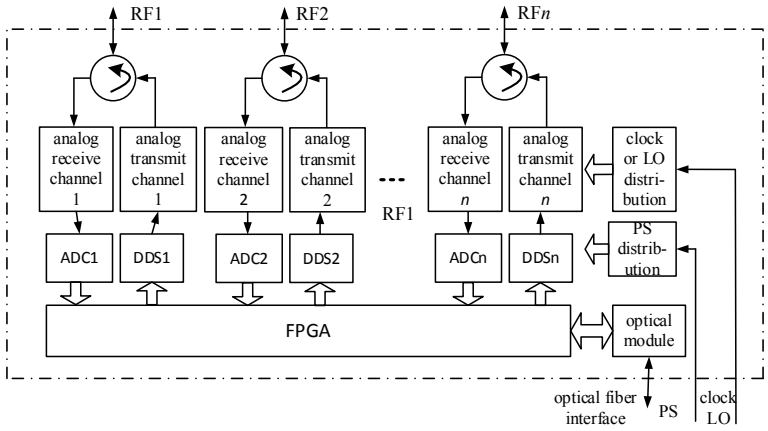


Fig. 7.2 Operation principle block diagram of DAM

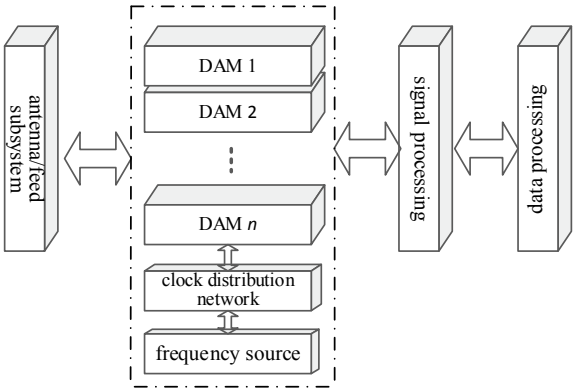


Fig. 7.3 A novel transmit/receive system integrated architecture

wavelength. However, the optical signal transmission system is basically interfered by microwave signal, so that the radar has stronger ECCM capability. On the other hand, the application of photoelectronic technique in radar field significantly reduces and gives facilities for system connections, which in turn bridges simple radar structure, flexible deployment, and easy and fast set-up/down.

At last, compared with the sub-array architecture in traditional phased array radar, the receiver has higher anti-saturation power. This is because the jamming signal has experienced a power combination before entering into low noise amplifier during sub-array synthesis and hence increases the difficulty of anti-jamming on the receiver end. Digital array radar has no sub-array synthesis.

In summary, digital array module is the one of the most important parts of digital array radar. Its performance determines in a high degree that a digital array radar can bring the advantages of full digital system into play or not. Its cost, reliability, and manufacturability are also important factors that must be taken into consideration in design.

7.3 RF Digitalized Transmitter Technique

7.3.1 Requirements of Digital Array Radar on Transmitter

The transmitter system of digital array radar is a multi-channel system. It can use numerous spaced antenna elements to transmit signals, and the power combining is realized in space through beam scheduling. This brings great flexibility for transmitter design and decreases the design requirement on a single transmit channel. In transmitter system design, considerations on the relation between the transmitter and the phased array antenna should be taken in account and attentions should be paid to the influences of the standing wave and loss of the transmission unit at its load end. Especially, the influence of the active standing wave of antenna mentioned

above should be evaluated. Being the mutual coupling between antenna elements, the active standing wave of antenna will present a great change when the transmit beam points to a large scan angle. If T/R switch instead of circulator/isolator is used, or the isolation of the circulator/isolator is poor, the traction certainly will produce on the power amplifier of transmit channel, resulting in changes of the amplitude and phase of its output signal with the beam direction. In severe condition, a heavy impact will be produced on the transmit pattern and sufficient attention should be paid.

In addition, the correlation between the transmit channels is also noticeable, that is, the amplitude and phase consistency between different ways of transmitters (usually after calibration). For this, radar should be equipped with relevant amplitude and phase monitoring, test, and adjustment device or means. For different transmitters, the differences in their operating parameters and characteristics will result in the differences and fluctuations in the amplitudes and phases between their output signals. In turn, the similarly amplitude and phase errors will be caused between antenna elements. The effects of amplitude and phase inconsistency of the transmitter output signals will be discussed hereafter. The relative errors of amplitude and phase distribution of antenna array caused by the amplitude and phase inconsistency will deflect the transmit beam direction, widen the transmit antenna mainlobe, and increase the sidelobe level of transmit antenna.

Take the linear array shown in Fig. 7.4 as an example. The linear transmit array has N elements that are fed by N transmitters. Set n to be sequence number of channel, $n = 1, 2, 3 \cdots (n-1)$. For simplification, assume the transmit antenna array to be a uniform array. The amplitude and phase errors of the output signal from each transmitter are Δa_m and $\Delta\phi_m$ respectively, where Δa_m is the relative amplitude fluctuation after normalization, $\Delta a_m < 1$.

The influences of amplitude and phase errors on antenna pattern are explained here. To further simplify computation, assume the pattern of antenna element is nondirectional, equal to 1. For a linear array with N elements, when the amplitude and phase errors of element are Δa_m and $\Delta\phi_m$ respectively, the pattern computation formula is

$$F(\theta) = \sum_{i=0}^{N-1} (1 + \Delta a_i) e^{j[i(\frac{2\pi}{\lambda} d \sin\theta - \frac{2\pi}{\lambda} d \sin\theta_B) + \Delta\phi_i]} \tag{7.1}$$

To confirm the maximum permissible values of amplitude and phase errors induced by each transmitter, it is necessary to perform this computation in designing transmit system. There are many factors to produce the amplitude and phase errors between transmitter channels, summarily they are:

(1) The inherent fluctuation between transmitter channels. The amplitude error in Δa_m is determined by the fluctuation of the final-stage power amplifier of transmitter. The dominant initial phase error can be eliminated by calibration. The residual is called as "phase calibration residual", usually it determines the phase error between transmit channels under radar operation state, $\Delta\phi_m$.

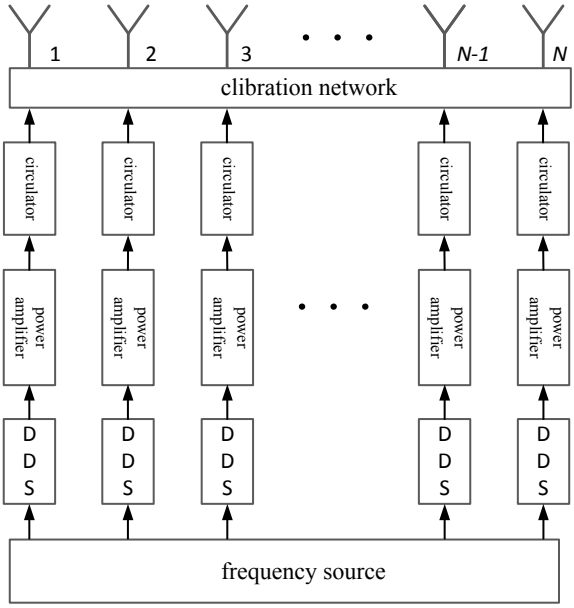


Fig. 7.4 Block diagram of transmit system of digital array radar

(2) The amplitude and phase errors of the feed lines (including calibration network, feed cable, and etc.) in transmit channel. The values of the amplitude and phase inherent errors can be obtained by test and modified in beamforming. The instrument test accuracy error is often small and thus the subordinate factor.

(3) DDS phase shift accuracy error. In digital array radar, the transmit system adopts digitalized transmitters, each transmitter corresponding to a DDS. Digital direct synthesis is used to produce the RF waveform signal required by radar. Channing the initial phase of the DDS output signal achieves the phase shift of the transmit signal. The phase shift accuracy is greatly higher than that of the traditional phase-shifter, up to 16 bits phase shift accuracy. This is also a subordinate factor.

(4) The amplitude and phase errors produced by the overlapping of jamming signal and desired signal in complex electromagnetic environment. In metric wave band, there is heavy electromagnetic interference inside or outside radar system due to complex environment, which will make the calibration signal and even the transmitting signal impure, and also produce the amplitude and phase errors between transmit channels. Additionally, there are many uncertain factors that cannot be predicted and computed. In a word, this problem should be resolved by strengthening electromagnetic compatibility design and filtering design at the scheme phase or design phase, because the measures are highly limited that can be taken at the production phase. Therefore, special attentions should be paid during radar system design.

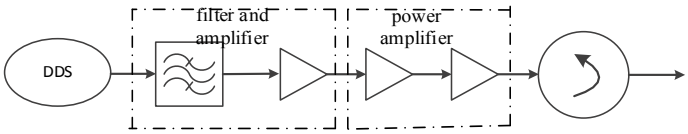


Fig. 7.5 Composition of RF digitalized transmitter

7.3.2 Realization of RF Digitalized Transmitter

With rapid development of semiconductor technology, nowadays RF digitalization can be realized in UHF band, VHF band, and even P band and L band, greatly reducing the equipment amount of radar transmit/receive channel. The RF digitalized transmitter is the typical feature of transmit/receive system of digital array radar. It is mainly composed of RF exciting signal generator (including DDS, filtering, and amplification), power amplification chain, and circulator (or isolator). The composition block diagram of a single-channel RF digitalized transmitter is shown in Fig. 7.5.

7.3.2.1 RF Direct Digital Frequency Synthesis Technique

Modern radar system requires a transmitting signal to have high frequency stability, large output dynamic range, good output frequency response, modulation function, and high frequency spectrum purity. Also it is required that the frequency, phase, and amplitude are all programmable controlled. Traditional analog signal source cannot meet these requirements. In the early of 1970s, American scholars J. Tiemey, C. M. Rader, and B. Gold firstly proposed a new frequency synthesis principle that uses full-digital technique and starts from phase concept to directly synthesize the required waveform, called as direct digital frequency synthesis (DDS). The DDS technique gets the advantages of high frequency resolution, fast frequency switching speed, continuous phase, and high frequency stability. It provides a new drive for modern radar technology. Thanks to high frequency agility speed, high frequency resolution, phase continuity in frequency switching, ability to output wideband orthogonal signal, and single-chip integration, DDS technique gets fast development and more and more applications.

DDS has two obvious defects due to its synthesis theory: the output frequency signal one has large spurious and the bandwidth of the output signal is limited. Therefore, researching the DDS chip with high operating clock frequency and excellent spurious performance becomes a development direction of DDS technology. The large DDS output spurious is resulted from the phase truncation error in signal synthesis process, the D/A converter quantization error, and the nonlinearity of D/A converter.

With the development of super high-speed GaAs devices, the DDS output bandwidth limitation is overcome gradually. But the spurious is determined by the

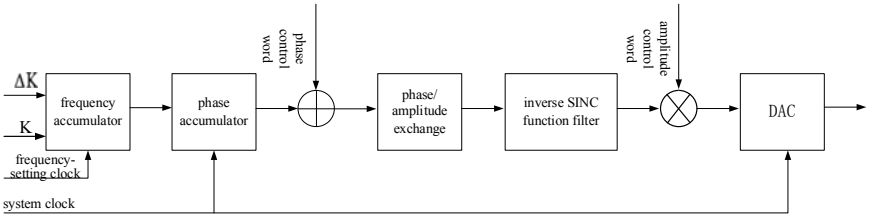


Fig. 7.6 Block diagram of DDS operating principle

characteristics of DDS itself, so it will become an important factor limiting the applications of DDS technology. When J. Tiemey et al. firstly proposed the DDS concept, they gave some statistic analysis results of frequency spectrum characteristics. Also, theory presented two major methods for low-spurious DDS design: single-quadrant sine wave storage and modified table look-up algorithm. Subsequently, the table look-up algorithm developed by Sunderland et al. is a very effective compressed storage and table look-up method, called Sunderland structure. Using single-quadrant sine wave storage structure and improved Sunderland structure, Nicholas et al. designed and developed a high-performance DDS with excellent spurious performance and high clock frequency. After that, Oleary proposed a modified DDS structure by use of noise shaping, effectively improving output frequency spectrum performance. In 1994, Harris et al. suggested to use noise feedback to reduce the error created by waveform table D/A converter quantization. Nowadays, the individual techniques for DDS chip are getting mature. Figure 7.6 depicts its operating principle.

Theoretically, DDS can generate arbitrary signal waveforms. That is, DDS technique can perform direct modulation on the one, two, or three of the generated signal waveform parameters (such as frequency, phase, and amplitude). Taking frequency modulation as an example, for a DDS system, its output frequency is given by

$$f_{out} = k \times \frac{f_{clock}}{2^n} \tag{7.2}$$

where, k is frequency control word, f_{clock} is input clock frequency into DDS, and n is the bit number of phase accumulator.

For a given DDS, the bit number of phase accumulator is a fixed value. Once the input clock frequency is set, its output frequency varies with control word k. So that, only making the frequency control work k change as the rule of modulation signal can realize the required frequency modulation signal. At the same time, the accurate phase control of the output signal can be achieved via the digital adder between the phase accumulator and the sine function table.

For the ideal DDS model, the output signal passing through the DAC can be expressed as

$$s(t) = \sum_{l=-\infty}^{+\infty} [\sin \omega_0 t \cdot \delta(t - lT_c)] * h(t - \frac{1}{2}T_c) \tag{7.3}$$

So the frequency spectrum obtained through Fourier transform of ladder wave $s(t)$ is

$$\begin{aligned} s(\omega) = &-j\pi \sum_{l=-\infty}^{+\infty} Sa(\frac{f_0 - lf_c}{f_c}\pi) \cdot \exp(-j\frac{lf_c - f_0}{f_c}) \cdot \delta(\omega + l\omega_c - \omega_0) \\ &+ j\pi \sum_{l=-\infty}^{+\infty} Sa(\frac{f_0 + lf_c}{f_c}\pi) \cdot \exp(-j\frac{lf_c + f_0}{f_c}) \cdot \delta(\omega + l\omega_c - \omega_0) \end{aligned} \tag{7.4}$$

It can be seen from expression (7.4) that the ideal DDS output spectral line only locates at $\omega_0 \pm l\omega_c$, where, $l = 0, 1, 2 \cdots$. And, all of the spectral lines fall into the envelope $Sa(\frac{f_0 + lf_c}{f_c}\pi)$. Figure 7.7 depicts the ideal DDS output frequency spectrum.

From Nyquist sampling theorem, we know that, if want to recover the ideal waveform, the output frequency cannot exceed $f_c/2$. Beyond $f_c/2$, the 1st order image frequency will fall into the Nyquist bandwidth, i.e. the range from DC to $f_c/2$. The $\sin(x)/x$ envelope brought from aperture distortion causes the DDS output amplitude to drop down several decibels in Nyquist bandwidth. So some DDS chips include a predistortion filter featured as $x/\sin(x)$. It has the ability to limit DDS output amplitude fluctuation within ± 0.1 dB.

When $l = 0$, the output of the ideal DDS is the required fundamental frequency signal. It has the maximum amplitude among all the spectral lines, and the value can reach up to $\pi\, Sa(\frac{f_0}{f_c}\pi)$. And we note that there is no spectral line at nf_c.

In RF digitalized transmitting system, on the basis of system requirement, DDS is needed to generate the RF signal with specific modulation, pulse width, bandwidth,

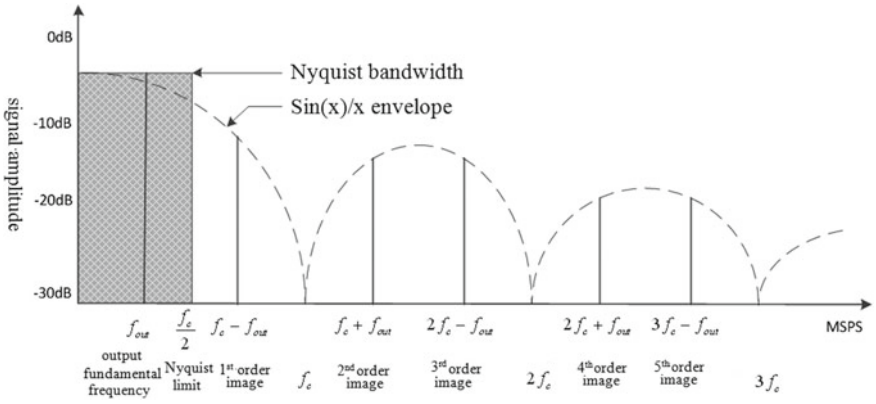


Fig. 7.7 Output frequency spectrum of ideal DDS

phase, and frequency. This leaves out the mixing step in the traditional transmitting channel, achieving a simpler channel design. In designing multi-way transmitting channels in digital array radar, what should be paid attention to is the synchronization of the output signals of multi-channel DDS. To realize the transmit beamforming in space, it should be ensured that the relative phases of the transmitting signals in individual channels are stable. Here, it is not required that the phases of individual channels hold absolute consistency. These fixed phase differences along with the phase differences in analog channels can be eliminated by system calibration. On the side, the importance should be attached to: because of the quantization precision problem existing in the accumulator stepping, when completing long pulse width waveform design, more accumulating times is needed. It is easy to enlarge the errors introduced by rounding to unacceptable degree. At this time, properly changing the step-span can limit the total amount of accumulative errors in an acceptable range.

7.3.2.2 Solid-State Transmitter Technology in Digital Array Radar

The transmitter that requires phase correlation is a master oscillator power amplifier (MOPA) transmitter. The active devices of the power amplifier can be the vacuum devices or the transistors. If the transistors are used, the transmitter is called as solid-state transmitter. Here, the emphasis is paid on the introduction to solid-state transmit amplification chain. Generally, it consists of front-stage amplifier, middle-stage amplifier, power divider, final-stage amplifier, power combiner, directional coupler, and circulator. As for a transmitter requiring harmonic suppression, its output end often has harmonic filter. The equipment amount can be properly reduced depending on practice equipment requirement.

Transistor is the heart of an amplifier and thus, it is necessary to make a brief description about it.

Transistor can be divided into two types: bipolar junction transistor (BJT) and field effect transistor (FET). The field effect transistor was invented by Shouey, Bardeen, and Britain in 1948. It is one of the semiconductor devices that are most widely used in radar field. At present, below S band, what has been widely used is Si BJT. BJT is a PN-junction device, formed by back-to-back junctions. It is a three-terminal device, may be PNP or NPN. For application at higher frequencies, NPN structure is preferable. This because the operation of the device depends on the diffusion ability of minority carrier to pass through the base region. The electron often has better migration characteristic than cavity, so the NPN structure is used.

In 1930, Lillienfeld brought forward the basic concept of field effect transistor (FET). Schokley invented the bipolar transistor in 1948 and presented the concept of FET in 1952. FET belongs to voltage-controlled device and it differentiates from BJT in conductive mechanism. Crystal triode is a current-controlled device and its conductive mechanism is contributed by majority carrier and minority carrier together, thus called as bipolar transistor. But the physical structure of FET is a whole piece of semiconductor material (like Si or GaAs). When its current path (also referred as conductive channel) is effected by external-applied voltage (electric field), only one

type of carrier acts. Different in physical structure of grid, the FET has three basic types:

(1) Junction field effect transistor (JFET);
(2) Metal semiconductor field effect transistor (MESFET);
(3) Metal-oxide-semiconductor field effect transistor (MOSFET).

Limited by manufacturing process, JFET usually is used in low-frequency circuit, as the component in low-frequency amplifier or switch-controlled circuit. MESFET is commonly used at the higher frequencies of microwave frequency band, for example, the GaAs MESFET currently in wide use can operate at millimeter wave.

MOSFET was initially used in digital integrated circuits. With the rapid development of transistor fabrication technologies and the continuos improvement of MOSFET fabrication and machining technologies, the operating frequency and output power of MOSFET are increased continuously. At the frequencies below S band, the output power of MOSFET has the trend towards exceeding BJT. Especially at the lower end of UHF band, VHF band, and short wave band, MOSFET power devices have very fast developments, while BJT technologies still hold in previous technical state.

The input and output impedances of microwave power transistor are often very low and include considerable reactance part. And the impedances will get lower with the output power increasing. To achieve the maximum transmission power, these impedances must be changed to 50 Ω, i.e., it is required to design impedance matching circuit. A proper impedance matching network not only can realize in-band optimal power transfer efficiency and reduce power loss, but also has additional functions, such as reducing noise interference, increasing power capacity, improving frequency response linearity, and etc. Thus the key factor of microwave power transistor amplifier design is impedance matching. That is, it is needed to achieve the conjugate matching of the input impedance of transistor amplifier and the inner impedance of signal source, the conjugate matching of the output impedance of transistor amplifier and the load impedance, and the conjugate matching of output impedance of front-stage transistor and the input impedance of back-stage transistor. If a high power transistor is needed, it is preferable to choose the device with high operating voltage. Due to high operating voltage, it has high output impedance accordingly, easy to achieve matching. In addition, if the operating voltage is high, its operating current is relatively low. The DC feeding loss will go down and the thinner wire can be used for DC feeding. Finally, under equivalent power, the high-voltage and small-current switching PS is easier to realize with lower cost than the low-voltage and big-current switching PS. Figure 7.8 gives the block diagram of a power amplifier.

The specifications of a power amplifier include operating frequency range, power, gain, gain flatness, P_{1dB} gain compressing point, efficiency, harmonic, spurious, and etc. The major specifications of a power amplifier will be discussed hereafter.

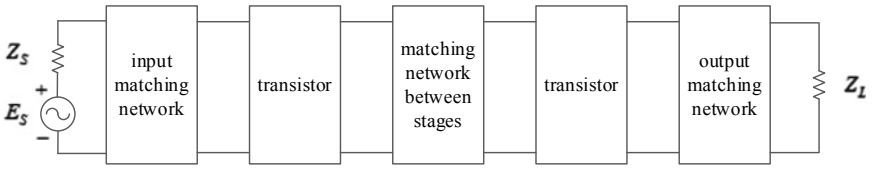


Fig. 7.8 Block diagram of power amplifier

(1) Operating frequency band

The operating frequency band means the frequency range operating in which an amplifier can meet its all specifications. The actual operating frequency of an amplifier could be beyond the defined operating frequency range.

(2) Output power at 1 dB compressing point, P_{1dB}

When the input power is small, there is a linear relation between the output power and the input power. The gain is referred as small signal linear gain, G_0. When the input power reaches a certain vale, the power amplifier will be saturated, as shown in Fig. 7.9. The power at the time that the output power falls 1 dB below the output power of the ideal linear amplifier is called as 1 dB compressing power, denoted by P_{1dB}. The gain at the 1 dB compressing point is marked as G_{1dB}, then we have $G_{1dB} = G_0 - 1$ dB. Generally, both power amplifier and transistor use P_{1dB} to present their power output capabilities, making dBm as its unit. The relation of P_{1dB} and input power is

$$P_{1dB} = P_{in(1dB)} + G_0 - 1 \tag{7.5}$$

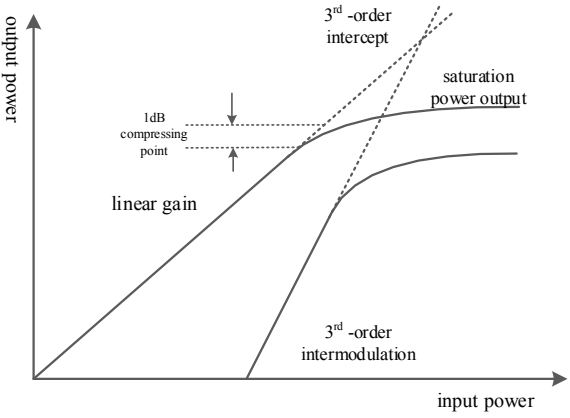


Fig. 7.9 Relation between linearity, 3rd-order intermodulation component and input signal

(3) Gain

Power gain usually means the ratio of the measured output power P_{out} and input power P_{in} when both signal source and load are 50 Ω, denoted by dB.

$$G(dB) = 10\log\frac{P_{out}}{P_{in}} \tag{7.6}$$

In designing power amplifier, the specifications related to gain also include gain flatness, gain stability, and out-band suppression. There is a bandwidth requirement for the most of power amplifiers and it is required that the gain of power amplifier maintains consistency within a given frequency bandwidth. Gain flatness means the fluctuation of gain within the operating frequency band, and is usually expressed by the difference of the highest gain and the lowest gain:

$$\Delta G(dB) = G_{\max} - G_{\min} \tag{7.7}$$

The gain flatness explains the magnitude of power amplifier gain changing within a frequency range, while the gain stability characterizes the stability of power amplifier gain changing with temperature and environment under normal condition. The out-band suppression reflects the suppression degree of power amplifier suppressing out-band signal.

On the other hand, in pulse radar, what the power supplying system commonly provides for the power amplifier is the average power of the transmitting signal. Then the energy storage capacitor should be added to the power supplying system so as to compensate for the changes in the transmitting pulse drop when the transmitting pulse width increasing. The energy storage capacitance necessary for the transmitting channels can be calculated by

$$c = \frac{I_P \times \tau}{d \cdot V_{CC}} \tag{7.8}$$

where, Ip is the peak current, τ is the pulse width, d is the voltage drop, and V_{cc} is the operating voltage.

(4) Power efficiency and power added efficiency

The power efficiency of power amplifier means the ratio of the RF output power of power amplifier and the DC power provided for the transistor, i.e.

$$\eta_P = \frac{P_{out}}{P_{DC}} \tag{7.9}$$

It reflects the capability of power amplifier transforming DC power into RF power. In the design of power amplifier, considering the influence of gain, the power added efficiency (PAE) is defined to be ratio of the difference between the output power P_{out} and the input power P_{in} of power amplifier and the provided DC power. That is,

$$PAE = \frac{P_{out} - P_{in}}{P_{DC}} \tag{7.10}$$

PAE is an important parameter of power amplifier. It reflects not only the capability of power amplifier transforming DC power into RF power, but also the capability of power amplifier amplifying RF power.

(5) Intermodulation distortion

Intermodulation distortion is the mixture components produced after two or multiple input signals of different frequencies passing through the power amplifier. It results from the nonlinearity of power amplifier. Assume that there are K input signals, and their frequencies are $f_1, f_2, \cdots f_k$ respectively. After passing through power amplifier, the output components include many mixture components due to the nonlinearity of power amplifier:

$$mf_1 \pm nf_2 \pm \cdots pf_k, \text{ where } m, n, \cdots p = 0, 1, 2 \cdots \tag{7.11}$$

These components are called as $(m + n + \cdots p)$ order components respectively. The stronger the nonlinearity of power amplifier is, the bigger the intermodulation components are. The magnitude of an intermodulation component can be denoted by intermodulation coefficient. If there are K equal amplitude signals, (m + n) order intermodulation coefficient can be expressed by

$$IM_{m+n} = 10\log(\frac{P_{m+n}}{P_1}) = 10\log(\frac{P_{m+n}}{P_2}) = \cdots = 10\log(\frac{P_{m+n}}{P_K}) \tag{7.12}$$

where, $P_1, P_2, \cdots P_K$ correspond to fundamental powers, respectively, P_{m+n} is $(m + n)$ intermodulation power, IM_{m+n} is measured by dBc. If the input signals into the power amplifier are equal-amplitude signals, among the above components, the ratio of the component with frequency of $2f_i - f_{i+1}$ or $2f_{i+1} - f_i$ and the fundamental component with frequency of f_i or f_{i+1} is called as third-order intermodulation coefficient IM_3. Similarly, the ratio of the component with frequency of $3f_i - 2f_{i+1}$ or $3f_{i+1} - 2f_i$ and the fundamental component with frequency of f_i or f_{i+1} is called as third-order intermodulation coefficient IM_5.

(6) Harmonic distortion

When the number of input signals increases to a certain degree, a series of harmonic waves will be generated due to the nonlinearity of power amplifier. For narrowband power amplifier, these harmonic waves are not located in the passband generally and can be filtered out easily by filter. For wideband power amplifier, these harmonic waves could fall into the passband. It is difficult to filter away them. The harmonic distortion is computed by

$$HD_n = 10\log\frac{P_{out(nf_0)}}{P_{out(f_0)}} \tag{7.13}$$

where, HD_n is n-order harmonic distortion, $P_{out(f_0)}$ is the output power of fundamental signal, and $P_{out(nf_0)}$ is n-order harmonic output power. Harmonic suppression is the specific value of fundamental power and harmonic power.

(7) Input/output standing wave ratio and echo loss

Input/output standing wave ratio is a key indicator that must be taken into consideration in microwave power amplifier. Both the input impedance and output impedance of power transmitter are small, presenting a big mismatching with the 50 Ω system. When the mismatching is severe, the instantaneous RF voltage or current at the output end of power amplifier could go beyond the rated value one-fold, causing the power transistor to be damaged. And the input/output standing wave ratio will also make the gain flatness and group delay of the system poor.

It is easy to measure the reflected power by the use of microwave instruments, so that, in the microwave frequency band, the echo loss is often used to represent the port matching. The echo loss means the specific value of the reflected power and the incident power, measured in dB. The relation between the echo loss ρ_α and the standing wave ratio ρ can be expressed as:

$$\rho_\alpha = 20\lg(\frac{\rho-1}{\rho+1}) \tag{7.14}$$

The modulus of reflection coefficient is

$$|\Gamma| = \frac{\rho-1}{\rho+1} \tag{7.15}$$

From (7.13) and (7.15), we can obtain the equivalent values between the standing wave ratio, echo loss, and reflection coefficient.

(8) Stability coefficient

The internal feedback of RF power amplifier will cause instable operation performance, even self-oscillation. To measure the stability of amplifier, the stability coefficient K is introduced.

$$K = \frac{1-|S_{11}|^2-|S_{22}|^2+|\Delta|^2}{2|S_{12}S_{21}|} \tag{7.16}$$

where,

$$\Delta = S_{11}S_{22} - S_{12}S_{21} \tag{7.17}$$

And we obtain the conditional expressions of RF power transistor being absolutely stable as:

$$K > 1 \tag{7.18}$$

$$\frac{1-|S_{11}|^2}{|S_{12}S_{21}|} > 1 \tag{7.19}$$

$$\frac{1-|S_{22}|^2}{|S_{12}S_{21}|} > 1 \tag{7.20}$$

When the three conditions are satisfied simultaneously, the amplifier is stable absolutely. That is, whatever values the source impedance Z_S and the load impedance Z_L are, the amplifier can work stably.

7.3.2.3 Stability Requirements on Transmitting in Digital Array Radar

In digital array radar, besides the conventional specification requirements mentioned above, the amplitude and phase stability of transmit branch is also a key factor that affects the tactical and technical performance of a radar system. It is necessary to explain that the amplitude and phase stability of a transmit branch here means the specification requirement on not only the solid-state transmit power transistor, but also the whole transmit channel including the exciting signal generation, filtering, amplification, and etc.

In the moving target indication (MTI) mode, a basic requirement on the transmitter is that the transmitting signal should have high amplitude and phase stability pulse-to-pulse. If the RF output signal of transmitter presents instable amplitude, phase or frequency, trigger pulse time jitter, and instable pulse width between adjacent pulses, the echoes from the stationary targets cannot be cancelled completely. This limits the performance of coherent MTI system. MTI performance is generally denoted by the improvement factor I'. I' is defined to be

$$I' = \frac{\bar{S}_o/C'_o}{S_i/C'_i} = \frac{\bar{S}_o}{S_i} CA \tag{7.21}$$

In the formula, $CA = \frac{C'_i}{C'_o}$ is called as the clutter suppression degree or cancellation ratio, and is the ratio of the input clutter power C'_i and the output clutter power C'_o of cancellation. $\bar{S}_o/S_i$ is called as signal gain and is the ratio of the average power of the output signal of cancellation across all the possible target speeds and the input signal power. S_o taking average value is because the cancellation system has different responses to different Doppler frequencies and the target speeds distribute in a certain range. The limits of the instable factors of transmitter to the MTI improvement factor are given in Table 7.1.

In addition, the amplitude and phase instable factors will also have effects on the amplitude and phase consistency between the transmitting channels, and further on the shape of the transmit pattern. Of course, here we mean the inconsistency of the amplitude and phase variations between the transmitting channels. The transmit stability is resulted from many causes, for example, temperature, vibration, clock signal

Table 7.1 Influences of instable factors of transmitter on MTI improvement factor

Instable factors between pulses	Limits to improvement factor
Phase instable	$I' = 20 \lg \frac{1}{\sigma_\varphi}$
Amplitude instable	$I' = 20 \lg \frac{A}{\sigma_A}$
Trigger pulse instable	$I' = 20 \lg \frac{\tau}{\sqrt{2}\sigma_t}$
RF pulse width instable	$I' = 20 \lg \frac{\tau}{\sigma_\tau}$
Transmitting pulse frequency instable	$I' = 20 \lg \frac{\sqrt{3}\tau}{(2\pi\tau)\sigma_f}$

jitter, and discreteness of devices. In general, radar is unable to make continuous calibration, thus the influences of these instable factor of the transmitting branch should be put under "calibration residue" and could produce error accumulative effect with time. Sufficient considerations should be given in the system design and validation.

7.4 RF Digitalized Receive Technique

7.4.1 Features and Composition of Advanced Metric Wave Radar Receiver

The advanced metric wave radar receiver is based on the mature realization and successful applications of the wideband RF digitalization techniques of software radio and recognitive radio. According to the idea of software radio, ADC sampling digitalization should approach to the output end of antenna element as close as possible, and for the best, should be just behind the antenna port so as to construct a universal open radar hardware platform by the use of wideband RF digitalized system. Among the traditional receivers, there are zero-IF receiver, low-IF receiver, and superheterodyne receiver. Currently, wideband RF direct sampling receiver has been developed. In metric wave radar, because of low carrier frequency and fast development of ADC devices, high resolution RF signal direct digitalization can be realized today. And, through variable sampling rate, sampling without blind zone can be carried out. The RF digitalization techniques based on software radio mainly include wideband RF signal direct processing technique, digital direct frequency synthesis technique, digital quadrature demodulation technique, and multi-rate signal processing technique. The block diagram of the basic compositions and the functions of advanced metric wave radar is shown in Fig. 7.10.

In the frequency band of metric wave radar, there are strong signal interferences resulted from broadcasting, television and mobile communications. To prevent RF front-end channel from saturating, a pre-selection filter or an antenna/feed filter is

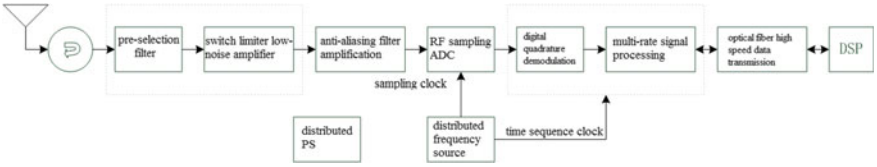


Fig. 7.10 Block diagram of basic composition and function of advanced metric wave radar

needed to filter out the strong out-band jamming signals and preserve the wanted signals. The pre-selection filter locates at the first stage of receiver and has direct effect on the noise figure of the whole receiver RF front-end. Considering the system linearity requirement, there should be no active components in the pre-selection filter. For highly integrated DAM module receiver design, which requires low insertion loss, easy realization, small volume, and no special superior out-band rejection, the passive LC filter can be adopted. For the case of low insertion loss, superior out-band rejection, and no strict volume limit, the cavity passive filter can be used.

In the radar with a duplex antenna, a circulator is used to achieve the transmitting and receiving isolation. To protect the receiving low-noise amplifier from damaging by the transmitting leakage power and the external strong jamming signals, it is also required to add a switch limiter before the low-noise amplifier. Microwave switches include PIN diode switch, Schottky diode switch, FET switch, and MEMS switch. Monopole double throw switch is often used in radar to prevent the power transistor in transmit branch from damaging by the reflected transmitting power under the off-state. The limiter is divided into active limiter and passive limiter. The former acts depending on the external control signal, while the later works depending on self-detection of RF signal. The switch limiter can be designed to be a hybrid switch limiter in which the active synchronous limiter prevents from the transmitting leakage power entering into the receiving front-end to burn it out during transmitting and the passive limiter protect the receiving front-end from damaging by the asynchronous signals from the neighbour radars or strong interference sources during receiving.

The low noise amplifier in RF front-end determines the noise figure of the digitalized receiver system cascade. To decrease the influences on the post-circuits, the low noise amplifier should not only meet the requirements of the dynamic range of the system and its stability, but also have gain as high as possible. In metric wave radar, to ensure that it is not easy to saturate under interference, its output 1 dB compression point should be set as high as possible. On the other side, the feedline and the insertion losses of the circulator, filter, and switch limiter before the low noise amplifier should be controlled as low as possible. In designing RF front-end, therefore, it is needed to choose good devices and make a comprehensive consideration of their parameters (gain, loss or standing wave) and positions based on the technical specifications of the radar system and the receiving system. The microwave GaAsFET low noise amplifiers based on MMIC have been found wide applications in the receiver RF front-ends of various radars. The modified GaAsFET—the high electron mobility transistor (HEMT) or the heterostructure field effect transistor (HFET)

appeared in 1990s. It has lower noise figure, higher gain and operating frequency and is compatible with MMIC. Nowadays, it dominates the low noise amplifiers in microwave band and millimeter wave band.

The ADC input bandwidth of RF digitalized receiver is wide generally and the sampling rate of high resolution ($\geq$14 bits) ADC is not beyond 500 MHz commonly. To achieve direct sampling of RF signal in metric wave band, bandpass sampling or under-sampling must be adopted. Thus analog anti-aliasing filter is needed to reject the interferences or noises from other Nyquist frequency bands, avoiding the effects of interference aliasing or noise folding on the output S/N ratio. For sampling without blind zone and decreasing the number of the jamming signals entering into the following circuits, the anti-aliasing filter is realized currently using electrically tunable filter or switch filter. The switch filter is realized by paralleling the filters in different frequency bands and gating via switch. As viewed from integration level and rectangle coefficient, the switch filter in metric wave radar is realized usually by SAW switch filter. The other anti-aliasing filter of RF digitalized receiver is the widely used electrically tunable filter, including current-type YIG electrically tunable filter and voltage-type varactor electrically tunable filter. As viewed from simpleness, miniaturization, and performance specifications, the varactor electrically tunable filter is preferred for the anti-aliasing electrically tunable filter in metric wave radar. Currently, a series of metric wave band electrically tunable filters produced by American PoleZero Company are excellent in performance specifications, volume, and weight, but costly. In China, there are electrically tunable filters based on GaAs varactor process, with similar performance specifications. The measured specifications and picture of an example product is given in Fig. 7.11. In addition, the electrically tunable filters based on Si cavity MEMS filter grow up gradually in recent years. Significant improvements are expected in volume and weight (Si based chip), performance specifications (e.g. rectangle coefficient), temperature characteristic, and cost.

ADC devices are the foundation and precondition of software radio, RF digitalized receiver, and future recognitive radio. ADC has different realizing architectures depending on different demands of speed, resolution, and bandwidth, including flash

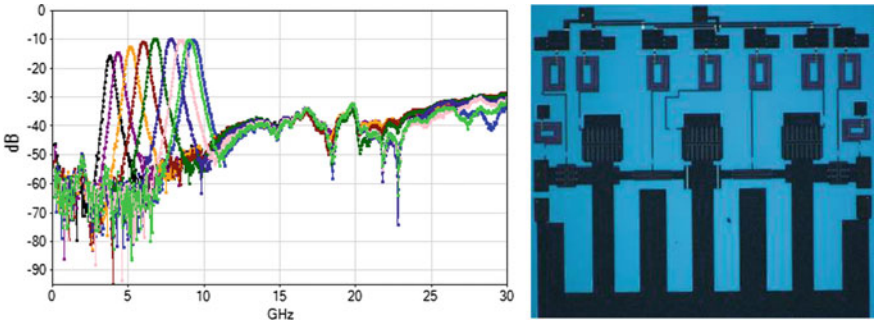


Fig. 7.11 An electrically tunable filter based on GaAs process made in China

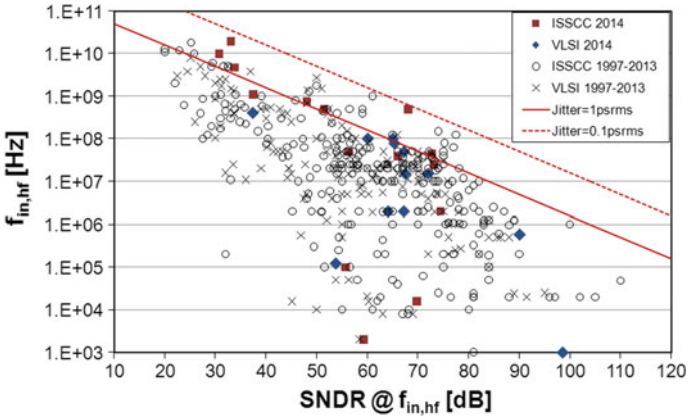


Fig. 7.12 SNDR and bandwidth distribution diagram of ADC devices

ADC, pipelined ADC, folding ADC, SAR ADC, Delta-Sigma ADC, time interleaved ADC, SCA/ADC, and so on. The main companies designing ADC include TI, ADI, E2V, Intersil, Linear Technology, Maxim, IDT, and No. 24 Research Institute of CETC. Professor Murmann of Stanford University collected the materials about ADC devices from 1997 to 2014 and gave the distribution diagram of the operating bandwidths and output SNDR indexes of different realizing architectures, as shown in Fig. 7.12. Metric wave radar operates in low frequency band and has no very strict bandwidth requirement, but suffers from severe interferences, which put forwards a high requirement on the instantaneous dynamic range of ADC. Thus high ADC sampling rate and resolution are required. At the same time, for digital array radar, considering its improved high integration level, multi-channel parallel high-resolution RF direct sampling ADC must be used.

RF digitalized receiver needs digital quadrature demodulation and multiple sampling rate signal processing to acquire the baseband complex signal matching with the transmitting signal, for use in the following signal processing, analysis, and target detection. Removed analog frequency conversion, the frequency conversion and filtering of RF digitalized receiver are done in digital domain. On the other hand, to accommodate different bandwidths and sampling rates of different systems and possible number of channelized channels, digital quadrature demodulation and multiple sampling rate signal processing need to build a universal digitalized IF signal processing platform. By setting the external controlled parameters, the real-time allocation of digital resources can be realized to adapt different system requirements. The devices commonly used to build this universal digitalized IF signal processing platform are the FPGA devices produced by Altera and Xilinx. Another approach is to use high performance multi-core DSP chips. The BWDSP 100 multi-core DSP chip designed by China can be use to construct this universal digitalized IF signal processing platform. Figure 7.13 shows a picture of the universal digitalized IF signal processing platform based on BWDSP 100 multi-core DSP chip.



Fig. 7.13 Processing platform based on BWDSP 100 multi-core DSP chip

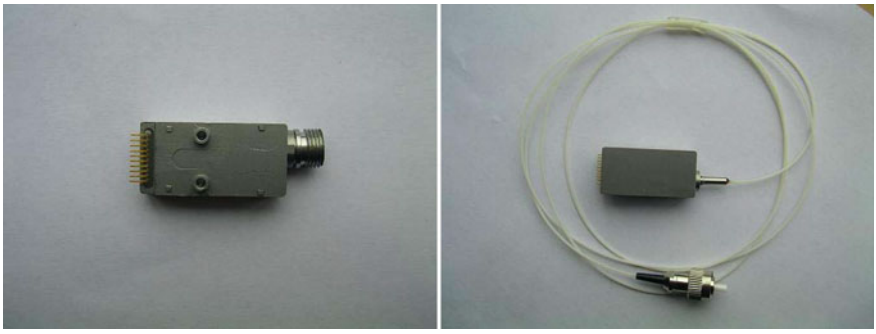


Fig. 7.14 Single-fiber bidirectional 2.5 Gbps optical module

The RF digitalized receiver of metric wave radar is usually placed on antenna array and multiple receiving channels are integrated into a receiver module. High digital signal data rate and long distance from signal processing unit require high speed optical transmission technology to transfer multiple channels of high speed digital signals to the signal processing unit. Thanks to rapid developments of optical transmission technology and devices, there are mature products with 10 Gbps (single-channel) and 6.5 Gbps (12-channel integrated/single-channel) and the optical modules with various wavelengths and connection modes. Figure 7.14 shows the pictures of a single-fiber bidirectional 2.5 Gbps optical module developed by No. 44 Research Institute of CETC.

7.4.2 Receiver Noise

Noise is the major factor to limit receiver sensitivity. Receiver noise is mainly composed of resistor noise, antenna noise, and the noise of receiver itself. According to Nyquist theorem, the resistor in circuit will produce open-circuit thermal noise voltage V_n at the temperature T (K).

$$V_n = \sqrt{4kTRB_n} \tag{7.22}$$

where, k is the Boltzmann constant ($1.380658 \times 10^{-23} J/K$), R is the resistance (Ω, and B_n is the receiver bandwidth (Hz). When the open-circuit voltage is applied to the matched load, the effective noise power is

$$P_n = 4kTB_n \tag{7.23}$$

The receiver noise is partly the thermal noise of resistor and also includes the noise produced by other active devices. They have the same spectrum and probability characteristics as the thermal noise, so that they are expressed by the thermal noise temperature.

$$T_n = P_n/4kB_n \tag{7.24}$$

For the convenience of computing signal noise, the output noise of system is viewed usually from the input. This is done by defining the system noise temperature T_s (K).

$$kT_sB_n = P_{no}/G_0 \tag{7.25}$$

where, G_0 is the effective gain of system, B_n is the system noise bandwidth, P_{no} is the system output noise power, T_s is the system noise temperature converted at the output end, and the product of kT_sB_n is the system output noise power converted at antenna input end. The antenna, transmission lines, receiver of the radar form a cascade system. For a cascade system of N stages, the system input noise temperature taking antenna as the system input end can be expressed by

$$T_s = T_a + \sum_{i=1}^{N} \frac{T_{e(i)}}{G_i} \tag{7.26}$$

T_a is the antenna noise temperature, $T_{e(i)}$ represents the equivalent noise temperature converted at the ith stage input end, and G_i is the effective gain between the system input end and the ith stage input end.

Antenna noise temperature includes the noise formed by the external electromagnetic waves received by the antenna and the thermal noise produced by the antenna resistor components. It depends on the noise temperature of various noise sources within the receiving antenna beam. When the beam is full of the noise sources of the same temperature, the antenna noise temperature is independent of the antenna gain and beamwidth, but dependent upon the space angle weithed average of the noise temperatures of all noise sources within the receiving antenna beam. In metric wave radar, especially the radar at lower metric wave band, its antenna suffers from strong noise mainly resulted from the solar noise and galactic noise. The big sources are the Sun and the center of Galactic System.

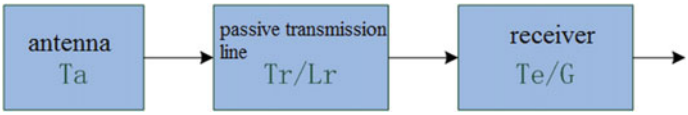


Fig. 7.15 Block diagram of an equivalent generalized radar receiver cascade for system noise temperature computation

When antenna beam points to the Sun or the center region of Galactic System, radar background noise has big effect on system noise temperature. At this time, spatial nulling can be considered to suppress antenna interference.

The receiver is a multi-stage transmission network and any stage of the receiver will produce noise. Define T_e to be the noise temperature of its internal noise converted at its input end, then the effective noise power of the internal noise converted at the input end, P_r (the receiver bandwidth is B_r), is

$$P_r = kT_eB_r \tag{7.27}$$

So an equivalent generalized noise temperature of radar receiver can be denoted to be

$$T_s = T_a + T_r + L_rT_e \tag{7.28}$$

The block diagram of an equivalent generalized radar receiver cascade is given in Fig. 7.15.

Noise temperature is often used in radar system analysis and receiver design. The engineering define is: if a linear two-port net has determinate input end and output end and when the input end source impedance is at 290 K, the specific value of input end SNR and output end SNR is defined to be noise figure of this net. Its explicit physical meaning is that the noise figure of the net is the degrading times of output signal SNR with respect to input signal SNR of the net. Using S_i/N_i to represent the input SNR of receiver and S_o/N_o to represent its output SNR, the noise figure, NF, is defined as

$$NF = \frac{S_i/N_i}{S_o/N_o} = \frac{N_o}{GN_i} = \frac{N_\infty + N_{ro}}{GN_i} = \frac{GN_i + GN_{ri}}{GN_i} = \frac{N_i + N_r}{N_i} = 1 + \frac{T_e}{T_o} \tag{7.29}$$

where, G is the gain of receiver, $N_i = kT_0B$ is the input noise power of antenna noise, and $N_r = kT_eB$ is the noise power of receiver output noise power converted at input end. So that the magnitude of noise figure is independent of signal power, but lies on the ratio of input noise power and output noise power.

In general, a receiver is composed of multiple stages of amplifiers, mixers, and filters. The noise figure or noise temperature of cascade circuit is determined by (G is the inverse of amplifier gain or mixer/filter loss)

$$NF_e = NF_1 + \frac{NF_2 - 1}{G_1} + \frac{NF_3 - 1}{G_1 G_2} + \cdots + \frac{NF_n - 1}{G_1 G_2 \cdots G_n} \tag{7.30}$$

$$T_e = T_1 + \frac{T_2 - 1}{G_1} + \frac{T_3 - 1}{G_1 G_2} + \cdots + \frac{T_n - 1}{G_1 G_2 \cdots G_n} \tag{7.31}$$

The noise figure is defined under the source temperature being the standard temperature $T_0 = 290$ K. For example, when the noise figure of receiver is 3 dB, the noise temperature of the receiver converted at input end is 290 K. When a radar is in operation, the source/antenna noise temperature T_a is generally not the standard temperature. At this time, the actual noise temperature corresponding to the receiver noise figure converted at the input end of receiver is

$$T_e = (NF - 1)T_a \tag{7.32}$$

Thus, in practical operation, the above expressions and (7.32) are used to calculate the noise temperature of the radar cascade receiving system, T_s, and its effect on radar system.

RF digitalized technology is used to realize metric wave radar receiver, so the calculation of the noise figure of RF digitalized receiver system should take the influences of the noise or noise figure of ADC and the following digital signal processing into account. The block diagram of noise analysis principle of RF digitalized receiver system is illustrated in Fig. 7.16.

Assume that the equivalent output noise power of ADC is N_{ADC}, the noise is band-limited noise, and the anti-aliasing filter before ADC can ensure no ADC sampling folded noise entering into ADC, then the output noise of ADC, N_s, is

$$N_s = N_o + N_{ADC} \tag{7.33}$$

So the noise figure of the system after cascading is

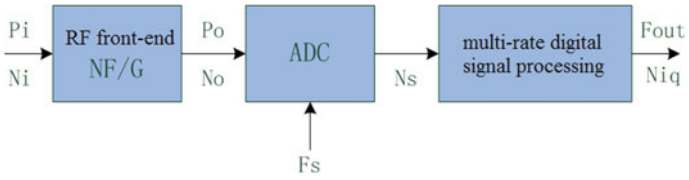


Fig. 7.16 Block diagram of noise analysis of RF digitalized receiver RF front-end Multi-rate digital signal processing

$$NF_s = \frac{N_s}{GN_i} = \frac{N_o + N_{ADC}}{GN_i} = NF + \frac{N_{ADC}}{GN_i} \tag{7.34}$$

Let $M = N_o/N_{ADC}$, substituting into the above expression, we have

$$NF_s = NF\left(\frac{1+M}{M}\right) = NF + 10\lg(1+M) - \lg M(dB) \tag{7.35}$$

That is, the degradation of ADC on noise figure is

$$\Delta NF = 10\lg(1+M) - \lg M(dB) \tag{7.36}$$

According to the define of noise figure, the noise figure of ADC can be given by

$$NF_{ADC} = P_{FS(dBm)} - SNR_{(dBFS)} - 10\lg(F_s/2) - KT_{(dBm/Hz)} \tag{7.37}$$

Thus the noise figure of ADC is not a fixed value. It is relative to the sampling clock/sampling rate, the amplitude and frequency of input signal, and the bandwidth of subsequent filter. Figure 7.17 gives the relation of ADC noise figure to different SNRs and sampling rates and Fig. 7.18 depicts the output noise spectrum of ADC under different input signal amplitudes.

It can be seen from the above analysis that, the effects of ADC of RF digitalized receiver on system noise is directly relative to the ratio of the front-end noise power and the noise power of ADC itself. The degradation of ADC on the cascading system noise figure can be reduced in two ways: decreasing the equivalent noise power of ADC or assuring that the input noise and signal of front-end can be quantized by ADC to the full through receiver system design.

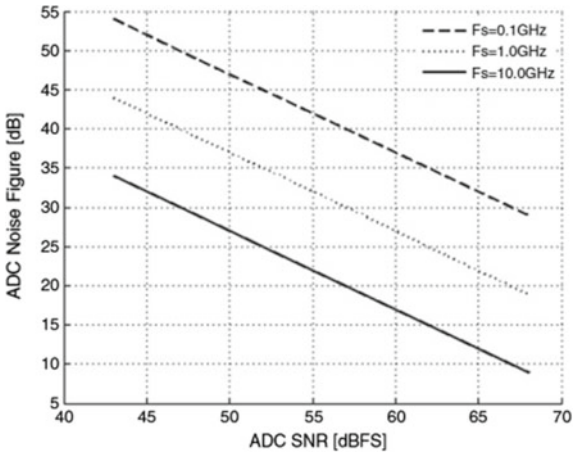


Fig. 7.17 Relation of ADC noise figure to SNR and sampling rate

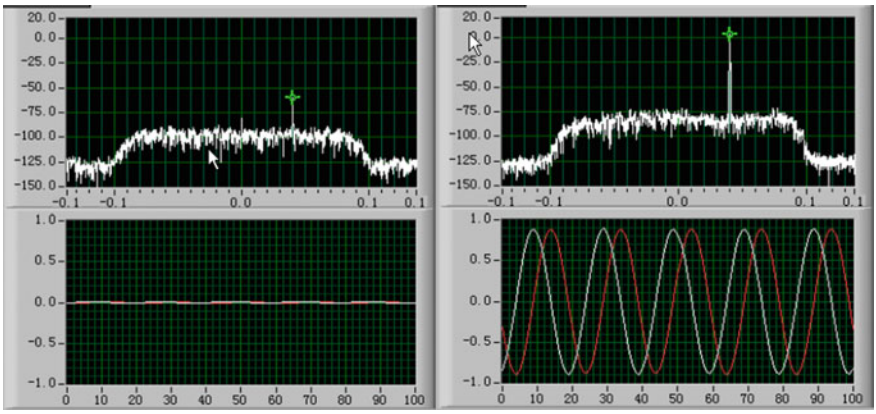


Fig. 7.18 ADC output noise levels under different input signal amplitudes

The equivalent noise power of ADC is not a fixed value, but changes w.r.t. its working environment. It can be expressed by

$$N_{ADC} = N_q + N_t + N_j \tag{7.38}$$

where, N_t is the thermal noise and N_q is the ideal quantization noise which is directly relative to the quantization level or ADC conversion sensitivity. For ADC with resolution of N and input peak-peak value of V_{p-p}, the quantization level is

$$Q = V_{p-p}/2^N \tag{7.39}$$

At this time, the maximum power of ADC is

$$P\text{max} = \left(\frac{V_{p-p}}{2\sqrt{2}}\right)^2 = \frac{2^{2N}Q^2}{8} \tag{7.40}$$

When the least bit of ADC is the noise bit and the noise takes uniform distribution, the quantization noise power is

$$N_q = \frac{Q^2}{12} \tag{7.41}$$

At this time, the maximum SNR of the ideal ADC is

$$SNR_{dBFS} = 10\lg\frac{P\text{max}}{N_q} = 10\lg\left(\frac{3}{2}\times 2^{2N}\right) = 6N + 1.76(dB) \tag{7.42}$$

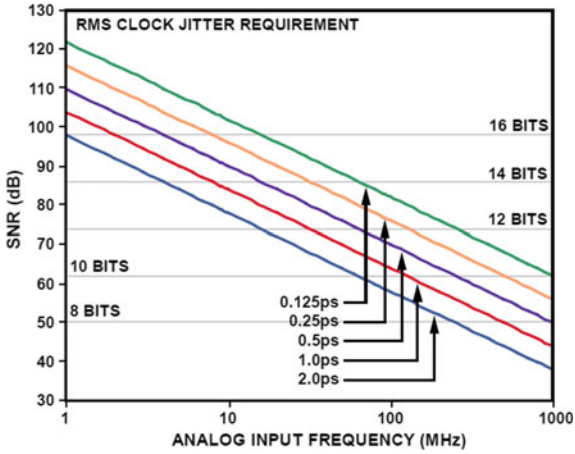


Fig. 7.19 Relationship of ideal ADC SNR to input frequency and clock jitter

The other key factor affecting the equivalent noise power of ADC is the noise resulted from the aperture uncertainty of clock. The aperture uncertainty involves the transform of the sampling and holding circuit of ADC itself and the upper/lower edge jitter of sampling clock. The clock jitter and the clock phase noise are the different formulations of a phenomenon and closely correlative to the thermal noise, phase noise, and spurious of clock source. In the case of point frequency input, the SNR of ADC limited by aperture jitter is

$$SNR_j = -20\lg(2\pi f_a \Delta t_{rms})(dB) \tag{7.43}$$

where, f_a is the frequency of analog input signal and Δt_{rms} is the rms of aperture jitter. Under the ideal condition, the relationship of the output SNR of ADC to the input frequency and the clock jitter is illustrated in Fig. 7.19.

On the other side, for reducing the degradation of ADC on the noise figure of RF digitalized receiver cascade system, the receiver system design is needed to assure that the front-end input noise plus signal can be quantized fully by ADC. This can be seen from the derivation of (7.45) and can also be interpreted from the noise back effect of ADC. When the weak signal below the lowest quantization hierarchy level and the strong signal over the lowest quantization hierarchy level but below the highest quantization hierarchy level go into ADC together, with the help of the back effect of the strong signal, the weak signal can pass through ADC together with the strong signal. The strong signal can be a signal or a noise and its intensity is required so that at least 90% energy can be quantized by ADC, generally about 6 times of the lowest quantization hierarchy level of ADC. In this case, the wanted weak signal is not lost basically. Using the noise back effect of ADC, if allowable, it may be considered to broaden the bandwidth of RF analog channel and increase the instantaneous dynamic range of the system, at the cost of high sampling rate and

digital baseband processing hardware. Figures 7.20, 7.21 and 7.22 give the simulation results of the noise back effect of ADC sampling signals.

The RF digitalized receiver of metric wave radar usually combines both the under-sampling and over-sampling, that is, the sampling frequency may be lower than the carrier frequency of RF signal but far higher than the instantaneous bandwidth of signal. When the output signal bandwidth after multi-rate signal processing matches to the instantaneous bandwidth of signal and all bandwidths of all filters in multi-rate signal processing match to the instantaneous bandwidth of signal as well as the out-band noise is rejected enough not to produce noise aliasing due to decimation, the final output noise power will be one fraction of $F_s/2B$ of ADC output noise power. Therefore, the ideal ADC output SNR after multi-rate signal processing can be expressed by

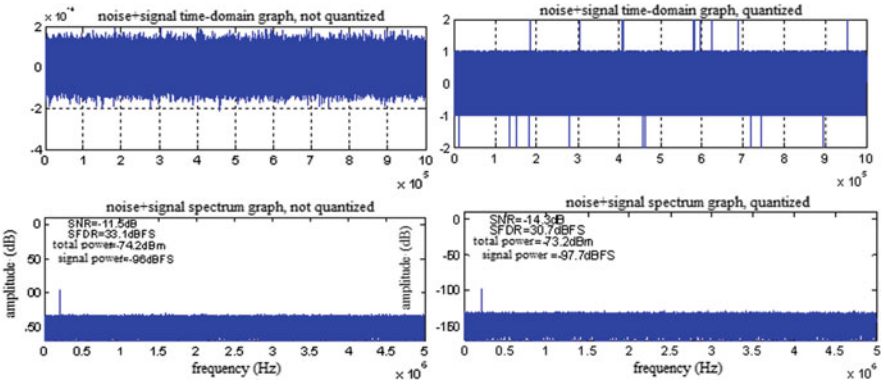


Fig. 7.20 Output SNR of ADC when signal power being −96 dBm and noise power being quantized 1 bit

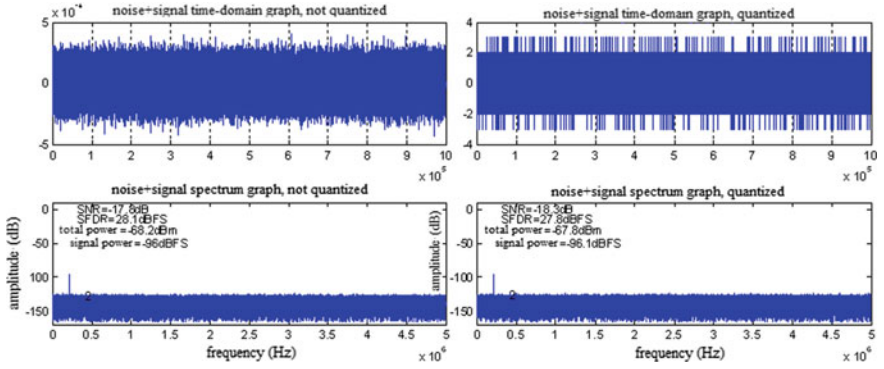


Fig. 7.21 Output SNR of ADC when signal power being −96 dBm and noise power being quantized 2 bits

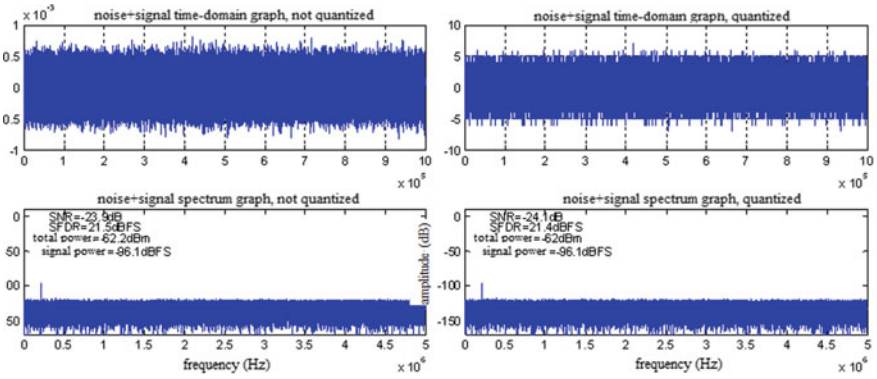


Fig. 7.22 Output SNR of ADC when signal power being −96 dBm and noise power being quantized 3 bits

$$SNR_{dBFS} = 6N + 1.76 + 10\lg(F_s/2B)(dB) \tag{7.44}$$

The multi-rate signal processing mainly includes fixed-point digital signal processing such as multi-stage filtering and decimation involves, so the bit-truncation process is involved consequentially. Similar to the previous analysis about ADC quantization noise, with SNR increasing, adequate bits are needed to guarantee that the output SNR meets requirement so as not to result in the loss of system SNR or the degradation of system noise figure. Figures 7.23 and 7.24 show the influences on SNR under different numbers of truncation bits.

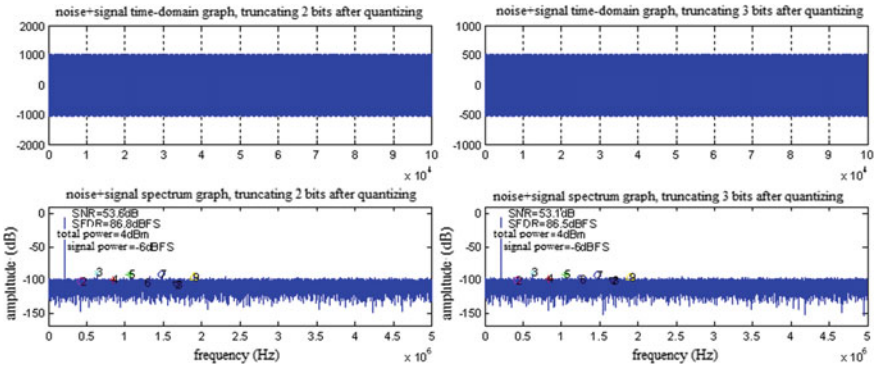


Fig. 7.23 Comparison between output SNRs in truncating 2 bits and 3 bits

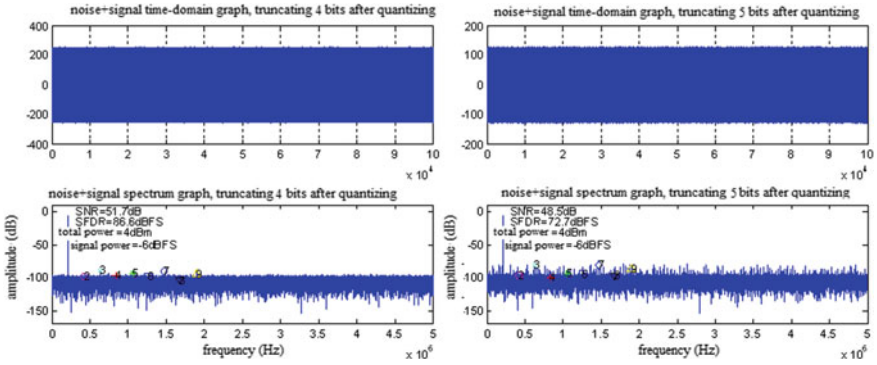


Fig. 7.24 Comparison between output SNRs in truncating 4 and 5 bits

7.4.3 Dynamic Range of Receiver

The dynamic range of receiver is chosen based on the total dynamic range of radar, radar system, signal processing mode, and so on. The total dynamic range of radar is decided by

$$D = D_r + D_\sigma + D_{S/N} + D_f \tag{7.45}$$

where,

D_r is the range of target echo signal changing with distance;
D_σ is the target's RCS changing range, decided by the RCS changing range of target/clutter;
D_{SIN} is the SNR required for target detection, relative to operation mode and target type;
D_f is the increment of dynamic range required under receiver bandwidth mismatching.

Currently, the metric wave radar adopts the fully digital phased array system based on RF digitalization technique. Active receiving, ADC sampling, digital down conversion are implemented at element level, then digital domain DBF processing is performed, followed by pulse compression and multi-pulse coherent integration. Assume that the benefit of DBF processing is D_{DBF}, the benefit of digital pulse compression is D_{DPC}, the benefit of multi-pulse integration is D_{CI}, then the instantaneous dynamic range of single-channel receiver of digital phased array radar, D_{dr} (the maximum output SNR of receiver), is required to be

$$D_{dr} = D - D_{DBF} - D_{DPC} - D_{CI} \tag{7.46}$$

As a comparison, in traditional analog phased array radar, the receiving beamforming is carried out in analog domain and is followed by ADC sampling and signal processing. If the signal processing modes are the same, the instantaneous dynamic range of receiver in analog phased array radar, D_{ar} is required to be

$$D_{ar} = D - D_{DPC} - D_{CI} \tag{7.47}$$

Therefore, under the same requirement on system dynamic ranges, the requirement on receiver dynamic range of digital phased array radar is by D_{DBF} lower than the requirement on receiver dynamic range of analog phased array radar, or, in another word, under the same receiver dynamic range, the total system dynamic range of digital phased array radar is by D_{DBF} wider than analog phased array radar. We can see that the digital phased array radar has the ability to improve the total system dynamic range greatly. Once the requirement on the instantaneous dynamic range of receiver has been determined, the design of receiver dynamic range can be carried out.

The usual representations of RF receiver dynamic range of are the dynamic range at 1 dB compression point, DR_{-1} (linear dynamic range of receiver), and the dynamic range without distorted signal, DR_{SFDR}.

The dynamic range at 1 dB compression point, DR_{-1}: It is defined as the ratio of the input signal power and the least detectable signal power or the equivalent noise power when the receiver output power is enough to produce 1 dB gain compression, that is,

$$DR_{-1} = \frac{P_{i-1}}{P_{i\min}} = \frac{P_{o-1}}{GP_{i\min}} = \frac{P_{o-1}}{GS_{\min}} = \frac{P_{o-1}}{GkT_0NFBM} \tag{7.48}$$

where, P_{i-1} is the signal power at the input end of the receiver when 1 dB compression producing, P_{o-1} is the output signal power of the receiver when 1 dB compression producing, G is the receiver gain, NF is the receiver note figure, B is the receiver bandwidth, M = 1 is the identification factor, and T_0 is the thermodynamic temperature. By derivation, we have

$$DR_{-1} = P_{o-1(dBm)} + 114 - NF_{(dB)} - 10\lg B_{(MHz)} - G_{(dB)}(dB) \tag{7.49}$$

$$DR_{-1} = P_{i-1(dBm)} + 114 - NF_{(dB)} - 10\lg B_{(MHz)}(dB) \tag{7.50}$$

The dynamic range without distorted signal, DR_{SFDR}, which denotes the ratio of the maximum input signal power of receiver and the 3th-order intermodulation signal power when the 3th-order intermodulation signal of receiver is equal to the least detectable signal, i.e.,

$$DR_{SFDR} = \frac{P_{isf}}{P_{i\min}} = \frac{P_{osf}}{GP_{i\min}} \tag{7.51}$$

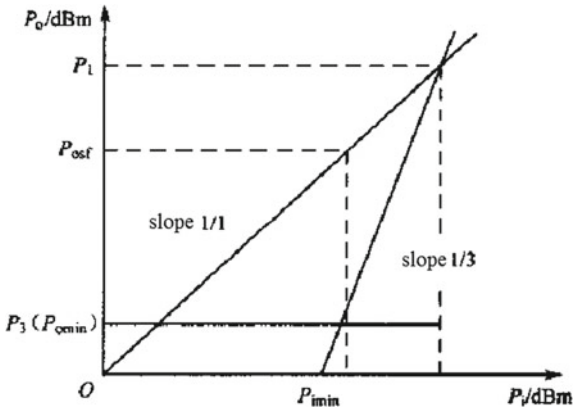


Fig. 7.25 Graphic representation of the dynamic range without distorted signal

Figure 7.25 shows the graphic representation method of the dynamic range without distorted signal, where, P_3 is the 3th-order intermodulation power level, P_{osf} is the maximum input signal power of receiver when the 3th-order intermodulation signal of receiver is equal to the least detectable signal. The 3th-order intermodulation intercept point is the intersection point of the input/output relationship curve of the fundamental frequency signal and the relationship curve of 3th-order intermodulation result and the input signal. P_1 is the power at 3th-order intercept point of the receiver. Ignoring the transformation of the phase distortion and the amplitude distortion resulted from the high-order components and nonlinearity, we have

$$DR_{SFDR} = \frac{2}{3}\left(P_1 - P_{o\min}\right) = \frac{2}{3}\left(P_1 - P_{i\min} - G\right) \tag{7.52}$$

$$P_{ofs} = P_{o\min} + DR_{SFDR} \tag{7.53}$$

$$P_1 = P_{o-1} + 10.65(dBm) \tag{7.54}$$

$$\begin{aligned} DR_{SFDR} &= \frac{2}{3}\left(P_{o-1} - P_{i\min} - G + 10.65\right) \\ &= \frac{2}{3}(P_{o-1} + 114 - NF - 10\lg B - G + 10.65) \\ &= \frac{2}{3}(DR_{-1} + 10.65) \end{aligned} \tag{7.55}$$

In designing the dynamic range of the RF digitalized receiver, the dynamic range of the receiver is required to match the dynamic range of the signal entering into the receiver. That is, the dynamic range of analog RF channel of receiver matches the dynamic range of the signal entering into the receiver, and the dynamic range of RF channel is also required to match the dynamic range of ADC. The dynamic range and the sensitivity of RF digitalized receiver are the two important indexes which

are correlative and restrictive with each other. It is required to make design through reasonable distribution of channel gain and reasonable selection of analog device and ADC specifications.

The ideal ADC dynamic range can be denoted as

$$DR_{ADC} = 10\lg\frac{P_{\max}}{P_{\min}} = \frac{2^{2N}Q^2/8}{Q^2/8} = 20N\lg 2 = 6N(dB) \tag{7.56}$$

The dynamic range of RF front-end matching the dynamic range of ADC requires that the maximum input signal does not cause ADC situation and the least signal can be fully quantized but does not cause receiver NF degradation after amplifying in RF front-end. The design of wide linear dynamic range of receiver should be started form aspects: reasonably distribute the gain of each stage in receiver and design or select the device with large dynamic range.

Modern early warning and detection radar usually has multiple operation modes and corresponding instantaneous signal bandwidths. Sometimes, the compatible wideband and narrowband operation modes are required (such operation modes as target image, target tracking, and target search). For simplifying the receiver design, the receiver channel is often designed in terms of the largest bandwidth. The sensitivity and dynamic range requirements are guaranteed under the largest bandwidth. The sensitivity and instantaneous dynamic range in narrowband operation mode can be achieved by the succeeding multi-rate signal processing. This requires the output I/Q signal after digital signal processing to have adequate noise bits. This wideband and narrowband integrated receiver design can achieve both high sensitivity and large linear dynamic range, which differentiates from the traditional analog receiver design.

7.4.4 Realization of Multi-Channel RF Digitalized Receiver

The design of multi-channel RF digitalized receiver is based on software radio RF digitalization technique and digital down conversion DDC technique (including the digital quadrature intermodulation technique and the multi-rate digital signal processing technique) to realize the conversion of an analog RF signal to digital baseband I/Q signal. Figure 7.26 illustrates the functional block diagram of a 16-channel RF digitalized receiver.

The RF digitalized receiver mainly includes bandwidth rejection low pass filter, IF sampling ADC, FPGA based digital down conversion (DDC), optical fibre interface, clock circuit, and PS circuit. The bandwidth rejection low pass filter adopts surface mount LTCC based low pass filter to limit the bandwidth of ADC input signal for out-band interference rejection. ADC is selected to be the 8-channel parallel 14-bit LTM9011 with 125 MHz sampling rate, the clock frequency is chosen as 120 MHz, and the center frequency of RF signal is 270 MHz, satisfying the optimal bandpass sampling theorem. The design requires that there are one 5 MHz tracking signal and

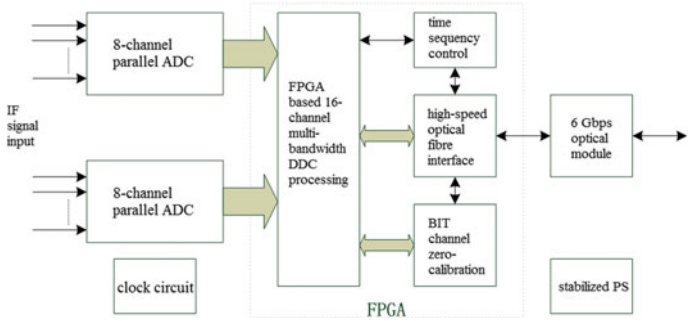


Fig. 7.26 Functional block diagram of a 16-channel RF digitalized receiver

one single-frequency signal or five 1 MHz searching signals simultaneously within a 20 MHz instantaneous bandwidth. The main specifications of the 8-channel parallel ADC are:

(1) 8-channel parallel ADC;
(2) The highest sampling rate is 125 MHz;
(3) Bit-width is 14 bits;
(4) SNR $\geq$ 71dBFS@fin = 270 MHz/fs = 125 MHz;
(5) SFDR $\geq$ 75dBFS@fin = 270 MHz/fs = 125 MHz;
(6) The input analog bandwidth is 800 MHz and the amplitude input signal is 1Vp-p/2Vp-p, selectable;
(7) Single PS 1.8 V/1.12 W, having PS bypass filtering capacitor inside the chip, without adding.

The DDC design requirements are as follows:

(1) IF: 270 MHz, sampling rate: 120 MHz, IF bandwidth: 20 MHz, satisfying the optimal sampling theorem;
(2) There are three instantaneous signal bandwidths: 5 MHz/1 MHz/0.2 MHz, corresponding to two baseband signal sampling rates: 5 MHz/1.25 MHz. There are five frequency division multiplexing subband signals with 1 MHz bandwidth each or there is only one signal with 5 MHz bandwidth in the 20 MHz IF bandwidth;
(3) A FPGA realizes 16-channel parallel DDC processing simultaneously.

Considering compatible wideband design, order reduction of filter, and resource saving, the realization of multi-sampling-rate, multi-band, and multi-channel DDC adopts the secondary mixing three-stage filtering and decimation structure. The block diagram of the realization and function of a single-channel DDC is shown in Fig. 7.27.

The functions of the individual modules are:

(1) The first-mixing wideband polyphase filtering & mixing post DDC processing module implements the digital down conversion of 20 MHz wideband IF signal. When the system operates in 5 MHz bandwidth, 1 MHz bandwidth, and 0.2 MHz

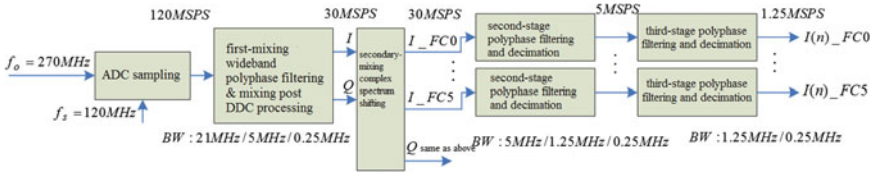


Fig. 7.27 Block diagram of multi-sampling-rate, multi-band, multi-channel DDC algorithm

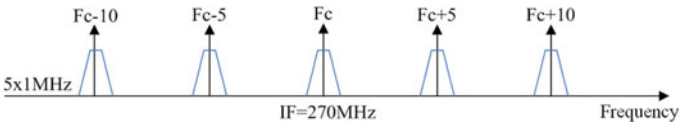


Fig. 7.28 Spectrum distribution in IF band under 1 MHz bandwidth mode

bandwidth, the filter corresponds to 5 MHz bandwidth, 21 MHz bandwidth, and 0.25 MHz bandwidth, respectively. The filtering of the signals of different bandwidths is realized by changing the filter coefficients through control signal.

(2) The secondary-mixing complex spectrum shifting module conducts the down conversion of five subband signals within IF band under the 1 MHz bandwidth mode. One of these subbands is compatible with three bandwidths: 5, 1, and 0.2 MHz. And under the 5 MHz mode, its center frequency is arbitrarily changeable. The spectrum distribution of the five signals under the 1 MHz bandwidth mode is shown in Fig. 7.28.

(3) The second-stage polyphase filtering and decimation module outputs 5MSPS sampling-rate signal. The filter coefficients can be changed according to operation bandwidth so as to filter signals of different bandwidths. There are three bandwidths: 5, 1.25, and 0.25 MHz.

(4) The third-stage polyphase filtering and decimation module outputs 1.25MSPS sampling-rate signal. The filter coefficients can be changed according to operation bandwidth so as to filter signals of different bandwidths. There are two bandwidths: 1.25 and 0.25 MHz.

In essentials, there are two methods to design low pass FIR filter. They are the time-domain windowing method and the frequency-domain Remez (or the Parks-McClellan method). Currently, the MATLAB software already has integrated the majority of conventional filter designs. The FDATool in the MATLAB can be used to conduct filter design. And the functions integrated inside can also be used to make design for the conveniency of joint simulation. The simulation parameters of the filters of different bandwidths 5, 1.25, and 0.25 MHz are given in Tables 7.2, 7.3 and 7.4. The simulation results can be seen in Figs. 7.29, 7.30 and 7.31.

The resources for realizing the DDC algorithm and its relative modules in FPGA are listed in Table 7.5.

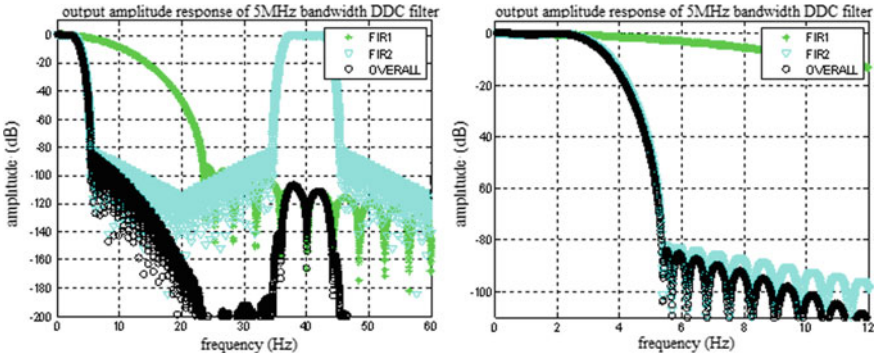


Fig. 7.29 Simulation result of two-stage cascading filters at 5 MHz bandwidth

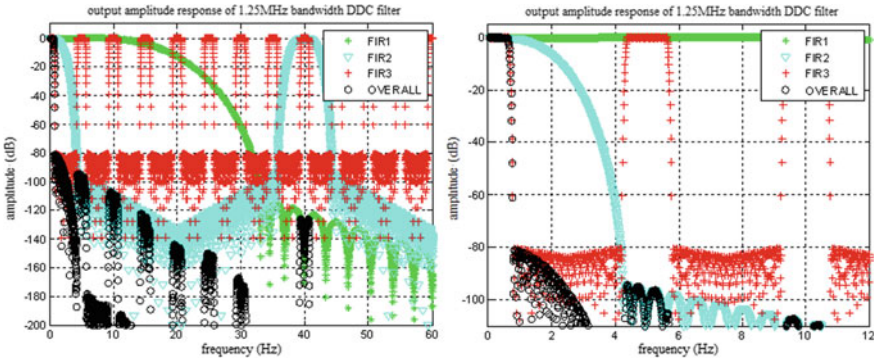


Fig. 7.30 Simulation result of three-stage cascading filters at 1.25 MHz bandwidth

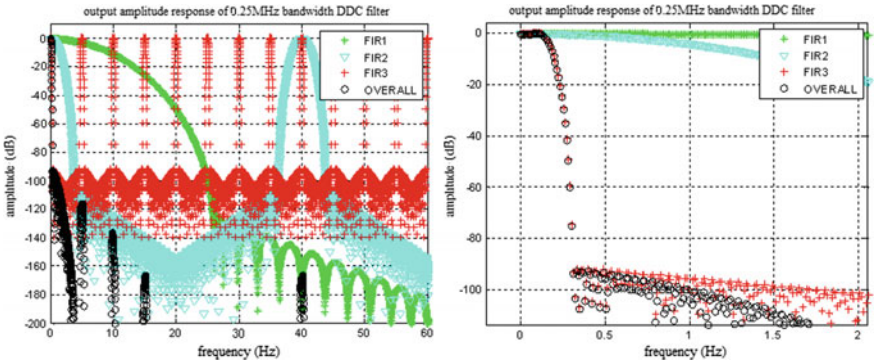


Fig. 7.31 Simulation result of two-stage cascading filters at 0.25 MHz bandwidth



Fig. 7.32 A multi-channel RF digitalized receiver

High speed optical fiber is used to connect the I/Q signal from the digital receiver to the signal processor. The output data rate with respect to a 5 MHz bandwidth is calculated as

$$5 \times 16\,bit \times 2(I/Q) \times 16(ch) \times 10/8(8B/10B) = 3.2\ \text{Gbps} \tag{7.57}$$

The computation of the data rate with respect to five 1 MHz bandwidths is

$$5 \times 1.25 \times 16\,bit \times 2(I/Q) \times 16(ch) \times 10/8(8B/10B) = 4.0\ \text{Gbps} \tag{7.58}$$

Taking the uniformity of FPGA internal clocks and the uniformity of the output data rates of high speed serial interfaces into consideration, all the input data rates in designing are treated as 120 MHz/32 bits. Thus, the serial data rate of optical fiber is

$$120(\text{MHz}) \times 32\text{bit} \times 10/8(8B/10B) = 4.8\ \text{Gbps} \tag{7.59}$$

Figure 7.32 shows a picture of a 16-channel RF digitalized receiver we designed.

Table 7.2 Parameter setting of two-stage filters at 5 MHz bandwidth

Parameter	FIR1	FIR2
Order of filter	23	47
Bandpass cut-off frequency (MHz)	5.0	5.0
Bandpass ripple (dB)	0.5	0.2
Stopband rejection (dB)	75	75
Stopband attenuation (dB)	55	45

Table 7.3 Parameter setting of three-stage filters at 1.25 MHz bandwidth

Parameter	FIR1	FIR2	FIR3
Order of filter	23	47	95
Bandpass cut-off frequency (MHz)	21	1.25	1.25
Bandpass ripple (dB)	0.5	0.2	0.4
Stopband rejection (dB)	80	85	80
Stopband attenuation (dB)	83	50	5

Table 7.4 Parameter setting of three-stage filters at 0.25 MHz bandwidth

Parameter	FIR1	FIR2	FIR3
Order of filter	23	47	95
Bandpass cut-off frequency (MHz)	0.25	0.25	0.25
Bandpass ripple (dB)	0.5	0.2	0.4
Stopband rejection (dB)	80	95	90
Stopband attenuation (dB)	102	60	15

Table 7.5 Realization of 16-channel parallel DDC algorithm in FPGA

Type of FPGA	EP4SGX180FF35I4
Multiplier (18 × 18)	800 (87%)
Logic element (LE)	93,403 (85%)
Highest operation clock rate (MHz)	148
Memory (Mb)	5.5 (49%)

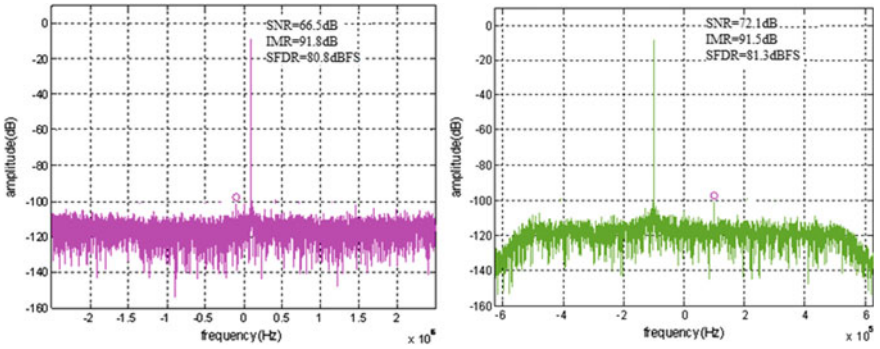


Fig. 7.33 Test results of DDC output at 5 MHz bandwidth and 1 MHz bandwidth (frequency offset: 0.1 MHz)

Figure 7.33 gives the test results of the RF digitalized receiver during its practical operation.

7.4.5 Optical Transmission and Synchronization of Data

7.4.5.1 High-Speed, Large-Capacity Optical Fiber Data Transmission

The fast development of RF digitalization technology has pushed the ADC and the succeeding multi-rate signal processing towards the antenna gradually. On the other hand, to reduce the transmission loss of analog signal, the RF digitalized receiver based on the RF front-end + ADC + multi-rate signal processing architecture will be directly located in the antenna array. A new generation of baseband radar signal

processing will be realized by high performance multi-core DSP or parallel computer. The high performance multi-core DSP or parallel computer is often located in the center processing cabinet far from the radar antenna array. Digital array module (DAM) is used to design the RF digitalized receiver for the purposes of increasing integration level and decreasing the volume, weight, and cost. Experiencing data fusion processing, the multi-channel baseband I/Q signals of RF digitalized receiver are transferred to the signal processing cabinet. In a module, 8, 16, or even more channels are integrated, so that the amount of the data to be transferred will be large. For example, in metric wave radar, the baseband I/Q data rate at the signal bandwidth 5 MHz will reach up to 6.4 Gbps after 16-channel fusion and 8B/10B coding.

As shown in Fig. 7.34, the bidirectional optical transmission system in metric wave radar mainly includes the FPGA based data serial-to-parallel and parallel-to-serial conversion portion and the optical module based optical-to-electric and electric-to-optical modulation/demodulation portion.

All of the main-stream FPGAs, produced by ALTERA, XILINX, and etc., integrate the high speed serial data interfaces with speed greater than 10 Gbps. Figure 7.35 illustrates the functional block diagram of high speed serial interface for V7 family FPGAs produced by XILINX.

The main-stream optical module also can support the signal transmission at 10 Gbps above. Then the FPGA can interface directly with optical module through AC coupling, which simplifies their applications. In addition, the hard core integrated in FPGA also reduces the difficulty in software design. Figure 7.36 shows a single-fiber bidirectional 2.5 Gbps optical module produced in China, and Fig. 7.37 is a double-fiber bidirectional single-channel 2.5–10 Gbps optical module produced in China.

To improve the transmission rate, capacity, and module integration level, many multi-channel integrated optical modules have been developed by the research institutes and corporations at home and abroad. Figure 7.38 is a 12-channel integrated transmit/receive optical module developed by Finisar Company. Also, to increase the assembly integration level and meet the miniaturization requirement, a research institute in China has developed a multi-channel SMT optical module, with single-channel rate of 6.25 Gbps and total rate of 75 Gbps, as shown in Fig. 7.39.

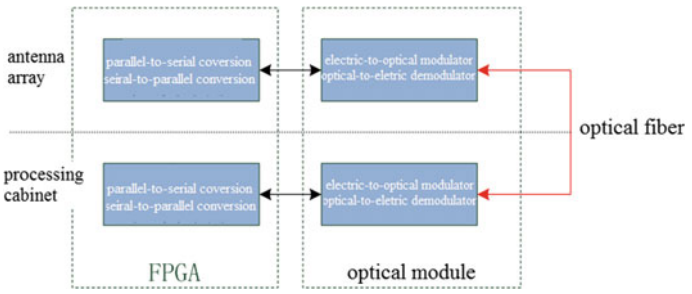


Fig. 7.34 Functional block diagram of radar optical transmission system

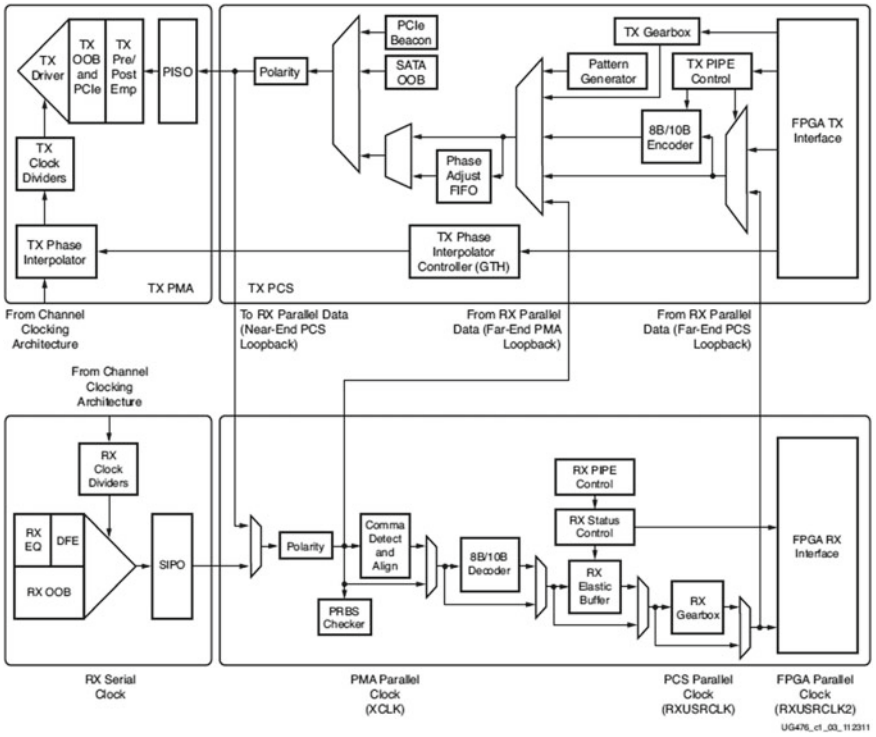


Fig. 7.35 Block diagram of high speed serial interface for V7 family FPGAs produced by XILINX

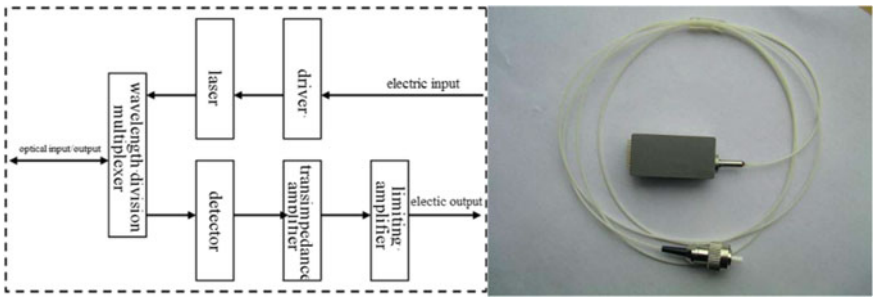


Fig. 7.36 A single-fiber bidirectional optical module produced in China

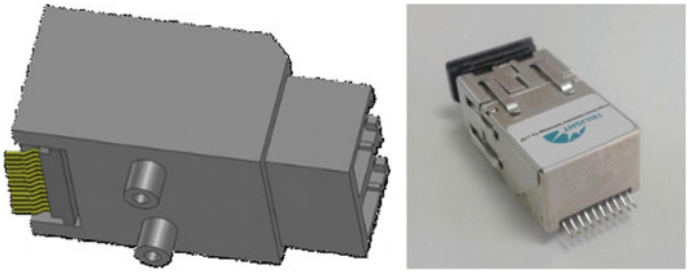


Fig. 7.37 A double-fiber bidirectional single-channel optical module produced in China



Fig. 7.38 A 12-channel transmit/receive optical module developed by Finisar

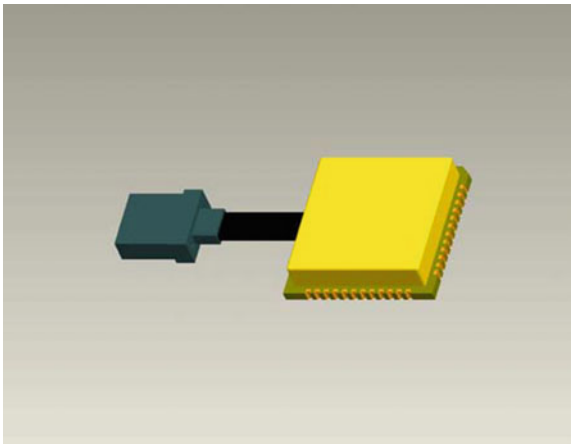


Fig. 7.39 A SMT 12-channel transmit/receive optical module

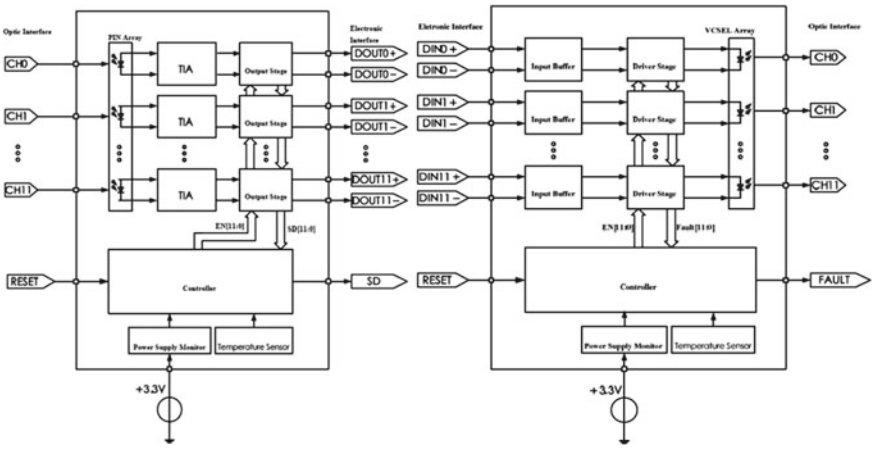


Fig. 7.40 Principle block diagram of multi-channel integrated optical module

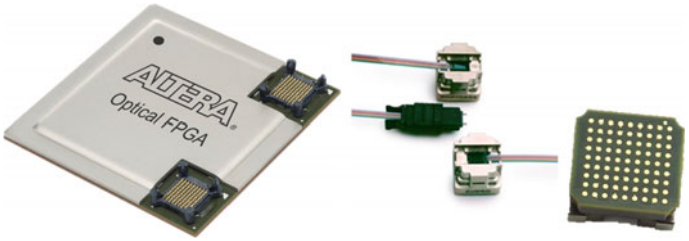


Fig. 7.41 Optical FPGA developed by ALTERA

Figure 7.40 gives the principle block diagram of multi-channel integrated optical module.

With the continuous upgrades of data transmission and capacity, the optical transmission and integration mode will evolve further. In the next generation of FPGA products of ALTERA, we can see optical FPGA. The single-channel 28 Gbps super high transmission rate is achieved by integrating multi-channel optical module onto the substrate of FPGA, seeing Fig. 7.41. As for short distance super high speed optical transmission, the chip-level 3D package direct free-space optical transmission developed by Avago will further increase integration level and transmission, as shown in Fig. 7.42.

7.4.5.2 Multi-Channel Data Synchronization Based on Optical Fiber Transmission

In the digital array radar which adopts transmit/receive DBF technique, the signal processing is based on multiple pulse repetition frequency (PRF) periods within a

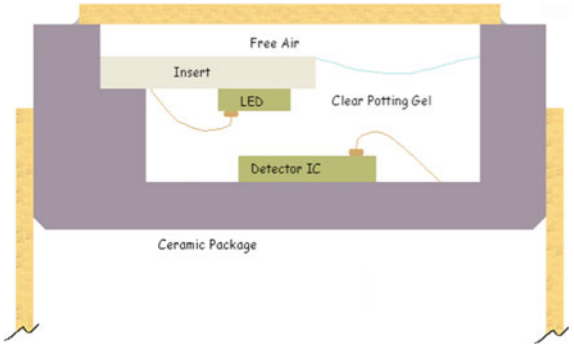


Fig. 7.42 Chip-level short distance free-space super high-speed optical transmission technology developed by Avago

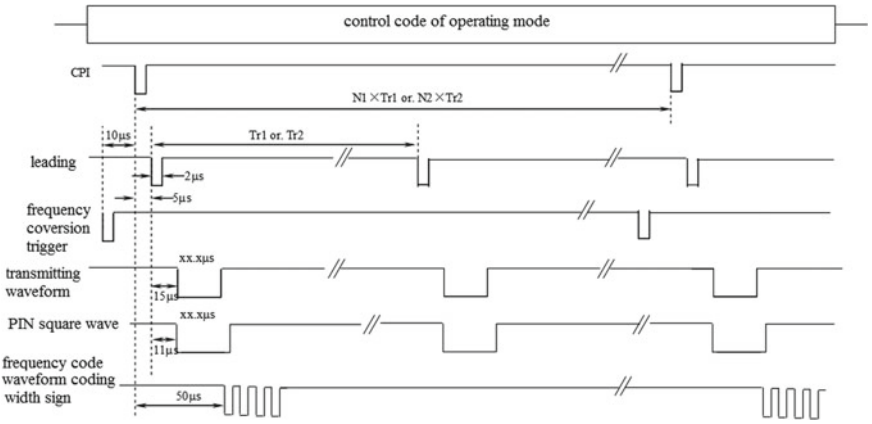


Fig. 7.43 Transmitting and receiving time sequences of pulse radar

coherent processing interval (CPI). The fixed phase relation should be kept between the transmitting channels. And the fixed phase relation for the echo signal or the test signal should also be kept between the receiving channels. Currently, the method to achieve the above fixed phase relations is that the multiple transmit/receive elements operate synchronously under the same timing pulse (leading) of the radar system and the synchronous clock, ADC sampling clock, DDS processing clock, and LO signal of each transmit/receive element are all generated by the same crystal oscillator. In this way, the phase relations of the timing pulse (leading) of radar system and the individual clock signals can be ensured to be fixed, and further, multiple transmit/receive elements can be ensured to operate synchronously under the timing pulse of radar system. Figure 7.43 shows the conventional transmitting and receiving time sequences of pulse radar.

Early phased array radar adopt the transmit/receive DBF technique because digital processing is performed at lower IF, both ADC sampling clock and DDS processing

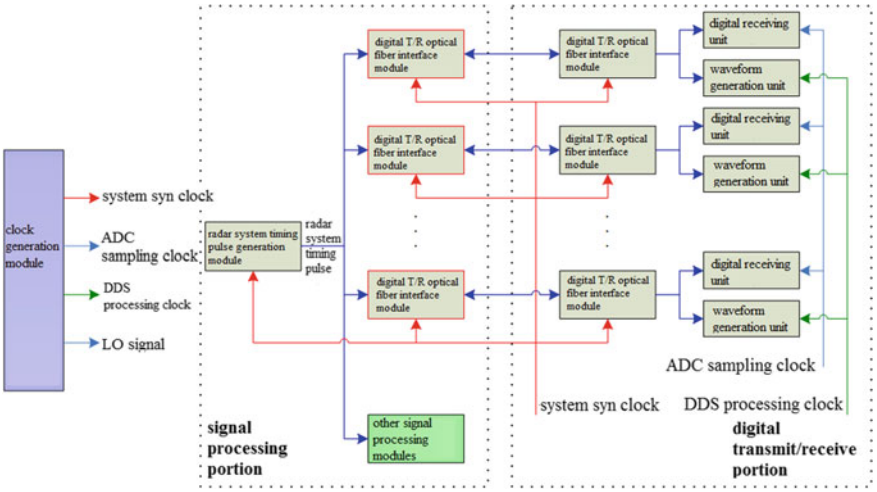


Fig. 7.44 Block diagram of timing signal and clock signal transferring and distribution

clock are low. Also as the timing pulse (leading) of radar system is distributed in the form of TTL signal, it is easy to achieve transmit/receive phase synchronization among multiple channels. However, the new metric wave digital array radar that uses RF digitalized receiver will face new problems: (1) large antenna array, which requires optical fiber to transfer the timing pulse (leading) of radar system; (2) High ADC sampling clock frequency and DDS processing clock frequency. Therefore, the difficulties must be overcome about transferring the timing pulse (leading) of radar system via optical fiber and stably sampling the timing pulse (leading) of radar system under high clock frequency.

In present digital array radar, the transferring and distribution of the timing signal and clock signal of radar system are shown in Fig. 7.44. First, the signal processing subsystem generates the timing signal of radar system required by radar according to the system synchronous clock. The leading signal is sent to the optical fiber interface module via the high-speed serial interface in FPGA and then to the optical fiber interface module of the digital transmit/receive portion at the far-end via optical fiber. Through deserialization by FPGA, the leading signal can be obtained. Second, the leading signal is transferred at a board level and distributed to the digital receiving module and the waveform generation module et al. To ensure that the radar operates stably under the timing pulse signal of a radar system and guarantee the multi-channel phase synchronization, it is needed to make consideration and design at the system level, circuit level, and chip level.

The design considerations at the system level mainly involve the following aspects:

(1) The radar pulse repetition period should be selected so that it is the integral times of there other clock periods except for considering the radar system performance requirement.

(2) The optical fiber for the leading signal transfer between the signal processing portion and the transmit/receive portion should be designed as long as possible so as to keep the delays of individual leading transfers consistent.
(3) The lengths of the RF cables for transferring the same kind of clock signals should be designed as consistent as possible to keep the phase delays of the same clocks to individual transmit/receive modules consistent.

The following considerations should be taken into consideration when conducting the circuit-level design:

(1) For multi-channel optical modules, the differential transmission lines form all optical modules should be equal in length so as to achieve identical delays.
(2) The board-level clock transfer should take the form of differential signal transmission to make the jitter introduced by the clock transferring at board level small.
(3) For PCB design, the transmission lines for transferring the sampling clock to ADC modules should be equal in length and the transmission lines for transferring the DDS processing clock to DDS chips should also be equal in length to ensure the identical delays of the clocks to individual modules.

The chip-level design considerations mainly involve the FPGA program design and the ADC chip and DDS chip application designs. The measurement that should be taken into account includes:

(1) The programs for sending the leading signal should work synchronously under the timing pulses generated themselves to realize the consistent delays of the timing signals sent by individual optical interfaces.
(2) The digital transmit/receive optical module gives a timing signal through deserialization. The timing signal is sampled by use of the system synchronous clock to obtain the timing signal for the digital transmit/receiver portion. The key of sampling the timing pulse by synchronous clock is to stably sample the signal, without metastable state occurring. When designing the programs, therefore, the synchronous logic design must be taken into consideration to ensure stable sampling. For this, the synchronous clock is used to make frequency multiplication of a high speed clock in FPGA and the clock is used to sample simultaneously the leading signals produced by the synchronous clock and the deserialization. Measuring the optimal phase relation through which the leading signal of synchronous clock sampling is obtained and using PLL to adjust the phase of synchronous clock can ensure that the metastable state will not occur when sampling the timing signal.
(3) After the timing pulse obtained by the synchronous clock sampling being stable, by regulating the phase relation of ADC sampling clock and the synchronous clock in FPGA, the metastable state will not occur when the ADC sampling clock samples the timing signal under the condition of the FPGA compiling satisfying the time sequence constraint. In this way, it can be ensured that the phase stability and channel-to-channel phase synchronization during the multiple repetition periods within a CPI in the digital receiving module.

(4) Once a stable timing pulse is obtained, it will be sent to individual DDS chips at the same time to make them work synchronously under the timing pulse. From this point, the DDS chip with synchronization function should be chosen.

Through the above design considerations divided into three levels, the multi-channel data synchronization problem in the RF digitalized receiver based on optical transmission can be well resolved.

7.5 Electromagnetic Compatibility Design

The radar operating in metric wave band has to face complex external electromagnetic environment. In this frequency band, the spectrum utilization rate is the highest and the distribution area is the widest. Also in this band, there are a mass of broadcast, TV, and communication users. Here, we take the TV signal as an example to make a brief explanation. In China, the TV adopts PAL D/K system and the TV channel frequency division is shown in Table 7.6.

We can see that the metric wave radar operates in a complex electromagnetic environment. Actually, it is unpractical that the radar site keeps enough distance from the TV base station to avoid interference each other. Consequently, in designing metric wave radar, it is necessary to take measures to reduce the interference as low as possible. Figures 7.45, 7.46, 7.47 and 7.48 give the measured frequency spectrums of the familiar interference signals in metric wave band.

Table 7.6 TV signal distribution in metric wave band

Band	Channel	Frequency range (MHz)	Image carrier frequency (MHz)	Sound carrier frequency (MHz)
I band (VHF)	DS—1	48.5~56.5	49.75	56.25
	2	56.5~64.5	57.75	64.25
	3	64.5~72.5	65.75	72.25
II band (VHF)	4	76~84	77.25	83.75
	5	84~92	85.25	91.75
III band (VHF)	6	167~175	168.25	174.75
	7	175~183	176.25	182.75
	8	183~191	184.25	190.75
	9	191~199	192.25	198.75
	10	199~207	200.25	206.75
	11	207~215	208.25	214.75
	12	215~223	216.25	222.75
UHF band	13~68	470~566 606~958		

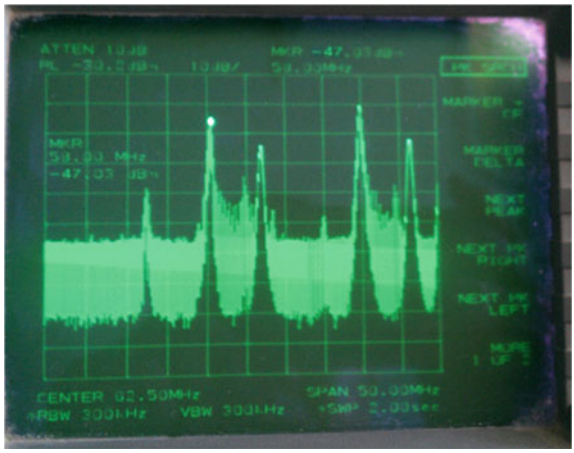


Fig. 7.45 Spectrum of channels 1–4 signals in VHF band (48.5–84 MHz)

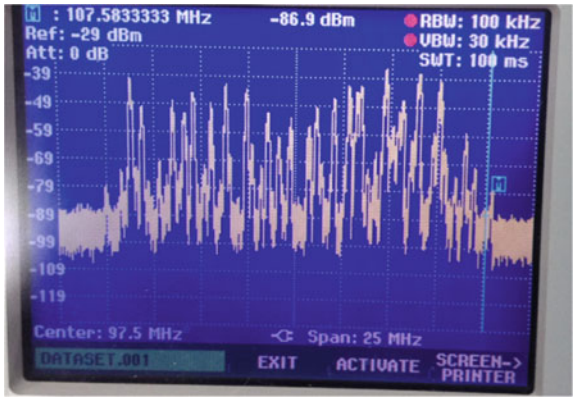


Fig. 7.46 Spectrum of FM broadcast signals in littoral (85–110 MHz)

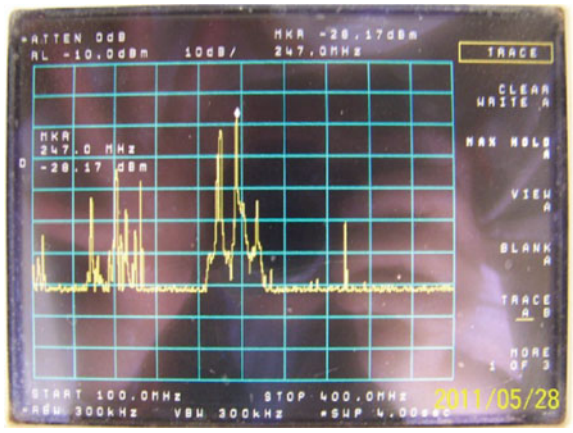


Fig. 7.47 Spectrum of channels 6–12 signals in VHF band (167–223 MHz)

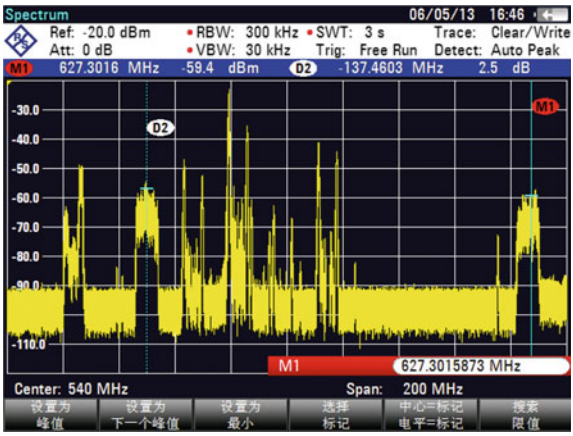


Fig. 7.48 Spectrum of analog/digital TV signals in UHF band (470–958 MHz)

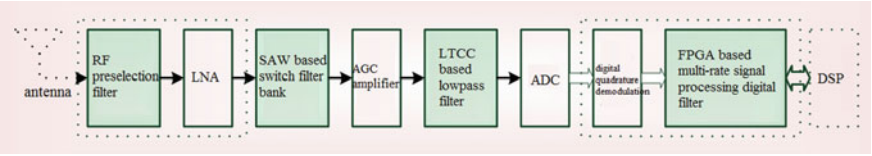


Fig. 7.49 Functional block diagram of RF digitalized receiver channel based frequency-domain multistage filters

The electromagnetic environment adaptability of metric wave radar includes two aspects: one is to reduce the interference from the external electromagnetic signals on the radar equipment; the other is that the radar equipment in operating should bring as few effects on civil apparatuses as possible. As viewed from the point of system, the interference rejection should be implemented comprehensively in multiple dimensions such as the mainlobe interference rejection, sidelobe cancellation, and temporal-domain interference cancellation realized by receiver multistage filtering in frequency domain and adaptive filtering in spatial domain. The main measure to suppress the in-band interference, out-band interference, adjacent channel interference, and external interference in RF digitalized receiver is the multi-stage filtering in frequency domain. The anti-interference design of RF digitalized receiver involves the frequency-domain multistage filtering anti-interference, the optimization and selection of RF digitalized sampling clock, and the suppression of internal interference.

(1) Frequency-domain multistage filtering anti-interference

The receiving channel realization of RF digitalized receiver of metric wave radar is shown in Fig. 7.49. The filters include RF preselection filter, SAW based switch filter bank, LTCC based lowpass filter, and FPGA based multi-rate signal processing digital filter.

RF preselection filter: It locates at the first stage of RF front-end. Its insertion loss has direct effect on the noise figure of receiver. The filter is mainly used to reject the strong out-band interference in far zone to avoid channel barrage, and to realize anti-aliasing filtering for RF samples together with the successive filter. Its design adopts LC filter and LNA1 + preselection filter + LNA2 architecture. In this wary, the enough out-band rejection can be achieved and the noise figure of LNA module can also be minimized. The amplitude-frequency response curve of RF preselection filter of a metric wave radar is given in Fig. 7.50.

SAW based switch filter bank: It has the excellences of small volume, easy integration, high rectangle coefficient, high in-band linearity, and good consistency. The direct-path signal is far greater than the echo signal. In designing channel, the received signals are amplified to approach the full range of ADC for amplifying the target echo signals and improving the detection of small signals. In the dense signal environment, the channel is susceptible to saturation with a high channel gain. Thus the analog channelization is needed to decrease the number of signals simultaneously entering into the following amplifier for an increased instantaneous dynamic range. In SAW based switch filter bank, the rectangle coefficient (BW_{40dB}/BW_{3dB}) of each sub-band filter can reach up to 2, so that the out-band interference and ADC sampling image spectrum can be rejected effectively, generally the rejection being greater than 40 dB. The amplitude-frequency response curves of its sub-band filters are shown in Figs. 7.51 and 7.52.

LTCC based lowpass filter: It adopts LTCC process and has laminated structure, small volume, and low insertion loss, suitable for highly dense surface mounting. Its sharp attenuation characteristic is beneficial to the rejection of interference and noise. In RF digitalized receiver, ADC input 3 dB analog bandwidth can cover the whole metric wave band, but the cut-off frequency of actual signal is not so wide. At the ADC input end, therefore, its input signal bandwidth can be limited by the lowpass filter with small volume and low insertion loss. The frequency range of ADC input signal can be further limited so as to reject the out-band interference by the LTCC based lowpass filter in combination with the RC lowpass filter at ADC input

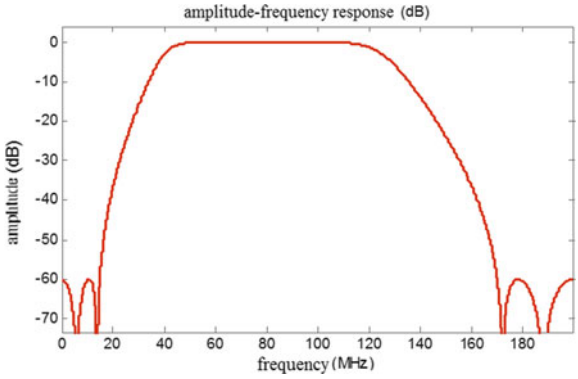


Fig. 7.50 Amplitude-frequency response curve of RF preselection filter

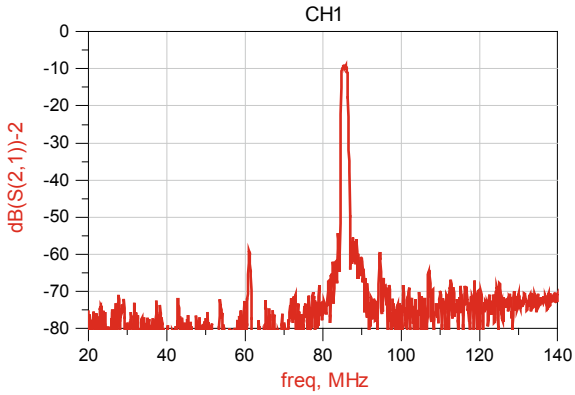


Fig. 7.51 Amplitude-frequency response of sub-band filters of narrowband switch filter bank

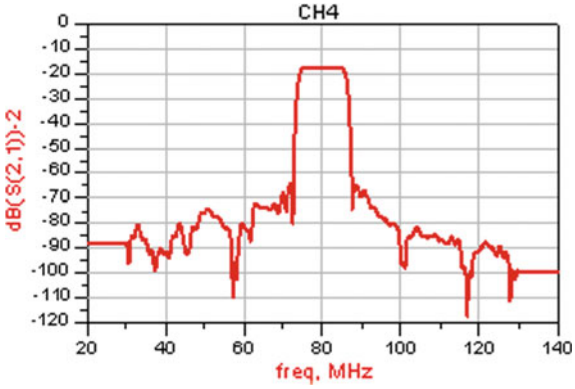


Fig. 7.52 Amplitude-frequency response of sub-band filters of wideband switch filter bank

interface. Also, the filter can reject the harmonic of ADC sampling clock to prevent it from entering the RF channel amplifier and producing intermodulation interference with input signal.

The FPGA based multi-rate signal processing digital filter: It is one of the core parts of the multi-rate signal processing. For digital receiving, the main action of this digital filter is to implement digital anti aliasing filtering before decimation and get the oversampling SNR benefit. Due to the high sampling rate of the RF direct sampling, the digital quadrature demodulation and the decimation filtering are needed to acquire the baseband I/Q signal matching the instantaneous signal bandwidth. It can be known from the previous analysis of analog filter that if the frequency band is divided too narrowly, the volume and cost of the analog filter will be increased significantly. So the adjacent-channel interferences near the operating frequency points of broadcast signal and the TV signal can be rejected only by digital filter. In a dense signal environment, the adjacent-channel interferences should be rejected enough to avoid the effects on SNR of the adjacent-channel interference signals folding in the frequency band after decimation.

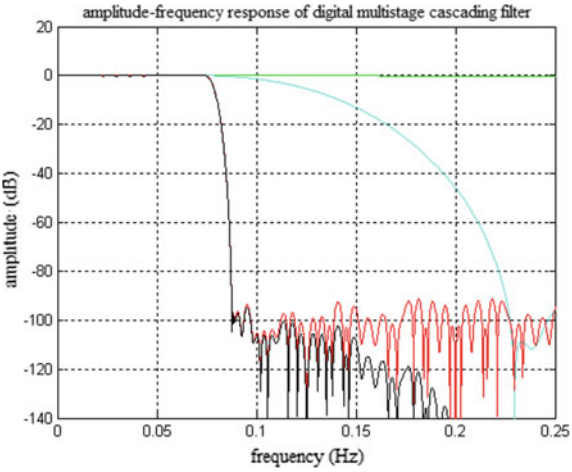


Fig. 7.53 Adjacent-channel rejection characteristic of digital multi-stage cascading filter

The design of the multi-rate signal processing digital filter should consider its high-effective realization and minimize resource occupation and power dissipation while holding performance. Today, the high-effective realizations of the multi-rate digital filter are CIC filter, half-band filter, and high-effective polyphase structure decimation filter. In the case of large decimation ratio, multistage cascading filters are needed to implement sampling rate conversion, SNR benefit, and interference rejection. In practical realization, the in-band ripple, out-band suppression, resource, and power dissipation should be considered. The suppression of the adjacent-channel interference requires a very narrow transition band of filter. The order of filter is directly related to the transition bandwidth. At this time, the spectral mask filter based on half-band filter or the spectral mask filter based on complementary filter can be used to achieve narrow transition bandwidth and adjacent-channel interference suppression. Figures 7.53 and 7.54 illustrate the amplitude-frequency response curves of the narrowband digital multi-stage cascading filter of a metric wave radar. We can see that, in the case of 150 kHz signal bandwidth, the rejection of digital filter on the adjacent-channel interference can reach about 100 dB, and even more nice rejection of in-band interference in far zone can be achieved.

(2) Optimization and selection of RF digitalized sampling clock

The optimization and selection of the sampling clock involves the optimization and selection of the clock frequency and the optimization and the selection of the relative specifications. The selection of the sampling clock of RF digitalized receiver should satisfy the bandpass sampling theorem firstly. In addition, because of the large analog bandwidth of RF direct sampling ADC, the multiple signals in Nyquist band will be aliased into the frequency band after sampling. Although there is an anti aliasing filter before ADC, when strong interference appears in a certain frequency band, the residues of interference signals after anti aliasing filtering and sampling could still be stronger than the target echo signals. Thus, in the case of strong interference out

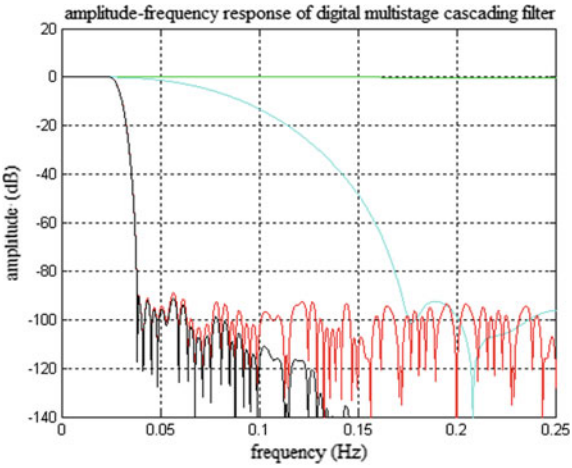


Fig. 7.54 Adjacent-channel rejection characteristic of digital multi-stage cascading filter

of the frequency band, the sampling clock should be selected such that the frequency band in which strong interference appears cannot be aliased into the frequency band of the operating signal through direct sampling.

Assume that a radar operates at 48–110 MHz, the far-zone interference can be suppressed effectively by the multi-stage analog filters of its RF digitalized receiver and its antenna response, but limited for suppression of the interferences resulted from TV channels 6–12 (167–216 MHz) in VHF band. Hence, on selecting the sampling clock, the emphasis is to avoid the signals in this frequency band directly aliasing into the operating frequency band. If the sampling aliasing is not considered, we can choose a 240 MHz sampling clock directly. At this time, the whole signal frequency band locates at the first Nyquist band, but the interferences resulted from TV channels 6–12 in VHF band will enter into the low frequency band of 48–85 MHz through sampling aliasing. In practical design, therefore, two sampling clocks or sampling clock switchover can be used to ensure no sampling aliasing, for example, 200 MHz sampling clock for 48–85 MHz and 240 MHz sampling clock for 85–110 MHz. The corresponding signal frequency bands and image interference frequency bands are shown in Figs. 7.55 and 7.56, the green indicating the operating frequency band and the red indicating the image interference frequency band. From the figures we can see that, when operating at 48–84 MHz frequency band and 200 MHz sampling clock, the FM broadcast signals and the VHF channels 6–12 signals are unable to alias into the operating frequency band through sampling directly; when operating at 85–110 MHz frequency band and 240 MHz sampling clock, the VHF channels 1–4 signals and channel 6–12 signals also cannot alias into the operating frequency band through sampling directly.

Operating in dense signal environment, the influence of phase noise also should be taken into consideration in designing the sampling clock of RF direct sampling receiver. The phase noise aliasing effect of multi-signal sampling clock will cause the noises of adjacent channels to superpose into the frequency band of the

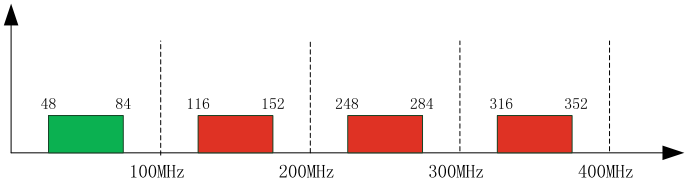


Fig. 7.55 Four Nyquist bands of 48–84 MHz signals before 200 MHz sampling

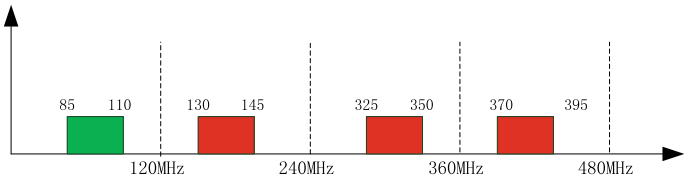


Fig. 7.56 Four Nyquist bands of 85–110 MHz signals before 240 MHz sampling

operating signal, especially in the case of narrow signal bandwidth and dense signals. Figure 7.57 shows the phase noise aliasing effect of multi-signal sampling. Considering the phase noise aliasing effect, the noise level near the short zone 100–200 kHz should be designed low enough. The crystal oscillator with high stability and low phase noise and the direct synthesis can be used to obtain the sampling clock with excellent phase noise performance. When the sampling phase-locking method is used to generate sampling clock, strict requirements should be applied for the loop filter bandwidth and its rejection.

(3) Suppression of internal interference

In the RF digitalized receiver of metric wave radar, it is easy to generate interferences, which should be minimized by reasonable electromagnetic compatibility design and device selection. The related analysis and design will be described as follows.

Multi-frequency intermodulation interference: It results from the harmonic and intermodulation generated by the multiple clock signals due to nonlinearity in active derives of the receiver entering into the operating frequency band. In RF digitalized receiver, the main clocks include the ADC sampling clock and its feedback synchronization clock, DAC/DDS conversion clock and its feedback clock, the system time sequence synchronization digital clock, the FPGA or DSP internal signal processing clock, optical transmission high-speed interface PLL reference digital clock, and the serial interface clocks collocated in the related chips. These clocks also can generate plenty of harmonic frequencies. If a RF digitalized receiver is designed improperly, the multiple clock foundational frequencies, harmonics, and their intermodulations will come into the transmit/receive frequency band and finally impact the stray and output SNR of the system. Then the design of receiver frequency source and the design of multi-channel RF digitalized receiver are required to achieve reliable isolation and screen from various interferences, preventing circuit coupling and leakage.

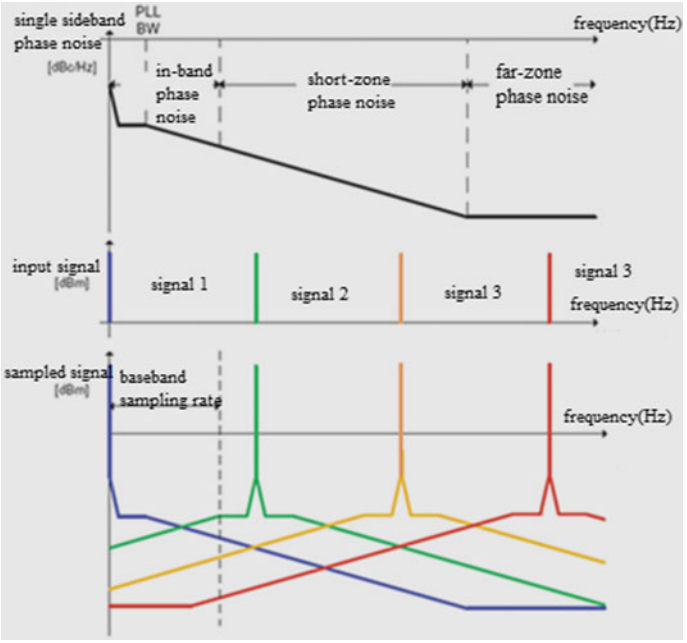


Fig. 7.57 Phase noise aliasing effect of multi-signal sampling

And all outputs are filtered to suppress their harmonics, avoiding the influences of the harmonics and their intermodulations on the system.

ADC nonlinearity: In multi-signal environment, harmonics and multitone intermodulation will produce. For an ADC, its single-tone stay, SNR, and multitone intermodulation characteristics are shown in Fig. 7.58. When the input power is −1 dBFS, the second harmonic suppression is more than 85 dBc and the third harmonic suppression is above 86 dBc. When the input dual-tone signal frequency is 46 MHz/50 MHz and the input power is −7 dBFS, the two-tone intermodulation suppression is above 97 dBc. When the input signal frequency is 185 MHz/190 MHz and the input power is −7 dBFS, the two-tone intermodulation suppression is more than 85 dBc. Therefore, on selecting an ADC, it is required to refer to its data book and make an assessment to determine whether the nonlinearity of the ADC itself affects the stray characteristic of the system or not.

Channel and filter nonlinearities: they will also cause the spurious in the received signal and the generation of interference signal, including the output harmonic characteristic of amplifier getting poor due to unsuitable distribution of channel gain and then generating interference. To avoid the interference, reasonable distribution of channel gain is required in designing channel. In the first stage of LNA, it is required to choose proper P_{-1} according to the maximum interference level. On the other hand, following the LNA, TV band filter and broadcast band filter should be designed respectively to reduce the signal components that will go into the next

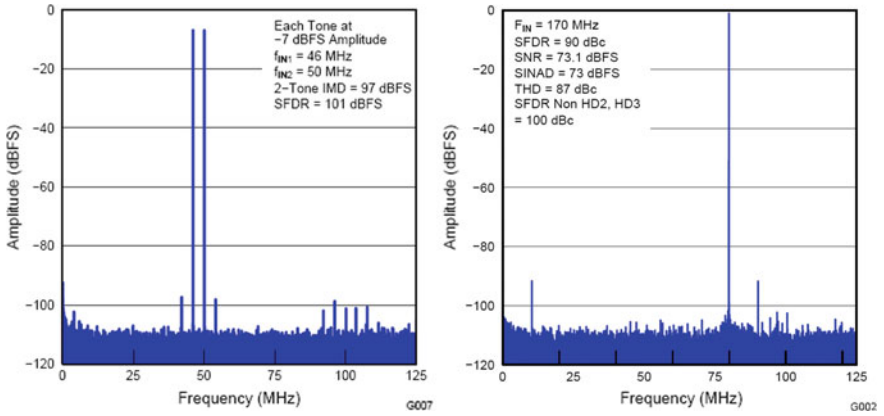


Fig. 7.58 Output characteristics of ADC single-tone and multitone signals

amplifier so as to prevent the generation of nonlinear signal. In addition, the phase nonlinearities of the channel and filter can also produce influences on the following DBF synthesis, cancellation, and correlation processing. Thus constraints should be applied to the phase nonlinearity index in the instantaneous bandwidth of each device, especially each filter.

PS switch frequency: can make intermodulation with the sampling frequency and produce symmetrical spurious frequency through ADC sampling. In multiple-signal environment, it will raise the noise level of the output signal and then affect the output SNR.

Except that the radar can suffer form the interferences due to other electronic equipments, its transmitting signal will also interfere with other electronic equipments. The spectrum purity of its transmitting signal must be controlled effectively. The indexes to measure the spectrum purity of its transmitting signal are the out-band spurious suppression and the harmonic suppression. Generally, the measures to improve the two indexes in design stage are as follows:

First, strict requirements must be applied to out-band spurious and harmonic suppression of power amplifier, which should be given full consideration in the design of amplification circuits. Moreover, the bandpass effect of the output circulator of transmitter can be utilized to improve the shape of the transmitting frequency spectrum, and then the bandpass effect of antenna element is used to further suppress the out-band spurious and harmonic of the transmitting frequency spectrum. If necessary, a high power filter can be added between the transmitting output and the antenna element. In phased array radar, owing to a large number of transmitters, the special attention should be paid to avoid self-excited oscillation in transmitter. Even if few transmitters produce self-excited oscillations, there will be a great influence on the synthesized transmitting frequency spectrum. In radar engineering design, the effective measures should be taken to monitor the operation status of each transmitter

and to feed the information back to the control system to shut down that transmitter in which the self-excited oscillation occurred.

During the phase of radar in service, the following measures can be taken: individual electronic equipments can be operated at different frequency points to make use of filtering to decrease the influences each other; the radar equipment can turn on the "sector silence mode" to reduce its effect on other electronic equipments; if allowable, to enlarge the distance between the electronic equipments or to use veil to achieve electromagnetic isolation.

7.6 Super-Low Phase Noise Frequency Source Technique

7.6.1 Analysis on the Effect of Frequency Source Phase Noise on Radar System

Frequency source is a necessary component of modern radar system. Its phase noise and spurious performances determine the accuracy and function realization of radar system to a high degree. With the development of radar technology, the requirement on the stability of frequency source posed by radar becomes more and more strict, especially the short-term stability. Only full-coherent frequency synthesizer can satisfy the requirement on the stability of frequency source. The short-term stability is measured commonly by single sideband phase noise spectrum density. Sometimes, the system designers may propose the requirement on the improvement factor. The relation between the phase noise and the improvement factor is

$$I = \frac{3}{16\int_0^F S_{\Delta\phi}(f_m)\sin^2(\pi\tau f_m)\sin^2(\pi T f_m)\mathrm{d}f_m} \tag{7.60}$$

where, I is the improvement factor at the secondary cancellation, $S_{\Delta\phi}(f_{\mathrm{m}})$ is the phase noise spectrum density of frequency synthesizer, τ is the round trip time, F is the half of IF bandwidth of receiver, and T is the pulse repetition period.

The improvement factor at the first cancellation is expressed as

$$I = \frac{1}{8\int_0^F S_{\Delta\phi}(f_m)\sin^2(\pi\tau f_m)\sin^2(\pi T f_m)\mathrm{d}f} \tag{7.61}$$

In RF digitalized receiver system, although the number of the signals provided by frequency source is decreased enormously compared with traditional superheterodyne system, the quality of the sampling clock (clock jitter) generated by frequency source also directly affects the ADC performance specifications. Theoretically, the signal-to-noise ratio (SNR) of ADC limited by the clock aperture jitter can be expressed as

$$SNR = -20\lg(2\pi f_a \Delta t_{rms}) \tag{7.62}$$

where, SNR is the signal-to-noise ratio (dB), f_a is the analog input frequency, and Δt_{rms} is the root mean square (rms) of aperture jitter.

Numerous factors affect random timing jitter, including noise sources such as broadband noise, phase noise, and spurs, as well as slew rate and bandwidth, which shown in the following figure. We can calculate the jitter through the phase noise curve inside the bandwidth of interest.

A sinusoid signal of a clock signal with phase noise can be written as:

$$\mathrm{C(t)} = A\sin(2\pi \mathrm{f_c} t + \theta(t)) = A\sin(2\pi \mathrm{f_c}(t + \frac{\theta(t)}{2\pi \mathrm{f_c}})) \tag{7.63}$$

and the period jitter is:

$$J_{PER} = \frac{\theta(t)}{2\pi \mathrm{f_c}} \tag{7.64}$$

the random quantity J_{PER} must have a zero mean. Thus the RMS of J_{PER} can be calculated by:

$$J_{PER-RMS} = \sqrt{< J_{PER}^2 >} = \frac{1}{2\pi \mathrm{f_c}}\sqrt{< \theta(t)^2 >} \tag{7.65}$$

where $< J_{PER}^2 >$ is the mean of J_{PER}^2 and $< \theta(t)^2 >$ is the mean of $\theta(t)^2$.

$$\mathrm{C(t)} = A\sin(2\pi \mathrm{f_c} t + \theta(t)) = A\sin(2\pi \mathrm{f_c} t)\cos(\theta(t)) + A\cos(2\pi \mathrm{f_c} t)\sin(\theta(t)) \tag{7.66}$$

As the $\theta(t)$ is always much smaller than $\pi/2$, Eq. (7.66) can be approximated as:

$$C(t) = A\sin(2\pi \mathrm{f_c} t) + A\theta(t)\cos(2\pi \mathrm{f_c} t) \tag{7.67}$$

The spectrum of C(t) is then:

$$S_c(t) = \frac{A^2}{4}[\delta(f - f_c) + \delta(f + f_c)] + \frac{A^2}{4}[S_\theta(f - f_c) + S_\theta(f + f_c)] \tag{7.68}$$

where $S_\theta(f)$ is the spectrum of $\theta(t)$. Using the definition of $L(\Delta f)$, we can find:

$$L(\Delta f) = L(f - f_c) = 10\log[S_c(f)/S_c(f_c)] \quad (\mathrm{dBc/Hz}) \tag{7.69}$$

that $L(\Delta f)$ presents the ratio of two power in 1 Hz bandwidth at frequency f and f_c, where $\Delta f = f - f_c$, following Eq. (7.68) above, therefore we can obtain $L(\Delta f)$ and $S_\theta(\Delta f)$:

$$L(\Delta f) = 10\log[\frac{\frac{A^2}{2}[S_\theta(f - f_c)}{\frac{A^2}{2}}] = 10\log[S_\theta(f - f_c)] = 10\log[S_\theta(\Delta f)] \tag{7.70}$$

$$S_\theta(\Delta f) = S_\theta(f - f_c) = 10^{\frac{L(\Delta f)}{10}} \tag{7.71}$$

we could also write Eqs. (7.72) as (7.72) when f means Δf in practice:

$$S_\theta(f) = 10^{\frac{L(f)}{10}} \tag{7.72}$$

following Eq. (7.65) above:

$$< \theta(t)^2 >= \int_{-\infty}^{+\infty} S_\theta(f)df = \int_{-\infty}^{+\infty} 10^{\frac{\mathrm{L(f)}}{10}} df \tag{7.73}$$

The $S_\theta(f)$ is symmetrical spectrum. We can calculate the jitter through the phase noise curve inside the bandwidth of interest

$$J_{PER-RMS} = \frac{1}{2\pi \mathrm{f_c}}\sqrt{< \theta^2(t) >} = \frac{1}{2\,\pi\,\mathrm{f_c}}\sqrt{2\int_0^{\mathrm{BW}} 10^{\frac{\mathrm{L(f)}}{10}} df} \tag{7.74}$$

where, f_c is the center frequency of the sampling clock (Hz), BW is the bandwidth of interest, f is the offset from f_c (Hz), $L(f)$ is the phase noise at the place where the offset from f_c (dBc/Hz).This is an integral operation and usually completed by the computer.

Besides, there are other approximate calculation methods, such as calculate broadband noise contribution to timing jitter, phase noise contribution to timing jitter and spurious noise contribution to timing jitter respectively. However, these computational models have certain limitations, which can be referred to in relevant literature.

In designing, frequency source indexes should be distributed in reason to meet the system design requirement according to the improvement factor index and ADC signal-to-noise ratio index required by radar system.

7.6.2 Realization of Frequency Source

Frequency synthesis technique means a process to generate one or more new frequencies by use of one or more reference frequencies. In essence, frequency synthesis is a technique for realizing analog or digital computation of frequency. It obtains a number of signals of the same precision with reference frequency through mathematical

operation of the reference frequency and then selects the wanted frequency depending on practical requirement. Frequency synthesis technique started from 1930s and has passed more than 80 years. The development of frequency synthesis technique can be divided into three stages:

The first stage is the direct frequency synthesis (DS). DS technique performs simple operations of reference frequency such as addition, subtraction, multiplication, and division and then conducts filtering to generate multiple frequencies for implementing frequency synthesis. On this account, direct frequency synthesis has the advantages of fast frequency conversion, low phase noise, high stability and reliability. However, because of the applications of a number of nonlinear devices such as mixers and frequency multipliers in the frequency synthesizing process, direct frequency synthesis has the disadvantages of complex circuits, large volume, high cost, and poor spurious suppression.

The second is stage the indirect frequency synthesis, also called as phase locked loop (PLL) frequency synthesis. PLL technique makes use of the linear servo loop of control theory and developed in 1940s. It realizes addition, subtraction, multiplication, and division of frequencies through phase locked loop. That is, one or more reference frequency sources are used to generate plentiful harmonic or combined frequencies via a series of nonlinear devices such as harmonic generator, mixer, and frequency divider, then the phase locked loop is used to lock the frequency of voltage controlled oscillator (VCO) to a harmonic or combined frequency, and finally the wanted frequency signal is output indirectly from VCO. The merits of this technique are high operating frequency, wide frequency band, low phase noise, good spurious performance, high frequency stability, and small volume. But it has low frequency conversion speed compared with DS and low frequency resolution.

The third stage is the direct digital frequency synthesis (DDS). Its development history has been introduced in Sect. 7.3.2.1. The outstanding advantages of the DDS are high frequency resolution and fast frequency conversion. The other superiorities are wide relative bandwidth of output signal, programmable frequency/phase control, and convenient single-chip integration. The full-coherent frequency synthesizer used in radar usually makes a highly stable crystal oscillator as reference so as to obtain a set of highly stable frequency signals. Hence the technical specifications of the crystal oscillator are very important. Currently, the short-term stability of crystal oscillator (measured in phase noise) is about -153 to -55 dBc/Hz@1 kHz offset. With the development of crystal oscillator technology, the crystal oscillator with super-low phase noise comes forth. PFC Company in Canada issues an 80 MHz constant temperature crystal oscillator, its phase noise is as low as -160 to -168 dBc/Hz at 1 kHz offset.

In designing, on the basis of the practical requirements of radar system on the technical specifications, cost, and reliability of the frequency synthesizer, proper realization scheme should be adopted to achieve the optimal effectiveness.

7.6.3 Techniques for Distributed Frequency Sources

To simplify the architecture of the digital array radar system and enhance its scalability, a novel frequency source design is proposed. That is, the frequency source host +N distributed frequency sources. The frequency host generates the reference signal for the distributed frequency sources, and then the distributed frequency sources produce the clock signals required for the transmit/receive system. In this way, the benefits are as follows:

(1) Simplify the external clock interface of the digital array module. Clock input only needs a cable, which is propitious to the array scalability and the transmit/receive system maintainability.
(2) Simplify the clock distribution network of antenna array. The reference clock commonly has low frequency and low transmission loss, so that the power division network of a large antenna array can be designed to be a passive network, improving the system reliability and decreasing the system complexity.
(3) In a radar system with separated transmit array and receive array, the reference clock signal can be translated into optical signal for optical fiber transmission. It is easy to realize long distance transmission of clock signal.
(4) The distributed frequency source technique is more propitious to large array antenna, which can decrease the weight and simplify the structure of large radar system.

It is noticeable that how to explore the noise decorrelation characteristic of the distributed frequency source is still under investigation. Once applicable, the spectrum purity of the synthesized transmit/receive beams in a radar system will be improved significantly.

Bibliography

1. Qiang Baihan, Wei Zhi. Theoretical Design and Practice of Modern Radar Transmitter[M]. Beijing: National Defense Industry Press, 1985.
2. Sivan L. Microwave Tube Transmitters[M]. Chapman and Hall, 1994.
3. Edward Ostroff, Michael Borkowski, Harry Thoms, et al. Solid-State Radar Transmitters[M]. Artech House Inc, 1985.
4. Skolnik M I. Radar Handbook[M]. McGraw-Hill, Inc, 1970.
5. Jed Rice. LDMOS Linearity and Reliability[J]. Microwave Joural, 2002(6).
6. Inder Bahl, Prakash Bhartia. Microwave Solid State Circuit Design[M]. 2nd ed. John Wiley & Sons Inc, 2003.
7. Wu Xiaobao, Wang Bing, Zheng Shilian, et al. Anti-Jamming Design of RF Digitalized Receiver in VHF Radar[J]. Radar Science and Technology, 2015(13):2.
8. Guo Chongxian. The Receiving Techniques for Phased Array Radar[M]. Beijing: National Defense Industry Press, 2009.
9. James Tsui. Special Design Topics in Digital Wideband Receivers[M]. Boston: Artech House, 2010.

10. Fredric J Harris. Multiple Sampling Rate Signal Processing in Communications System[M]. Translated by Wang Xia, Zhang Mei, Liu Shutang. Xi'an: Xi'an Jiaotong University Press, 2008.
11. Ljiljana Milic. Multirate Filtering for Digital Signal Processing: Matlab Applications[M]. New York: Information Science Reference, 2009.
12. Yang Xianiu, Lou Caiyi, Xu Jianliang. Principle and Application of Software Defined Radio[M]. Beijing: Publishing House of Electronics Industry, 2001.
13. Hu Mingchun, Zhou Zhipeng, Gao Tie. Radar Microwave New Techniques[M]. Beijing: Publishing House of Electronics Industry, 2014.
14. Tierney J, Rader C M, Gold B. A Digital Frequency Synthesizer[J]. IEEE Trans on Audio and Electroacoustics, 1971(AU-19):48–57.
15. Sunderland D A, et al. CMOS/SOS Frequency Synthesizer LSI Circuit for Spread Spectrum Communication[J]. IEEE J. Solid-State Circuits, 1984(19):497–505.
16. Zheng Xin, Li Wenhui, Pan Houzhong, et al. Radar Transmitter Techniques[M]. Beijing: Publishing House of Electronics Industry, 2006.
17. Inder Bahl, Prakash Bhartia. Microwave Solid-State Circuit Design[M]. Translated by Zheng Xin. Beijing: Publishing House of Electronics Industry, 2006:176–274.
18. Guillermo Gonzalez. Microwave Transistor Amplifiers: Analysis and Design. Upper Saddle River, N.J.: Prentice Hall, 1997.
19. Gardenghi R A, Houlne R C. Power Supply Consideration for Pulse Solid State Radar[J]. IEEE Conference Record of the 1990 Nineteenth, 1990 (26–28):146–152.
20. Guerci J R. Cognitive Radar: The Knowledge-aided Fully Adaptive Approach[M]. Translated by Wu Shun-jun. Beijing: National Defense Industry Press, 2013.
21. Olivier Jamin. Broadband Direct RF Digitization Receivers[M]. Springer International Publishing Switzerland, 2014.
22. Chen Shunyang, Yang Xiaoniu. Study on a New RF Digitalizing Framework and Its Key Techniques[J]. Electronic Counter measurements, 2014(1):1–6.
23. Yi Wen. Radar Receiver Techniques[M]. Beijing: Publishing House of Electronics Industry, 2005.
24. Hu Mingchun, Zhou Zhipeng, Yan Wei. Transmit/Receive Module Technology[M]. Beijing: National Defense Industry Press, 2010.
25. Murmann B. ADC Performance Survey 1997–2014[EB/OL]. www.stanford.edu/murmann/adcsurvey.html.
26. Nyquist H. Thermal Agitation of Electric Charge in Conductors[J]. Phy. Rev., 1928(32):110–113.
27. Wang Hong. Research on Wideband Digital Receiver and System Implementation[D]. Chungdu: University of Electronic Science and Technology of China, 2007.
28. Pang Jiantao. Study and Realization of the Frequency Synthesis Technique of the Modern Coast Defense Radar Based on DDS[D]. Xi'an: Xidian University, 2008.
29. Yin Lei. Design of High Precision Signal Generator Based on DDS[D]. Jinhua: Zhejiang Normal University 2009.
30. Liu Dengbao. Design and Research on High Power Solid-State Transmitter at SW Band[D]. Nanjing: Nanjing University of Science and Technology, 2008.
31. Hong Tao. Design of Full Solid-State Transmitter for Ground-Wave over the Horizon Radar[D]. Xi'an: Xidian University, 2007.
32. Xu Ming. The Application Analysis of LDMOS Power Devices in P Band Radar transmit System[D]. Nanjing: Nanjing University of Science and Technology, 2012.
33. Chen Guiqiang. Linearization Technology for Microwave Power Amplifier[D]. Chungdu: University of Electronic Science and Technology of China, 2004.
34. Luo Wantuan. Research on a Small-Signal Detection System Based on Electric Field Sensor[D]. Chungdu: University of Electronic Science and Technology of China, 2009.
35. Gu Xingwang. Design of a Millimeter-Wave High Sensitivity Receiver[D]. Nanjing: Nanjing University of Science and Technology, 2008.

36. Yuan Shunyi. Study on Large Dynamic Range and High Sensitivity Digital Receiver[D]. Chungdu: University of Electronic Science and Technology of China, 2006.
37. Zhang Juan. Synthesized Frequency Sources Research and Implementation[D]. Chongqing: Chongqing University, 2011.
38. Clock Jitter and Phase Noise Conversion[EB/OL]. https://www.maximintegrated.com/en/app-notes/index.mvp/id/3359.
39. Walt Kester. Converting Oscillator Phase Noise to Time Jitter[EB/OL]. http://www.analog.com/media/en/training-seminars/tutorials/MT-008.pdf.
40. Random Noise Contribution to Timing Jitter Theory and Practice[EB/OL]. http://pdfserv.maximintegrated.com/en/an/AN3631.pdf.
41. Design a Low-Jitter Clock for High-Speed Data Converters[EB/OL]. https://www.maximintegrated.com/en/app-notes/index.mvp/id/800.
42. Ali Hajimiri, et al. Jitter and Phase Noise in Ring Oscillators[J]. IEEE Journal of Solid-State Circuits, 34(6):790–804.

Chapter 8
Target Classification and Identification Techniques for Advanced Metric Wave Radar



8.1 Overview

8.1.1 Status of Radar Target Classification and Identification

The research on radar target identification requires profound theoretical basis and numerous field tests, which certainly will promote the modern radar theory and modern radar technology to a new stage. The research on radar identification techniques around the world has passed 50 years since Barton made an exact judgment of the shape feature of the Soviet Union satellite Spuknit II by use of AN/FPS-16 radar. During this period, a series of important progresses in this field have been made in many countries.

The target identification technique has been determined as one of the twenty key defense technologies by American Department of Defense for a long time. In the 1990s, DoD set up a target identification workgroup to take charge of radar target data standardization and identification performance assessment. The target database includes multiple military aircraft and missile targets. In 1995, Canadian Leung designed a set of automatic target identification system for the sea surface surveillance radar in Ottawa, capable of achieving detection, tracking and classification of sea surface target. In 1996, American Teti set up a target identification system based on AWG-10 radar. By extracting six-dimensional joint features of target, quasi realtime identification of F-18 aircraft was realized through multi-feature comprehensive decision-making. In 2000, the research results announced by Lincoln Laboratory showed that the imaging resolution of USA radar reconnaissance satellite reached 0.1 m, capable of monitoring and identifying ships, military vehicles, and mobile intercontinental missiles, finding the targets at several meters underneath dry sand and shallow sea, and distinguishing the false targets. Russia has engaged in the study on target identification since World War II. It is reported that they achieved the accuracy of 90% for identifying aircraft and the accuracy of 99% for identifying the warhead of ballistic missile. In addition, many other countries also have made

© National Defense Industry Press, Beijing and Springer Nature Singapore Pte Ltd. 2020

J. Wu, *Advanced Metric Wave Radar*, https://doi.org/10.1007/978-981-10-7647-3_8

efforts to study the target classification and identification techniques such as Japan, Australia, France, Poland, Israel, and etc.

There are many methods for radar target identification. Based on resonant frequency characteristics, Baum proposed the singularity expansion method to explore metaphase and anaphase transient responses and used the concept of poles to characterize the electromagnetic characteristics in 1971. In 1975, Blaricum and Mittra firstly put forward the Prony method for directly extracting the poles of target from a set of transient response temporal-domain data. Afterwards, Jain presented the function bundle method of target poles while Hua et al. extended it to the generalized function bundle method. In order to avoid direct extraction of poles from noisy target scattering data, Kennaugh proposed the K-pulse concept, that is, the excitation signal of limited duration is used to act on target. The K-pulse characterized the pole spectrum of target. Meanwhile, Chen proposed the E-pulse method (also called S-pulse method), which is an inverse solution of K-pulse. That is, the characteristic waveform measured in advance is stored in computer through waveform synthesis method, and then the target scattering echo acquired online is made a convolution with it to find the target features for identification. The resonant-frequency-based identification method can be used for airplane type judgment based on a certain scale of database.

For the polarization identification, the concept of polarization scattering matrix has been proposed for a long time. The two-dimensional complex scattering matrix is used to represent the target scattering characteristics in the case of specific attitude and radiation source frequency. The polarization invariables capable of characterizing the polarization scattering characteristics of target was early presented by Brickel. These invariables are not affected by Faraday rotation (polarization plane rotation) or target rotation around the radar line of sight and antenna polarization errors, so as to be widely applied in target identification. The polarization invariables perfectly determine the target's backscattering characteristics and contain the maximum target information for radar observation along the line of sight. The methods based on polarization features play an important role in fine target classification.

With respect to micro-Doppler-based identification, Chen et al. analyzed the micro-Doppler modulation features of target by utilizing the time-frequency analysis tool. Micro-Doppler modulation features have been widely used in the detection and identification of space targets, ballistic missiles, and aerodynamic targets. The rotary parts of airborne target are always in periodical movement in respect of the rotation center of target, thus they will produce periodical modulation on the amplitude and phase of target's signal echo. This micro-Doppler modulation is widely applied in the narrowband radar target identification research as a very effective target signature.

In China, the research on radar target classification and identification has been experienced for several years, with achievements in such areas as resonant frequency identification, polarization identification, micro-Doppler modulation identification, and wideband feature identification. For resonant frequency features, the pole extraction methods and the pole database construction methods of the radar target in resonance zone are achieved in National University of Defense Technology, Harbin Institute of Technology, and Air Force Radar Academy. For polarization features,

Zhuang Zhaowan proposed a method for intrinsic coefficient extraction of target in polarization domain. Based on the single-frequency multi-polarization amplitude response equation, this method could to obtain a set of absolute polarization invariables using the concept of poles that do not vary with target attitude. Wang Xuesong et al. of National University of Defense Technology developed the first experimental instantaneous polarimetric radar system by themselves in the world. They carried out a series of field experiments to measure the polarization features of target. The basic and common difficult problems in target polarization scattering feature extraction and identification were solved preliminarily. For polarization identification, the research group used the polarization invariables to realize the classification and identification of 5 types of aircraft. Moreover, they have accumulated rich experiences of polarization feature analysis and measurement. For micro-Doppler feature identification, Xidian University, National University of Defense Technology, and Tsinghua University have performed a number of effective researches. They have gained valuable experiences in the analysis, extraction, and classification of micro-Doppler features, which have been applied well in narrowband radar for classification and identification of jet airplane, propeller-driven aircraft, and helicopter. In the real applications of radar target identification, a radar manufacturer and Xidian University jointly developed a signal processor, which has preliminary classification and identification functions (assistant artificial judgment) based on narrowband (L band) and wideband (C band) signal echo. The processor is tested to be able to identify jet airplane, propeller-driven aircraft, and helicopter. Overall, the study on target identification theory gained more achievements about classification than identification. For identification, the effective accumulation of large scale template library is still required.

We have investigated a number of active explorations in the field of target identification. In 2006, we used a metric wave radar system for data acquisition of civil aviation jet airplanes, propeller-driven aircraft, and helicopters. The analysis based on these effective data of near 200 tracks shows that the target classification and identification method based on multiple modulation features can achieve identification accuracy of 90% or more for the targets as the jet airplane, the propeller-driven aircraft, and the helicopter. In 2011, we further used a 3D radar to collect the measured data of near 300 tracks of helicopter and levitated globular reflector, and validated the effectiveness of extraction and selection methods for typical modulation features. Moreover, we proposed a modification solution for the radar operating parameters to improve its target identification capability. In 2012, a radar prototype was used to gather the measured data of near 500 tracks of aircraft targets. Based on the modulation features such as spectral line interval and waveform entropy, the classification and identification accuracy for jet airplane, propeller-driven aircraft, and helicopter targets could be up to 90%. In 2012, a P-band phased array radar acquired the measured data of ballistic missile targets. Based on the statistic features of RCS, energy entropy features, and time-frequency analysis, the radar could distinguish warhead group targets from missile body targets effectively. During the observation of "Light Star 3" of North Korea, the radar realized successfully the classification of the rocket and separator based on the trajectory features. In addition, a metric wave radar prototype collected a large quantity of single-frequency single-polarization measurement

data in 2012 and 2013. The data analysis shows that the classification and identification accuracy of multi-feature synthesis identification method for jet airplane, propeller-driven aircraft, and helicopter targets is better than 90%. Meanwhile, the dual-polarization (horizontal polarization and vertical polarization) data were also gathered. The effective judgments of bulk, thickness, scattering-point number, and symmetry of targets were realized through extracting polarization invariables of polarization scattering matrix. The resonance data of typical targets were also collected through frequency sweep to verify the effectiveness of the methods for resonant frequency feature extraction and analysis.

8.1.2 Target Classification and Identification Process in Metric Wave Radar

For metric wave band, the majority of targets fall in resonance scattering region. In this case, the analysis of principle information such as shape, size, and symmetry of target can be made based on "poles". Within the resonance region, the RCS of target varies rapidly with the frequency of detection signal, appearing the wave characteristics with spikes and notches. The strong scattering represented by spikes is the result from the resonance between the operating frequency of radar and the inherent frequency of target. The set of the frequencies at all spikes reflect the inherent frequency structure characteristics of target, that is, the poles of target. The radar can extract pole feature through frequency sweep mechanism as well as micro-Doppler modulation feature through transmitting high PRF waveform. For polarization feature extraction, it could be achieved by transmitting horizontal and vertical polarization waveforms in time-sharing and receiving dual-polarization signals at the same time. Through synthesis, extraction, selection, and classification of time domain, frequency domain, and polarization domain features of target, the resonance frequency identification (also called as pole identification) decision, micro-Doppler modulation identification decision, and polarization identification decision can be obtained.

The target classification and identification process are shown in Fig. 8.1. For a target with an uncertain attribute, the operator sends an target identification request and then the radar receives and stores the target attributes sent back from the responder of cooperative target. For an uncooperative target, the radar will switch into the target classification and identification processing mode, that is, the identification waveform is transmitted to the target and then the target echo is received. After pre-processing and synthesis feature extraction and making synthesis decision based on the obtained target features, the result will be sent back to the operator.

The key point of target classification and identification is the effective feature extractions. The radar characteristics of target embody in the amplitude, phase, frequency, and polarization of the target's backscattered echo signal. The radar characteristics of target echo are closely relative to the physical features of target (electromagnetic characteristics of size, shape, and material), radar parameters (transmitted

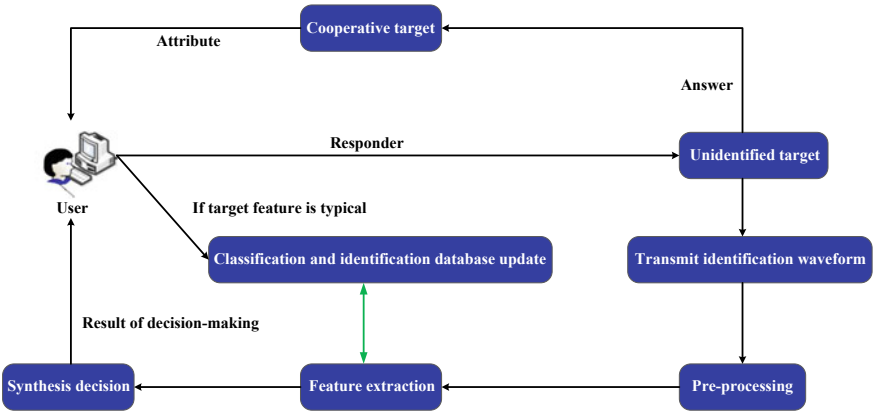


Fig. 8.1 Target classification and identification process in radar

signal form, polarization mode, radar operating mode, and so on), and detection environment (range, jamming, and weather). The radar must make comprehensively use of the information in Doppler domain, frequency domain, and polarization domain to conduct target classification and identification. The Doppler domain information is straightly relative to the motion characteristics of target, and the frequency domain information and the polarization domain information are embodied by RCS of target.

8.2 Feature Extractions

8.2.1 Basic Motion Features

8.2.1.1 Height

The height of aircraft target is usually below 30 km. The height of tactical ballistic missile is lower than 350 km. The height of near space target is in the range of 30–100 km. The space target has the greatest height among them, and the height of high-orbit satellite can reach up to several thousands of kilometers or even tens of thousands of kilometers.

8.2.1.2 Velocity

The velocity of aircraft target is usually within 3 Mach. The velocity of near space target is 5–20 Mach. The velocity of tactical ballistic missile is 3–20 Mach. The velocity of space target has faster velocity. The velocity of space target is commonly in the range of 20–30 Mach.

Table 8.1 Kinematic features of airplanes

Type	Height (km)	Velocity (Mach)	Target type
1	<10	<0.8	Propeller-driven aircraft
2	<5	<0.3	Helicopter
3	Uncertain	About 2	Jet airplane
	5–13	0.5–1	Civil Jet airplane

The typical kinematic features of jet airplane, propeller-driven aircraft, and helicopter are given in Table 8.1.

8.2.1.3 Change Rate of Height

The height of airplane target changes slowly and the absolute value of height change rate is smaller than 0.6 km/s commonly. When the height of tactical ballistic missile ranges 0–100 km, its vertical motion is dominant with the absolute value of height change rate beyond 0.6 km/s. The orbit height of space target is stable generally, with a weaker height change.

8.2.1.4 Change Rate of Horizontal Position

The target's horizontal velocity satisfies

$$v_h = \sqrt{v^2 - v_v^2} \tag{8.1}$$

where, v and v_v are the target's velocity and vertical velocity, respectively.

The change rate of height and the change rate of horizontal position should be used in the limited scenes. For maneuverable aircraft targets, there is no fixed relation between the change rate of height and the change rate of horizontal position; the near space target mainly makes horizontal movement, the absolute value of the change rate of horizontal position is generally greater than that of the change rate of height; the ballistic missile is in vertical motion commonly below 100 km, so that the absolute value of the change rate of horizontal position is generally smaller than that of the change rate of height.

8.2.1.5 Acceleration Change Curve

The change curve of acceleration reflects the maneuver of target. The acceleration of conventional aircraft target shows a very slow change. The tactical ballistic missile

has different accelerations in boost phase, unpowered phase, and reentry phase, but there is only a small change in the same phase. The near space target makes long endurance flight usually along inertial trajectory or boost-glide trajectory, thus large change in its acceleration occurs, and the track of target shows "leapfrogging".

8.2.2 *Resonant Frequency Features*

The same target shows different scattering features for the incident electromagnetic waves of different frequencies. On the basis of the relation of the incident wavenumber of $k = 2\pi f/c$ and the target's feature size of a, the scattering characteristics of target can be divided into three types: Rayleigh region scattering ($ka \leq 1$), resonance region scattering ($1 \leq ka \leq 10$), and optical region scattering ($ka \geq 10$), as shown in Fig. 8.2.

The Rayleigh region, also called as low frequency region, is characterized by very small feature size of target compared with radar wavelength. In this region, RCS of target increases as wavelength decreases, in direct proportion to the forth power of frequency. However, for most military applications, the wavelength is usually smaller than the size of object.

The optical region is also called as high frequency region. The ka is generally assumed to be satisfied with $ka \geq 10$. Within the region, the electromagnetic coupling between different portions of target is small, satisfying the locality principle. The scattering characteristics of target can be formed by coherent overlapping of some

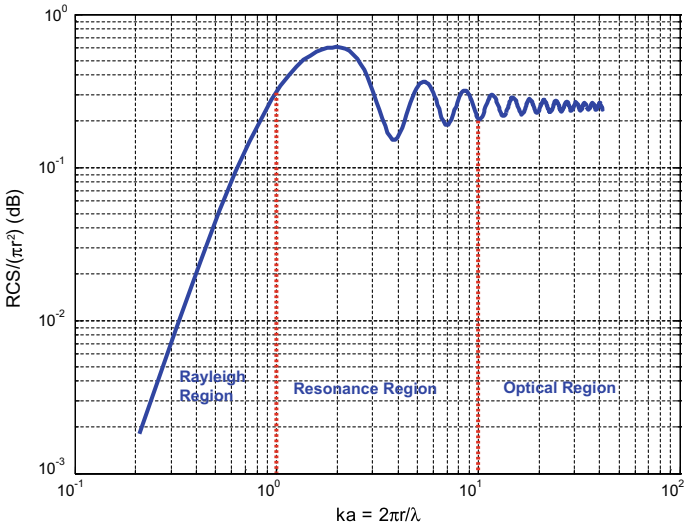


Fig. 8.2 Curve of perfect conducting sphere RCS varied with radar wavelength

independent scattering centers on target surface, which is very important for the shape feature extraction of target.

The resonance region is also called as Mie scattering region. The *ka* is generally considered as to be $1 \leq ka \leq 10$. In this region, the incident wavelength and the target size are in the same order of magnitude. With wavelength decreasing, RCS presents oscillating attenuation characteristics. It can be seen from Fig. 8.2 that, in the resonance scattering region, the RCS of target generates oscillation phenomenon with the frequency. The set of frequencies at oscillation peaks (its magnitude is depended on the operating frequency range of radar or the signal bandwidth) reflects the inherent frequency characteristics of target. The frequencies at the peaks are called as the poles of target. These poles only rely on the shape, size, and material of target, and these features in resonance region can be effectively applied in target r identification for the radar.

There are generally two research contents for target identification by use of the pole features. One is to directly extract target poles from radar echo as the features for matching. The other one is to synthesize a characteristic waveform as the characteristic signal for storing in library. The identification process is that the received target echo is made convolution computation with the stored characteristic waveform and the type of target is determined according to the desired output of convolution result.

For example, an electromagnetic simulation is performed on the electromagnetic model of a typical aircraft shown in Fig. 8.3, and the simulation parameters of the aircraft are given in Table 8.2.

Figure 8.4 gives the curves of echo amplitude varying with frequency about the aircraft at different elevations. The simulation environment is set to be far-field and the elevation is set in the range of 0–20°. It can be seen that the cross-polarization

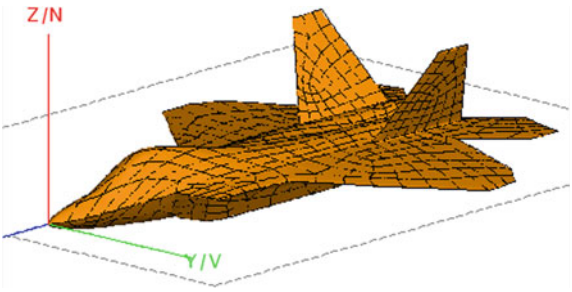


Fig. 8.3 Electromagnetic simulation model of a typical aircraft

Table 8.2 Identification related parameters of a typical aircraft

Aircraft type	Length (m)	Wingspan (m)	Height (m)	Max cruise velocity (Mach)	Practical ceiling (m)
A typical aircraft	18.9	13.56	5.08	2.25	19,812

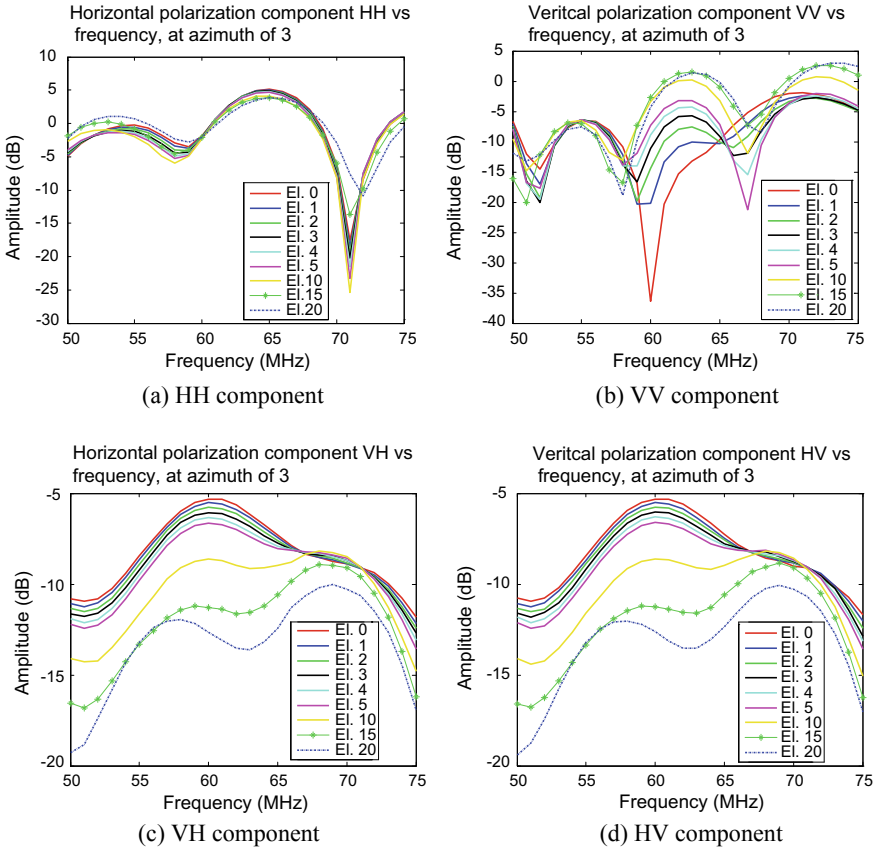


Fig. 8.4 Curves of echo amplitude varying with frequency about a typical aircraft at different elevations

components of HV and VH are nearly equal and the HH component does not change with elevation basically. The VV component is above 0 dB, and the RCS frequency response curve does not present a large change while the elevation in the range of 0–5°. Therefore, a small elevation change only produces a few effect on target poles.

Figure 8.5 shows the curves of echo amplitude varying with frequency about the aircraft at different azimuths. It can be seen that the echo amplitude of co-polarization components (HH and VV) of target produces significant oscillation phenomenon with frequency, and a small azimuth change only produces a small effect on target poles.

It can be seen from above that, in a certain angle range, the poles present slight changes with azimuth and elevation. Therefore, the resonance frequency characteristic can be taken as the important feature to effectively identify typical fighter targets.

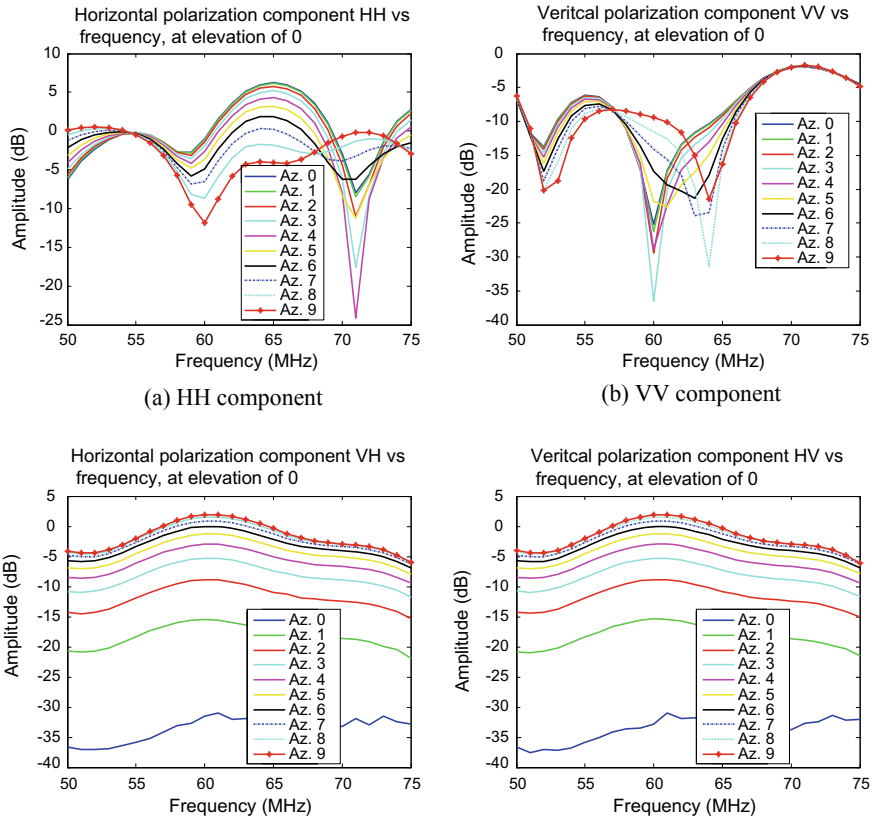


Fig. 8.5 Curves of echo amplitude varying with frequency about a typical aircraft at different azimuths

8.2.3 Micro-Doppler Modulation Feature

Micro-motions are involved in target detection, such as the rotation of helicopter rotor, the rotation of propeller blades, and the precession of warhead. The periodical modulation of rotation parts on target echo could be well applied in target identification. Currently, this kind of study mainly focuses on the target in optical scattering region. The setup of modulation echo model of rotation parts is based on the linear overlapping of the models of strong scattering points. When rotation part falls in resonance region, the physical size of target is in the same order of magnitude as incident wavelength. The phase of incident field changes significantly along the length of target. Each portion of scatter makes effects on other portions. The total result of mutual effects of all scatter portions determines the final current density distribution. Here, the mathematical model based on "scattering point" is no longer

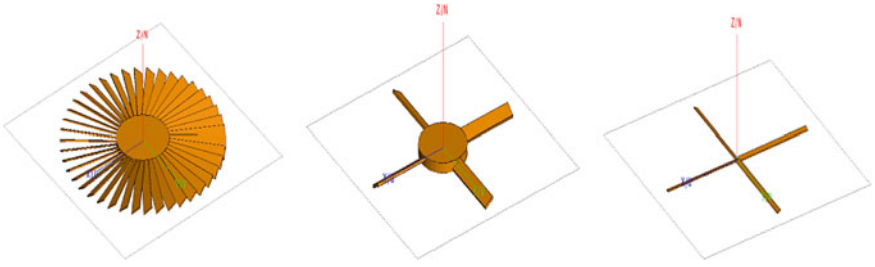
applicable. Thus, for the micro-motion effect of rotation parts of airplane target in resonance region, the electromagnetic simulation software is required currently to simulate the rotation parts in resonance region and generate echo data for theoretical analysis.

Figure 8.6 shows the electromagnetic scattering models of rotation parts of typical aerodynamic targets. Through electromagnetic simulation, the echoes of these models in optical region and resonance region can be obtained. The time-domain modulation echoes obtained is shown in Fig. 8.7.

It can be found from Fig. 8.7 that, compared with optical region, the peaks of modulation echoes from target in resonance region are expanded obviously. The superposition of large sidelobes near the dominant peak makes the echo modulation characteristic produce a great change. The sidelobes between the dominant peaks of helicopter echoes become large markedly in resonance region due to the influence from the superposition of large sidelobes. However, the echo modulation characteristic of propeller-driven aircraft becomes weak evidently. The echo from jet airplane approximates a straight line, just being modulated very slightly.

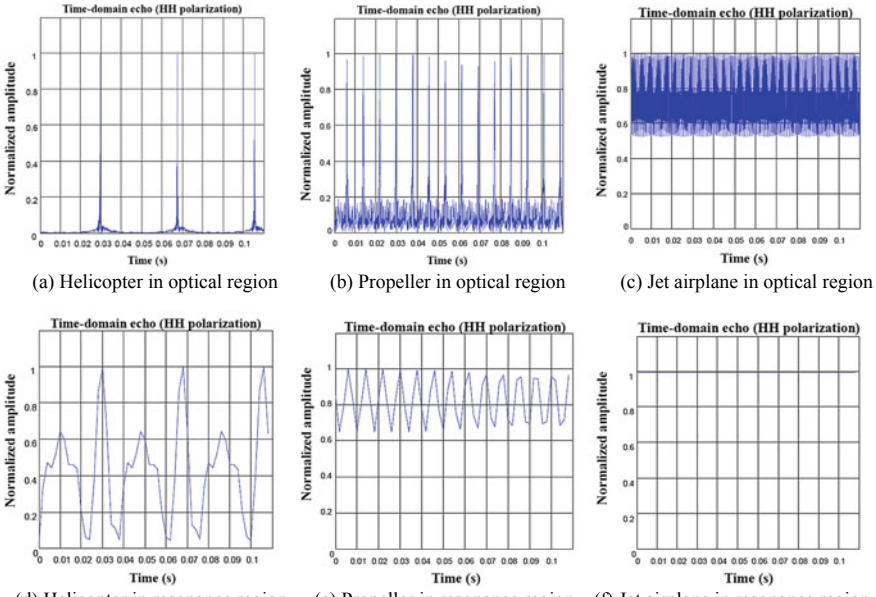
Figure 8.8 depicts the frequency spectrum of rotation parts of typical aerodynamic targets. It can be seen that these three types of aerodynamic targets present significant differences. The number of spectrum lines of helicopter is the most. The jet airplane has the least spectrum lines, and the Doppler spectrum nonoverlapping condition can not be satisfied except for high PRF. In resonance region, the three types of targets are still different in their modulation characteristics and the frequency spectrum nonoverlapping condition can be satisfied in low PRF.

Through the above simulations and analysis, it is feasible that the metric wave radar uses micro-Doppler modulation features to classify aerodynamic targets. Hereafter, we will give brief descriptions of the typical modulation features.



(a) Jet air plane (b) Propeller (c) Helicopter

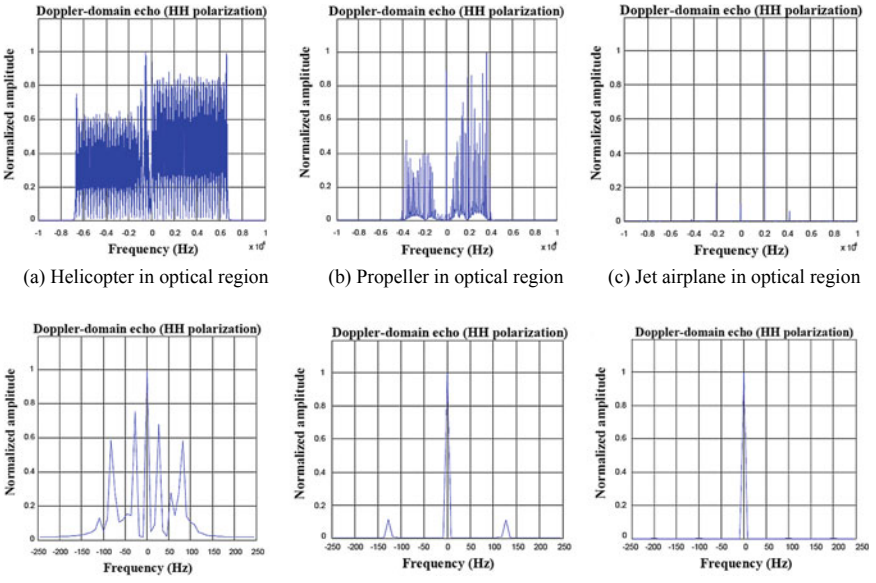
Fig. 8.6 Electromagnetic scattering models of rotation parts of aerodynamic targets



(a) Helicopter in optical region (b) Propeller in optical region (c) Jet airplane in optical region

(d) Helicopter in resonance region (e) Propeller in resonance region (f) Jet airplane in resonance region

Fig. 8.7 Time-domain echoes from rotation parts of typical aerodynamic targets



(a) Helicopter in optical region (b) Propeller in optical region (c) Jet airplane in optical region

(d) Helicopter in resonance region (e) Propeller in resonance region (f) Jet airplane in resonance region

Fig. 8.8 Frequency spectrum of rotation parts of typical aerodynamic targets

8.2.3.1 Spectral Line Interval

Electromagnetic wave generates a series of spectral lines due to the periodical modulation by propeller blades. The relationship between the modulation period and the interval of spectrum lines can be written as

$$f_T = P \cdot N \cdot f_r \tag{8.2}$$

Here, N is the number of blades (when N is an odd number, $P = 2$; when N is an even number, $P = 1$), f_r is the rotation speed of blades.

The interval of spectral lines reflects the periodic feature of modulation spectrum. The number and rotation speed of blades of modern aircraft are designed to be optimal in aerodynamics and the rotation speed is usually constant in normal cruise. Thus, for specific types of aircraft and radar, their periodic feature of modulation spectrum f_T is fixed. Generally, the interval of spectral lines of helicopter is 10–50 Hz, the interval is 60–300 Hz for propeller-driven aircraft, and the larger for jet airplane.

8.2.3.2 Spectral Line Width

The Doppler shift will be created between the linear velocity of the end of rotation part and the radial projection velocity of radar. The spectral line width reflects the shift. It is defined as

$$\mathrm{B} = \frac{4\pi \cdot \mathrm{P} \cdot f_r \cdot L \cdot \cos\beta}{\lambda} \tag{8.3}$$

where, L is the effective length of blade, β is the elevation.

Hence, the feature is the comprehensive reflection of the linear velocity of the end of rotation blade and the transmitted frequency of radar.

8.2.3.3 Number of Spectral Lines

The number of spectral lines reveals the position and attitude of aircraft in a certain extent. It is defined to be

$$\mathrm{N}_1 = \frac{8\pi \cdot L \cdot \cos\beta}{N \cdot \lambda} \tag{8.4}$$

The number of spectral lines reflects the modulation effect of rotation blade.

8.2.3.4 Features Based on Empirical Mode Decomposition

The features based on empirical mode decomposition (EMD) mainly include the waveform entropy, the center moment, and the energy ration. For a signal $x = \{x_i\}_{i=1}^{N}$, the waveform entropy takes the Doppler-domain waveform entropy of the first EMD component M_1, as the feature, which is defined as

$$S_{entropy} = -\sum_{i=1}^{N} p_i \log(p_i) \tag{8.5}$$

where $p_i = x_i / \sum_{i=1}^{N} x_i$.

The waveform entropy feature can be used to reveal the energy distribution; the more centralized the energy, the smaller the entropy.

The center moment takes the second-order center moment of M_r (the Doppler spectrum of the sum of the rest EMDs except for the first EMD). It is defined as

$$u^2 = \sum_{i=1}^{N} (i - i_0)^2 \overline{x_i} \tag{8.6}$$

where, $\overline{x_i} = \frac{x_i}{\sum_{i=1}^{N} x_i}$, $i_0 = \sum_{i=1}^{N} i \cdot \overline{x_i}$. The second-order center moment feature in Doppler domain reflects the deviation of target echo in Doppler domain with respect to its geometric gravity center.

The energy ratio takes the specific value of M_1 and M_r. It reveals the relation of fuselage component and micro-motion component. It is defined by

$$\frac{E(M_1)}{E(M_r)} = \frac{\|M_1\|_2}{\|M_r\|_2} \tag{8.7}$$

8.2.3.5 4D Features Based on Singular Value Decomposition (SVD)

The first-dimension feature is taken to be the number of large eigenvalues with the signal energy of 98% and the noise energy of 2%. That is

$$f_1 = \arg_i \left(\sum_{n=1}^{i} \lambda_n^2 / \sum_{n=1}^{N_e} \lambda_n^2 = 0.98 \right) \tag{8.8}$$

The second-dimension feature is taken to be the self-adjusting period factor. It is defined by

$$f_2 = \varsigma \times \delta_{rperi} \tag{8.9}$$

where, $\varsigma = \widehat{\varsigma}/\log N_e$, denotes the normalized energy entropy, $\widehat{\varsigma} = -\sum_{j=1}^{N_e} \varepsilon_j \log\left(\varepsilon_j\right)$, $\varepsilon_i = E_i/\sum_{j=1}^{N_e} E_j$, E_i denotes the signal energy used to estimate the sample of covariance matrix; $\delta_{rperi} = 1 - N_e\delta_{peri}/(1 - N_e)$, denotes the normalized period factor, $\delta_{peri} = \lambda_1^2/\sum_{i=1}^{N_e} \lambda_i^2$.

The third-dimension feature is the characteristic spectrum, that is

$$f_3 = -\sum_{i=1}^{N_e} p_i \log(p_i) = -\sum_{i=1}^{N_e} \left(\lambda_i^2/\sum_{j=1}^{N_e} \lambda_j^2\right) \cdot \log\left(\lambda_i^2/\sum_{j=1}^{N_e} \lambda_j^2\right) \tag{8.10}$$

The fourth-dimension feature is taken to be the sum of eigenvalues of the normalized large eigenvalues, that is

$$f_4 = \sum_{i=1}^{N_e} \lambda_i/\lambda_1 \tag{8.11}$$

8.2.3.6 Phase Modulation Feature

The relative movement of the airplane rotation blade in high frequency region results in relative phase variation of equivalent scatter center, which in turn causes variations in amplitude and phase components of complex envelops of echoes.

The amplitude deviation coefficient is defined by

$$g_a = \frac{\sigma_a}{\bar{a}} \tag{8.12}$$

Here, $\bar{a}$ is the mean amplitude, and σ_a is the amplitude variance.

The greater its value, the greater the fluctuation of echo amplitude. That means that the rotation parts are remarkable for a airplane target. Inversely, the stable fuselage components are dominant in target echoes.

The phase-shift scattering angle is defined by

$$g_{\mathrm{p}} = \arctan\left[\left(\frac{N_a}{N_a - 1} \cdot \frac{1 - r^2}{r^2}\right)^{\frac{1}{2}}\right] \tag{8.13}$$

where, $r^2 = \frac{1}{N_a^2}\left[\left(\sum_{i=1}^{N_a} \cos(\Delta\phi_i)\right)^2 + \left(\sum_{i=1}^{N_a} \sin(\Delta\phi_i)\right)^2\right]$, N_a is the number of effective echoes when antenna scanning over the aircraft, $\Delta\phi_i$ is the pulse-to-pulse phase variation. They both can reflect the aircraft complexity in a certain context, that is, the structural and proportional relation of rotation parts and fuselage.

8.2.3.7 Fractional Brown Fractal Dimension Feature

Amplitude fluctuation is viewed as the result of random walks and satisfies that the amplitude difference obeys zero mean value. The variance is the Gaussian distribution of fractal exponent of time difference, that is, the variance of pulse-to-pulse amplitude variation is in inverse proportion to the fractal exponent of time difference. The fractional Brown fractal dimension is defined as

$$\ln[\mathrm{var}\{a(t+\Delta r)-a(t)\}] = 2H\cdot\ln(\Delta r)+C \tag{8.14}$$

where, $a(t)$ is the amplitude, Δr is the time interval, C is a constant, and H is the slope. This feature is mainly used to identify helicopter target.

8.2.3.8 Asymmetry

Define the frequency point in negative frequency region to be $x^{(1)} = [x_1^{(1)}, x_2^{(1)}, \ldots, x_N^{(1)}]$ and the frequency point in positive frequency region to be $x^{(2)} = [x_1^{(2)}, x_2^{(2)}, \ldots, x_N^{(2)}]$, then the asymmetry feature can be defined by

$$F_1 = \frac{1}{N}\sum_{i=1}^{N}\left|x_i^{(1)} - x_i^{(2)}\right| \tag{8.15}$$

The asymmetry feature reflects the asymmetry of Doppler distributions in negative and positive regions, which indirectly reflects the physical structure of aircraft and is effective for helicopter identification.

8.2.3.9 Multi-fractal Features

For airplane identification based on multi-fractal spectral lines, the symmetric degree of mass index is defined by

$$R_\tau = \left|\frac{\max\tau(q)}{\min\tau(q)}\right| \tag{8.16}$$

where $\tau(q)$ is the mass index. The spectral width is defined as $\Delta\sigma = \sigma_{\max} - \sigma_{\min}$. The fractal dimension difference of the minimax probability subset is $\Delta f = \left|f(\sigma_{\min} - f(\sigma_{\max}))\right|$, and the symmetry index is

$$R_\sigma = \frac{\Delta\sigma_L - \Delta\sigma_R}{\Delta\sigma_L + \Delta\sigma_R} \tag{8.17}$$

where, $\Delta\sigma_L = \sigma_0 - \sigma_{\min}$, $\Delta\sigma_R = \sigma_{\max} - \sigma_0$.

8.2.3.10 Doppler-Domain Integral

Based on the differences in Doppler domain of jet airplane, propeller-driven aircraft, and helicopter, the Doppler-domain curve quadrature can obtain the area of the curve and coordinate axis. The value approximatively reflects the magnitude of total energy backed from target. It is defined as

$$\mathrm{d}I = \sum_{i=1}^{n} y_i \tag{8.18}$$

In similar echo collections, because of different shapes, the Doppler integral value of jet airplane is the largest, the next is for propeller-driven aircraft, and the smallest is for helicopter.

8.2.4 Polarization Features

Polarization features are taken commonly from polarization scattering matrix (PSM). The elements in the scattering matrix are usually complex. Each of them represents an electric field component relative to RCS (measured in power). Its value depends on the transmit/receive polarization state, target aspect angle, and scattering characteristics. Under certain radar aspect angle and incident frequency, a target determines a scattering matrix, which can be expressed as

$$[S] = \begin{bmatrix} S_{11} & S_{12} \\ S_{21} & S_{22} \end{bmatrix}$$

where, the subscripts "1" and "2" denote a set of orthogonal polarization components. The first subscript denotes the polarization mode of receive antenna and the second denotes the polarization mode of transmit antenna. Let $S_1 = S_{11} + S_{22}$ and $S_2 = S_{11} - S_{22}$, which denote the trace and the inverse trace of PSM.

The polarization invariants perfectly determine the backscatter characteristics of target at a given orientation and characterize maximum target information obtained by radar observation at the line of sight direction. The polarization invariants are unchangeable with pitching angle and radar polarization basis, which include the scattering matrix determinant, the trace of power matrix, depolarization coefficient, eigenpolarization direction angle, and eigenpolarization ellipticity.

8.2.4.1 Scattering Matrix Determinant

The scattering matrix determinant is defined as

$$\Delta = \det[S] = S_{11}S_{22} - S_{12}^2 \tag{8.19}$$

In the case of target rotating around radar line of sight or radar rotating around target line of sight, the scattering matrix determinant remains the same. For the line target, like a metal wire, $\Delta = 0$; for isotropy target, such as a metal ball, $\Delta = A^2$ (A is a real number); for symmetric target, $\Delta = S_{11}S_{22}$. Hence, the invariant Δ could generally reflect the target being big or small, and fat or thin.

8.2.4.2 Trace of Power Matrix

The power scattering matrix defined by Graves is

$$[P] = [S^*]^T[S] \tag{8.20}$$

where, * stands for the conjugate and T represents the transpose. The trace of power matrix is unchanged when target rotating around line of sight of radar. It represents the total power received by a pair of orthogonal polarization antennas. The trace of power matrix of P_1 can be expressed as

$$P_1 = |S_{11}|^2 + |S_{22}|^2 + 2|S_{12}|^2 \tag{8.21}$$

The trace of power matrix characterizes the RCS value of target under full-polarization, and is able to reflect the size of target approximatively.

8.2.4.3 Depolarization Coefficient

Depolarization coefficient is defined by

$$D = 1 - \frac{|S_1|^2}{2P_1} = \frac{\frac{1}{2}|S_2|^2 + 2|S_{12}|^2}{|S_{11}|^2 + |S_{22}|^2 + 2|S_{12}|^2} \tag{8.22}$$

Both S_1 and P_1 are the polarization invariants, so is the depolarization coefficient reflects the number of target scattering centers approximatively. For isolated scattering center, D is commonly smaller than 0.5. The large value ($0.5 < \mathrm{D} \leq 1$) corresponds to the combinative target with multiple scattering centers generally.

8.2.4.4 Eigen Polarization Direction Angle

Eigen polarization direction angle is defined to be

$$\varphi_d = \frac{1}{2}\text{arctg}\frac{2\text{Re}(S_1^* S_{12})}{\text{Re}(S_1^* S_2)} \tag{8.23}$$

where $\text{Re}(\cdot)$ is the operator of taking real part.

Eigen polarization angle reflects the polarization direction of target.

8.2.4.5 Eigen Polarization Ellipticity

Eigen polarization ellipticity is expressed by

$$\tau_d = \frac{1}{2}\text{arctg}\frac{\text{j}2S'_{12}}{S_1} \tag{8.24}$$

where $S'_{12} = S_{12}\cos(2\varphi_d) - \frac{1}{2}S_2\sin(2\varphi_d)$.

The feature of eigen polarization ellipticity represents the symmetry of target. Among the above five polarization invariants, the eigen polarization direction angle and the eigen polarization ellipticity are relative to the eigen problem of scattering matrix. The eigen polarization is the input polarization that can make the output coincident with the input. At this time, the corresponding scattering matrix is called as eigen polarization scattering matrix of target and can be expressed by

$$[S]_d = \begin{bmatrix} \lambda_1 & 0 \\ 0 & \lambda_2 \end{bmatrix}$$

where both λ_1 and λ_2 are the eigenvalues.

Any target has eigen polarization direction angle and the eigen polarization ellipticity. When the transmitted polarization matches with the eigen polarization of target, the target echo polarization direction parallels to the transmitted polarization direction. The maximum RCS and the minimum RCS of target are λ_1 and λ_2 respectively. The eigenvalues do not vary with target rotating around the line of sight of radar or polarization basis, so that the eigen polarization direction angle and the eigen polarization ellipticity also have the polarization invariability.

Figure 8.9 shows the feature distributions in two-dimensional polarization plane of the determinant and the trace of power matrix for F-22 and Boeing 737 based on electromagnetic simulation computation. It can be seen that the determinant and the trace of power matrix of conventional jet airplane are obviously larger than those of the stealth aircraft F-22.

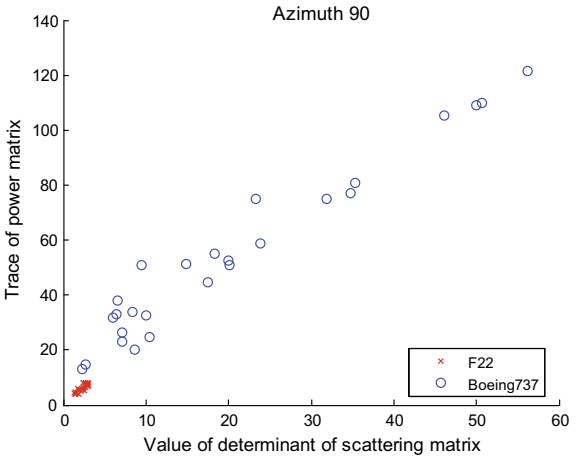


Fig. 8.9 Typical polarization feature 2D distribution of aerodynamic targets

8.3 Target Classification and Identification

The classification and identification methods for aerodynamic targets can be divided in the following categories:

(1) The methods based on target movement features, mainly make use of such information as velocity, height, and acceleration. The precision of this kind of methods relies on the velocity measurement precision and height finding precision of radar.

(2) Based on target RCS features. RCS is suffered from large influence of target aspect and the statistic characteristics of single-echo RCS and serial-echo RCS, which require the long observation time and large storage space. For fast aircraft targets, therefore, there are limitations in direct use of RCS features in target classification.

(3) Identification based on resonant frequency features, also called as identification based on pole features. As the most important foundations for radar target identification are in resonance region, the poles are determined by the characteristics of target itself such as shape, size, material, and so on, independent of radar polarization modes. The method can reveal the intrinsic frequency structure of target.

(4) Based on micro-Doppler modulation features. The periodical movements of propellers, rotation blades, or rotors of dynamic targets such as propeller-driven airplane, jet aircraft, or helicopter, will produce periodical modulation on radar echoes. There are very different periodical modulation spectrums for different targets. These methods could be found the wide applications in the classification and identification of propeller-driven airplane, jet aircraft, and helicopter.

(5) Based on target polarization features. This kind of methods commonly classify the targets into spheroid, dipole, two-faced right angle reflector on the basis of

target polarization or characteristic polarization information defined by PSM. The extraction method requires the radar to have dual-polarization transmit and receive. With the development of the foundational theory and technology of radar polarization measurement, more and more attentions are paid to this class of methods.

8.3.1 Decision Synthesis

The essence of target classification and identification is to make a judgment about the type of target based on the given eigenvector. The decision-making criteria are determined by the decider, as illustrated in Fig. 8.10. There are two major methods to design the decider: determinate discriminant and statistic discriminant. The realization of the former is simple, with representative methods such as decision tree and nearest-neighbor. This sort of deciders requires more prior knowledge about target features. In addition, the radar echoes of airplane targets usually have the property of statistics, thus the statistic discriminant could be applied in the classification and identification for this sort of targets. However, the statistic judgment method based on probability model relies strongly on prior knowledge.

An effective means of removing prior uncertainty is to use special training algorithms to conduct iterative learning. The training algorithms include two sorts: the supervised and the unsupervised. The former is employed here, that is, the training sample of the target is known in the learning process. The typical kernel classifier, for example, the support vector machine, has found wide and successful applications in target identification.

Classification and identification of three typical aerodynamic targets can be constructed as a multi-class pattern recognition problem: the input sample is x, and the output is the corresponding label of the vector, namely

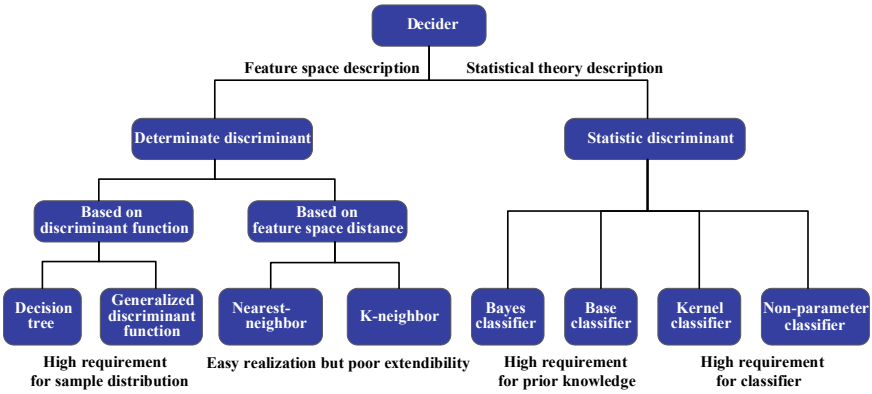


Fig. 8.10 General decider for target classification and identification

$$y = \begin{cases} 1, & \text{Propeller-driven aircraft} \\ 2, & \text{Helicopter} \\ 3, & \text{Jet airplane} \end{cases} \tag{8.25}$$

Once master the mapping rule from input x to output y, the automatic classification and identification of target can be achieved. The radar can make comprehensive use of motion feature, resonant frequency feature, polarization feature, and modulation feature to conduct synthesis judgment. Modulation feature, as the main classification feature, is used for the judgment of jet airplane, propeller-driven aircraft, and helicopter. As the fine features, resonant frequency feature and polarization feature provide the principle information about structure, size, and inherent frequency of target through matching with the classification and identification database, which can be used for the judgment of the aircraft type.

Modulation feature judgment is complemented by SVM classifier. In practical applications, the multi-class problem is commonly translated into sub-problems of multiple binary classifications. Here, take the linear SVM as an example to expatiate its training process. For the samples $\{x_i, y_i\}_{i=1}^n$, its classification decision is determined by

$$y_i = sign(w^T \cdot x_i + b)\ i = 1, \ldots, n \tag{8.26}$$

where, w and b are weight and bias. The optimal combination can be solved through the following quadratic programming problem:

$$\min_{w,b} \tfrac{1}{2}\|w\|^2 s.t.\ y_i(w^T \cdot x_i + b) \geq 1,\ \ i = 1, \cdots, n \tag{8.27}$$

The complete target classification and identification process can be divided into two steps: training and testing. In the training process, w and b are obtained by solving the provided samples $\{x_i, y_i\}$, and namely, the decider model is obtained. After training, the model is used to make prediction of the unknown test samples to make decision of the target type. Figure 8.11 depicts the performance test strategy of classification and identification of airplane targets:

(1) Divide the eigenvectors set into independent training set and test set (at a proportion of 1:4);
(2) Perform model leaning on the training set, and save the obtained decider model;
(3) Use the obtained model to make class prediction of the samples in the test set;
(4) Make comparison between the predicted class and the practical class to test the accuracy of the decider model;

Repeat the above steps till to achieve stable statistics performance.

There are two important indexes to measure the performance of classification and identification algorithms: accuracy and variance. The former characterizes the accuracy of classification and identification algorithms, and the latter measures the stability of algorithm. The smaller the variance, the more stable the algorithm.

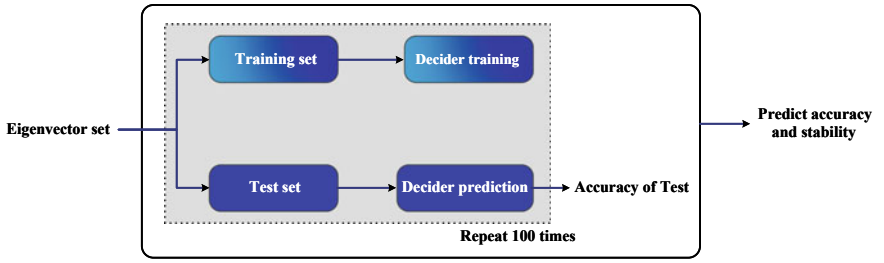


Fig. 8.11 Block diagram of performance test of airplane target classification and identification system

Taking comprehensive use of multiple features, the criterions of radar judging jet airplane, propeller-driven aircraft, and helicopter are as follows:

(1) Jet airplane: If the extracted modulation features are effective, the judgment of a target being a jet airplane is given when the output from the modulation feature classifier is 3. In aerodynamic targets, the target with the flight at a stable velocity over 1 Mach is determined to be a jet airplane. When the flight height is more than 10 km, the target is determined to be the jet airplane. When its polarization feature and resonant frequency feature match with the characteristic parameters of the jet airplane target in the classification and identification database, the target is judged to be a jet airplane.
(2) Propeller-driven aircraft: If the extracted modulation features are effective, the judgment of a target being a propeller-driven aircraft is given when the output from the modulation decision classifier is 1. When its polarization feature and resonant frequency feature match with the characteristic parameters of the propeller-driven aircraft target in the classification and identification database, the target is judged to be a propeller-driven aircraft.
(3) Helicopter: If the extracted modulation features are effective, the judgment of a target being a helicopter is given when the output from the modulation decision classifier is 2. When its polarization feature and resonant frequency feature match with the characteristic parameters of the helicopter target in the classification and identification database, the target is judged to be a helicopter.

In addition, the synthesis decision-making module makes synthesis of multiple features and then gives the decision about the type of aerodynamic target.

8.3.2 Data Analysis

In this section, the ability to extract resonant frequency features, polarization features, and micro-Doppler features is firstly demonstrated on the basis of the measured

data of a metric wave radar. And then the classification and identification of jet airplane, propeller-driven aircraft, and helicopter are made based on the extracted target features.

8.3.2.1 Resonant Frequency Data Analysis

Figure 8.12 shows the frequency resonance curves of two data sets of civil aviation airplane. Compared with the frequency resonance curve acquired from electromagnetic simulation model of Boeing 737, the three curves are very approximative in both amplitude and pole position. Because the measured target and the simulated target are similar in physical size and structure, their frequency resonance curves are also in very close.

For analyzing the frequency resonance characteristics of stealth target under different azimuth angles, the resonance response curves of HH and VV principle components of a typical stealth aircraft are simulated. The results are given in Fig. 8.13. In the figure, the azimuth angle of 0° means that the radar line of sight aims at the nose cone direction of aircraft. The azimuth angle of 90° corresponds to the line of sight of radar against the side of aircraft. The azimuth angle of 180° represents radar illumination at the direction of aircraft tail. The statistical values of position and amplitude of each pole is given in Tables 8.3 and 8.4.

Table 8.3 gives the resonance frequency statistics in horizontal polarization of a typical aircraft under elevation of 0°, which reflects the horizontal structure characteristics of the target. This typical aircraft is left and right symmetrical in

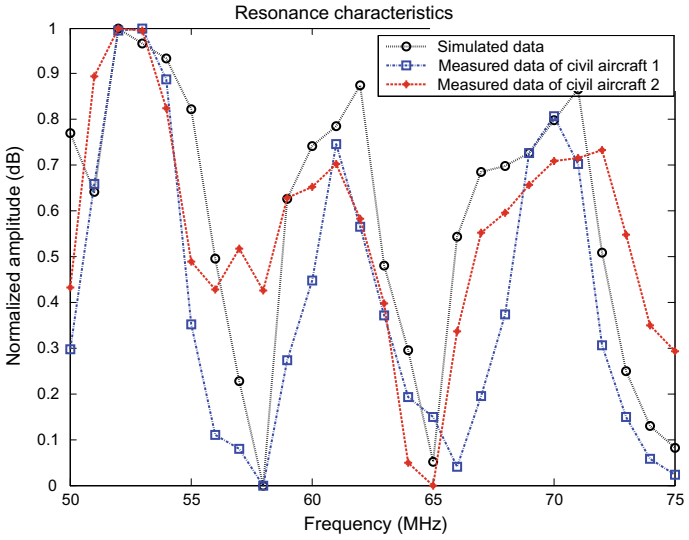
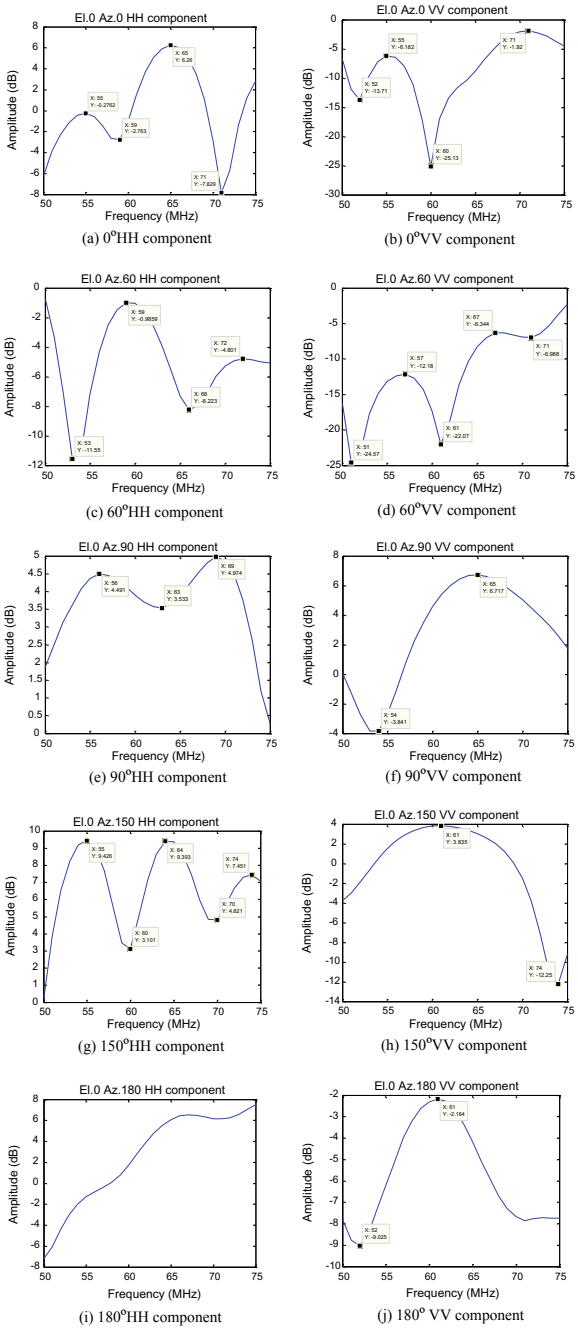


Fig. 8.12 Frequency resonance curves of measured data and simulated data of Boeing airplanes



(a) 0°HH component (b) 0°VV component

(c) 60°HH component (d) 60°VV component

(e) 90°HH component (f) 90°VV component

(g) 150°HH component (h) 150°VV component

(i) 180°HH component (j) 180° VV component

Fig. 8.13 Resonance response curves in HH and VV channels of a typical aircraft under typical azimuth angles

Table 8.3 Extreme point distribution of HH component of a typical aircraft at different azimuth angles

Azimuth (°)	Peak value 1		Peak value 2		Peak value 3	
	Frequency (MHz)	Amplitude (dB)	Frequency (MHz)	Amplitude (dB)	Frequency (MHz)	Amplitude (dB)
0	55	−0.2762	65	6.26	–	–
60	59	−0.9859	–	–	72	−4.801
90	56	4.491	69	4.974	–	–
150	55	9.426	64	9.393	74	8.451
180	–	–	65	6.081	–	–

Table 8.4 Extreme point distribution of VV component of a typical aircraft at different azimuth angles

Azimuth (°)	Peak value 1		Peak value 2	
	Frequency (MHz)	Amplitude (dB)	Frequency (MHz)	Amplitude (dB)
0	55	−6.182	71	−1.92
60	57	−12.18	68	−6.343
90	65	6.717	–	–
150	61	3.835	–	–
180	61	−2.184	–	–

its structure, so that almost the same poles appear when azimuth angles are 0° and 180°.

Table 8.4 shows the resonance frequency statistics in vertical polarization of a typical aircraft. The extreme points reflect the vertical structure characteristics of the target. When the elevation is 0°, the projection of vertical structure of a typical aircraft with respect to the line of sight of the radar is almost aptotic. As a result of different shielding effects of the wings, and etc., however, the distributions of resonant frequency points of VV component are few different at different azimuth angles.

From the above analysis, we can see that the resonant frequency feature directly reflects the principle information of target including its structure, and etc. The distribution of resonant frequency points at different azimuth angles can reflect the overall structure status of target, which provides important support for classification and identification of target.

8.3.2.2 Polarization Feature Data Analysis

To prove the possibility to pick up the polarization feature, the electromagnetic simulation software is used to generate the dual-polarization data of three types of aircrafts including MTA, Drone, L15. MTA is a multi-purpose large transporter,

Drone is an unmanned aerial vehicle (UAV), and L15 is an advance training plane. Their size parameters are given in Table 8.5.

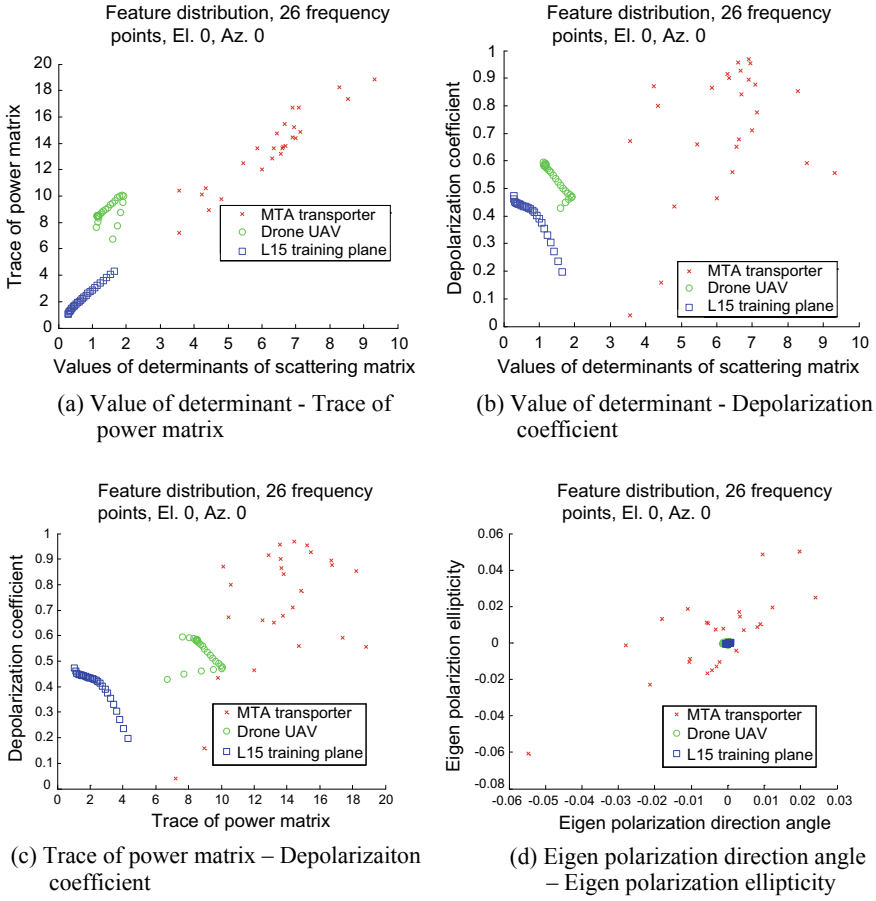
In Table 8.5, the three types of aircraft are arranged in a descending order according to their length, width, and wingspan. From the aspect of "thickness and thinness" (refer to fuselage width), MTA transporter is the most "thick", the second is Drone UAV, and L15 training plane is the "thinnest". As for the determinants of their polarization scattering matrixes, in theory, MTA transporter is the most, the next is Drone UAV, and L15 training plane is the least. From the point of view of "big and small" (by reference to fuselage length), MTA transporter is the "longest", Drone UAV is the next, and L15 training plane is the "shortest". Therefore, as for the traces of their power matrixes, MTA transporter is the most, the next is Drone UAV, and L15 training plane is the least.

Figure 8.14 shows the two-dimensional feature distributions of polarization invariants at successive 26 integral frequency points within the radar frequency range under typical azimuth and elevation. It can be seen that high separability on the three types of targets is achieved based on the polarization invariants in the case of azimuth of 0° (at the direction of nose cone). For further analysis of classification and identification capability of the polarization invariants on the three types of targets, the statistic results of the eigenvalues at each integral frequency points (26 points in total) are given in Table 8.6.

From Table 8.6, the average value of the PSM determinants at different frequency points is the greatest for MTA transporter, the least for L15 training plane, and Drone UAV is the medium. The results are consistent with the theoretical computation. The average traces of power matrix at 26 integral frequency points accord with the relationship of MTA transporter the greatest, Drone UAV the next, and L15 training plane the least. The results also coincide with the theoretical computation, indicating that the eigenvalues can measure directly the structure information about the size dimension of target. The average the depolarization coefficients at 26 integral frequency points also follow the relationship of that MTA transporter is the greatest, Drone UAV is the next, and L15 training plane is the least. This results accord with the theoretical computation. MTA transporter is complex in structure; its vertical tail makes the number of scattering centers significantly increase. The structure of L15 training plane is the most simple and its depolarization coefficient is also the least. Both eigen polarization direction angle and eigen polarization ellipticity reflect the symmetry of target at a certain extent.

Table 8.5 Size information of three types of aircraft

Type	Length (m)	Width (m)	Wingspan (m)	Height (not including undercarriage) (m)
MTA transporter	42.35	39.76	17.29	12.87
Drone UAV	9.5	14.05	6.4	1.8
L15 training plane	7.59	5.28	1.92	2.15


Feature distribution, 26 frequency points, El. 0, Az. 0
Trace of power matrix
Values of determinants of scattering matrix
MTA transporter
Drone UAV
L15 training plane
Feature distribution, 26 frequency points, El. 0, Az. 0
Depolarization coefficient
Values of determinants of scattering matrix
MTA transporter
Drone UAV
L15 training plane
Feature distribution, 26 frequency points, El. 0, Az. 0
Depolarization coefficient
Trace of power matrix
MTA transporter
Drone UAV
L15 training plane
Feature distribution, 26 frequency points, El. 0, Az. 0
Eigen polariztion ellipticity
Eigen polarization direction angle
MTA transporter
Drone UAV
L15 training plane

(a) Value of determinant - Trace of power matrix

(b) Value of determinant - Depolarization coefficient

(c) Trace of power matrix – Depolarizaiton coefficient

(d) Eigen polarization direction angle – Eigen polarization ellipticity

Fig. 8.14 2D feature distribution of polarization invariants under azimuth of 0°

The RCS is the greatest when azimuth is 90°. Figure 8.15 shows the 2D feature distributions of polarization invariants at azimuth of 90° for MTA transporter, Drone UAV, and L15 training plane. It can be seen that the high separability on the three types of targets is also achieved based on the polarization invariants in the case of azimuth of 90° (from the side direction of fuselage).

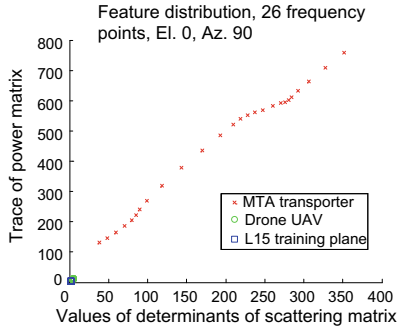
For further measuring the differences of the three types of target in the number of scattering points of fuselage side and the symmetry, Table 8.7 gives five-dimensional polarization invariants of the three types of targets at 26 integral frequency points in the radar frequency range. From the table, both the eigen polarization direction angle and the eigen polarization ellipticity of the three types of targets are increased greatly compared with those in the case of azimuth of 0°, which indicates that the asymmetry of side fuselage increase significantly.

Table 8.6 Eigenvalue distribution of polarization invariants of three types of target under azimuth of 0°

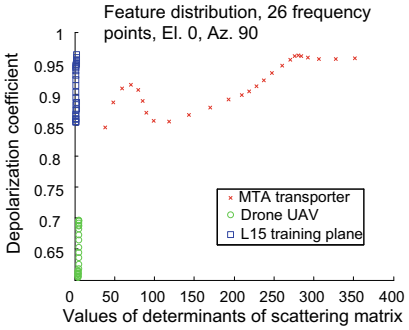
Polarization invariant	Type	Mini value	Max value	Mean value
Value of determinant	MTA transporter	3.5607	9.3296	6.2525
	Drone UAV	1.1096	1.9127	1.4419
	L15 training plane	0.2879	1.6466	0.7712
Trace of power matrix	MTA transporter	7.2062	18.8383	13.5760
	Drone UAV	6.7246	10.0779	8.8040
	L15 training plane	1.0587	4.299	2.3438
Depolarization coefficient	MTA transporter	0.0397	0.9697	0.7148
	Drone UAV	0.4292	0.5943	0.5344
	L15 training plane	0.1979	0.4731	0.3979
Eigen polarization direction angle	MTA transporter	−0.0116	0.0108	−0.0015
	Drone UAV	−0.0015	0.0003	−0.0004
	L15 training plane	−0.0003	0.0007	0.0003
Eigen polarization ellipticity	MTA transporter	−0.0136	0.0095	−0.0033
	Drone UAV	−0.0011	0.0010	0.0001
	L15 training plane	−0.0004	−0.0000	−0.0003

Table 8.7 Eigenvalue distribution of polarization invariants of three types of target under azimuth of 90°

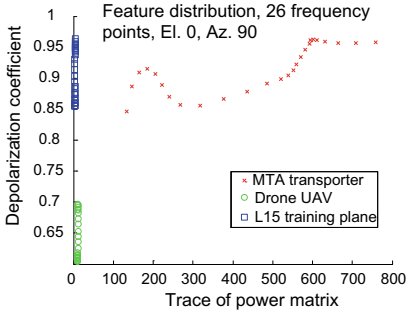
Polarization invariant	Type	Mini value	Max value	Mean value
Value of determinant	MTA transporter	37.9267	351.6079	191.7428
	Drone UAV	3.9651	5.4654	4.6483
	L15 training plane	1.5274	2.1531	1.7511
Trace of power matrix	MTA transporter	132.8602	759.1112	448.9419
	Drone UAV	9.3148	12.4517	10.6615
	L15 training plane	3.4463	4.6524	3.8123
Depolarization coefficient	MTA transporter	0.8463	0.9624	0.9138
	Drone UAV	0.6047	0.6966	0.6413
	L15 training plane	0.8547	0.9633	0.9080
Eigen polarization direction angle	MTA transporter	−0.0169	0.6099	0.1633
	Drone UAV	0.0065	0.0567	0.0156
	L15 training plane	0.1283	0.2478	0.2851
Eigen polarization ellipticity	MTA transporter	0.0066	0.2106	0.1245
	Drone UAV	0.0467	0.1105	0.0682
	L15 training plane	0.0407	0.2851	0.1472


Feature distribution, 26 frequency points, El. 0, Az. 90
Trace of power matrix
Values of determinants of scattering matrix
MTA transporter
Drone UAV
L15 training plane

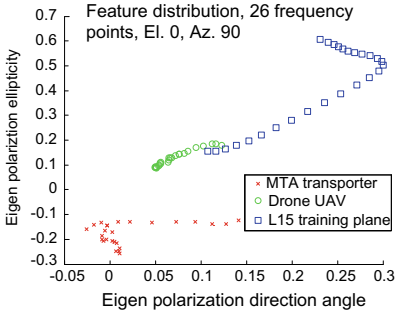
(a) Value of determinant - Trace of power matrix


Feature distribution, 26 frequency points, El. 0, Az. 90
Depolarization coefficient
Values of determinants of scattering matrix
MTA transporter
Drone UAV
L15 training plane

(b) Value of determinant - Depolarization coefficient



(c) Trace of power matrix – Depolarizaiton coefficient



(d) Eigen polarization direction angle – Eigen polarization ellipticity

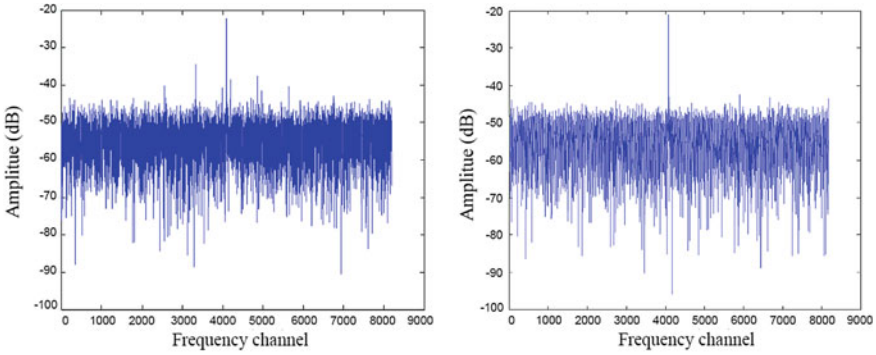
Fig. 8.15 2D feature distribution of polarization invariants under azimuth of 90°

It can be found from the above analysis that the polarization invariant can reflect the structure characteristics of target, such as "thick or thin", "big or small", symmetry, and scattering point distribution. The polarization invariants under different azimuths and elevations can reflect the whole structure of target.

8.3.2.3 Modulation Feature Data Analysis

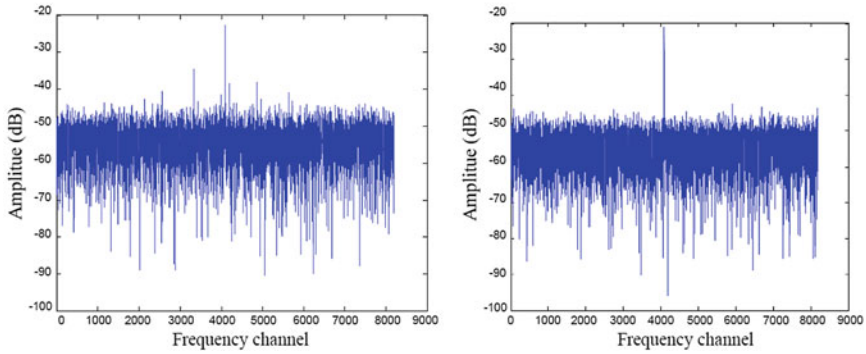
Figure 8.16 depicts the frequency spectrum of typical jet airplane. As shown in the figure, it is difficult to obtain modulation spectrum lines when a jet airplane flies backwards the radar station (away from the radar) or makes a tangential flight. While in flying towards the radar station, the modulation spectrum lines can be gained, and the spectrum lines of each target is relatively stable.

Figure 8.17 shows the typical frequency spectrum of the propeller-driven aircraft. As shown in the figure, the modulation spectrum lines can be obtained when an aircraft flies backwards the station, towards the station, or makes a tangential flight.



(a) Towards station (spectrum line interval 375Hz)

(b) Backwards station (no modulation)



(c) Towards station (spectrum line interval 375Hz)

(d) Tangential flight (no modulation)

Fig. 8.16 Frequency spectrum of measured data of jet airplane

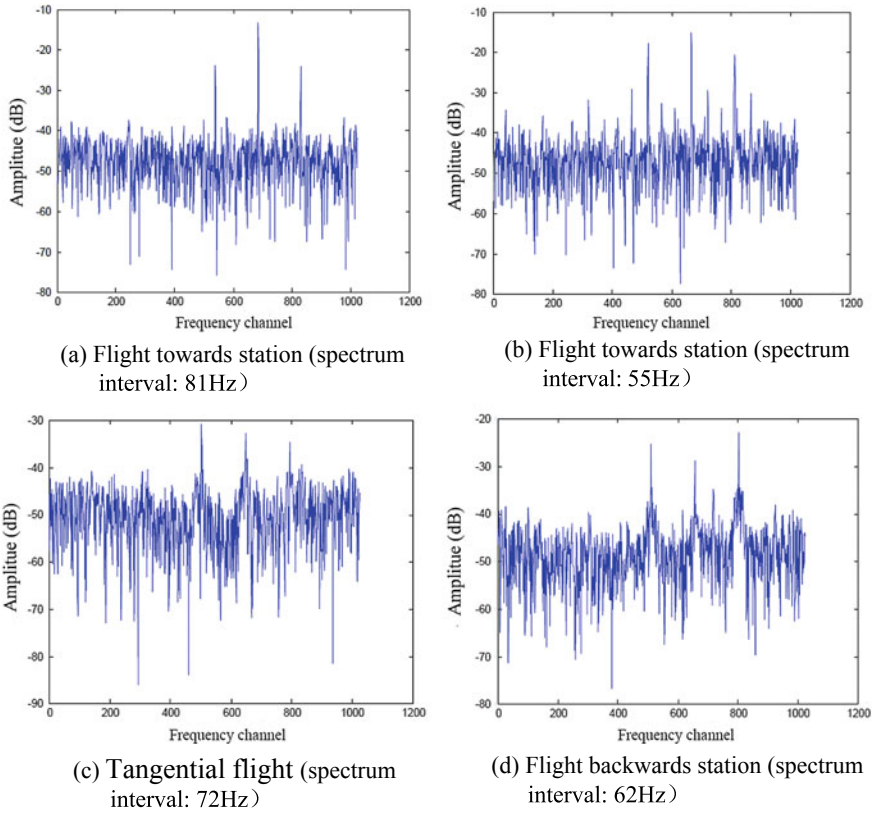
Due to the shielding effect of fuselage, there are some differences in the distributions of modulation spectrum lines and the amplitude intensities achieved, but the interval of spectrum lines is in a stable range.

As shown in Fig. 8.18, the typical frequency spectrum of helicopter is given. The stable modulation spectrum lines can be obtained in all the cases of helicopter with the flights towards and backwards the radar station, or tangential flight.

Through the above analysis, we can see that the micro-Doppler modulation features can be extracted from radar data effectively.

8.3.2.4 Data Analysis of Aerodynamic Target Classification and Identification

Figure 8.19 shows the two 2D distributions using three features of amplitude deviation coefficient, frequency-domain entropy, and Doppler-domain integration for



(a) Flight towards station (spectrum interval: 81Hz）

(b) Flight towards station (spectrum interval: 55Hz）

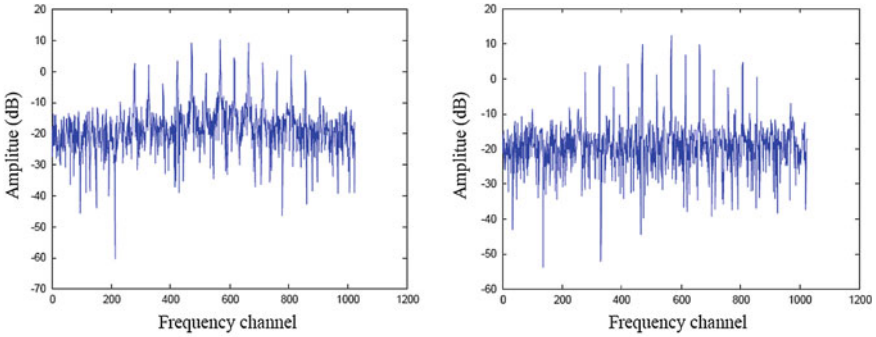
(c) Tangential flight (spectrum interval: 72Hz）

(d) Flight backwards station (spectrum interval: 62Hz）

Fig. 8.17 Frequency spectrums of measured data of propeller-driven aircraft

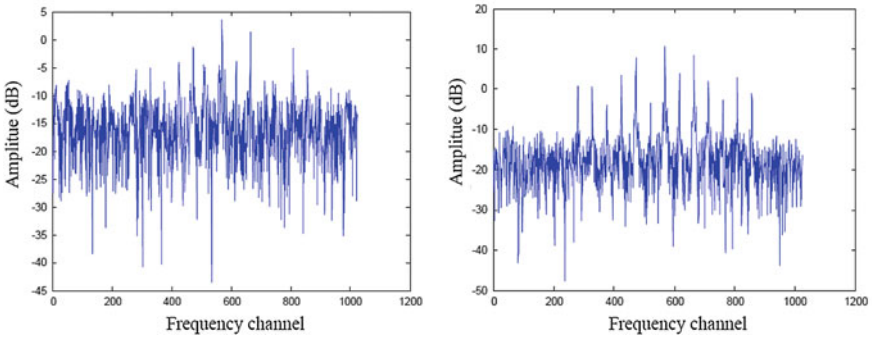
helicopter, jet airplane, and propeller-driven aircraft. From Fig. 8.19a, the Doppler-domain integration is the greatest for jet airplane, the next for propeller-driven aircraft, and the least for helicopter, which is in accordance with the physical size, that is, the echo energy returned from jet airplane is the greatest, the least from helicopter. The amplitude deviation coefficient reflects the structural proportional relation between the rotation parts and the fuselage. As shown in the figure, the proportion of helicopter is the greatest, then the propeller-driven aircraft, and the least is jet airplane. In Fig. 8.19b, for the frequency-domain entropy feature, the least is civil aviation airplane and the greatest is helicopter, which indicates that the echo energy from jet airplane target is the most concentrative and the echo energy from helicopter is the most dispersive, coinciding with the physical size.

We can see from Fig. 8.19 that helicopter, jet airplane, and propeller-driven aircraft can be differentiated in feature space. The motion feature judgment can make auxiliary correction on the results in real time so as to adapt such recognition scene that severe shielding effect occurs due to rotation parts of few targets. The frequency



(a) Flight towards station (spectrum interval: 24Hz）

(b) Flight backwards station (spectrum interval:23.5Hz）



(c) Tangential flight (spectrum interval: 24.5Hz）

(d) Flight backwards station (spectrum interval: 22.5Hz）

Fig. 8.18 Frequency spectrums of measured data of helicopter

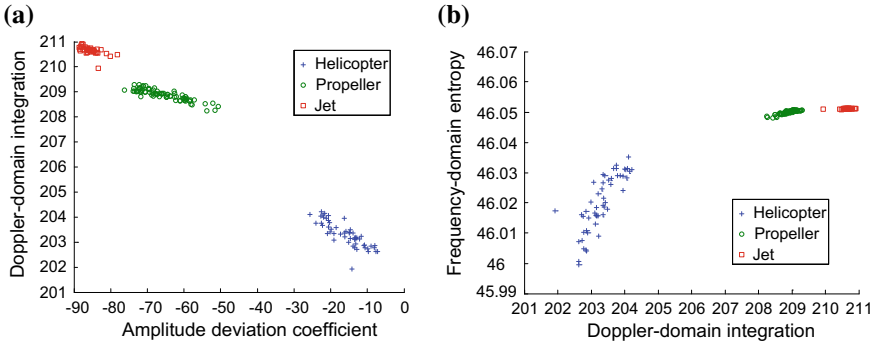


Fig. 8.19 2D distribution of modulation features of measured data

resonance feature and the polarization feature are made match decision with the target features in the identification database to achieve decision on the fine information about shape, size, symmetry, and etc.

Using different feature combinations to constitute input vectors can improve the classification and identification accuracy of various modulation features on the three types of airplane targets. Through comprehensive applications of basic motion feature, resonant frequency feature, micro-Doppler modulation feature, and polarization feature, selecting appropriate features and making combinations, the radar can achieve the classification and identification accuracy beyond 90% on jet airplane, propeller-driven aircraft, and helicopter. As a result, target classification and identification is able to give reliable output through multi-frame integrated decision.

8.4 Classification and Identification Database

The complexity and the scale of the target classification and identification database depend on the degree of confidence required by decision-making and the complexity of targets.

8.4.1 Construction Approach

Target signatures constitute the foundation of target classification and identification. Perfect database of target signatures is very important for the target recognition based on template matching and feature extraction. Based on difference in the generation modes of such characteristic signals, the construction approaches of classification and identification database are divided into several kinds as follows:

(1) Practical measurement on target. Here, the difference between far field measurement and near field measurement, the influences of clutter and ground reflection, the different flight attitudes of target, and the difference in the angle of view between radar and target should be taken into consideration. Comprehensive use of the time-domain, frequency-domain, and polarization-domain information of target is made to perform classification and identification. The characteristic signals cover time-domain echo signal or RCS, the frequency spectrum signal of target under specific radar operating parameters (carrier frequency, PRF, dwell time, SNR, and etc.), the frequency resonance response curve, and the polarization scattering matrixes obtained at different azimuths, elevations, and operating frequencies under dual-polarization operation mode. The setup of the characteristic signal database is of importance for the expansion and update of classification and identification function. From each kind of characteristic signal, multiple signal features can be derived. There are differences in generation

time and scene for various features. The target classification and identification present different combining modes at different stages.

(2) Electromagnetic modeling on target. The approach is based on target's geometric size, shape, and dielectric constant and electrical conductivity of material. It is important for this kind of approach to calculate the reflected signal by solving the Maxwell equation and extract the scattering features of target according to the known incident signal. Commercial software mainly including Feko Suite of EMSS Ltd and the CST software of CST workroom could be used to generate the characteristic signal of the known model. The simulations technologies in common use are the finite difference time-domain (FDTD) method and the moment method. The former split the target into 3D meshes and uses the Maxwell equations to perform computer simulation on the electromagnetic field of each mesh, which is suitable for the target with internal structure. The latter segments the target surface into plane geometry shapes (such as triangles) and forms subdomains, and then calculates the reflection electric field based on the current of subdomain. Table 8.8 gives the size information of typical targets available for electromagnetic modeling.

(3) Measurement at higher frequency band on reduced scale model of target in specific experiment place (such as microwave anechoic chamber). Due to the limit of size, the reduced scale model is used in the majority of microwave anechoic chambers.

Table 8.9 gives the electromagnetic reduced scale relationship between the perfect conducting full-size target and the reduced scale target model, where the s is the reduced scale factor to perform measurement.

The relationship between the RCS (σ') of the reduced scale model (at a scale of 1: s) and the RCS (σ) of the converted real-size target is

$$\sigma = \sigma' + 20\lg(s)\ (\text{dB}) \tag{8.28}$$

Accordingly, the test frequency f′ for the reduced scale target should be s times of that for the real target.

Table 8.8 Size information of typical targets

Type	Length (m)	Height (m)	Wingspan (m)
F-35	15.47	4.57	10.70
Mirage 2000 (A)	14.36	5.20	9.13
Rafale	15.27	5.34	10.8
J-10	14.57	4.78	8.78
Y-12	14.86	5.575	17.235
Yak-42	36.38	9.83	34.88
Boeing 777	63.73	18.50	60.90

Table 8.9 Electromagnetic reduced scale relationship between full-size target and reduced scale model

Parameter	Full-size model	Reduced scale model
Length	l	$l' = l/s$
Time	t	$t' = t/s$
Frequency	f	$f' = fs$
Wavelength	λ	$\lambda' = \lambda/s$
Conductivity	σc	$\sigma' c = s\sigma c$
Resistance	R	$R' = R^a$
Dielectric constant	ε	$\varepsilon' = \varepsilon^a$
Magnetic conductivity	μ	$\mu' = \mu^a$
Phase velocity	ν	$\nu' = \nu$
Propagation constant	k	$k' = sk$
Antenna gain	g	$g' = g$
RCS	σ	$\sigma' = \sigma/s2$

[a]Theoretical relationship, the parameters of practical material vary with frequency

8.4.2 Content and Storage Rule

For a radar system, the resonant frequency feature, polarization feature, micro-Doppler modulation feature, and motion feature could be used to perform classification and identification on jet airplane, propeller-driven aircraft, and helicopter. Correspondingly, the characteristic signal database is divided into the frequency resonance curve database, polarization scattering matrix database, and micro-Doppler modulation frequency spectrum database. To a certain degree, all the three kinds of characteristic signal have dependency on target's angle of view. Thus, the angle of view is taken as an important flag bit for use in classification and storage. Table 8.10 gives an exemplary characteristic signal database of three types of targets. It takes as a form of 2D database and also can be expanded to be a 3D database that covers the elevation and azimuth information of targets. In the table, P_{ij} represents the characteristic signal of the *ith* type of target at the *jth* angle of view. For resonant frequency curve database, P_{ij} is the frequency response curve of a specific target at a specified angle of view. For polarization feature database, P_{ij} corresponds to the elements in polarization scattering matrix. For micro-Doppler modulation feature database, P_{ij} is micro-Doppler modulation frequency spectrum. When entering into the database, each of the characteristic signals P_{ij} indicates the kind and value of its derived feature.

In current investigations, there are many target features and the generation conditions, the recognition effectiveness (i.e. separability of target types) of these features are different from each other. The extracted feature from characteristic signal can

Table 8.10 Exemplar characteristic signal database of three types of target at *n* angles of view

Type of target	Target's angle of view			
	Angular domain 1	Angular domain 2	…	Angular domain n
1	P11	P12	…	P1n
2	P21	P22	…	P2n
3	P31	P32	…	P3n

be stored in database as feature template. The derived features and motion features (including velocity, height, and acceleration) are stored in the form of feature parameter set. The storage mode is

$$\text{feature} = \{\text{class, name, value, LB, UB}\}$$

where, the "class" is the class of target, the "name" is mark of feature name, "value" is the eigenvalue, LB is the lower limit of this class of features, and UB is the upper limit.

In target recognition process, if a new target measurement sample is determined to be in high degree of confidence, it can be used as a new sample. Then the characteristic signal and the eigenvalue are stored in the database. On the other hand, it is possible to eliminate the unapt sample from the database on a dynamic basis. To prevent from frequent update, the radar target classification and identification database can be updated in a manual mode.

8.4.3 Realization Measures

To ensure easy scale expansion, the radar can use non-relation database to store data file. The database performs parallel storage based on distributed file system. Combined with the management method, database management service is provided for upper applications. In the distributed storage process, the consistent hashing algorithm is adopted to realize the data distribution to multiple nodes.

As shown in Fig. 8.20, the consistent hashing algorithm firstly computes the hashing values of individual storage nodes and maps the hashing values into an annular address space. Then the same hashing function is used to acquire the hashing values of data objects which are also mapped into the same address space. On the hashing ring, departing from a data object node, the first storage node along the clockwise direction is the storage position of this data node. Each storage node is responsible for storing the data object between this node and its predecessor node. If a new storage node is added (i.e., adding a new sample), it is mapped firstly onto the hashing ring. Then departing from the new node, the data object between the first node met along the counter-clockwise direction and the new node constitutes a data set. Transfer the data object in the set from the original node to the new node

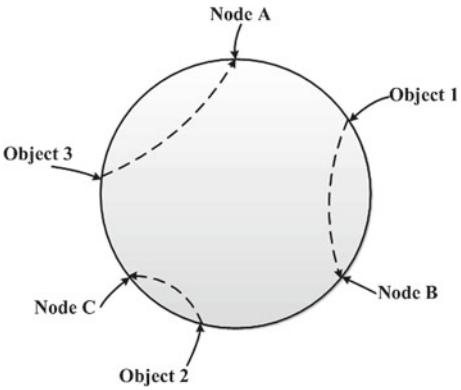


Fig. 8.20 Data distribution realized by consistent hashing algorithm

to complete node adding. When deleting a storage node (i.e., removing the unapt sample from original database), it is only required to assign the data object of this node to its next storage node. Then the deleting operation is completed. It can seen that, when adding or deleting a storage node, only this node and its neighboring nodes suffers from influence, the states of other nodes on the hashing ring have no change. The data distribution realized by use of the consistent hashing algorithm can reduce the influence of the change of storage node on the system.

The number of storage nodes of target classification and identification database is limited in initial training phase, so that it is difficult to achieve a uniform distribution on the hashing ring. The virtual node distribution method can be used to avoid load unbalancing. That is, each storage node can possess multiple virtual nodes and they are also mapped onto the hashing ring. This method can ensure that the nodes on the hashing ring are still in uniform distribution even in the case of few nodes.

The characteristic signals are stored as per the unit of storage object. By horizontal partitioning and taking a row of data record (tuple of relational database) as a unit, they are distributed on individual nodes. The flow to visit the target classification and identification database is depicted in Fig. 8.21. Once the characteristic signal of target is acquired, the database visit instruction is triggered and sent to the meta-database server. The server is responsible for mapping the visit operation into the data nodes. Received the construction, each node completes the relative operations and then sends the result to the data collector. The data collector collects all node data and performs data combination. The result is returned back to the user. That is, the result of template matching or the extracted eigenvector is returned back to the feature extraction/selection module of target classification and identification.

The manual update of target classification and identification database is to add new samples through adding virtual nodes by use of "Add_vnode". Along with the system operation, when some characteristic signal nodes have great changes and therefore need to delete, use "Del vnode" to delete this nodes. And the number of virtual nodes is adjusted by use of "Update" according to the performance quantizing parameters.

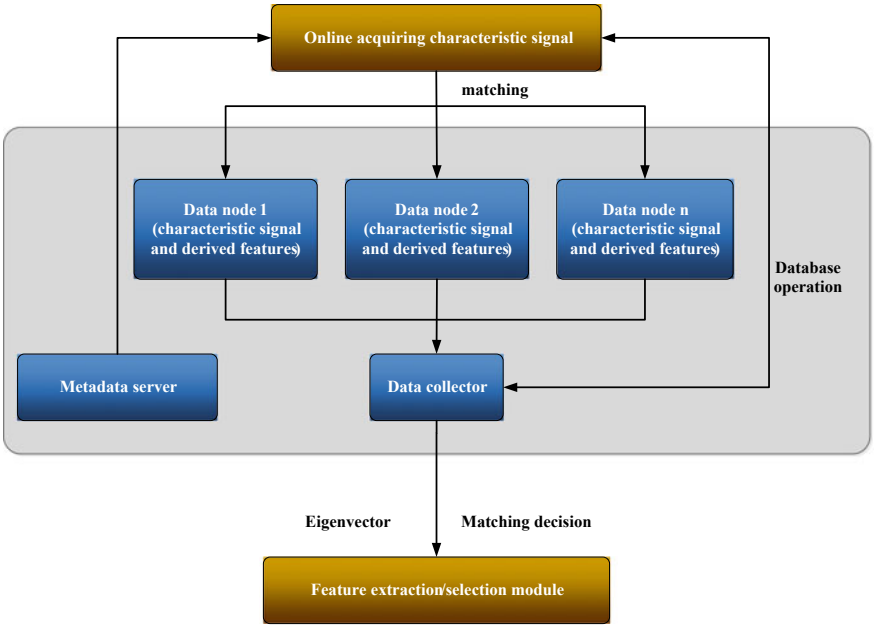


Fig. 8.21 Operation flow of distributed target classification and identification database

Bibliography

1. Ding J J. Target Recognition Techniques of Surveillance Radar [M]. Beijing: National Defense Industry Press, 2008.
2. Ma L. Review of Radar Automatic Target Recognition [J]. Modern Radar, 2011, 33(6):1–7.
3. Wu G X. Radar Target Features Extraction and Target Identification in Resonance Region [D]. Harbin: Harbin Institute of Technology, 2008.
4. Baum C E. On the Singularity Expansion Method for the Solution of Electromagnetic Interaction Problems[R]. AFWL Interaction Notes, Note 88, 1971.
5. Van Blaricum M L, Mittra R. A Technique for Extracting the Poles and Residues of a System Directly from Its Transient Response [J]. IEEE Trans on Antennas and Propagation, 1975, 23(6):777–781.
6. Jain V K, Sarkar T K, Weiner D D. Rational Modeling by Pencil-of-Function Method [J]. IEEE Trans on Acoustics, Speech and Signal Processing, 1983, 31(3):564–573.
7. Hua Y B, Sarkar T K. Generalized Pencil-of-Function Method for Extracting Poles of an EM Systems From Its Transient Response [J]. IEEE Trans on Acoustics, Speech and Signal Processing, 1989, 37(2):229–234.
8. Kennaugh E M. The K-Pulse Concept[J]. IEEE Trans on Acoustics, Speech and Signal Processing, 1981, 29(2):327–331.
9. Chen Y F, Nyquist D P, Westmoreland D, et al. Radar Waveform Synthesis for Single-Mode Scattering by a Thin Cylinder and Application for Target Discrimination [J]. IEEE Trans on Acoustics, Speech and Signal Processing, 1982, 30(5):867–880.
10. Sinclair G. The Transmission and Reception of Elliptically Polarized Waves [J]. Proceedings of the IRE, 1950, 38(2):148–151.
11. Brichel S H. Some Invariant Properties of the Polarization Scattering Matrix [J]. Proceedings of the IEEE, 1965, 53(8):1070–1072.

12. Huang P K. Radar Target Signatures [M]. Beijing: China Astronautic Publishing House, 1993.
13. Chen V C, Li F Y, Ho S S, et al. Micro-Doppler Effect in Radar: Phenomenon, Model and Simulation Study [J]. IEEE Trans on Aerospace and Electronic Systems, 2006, 42(1):2–21.
14. Bell M R., Grubbs R A. JEM Modeling and Measurement for Radar Target Identification[J]. IEEE Trans on Aerospace and Electronic Systems, 1993, 29(1):73–87.
15. Wang S G, Guan X P, Ma X Y, et al. A Method of Extracting Radar Target's Poles and the Poles' Characteristics [J]. Signal Processing, 2007, 23(4):516–520.
16. Wu N, Wang D W, Qin J M. Identification of Radar Targets with Pole Characteristics-Based Likelihood Ratio Test [J]. Journal of Air Force Radar Academy, 2009, 23(1):31–35.
17. Zhuang Z W. Research on Target Recognition of Frequency Domain and Polarization Domain for Radar [D]. Beijing: Beijing Institute of Technology, 1989.
18. Wang X S, Li Y Z, Dai H Y, et al. Research on Instantaneous Polarization Radar System and External Experiment [J]. Chinese Sci Bull, 2010, 55(10):937–944.
19. Xiao S P, Wang X S, Zhuang Z W. Aircraft Target Recognition Based on Polarization Invariant [J]. Journal of Infrared and Millimeter Waves, 1996, 15(6):439–444.
20. Zhuang Z W, Xiao S P, Wang X S. Radar Polarization Information Processing and Application [M]. Beijing: National Defense Industry Press, 1999.
21. Liu Y. Study on Moving Target Polarization Characteristic Measurement and Polarization Radar Anti-Jamming Techniques [D]. Changsha: National University of Defense Technology, 2011.
22. Wang B S, Du L, Liu H W, et al. Aircraft Classification Based on Empirical Mode Decomposition [J]. Journal of Electronics & Information Technology, 2012, 34(9):2116–2121.
23. Chen F. Radar Target Recognition Based on HRRP and JEM Signal [D]. Xi'an: Xidian University, 2009.
24. Du L, Bao Z, Xing M D. Analysis and Detection of Radar Echoes from Helicopters [J]. Journal of Xidian University, 2003, 30(5):574–580.
25. Chen X Y. Research on Radar Signature Extraction from Target with Micro-Motions [D]. Changsha: National University of Defense Technology, 2006.
26. Li K L. Research on Feature Extraction and Parameters Estimation for Radar Targets with Micro-Motions [D]. Changsha: National University of Defense Technology, 2010.
27. Xiang D P. Research on Micro-Doppler Echo Simulation and Micro-Motion Signature Extraction Technology [D]. Changsha: National University of Defense Technology, 2010.
28. Ding J J, Zhang X D. Studies of Modulation Characteristics of Propeller Aircraft Returns in the LRR [J]. Journal of Electronics and Information Technology, 2003, 25(4):460–466.
29. Ding J J, Zhang X D. Jet Engine Modulation Signatures of Propeller Aircraft in Air-Defense Radar Signals [J]. Journal of Tsinghua University (Science and Technology), 2003, 43(3): 418–421.
30. Ding J J, Zhang X D. Complex AR Bispectrum and Application to Target Classification in the Conventional Radar [J]. Signal Processing, 2002, 18(6):556–559.
31. Sun Y, Duan G R, Zhang M R, et al. Modified Aerodynamic Coefficient Models of Hypersonic Vehicle in Reentry Phase [J]. Systems Engineering and Electronics, 2011, 33(1):134–137.
32. Du L. Study on Radar HRRP Target Recognition [D]. Xi'an: Xidian University, 2008.
33. Ni J, Zhang S Y, Miao H F, et al. Target Classification of Low-Resolution Radar Based on Fractional Brown Feature [J]. Modern Radar, 2011, 33(6):46–48.
34. Li Q, Xie W. Target Classification with Low-Resolution Surveillance Radars Based on Multifractal Features [J]. Progress in Electromagnetics Research B, 2012, 45(1):291–308.
35. Liang H N. Study on Measurement Topography Using Polarization SAR Images [D]. Chengdu: University of Electronic Science and Technology of China, 2001.
36. Meng Q Y. Study on Wide-Band Polarimetric Radar Targets Recognition [D]. Chengdu: University of Electronic Science and Technology of China, 2007.
37. Zhang X L. Research on Anti-Stealth and Polarization Information Processing of Quad-Polarization Meter-Band Radar [D]. Xi'an: Xidian University, 2010.
38. Yao Y P, Shen J J, Zhou L Q, et al. Progressively Extended Distribution Strategy for Non-Relational Database [J]. Journal of Information Engineering University, 2013, 14(4):499–503.

Chapter 9
Cooperative Detection Metric Wave Radar Techniques



9.1 Overview

The wavelength characteristic of metric wave radar makes it have the advantages of anti-stealth, anti-ARM, and long detection range. However, because of its narrow bandwidth and wide beam, there are some limitations in improving angular resolution and locating precision by single metric wave radar. The metric wave radar adopts cooperative detection technique to enhance the performance of metric wave radar.

The cooperative detection metric wave radar consists of multiple metric wave radar transmitting/receiving node cooperative processing centers and high-speed communication links, shown in Fig. 9.1. Using spatial diversity and waveform diversity techniques, the receiving node is able to process the target echoes of multiple transmitting nodes. Using high-speed communication technique and high-performance computation technique, multiple cooperative detection nodes are combined through resource management and control into a cooperative detection metric wave radar system capable of high-effective interconnections and intercommunications. Based on such cooperative processing technology, the information detected by individual nodes will be processed jointly. In this way, there are obvious superiorities in stealth target detection, target location precision, ECCM, battlefield survivability, and etc.

Compared with the traditional metric wave radar, the cooperative detection VHF radar possesses the advantages as follows:

(1) Strong ability to detect stealth target: The cooperative detection metric wave radar can make effective use of the multi-direction scattering characteristic of stealth target, such as the scattering characteristic of lateral RCS being 20 dB larger than nose cone RCS, and can suppress the strong fluctuation of RCS with spatial position, greatly enhancing the ability to detect stealth target.
(2) Higher angular resolution: With the employment of multiple radar nodes deployed dispersively to distinguish target cooperatively or in short baseline to make coherent synthesis, the radar could achieve higher angular resolution, which improves the target location precision.

© National Defense Industry Press, Beijing and Springer Nature Singapore Pte Ltd. 2020

J. Wu, *Advanced Metric Wave Radar*, https://doi.org/10.1007/978-981-10-7647-3_9

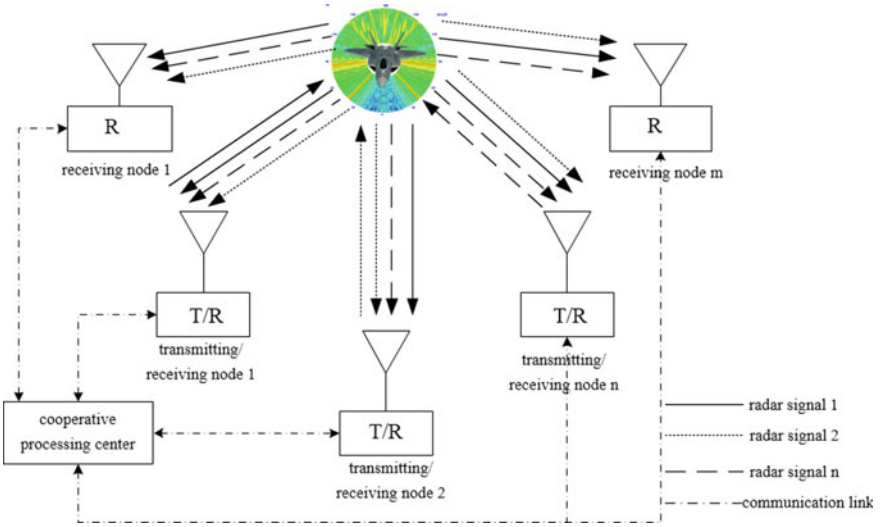


Fig. 9.1 Schematic diagram of cooperative detection metric wave radar composition

(3) Strong ECCM capability: Making use of the homologous correlation and multi-station cooperative processing can realize mainlobe jamming cancellation, which breaks through the technical bottleneck existing in monostatic radar.
(4) High economical efficiency: Effective detection of stealth target requires large radar power-aperture product, which results in high cost and poor mobility. The radar nodes of cooperative detection metric wave radar are relatively small and easy to manufacture, thus the cost is low.
(5) Good mobility: Each radar node possesses good mobility, so that the whole system has good mobility.
(6) Good flexibility: The radar nodes in the system are able to operate in self-transmitting/self-receiving form, bistatic/mutistatic form, MIMO form, and full-coherence mode. The whole cooperative detection metric wave radar can take a single form or be the hybrid of several forms above. Its configuration is flexible and changeable, that is, it can be deployed in either centralized mode or decentralized mode. Due to the flexibility, the system can be reconfigured dynamically with mission changing.
(7) Excellent scalability: The system detection capability can be expanded by adding the number of radar nodes; even the radar function can be expanded.
(8) Higher reliability: Multiple distributed radar nodes work jointly. Even if some radar node malfunctions, the system can still work.

9.2 Development Trend of Cooperative Detection Technique

Once the multi-radar cooperative operation mode was proposed, it become a development direction of modern radar detection techniques. A series of detection concepts were put forward such as cooperative engagement capability, MIMO radar, distributed full-coherent radar, and etc., which establish the foundation for the design and realization of cooperative detection VHF radar system.

9.2.1 CEC System Technique

CEC stands for "cooperative engagement capability". It is featured by fully making use of the superiorities of various platforms that are located at different places and equipped with different sensors and weapons, taking full advantage of the shared observation data (e.g., unfiltered range, azimuth, height, and Doppler) from every sensor on each platform, and maintaining the key characteristics of the data such as precision and real time. These data are integrated into the combat system of each platform and can be used in the same fashion as the data from the sensors of the platform itself. All combat platforms are netted in this manner to form an integrated theater defence system.

The initial intention of the CEC system is to solve the air defence issues in littoral operations of naval fleet. Its basic design is that the combat units share the data from each sensor in the battle group and the whole battle group works in a network manner so as to enhance the air defence capability greatly. Developed for years, US Navy equipped its aircraft carriers, Aegis destroyers, and cruisers with CEC system. At present, American multiple services conduct a joint investigation to introduce the CEC system into the Patriot missile system, corps air defence missile system, E-3 early warning airplane, theater high altitude air defence/ground based radar (THAAD/GBR) system, and etc., constructing a real seamless theater air defence and anti-missile system (Fig. 9.2).

CEC has three basic functions, i.e., accurate cueing, joint tracking, and cooperative engagement. In 1990s, with the CEC concept being introduced into ballistic missile defence system, new operation functions had been developed, that is, cooperative localization, beyond-visual-range combat, and cooperative discrimination. On the basis of CEC multisenor fusion tracking, Lincoln Laboratory proposed the fusion recognition theory. The observation data of distributed sensors at different bandwidths and different angles are fused coherently to generate ultra wideband, large rotation angle target 2D image, which significantly improves the target identification capability and precision.

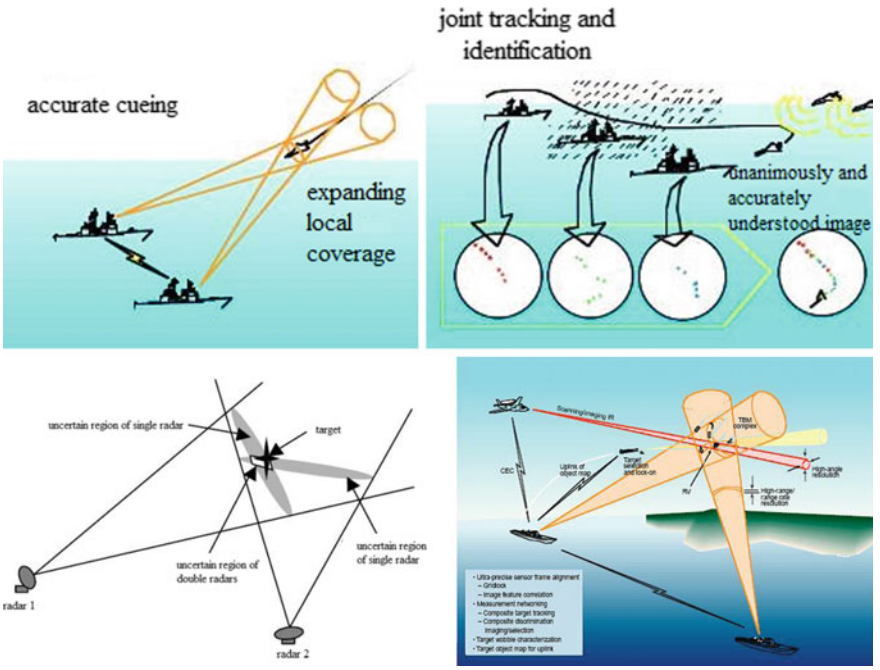


Fig. 9.2 Schematic diagram of CEC system functions

9.2.2 MIMO Radar Techniques

As a sign of new concept radars, multiple-input multiple-output (MIMO) radar nowadays has become the research hotspot in radar community. Different from the traditional phased array radar, MIMO radar has the advantages of multiple channels in space, added freedom of system, improved resolution of airborne target, effectively-resisted target RCS scintillation, and enhanced detection performance of system.

1. **Coherent MIMO radar techniques**

(1) Investigations on coherent MIMO radar in France and China

In the late of 1980s, French ONERA and Thomson–CSF Company jointly developed a prototype of synthetic impulse and aperture radar (SIAR), shown in Fig. 9.3. Actually, it presented the idea of coherent MIMO radar although the concept of coherent MIMO radar hasn't been proposed yet. It can be viewed as the rudiment of coherent MIMO radar. Whose basic ideas can be summarized as: ① The signals of individual nondirectional radiation elements are encoded to enable full-airspace isotropic illumination while using large antenna array; ② In the receiving system, the signal components radiated by individual radiation elements are decomposed according to the codes. Through time delay calibration via the element set in space, the signal



Fig. 9.3 SIAR prototype in France

components are recombined coherently to obtain the narrow pulses of target echoes, that is, the equivalent transmitting beams. However, for the reasons including budget, the SIAR development and experiment were terminated in the late of 1990s.

In China, the SIAR research was started in the early of 1990s and its experimental study was completed in 2000. After then, the demonstration and development of a practical system was initiated. In 2011, the first large practical SIAR system in the world was completed. It is also the first large practical MIMO radar system around the world.

(2) Coherent MIMO radar research in America

Sponsored by US Missile Defense Agency, MIT Lincoln Laboratory carried out the theory study and experiments of MIMO radar and developed L-band and X-band MIMO radar prototypes, as shown in Fig. 9.4. Then, the researchers of University of Florida and University of Washington carried out deep studies on transmitting/receiving joint adaptive algorithm, estimation of target parameters, and transmitting beam synthesis, which provides theoretical basis for the performance advantages of coherent MIMO radar.

2. **Noncoherent mimo radar techniques**

(1) Noncoherent MIMO radar research in New Jersey Institute of Technology

The concept of noncoherent MIMO radar was proposed firstly by the research team of New Jersey Institute of Technology (NJIT) in IEEE radar conference 2004. In their following work, deep researches on signal detection, estimation of target parameters, and waveform design were conducted. Their studies provide the theoretical basis for the performance superiority of noncoherent MIMO radar.

(2) Noncoherent MIMO radar research in University College London

C. J. Baker et al. of University College London made profound analysis about the performance superiorities of noncoherent MIMO radar in relation to traditional radar

from coverage, resolution, and location precision. They constructed a small experimental system using COTS products and carries out a number of target observation experiments and clutter measurement studies (Fig. 9.5).

Except for the above researches, the scholars of US Naval graduate school and University of Arizona also made deep theoretical studies on the cooperative operation mode and optimal detector.

9.2.3 Distributed Array Coherent-Synthesis Radar Technique

Distributed array coherent-synthesis radar system is composed of some mobile radar nodes and a center control processing system. These radar nodes are arranged in a mode with their beams directing at the same region. Through center control

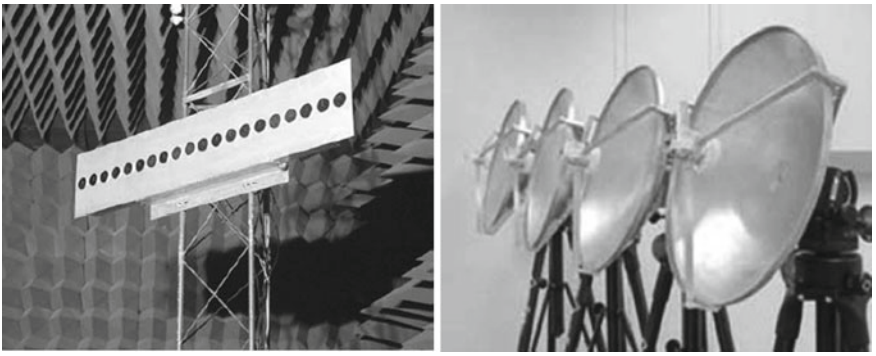


Fig. 9.4 L-band and X-band coherent MIMO radar prototypes developed by MIT Lincoln Laboratory



Fig. 9.5 Coherent experimental MIMO radar system of University College London



Fig. 9.6 Distributed array coherent-synthesis radar of Lincoln Laboratory

processing system, the radar nodes can realize joint coherent operation and signal-level coherent synthesis to form equivalently a large coverage detection radar system.

Lincoln Laboratory released a report in 2004 about distributed array coherent-synthesis radar to firstly open its preliminary study result. A paper released in 2006 by Lincoln Laboratory reported its important breakthrough: two wideband radars realized coherent transmitting and receiving completely, achieving the maximum gain of 9 dB (Fig. 9.6). Different from traditional radar, each radar node of the distributed coherent-synthesis radar transmits orthogonal waveforms. A radar node receives the echoes of other radar nodes while receiving the echoes of the radar node itself. By matched filter processing of all transmitted waveforms respectively and simultaneously, the phase and time delay of each echo is obtained. Then the receiving coherent-synthesis is performed to achieve the maximum system gain N^2 (N is the number of radar nodes). This is called as the receiving coherence mode. On the basis of the receiving coherence mode, when the time delay and phase estimations reach to some degree, each radar node starts to transmit in-phase waveforms. Controlling and adjusting the moment and phase of each radar node transmitting signal can realize both transmitting coherence and receiving coherence, i.e., full coherence, to achieve the maximum system gain N^3. This is called as transmitting/receiving coherence mode (Fig. 9.7).

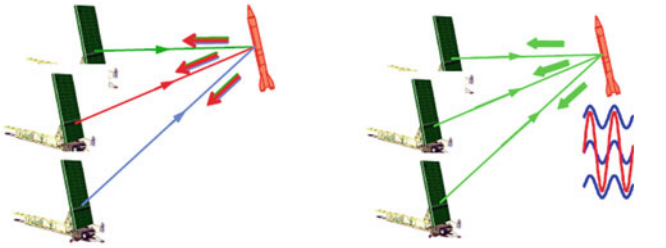
9.3 Typical Operation Modes

On the basis of system configuration and detection mission requirement, the cooperative detection metric wave radar is able to operate in several typical operation modes: self-transmitting/self-receiving, multiple-transmitting/multiple-receiving, and transmitting/receiving full coherence. Hereafter, we will analyze the connotation, information fusion mode, and performance of each operation mode.

9.3.1 Self-transmitting/Self-receiving Mode

When the cooperative detection metric wave radar operates in self-transmitting/self-receiving mode, each radar node works as a monostatic radar under the scheduling of the cooperative processing center. It performs pre-processing for the detected echo information. And the cooperative processing center conducts fusion processing of the information from each radar node to generate united track situation (Fig. 9.8).

Depending on the different levels of the information transferring from a single radar node to the cooperative processing center, the different processing methods, such as the track fusion, plot fusion, and distributed detection, can be used in the cooperative processing center. The plot/track fusion processes the plot information



(a) Receiving coherent gain N^2 (b) Transmitting/receiving coherent gain N^3

Fig. 9.7 Basic principle of coherent synthesis

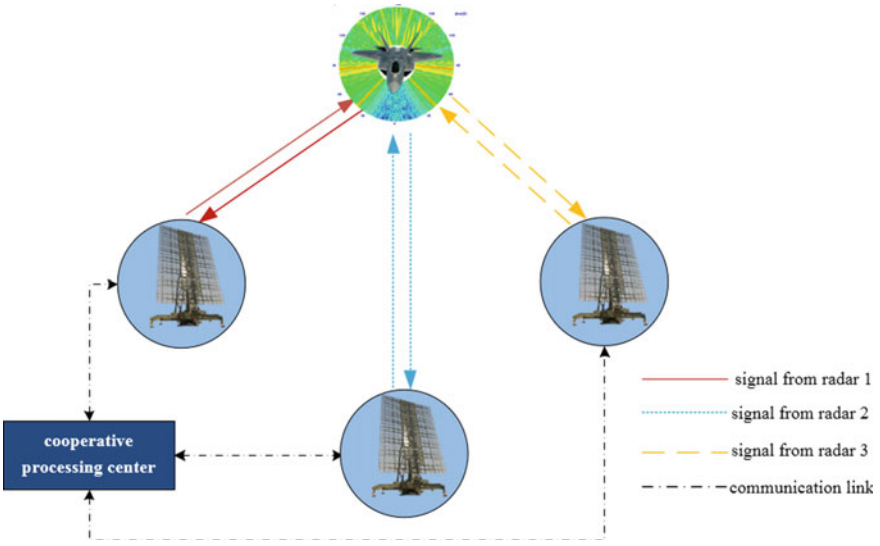


Fig. 9.8 Self-transmitting/self-receiving mode

sent from individual radars that are not determined to be target or not. The cooperation for all radars in the system can increase detection probability, enlarge detection range, and improve track quality. In distributed detection method, each radar node performs pre-processing for its observation data and then sends the data to the cooperative processing center in which the local observation data from individual radar nodes are synthesized and the final decision is given according to some judging criteria. In cooperative detection VHF radar system, distributed detection has the ability to improve the response speed and survivability and increase the coverage areas and the number of targets to be detected. Also the system reliability could be improved and a higher total SNR can be provided even some nodes are in failure. The typical net structure of the distributed detection algorithm is the feedback parallel structure (Fig. 9.9). The detection center feeds the final judgement result back to each radar node for use as one of the judgements baises to make local judgement at next moment. This structure can obviously improve the quality of the information provided by radar nodes.

Here, through simulation, we will make a comparative analysis on the detection performance and plot fusion detection performance of the cooperative detection metric wave radar system using the distributed detection algorithm and a single radar node in self-transmitting/self-receiving mode. The simulation conditions are: the radar nodes in the system are deployed dispersively, the target echoes satisfy decorrelation condition, the radar cross section of target belongs to type SWL-I, and

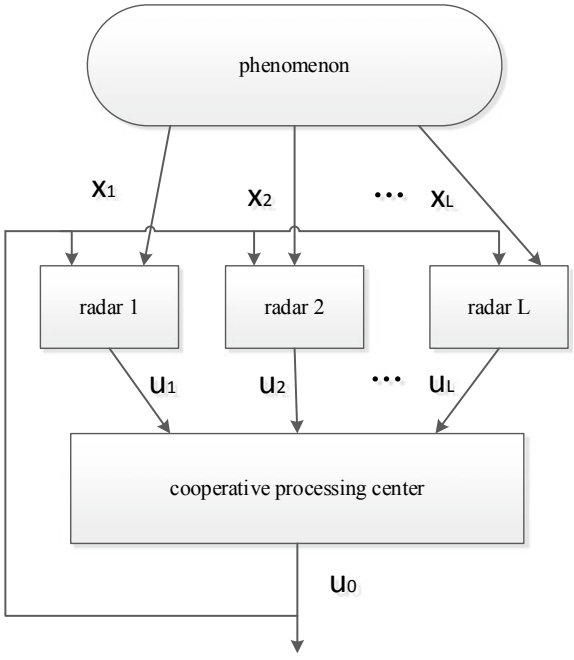


Fig. 9.9 Schematic diagram of the distributed detection algorithm with parallel structure

the radar cross sections related to different radar nodes are independent each other. The distributed detection model used in the system is

$$Pd = 1 - \frac{a^N}{\Gamma(N)\Gamma(M-N)} \int_0^T dy \int_0^1 dt G(y,t)$$
$$G(y,t) = \exp(-y[1-(1-a)t]) y^{M-1} t^{N-1} (1-t)^{M-N-1} \tag{9.1}$$

$$a = \frac{1}{1 + K * SNR}$$

where, M is the total number of pulses in distributed detection, N is the number of radar nodes (for two metric wave radars, N = 2), and K = M/N, the number of the pulses output from each radar.

Plot fusion detection adopts "or" fusion criterion. The detection probability and false alarm probability of the cooperative processing center are expressed as follows:

$$P_d = 1 - \prod_{i=1}^{N} (1 - P_{di}); \quad P_{fa} = 1 - \prod_{i=1}^{N} (1 - P_{fai}) \tag{9.2}$$

The simulation parameters are set to be: M = 16, N = 2, and K = 8. That is, for distributed detection, there are 16 pulses in total, 8 pulses in a radar node. When the false alarm probability is 10^{-6}, the detection threshold of the fusion center is 42.62 through calculation. The simulation results of detection performances of a single radar node, plot fusion detection, and distributed detection in the case of false alarm probability being 10^{-6} are given in Fig. 9.10.

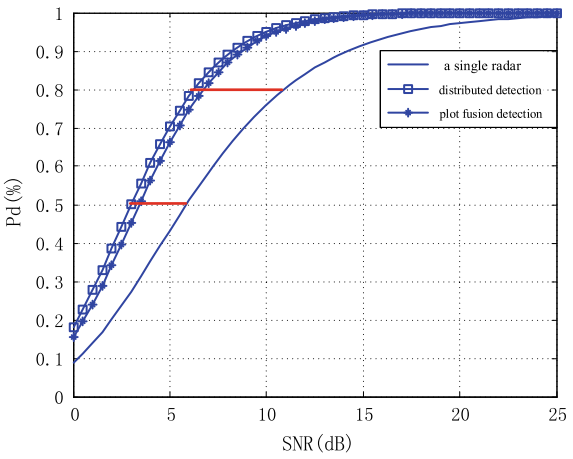


Fig. 9.10 Detection probability curves under false alarm probability of 10^{-6}

It can be seen from Fig. 9.10 that, when the false alarm probability is 10^{-6} and the detection probability is 0.5, the monopulse detectable SNR of distributed fusion detection decreases by 2.8 dB compared with single radar detection. When the detection probability is 0.8, the monopulse detectable SNR outperforms about 4.5 dB compared with single radar detection. The higher the detection probability is, the larger the detection gain is. Compared with plot fusion detection, when the detection probability is 0.5–0.8, the monopulse detectable SNR reduces by 0.4 dB.

As long as the nodes in cooperative detection VHF radar system possess target detection capability, they can work in this cooperative operation mode. In contrast to plot/track fusion detection mode, the distributed detection mode has lower information loss, but proposes higher requirements on the transmission bandwidth and time synchronization precision of the system.

9.3.2 MIMO Mode

When the cooperative detection VHF radar operates in MIMO mode, each of its radar nodes transmits orthogonal coded waveforms and works in N-transmitting/N-receiving MIMO operation mode to form N^2 channels to receive the echo of a target (Fig. 9.11). In short-baseline deployment, using coherent integration, the echo SNR can reach N^2 performance gain in theory compared with single radar. In long-baseline deployment, N^2 receiving channels correspond to different transmitting paths and receiving paths. Through reasonable deployment, the target signals in different channels may satisfy independence condition. The noncoherent integration detection model can then be used to enhance detection performance greatly.

We have conducted several experiments. Simulation analysis conditions: For the same receiving channel, assume that radar cross section of target belongs to type SWL-I, the target echo signals of different pulses in a scan are completely correlated, and the radar cross sections in different scans are independent each other. In MIMO mode, the target echo signals in different channels are independent each other. For the same receiving channel, coherent integration is adopted, while noncoherent integration is used in the case of 4 receiving channels.

Simulation parameters setting: $M = 32$, $N = 2$, and $K = 8$. That is, for noncoherent integration detection, there are 32 pulses in total, 8 pulses in a receiving channel; when the false alarm probability is 10^{-6}, the detection threshold of the fusion center is 66.40 through calculation. The simulation results are shown in Fig. 9.12.

It can be seen from Fig. 9.12 that, when the false alarm probability is 10^{-6} and the detection probability is 0.5, compared with single radar detection, the monopulse detectable SNR of signal-level fusion detection in MIMO mode decreases by 4.8 dB. In contrast to plot fusion, the monopulse detectable SNR is reduces by 2.4 dB. When the detection probability is 0.8, the monopulse detectable SNR reduces by about 7.9 dB compared with single radar detection, or 3.7 dB in contrast to plot fusion. The higher the detection probability is, the larger the detection gain is.

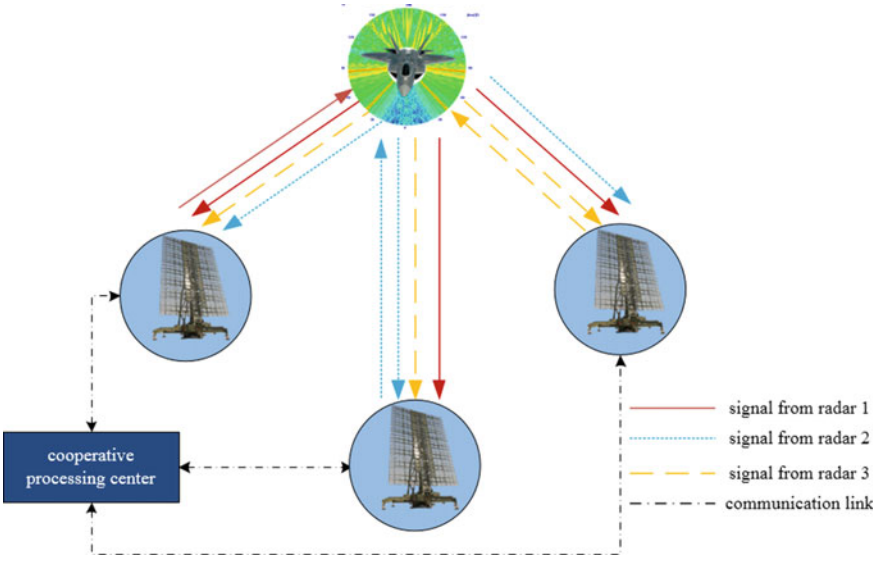


Fig. 9.11 Schematic diagram of MIMO mode

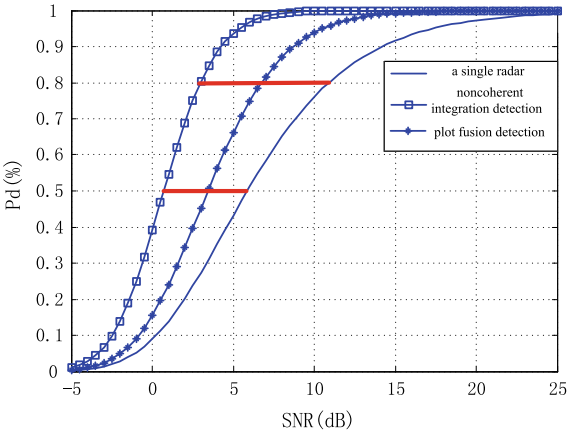


Fig. 9.12 Detection probability curves under false alarm probability of 10^{-6}

9.3.3 Transmitting/Receiving Full-Coherence Mode

Operating transmitting/receiving full-coherence mode, the radar nodes are arranged in such a way to meet "spatial correlation" distribution condition strictly. These nodes transmit in-phase waveforms. Controlling and adjusting the moments and phases of the radar nodes transmitting signals can realize both transmitting coherence and receiving coherence, i.e., full coherence. The SNR of target echoes can be increased N^3 folds at most.

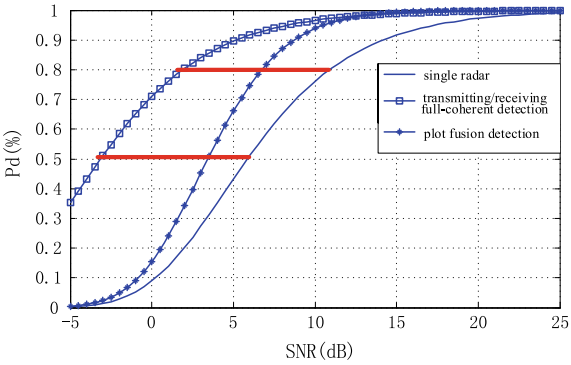


Fig. 9.13 Detection probability curves under false alarm probability of 10^{-6}

(1) Detection performance

Based on the radar detection equation, in transmitting/receiving full-coherence mode, the detection equation of the cooperative detection metric wave radar is

$$R_{\max}^4 = N^3 \frac{P_t \tau G_t G_r \sigma \lambda^2 F_t^2 F_r^2}{(4\pi)^3 k T_s V_o C_B L} \tag{9.3}$$

where, P_t, G_t, and G_r are respectively the transmitting power, transmitting gain, and receiving gain of each radar node.

Assume that two radar nodes operate in transmitting/receiving full-coherence mode, and there are 8 pulses. When the false alarm probability is 10^{-6} and the detection probability is 0.5, in contrast to plot fusion detection, the monopulse detectable SNR is reduced by 6.5 dB; when the detection probability is 0.8, it is reduced by 4.9 dB (Fig. 9.13).

(2) Angle measurement precision

The distributed array coherent-synthesis method is used to form an equivalent large-aperture antenna, so as to implement high-precision angle measurement. If n radar nodes are in linear arrangement and the phase centers of their antenna arrays are equally separated, then the horizontal pattern model of coherent synthesis is

$$|Y(\theta)| = \left| \frac{\sin(\pi kn \sin\theta)}{\sin(\pi k \sin\theta)} \frac{\sin(\frac{\pi}{2} m \sin\theta)}{\sin(\frac{\pi}{2} \sin\theta)} \right| \tag{9.4}$$

where, m is the number of array elements of a single radar array in horizontal direction, λ is the wavelength, D is the distance between the phase centers of adjacent radar nodes, θ is the angle, and k = D/λ.

According to the pattern expression, the null beamwidth is determined by the two nulls most approached by $\frac{\sin(\pi kn \sin\theta)}{\sin(\pi k \sin\theta)}$. That is, the two nulls satisfy $kn \sin\theta = \pm 1$, thus the null beamwidth approximates $\frac{2}{kn}$ rad and the 3 dB beamwidth approximates $\frac{1}{kn}$ rad.

When the pattern pointing direction is not the array normal direction, the mainlobe will widen and the distance between the mainlobe and the first grating lobe will enlarge. On the other hand, when the pattern pointing direction is the array normal direction, the mainlobe is the narrowest and the distance between the mainlobe and the first grating lobe is the least.

Simulation parameters: $m = 20$, $n = 2$, and $k = 50$; if calculate at the operating frequency of 240 MHz, then, when $k = 50$, the distance between the array centers of two radars is 62.5 m. The azimuth lobe pattern of single radar and the azimuth lobe pattern synthesized coherently by two radars are illustrated in Fig. 9.14.

It can be seen from Fig. 9.14 that, in the case of uniform weighting, the synthesized pattern has some grating lobes in the mainlobe width of single radar. The 3 dB beamwidth of single radar is about 5.07° and the coherently synthesized 3 dB beamwidth approximates 0.57°. Computing at the angle measurement precision being 1/10 of beamwidth, the direction measurement accuracy of single radar is about 0.5°. The angle accuracy could achieve 0.057° by employing coherent synthesis with the ambiguity eliminated synchronously. It is obvious that, by using coherent synthesis in angle measurement processing, the cooperative detection metric wave radar can improve the angle measurement accuracy significantly.

There are many methods to solve the angle measurement ambiguity. Here, we will introduce the simplest one. Choose proper baseline length of two radars in such a manner to make the angle measurement accuracy of single radar higher than the mainlobe beamwidth in coherent synthesis. Take the angle measurement result of single radar as the coarse measurement result. Then the synthesized beam is used to make high-precession monopulse angle measurement. The angle measurement accuracy achieved finally will be higher than the single radar about one order of magnitude.

To form the synthesized beam effectively, the arrays of the cooperative detection VHF radar must be calibrated so as to eliminate the amplitude and phase errors existed between different radar arrays and inside the arrays. The key to make the calibration between different radar arrays is the measurement of their relative positions, which can be realized by use of optical means, GPS, and geodetic survey.

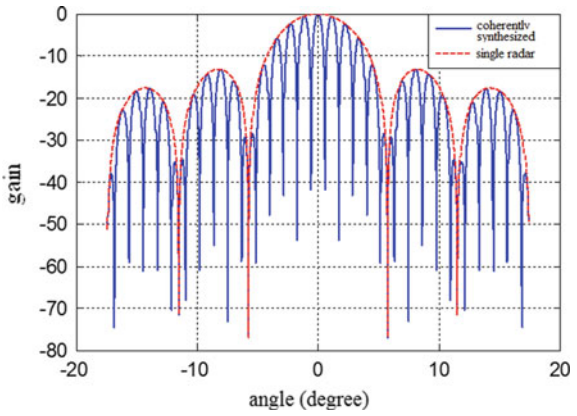


Fig. 9.14 Comprison between the azimuth lobe pattern of single radar and the coherently synthesized azimuth lobe pattern

Bibliography

1. CHEN Dejun, RAO Jie, SHAO Xijun. Radar Coordinated Detection Based on Information Grid[J]. Fire Control and Command Control, 2011(2):24–27.
2. LIU Zhanglin, CHEN Baixiao. Study on Maximum Likelihood Supper Resolution Height Finding Technique for Metric Wave Radar[J]. Radar Science and Technology, 2011, 9(4): 308–310.
3. SONG Shiping, Zhao Jianchuan. Cooperative Engagement Capability and Its Advance[J]. Ship Electronic Engineering, 2001(1):4–11.
4. Rivers B P, Puttre M. Victory at CEC: United States Navy Cooperative Engagement Capability, Development and Analysis[J]. Journal of Electronic Defense, 2001(9):20–26.
5. The Cooperative Engagement Capability[EB/OL]. [2010212205]. http://www.jhuap.edu/techdigest/td/td1604/aplteam.pdf.
6. Hammad A Khan, Wasim Q Malik, David J Edwards, et al. Ultra Wideband Multiple-Input Multiple-Output Radar[C]//Proceedings of IEEE Radar Conf, 2005(1):900–904.
7. Baker C J, Hume A L. Netted Radar Sensing[J]. IEEE Aerosp. Electron. Syst. Mag., 2003, 18 (2):3–6.
8. D. W. Bliss, K. W. Forsythe. Multiple-Input Multiple-Output (MIMO) Radar and Imaging: Degrees of Freedom and Resolution[C]//Proc. 37th Asilomar Conf. Signals, Systems and Computers, Pacific Grove, CA, 2003 (1):54–59.
9. E Fishler, A Haimovich, R Blum, et al. MIMO Radar: An Idea Whose Time Has Come[C]//Proc. IEEE Radar Conf. April 2004:71–78.
10. Mcharg J C, Cuomo K M, Coutts S D, et al. Wideband Aperture Coherence Processing for Next Generation Radar[R]. MIT Lincoln Laboratory, 2004.
11. Coutts S, Cuomo K, Mcharg J, et al. Distributed Coherent Aperture Measurements for Next Generation BMD Radar[C]// IEEE Workshop on Sensor Array and Multichannel Signal Processing, 2006:390–393.
12. Eli Brookner. Phased-Array and Radar Astounding Breakthroughs - an Update[C]//2008 IEEE Radar Conference, 2008:1–6.
13. Hai Deng. Polyphase Code Design for Orthogonal Netted Radar Systems[J]. IEEE Trans on Signal Processing, 2004, 52 (11): 3126–3135.
14. GAO Hongwei, CAO Zhe, Lu Yaobing. Study and Demonstration of Distributed Array Coherent Synthesis Radar[C]//12th China Radar Conference, 2012:129.134.
15. CAO Zhe, CHAI Zhenhai, GAO Hongwei. Technology and Tests on Distributed Aperture Coherence-Synthesizing Radar[J]. Modern Defence Technology, 2012, 40(4):1–11.
16. JIANG Wei, WU Siliang, YUAN Haojuan. Coherent Detection for Frequency Diversity Separated Sub-Array Radar[J]. Transactions of Beijing Institute of Technology, 2010, 30(1):96–80.
17. CHEN Genhua, CHEN Baixiao, YANG Minglei. High Accuracy 2-D Direction Finding Using Interferometric-Like L-Shaped Array[J]. Systems Engineering and Electronics, 2012, 34(01):17–23.
18. CHEN Genhua, CHEN Baixiao, YANG Minglei. High Accuracy 2-D Angle Estimation Using Distributed Coherent Arrays[J]. Journal of Electronics & Information Technology, 2012, 34(11):2621–2627.
19. CHEN Baixiao. Modern Radar System Analysis and Design[M]. Xi'an: Xidian University Press, 2012.
20. CHEN Genhua. Study on High Accuracy Angle Estimation for Distributed Subarrays Antennas VHF Radar[D]. Xi'an: Xidian University, 2013.
21. Ma Peng, Zhang Ke, Hong Zhenqing, et al. Array Optimizing in Distributed Coherent MIMO Radar Based on Multi-Target Cramer-Rao Lower Bound[J]. Journal of Data Acquisition and Processing, 2012, 27(4):410–416.
22. Zhao Guanghui. Study on Sparse Array Meterwave Radar Based on SIAR[D]. Xi'an: Xidian University, 2008.

Chapter 10
Structural Design of Large Metric Wave Radar



10.1 Introduction

Radar structural design takes an important part of radar development, determining the mobility, reliability, security, environment adaptability and manufacturability of a radar, and playing an important role in the performance and quality. As metric wave radar technology is developing, structure of metric wave radar is also significantly changing. According to telecommunication regime, metric wave radars are divided into 2D metric wave radars and 3D metric wave radars, their difference is whether having a height finding capability; according to structure, divided into array metric wave radars and aperture sparse metric wave radars, the array metric wave radar is a large planar array radar, and the aperture sparse radar uses tower-type array antennae, which can randomly be set up on a flat area; according to mobility, divided into mobile metric wave radars and fixed metric wave radars, the mobile metric wave radar can use a vehicle chassis for transportation, and because of the large array, the fixed metric wave radar usually doesn't use the mechanical scanning mode and can't be transported.

At the beginning, most metric wave radars were 2D radars, using small antenna aperture and sparse trussed type antenna structure. Their requirements of stiffness and mobile set-up were low. The advanced 3D metric wave radar uses digital phased array and super resolution signal processing, and has some new structural features: (1) large antenna aperture, increasing requirements of radar power, and contrast to a traditional 2D radar's 100 m^2 antenna aperture, the antenna aperture of a mobile 3D metric wave radar is more than 200 m^2; (2) instead of traditional concentrated emission metric wave radars, the digital phased array modules, many accessories and cables are put on the antenna, leading to a large number of front equipments and more complex structure, so the focus of the metric wave radar antenna design is suitable overall layout; (3) as a result of the 3D radar's height finding capability, the deformation precision of the array is improved from meter level to millimetre level, and with the antenna aperture increasing, it is very important to make the deformation precision achieve a high level; (4) the requirements of mobility, to a mobile metric

© National Defense Industry Press, Beijing and Springer Nature Singapore Pte Ltd. 2020

J. Wu, *Advanced Metric Wave Radar*, https://doi.org/10.1007/978-981-10-7647-3_10

wave radar, deployment and roll-up modes of the antenna element are improved from manual and semi-manual modes to auto modes, and the mobility requirement is also improved from several hours to less than 1 h; (5) high environment adaptability requirements, the survivability has to be enhanced in the bad weather, for example, in high wind, the antenna of a 3D metric wave radar has significantly larger wind drag coefficient than a 2D radar, making the overturning moment of a large mobile wave radar rapidly increased from less than 490 kN m to more than 980 kN m, and strictly challenging the security of antenna design. Moreover, the antenna array of a metric wave radar is exposed, and usually don't have a protective radome, so in the bad weather, it is very important to seal antenna elements.

At present, the structure of metric wave radar is trending to high precision, high automation, high reliability and low cost. This requires that as the power and size of the advanced metric wave radar antenna are increasing, the radar power and precision of the array are higher and higher; the deployment time is shorter and shorter, the automation is higher and higher; the reliability and service life of the radar are higher and higher, working in all-weather and all-day; the radar's operating and maintenance cost is lower and lower.

When advanced metric wave radars are developing, we have to encounter some new technology problems, including formative design technology, safety design technology, auto-erecting technology and cooling technology, etc. We must explore, study and break through important problems, improving the structural design of advanced metric wave radars.

10.2 Overall Design of Metric Wave Radar

10.2.1 Outline of Overall Design

The overall structural design is the key element of radar product development. The system structure participates in the full development process, including feasibility study, system structure scheme demonstration, key technology breakthrough, prototype development, system assembly and joint test, product typification evaluation and after-sale service.

The basic requirements of overall structural design involve technical parameters, standardization and mechanics engineering designs, and the mechanics engineering designs include mechanical structure and modelling design, reliability design, thermal design, anticorrosion and protection design, vibration isolation and cushioning design, electromagnetic compatibility (EMC) design and manufacture ability design.

10.2.2 Overall Layout Design

The overall layout is the most important part in the overall structural design, mainly including position layout, partition of elements, overall layout (the relative location and assembly relationship of each element), interface and interface module designs etc. When designing overall structural layout, we must make the equipments compact, use integration design methods, and strictly control the centroid position of top loading, especially the antenna structure. When the quality and the size of the electronic equipment and other electronic devices are controlled and confirmed, according to their respective functions and the relation to each other, we can design the layout of the working state and transportation state of the upper units from top to bottom, select the mode of state transformation, and repeatedly check the mobility and stability indices until the requirements are finally met. In mobile 3D metric wave radar, the focus and difficulty of overall layout design are layout design of the antenna vehicle unit. The antenna vehicle unit is comprised of a radar bearing platform with a transportation chassis function, an antenna pedestal and a rotary turntable, a large tonnage lifting mechanism, and an antenna system.

Wind resistance stability is the first problem to be focused on in the layout design of the large metric wave antenna vehicle. According to the radar scale, we can select the wind resistance mode. When the scale of the radar is within 300 m^2, the overturning moment is not more than 200 ton m, and the requirement of maneuver index is high, the wind resistance method is the anti-overturning legs with large span to enable stability on the ground, and the anti-overturning legs are arranged around the chassis, using the folding/deploying mode to improve the mobility of the antenna unit. When designing the leveling legs layout, we also consider the outline size and the center of gravity of radar in lodging state, working state and transportation state. The position of the center of gravity must fall within the range which the leveling legs enclose, to make the antenna operate safely and reliably. If the radar is too large, we recommend to use the fixed array.

In order to improve the dynamic pointing precision of the radar, the chassis rigidity should be as high as possible. At the same time, to provide the upper structure enough space, the height of its loading surface is also required to be as low as possible. In order to coordinate the pair of contradictions, when designing the overall layout, we need to determine the height of the chassis and the specific stiffness requirements. For the chassis of a large metric wave radar, we can use the layout that makes the leveling legs and the anti-overturning legs apart. This method uses the leveling legs to provide leveling function, while improving the stiffness of the radar chassis.

When the weight distribution of the antenna vehicle is carried out, the weight of all the equipments on the array surface should be strictly controlled. The chassis of the antenna vehicle should be heavy and stable, and the equipments above the turntable should be rigid and light. The light antenna is beneficial to reduce the scale of the lifting mechanism and the azimuth driving mechanism, so as to control the overall weight of the antenna vehicle unit. The heavy equipments on the antenna are arranged near the bottom of the radar antenna or near the rotation center, so as to reduce the

inertia of the antenna. We should choose the suitable antenna structure and layout, as large as possible section stiffness, and reliable connection structure design. Because the antenna array of the large metric wave radar is very large, multiple transportation units are needed to transport the antenna. The main bearing framework is arranged on the antenna vehicle. When the antenna surface is transported, it is moved to other vehicles, and connected with the main bearing framework by fast-locks.

In order to improve the stiffness of the antenna array, the supporting points of the antenna should be as high as possible in the working state. But because of the limit of the lifting mechanism, we can consider to set the auxiliary supporting structure for the antenna. At the same time, the chief designer of the telecommunications system can adjust the elevation angle of the antenna and suitably deploy equipments to ensure the center of gravity of the antenna near the rotation center. In order to improve the mobility, the auxiliary supporting structure can be driven by automatic driving mode. The mechanism itself can lock, or the driving mechanism has safety lock, to ensure the stability of the supporting mechanism under the large wind.

10.2.3 Radar Erection and Assembly

The mobility requirement of modern military ground radar is higher and higher. After the radar is transferred, we must enable the conversion between transportation state and working state in the given time, and the rapid erection and assembly are important problems in the overall design of radar structure. When the site transition is carried out, the erection of large radar generally includes the following steps: the antenna unit in place—the separation of the tractor and the trailer—connecting the units by the cables, powering the units—expanding the legs of the antenna vehicle platform—leveling the legs—expanding the bearing framework, locking—transferring the antenna among the different units, assembling—connecting the antenna units with the cables—the antenna automatic lifting—unlocking the turntable—turning on the antenna to rotate. The disassembly process is opposite. The maneuverability requirement of the large 3D metric wave radar has been significantly improved, usually within 1 h.

In the overall design, we need to decompose the time index of each step, and determine the specific technical requirements: the makeup of the radar posture conversion mechanism, the size of the structure and the interface, the mode of action and the driving force, to make the automatic erection mechanism stably, coordinately and reliably operate and lock, and do not interfere with the other equipments and components.

Taking a large mobile 3D metric wave radar as an example, the antenna array needs to occupy a number of transportation units. When the radar site is set up, the antenna subarrays are hoisted and transferred among different transportation units, taking up the most time. In the overall design, the automation method is adopted to significantly improve the erection efficiency. In structural design, when manually driving the folding and locking mechanisms, we should pay attention to the

accessibility and operational safety in the erection process. Besides, the 3D radar antenna array has a large number of cables. In the early design, a large number of cables need to be suitably combined to reduce the number and time of disassembly, effectively shortening the erection time of the transferred radar. The automatic erection also includes the fully automatic expansion and leveling of the bearing multi-leg system of the radar platform, the expansion and folding of the auxiliary supporting legs of the antenna, the expansion/folding of the antenna framework, the automatic erection/disassembly of the large antenna. The Sect. 10.3.3 gives the details.

10.2.4 Transportation and Packing Design

Mobile metric wave radar usually uses the highway and railway transportation. The antenna aperture of a large metric wave radar is hundreds of square meters. It is necessary to use a small number of transportation units to complete the loading of the antenna, and make full use of the size and bearing potential of each transportation unit.

In the highway transportation state, the metric wave radar is comprised of multiple transportation units, including the antenna frame transportation units, the antenna subarray transportation units, the electronic equipment transportation units and the power station transportation units. The weight, size, axle load distribution and passing ability of all highway transportation units meet GJB2948-97 “transportation loading size and weight limit”, GB1589-2004 “highway vehicle outline size, axle load and quality limit”, JTGB01-2003 “highway engineering technical standard”, GB7258-2004 “motor vehicle operation safety technical condition”, JTG D60-2004 “general specification for highway bridge and culvert design” (The first or second grade highway bridge and culvert are 5.0 m high, and the third or fourth grade highway bridge and culvert are 4.5 m high), and can successfully pass the third grade highway (The two-lane highway is 6.5 m wide, the speed is 30 km/h, the minimum turning radius is 15 m, the maximum longitudinal gradient is 8%, the side slope is 20%, the wharf approach slope is 8.9–10%, the bridge longitudinal slope is less than 4%, and the bridge head approach longitudinal slope is less than 5%).

In the railway transportation state, it can be transported by the flatbed trucks, and when transported, is not beyond the loading limit of basic goods. All the transportation vehicles are separately suspended and reinforced on the train. The transportation pallets of the antenna subarrays, the electronic equipment shelters and the power stations are directly placed and reinforced on the train platform.

The radar packaging design should be convenient for transportation, loading and unloading, storage, use and management. If special packaging containers and loading/unloading equipments are needed, the design constraints should be determined.

10.3 Key Technologies in Structural Design of Metric Wave Radar

10.3.1 Antenna Framework Configuration Design Technologies

The antenna structure is an important part of radar products. The configuration of the antenna framework plays an important role in the design of the structure, and even to a great extent, it has become a distinct mark of the whole radar. Although the size of its aperture is subject to the telecommunication indices, how to choose the appropriate structure, to reasonably reduce the weight, to address the sharp contradiction between the rigidity and the quality, to choose the optimal structure scheme and to realize the reasonable design of the whole radar is the duty of the structural designers.

10.3.1.1 Aesthetic Configuration Design

For a complex and large military metric wave radar with a complex structure, the configuration design should pursue the design concept combination the function and the space aesthetics into one, emphasize the sturdiness of the military equipment, and achieve the perfect unity of the advanced technology feeling and the military temperament in the metric wave radar system. The idea is based on the aesthetic principles and expressive techniques of spatial configuration, including:

(1) Unity and change

For the metric wave radar, especially the fixed metric wave radar, the antenna subarrays has large volume and large number, so the antenna arrays of most metric wave radars are very large. The subarrays are arranged regularly on the hundreds of square meters, and the visual senses of order and oppression are felt. On the other hand, the auxiliary equipments such as the lightning rods, the blanking antennas, or the small antenna arrays of the second radar arranged at the bottom, provide the highly unified array with additional varying elements. As shown in Fig. 10.1, the Russian "Voronezh-M" fixed radar has the different color blocks on the antenna array, which not only helps the radar stealth in the open area, but also perfectly combines the unity and change into its spatial configuration.

(2) Symmetry and balance

In mobile metric wave radar configuration, the aesthetic principle of symmetry and balance is particularly evident. Due to the limitation of the area and stability of the vehicle platform, the deployable antenna should be symmetrical as far as possible along the central axis, so as to ensure the center of mass of the antenna on the central axis, reduce the risk of the overturning of the vehicle platform, and also make the modeling have civilized and sturdy visual senses. Moreover, if the structure can not be completely symmetrical (Fig. 10.2), for the antenna subarrays with different



Fig. 10.1 Russian "Voronezh-M" fixed metric wave radar

structures, the mechanical balance is satisfied, and the antenna's overall visual layout should be stable and balanced along the central axis.

(3) Contrast and harmonization

As shown in Fig. 10.3, a foreign fixed metric wave radar, the frame type antenna array is located on the cement base, and a row of equipment rooms are at the rear of the base. The antenna array and the cement base, the equipment rooms form a virtual-real contrast, which highlights the lightness of the antenna and the solidness of the base. Although the whole radar is large, the sense of body volume is greatly weakened. At the same time, because of the great disparity between the antenna



Fig. 10.2 A metric wave 3D radar made in China



Fig. 10.3 A foreign fixed metric wave radar

array and the base, to reconcile this strong contrast, the control building with the dark walls stands in the middle of the equipment rooms, serving as a link and a transition between the antenna and the bottom equipment rooms. This makes the whole radar system not only tall and straight, but also have a table visual image.

(4) Cadence and rhythm

The configuration of the metric wave radar mostly is relatively sparse frame type. As the supporting frames of the antenna array, they usually have the longer distance apart and are arranged in a straight line, such as the US OTH-B over the horizon radar, as shown in Fig. 10.4.

The supporting frames with great structural senses and the "white" between the supporting frames alternately repeat combination, which functionally ensures the windward blowing through the supporting frames, to reduce the wind resistance of the antenna array and make a sense of strict and orderly rhythm of the configuration.

10.3.1.2 Configuration of Bearing Structural Parts

1. Configuration optimization

In the stage of the overall scheme demonstration of the radar structure, in addition to the necessary aesthetic design, we also need to considerer several aspects according to the antenna electrical performance, the working state, the mechanical performance, the reliability and the manufacturing process requirements. The configuration optimization is based on satisfying the structure and function of the radar, and designs the optimal force transfer path and material distribution of the structure. The configuration optimization is at the initial stage of the design of the radar mechanism. Although it does not involve the size design of the specific structure,



Fig. 10.4 US OTH-B over the horizon radar

the overall consideration of the product's performance (array size, equipment layout, maintenance space, stiffness, strength, weight, etc.) can be carried out by the configuration optimization, which can make the design in the right direction at the beginning and avoid most repeats at the final stage of the design, so as to shorten product design cycle and save design cost effectively.

At present, the topology optimization is mainly used to optimize the configuration of radar. As a high level optimization design technology, the topology optimization theory has been developing rapidly in the past twenty years. All kinds of new theories and computing methods are constantly emerging, and have been applied to the fields of automobile and aerospace. Topology optimization is a mathematical method, which can transfer the external loads to the positions of the structural support in a given space structure, and make the performance of the structure optimal. It not only optimizes the shape of the structure's boundaries, but also optimizes the number and distribution of the holes within the structure. Some common finite element softwares such as OPTISTUCT, TOSCA and ANSYS, provide the topology optimization simulation modules to process and calculate before and after the topology optimization. For example, in Fig. 10.5, in order to obtain the antenna framework which has the simple structure, the clear force transfer path and light weight, the configuration of the antenna framework is optimized by the finite element software in the scheme stage. The initial model of the optimization is the trapezoid supporting structure. The maximum deformation is the constraint premise, and the minimal material is the optimal goal. In the trapezoidal design space, the optimal material area distribution

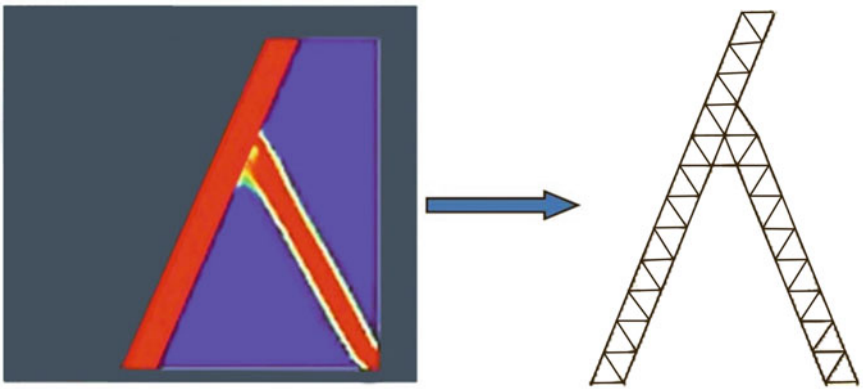


Fig. 10.5 The topology optimization diagram of the antenna framework configuration

map is achieved by the topology optimization. On this basis, through engineering feasibility analysis, we finally get the "人" (a chinese character, meaning human) font structure which has the concise configuration and meets the requirements of the force transfer path.

2. Particular structural form

The main function of the antenna framework is to install and fix the antenna subarrays, and ensure the accuracy of the array under loading. Considering the result of the configuration design and the topology optimization based on aesthetics, we can reasonably choose the particular form and material of the bearing structure. At present, the metric wave radar bearing structure mainly has the following several forms:

(1) Tower mast structure

In general, the tower mast structure is widely used as a radar bearing structural form. Generally, the structure is high, the cross section is relatively small, and the horizontal load (especially the wind load) is the main basis of the structural design. According to its structural form, it can be divided into two kinds: the pulling mast structure and the self supporting tower.

The stability of the pulling mast structure depends on the ropes, because of the support of the ropes, the mast can be thin and light. The body of mobile mast antenna is usually assembled by several sections. When erected, it can be raised one by one, and when transported, it can be divided into several sections which are not long. The mast not only supports the antenna, but sometimes the body of the mast is also used as an emitter. In general, the steel cords or steel strands are used as the ropes, and the layout is divided into two kinds: three ropes and four ropes, which are respectively applied to the triangular section mast and the quadrangular section mast. The elevation arrangement of the ropes mainly includes the layers and the elevation design. It is necessary to comprehensively consider the overall stability,



Fig. 10.6 A pulling mast radar structure

the installation and maintenance workload, the number of the ropes and the total weight of the ground anchor. Figure 10.6 is the structure of a large radar. The main mast adopts truss structure, and both sides use the ropes to increase the support, which makes the whole structure stable and the wind resistant capacity excellent.

A self-supporting tower is a space truss structure whose cross-section is a positive polygon (a triangle, a square, a hexagon and an octagon). The cross-section size varies with the height, and a suitable curve shape can be determined according to the stress condition, as shown in Fig. 10.7. The tower is usually used to support antennas, such as the radar antenna tower.

(2) Truss structure

The truss structure is a structure composed of the rods connected to each other by hinges. In general, the truss is comprised of the straight rods, and has a plane or space structure with triangular elements. The truss components are mainly subjected to axial tension or pressure, which can make full use of the strength of the material and reduce the weight and rigidity of the material in a larger span than the real abdominal beams.

In the truss structure, the stress of each truss component is mainly dominated by unidirectional tension and pressure. Through the rational arrangement of the upper and lower chords and the abdominal rods, the bending moment and the shear force distribution in the structure can be adapted to the structure. The structure



Fig. 10.7 A self supporting radar tower

is flexible and widely used. Contrast with the real abdominal beams (that is, the beams that we generally see), in the bending aspect, because the internal force arm is increased by placing the cross sections which are tensioned and compressed in the upper and lower ends, the truss beams with the same amount of material achieve more bending strength. In terms of shearing resistance, the shearing force can be gradually transferred to the bearing by rationally arranging the abdominal rods. In this way, whether bending resistance or shearing resistance, truss structure can make full use of material strength. The more important meaning is that through the effect of transverse bending, it transforms the complex stress state within the real abdominal beams into the simple tension stress state within the truss components, so that we can intuitively understand the distribution and transfer of the force, and facilitate the change and combination of the structure. Figure 10.8 is a typical truss structure, which is supported by triangular truss. Its characteristics include light and compact structure, great rigidity, and high stability.

(3) Rigid frame structure

The rigid frame is a structure composed of several straight rods with rigid nodes (part of which can be hinge nodes). Contrast with truss structure, the rigid frame structure bearing capacity is greater, the constraint deformation ability is stronger, the structure is relatively simpler, the construction is more convenient, but the rods coordination ability is weak, the force transmission is poor, and the amount of steel is relatively larger. In the design of the rigid frame structures, the rods connection is an important part in the design of such structures. The connection methods concern the force transmission and use requirements of the structures. Therefore, the rational selection of the rigid frame structure connection method should not only make the



Fig. 10.8 A long range radar station with a truss structure

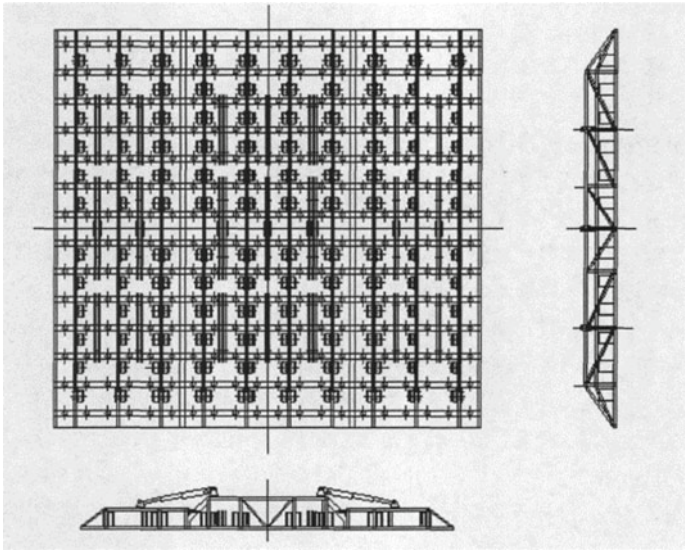


Fig. 10.9 The structure of an antenna array surface

force transmission clear, concise, reliable and safe, but also make the structure simple, the material saving and the construction convenient. The 3D metric wave radars mostly use planar array antennas, and the antenna faces are more regular. The primary and secondary beams are rigidly connected to form a well pattern structure, whose shape is like a vertical and horizontal "door plank", as shown in Fig. 10.9.



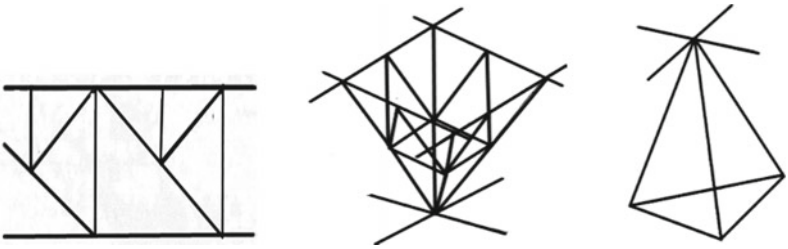
Fig. 10.10 The plate and shell structure of a type of radar

(4) Plate and shell structure

Plate and shell structure is a structure whose thickness is smaller than the length and width. A plane surface is the plate, and a curved surface is the shell. In the radar structure, the thin shell structure has beautiful shape, simple force transmission line, and great bearing performance. In addition to bearing structure, it can maintenance the structure, combing the two functions into one, and saving more materials. In the design of the radar structure, the wind resistance of the plate and shell structure is not very well, it is generally applied to the smaller size structures and components. Figure 10.10 is the radar antenna shell structure designed by the plate structure. This structure is generally not used in the large metric wave radar structure.

(5) Grid structure

The grid structure is a double-layer or multi-layer high-order statically indeterminate space system composed of multiple nodes connected in a certain grid form. It is usually made of the steel pipes or profiled steel materials. The grid structure can be classified into planar truss system, triangular pyramid system, four pyramid system and six pyramid system. Its general structure is shown in Fig. 10.11. Because of spatiality, simple force transmission, and good bearing performance, the grid structure has the advantages of large rigidity, great aseismic performance, light weight, easy



(a) planar truss system (b) four pyramid system (c) triangular pyramid system

Fig. 10.11 The grid structure system

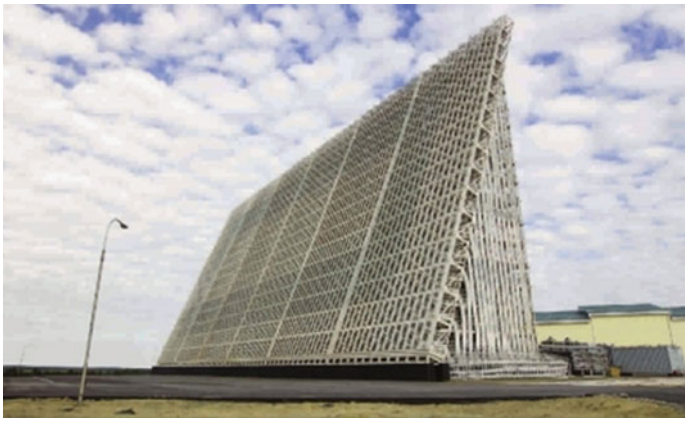


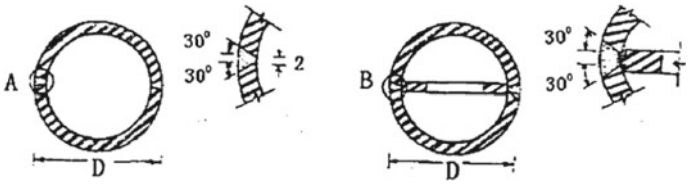
Fig. 10.12 Grid bearing radar antenna

fabrication and installation, and low cost. It has been widely used in the large metric wave radar.

Figure 10.12 is the antenna structure of a type of radar. The structure of the antenna adopts space grid structure, and has excellent overall stiffness, wind resistance capability and aseismic performance.

10.3.1.3 Key Connection Configuration Design

The bearing structure of the metric wave radar is mainly composed of components (such as rods, beams, trusses, etc.) which are made up of plates and section steels through necessary connections, and then form a whole structure through a certain installation. The joint nodes play the role of connecting the components and transferring the internal force in the formation of the bearing structure, and also play the role of transferring load at the joints of different parts, so the nodes are an important part of the bearing structure. When selecting key connection configurations, we need to



(a) non-ribbed form (b) ribbed form

Fig. 10.13 The welded hollow sphere nodes

comprehensively consider different aspects, including mechanics, machining, manufacturing, material and construction. At present, the connection points of the metric wave radar mainly include spherical nodes, plate nodes, tube nodes and intersecting nodes.

1. Spherenode

The sphere node is used most widely in the radar bearing nodes. It is often used for the intersection of three or multi direction components. According to the connection forms of the components, it can be classified into three types: welded hollow sphere node, ordinary bolt sphere node and new type bolt hollow sphere node. Of them, the welded node is mostly used in permanent rigid frame bearing components of the radar structure, and bolt node is mostly used in detachable truss components. The sphere node has large stiffness and great adaptability. Because of the non directional property of the sphere, the node is subjected to uniform force and has the advantage of automatic centering, not producing eccentricity. The main disadvantage is that the structure of the node is complex and consumes time and materials.

(1) Welded hollow sphere node

The node is made of two round steel plates, which are manufactured into two semicircular spherical shells by hot or cold pressure, and then welded to form a sphere structure. This is classified into ribbed form and non-ribbed form, as shown in Fig. 10.13. When the sphere diameter is too large or the internal force of the rod is large, the rib stiffener can be welded in the middle of the two hemispheres to increase the rigidity and strength of the sphere. The rib stiffener is usually placed in the maximum stress plane, and the mid material is removed to reduce the self weight of the structure. The physical structure of a welded hollow sphere node is shown in Fig. 10.14.

The structure of the welded hollow sphere node does not require special surface treatment for the rods and the spheres and complex processing for the nodes, so is connected simply. This advantage is more prominent when the nodes of the intersection are more. The sphere node has an isotropic structure. The bearing of the node is reasonable and the force transfer path is clear. The single welding seam makes the node stiffness larger and the overall stability better. Therefore, this kind of node is widely used in the connection of all kinds of grids.



Fig. 10.14 The physical drawing of a welded hollow sphere node

(2) Ordinary bolt sphere node

The bolt node is made up of bolt connections, and mostly used for the detachable connection and the connection structure of the framework itself. The advantage is that the assembly and disassembly is simple. The disadvantages are that the manufacturing process is increased and the section of the component is weakened. The ordinary bolt sphere nodes consist of bolt spheres, steel spheres, pins, bushings, high strength bolts and cone head components. The bolt sphere nodes have definite bearing, and the spheres have no directivity. They can connect with any rod in any direction without eccentricity. The advantages are strong generality and high degree of standardization. The disadvantages are the complex structure of the node, the large amount of steel, and the high requirement of the process, and there are the long force transfer path in the mechanical properties and the stress concentration in the joint section of the pins, as shown in Figs. 10.15 and 10.16.

(3) New bolt hollow sphere node

The new bolt hollow sphere node is mainly composed of regular shells, cover plates, bolts, inner and outer gaskets and cone heads, as shown in Fig. 10.17. Compared with a solid sphere node, the hollow spherical node is easy to construct and

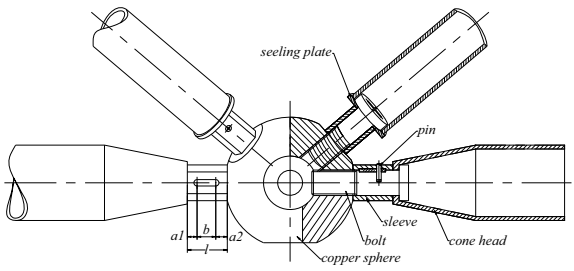


Fig. 10.15 The solid sphere node structure drawing



Fig. 10.16 The physical drawing of solid bolted sphere node

fit, and has less steel consumption and lower technological requirements. The bolts and the rods are connected by separating the sphere covers. This node is suitable for the grid shell structure and the truss structure which use the steel pipes as the rod, and the steel pipes and the hollow spheres are not eccentric in nature.

2. Plate node

The plate node is made up of welded or bolted steel plates, as shown in Fig. 10.18. This kind of node is mainly applied to the plate and shell structure and truss structure of common steel members, such as angle steel and I-beam, and it has flexible and changeable characteristics.

3. Tube node

The tube node refers to that the connectors are hollow cylinders, and the nodes are formed by directly welding on the cylinder surface of intersection, as shown in

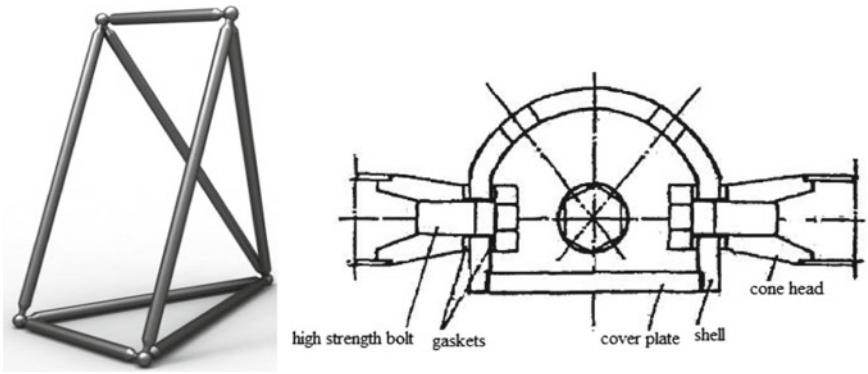


Fig. 10.17 The hollow bolt sphere node

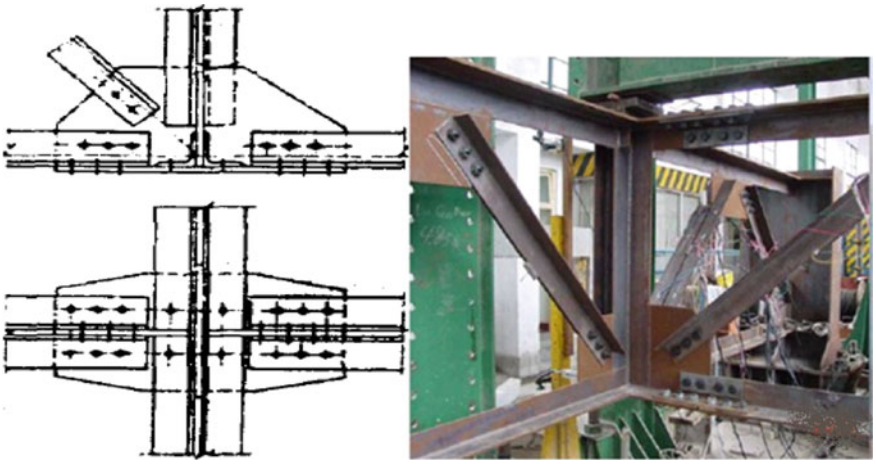


Fig. 10.18 The plate node

Fig. 10.19 The tube node

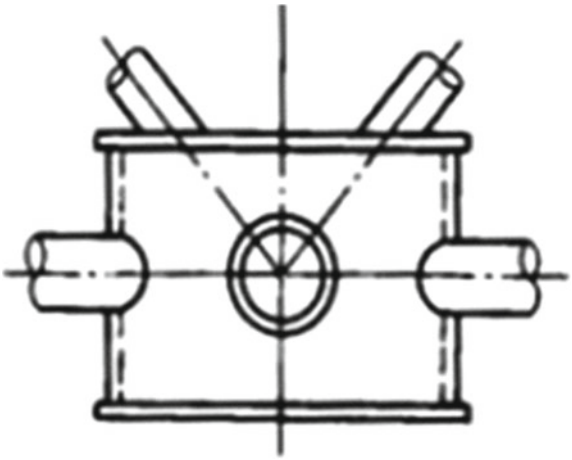


Fig. 10.19. The form of the node is similar to the foregoing welded hollow sphere node. The difference is that the hollow cylinder connectors can be welded directly, thus reducing the process of making the hollow spheres and the amount of steel, so it has the advantages of simple connection and saving material. Its disadvantages are that the intersection of cylinders lead to a curved surface between the end of the rod and the steel tube, and the cutting of the rod is complicated. At the same time, it no longer possesses the automatic centering characteristics of the spherical nodes, and the eccentric force is easy to produce. Therefore, the tube node is mainly used for the connection between the smaller size components to reduce the use of materials.

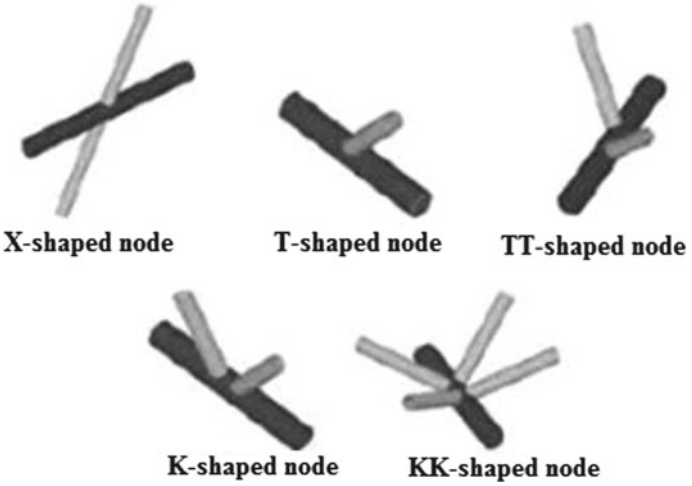


Fig. 10.20 The intersecting nodes

4. Intersecting node

The intersecting nodes are mainly used for the connection of the grid structure. To form the intersecting nodes, we firstly mechanically machine the ends of grid abdominal rods so as to intersect them each other, and then directly weld them to the walls of the main tubes, or we directly weld a main tube at one direction to the other main tube, as shown in Fig. 10.20.

In mechanical properties, the transfer force path of the intersecting node is simple and clear, which is convenient for the calculation and design of the node bearing; the node can connect the rods in any direction, so it has a strong adaptability. Its disadvantages include large installation work, difficulty in machining and positioning of the rods, large residual stress of the structure. These shortcomings are mainly caused by welding connection.

The intersecting nodes have many disadvantages, but the nodes are widely applied in practice due to its convenient design and beautiful appearance.

There are various forms of nodes. In actual use, we can choose a reasonable node form according to the site conditions, or design a new form of nodes. In the design process of key connection points of radar structure, first of all, the connection of the nodes should be designed according to the structural bearing characteristics and the requirements of use. The following design principles should be followed in the design.

(1) Avoid setting interfaces in the areas where stress is large, stress is complex and space is narrow.
(2) The node construction should be simple for construction, with little additional stress and no easy to accumulate water.

(3) The detachable connections should be flanged as far as possible, and the cementation should not be used alone in the field work.
(4) Treat seriously the problems of component eccentricity, two-force rod bending and welding stress.
(5) Punching, slotting and tinkering in the important parts, or local connection on the thin wall are strictly prohibited.
(6) When designing, avoid the corrosive connection nodes, causing connection performance degraded.

10.3.2 Wind-Resistant Safety Design Technology

For the structure of the metric wave radar, the wind load is the uppermost load. The safety design of wind resistance is primary in the structural safety design. Wind resistance design is directly related to the safety of the whole structure, which is a key factor in determining the success or failure of the overall structure design. It must be considered and demonstrated in the design phase of the scheme.

The wind load of a body is comprised of frictional resistance and pressure drag (including form drag, induced drag and wave resistance). For the non-streamlined antenna structure, the frictional resistance is much smaller than the pressure drag, and the wind load is derived from the form drag related to its configuration. The factors that affect wind force are very complex. Through theoretical formulas, it is difficult to calculate the wind force which the antenna structure bears with, and the experiments usually determine it. According to similarity theory and dimensional analysis, the formula of wind force and wind moment can be expressed as

$$F = C_F q A \tag{10.1}$$

$$M = C_M q A D \tag{10.2}$$

Among them, C_F and C_M are the wind force coefficient and the wind moment coefficient respectively, related to the structure shape and Reynolds number; and q is the dynamic pressure, related to the air density, $q = \nu^2/16$ is used in the inland areas, $q = \nu^2/17$ is used in the coastal areas, and $q = \nu^2/19 \sim \nu^2/18$ is used in the plateau and the alpine areas. A is the characteristic area (m^2) of the antenna; D is the dimension (m) of the antenna aperture that is vertical to the azimuth axis; ν is the wind speed (m/s). As shown above, as long as the wind force and wind moment coefficients are obtained by the experiments, the wind force of similar objects can be calculated. The antenna wind force test is usually carried out in the wind tunnel, and the scale-down model is used to replace the structure, as shown in Fig. 10.21. In addition to the geometric similarity, the scale-down model should be similar to the boundary condition and the air flow condition. The experimental data obtained



Fig. 10.21 The radar wind tunnel test

at this time is by the actual conditions and meets the requirements of the engineering application.

The metric wave radar's safety problems under strong wind mainly include two aspects: one is stability, and the other one is stiffness and strength. The stability problem mainly refers to the anti overturning ability of the whole radar structure and the bending-resistant ability of the local main supporting structure, and the stiffness and strength problem refers to the stiffness and structural strength failure of the radar antenna array. Next, we will expatiate on these two aspects respectively.

10.3.2.1 Wind-Resistant Stability Design

1. Anti overturning design of the whole radar structure

For the small antenna array structure, its bearing overturning moment caused by the wind is relatively small, and the overturning problem of the whole structure in high wind is not outstanding. For the metric wave radar, whose antenna array has increased aperture and weight, its overturning moment under the high wind has exceeded 100-ton m. The anti overturning problem of the whole radar has gradually emerged, and it has become a new problem for the designers. To improve the structure of the anti overturning ability of the metric wave radar, we mainly adopt the following design principles:

(1) We strictly control the position of the center of gravity of the radar in various conditions and make it always fall within the overturning edge, which is the key to ensure the stability of the radar.

(2) Improve chassis rigidity, lower the bearing surface height and reduce the inertia of the antenna.
(3) The main bearing back frame adopts open truss structure, and the antenna subarray is individually packaged, to increase the air permeability and the wind load.
(4) We strictly control the weight of the equipment on the array. The lightweight helps to reduce the scale of the antenna lifting mechanism and the azimuth driving mechanism, to control the weight of the whole machine.
(5) Take the long span supporting legs, increase the number of supporting legs, and arrange the distribution of the supporting legs reasonably.
(6) When the site condition is suitable, we can flexibly use other vehicles for rigid splicing, to increase the stability radius and weight of the chassis and improve wind resistance.
(7) According to the military standards, we should consider the weight and size limits of the transportation units; and according to the tactic indexes, we should considering the requirements for the number of transportation units and the dynamic erection, so the weight of the antenna and the length of the chassis should be controlled within a reasonable range.

The following three methods can be used to calculate the stability of wind resistance.

(1) Moment method

The moment method is used to check the anti overturning stability. In the whole machine, the algebraic moment sum of the external loads (including wind force, eccentricity force and inertia force) on dangerous overturning edges must be not less than the corresponding moment caused by self-weight.

$$\sum M_{total} = M_{wind} + M_{\text{eccentricity}} + M_{\text{inertia}} \geq M_{\text{self - weight}} \tag{10.3}$$

The moment method uses rigid hypothesis for the structural deformation of the whole machine, and more than two safety factors should be taken in the actual design.

(2) Multi-body dynamic method

The radar system is a complex multi-body system, involving a series of complex conditions such as mechanical motion and system control. Therefore, a multi-body dynamic analysis of the radar system should be carried out to fully consider the bearing characteristics of the whole radar in a complex external environment. Taking a metric wave radar as an example, by establishing a reasonable dynamic topological relationship (Fig. 10.22), a correct multi-body dynamic model is obtained, and the stability of the whole vehicle is judged by the pressure value of each axle of the vehicle. It is necessary to point out that the rigid hypothesis of the whole machine structural deformation is also adopted in multi-body dynamics, and we don't consider the influence caused by the elastic deformation of the structure, so the method is suitable for the radar structure with the stronger overall stiffness.

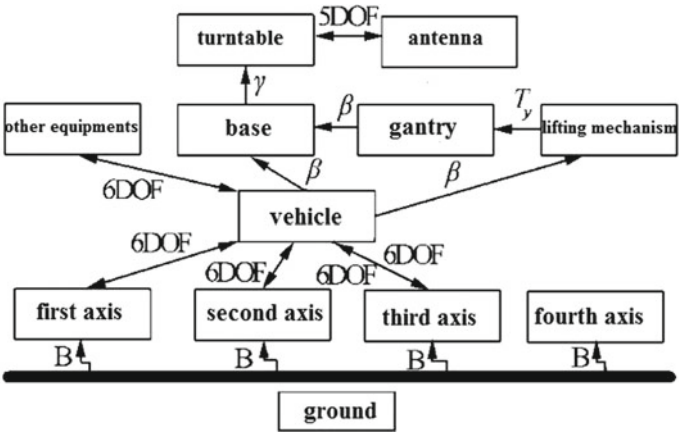


Fig. 10.22 The topological relationship diagram of the radar system

(3) Computational mechanics method

Considering the structural deformation, we use the computational mechanical method to investigate the stability of the local supporting legs, which includes the repeated iterative method based on the linear problem and the contact mechanics based on the nonlinear problem. Firstly, the iterative method based on the linear problem is used to complete the full constraint on all legs to calculate the reaction force of each leg, and then remove the reaction force of the legs to recalculate the corresponding constraint of the pulling force. The calculation cost of each linear iterative analysis step is small, however, because of needing more manual intervention, especially increasing the supporting legs of the large equipment, the iterative process of manual judgment becomes more and more complex. At the same time, the method applies or relieves the freedom degree of all nodes on the contact surface of the whole leg at each iteration step, and can not simulate the local upswept phenomenon of a single leg, which may appear in the actual working state. When the contact mechanics method is used to solve the stability problem of multi supporting legs, we can only one time solve for the contact state of all the legs and the force-deformation of the legs, so as to avoid more cost of manual intervention, and can obtain the structural mechanical response behaviors that can simulate the local upswept phenomenon of a single leg. Figure 10.23 is wind stability analysis model is established on the contact algorithm for a vehicle based large metric wave radar.

2. Stability design of the main supporting structure

There are often some lifting mechanisms or tower mast configurations in the structure of the metric wave radar, and the bearing force is determined by the stability conditions of the main supporting structure in the case of high wind. In the structural design, both the overall stability and the local stability should be simultaneously

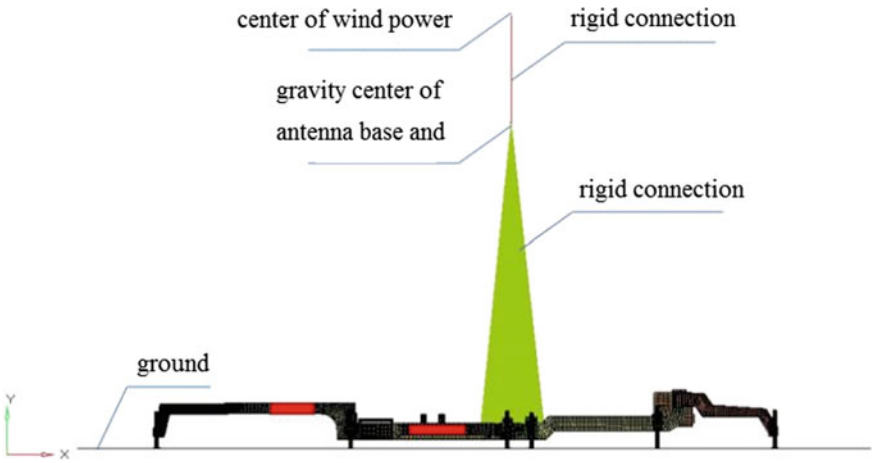


Fig. 10.23 The wind resistant stability analysis model based on contact algorithm

satisfied. In the past, the structural engineering accidents caused by the instability of components at home and abroad happen repeatedly.

The overall stability of the metric wave radar structure refers to that the critical state of the supporting structure, which is subjected to the larger pressure load under the action of the wind load, causes the indefinite deformation of the structure through a little increase of the external force, making the structure lose stability and causing the overall failure. The overall stability of a single component can be guaranteed by selecting the proper section of the component. However, for the increase of the aperture and the difference of the configuration, in the metric wave radar, there are more structural design components, so the structure overall stability problem is difficult to solve. At present, it is mostly verified by the modern numerical analysis methods or test methods. When the structure is preloaded, such as the pre-stressed ropes around the mast, the preload should be considered in the buckling analysis. Otherwise, the calculation result may have large error. In Fig. 10.24, the buckling mode of a large metric wave array structure is calculated. The different order modes correspond to different local possible unstable parts. When the buckling load coefficient is more than 1, it means buckling-restrained. The greater the coefficient is, the better the stability is. According to the buckling stability analysis of the rods, the first-order buckling load coefficient is 16, and the overall stability of the antenna frame work is large.

For a main supporting structure subjected to complex loads, it is possible not only to lose overall stability, but also to lose local stability. The local stability is the phenomenon that when the load is achieved to a certain value, under the loading action, the plate parts which constitute the component can not continue to maintain the plane balance state and produce the convex curve. The result of losing local stability is that it can lead to losing the structure bearing force immediately, though the overall stability is not lost. The loss of local stability changes the bearing status

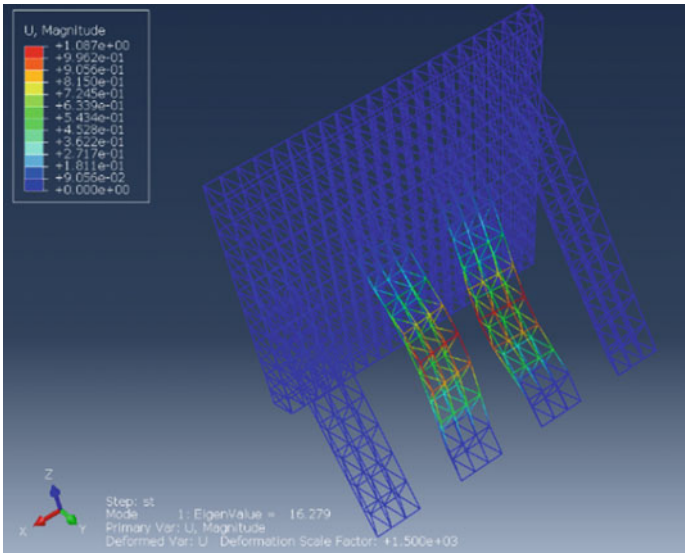


Fig. 10.24 The buckling mode of a large metric wave antenna array structure

of the structure, and reduces the overall stability and the stiffness of the structure. In the structural design, the local stability of the structure is mostly limited by the width to thickness ratio of the plates, and the rate does not exceed the allowable value. In some locations, various rib stiffeners can also be used to improve the local stability of the panels.

10.3.2.2 Wind-Resistant Stiffness and Strength Design

The design of the antenna structure needs to solve a series of contradictions and problems, but in comparison, the weight of the stiffness and strength problem is greater. It is often the control factor in the structural design. By optimizing the design, the main contradiction that the designer faces is to use the minimum mass to realize the specified stiffness and strength index.

1. Stiffness design

The deformation of radar antenna array directly determines the electronic performance of the radar, and how to ensure the stiffness of the radar in the case of high wind is the main work of the wind resistant design of the radar structure. The core of the antenna structure design is the precision, and the realization of the precision mainly depends on the stiffness of the structure, that is, the ability of the structure itself to resist deformation under the specified load conditions. To improve the stiffness of the metric wave radar antenna structure, the following methods can be utilized:

(1) Reduce the influence of the external load: accurately estimate the scale and influence of wind coefficient and wind load by the rational design wind speed, the scientific use of experimental means and calculation methods; and adopt sparse and slender components to reduce the wind coefficient.
(2) Select the rational structural form and layout: from the rationality of bearing force, the truss should be selected as the first choice, the design and calculation are simple, and the processing and assembly are convenient; the layout should be in the proper statically indeterminate state, and no geometric variable phenomena are allowed to appear in any part.
(3) Select material: light mass, high strength, high modulus, temperature resistance and three protection metal materials or advanced composite materials are preferred.
(4) Increase the inertia moment of the section: design the section shape reasonably, use the stiffeners correctly, and strengthen the bending stiffness.

For the metric wave radar, when its height is greater than 30 m and the vertical to horizon ratio of the antenna is greater than 1.5, or the basic self-vibration cycle of the radar structure is lower than 4 Hz, because of wind pressure fluctuation on the structure, the effect of the tail wind vibration should be considered. The deformation distribution of the array can be accurately calculated by using the finite element method, and it is an important basis for design optimization and weight reduction. Figure 10.25 shows the deformation distribution of a large metric wave antenna array is calculated by using the finite element method.

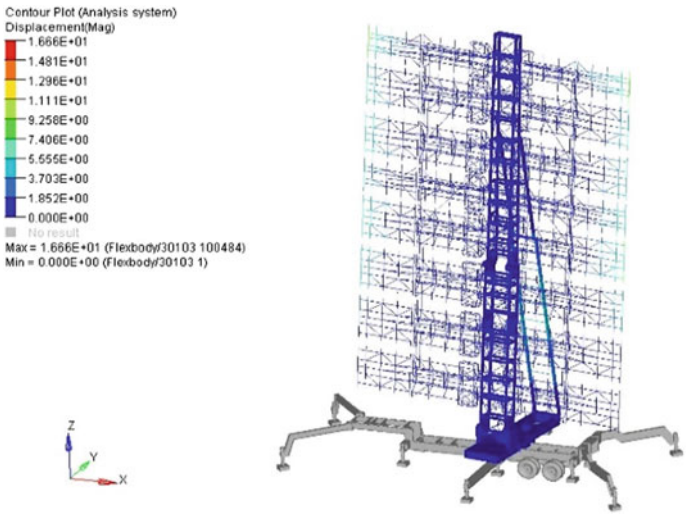


Fig. 10.25 The deformation distribution of a large array

2. Strength design

Generally, the structure of the metric wave radar is large. In order to achieve better maneuver performance, the whole machine structure also undergoes large movements such as transportation, erection, lifting and turning, and especially in the case of high wind, the bearing force is even larger. The main content of strength design is to design a reasonable layout structure and ensure that the structure of the radar is not damaged under any limit condition. For the strength design of a metric wave radar structure, we should pay attention to the following aspects:

(1) Avoid setting interfaces in the areas where stress is large, stress is complex or space is narrow.
(2) The interface design between components and the interface design between whole parts should be closely calculated and simple for construction.
(3) The detachable connections should be flanged as far as possible.
(4) Treat the problems of component eccentricity, two-force rod bending and welding stress seriously.
(5) Punching, slotting and tinkering in the important parts, or local connection on the thin wall are strictly prohibited.

The structure strength design belongs to the problem of mechanical analysis. The mechanical analysis of radar structure is often complex, and the exact solution must be aided by the numerical methods, such as finite element method. However, in the stage of scheme demonstration, when we grasp the main contradictions, omit the secondary factors, and reasonably put forward the simplified structure, it is often feasible and time-saving to use the knowledge of the material mechanics and the structural mechanics to carry out the primary design. In the detailed design stage, when the structure configuration design is complex, the detailed mechanical strength analysis can be carried out for the whole machine structure, or the detailed demonstration of the weak links is carried out to improve the structure strength. The detailed finite element analysis and demonstration of the strength of a large vehicle metric wave radar's turntable in wind load is shown in Fig. 10.26, including bolt connections, inner reinforcement plates, oil cylinder supporting ears, antenna supporting ears and back supporting ears. Through this detailed demonstration, the structural designers can gain effective data support and theoretical foundation.

10.3.2.3 Wind-Resistant Safety Design Method

With the increasing complexity and integration of radar equipment, the requirement of radar structure design in modern engineering is also improving. In the design process, the combination of CAD and CAE technologies plays a significant role in improving the design level and design efficiency of the structural radar equipment and shortening the cycle of product development. CAE technology is the result of the deep development of CAD technology. Designers can replace the traditional "design-verification design-redesign" cycle with the modern design method of "design-simulation design-improved design". The structure of the large metric wave radar is complex and the number of components is large. The cost of traditional

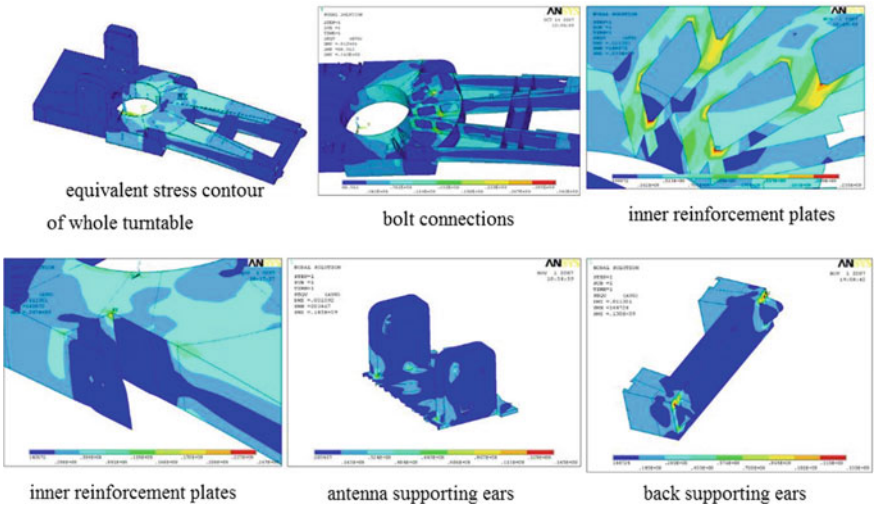


Fig. 10.26 The stress distribution of a large array

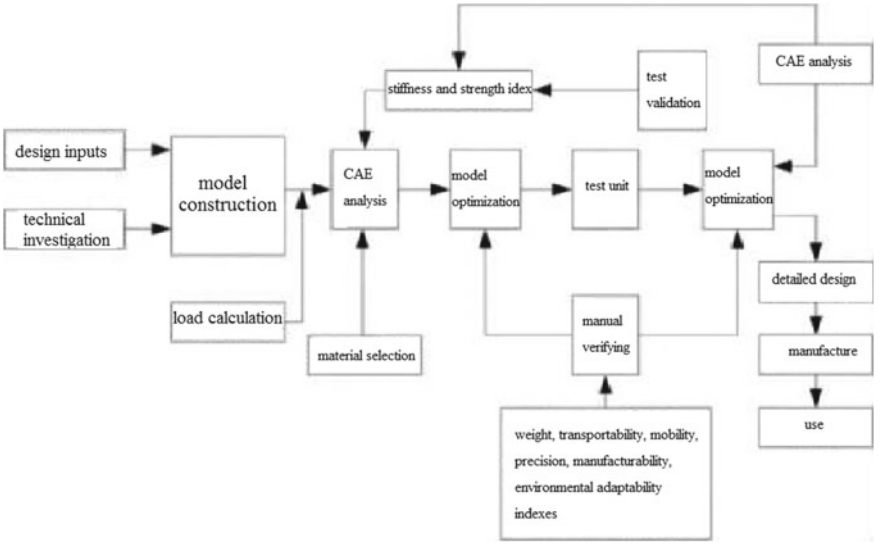


Fig. 10.27 The process of radar structure safety design based on simulation technology

safety verification experiment is high and the cycle is long. In the structure design, it is more necessary to introduce the simulation design technology to consider the structure safety performance. A flow chart of radar structure safety design based on simulation technology is shown in Fig. 10.27.

After solving the deformation and stress of the metric wave radar through the finite element method, we can carry out the optimization design for the antenna

structure. The mathematical description of the antenna structure optimal design is the quantitative expression of the optimal design model given after the comprehensive analysis of its design variables, performances, shape constraints and objective functions. The design variables include the size of the sections reflecting the thickness of the rods and the plates and shells, the coordinate variable of the chord nodes under the back frame, and the generalized design variables which are expressed by the shape of the continuum. The constraints include the quality limit, the square root of the reflection surface, the stress constraint, the inherent frequency constraint. The object functions include the structural quality, the reflection surface precision, and structural reliability.

We take the section size optimization as an example and introduce the metric wave radar structural safety optimization design method. The section size has a direct and decisive influence on the stiffness of the whole radar. The main problem of designers is that in the antenna structure design, how to realize the specified stiffness index through optimization design and the minimum quality. The size optimization is generally called parameter optimization (changing the parameter value of the model and keeping the grid model unchanged). It can optimize the parameters of the finite element model, such as the thickness of the plate, the section size of the beam, and the material properties. According to the design stage, it can be separated into two types.

(1) Free size optimization for the concept design. This technology is used to determine the thickness distribution of non-equal thickness thin wall parts (plate and shell element), such as the thin-walled space of the digital array module box.
(2) Size optimization for detailed design. At this time, the antenna structure has been determined, and only a few specifications and parameters need to be determined. In practical engineering applications, the discrete variables are often used to optimize.

When designing the antenna, by the product stage (the technical state of the antenna structure), the designers can carry out the size optimization for the design variables according to the design objective under the design constraints. The typical optimization process is shown in Fig. 10.28.

10.3.3 Automatic Erection Design Technology for Metric Wave Radar

An important index of the ground mobile metric wave radar is the erection time, and the automatic radar erection is an important means to reduce the erection time and improve the mobility of the radar. It is also the key technical difficulty of the radar structure design. This book mainly introduces the automatic erection of the metric wave radar working platform, the automatic erection technology of the antenna array and the automatic splicing technology of the antenna array.

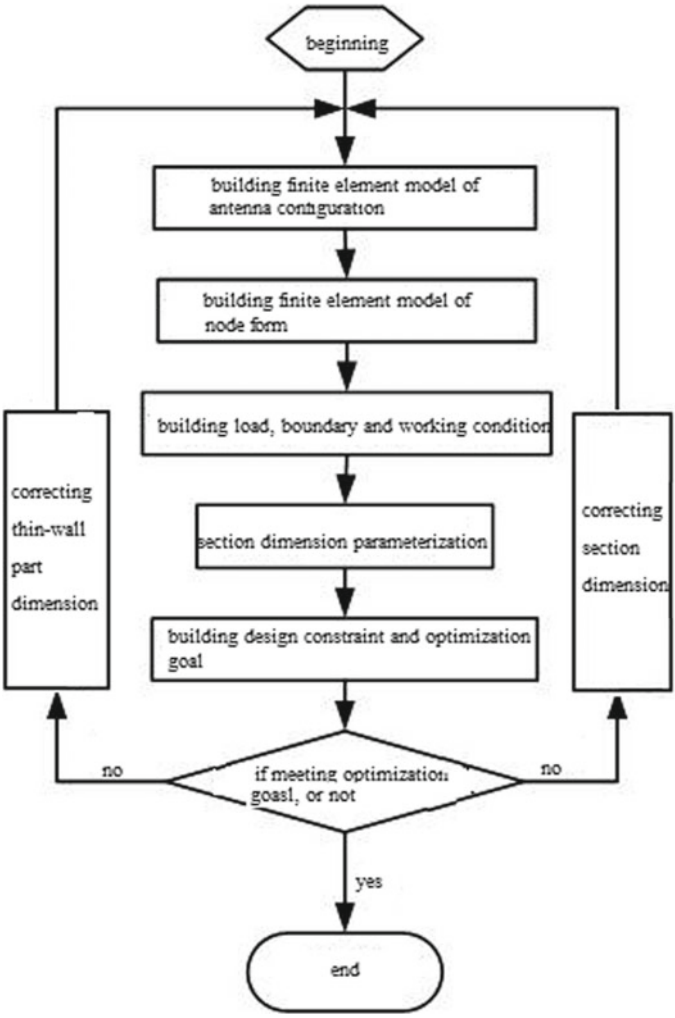


Fig. 10.28 Typical size optimization design process

10.3.3.1 Working Platform Automatic Erection

The main function of the radar antenna working platform is to provide reliable structural support for the antenna and turntable. It has automatic leveling function to meet the levelness requirements of the carrying equipment and has good maneuverability. It can be erected and withdrawn during the required time. There are various similar platforms at home and abroad. They are separated into three points supporting, four points supporting and six points supporting according to the supporting structure; they are separated into manual leveling and automatic leveling according to

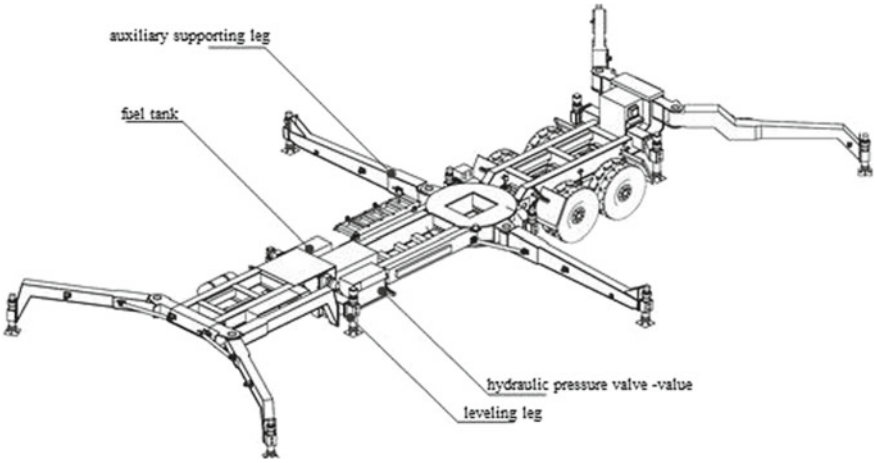


Fig. 10.29 Working platform layout

the leveling form, and four legs leveling and six legs leveling are the commonly used automatic leveling forms; they are separated into the electro-mechanical and electro-hydraulic types according to the actuating mechanism.

Due to the huge antenna array and heavy upper units of the large metric wave radar, the traditional four leveling legs cannot meet the requirements of the work. It is necessary to adopt the structural form of leveling legs plus auxiliary supporting legs, which can be designed as four, six, eight auxiliary supporting legs according to the needs, as shown in Fig. 10.29.

The servo control of platform automatic erection mainly uses the automatic leveling and auxiliary supporting to complete the antenna platform automatic erection together. The platform control system is generally composed of platform control box, hydraulic system, sensors and actuators. The platform control box is the main control unit, which controls the hydraulic system to perform the corresponding actions according to the operation instructions, and detects all kinds of state information in real time, including control modules, circuit breakers, relays, operation panels and so on. The hydraulic system is the actuating mechanism, mainly including hydraulic pump stations, solenoid valve groups, supporting leg hydraulic motors and corresponding pipelines, as shown in Fig. 10.30.

We take four points leveling plus eight auxiliary supporting legs as an example to explain the platform erection control. The four leveling legs are located on the front and back sides of the antenna vehicle. The front, middle and rear parts of the antenna vehicle respectively have a pair of manual unfolding supporting arms and the corresponding auxiliary supporting legs. In the middle of the antenna vehicle, a couple of auxiliary supporting legs are also installed, which can ensure the anti overturning force of the antenna under various conditions. The structural design of the leveling legs plus the auxiliary supporting legs improves the stability, but it also

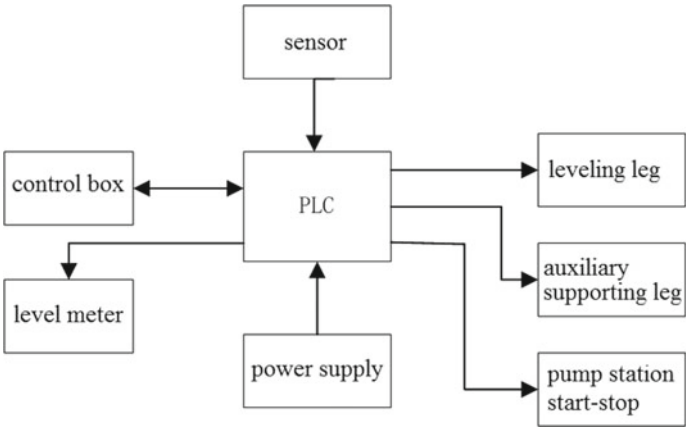


Fig. 10.30 Platform automatic erection block diagram

brings the problem that how to make the auxiliary supporting legs fall to the ground without destroying the leveling precision and play the auxiliary supporting role.

The platform supporting control process mainly has the following steps. The antenna vehicle arrives at the working position, deploys the supporting arms, manually unfold the locks, and then the system is power on. Four leveling is supporting legs extend, and after falling to the ground, they are automatically leveling to stop, achieving the leveling precision. Eight auxiliary supporting legs extend to the ground and support the whole platform.

When the four point leveling system begins to level, the four falling points are tested to ensure that the four leveling supporting legs reliably fall to the ground. Then, according to the numerical value of the horizontal sensors, we use four points rising automatic leveling method, that is, all of the four supporting legs participate in leveling, and follow the "only rising, no falling" principle. According to the information of the horizontal sensors' X axis and the Y axis, the highest point is found, the highest point is kept, and the other low points are controlled to approach the highest point regarding a certain control algorithm. The stopping condition is that when the platform meets the leveling accuracy, the leveling ends. After the leveling is completed, the auxiliary supporting legs need supporting for grounding, which cannot appear the false grounding phenomenon and affect the leveling accuracy. In order to solve the problem of the auxiliary legs grounding and avoid the false grounding, the grounding switches are designed inside the auxiliary supporting legs. When the supporting legs touch the ground, the switches close to stopping the supporting legs, making them fall to the ground without affecting the leveling precision.

10.3.3.2 Antenna Array Automatic Erection

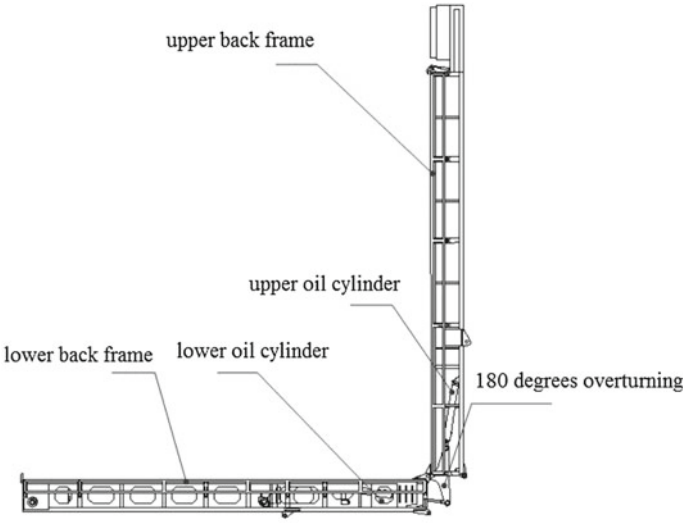
The antenna array automatic erection is comprised of the antenna array automatic deploying/folding, the antenna array automatic stitching/decomposition, the antenna array automatic lifting/recovery and the antenna array auxiliary support. The antenna array automatic deploying/folding technology is often used in a single vehicle transportation mode, enabling the radar to rapidly response. The antenna array automatic splicing/decomposing technology is often used in the multi-vehicle, multi-antenna decentralized transportation mode, and all parts of the antenna array are combined in the radar site. The antenna array automatic lifting/recovery technology is used as the basic operation of the antenna array automatic erection, and the antenna array auxiliary supporting technology is mainly used to enhance the stability of the antenna array in the working state.

To ensure the stability, the main bearing framework of the antenna is separated into two parts, the upper back frame and the lower one. In the transportation state, the antenna's upper and lower back frames are folded and need to overturn and deploy when working. Therefore, the antenna back frame needs to have the 180° overturning and folding function. The basic overturning and folding structure include an upper back frame, a lower back frame, two groups of overturning cylinders and locking mechanisms. A group of oil cylinders between the lower back frame and the rocker arm can be turned over 90°, another group of oil cylinders between the upper back frame and the rocker arm can be turned over 90° again, and then the combined 180° overturning and folding are completed. In order to ensure the location and lock, two groups of positioning and locking devices are set up between the upper and lower back frames, one group are the positioning pins and the other are locking latches, as shown in Fig. 10.31.

Generally, the antenna lifting is achieved directly by the three-stage oil cylinder with a large diameter. When the lifting oil cylinder works, the auxiliary back support and its three groups of supporting rods act accordingly. After completing the antenna lifting, the lifting cylinder stops, and the auxiliary supporting rods reach the supporting positions under the action of the supporting rod cylinder, which has the self-locking devices. When working, the antenna relies on the lifting cylinder and the auxiliary back support to ensure its rigidity and stability. The antenna array of the metric wave radar has large size and high weight, so when designing the lifting mechanism layout, we should increase the lifting arm of an antenna as far as possible in order to reduce the lifting force which the antenna frame bears. But this leads to a problem that the lifting mechanism needs the larger telescopic ratio, and it is difficult to adopt the single stage lifting mechanism to meet the stroke need. The lifting mechanism can adopt multistage hydraulic direct lifting technology, connecting rod combination lifting technology or main and auxiliary multi-point relay lifting technology to solve the larger telescopic ratio problem. When using these techniques, we must accordingly adopt the position protecting mechanism and the auxiliary supporting mechanism, to ensure the rigidity, stability and safety of the antenna system. The auxiliary supporting mechanism can adopt a wire rope retractable mechanism,



(a) the folding back fame



(b) the back frame overturning 90 degrees



(c) the back frame overturning 180 degrees

Fig. 10.31 The back frame overturning

a single link mechanism or a multi-link coordinated lifting mechanism to achieve erection/withdrawal.

For the 3D metric wave radar, the precision of the antenna framework planar array is high, and the auxiliary back support on the array surface can effectively reduce the antenna cantilever, and improve the stiffness of the framework and the precision of the array surface. The auxiliary back support is fully deployed and folded by an automatic erection system, which is easy to reduce the risk of personnel operation. As shown in Fig. 10.32, the auxiliary back support of a metric wave radar uses a multi-link coordinated lifting mechanism and emplaces to forma stable support structure for the array surface. The safety lock is set in the oil circuit, and the mechanical lock is set in the cylinder.

The overturning, lifting and auxiliary support of large antenna usually adopt hydraulic control system, which is mainly composed of an array surface control box, a hydraulic system, and its actuators. The array surface control box is the main control unit, which controls the hydraulic system to perform the corresponding actions according to the operation instructions, and mainly includes the control modules,

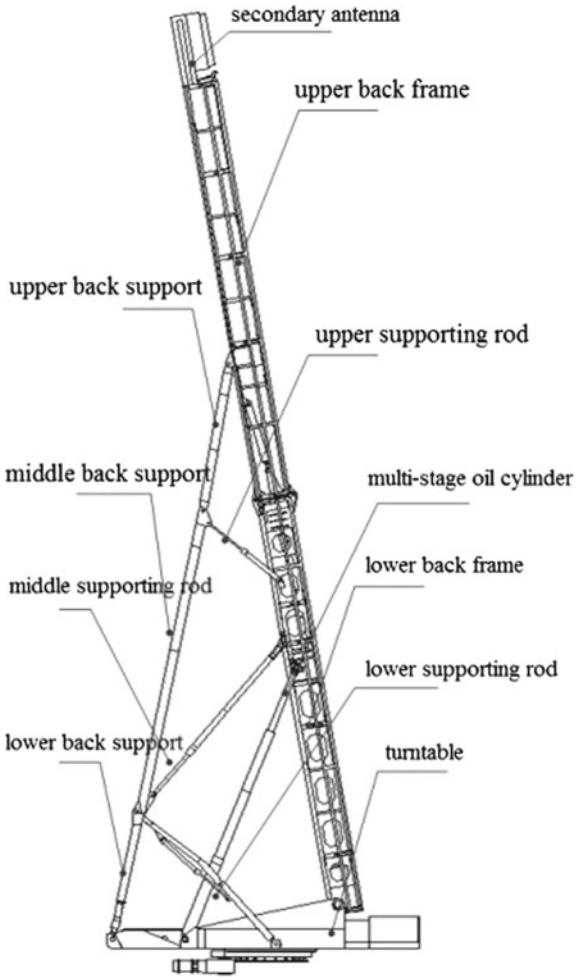


Fig. 10.32 The lifting mechanism schematic diagram

circuit breakers, and relays. The hydraulic system is the actuator of the action, mainly including the hydraulic pump station, solenoid valve group, overturning mechanism, lifting mechanism, auxiliary supporting rods, locking/unlocking mechanism and the corresponding pipelines, as shown in Fig. 10.33.

The control process of the antenna array automatic erection mechanism is complicated. The lifting cylinder needs to take different speeds according to the different angles. At the same time, in order to complete the action function, each supporting rod and the back supporting cylinder need to cooperate. In the control process, the multichannel sensors are used to carry out the position sampling to ensure the correct position in the action process, avoiding the stuck phenomenon.

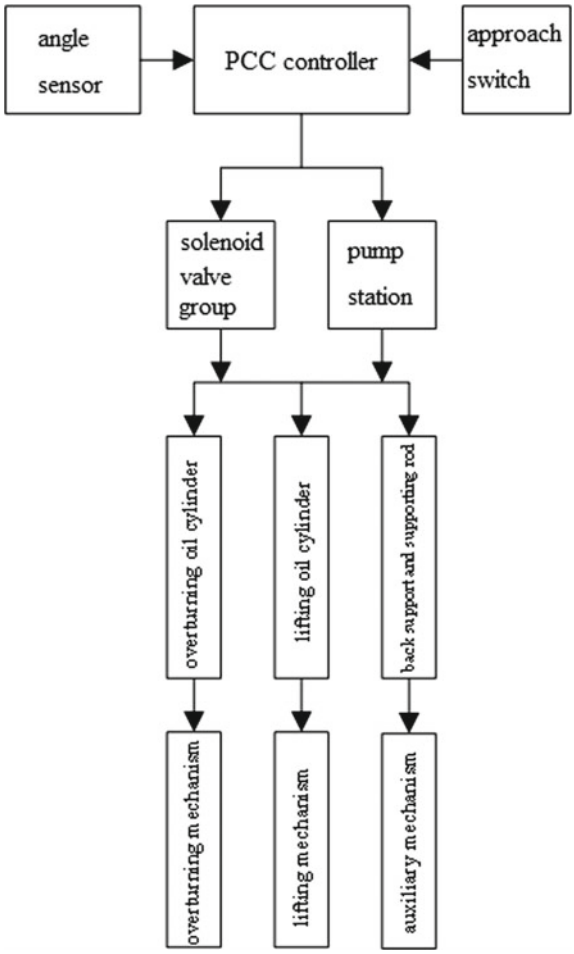


Fig. 10.33 The antenna automatic erection block diagram

10.3.3.3 Antenna Array Surface Automatic Stitching

The antenna array surface of the large metric wave radar is mostly stitched with multiple antenna array surfaces and mainly erected by two ways: crane lifting and automatic splicing. The crane lifting requires operators to have a professional qualification, and need long erection time, so this method restricts the mobility of the large radar. The antenna array surface automatic stitching technique uses the integrated design method of electromechanical, hydraulic, photoelectric and image analysis to complete the automatic splicing and assembling of the large vehicular radar antenna through the automatic splicing mechanism.

There are two partitioning ways of the antenna array surface, namely vertical partitioning and horizontal partitioning. When the antenna array is divided into three blocks on the left, middle and right, or more blocks, the middle block can be directly

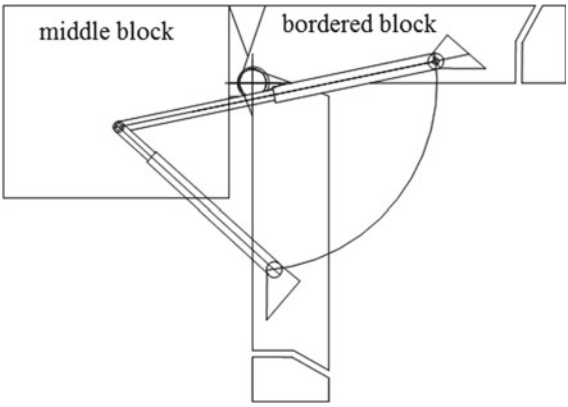


Fig. 10.34 The 90° deploying mechanism schematic diagram

arranged on the main bearing framework, and the sub-block and the middle block can be connected by the automatic deploying/folding mechanism when the antenna is assembled. The mechanism can be driven in two ways: cylinder drive and motor drive. As shown in Fig. 10.34, the hydraulic deploying mechanism is adopted, and the quick pull-out joint is used in the hydraulic system to realize the combination and separation of the system.

The aim of the antenna array surface automatic stitching is to realize the automatic, accurate and quick assembly when the precision of the antenna array is ensured, and the stitching is reliable. The automatic antenna splicing mainly includes digital automatic measurement, servo control, and position and orientation automatic adjustment. The basic working principle is shown in Fig. 10.35.

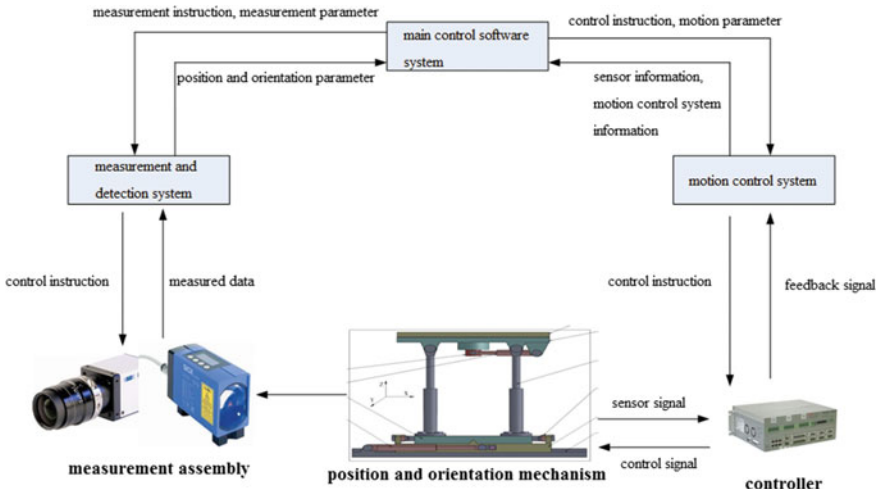


Fig. 10.35 The antenna butting schematic diagram

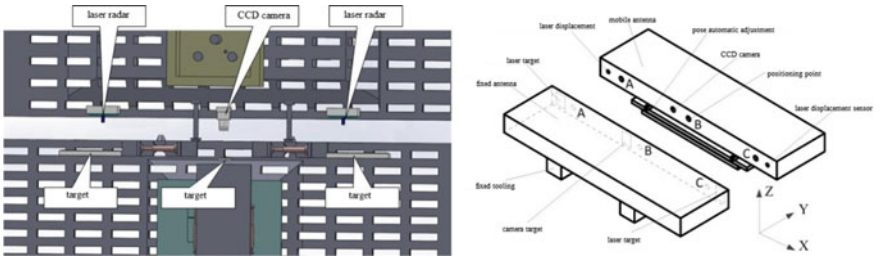


Fig. 10.36 The digital automatic measurement system layout diagram

(1) Accurately measure the posture data between a fixed antenna and mobile antenna through a digital automatic measurement device.
(2) The measured position and orientation data is transformed into the spatial 6-DOF relative position and digital orientation information through data processing and analyze, and is transferred to the servo control system.
(3) The servo control main control system sends out motion control instructions according to the position and orientation information and the set procedure and completes the mobile antenna posture adjustment and closing through the antenna position and orientation automatic adjustment mechanism. During the period, the digital automatic measuring device also needs to measure the position and orientation data between the fixed antenna and the mobile antenna in real time, in order to carry out the adjustment in real time.
(4) Finally, the two antenna array surfaces are accurately positioned and locked by the positioning and locking mechanism.

(1) Digital Automatic Measurement Technology

Considering the actual index, environmental adaptability and cost of the antenna array surface, we can use the method combining laser radars with a CCD camera to automatically measure the position and orientation of the antenna array surface. The measurement system layout, as shown in Fig. 10.36, can accurately measure the distance (Y direction in Fig. 10.36) and the position and orientation information of the parallelism between the butting antenna array surfaces through a group of laser radars, then capture the presupposed targets on the fixed array through a wide viewing angle CCD camera, and obtain the position and orientation information including the altitude difference (Z direction in Fig. 10.36) and the spacing (X direction in Fig. 10.36) between the butting antenna array surfaces by calculating the captured images. Through the combination of these measurements, we realize an antenna array surface automatic butting digital measurement system with good environmental adaptability and low cost.

Through these measurements, we can get the position and orientation parameters of each direction between the automatic stitching antenna array surfaces, to provide the foundation for automatic control.

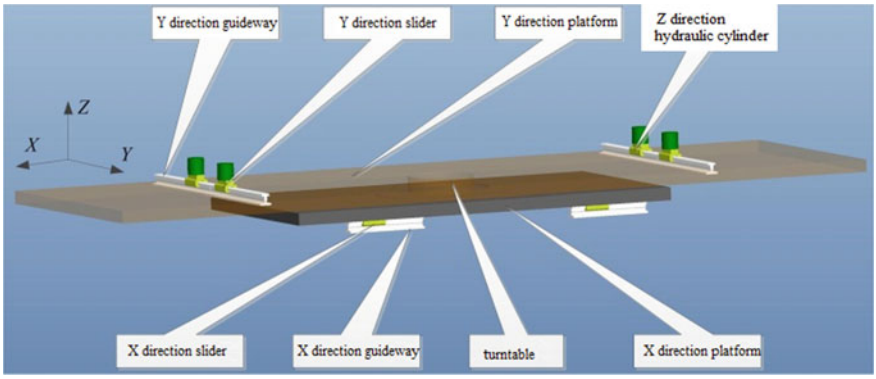


Fig. 10.37 The antenna automatic splicing mechanism

(2) Antenna Position and Orientation Automatic Adjustment Mechanism

The position and orientation automatic adjustment mechanism of the large antenna can automatically accomplish the adjustment, splicing and positioning locking of the relative position and orientation of the assembled antennas. The antenna position and orientation automatic adjustment mechanism adopts a motion platform with multi-degrees of freedom to achieve the position and orientation adjustment of the butting antenna in all directions, and complete the precise butting of the assembly. As shown in Fig. 10.37, the butting mechanism is composed of the driving sliders, turntable, lifting columns and bearing platform. The driving sliders are divided into X direction sliders and Y direction sliders, and they can drive the X and Y bearing platforms respectively so that the antenna can move in X and Y directions. The turntable can realize the rotation of the antenna around the Z axis. On the horizontal plane, the position control and location of the antenna can be realized by the driving sliders and the turntable. There are four lifting columns, and the four points supporting leveling solution is used to complete the leveling of the antenna and the translational motion in the Z direction. Compared with the three points leveling method, the supporting surface of the four points supporting leveling method is bigger, and the supporting points are less stressed. The butting mechanism has the advantages of simple structure, easily assured strength and rigidity, less driving links, and easily assured accuracy.

(3) Driving Control Technology of Position and Orientation Adjustment Mechanism

The servo control system in the automatic splicing system is the control backbone. It is a collection of special electronic equipment for performance detection, operation control and Safety protection, and is comprised of the control computer, servo control circuits, logic protection circuits, input and output interfaces. The schematic diagram of the electrical control system of the butting verification system is shown in Fig. 10.38. After the butting process starts, the control computer collects all kinds

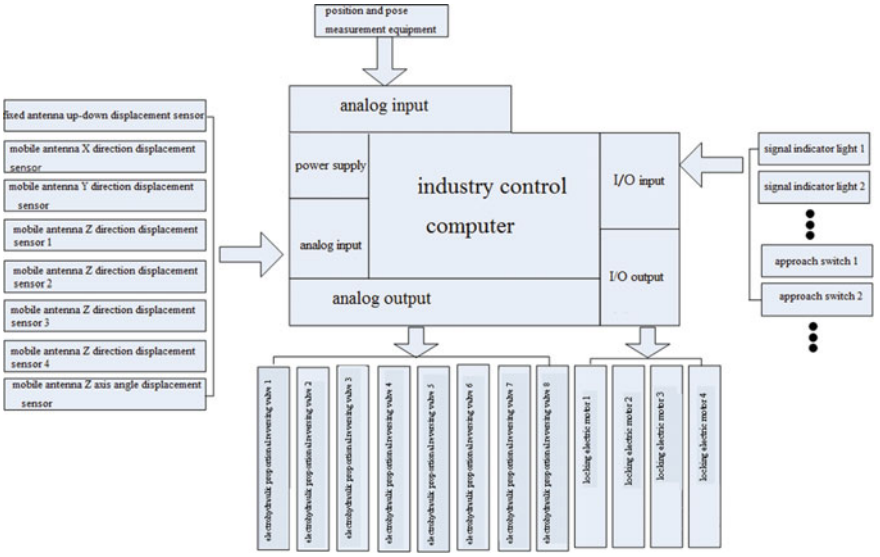

position and pose measurement equipment
analog input
power supply
industry control computer
I/O input
analog input
I/O output
analog output
fixed antenna up-down displacement sensor
mobile antenna X direction displacement sensor
mobile antenna Y direction displacement sensor
mobile antenna Z direction displacement sensor 1
mobile antenna Z direction displacement sensor 2
mobile antenna Z direction displacement sensor 3
mobile antenna Z direction displacement sensor 4
mobile antenna Z axis angle displacement sensor
signal indicator light 1
signal indicator light 2
approach switch 1
approach switch 2
locking electric meter 1
locking electric meter 2
locking electric meter 3
locking electric meter 4

Fig. 10.38 The system diagram of antenna array surface automatic splicing

of sensor data and calculates the relative positions of the cutting mechanism in the X, Y and Z axis directions. The data fusion is done according to a certain strategy algorithm, and the position errors of the butting mechanism in all directions are calculated. The butting process is sequentially carried out in the three directions following the order of X, Y and Z, and is completed by two steps: coarse positioning and accurate positioning.

According to the control strategy, the control software is designed by the modularization method, which is divided into modules such as initialization, data acquisition and processing, X-axis direction control, Y-axis direction control, and Z-axis direction control. The functions of each module are as follows.

(1) The initialization module: system reset, the initialization operation of input and output and internal variables of the PLC module.
(2) The data acquisition and processing: collecting external information, such as instruction input, sensor data.
(3) The X-axis control: controlling the X-axis direction according to the collected data.
(4) The Y-axis control: controlling the Y-axis direction according to the collected data.
(5) The Z-axis control: controlling the Z-axis direction according to the collected data.

10.3.4 Cooling Design Technology

Like the requirements of all other radar systems, in order to ensure the proper operation of a metric wave radar system, we need to ensure the proper and stable operation of the related electronic components. The necessary condition for the stable operation of a metric wave radar system is that the power electronic components work at the appropriate temperature, so the feasible and reliable cooling design has become the key of the high reliability indexes of the metric wave radar.

The common cooling design technology, based upon the primary cooling technology, mainly includes natural cooling design technology, forced air cooling design technology and liquid cooling design technology.

10.3.4.1 Natural Cooling Design Technology

The natural cooling is one of the most widely used methods in the electronic equipment cooling. The radiation convection technology and the natural convection cooling technology belong to natural cooling technology. The cooling technology has the advantages of safety, reliability, low price and low maintenance cost. Therefore, when selecting the cooling form of electronic equipment, we should give priority to it when meeting the requirement of temperature rise control. The cooling technology of VHF radar control cabinet heat consumption is very low for electronic equipment.

10.3.4.2 Forced Air Cooling Design Technology

When the natural convection cooling is unable to stop the temperature rise of the device, it is necessary to rely on the external power (such as a fan) to provide cooling (i.e. forced cooling). Compared with the natural cooling technology, the heat dissipation capability of the forced air cooling technology is 10 times larger than that of the natural convection, although it faces the problem of cost, noise and complexity.

For the forced air cooling technology, two problems should be considered: the fan selection and the duct design. The commonly used fans for electronic equipment are mainly separated into two kinds: the centrifugal fans and the axial fans. The working characteristics of the centrifugal fans are small air volume and high wind pressure. The working characteristics of the axial fans are large air volume and low wind pressure. The selection of the fans needs to be considered with the actual needs.

Because the array surface of a metric wave radar has the characteristics of large heat source dispersion and good permeability, most electronic equipment of the array surface are cooled by forced air cooling. Although the heat dissipation capacity of the conventional forced air cooling technology is still greatly limited, in recent years, with the continuous advancement of heat conduction and expanded materials, such

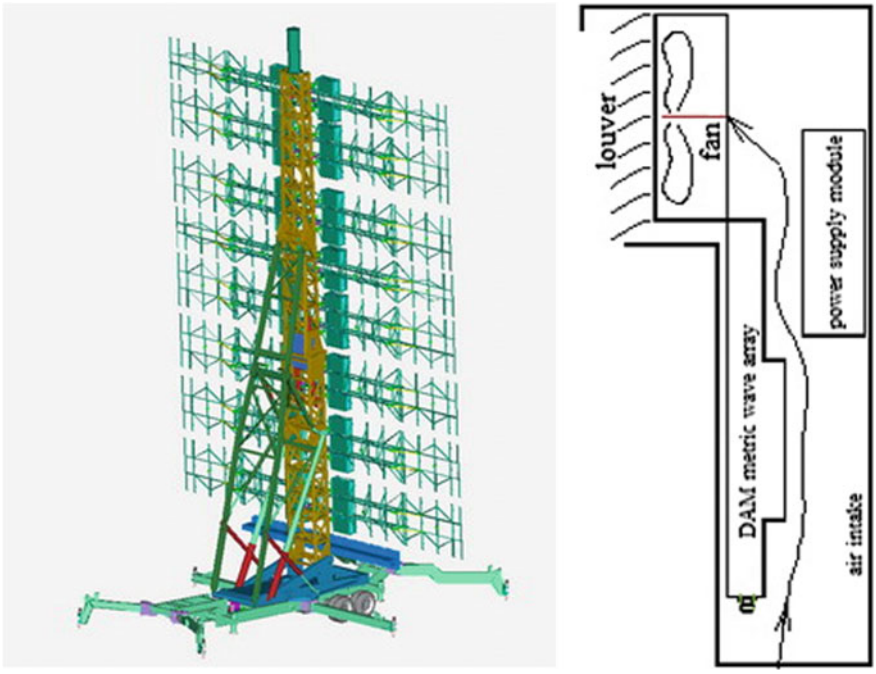


Fig. 10.39 The antenna of a air-cooled metric wave radar

as heat pipe, heat mean cavity and graphene, the heat dissipation capacity of forced air cooling can be further improved. The antenna of a Chinese 3D metric wave radar is shown in Fig. 10.39, which adopts the forced air cooling design.

10.3.4.3 Liquid Cooling Design Technology

Compared to the forced air cooling technology, the heat dissipation capacity of the liquid cooling technology can be further improved. The cooling technology can be used for the heat dissipation of the high heat flux density power devices. The liquid cooling technology can be separated into the direct liquid cooling technology and the indirect liquid cooling technology.

The direct liquid cooling technology refers to that the heating parts of the electronic devices are directly in contact with the coolants. For example, the electronic devices are directly impregnated in the inert liquids (such as fluorocarbons) or directly scoured by the inert droplets and jet flows, such as the liquid jet cooling technology and the liquid spray cooling technology. Generally, because of direct contact between the coolants and the electronic equipments, the direct liquid cooling technology has no intermediate heat transfer resistance, so it has very high heat dissipation capability. For example, if the liquid jet cooling is carried out by the scour of high speed

fluid, the heat transfer performance is closely related to the jet speed. When water is used as the cooling medium and the jet velocity reaches 47 m/s, its heat dissipation capacity is as high as 1700 W/cm^2. Though the cooling capacity of the direct liquid cooled cooling technology is very high, the direct liquid cooling technology is still in the exploration stage for the heat dissipation of a radar array surface, due to the limitations of inertia, insulation, electrical conductivity and reliability.

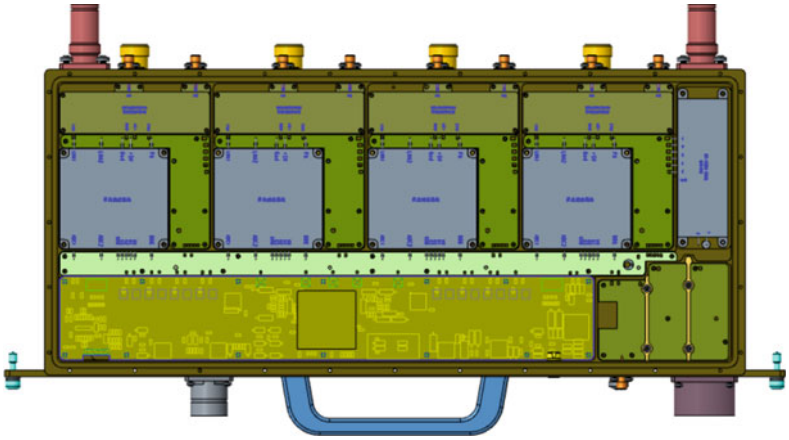
The indirect liquid cooling technology is that the liquid coolants don't directly contact with the heating elements, but firstly transfer heat to the heat exchangers through the heat conduction mode, then the heat is taken away by the cooling coolants of the heat exchangers, the cooling liquid is returned to the cold plates again, and finally the cooling effect is achieved through the circulation reciprocating mode. The liquid cooling system with this cooling technology is mainly composed of the cold plates, circular pipes, pumps and external heat exchangers. The cold plate indirect cooling is a relatively mature cooling technology, which is widely used for the radar array surface cooling. The cooling system with this cooling technology has the characteristics of simple structure, compact, high surface heat transfer coefficient, small temperature gradient, uniform heat load and large heat exchange area. The usual coolants include water, fluorocarbon, grease, ethanol, ethylene glycol solution etc.

In recent years, because the heat flux density of the power devices in the metric wave radar is increasing, the heat flux density of the electronic devices in some metric wave radars can be 100 W/cm^2 or even higher, and it is also necessary to use the liquid cooling technology. Currently the liquid cooling technology mainly used in the metric wave radar is the indirect liquid cooling technology (Fig. 10.40). In addition, the metric wave radar has the characteristic of large heat source dispersion, so the distributed liquid cooling system can be used to replace the traditional centralized liquid cooling system to improve the flow distribution accuracy.

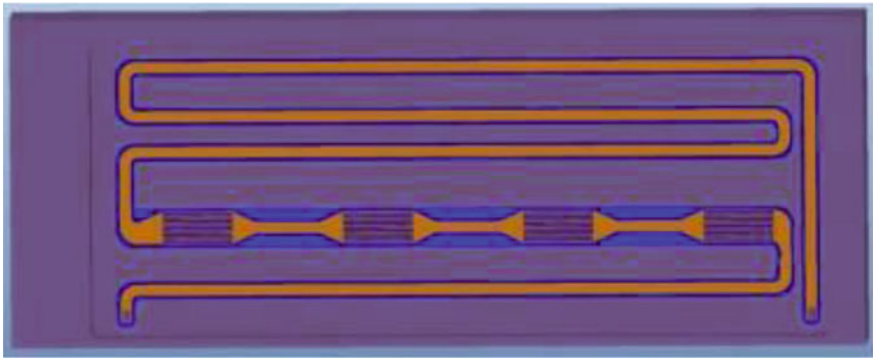
10.3.4.4 Other Cooling Design Technology

(1) Heat Pipe Technology

The heat pipes developed in recent decades are the heat transfer elements with high thermal conductivity. The heat transfer between cold fluids and hot fluids is coupled by the phase transition processes of the working medium evaporation and condensation in the heat pipes, and its equivalent thermal conductivity can be 103–104 times as great as that of the metal. The ordinary heat pipes are made up of the pipe shells, capillary porous materials, working liquids and cooling fins. The air in the tubes is removed to form the vacuum and fill up the pores in the capillary material with the liquids, and the tubes also need to be sealed. When the evaporation section is heated, the liquid in the capillary material evaporates, and flows from the adiabatic section to the condensing section. After cooling, the liquid depending on the capillary force action flows back to the evaporation section along the porous material. In this cycle, the heat is transferred from the heat pipe shell to the tube core, then transferred to the working medium, after that, transferred to the condensing section, and the



(a) the DAM outline diagram



(b) the DAM cold plate liquid flow channel

Fig. 10.40 The DAM structure diagram of a liquid cooling metric wave radar

condensing section releases the heat through the condensation action. The heat pipe technology can transfer and expand the heat at specific locations, thus reducing the design difficulty of the cooling system. In the metric wave radar, the technology can be used in the DAMs and the DBF boxes (Fig. 10.41), for which it is difficult to achieve heat dissipation.

(2) Semiconductor Refrigeration Technology

The semiconductor refrigeration technology is also called the thermoelectric refrigeration technology, which uses thermoelectric effect (Peltier effect). It has some advantages, for example, it does not require any refrigerant and can achieve high precision temperature control. It is suitable for some places which have restricted spaces and no refrigerant pollution, such as the semiconductor refrigeration closed cabinet

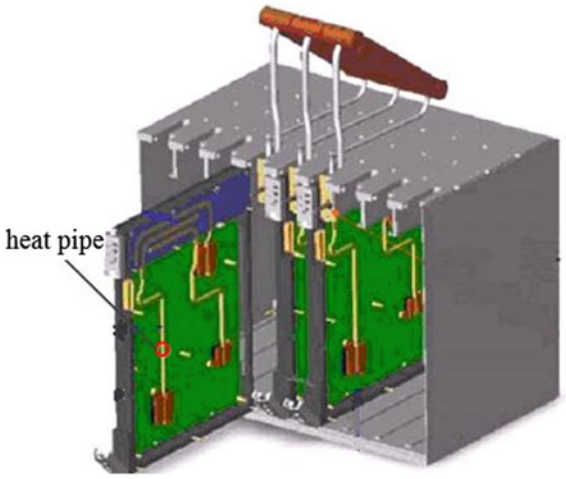


Fig. 10.41 The schematic diagram of the heat pipe used in the DBF inserting box

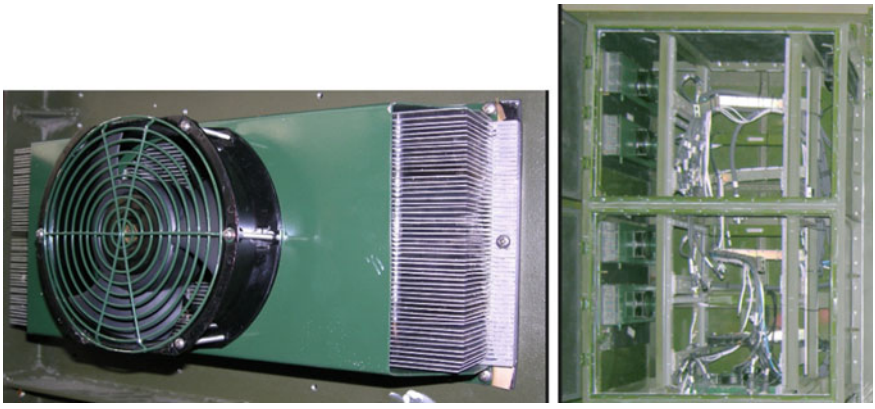


Fig. 10.42 A semiconductor refrigeration closed cabinet

shown in Fig. 10.42. However, the cooling efficiency of semiconductor refrigeration technology is generally not high, and the power of a single semiconductor refrigeration element is very small, which can only slightly reduce the system temperature. In order to use semiconductor refrigeration technology to achieve high power heat dissipation, a large number of semiconductor refrigeration elements are required to be combined into the electric stacks, which have the disadvantages of high cost and large volume. At present, the maximum heat dissipation capacity of the semiconductor refrigerator is only 100w/cm^2, and the integrated thermoelectric film cooling technology has been used for cooling the high power lasers.

Bibliography

1. Yu Zujian. Thermal Design and Analysis Technology of Electronic Equipments[M]. Beijing: Beihang University Press, 2008.
2. Qiu Chengti, Zhao Dunyi, Jiang Quanxing. Structural Design Principle of Electronic Equipments[M]. Nanjing: Southeast University Press, 2001.
3. Zhang Bin. Research on Thermal Design for Electronic Equipment[J]. Equipment Manufacturing Technology, 2012(1):63–65.
4. Liu Yibing, Huang Xinmin, Liu Anning, etc. Research Based on New Heat Release Technology of Electron[J]. Cryogenics & Superconductivity, 2008(3):57–57,61.
5. Zhu Bin, Sheng Jun, Wei Tao. Design and Optimization of a Cold Plate with High Thermal Density[J]. Electro-Mechanical Engineering, 2014(4):15–18.
6. Zhang Hong, Zhuang Jun. Research, Development and Industrial Application of Heat Pipe Technology[J]. Journal of Nanjing Normal University (Engineering and Technology), 2002(2):1–13.
7. Huang Huanwen, Feng Yi. Study of Heat Transfer Enhancement about Semiconductor Refrigeration[J]. Cryogenics and Superconductivity, 2010, 38(8):60–63.
8. Chen Ji. Stability Theory and Application of Steel Structure[M]. Beijing: Scientific and Technical Documentation Press, 1994.
9. Wu Fugao. Structural Design of Antenna Pedestal[M]. Beijing: National Defense Industry Press, 1980.
10. Yin Deyu, Liu Shanwei, Qian Ruojun. Structural Design of Latticed Shell[M]. Beijing: China Architecture & Building Press, 1996.
11. Ping Lihao, Huang Puqing, Zhang Runkui, etc. Radar Structure and Technology[M]. Beijing: Publishing House of Electronics Industry, 2007.
12. Ye Shanghui, Li Zaigui. Structural Design of Antenna[M]. Xi'an: Xidian University Press, 1986.
13. Hao Fei. The Main Forms and Characteristics of Long-Span Space Structure[J]. Inner Mongolia Petrochemical Industry, 2011(3):82–83.
14. Shen Zuyan, Chen Yangji, Chen Yiyi. Basic Principles of Steel Structure[M]. Beijing: China Architecture & Building Press, 2000.
15. Wang Ju. Study on Space Truss Structure Design and Reinforcement[D]. Changsha: Central South University, 2012.
16. Dong Shilin, Zhao Yang. Discussion on Types and Classifications of Spatial Structures[J].China Civil Engineering Journal, 2004, 37(1):7–12.
17. Zhou Daoming. Development and Application of Membrane Structure Engineering[J]. Industrial Construction, 1999, 29(11):28–30.
18. Industry Standard of The People's Republic of China. Grid Structure Design and Construction Code(JGJ-91)[S]. 1994.
19. Lan Tian. Application and Developments of Steel Spatial Structures[J]. Journal of Building Structures, 2001, 22(4):2–7.
20. Li Ming. Research on the Arrangement for Prestressed Cables of Prestressed Latticed Structures[J]. Industrial Construction, 2005, 35(5):47–55.
21. Vasant Mistry, Atorod Azizinamimi. Development of Space Truss Structure Using Glass Fiber Reinforced Plastics[J]. 2005(11):1–2.
22. He Xixia. Effective Lengths of Compressed Members in Multi-Planar Tubular Truss with Simple Joints[D]. Xi'an: Xi'an University of Architecture and Technology, 2003.
23. Wang Guozhou, Qu Lyuqian. Principles and Designs of Steel Structures[M]. Beijing: Tsinghua University Press, 1993.
24. Luo Yilin. Design and Loading Capacity Analysis in Integrated Joints of Composite Truss[D]. Harbin: Harbin Institute of Technology, 2013.
25. Yu Weijiang. Study on New Polyhedron Spatial Frame Structures[D]. Hangzhou: Zhejiang University, 2005.

26. Xie Mingjiu. Composite Connection[M]. Shanghai: Shanghai Jiao Tong University Press.
27. Si Hongwei. Research on Dynamic Modeling and Active Fuzzy Control of Large Flexible Space Truss[D]. Changsha: National University of Defense Technology, 2006.
28. Kazuhide Ando, Jin Mistsugi, Yumi Senbokuya. Analyses of Cable Membrane Structure Combined with Deployable Truss. Computers & Structures, 2000, 74(1):21–39.
29. Wang Jie. Stability Design of Truss[D]. Kunming: Kunming University of Science and Technology, 2011.
30. Wu Changdong, Chen Yunbo. Applications of Steel Tube Structure on Engineerings[J]. Industrial Construction, 1997(2):10.24.
31. Ding Yunsun. Discussion on Some Design Problems in Circular Tubular Joints[J]. Spatial Structures, 2002, 8(2):56–64.
32. Liu Dianzhong, Liu Canjun. Applying Investigation for Triangle Steel Tube Truss[J]. Journal of Jilin Architectural and Civil Engineering Institute, 2000(3):1–4.
33. Sun Huanchun, Wang Yuefang. Comment on Classical Theory of Stability Analysis for Truss Structures[J]. Chinese Journal of Computational Mechanics, 2005, 22(3):316–319.
34. Zhu Run. Topology Optimization for Plate and Shell Structure Under Static Loads[D]. Beijing: Beijing University of Technology, 2011.
35. Li Yongsheng. Study on Mechanical Properties of a Shipborne Radar[D]. Nanjing: Nanjing University of Science and Technology, 2011.
36. Tao Fuyu. Brief introduction to Modern Metric Wave Radars[J]. Land-Based Air Defence Weapons, 2002(4):34–38.
37. Zhao Dechang. Structural System Design of Ground-Based High-Mobility Radar[J]. Electro-Mechanical Engineering, 2007, 23(3):19–23.
38. Zha Jinshui. Structural Design of Antenna System of a Meter Wave Radar[J]. Electro-Mechanical Engineering, 2012,28(2):26–29.
39. Zhu Haibo, Pan Kai. Summery for the Structural Design of X Band Vehicle-borne Doppler Weather Radar System[J]. Electro-Mechanical Engineering, 2003, 19(4):8–10.
40. Ke Qiuhong, Liu Feng, Li Lijuan, etc. Stability Analysis of a Three-Dimensional Truss Arch Structure[J]. Spatial Structures, 2006, 12(2):44–48.
41. Guo Yanlin. Modern Structure System and Application[J]. Steel Structure and Construction Industry, 2004(4):8–14.
42. Tang Weibin. Kinetic Analysis and Optimal Design of a Airborne Avionic Equipment Bracket[D].Chengdu: University of Electronic Science and Technology, 2008.
43. Gu Songnian, Xu Bin, Rong Jianhua, etc. Recent Progresses on Structural Dynamic Design Methods[J]. Journal of Mechanical Strength, 2005, 27(2):156–162.
44. Ye Hongling, Sui Yunkang, Liu Zhaomiao. Topological Optimization Analysis of Two-Dimensional Continuum Thin Plate Structure[J]. Journal of Beijing University of Technology, 2007, 33(8):785–790.
45. Ben Shaoyu. Key Technology Analysis and Study for Helicopter Borne Radar Structure Design[D]. Nanjing: Nanjing University of Science and Technology, 2011.
46. Balajti, Gy. Kende, Ed. Sinner. Increased Importance of VHF Radars in Ground-Based Air Defense[J]. IEEE A&E Systems Magazine, 2012(1):4–18.
47. Li Jinliang, Li Yongzhen, Wang Xuesong. Study on Anti-Stealth with Meter-Band Polarimetric Radar[J]. Radar Science and Technology, 2005, 3(6):321–326.
48. Sun Ying, Chen Li, Li Jialu. Finite Element Analysis on Loading Properties of Intersecting Tubular Joint with Carbon/Epoxy 3D Multidirectional Braided Composite[J]. Journal of Solid Rocket Technology, 2008, 31(3):266–274.
49. Yang Yibin. Effect of Joint Stiffness on the Portal Frame Stability[D]. Shanghai: Shanghai Jiao Tong University, 2010.
50. Chen Shaofan. Stability Design Guide of Steel Structure[M]. Beijing: China Architecture & Building Press, 2004.
51. Tang Weimin. Study on Auto Assembly Technology for Large Array Antenna of Mobile Radar[J]. Radar Science and Technology, 2014, 12(3):338–342.

52. Wang Xianquan. Research on Stability of Cold-Formed Thin-Walled Steel[D]. Wuhan: Wuhan University of Technology, 2008.
53. Zhang Zhongxing. Frame Structure Optimization of an Out Door Enclosure[D]. Shanghai: Shanghai Jiao Tong University, 2009.
54. Teng Hui. The Research of the Electro-Hydraulic Automatic Level System of the High-Altitude Working Machine[D]. Hangzhou: Zhejiang University, 2006.
55. Tan Guihong. Discussion on Large Mobile Meter-Wave Radar Structure System Design[J] Electro-Mechanical Engineering, 2010, 26(3):1–4.
56. Wang Yaqing. Studying the Heat Transfer Performance in the Non-Boiling Regime of Spray Cooling[D]. Hefei: University of Science and Technology of China.

Chapter 11
System Tests and Demonstrations



11.1 Introduction

This chapter describes the antenna calibration tests and demonstrations, the radar airspace coverage, and the height-finding under different terrain conditions.

11.2 Test and Demonstration of Transmitting/Receiving Calibration

Because of the different components, the manufacturing tolerance, the assembly errors, etc., there are variations of initial amplitudes and phases among the phased array radar channels. To ensure good performances, it is required to accurately measure the differences of initial amplitudes and phases among the channels and conduct relevant compensations so as to make the antenna beams meet the design requirements.

11.2.1 Interior Field Calibration of the Transmitting Channel

When conducting the interior field calibration of the main radar transmitting channels, the transmitting channels transmit according to a time sequence control. The transmitted power is sent to the calibration receiver (multiplexing with the blanking receiver) via calibration network coupler, power divider, and attenuator. The I/Q data output from the receiver are sent to the signal processing system to obtain the relative amplitudes and phases values of each transmitting channel under different frequencies. These data are saved in the signal processing system in order to be used during the transmitting.

© National Defense Industry Press, Beijing and Springer Nature Singapore Pte Ltd. 2020

J. Wu, *Advanced Metric Wave Radar*, https://doi.org/10.1007/978-981-10-7647-3_11

11.2.2 Interior Field Calibration of the Receiving Channel

When conducting the interior field calibration of the main radar receiving channels, the calibration signal sources of the transmitting/receiving system separately generate RF signals of different frequencies under the control of the receiving calibration triggering signal and frequency code generated in the signal processing system. The signals are coupled into individual receiving channels via attenuator, power divider, and calibration network. The digital I/Q calibrated data of each receiving channel are collected by the signal processing system, where they are analyzed to obtain the relative values of amplitudes and phases of the individual receiving channels for different frequencies. These data are stored in the signal processing system to be utilized during the receiving beamforming.

11.3 Antenna Test and Demonstration

11.3.1 Antenna Outfield Calibration Test and Demonstration

The metric wave radar usually has a large antenna aperture. Because of the antenna structure limitation, the test of vertical plane beam cannot be conducted lying at horizontal direction. Hence, the slant-range field measurement method is generally used to carry out the far-field beam test of the metric wave radar antenna. Using a transmitting signal source mounted on a test tower, the receiving antenna horizontal plane beam is measured through the mechanical scanning of the antenna rotation pedestal whereas, the measurement of the vertical plane beam is accomplished via an electronic scan.

11.3.1.1 Test Site

When using the slant range measurement method for the antenna test, the test tower height is exploited to build the slant range antenna test site (the schematic diagram of the test site is shown in Fig. 11.1). The main site requirements are described as follows.

The view factor requirement of the test site: There should be no barriers around the test site, such as high buildings, trees, etc., and only small stray electric waves exist. The test range is

$$R \geq \frac{2 \cdot K \cdot D^2}{\lambda}.$$

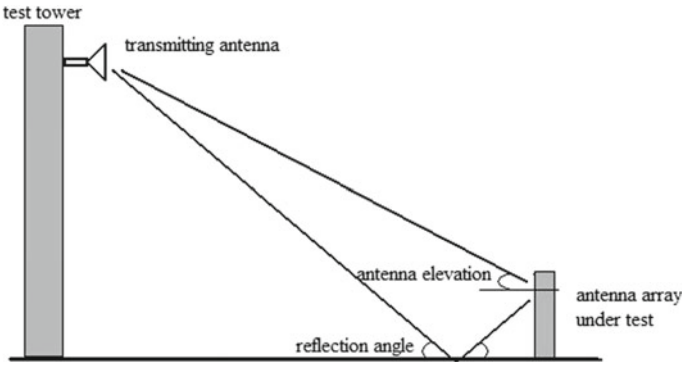


Fig. 11.1 Schematic diagram of slant range measurement method

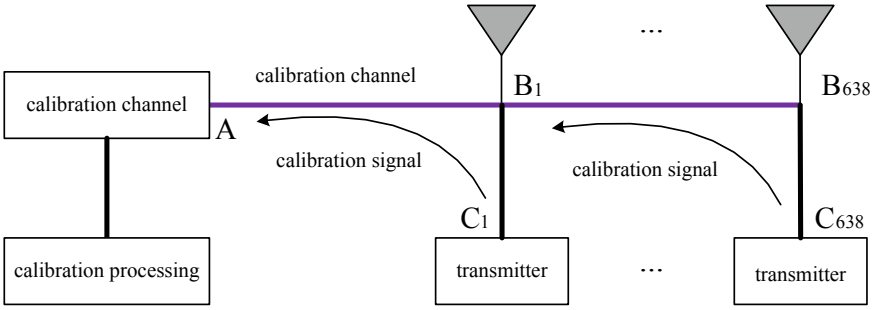


Fig. 11.2 Block diagram of transmitting calibration coefficient processing

The transmitting antenna is designed to have large vertical aperture so as to decrease its the ground-touch level. The shielding net is mounted in the main reflection area to reduce ground reflections.

11.3.1.2 Test Procedures

(1) As illustrated in Fig. 11.2, when performing antenna outfield calibration test, switch on the system to conduct the transmitting external calibration and gain CB. Under the same state, perform the internal calibration and gain CA. Then the value of CB/CA = B/A can be obtained. The value is completely generated by passive components and can be used for long.

(2) As shown in Fig. 11.3, when conducting antenna outfield calibration test, switch on the system to perform the receiving external calibration and obtain BC. At the same time, conduct internal calibration and obtain AC. Then the value of BC/AC = B/A can be obtained. This value is completely generated by passive components and can be used for long.

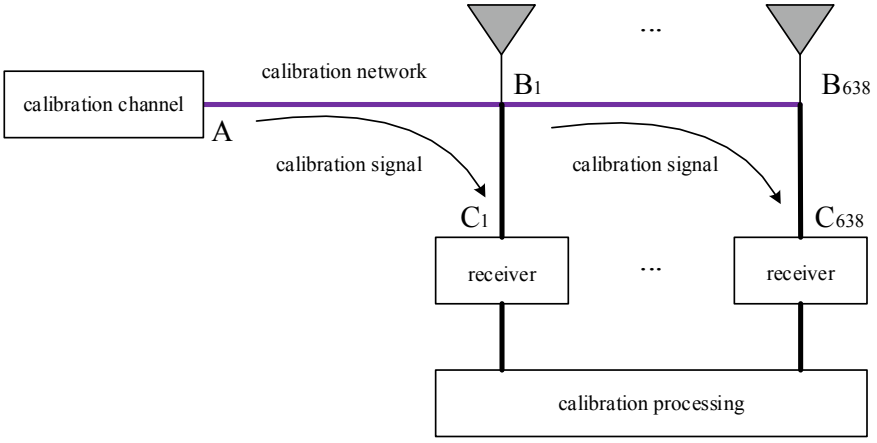


Fig. 11.3 Block diagram of receiving calibration coefficient processing

(3) When the radar is in normal mode, switch on the system every time to perform an internal calibration. The value of AC is obtained by measurement. This value is multiplied by B/A to obtain the amplitude and phase errors of the BC channel. Then the calibration coefficient W can be found using these values.

11.3.2 Low Sidelobe Antenna Outfield Test

For the metric wave 3D radar that uses digital beamforming (DBF) technique, the receive beamforming of the antenna is done in the system signal processing subunit and the transmitting beamforming is implemented by controlling the amplitude and phase parameters of multiple transmitting channels. The far field test of the antenna pattern is conducted on the whole system.

11.3.2.1 Test of the Receiving Pattern

When testing the antenna receiving pattern, the signals are received by the different elements of the antenna under test. These signals will go to DAM through both feedline and coupling calibration networks to be processed; after that, they are transferred to the signal processing subunit via the optical fiber system to perform the digital beamforming; finally, the antenna pattern is obtained on the signal processing computer.

The antenna horizontal receiving pattern test procedures are:

(1) Set up the transmitting antenna on the antenna test tower platform. Set the pointing direction of the transmitting antenna (horizontal normal direction) at

the radar antenna and connect the test instruments according to the antenna test block diagram illustrated in Fig. 11.4.

(2) Level the radar rotation pedestal and aim the antenna horizontal pointing direction to the transmitting antenna position on the test tower. Test the relative azimuth relation between the radar antenna and the transmitting antenna. At the same time, test the elevation relation between the radar antenna and the transmitting antenna. The angular relations are sent to the signal processing system.

(3) Switch on the radar system and turn on the test equipments and instruments. After conducting the internal calibration of the receiving channel, lift up the antenna to the normal operation mode.

(4) Adjust respectively the frequency of the transmitting antenna source signal and the radar operating frequency to the required test frequency. Using signal processing operations, adjust the antenna horizontal beam pointing direction to the test beam position and adjust the beam vertical plane to point at the transmitting antenna.

(5) Rotate the antenna by 360°. The antenna horizontal receiving pattern can be obtained directly on the signal processing computer via the signal acquisition system.

(6) By repeating the procedures (4)–(6), the antenna patterns at different frequencies can measured.

(7) Process the measured antenna patterns to determine the antenna parameters such as the horizontal beamwidth, horizontal sidelobe level, etc.

As an example, the receiving horizontal sum/difference pattern test results of a metric wave radar at a specific beam position is given in Fig. 11.5. Its receiving horizontal pattern test results at individual beam positions are shown in Fig. 11.6.

The procedures for testing the antenna vertical receiving pattern are:

(1) Set up the transmitting antenna on the antenna test tower platform. Aim the pointing direction of the transmitting antenna (horizontal normal direction) at

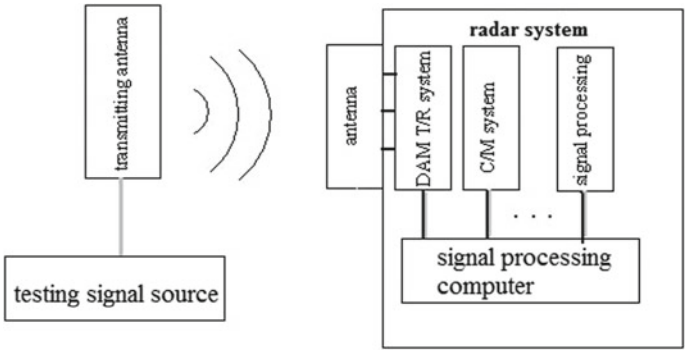


Fig. 11.4 Block diagram of the antenna receiving pattern test

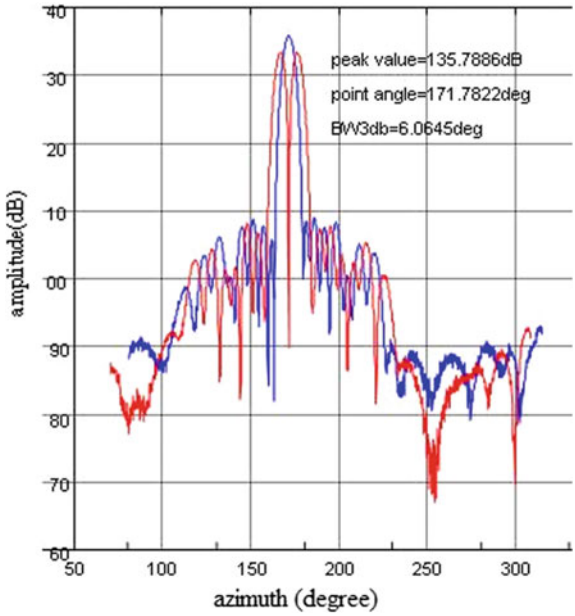


Fig. 11.5 Tested receiving horizontal sum/difference pattern at single beam position

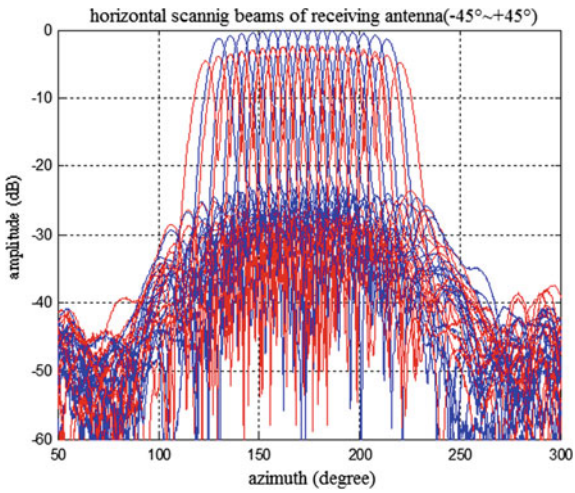


Fig. 11.6 Receiving patterns at individual beam positions

the radar antenna and connect the test instruments according to the block diagram of antenna test illustrated in Fig. 11.4.

(2) Level the radar rotation pedestal and aim the horizontal pointing direction of antenna at the transmitting antenna position on the test tower. Test the relative azimuth relation between the radar antenna and the transmitting antenna. At the same time, test the elevation relation between the radar antenna and the

transmitting antenna. The angular relations are sent to the signal processing system for use.

(3) Switch on the radar system and turn on the test equipments and instruments. After conducting the internal calibration of receiving channel, lift up the antenna to the normal operation state. The horizontal normal direction of the antenna aims at the transmitting antenna.
(4) Adjust the frequency of the transmitting antenna source signal and the radar operating frequency to the required test frequency.
(5) Adjust the antenna beam to perform the receiving beam scanning in the range of 0–40° along vertical direction. Via the signal acquisition system, the vertical receiving pattern of the antenna can be obtained directly on the signal processing computer.
(6) By repeating the procedures (4)–(6), the vertical patterns at different frequencies can measured.
(7) Process the measured antenna patterns data to extract the antenna parameters such as the vertical beamwidth, sidelobe level, and so on.

11.3.2.2 Test of the Transmitting Pattern

During the antenna transmitting pattern test, the signal flow is: aim the antenna under test at the testing antenna. Switch on the radar transmitter. At the same time, Transfer the azimuth signal of the antenna rotation pedestal (or the antenna scanning pulse signal) to the test point on the tower. After the testing antenna received signal, use the azimuth pulse signal from the antenna under test as a trigger. The received RF signal is collected directly on the peak power meter. Finally, the antenna transmitting pattern can be obtained on the test computer.

The procedures for testing the antenna horizontal transmitting pattern are:

(1) Set up the transmitting antenna on the antenna test tower platform. Aim the pointing direction of the transmitting antenna (horizontal normal direction) at the radar antenna and connect well the test instruments according to the block diagram of antenna test illustrated in Fig. 11.7.
(2) Level the radar rotation pedestal and aim the horizontal pointing direction of antenna at the transmitting antenna position on the test tower. Test the relative azimuth relation between the radar antenna and the transmitting antenna. At meanwhile, test the elevation relation between the radar antenna and the transmitting antenna. The angular relations are sent to the signal processing system for use.
(3) Switch on the radar system and turn on the test equipments and instruments. After conducting the internal calibration of receiving channel, lift up the antenna to the normal operation state.
(4) Adjust the radar operating frequency to the required test frequency. Through the signal processing control instructions, aim the pointing direction of the antenna

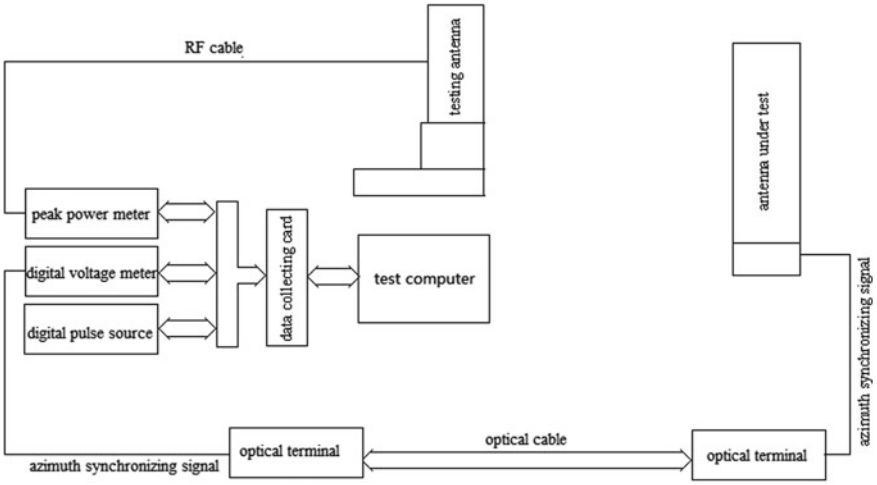


Fig. 11.7 Block diagram of transmitting pattern test

vertical beam at the test antenna on the test tower. Meanwhile, transfer the azimuth pulse signal of the rotation pedestal to the test point on the tower.

(5) Start the antenna pedestal and control its rotation speed within a proper range.
(6) Start the software test. Through the signal acquisition system, the horizontal transmitting pattern of the antenna can be obtained directly on the signal processing computer.
(7) Repeating the procedures (4)–(7), the horizontal patterns at different frequencies can measured in turn.
(8) Conduct data processing of the measured horizontal transmitting patterns of the antenna to produce the parameters such as the horizontal beamwidth, sidelobe level, scanning range of transmitting beam, and so on.

The test results of the horizontal transmitting patterns of a metric wave 3D radar at individual beam positions are given in Fig. 11.8.

The procedures for testing the antenna vertical transmitting pattern are:

(1) Set up the transmitting antenna on the platform of the antenna test tower. Aim the pointing direction of the transmitting antenna (horizontal normal direction) at the radar antenna and connect well the test instruments according to the block diagram of antenna test illustrated in Fig. 11.7.
(2) Level the radar rotation pedestal and aim the horizontal pointing direction of antenna at the transmitting antenna position on the test tower. Test the relative azimuth relation between the radar antenna and the transmitting antenna. At meanwhile, test the elevation relation between the radar antenna and the transmitting antenna. The angular relations are sent to the signal processing system for use.

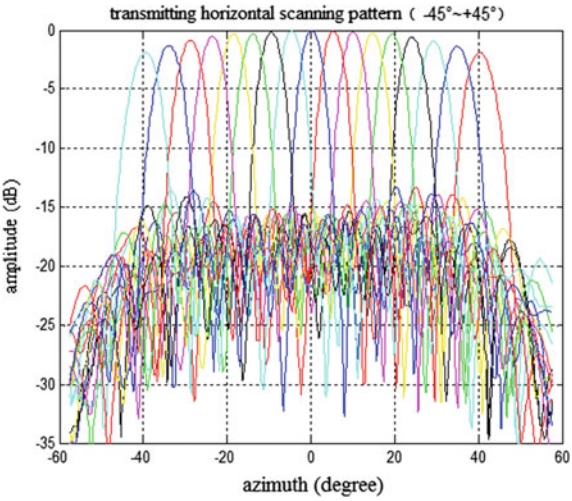


Fig. 11.8 Horizontal transmitting patterns at individual beam positions

(3) Switch on the radar system and turn on the test equipments and instruments. After conducting the internal calibration of transmitting channel, lift up the antenna to the normal operation state. Aim at the horizontal normal direction of antenna at the testing antenna.
(4) Adjust the radar operating frequency to the required test frequency. Through the signal processing control instructions, make the antenna beam perform scanning in the range of 0–40° along vertical direction. At the same time, transfer the beam scanning control pulse signal via optical cable to the test point on the tower to control the scanning speed in a proper range.
(5) Start the test software. Through acquisition system, the vertical transmitting pattern of the antenna can be obtained directly on the signal processing computer.
(6) Repeating the procedures (4)–(6), the vertical transmitting patterns at different frequencies can measured in turn.
(7) Conduct data processing of the measured antenna patterns to produce the parameters such as the vertical beamwidth, sidelobe level, and so on.

11.3.3 Test of the Sidelobe Cancellation Performance

Modern radars are required to be able to cancel multiple jamming sources at the same time and reject any interference. In general, simulations are conducted to test the radar sidelobe cancellation performance in an open environment with no strong radiation objects.

11.3.3.1 Test Site

The site requirements for the sidelobe cancellation test are as follows:

(1) The radar site should bean open environment without any obstacles. For metric wave radars, there should be a flat ground between the jamming antenna and the radar antenna. The ground roughness should meet the Rayleigh criterion: $\Delta H \leq \lambda/(M \sin\psi)$, where, ψ is the grazing angle, and M is the flatness coefficient (generally taking 8–32);
(2) The jamming antenna points to the $\pm 60^\circ$ plane range of the radar antenna direction with no obvious reflecting points;
(3) Far from the range $R \geq \frac{2D^2}{\lambda}$ (D is the horizontal aperture of the radar antenna), i.e., the two jamming antenna should be positioned around 300 m, from the radar so as to meet the antenna far-field test conditions.

11.3.3.2 Test Procedures

The procedures of the sidelobe cancellation performance test are:

(1) Under far-field test conditions, set multiple jamming sources around the radar according to the radar under test specification requirements. The polarization of the jamming source antennas are the same as the polarization of the radar antenna. The jamming sources are spaced in azimuth by a distance no less than three times the radar antenna azimuth beamwidth, as shown in Fig. 11.9;
(2) The height of the jamming antenna should not be lower than the lower edge of the radar antenna to ensure that the jamming antenna is in the beam;
(3) The frequency of the jammer is set to be equal to the radar operating frequency. The jamming signal is chosen to be a noise modulation signal or a frequency

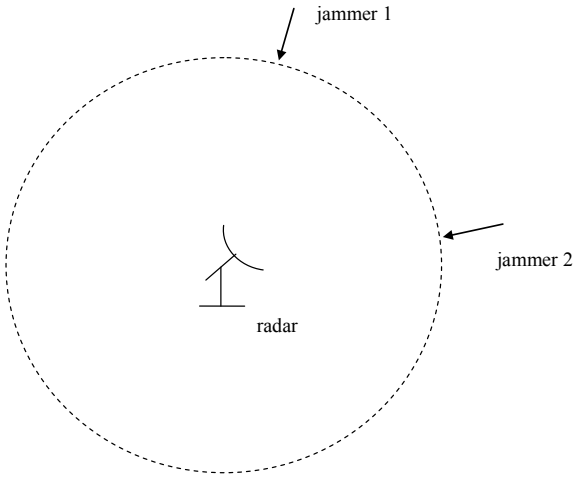


Fig. 11.9 Schematic diagram of jammer allocation in the radar sidelobe cancellation test

modulation continuous wave signal. The bandwidth of the jamming signal is equivalent to the radar waveform bandwidth;

(4) Switch on the radar system. Turn on the jamming source and observe the raw video output. Rotate the radar antenna. When the antenna large azimuth sidelobe aims at the jammer, adjust the output signal power of the jammer to obtain a jamming-noise-ratio greater than 30 dB for. Adjust the other jammers so as to get the same jamming intensities;

(5) Switch on all of the jammers and rotate the radar antenna. Aim the mainlobe of the beam under test at each jammer in turn and observe the raw video output of the beam under test. Choose the maximal value of the jamming signal intensity and mark it as Nmax;

(6) Rotate the radar antenna slowly and observe the raw video output of the beam under test. When the mainlobe departs from the jammer direction by more than one azimuth resolution beamwidth, switch on one or more jammers respectively. When the jamming-noise-ratio is more than 30 dB, note the jamming signal intensities at this direction before and after sidelobe cancellations as N1 and N2 respectively in the case of one or more jammers;

(7) Continue to rotate the radar antenna slowly. Test and record the next N1 and N2 at a given azimuth interval;

(8) Compute the N1−N2 at all directions, which is the jamming suppression ratio of the radar after sidelobe cancellation in the case of multiple jammers.

Figures 11.10 and 11.11 show examples of pictures on the terminal of a metric wave radar before and after sidelobe cancellation. Figure 11.12 shows the jamming suppression ratio test result of this radar after sidelobe cancellation in the case of two jammers.

11.4 Test and Demonstration of Metric Wave Radar Airspace Coverage

11.4.1 Test Method

The airspace coverage performance of metric wave radar can be demonstrated by target flight detection at different altitudes. In practice, further demonstration of the metric wave radar actual detection capabilities can be made by the observing the routine training flights and civil airline flights, and accurately record the typical air situations.

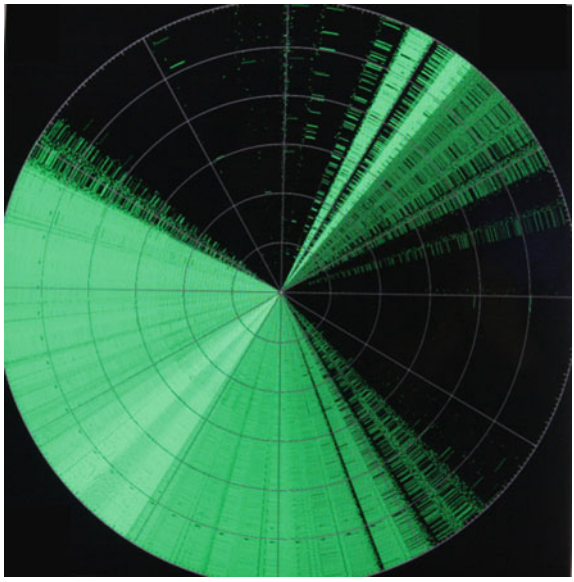


Fig. 11.10 Jamming situation on a metric wave radar before sidelobe cancellation

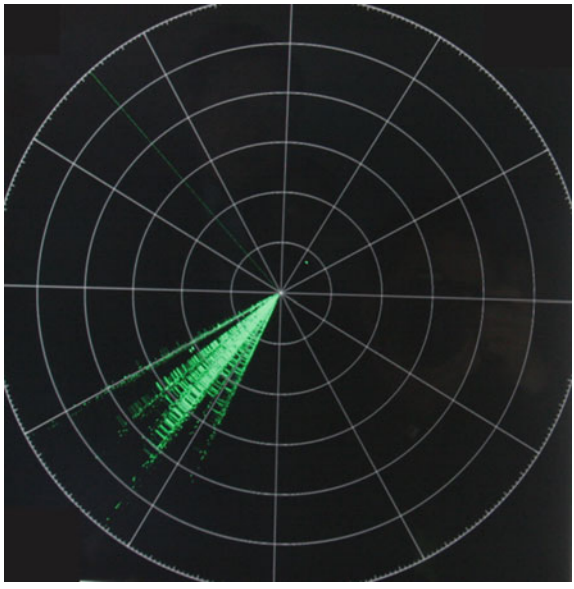


Fig. 11.11 Jamming situation on a metric wave radar after sidelobe cancellation (only mainlobe suffers jamming)

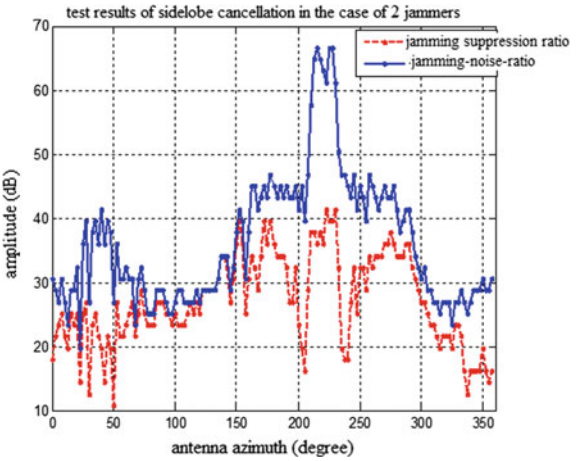


Fig. 11.12 Test results of sidelobe cancellation in the case of two jammers

11.4.2 Performance Evaluation Based on Tested Data

(1) Selection of the test flight route

The target aircraft should perform radial flights forward and backward with respect to the radar station at different constant altitudes. Its speed should meet the specified flight speed requirement. Likewise, the heading error and altitude fluctuation should be small enough so as to meet the requirements. The actual altitude is the altitude measured by the GPS onboard the target aircraft.

(2) Number of test flights

The number of test flights is computed by:

$$F_N = \frac{NVT}{3600 \times \Delta R} \tag{11.1}$$

where, ΔR—the range sampling interval;

N—the number of observation points; for a probability of detection Pd = 0.8, a confidence level 1−α of 90%; a confidence interval of 0.683–0.888, the number of observation points N within the sampling interval is not less than 50. Moreover, if the probability of detection Pd = 0.5, the confidence level 1−α = 90%, and the confidence interval is 0.375–0.621, the corresponding number of observation points N within the sampling interval is not less than 50;

T—observation period;

V—aircraft relative speed (with respect to the radar);

F_N—number of test flights, i.e., number of test flights required for each flight altitude.

The number of test flights for the radar, in different operating modes can be calculated by the formula.

(3) Data collection

Data collection is conducted in the automatic extraction mode. The data measured and reported by the operator on the display are viewed as the standard data. The target position data provided by the printer or recorded in the hard disk of the automatic extraction equipment are viewed as the reference data.

(4) Data processing

a. Computing the probability of detection
The whole flight route at a specific test altitude is segmented with a range sampling interval of 20 km and the neighboring sampling intervals overlap 10 km. The probability of detection at each sampling interval is given by

$$P = M/N \tag{11.2}$$

where, P—probability of detection,
N—number of observation points within range sampling interval,
M—number of found points within range sampling interval.
The value is taken as the probability of detection at the center of this range sampling interval.
In the same way of counting the number of observation points and the number of found points, the data at different altitudes is counted. Likewise, for a given altitude, the data is also counted respectively forwards or backwards radar station. For the observation point at the intersection of range sampling intervals, the counting is done only one time, and is considered as the observation point within the close range interval.

b. Plotting the probability of detection curve
Take the range as abscissa and the probability of detection as ordinate, and then plot the variation of the probability of detection with respect to the range in case of a target moving forward or a backward with respect to the radar station for specific test flight altitudes. After smoothing, find out the radar detection range R_0 corresponding to the probability of detection specified in tactical and technical specifications.

c. Calculating the maximal detection range of the radar in free space
Take the coverage data at a specific altitude as a benchmark and the coverage data at other altitudes as references. Calculate the maximal detection range of the radar in free space and compute the confidence interval estimation.

d. Plotting the vertical detection coverage diagram (coverage diagram)
Select the exponential atmosphere model range-altitude-elevation relation drawing paper as the base map of the vertical detection coverage diagram of radar. The atmospheric refraction mode follows the exponential mode in GJB/z 87, where the coefficients Ns and Ce take the annual average values around China.
On the selected base map, plot the vertical detection coverage diagram according to the following formula:

$$R = R_{max} * F \tag{11.3}$$

where, R—radar detection range;
R_{max}—the maximal detection range of radar in free space;
F—pattern propagation factor.

(5) Test results

On the basis of the actual number of observation points within the range sampling interval, check the relationship between the probability of detection confidence interval and the number of observation points to get the probability of detection confidence interval under the given confidence level.

According to the probability of detection curve and the probability of detection confidence interval obtained by test, the detection range confidence interval under the given confidence level can be computed by the following expression:

$$\begin{aligned} R_H - R_O &= \frac{\Delta R}{\Delta P}|_{P=P_0}(P_L - P_0) \\ R_L - R_O &= \frac{\Delta R}{\Delta P}|_{P=P_0}(P_H - P_0) \end{aligned} \tag{11.4}$$

where, P_H—upper limit of detection probability;
$\frac{\Delta R}{\Delta P}|_{P=P_0}$—the reciprocal of the slope of detection probability at P_0;
P_L—lower limit of detection probability;
P_0—the specified detection probability;
R_H—upper limit of detection range confidence;
R_L—lower limit of detection range confidence.

11.4.3 An Example of Performance Evaluation

Take the performance evaluation test of the airspace coverage of a metric wave radar as an example. Figures 11.13, 11.14, 11.15 and 11.16 respectively give the test pictures and the probability of detection statistics of the radar at different altitudes.

Based on the above performance evaluation method, the statistic diagram of the probability of detection is formed using the test data. From the diagram, it is easy to obtain the radar detection range corresponding to the required probability of detection. On this basis, the maximal detection range of the radar in free space under different test flight altitudes can be calculated. According to the probability of detection statistic diagram, the radar's airspace coverage continuity and low-elevation coverage performance can be checked. It is shown from a number of tests in different terrain conditions that the advanced metric wave radar performed airspace coverage continuity and low-elevation line-of-sight detection performance.

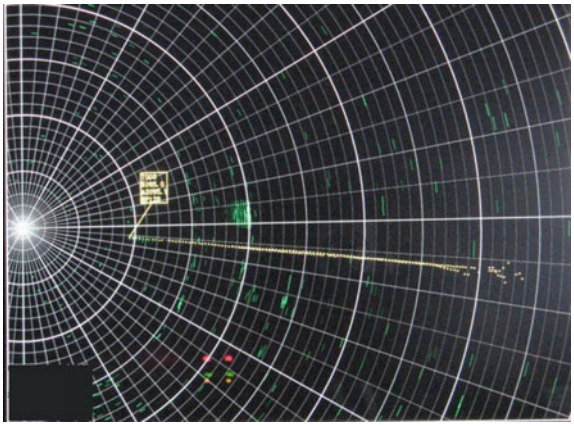


Fig. 11.13 Test picture of a metric wave radar with a target at 11,300 m in altitude

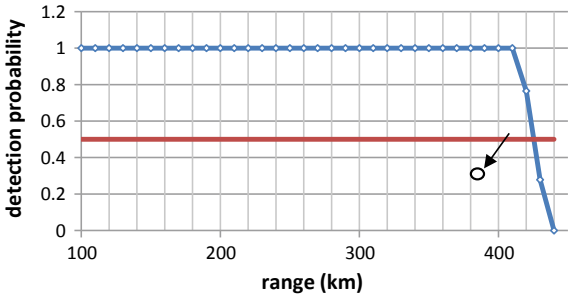


Fig. 11.14 Detection probability statistics of a metric radar with a target at 11,300 m in altitude

11.5 Height-Finding Tests and Demonstrations in Different Terrain Environments

11.5.1 Test Method

A metric wave radar is set up on different sites. The data collected under several typical sites are analyzed to demonstrate the height-finding effect of the metric wave radar for different reflection surfaces.

The height-finding algorithms includes: alternating projection maximum likelihood (APML) algorithm, synthetic steering vector maximum likelihood (SVML) algorithm, spatial smoothing MUSIC (SSMUSIC) algorithm, synthetic steering vector MUSIC (SVMUSIC) algorithm, multi-dimensional

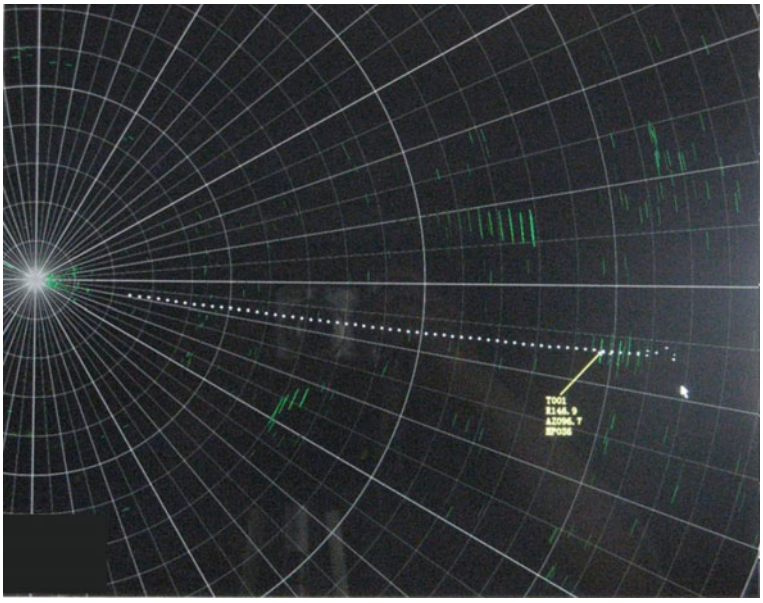


Fig. 11.15 Test picture of a metric wave radar with a target at 2100 m in altitude

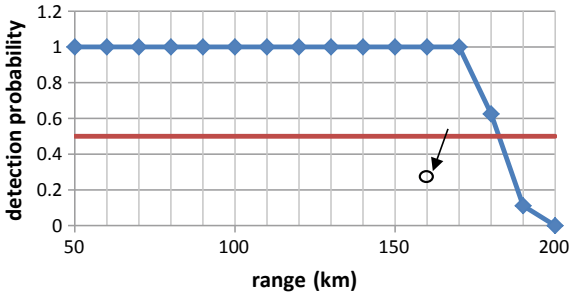


Fig. 11.16 Detection probability statistics of a metric radar with a target at 2100 m in altitude

alternating projection synthetic steering vector maximum likelihood (AP-SVML) algorithm, and adaptive beamforming (ADBF) algorithm. The feasibilities and application ranges of these algorithms are demonstrated through the measured data.

11.5.2 Performance Evaluation Based on Test Data

(1) Flat and smooth reflection surface (water surface)

The radar is set up near a lake and the lake surface becomes the reflection surface. The APML algorithm and the SVML algorithm are used to process the measured

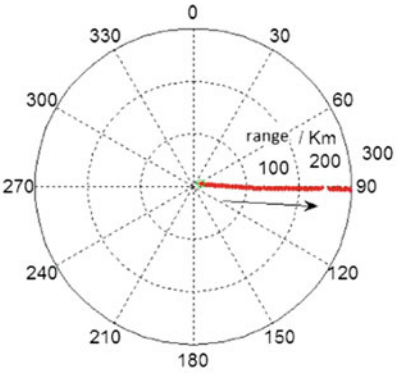
data. The results are shown in Fig. 11.17. Figure 11.17a is the target flight trajectory, the arrowhead indicates the target motion direction, and the target is flying away from the radar station toward the east; Fig. 11.17b–e show the variation with respect of the target range, of the elevation measurement value, the elevation measurement error, the height measurement value, and the height measurement error respectively.

It can be seen from the data processing results that, in general, both APML algorithm and SVML algorithm can implement metric wave radar height finding in the case of flat reflection surface, but the APML algorithm has a great fluctuation in angle measurement due to the effect of the multipath echo and the beam splitting. As a comparison, the SVML algorithm can achieve higher angle measurement accuracy and height finding accuracy. Statistically, along the whole flight route, the rms errors of angle measurement and height finding of APML algorithm are 0.26° and 587.8 m respectively; the corresponding rms errors of SVML algorithm are 0.13° and 353.6 m respectively. The measured data show that the SVML algorithm based on terrain matching can estimate the target elevation in multipath environment effectively and achieve higher angle measurement accuracy and height finding accuracy.

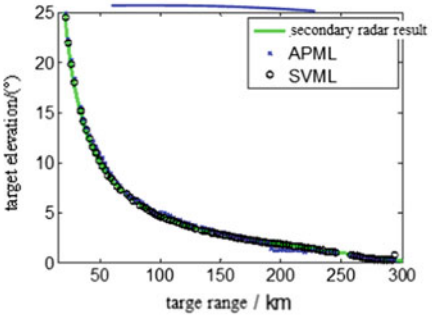
(2) Fluctuant and gentle ground surfaces

The radar is set up in a clear field and the reflection surface is fluctuant and gentle ground surface. The SSMUSIC algorithm and the SVMUSIC algorithm are used to process the measured data. SVMUSIC-1 and SVMUSIC-2 represent the terrain-ignored synthetic steering vector MUSIC algorithm and terrain-matched synthetic steering vector MUSIC algorithm respectively. The results are shown in Fig. 11.18. Figure 11.18a is the target flight trajectory, the arrowhead indicates the target motion direction, and the target is flying away from the radar station toward the east; Fig. 11.18b is the curve of the elevation measurement value changing with the target range; Fig. 11.18c is the curve of the elevation measurement error changing with the target range; Fig. 11.18d is the curve of the height measurement value varying with the target range; and Fig. 11.18e is the curve of the height measurement error varying with the target range.

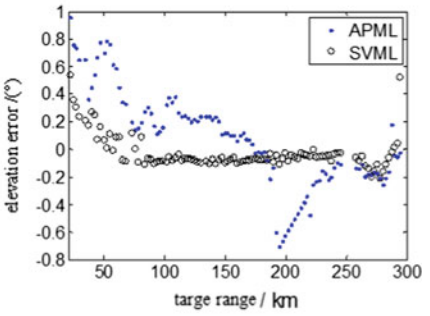
It can be seen from the measured data that, when the target is in high elevation region, that is, flying along the flight route 50–160 km, there is an influence of terrain on the angle estimation. The SVMUSIC-1 has the maximal angle measurement error. The result provided by secondary radar is taken as the true value, then the elevation rms error and height rms error are 0.31° and 495.8 m respectively. The SSMUSIC algorithm is impacted by multipath echoes and there is a large fluctuation in angle measurement. The elevation rms error and height rms error are 0.12° and 217.2 m. When the target is in low elevation region, that is, flying along the flight route 160–500 km, the SSMUSIC algorithm is impacted strongly by multipath and beam splitting, which results in irresolution of the target and its mirror-image as well as large height measurement error. In comparison, the SVMUSIC-2 algorithm is able to estimate the elevation of the target under multipath environment effectively and also can achieve higher angle and height measurement accuracies. In high elevation region, the elevation rms error and the height rms error are 0.05° and 68.5 m respectively. In low elevation region, the elevation rms error and the height rms error are



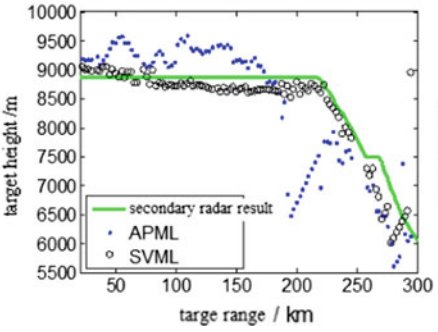
(a) Target flight trajectory



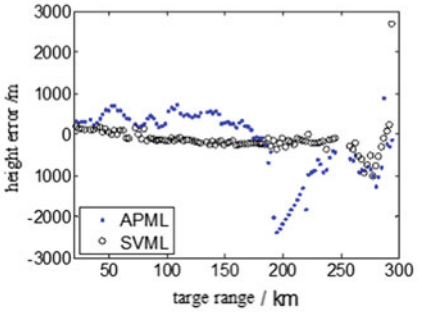
(b) Target elevation varying with range



(c) Elevation error varying with range

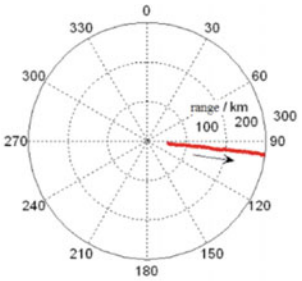


(d) Target height varying with range

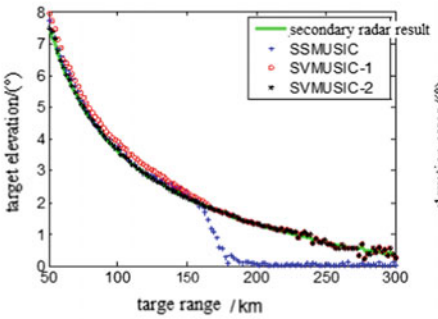


(e) Height error varying range

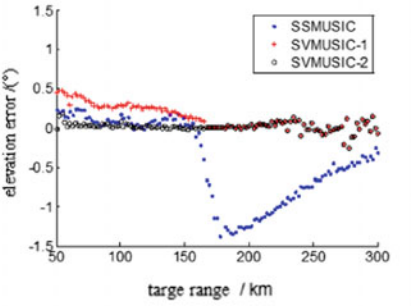
Fig. 11.17 Processing results of the measured data in water surface scene



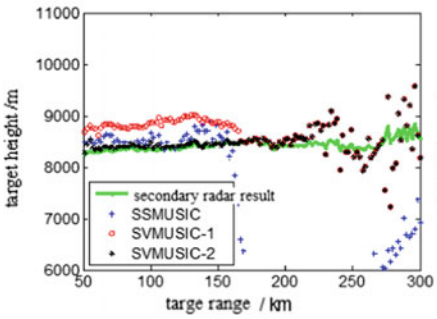
(a) Target flight trajectory



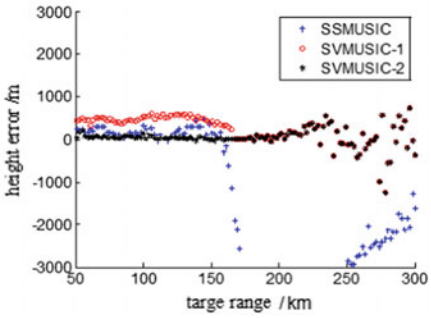
(b) Target elevation varying with range



(c) Elevation error varying with range



(d) Target height varying with range



(e) Height error varying range

Fig. 11.18 Processing results of the measured data condition of fluctuant and gentle ground surface scene

0.06° and 329.6 m respectively. The measured data proves that the synthetic steering vector MUSIC algorithm based on terrain matching can estimate target elevation in multipath environment effectively and achieve higher angle and height measurement accuracies.

(3) City reflection surface

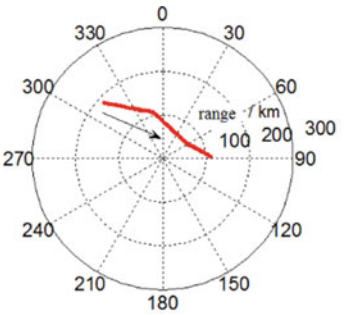
The radar is set up near a city. The buildings and trees constitute irregular reflection surfaces. The synthetic steering vector maximum likelihood (SVML) algorithm only counting in specular reflection and the multi-dimensional alternating projection synthetic steering vector maximum likelihood (AP-SVML) algorithm counting in diffuse reflection are used to process the measured data. The processing results are given in Fig. 11.19. Figure 11.19a is the target flight trajectory, the arrowhead indicates the target motion direction, and the target is flying tangentially toward the east; Fig. 11.19b is the relationship curve of target's plot and range; Fig. 11.19c is the curve of the elevation measurement value changing with the target plot; Fig. 11.19d is the curve of the elevation measurement error varying with the target plot; Fig. 11.19e is the curve of the height measurement value varying with the target plot; and Fig. 11.19f is the curve of the height measurement error varying with the target plot.

It can be seen from the measured data that, when the reflection surface is complex, the synthetic steering vector maximum likelihood (SVML) algorithm counting in specular reflection only cannot achieve good results. This is because the signal from rough surface is the sum of the specular reflection component and the diffuse reflection component when the ground surface roughness fails to meet the Rayleigh criteria. But the diffuse reflection component takes large proportion. Comparatively, the multi-dimensional alternating projection synthetic steering vector maximum likelihood (AP-SVML) algorithm counting in diffuse reflection can achieve higher angle and height measurement accuracies. Statistically, along the whole flight route, the rms errors of angle measurement and height measurement of the SVML algorithm are 0.56° and 1315.6 m respectively and the rms errors of angle measurement and height measurement of AP-SVML algorithm are 0.18° and 320.2 m respectively.

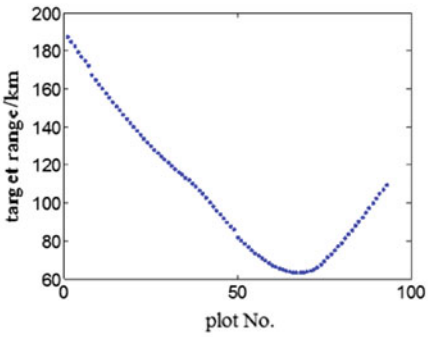
(4) Mountain reflection surface

The radar is set up on the top of a hill (163 m above the sea level) and the reflection is the fluctuant and steep ground surface. The terrain matching maximum likelihood algorithm and the adaptive beamforming algorithm are used to process the measured data. The results are shown in Fig. 11.20, where, Fig. 11.20a is the target flight trajectory; Fig. 11.20b is the relationship between the target plot and range; Fig. 11.20c is the curve of the elevation measurement value changing with the target plot; Fig. 11.20d is the curve of the elevation measurement error changing with the target plot; Fig. 11.20e is the curve of the height measurement value varying with the target range; and Fig. 11.20f is the curve of the height measurement error varying with the target plot.

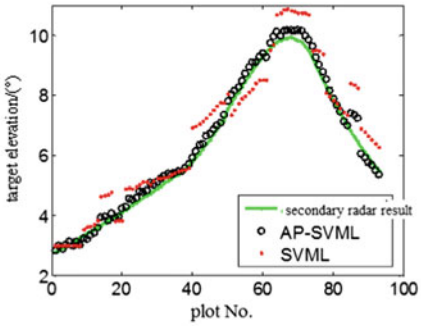
It can be seen from the measured data that, when the radar is set up on the hill and the reflection surface is very complex, the synthetic steering vector maximum



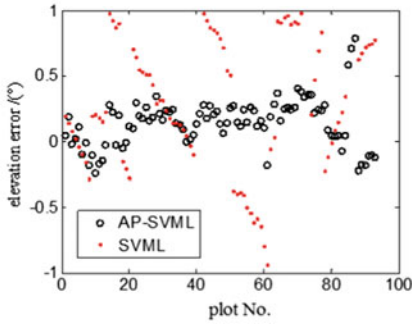
(a) Target track



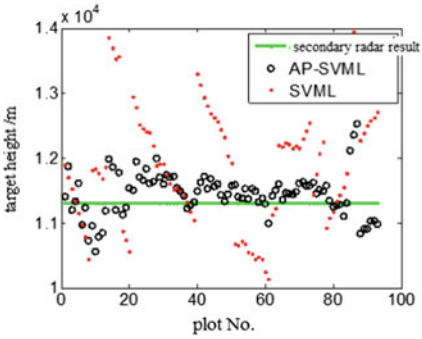
(b) Relationship between plot and range of target



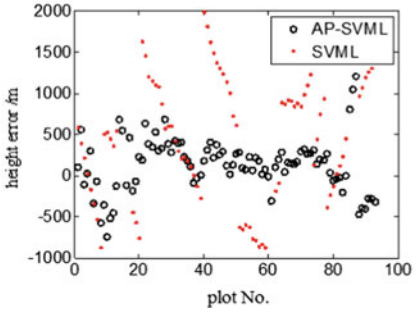
(c) Target elevation varying with plot



(d) Elevation error varying with plot

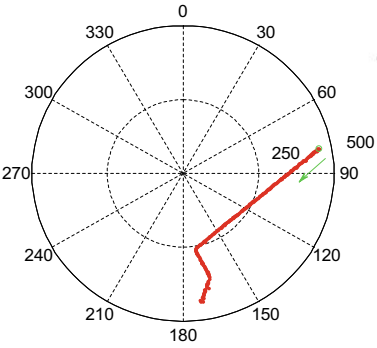


(e) Target height varying with plot

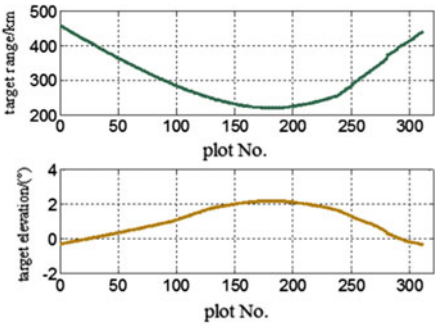


(f) Height error varying with plot

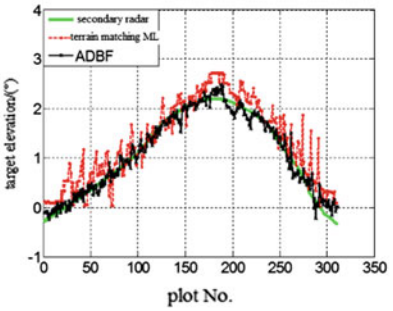
Fig. 11.19 Processing results of the measured data in city reflection surface scene



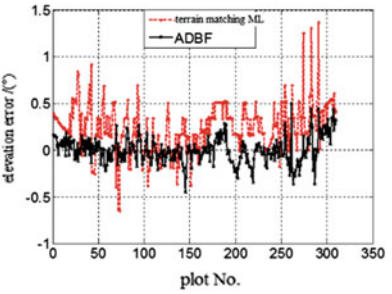
(a) Target track



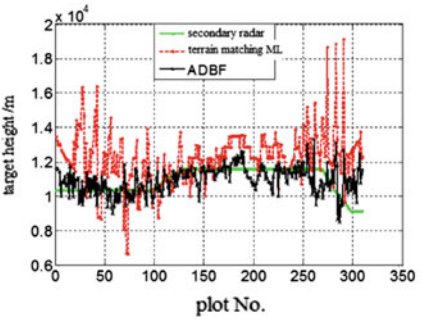
(b) Relationship between plot and range of target



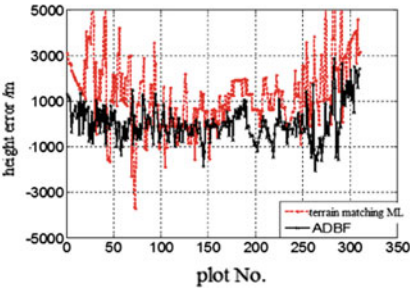
(c) Target elevation varying with plot



(d) Elevation error varying with plot



(e) Target height varying with plot



(f) Height error varying with plot

Fig. 11.20 Processing results of the measured data in mountain reflection surface scene

likelihood algorithm based on terrain matching fails to obtain good results. Comparatively, the adaptive beamforming algorithm can achieve higher angle and height measurement accuracies. Statistically, along the whole flight route, the rms errors of angle measurement and height measurement of the maximum likelihood algorithm based on terrain matching are 0.53° and 1215.6 m respectively and the rms errors of angle measurement and height measurement of the adaptive beamforming (ADBF) algorithm are 0.22° and 654.2 m.

Based on the analysis of the measured data, the reasonable design can be made regarding the low-elevation height-finding in metric wave radar. For flat site, the ML algorithm based on terrain matching can be used. For rough site, the multi-dimensional alternating projection synthetic steering vector ML algorithm counting in diffuse reflection can be selected. For high mountain site, the height finding algorithm based on adaptive beamforming is a good candidate. The processing methods for the above three classes of sites involve all of the possible site conditions and basically resolve the height finding issues of metric wave radar under different sites.

In practice, most sites are not solely flat, rough, or high mountain sites, but are a hybrid of multiple terrains, i.e., the complex site environments. Any of the above height-finding algorithms cannot meet the height-finding requirement of a complex site. Aiming at the complex site environment including multiple terrains, it is needed to uniformly divide the azimuth zone into N sectors and set the algorithm selection flag bits for selecting the effective algorithm suitable for each sector. For a target located in a specific azimuth sector, the corresponding algorithm is chosen to perform height-finding processing. By reasonable choice and combined utilization of the three height-finding algorithms, the optimal height-finding effect can be achieved.

The comprehensive utilization of the three algorithms not only holds the height finding advantage of the terrain matching maximum likelihood algorithm, but also enhances the site adaptability and solves the difficult problem of the radar height finding in fluctuant sites and high mountain sites. The solution is suitable for hybrid and complex site environments. The three algorithms form a complete height finding algorithm system and provide robust height finding algorithms for metric wave radar.

Bibliography

1. Schmidt R. Multiple Emitter Location and Signal Parameter Estimation [J]. IEEE Trans on Antennas and Propagation, 1986, 34(3):276–280.
2. Roy R, Kailath T. ESPRIT-Estimation of Signal Parameters via Rotational Invariance Techniques [J]. IEEE Trans on Acoustics, Speech and Signal Processing, 1989, 37(7):984–995.
3. Wang Yongliang. Spatial Spectrum Estimation Theories and Algorithms [M]. Beijing: Tsinghua University Press, 2004.
4. Stoica P, Arye N. MUSIC, Maximum Likelihood, and Cramer-Rao Bound [J]. IEEE Trans on Acoustics, Speech and Signal Processing, 1989, 37(5):720–741.
5. Krim H, Viberg M. Two Decades of Array Signal Processing Research: the Parametric Approach [J]. Signal Processing Magazine, IEEE, 1996, 13(4):67–94.
6. Ziskind I, Wax M. Maximum Likelihood Localization of Multiple Sources by Alternating Projection [J]. IEEE Trans on Acoustics, Speech and Signal Processing, 1988, 36(10):1553–1560.

7. Lo T, Litva J. Use of a Highly Deterministic Multipath Signal Model in Low-Angle Tracking [C] // Radar and Signal Processing, IEE Proceedings, 1991, 138(2):163–171.
8. Meng Y, Wong K M, Wu Q. Estimation of the Direction of Arrival of Spread Source in Sensor Array Processing [C] // Proc. ICSP, 1993(10): 430–434.
9. Yang Xueya. Study on Array Super-Resolution and Altitude Measurement in VHF Radar [D]. Xi'an: Xidian University, 2011.
10. Zhu Wei. Study on Low-Angle Altitude Measurement in VHF Radar [D]. Xi'an: Xidian University, 2013.